



## Full Length Article

# A universal substrate for the nanoscale investigation of two-dimensional materials

Tuan-Hoang Tran<sup>a</sup>, Raul D. Rodriguez<sup>a,\*</sup>, Dmitry Cheshev<sup>a</sup>, Nelson E. Villa<sup>a</sup>,  
Muhammad Awais Aslam<sup>b</sup>, Jelena Pešić<sup>c</sup>, Aleksandar Matković<sup>b</sup>, Evgeniya Sheremet<sup>a</sup>

<sup>a</sup> Tomsk Polytechnic University, Lenina ave. 30, Tomsk, Russia

<sup>b</sup> Institute of Physics, Montanuniversität Leoben, Franz Josef Strasse 18, 8700 Leoben, Austria

<sup>c</sup> Institute of Physics Belgrade, University of Belgrade, Pregevica 118, 11080 Belgrade, Serbia

## ARTICLE INFO

## Keywords:

Highly-oriented pyrolytic graphite  
Graphene substrate  
2D materials  
Straintronics  
Nanoscale characterization

## ABSTRACT

Since discovering two-dimensional materials, there has been a great interest in exploring, understanding, and taking advantage of their unique properties. Si/SiO<sub>2</sub> is one of the most used substrates for the deposition and characterization of 2D materials due to its availability and optical contrast. This work goes beyond the conventional substrate and introduces highly-oriented pyrolytic graphite (HOPG) as universal support for investigating two-dimensional materials due to several unique properties such as chemical and temperature stability, intrinsic high flatness, reusability, electrical conductivity, ease of use, availability, and enhanced adhesion of two-dimensional materials. We demonstrate this by analyzing several 2D materials with advanced atomic force microscopy methods, Raman and photoluminescence spectroscopy with hyperspectral imaging, and scanning electron microscopy with elementary analysis imaging. The strong adhesion to HOPG allowed the instant deposition of different two-dimensional materials GaSe, MoS<sub>2</sub>, Zn<sub>2</sub>In<sub>2</sub>S<sub>5</sub>, talc, and h-BN. This feat is hard to accomplish on the conventional SiO<sub>2</sub> substrate without polymer-assisted transfer. Moreover, this strong interaction can strain 2D materials deposited on HOPG, giving localized changes in reactivity, optical, and electronic properties. This effect is explored for selective Ag deposition on strained regions of 2D materials to activate photocatalytic reactions.

## 1. Introduction

Two-dimensional (2D) nanomaterials keep on attracting great interest thanks to their remarkable electrical, optical, mechanical, and chemical properties, exploitable in diverse applications [1]. Their studies shot up thanks to analytical methods that allowed us to investigate the intrinsic properties of 2D materials [2]. Most studies have used insulating materials such as h-BN and Si/SiO<sub>2</sub> as default substrates. Thanks to its flatness, chemical stability, optical properties, and relatively low cost, Si/SiO<sub>2</sub> is beneficial for several analytical methods [3,4]. However, the surface of the commonly used Si/SiO<sub>2</sub> substrates involves many configurations due to its amorphous nature with possible both O-polar and Si-polar defects. The surfaces with uncontrolled or unwanted defects strongly affect the electronic properties of 2D materials. To avoid this, SiO<sub>2</sub> is H-passivated to minimize the effects on the electronic properties of the 2D materials deposited on top, [5] or passivated via self-assembled hydrophobic monolayers, as hexamethyldisilazane [6].

Its electrically insulating nature makes the 2D electron gas decouple from the surroundings, allowing to study of the intrinsic properties of 2D materials. On the other hand, this makes conventional insulating substrates inconvenient for nanoscale electrical characterization methods such as Kelvin probe force microscopy (KPFM), conductive atomic force microscopy (C-AFM), and scanning electron microscopy (SEM).

Gold is also a choice; however, gold has to be evaporated on flat substrates such as glass, mica, or silicon, where adhesion layers such as Ti, Cr, or Pt have to be used, limiting reusability. Moreover, gold surfaces must be annealed to obtain crystalline flat planes, which are also limited to a smaller lateral size of 100 nm [7]. Compared to Au and Si/SiO<sub>2</sub> substrates, a freshly cleaved highly-oriented pyrolytic graphite (HOPG) surface obtained by mechanical exfoliation is the flattest, cleanest and easiest support for 2D materials one could get. Furthermore, HOPG has an excellent electrical conductivity that allows studying the electrical properties of conductors, semiconductors, and insulators at the nanometer scale. Due to the van der Waals force, we

\* Corresponding author.

E-mail address: [raul@tpu.ru](mailto:raul@tpu.ru) (R.D. Rodriguez).

<https://doi.org/10.1016/j.apsusc.2022.154585>

Received 24 June 2022; Received in revised form 13 August 2022; Accepted 16 August 2022

Available online 18 August 2022

0169-4332/© 2022 The Authors. Published by Elsevier B.V. This is an open access article under the CC BY license (<http://creativecommons.org/licenses/by/4.0/>).

expect that 2D materials will strongly couple to HOPG, forming vdW heterostructures that allow us to investigate such systems' novel properties [8]. This expectation of heterostructures' formation is justified by density functional theory (DFT) calculations in previous studies for various 2D materials combined with graphene [9,10].

Previous works showed HOPG as a substrate for synthesizing and studying nanostructures [11,12]. Those studies were motivated by HOPG chemical and temperature stability critical to synthesis processes. For example, HOPG benefits as a substrate were shown by the electro-deposition of various chalcogenides, especially on graphite steps, [13] or by investigating structural and local electronic properties of  $\text{WS}_2/\text{WSe}_2$  heterostructures [14].

Thus, there seems to be an untapped potential in HOPG that could allow the systematic study of physical, chemical, electrical, and structural properties using the same van der Waals support typical for 2D material heterostructures. We investigated this possibility by atomic force microscopy (AFM)-based methods, including scanning capacitance microscopy (SCM), KPFM, and IV-curves at the nanoscale. HOPG as a

substrate allowed us to obtain optical and structural properties of different 2D layers by photoluminescence (PL) and Raman micro-spectroscopy. Without spectral overlap between 2D materials and the substrate, these analyses were possible since, except for the shear mode of multilayer graphene, HOPG does not have any Raman modes in the frequency range of most 2D materials ( $10\text{--}600\text{ cm}^{-1}$ ). In addition, the excellent thermal conductivity of HOPG helps with heat dissipation, preventing burning or modifying heat-sensitive materials. The surface morphology and elemental content were investigated by SEM and energy dispersive X-ray (EDX) spectroscopy without resorting to deposition of a conductive coating that would be otherwise required with insulating substrates. Our results are not limited to a single 2D material, but we demonstrate its universality by investigating different layered systems mechanically exfoliated from bulk crystals. Our results show not only the nanoscale analysis of a widely-studied 2D material like  $\text{MoS}_2$  or its well-known cousin GaSe, but we also report for the first time a new 2D material never investigated before in its 2D nanosheet van der Waals form,  $\text{Zn}_2\text{In}_2\text{S}_5$  (ZIS). Surprisingly, we found that the strong interaction

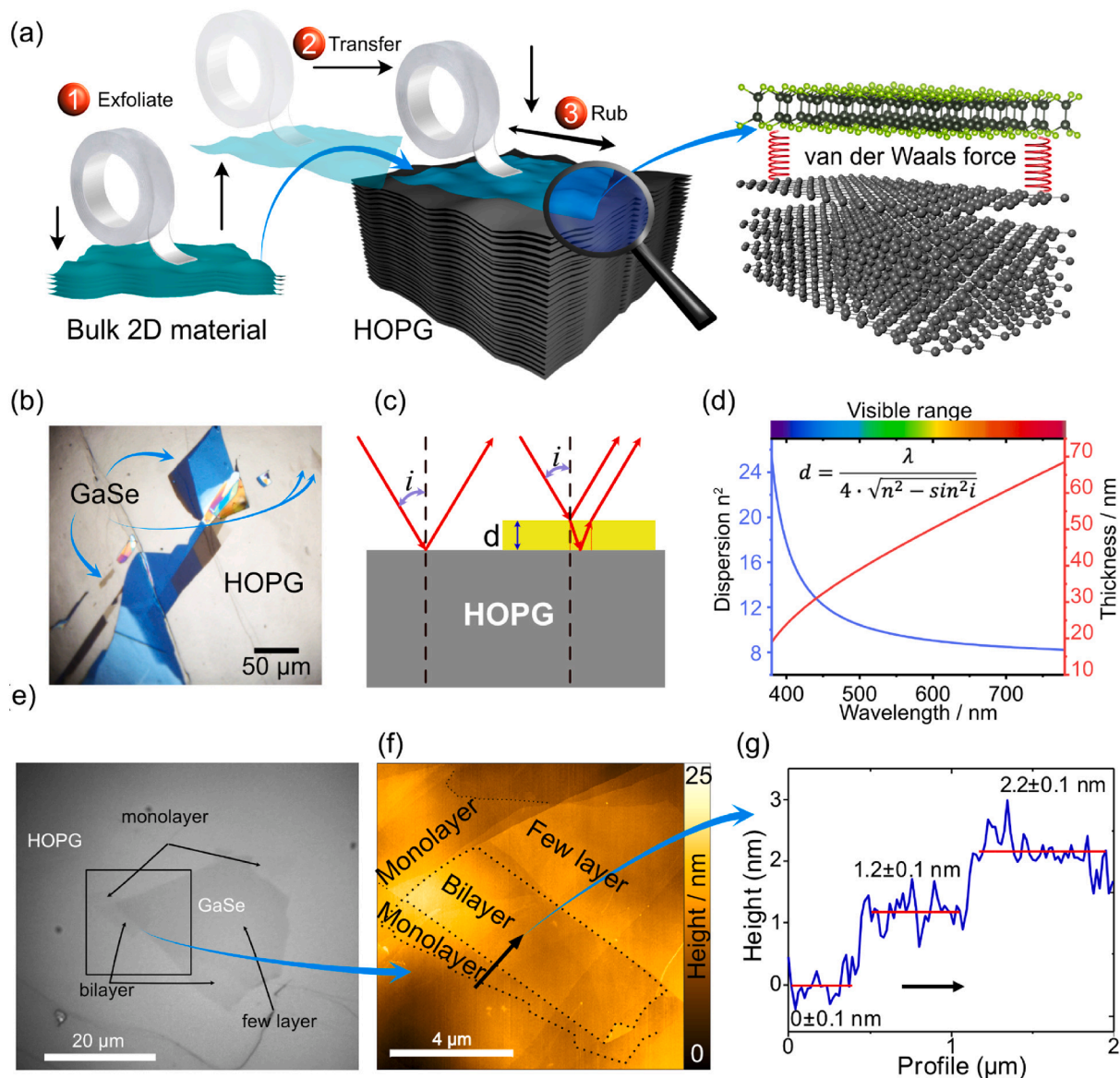


**Fig. 1.** a) Deposition of 2D materials on HOPG, b) Optical image of GaSe layers with different thicknesses on HOPG. c) Optical interference schematics showing the optical paths in the system of 2D materials on HOPG. d) A plot of refractive index dispersion dependence on wavelength and GaSe thickness according to the interference maxima wavelength for zero order. e) Optical image of the region of interest with a 100x objective shown in brown color scheme for improved contrast. f) AFM topography of GaSe. g) Cross-section profile showing thicknesses corresponding to bilayer and monolayer GaSe.

between the 2D materials and HOPG leads to complete imprinting of the substrate's structural defects on the 2D layer deposited on top. Consequently, the 2D material properties could be tuned by pre-patterning or pre-straining/wrinkling the HOPG substrate [15]. Finally, we illustrate this application with the modification of GaSe on HOPG, showing the change in optical, electronic, and catalytic properties due to the strong surface/2D material interaction as a proposal to straintronics.

## 2. Results and discussion

### 2.1. Contaminant-free direct deposition of 2D materials and layer thickness determination by optical contrast

Polydimethylsiloxane (PDMS) is often used to transfer 2D layers to different substrates with the so-called dry transfer method or PDMS stamp method [16]. Despite its convenience that allows transfer to arbitrary substrates, this method is prone to sample contamination by PDMS residues affecting the characterization results [17]. Therefore, we wondered if HOPG could help develop a transfer method for 2D materials that is PDMS residue-free, inexpensive, fast, and easy to implement. We investigated the 2D material deposition directly on HOPG with the hypothesis that a strong interaction between the two materials makes the instant deposition of 2D layers possible. We verified this hypothesis by touching the HOPG surface with different layered crystals (see Video S1 in the Supporting Information and Fig. 1a). In a matter of seconds, we obtained a large number of thin layers deposited over an extended area without adhesive tape or other transfer residual contamination (see Fig. 1b and 1e). The many different colors are due to light interference in the layers with different thicknesses, as schematically presented in Fig. 1c. This feature allows us to estimate the flake thickness from an optical microscopy image alone. The interference maximum is given by  $m\lambda = 2d\sqrt{n^2 - \sin^2 i} - \frac{\lambda}{2}$ , where  $d$  – flake thickness,  $n$  – refractive index,  $i$  – angle of incidence, and  $m$  – order of interference maximum. Considering that  $m = 0$  and  $i = 22^\circ$  (half of beam convergence angle), the 2D layer thickness can be defined as  $d = \frac{\lambda}{4\sqrt{n^2 - \sin^2 i}}$ . The dispersion equation for GaSe was defined by Kato *et al.* and expressed as  $n^2 = 10.6409 + \frac{0.3788}{\lambda^2 - 0.1232} + \frac{7090.7}{\lambda^2 - 2216.3}$  [18]. Fig. 1d shows the dependence on the wavelength that defines the flake color as a function of layer thickness. We notice that the objective has a set of angles. It leads to a small error ( $\pm 0.4$  nm) in the thickness calculation.

For ultrathin sub-10 nm layers, the interference condition set by equation (1) obviously cannot be achieved for visible light; instead, we observe these layers in grayish color. Realizing this point allows us to quickly inspect and select those ultrathin layers for which remarkable properties are often observed.

This visual observation can be explained by optical contrast. For instance, Li *et al.* used the optical contrast to identify 1L – 15L ultrathin 2D layers made of graphene, MoS<sub>2</sub>, WSe<sub>2</sub>, and TaS<sub>2</sub> on 90 and 300 nm Si/SiO<sub>2</sub> [19]. Complex reflectivity defines the effect of substrate, with low substrate reflectivity generally giving a high contrast [20]. This is why 2D layers and graphene are so hard to see on highly reflective surfaces like Au or Ni [21]. The optical contrast of 2D materials on a substrate depends on the number of layers, numerical aperture of the objective, wavelength, and optical properties of the layer and the substrate [22]. Contrary to HOPG, the optical contrast of 2D materials on Si/SiO<sub>2</sub> has been studied extensively [22,23]. Thanks to the low substrate reflectivity, graphene is readily visible on Si/SiO<sub>2</sub> with an optimal thickness of 90 or 280 nm enhanced with green filters or without filters under white light illumination [24]. For MoS<sub>2</sub> monolayers, the optimal thickness of SiO<sub>2</sub> is 55 or 220 nm [4]. Interestingly, the optical contrast of 2D materials on HOPG has not been investigated so far. We expected that because of its low reflectance of 0.26804 at 587.6 nm, which is approximately equal to that of Si/SiO<sub>2</sub> [25]. This is an exciting and valuable result since we can still visualize ultrathin layers despite the lack of optical interference in HOPG.

Fig. 1e shows a visual image of GaSe flakes on HOPG with the dark brown color observed under a 100x microscope objective with a halogen lamp and objective NA = 0.7. AFM imaging results of the gray region in Fig. 1f show that these are ultrathin GaSe layers with thickness down to 2.2 nm and 1.2 nm (see Fig. 1e), which correspond to bilayer and monolayer GaSe, respectively [26]. In addition, MoS<sub>2</sub> monolayer was also visually observed on HOPG, as discussed later on. Herein, we perform a layer thickness vs optical contrast evaluation that shows the possibility for fast characterization of the 2D material thickness using HOPG as a substrate. The optical contrast (OC) is defined  $OC = 1 - \frac{R_{2dm+Sub}}{R_{sub}}$ , where  $R_{2dm+Sub}$  and  $R_{sub}$  are the reflection intensity from 2D material on the substrate and bare substrate, respectively. The OC for monolayer and bilayer GaSe was calculated as  $3 \pm 1\%$  and  $8.0 \pm 1\%$ , respectively.

Optical and AFM topography images were also obtained for h-BN and talc, showing the HOPG universality for 2D materials deposition and optical observation from multilayer to ultrathin (see Figure S1 in Supporting Information). Thus, HOPG as a substrate allows the quick identification of ultrathin 2D layers that appear grayish under a conventional optical microscope.

### 2.2. Electronic characterization of two-dimensional layers on HOPG substrates with KPFM and SCM

Since Nonnenmacher *et al.* first introduced Kelvin probe force microscopy (KPFM) in 1991, [27] KPFM has become more and more popular in the electronic characterization of semiconductor, metal, organic, and 2D material devices [28,29]. In KPFM, as shown in Fig. 2a and 2b, the sample is grounded, and a direct (DC) potential is applied at the tip to nullify the first harmonic electrostatic force  $F_\omega = \frac{dC}{dz}(V_{DC} - V_{CPD})V_{AC}\sin(\omega t)$ , where  $V_{DC}$  and  $V_{CPD}$  are direct potential and contact potential difference (CPD) between the tip and sample, respectively.

Therefore, KPFM allows evaluating the work function of materials since under these conditions  $V_{CPD} = \frac{\Phi_{tip} - \Phi_{sample}}{e}$ , where  $\Phi_{tip}$  and  $\Phi_{sample}$  are the work functions of tip and sample, respectively, and  $e$  is the electronic charge [30]. When the two materials are not connected, their vacuum levels are aligned, but their Fermi levels differ. When electrically connecting both materials, the Fermi levels align by charge flow between the two materials (see Fig. 2b). After both materials become charged, an electrostatic force arises between the tip and the sample. In KPFM, this force is nullified by applying an external DC voltage that matches the contact potential difference. GaSe is one of the 2D group-III metal monochalcogenides and has been used in nonlinear optical applications [31]. The electronic properties of 2D materials strongly depend on the number of layers. For instance, bulk GaSe has a bandgap of 2.1 eV, while monolayer GaSe is predicted to have a bandgap of 3.5 eV [32]. Therefore, knowing the work function of GaSe flakes for different layer thicknesses is essential so that appropriate metals can be chosen to tune the band alignment and design devices with desired properties. The AFM topographies of monolayer, trilayer, and bulk GaSe, along with their height profiles, are presented in Fig. 2c. The thickness of the GaSe monolayer is  $(1.2 \pm 0.2)$  nm, in excellent agreement with values reported in the literature [26,33]. The corresponding KPFM surface potential map is shown in Fig. 2d. HOPG domains in the CPD image are related to water and hydrocarbon adsorption on twisted graphene in HOPG [34]. Interestingly, the CPD of bulk GaSe with a thickness of 42.5 nm is  $(29.8 \pm 0.5)$  mV. The CPD of GaSe decreases when decreasing layer thickness from  $(-36.5 \pm 0.4)$  mV to  $(-51 \pm 0.5)$  mV for trilayer and monolayer GaSe, respectively. A PtIr-coated AFM tip (Fermi level 4.83 eV) was used to measure the sample's CPD, which allowed us to deduce that the GaSe work function increases from 4.8 eV for the bulk ( $42.5 \pm 0.3$  nm layer) to  $4.88 \pm 0.01$  eV for trilayer and monolayer. These values are significantly different from Chong and coauthors' work, [35] who reported that the GaSe work function increases from

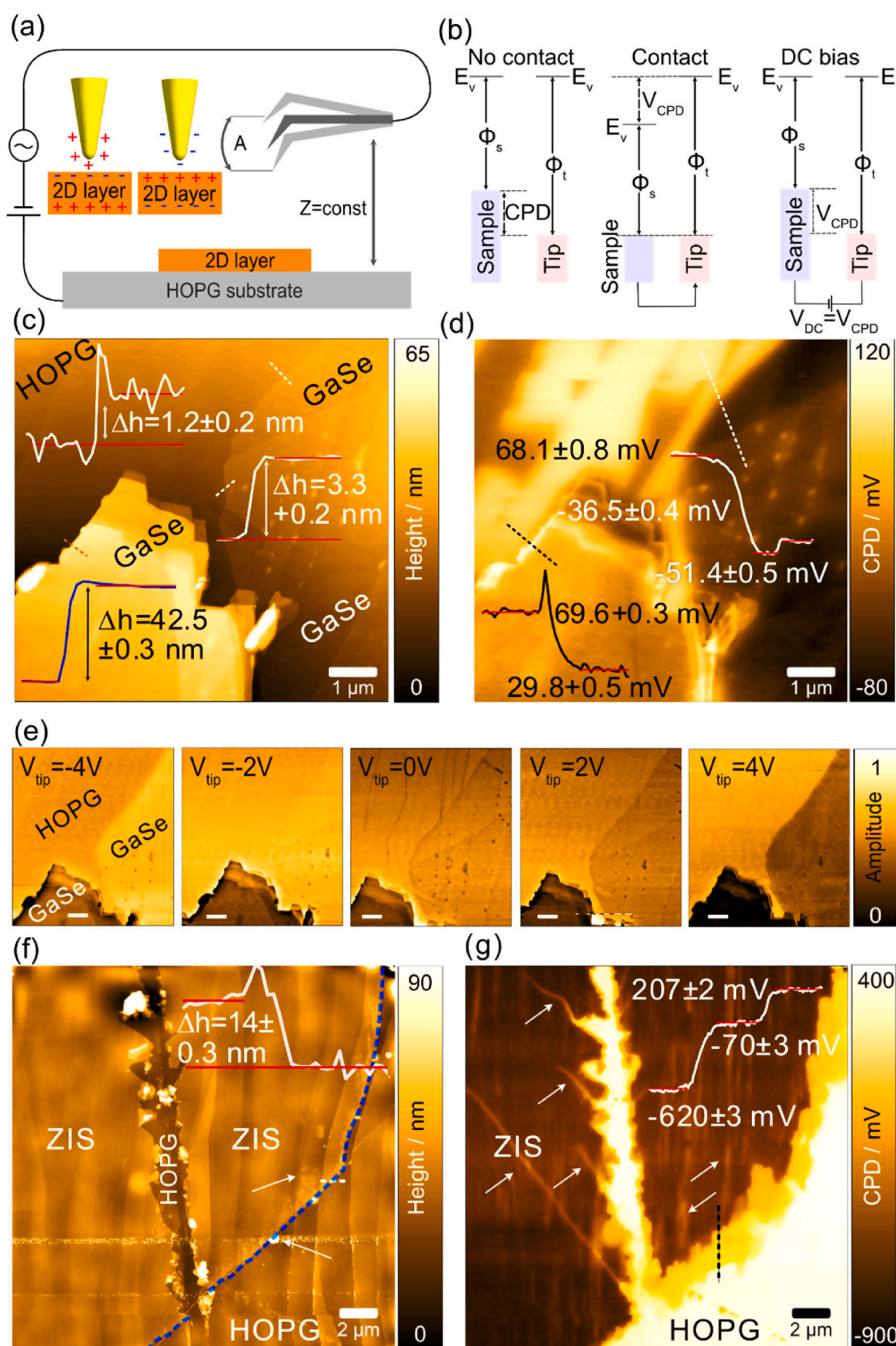


**Fig. 2.** a) General schematic of KPFM and SCM modes measurement setup. b) KPFM energy diagram. c) AFM topography image of GaSe on HOPG (inset - height profile). d) CPD image of GaSe on HOPG (inset - CPD profile). e) SCM imaging GaSe layers at different applied DC voltages; the scale bar is 2  $\mu\text{m}$ . f) AFM topography image of  $\text{Zn}_2\text{In}_2\text{Z}_5$  on HOPG (inset - height profile). The blue-dashed line shows the ZIS/HOPG interface. g) CPD image of ZIS. White arrows show contamination, inset - CPD profile. (For interpretation of the references to color in this figure legend, the reader is referred to the web version of this article.)

4.35 eV to 4.51 eV when the thickness decreases from 15 to 4 layers and then increases to 4.7 eV but for a higher number of layers up to 38. However, in that work, the authors measured samples on a Si/SiO<sub>2</sub> substrate without an external electrical contact that leads to sample charging. In such a case, the CPD becomes more sensitive to surface dipoles and charging effects than the work function.

Controlling the electronic properties of semiconductors and their doping level made possible the technological revolution brought by microelectronics [36]. Further progress is being made by shrinking

device dimensions and exploring the potential of 2D materials in nanoelectronics [37]. In this context, we used scanning capacitance microscopy (SCM) to study the charge carrier distribution in a GaSe flake. This was possible thanks to the excellent electrical conductivity of HOPG that provides an opportunity to perform electrical measurements of 2D semiconductors and distinguish them on a well-defined flat background showing only typical terraces of HOPG. Fig. 2a shows a simple scheme of the SCM working principle. The sample's topography is recorded in the first pass. Then, in SCM, the tip is lifted by 10 nm in a

second scan pass while the tip-sample electrostatic force is recorded at the second harmonic under a potential bias  $F_{2\omega} = -\frac{1}{4} \frac{dC}{dz} V_{AC}^2 \sin(2\omega t)$ . In this experiment, it is easy to see the difference in capacitance between the 2D sample and the substrate (see Fig. 2e). The SCM amplitude signal is related to the local conductivity of the sample, and thus, to the charge carrier mobility and charge carrier density [38]. Regions with bright and dark contrast correspond to high and low conductivity, respectively. The metal-like conductivity of HOPG allows it to be used as a reference to identify n- or p-type regions in the 2D material placed on top. This is the first time that n- or p-type identification has been conducted on a HOPG substrate since mainly Si/SiO<sub>2</sub> was employed before for this purpose which can be inaccurate due to surface charging [39,40]. The SCM results at different biases in Fig. 2e show that the local conductivity of GaSe decreases as the applied DC voltage to the tip changes from -4 V to 4 V. While the negative bias voltage induces the accumulation of holes on the surface, the positive bias voltage produces an accumulation of electrons, leading to a low dielectric response. This behavior arises from the p-type conductivity of GaSe [35]. Interestingly, at  $V_{DC} = -4$  V, the local conductivity of monolayer and trilayer GaSe is even higher than the local conductivity of HOPG. We attribute this result to the higher hole concentration of p-type GaSe/HOPG than HOPG due to hole doping induced on graphene by GaSe [41].

At -4 V bias, the local conductivity of GaSe decreases as its thickness decreases due to quantum confinement [42]. We can see that the conductivity of monolayer GaSe is considerably higher than trilayer GaSe at  $V_{DC} = -4$  V. However, when  $V_{DC} = 4$  V, we do not see differences in charge concentration and mobility of monolayer and trilayer GaSe because of charge carriers' depletion. In addition, the charge carrier density and mobility of a few-layered GaSe is still higher than in bulk GaSe at a bias voltage of 4 V. This result is somewhat unexpected considering that monolayer and few-layer GaSe readily oxidize in air a short time after exfoliation [33,43] so that we expect to see oxidized GaSe with decreased conductivity. High conductivity could occur if oxygen incorporation increases charge carrier density, like in indium tin oxide [44]. Another possibility is that previous reports on the oxidation of GaSe in air are based mainly on Raman spectroscopy. Despite the low laser power used in those reports to avoid oxidation, the laser exposure of GaSe could still induce photooxidation [33,43]. Since our ultrathin GaSe layers were not exposed to laser light during or before our KPFM experiments, we suspect their stability is higher than previously reported. Besides, a bottom graphene layer on SiO<sub>2</sub> significantly reduces the degradation of GaTe layers deposited on top due to the hydrophobic nature of graphene [45]. We are now closely looking into this question and plan to report our findings in a separate work.

The changes in electronic properties due to substrate-induced defects by HOPG on GaSe were also investigated by KPFM and SCM. The optical microscopy image and a sketch of the structure are shown in Figures S2a and S2b. The AFM topography of GaSe on HOPG defects is shown in Figure S2c. The GaSe layer thickness is  $6.9 \pm 0.2$  nm, and the height difference on the step of HOPG is  $216.7 \pm 0.3$  nm (see the profile in Figures S2d and S2e). Despite the large step defect size, the thin GaSe flake follows the HOPG topography perfectly. KPFM, SCM, and phase images are presented in Figures S2f, S2g, and S2h. The CPD contrast shows that the charge concentration in GaSe is higher in the regions over the HOPG step defect than on the flat HOPG. Moreover, these steps also change the mechanical properties of GaSe as we see the difference of GaSe on the defects and flat HOPG in the phase image in Figure S2h.

Zn<sub>2</sub>In<sub>2</sub>S<sub>5</sub> is a novel 2D material with applications such as photocatalysis in nanoparticle form [46]. However, ZIS has not been investigated in the large-scale highly crystalline 2D-layered form, like graphene or MoS<sub>2</sub> mechanically exfoliated from bulk crystals. Nevertheless, there is an interesting report by Zhang *et al.* [47] who obtained ZIS nanolayers with sub-micrometer lateral dimensions and showed excellent photocatalytic performance against other zinc sulfide indium phases (Zn<sub>m</sub>In<sub>2</sub>S<sub>m+3</sub>, m = 1–3).

Beyond the sample topography information provided by conventional AFM, with its 3D mapping capabilities at the nanoscale, we chose KPFM analysis as a complementary method to map the electronic properties of ZIS on HOPG. The topography image in Fig. 2f shows defects and edges of HOPG that are visible through the 14 nm thick Zn<sub>2</sub>In<sub>2</sub>S<sub>5</sub> layer placed on top. The strong van der Waals force between Zn<sub>2</sub>In<sub>2</sub>S<sub>5</sub> and HOPG deforms Zn<sub>2</sub>In<sub>2</sub>S<sub>5</sub> and makes it follow the HOPG topography. This remarkable observation is highly significant since straintronic applications could be developed by first patterning HOPG and then depositing the 2D nanomaterial to mimic the pre-patterned substrate developing predefined strained regions [48]. This way of indirect patterning a 2D material was never attempted before with HOPG and may offer a high-quality crystalline lattice engineering due to the non-invasive approach for introducing strain.

Motivated by the strong adhesion force between 2D material and HOPG, we tested the robustness of this interaction by using force lithography that is remarkably demanding on the 2D material/substrate adhesion. During scratching, a sharp needle effectively removed part of Zn<sub>2</sub>In<sub>2</sub>S<sub>5</sub> and created cracks on the surface visible in the topography image Fig. 2f. Making such a mechanically-induced scratch is challenging when using Si/SiO<sub>2</sub> wafers as supports since the 2D material just gets dragged over the substrate or folded over the edge due to the strong indenter-sample shear force and weaker 2D/SiO<sub>2</sub> adhesion [49]. Fig. 2g shows the sample's CPD image (with a CPD value of  $(-207 \pm 2)$  mV for HOPG), where a similar contrast is observed all over Zn<sub>2</sub>In<sub>2</sub>S<sub>5</sub> except for the regions at the edges and mechanically induced defects. The work function of HOPG is calculated at  $(4.633 \pm 0.002)$  eV. Due to airborne contamination when measuring in the air, this value is 20 meV higher than in previous reports [34,50]. From the value of Zn<sub>2</sub>In<sub>2</sub>S<sub>5</sub>'s CPD of  $(620 \pm 3)$  mV, we can evaluate the work function of Zn<sub>2</sub>In<sub>2</sub>S<sub>5</sub>, at  $(5.460 \pm 0.003)$  eV. Around the edge on the right side (see the arrow in Fig. 2f), the regions with lower CPD are more prominent than around the defects and cracks. The areas with low CPD coincide with the ZIS layer edge at the HOPG interface. The contrast in these regions is due to debris and contaminants observed in the topographic image (Fig. 2f). Being able to spatially control the reactivity, surface potential, and surface affinity of 2D materials by lithography is of significant value for nanoelectronics. The KPFM results show that defects propagating from the scratch and defects induced by the substrate have lower CPD than non-defective terraces. Thus, it seems promising to use defects on the HOPG substrate to tune the properties of the 2D material on top as a sort of indirect lithography.

### 2.3. Photoluminescence and Raman imaging of MoS<sub>2</sub>

The chemical purity and stability of HOPG in contact with multi-layered and two-dimensional materials enable conducting micro-Raman spectroscopy, photoluminescence spectroscopy, and other optical and structural analyses of 2D materials without background signals. This is important because no other Raman modes or emission peaks will arise in HOPG since it remains stable during the spectroscopic analysis. Background-free spectroscopy is possible since there is no spectral overlap between the high-frequency G and 2D modes of HOPG substrate with the low-frequency modes of most 2D materials in the spectral range  $< 600$  cm<sup>-1</sup>. Photoluminescence (PL) and Raman spectroscopies are widely used to detect monolayers of 2D materials and other effects such as doping, strain, temperature, and compositional changes [51,52]. Much attention has been given to the optical properties of MoS<sub>2</sub> that we use as a layered model system here. MoS<sub>2</sub> was exfoliated and transferred to HOPG by the PDMS transfer method, demonstrating the compatibility of HOPG with this widespread transfer method. The sample consists of a monolayer, few-layer, and bulk MoS<sub>2</sub>. The sample's topography and phase images are shown in Fig. 3a and 3b. We can distinguish MoS<sub>2</sub>, HOPG, and PDMS residues on HOPG. The phase contrast from PDMS-transfer residues is higher than that of HOPG and MoS<sub>2</sub>, related to the higher tip-sample adhesion force for the transfer residues. It is precisely

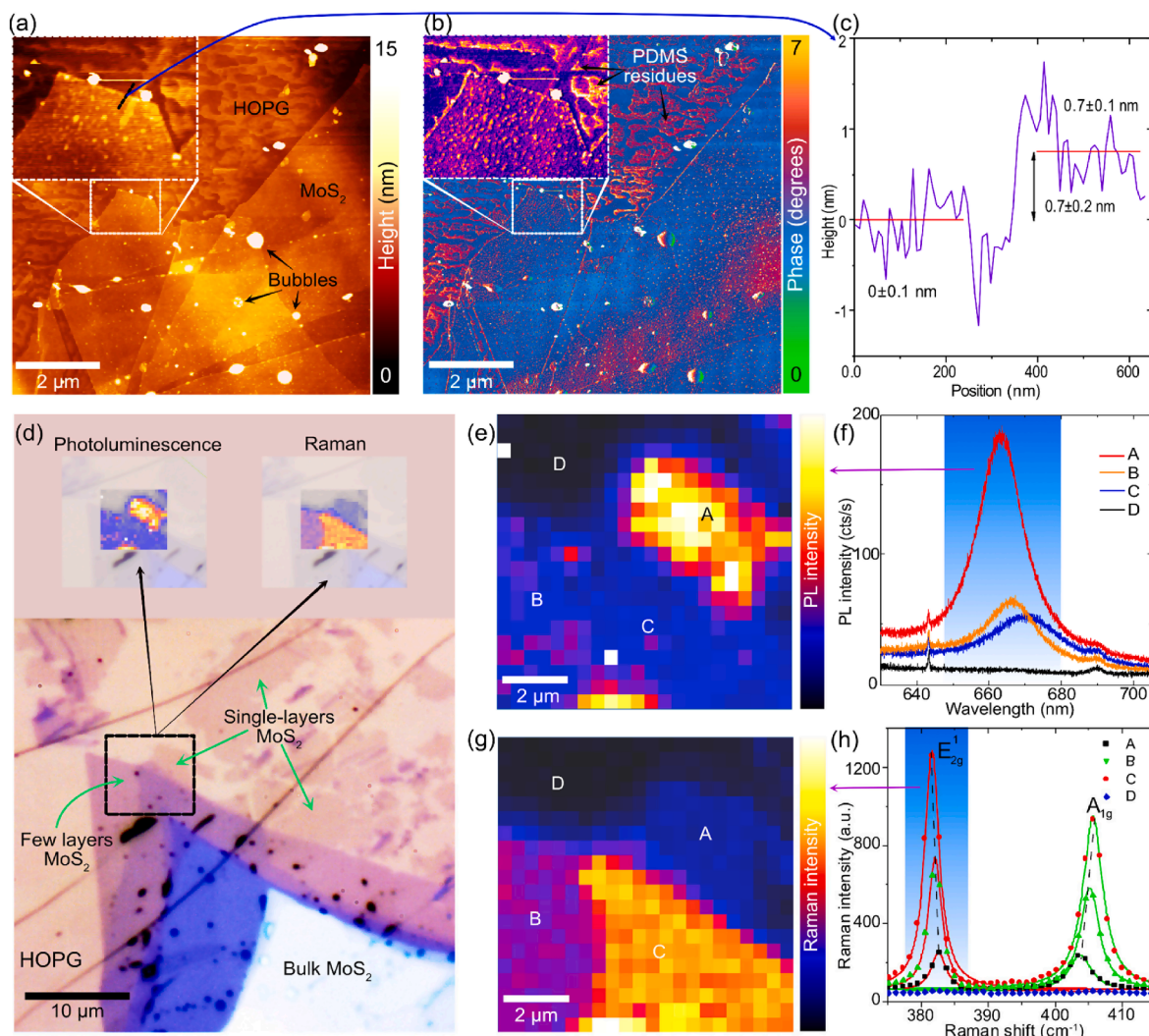


**Fig. 3.** PL and Raman maps of MoS<sub>2</sub> on HOPG. a) AFM topography and b) phase images. c) Single-layer height profile of the regions visible in d) the optical microscopy image. The red lines are linear fits for the substrate and MoS<sub>2</sub> monolayer profile with the fitting errors. e) PL map with regions of interest labeled: A - monolayer MoS<sub>2</sub>, B - bilayer MoS<sub>2</sub>, C - trilayer MoS<sub>2</sub>, and D - HOPG. f) PL spectra from different regions of interest. g) Raman intensity map. h) Raman spectra from different regions. (For interpretation of the references to color in this figure legend, the reader is referred to the web version of this article.)

this kind of sample contamination that our rubbing method on HOPG entirely avoids using PDMS or adhesive tape (see Fig. 1 and Fig. 2). In addition to leaving residues, PDMS transfer produces micro- and nanobubbles on MoS<sub>2</sub> [53,54]. These bubbles can be easily noticed in topography and phase images (see Fig. 3a and 3b). Despite the residues on HOPG, the 0.7 nm monolayer thickness was determined by the cross-sectional analysis presented in Fig. 3c [55,56]. The uncertainties were determined from the linear fits in the cross-sections; we can see that the uncertainties in height profile when using PDMS are more significant than the height value deduced when using our method. From the optical image in Fig. 3d, we again see how easy it is to identify 2D monolayers on HOPG despite the absence of optical interference contrary to Si/SiO<sub>2</sub>.

Fig. 3e and 3f show the photoluminescence map and spectra at different sample points: A - monolayer MoS<sub>2</sub>, B - bilayer MoS<sub>2</sub>, C - trilayer MoS<sub>2</sub>, D - HOPG. Monolayer MoS<sub>2</sub> shows the strongest PL signal due to the indirect to direct bandgap transition. The PL signal decreases with the increase in the number of MoS<sub>2</sub> layers following the literature [55–57]. The PL spectra of few-layer MoS<sub>2</sub> on SiO<sub>2</sub> substrates exhibit two prominent peaks around 627 and 670 nm [55]. In our system, the second peak is located at 663 nm for the monolayer and shows redshift as the number of layers increases (Fig. 3f). This behavior can be related to the strong van der Waals interaction between MoS<sub>2</sub> and HOPG.

Although the first prominent PL peak of MoS<sub>2</sub> coincides with the 2D Raman peak of HOPG at the laser wavelength we used, this overlap could be avoided by changing the laser wavelength.

The Raman map and spectra of a few-layer MoS<sub>2</sub> are shown in Fig. 3g and 3h, respectively, perfectly matching previous reports with the E<sub>2g</sub><sup>1</sup> and A<sub>1g</sub> phonons around 380 and 400 cm<sup>-1</sup>, and a prominent peak at approximately 450 cm<sup>-1</sup> [56]. For monolayer MoS<sub>2</sub>, the E<sub>2g</sub><sup>1</sup> mode at 382.6 cm<sup>-1</sup> has a blue shift compared to monolayer MoS<sub>2</sub> measured on SiO<sub>2</sub>; we attribute this shift to the strong interaction with the substrate. The peak intensity and position show a monotonous change with the number of MoS<sub>2</sub> layers. The intensity of all peaks increases when increasing the MoS<sub>2</sub> thickness; the E<sub>2g</sub><sup>1</sup> Raman mode is blue-shifted while the A<sub>1g</sub> mode shows the expected redshift. Besides the peak shift differences between MoS<sub>2</sub> on HOPG and SiO<sub>2</sub>, these results demonstrate the versatility of HOPG as a substrate for optical spectroscopic analysis of 2D materials. This clean spectroscopic background was critical to acquiring the Raman spectra of talc (10 nm thick) on HOPG in addition to the heat-dissipating, inert, and high adhesion HOPG nature [58].

## 2.4. Stretching out 2Ds: Straintronics - a multistep defect on HOPG activates the chemical reactivity of a GaSe layer

In recent years, the design of 2D materials has been flourishing thanks to advances in the fundamental understanding of these nanomaterials at the atomic scale. The catalytic activity of materials depends on the number of active sites on the surface [59]. The active sites are defined by their electronic properties on the surface, which can be

increased by structural modifications such as surface microstructure. One emerging strategy for structural modification is strain engineering, which allows controlling interfacial charge transfer, surface reactivity, and electronic and photonic performance [60]. Strain can be induced purposely or accidentally like nanolayers over HOPG graphite steps. Stress causes changes in the 2D system, such as increased interatomic distances that make atomic bonding surfaces softer. Moreover, electronic properties also change. For instance, as recently summarized by

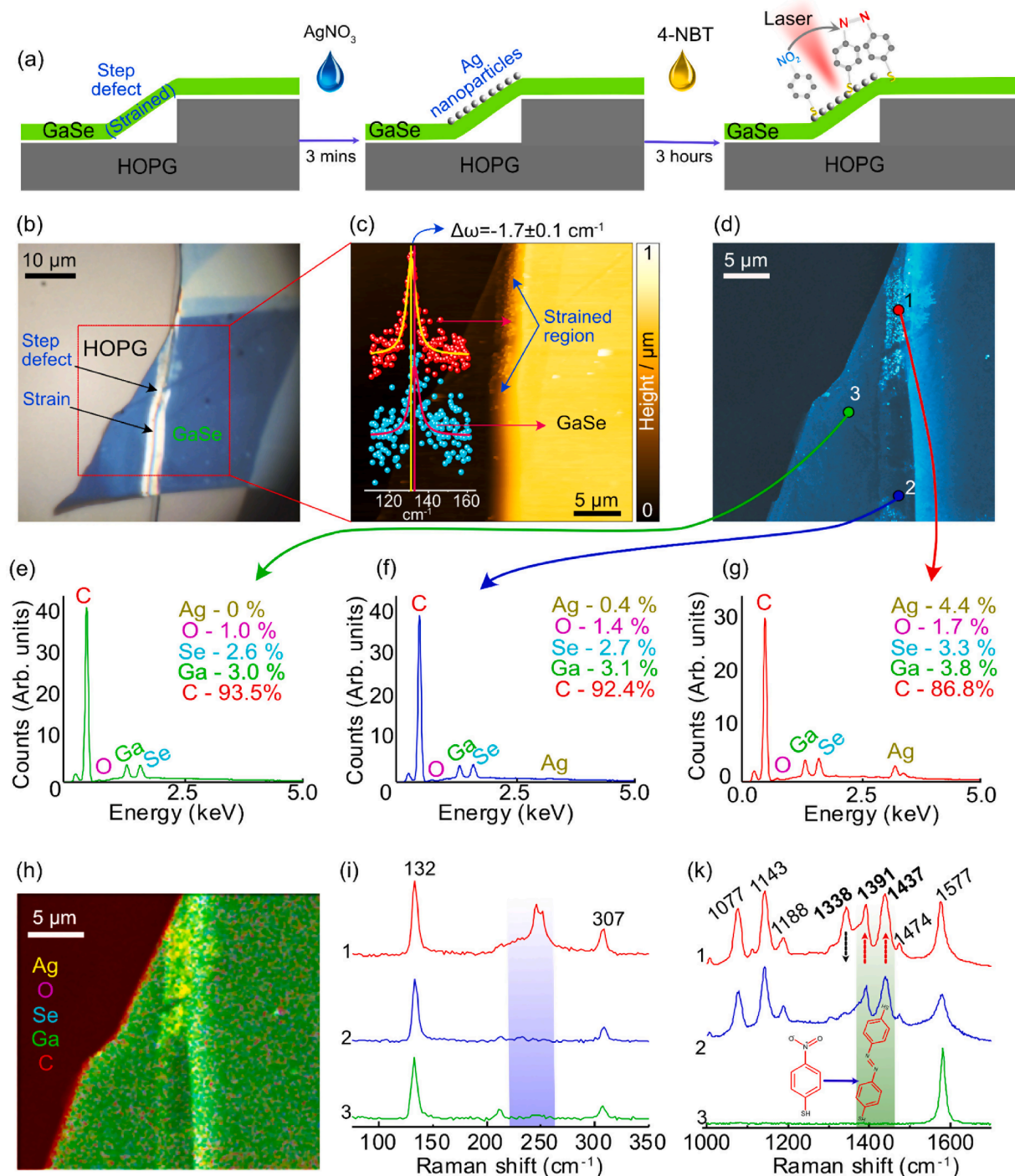


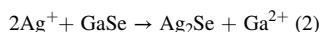
**Fig. 4.** a) Experimental scheme representing the process of  $\text{AgNO}_3$  solution deposition, Ag nanoparticles formation, and functionalization with 4-NBT, b) Optical image of GaSe on HOPG after modification by  $\text{AgNO}_3$ , c) AFM and d) SEM images of the region of interest. The inset in c) shows the Raman spectra with a down-shift of the  $\text{A}'_1$  peak for the strained region. (e-g) EDX spectra represent non-strained region e), strained region f), and strained region with Ag nanoparticles. h) Elemental map obtained by EDX. i) Raman spectra of the sample after modification by  $\text{AgNO}_3$ . k) Raman spectra of the sample at different locations after exposure to 4-NBT for 3 h.

Wu *et al.*, charge carriers' concentration, band gap, and phonon modes all get affected by strain [61]. We show in this section that the strong interaction between the 2D material and the HOPG substrate can be exploited to enhance the catalytic activity of GaSe radically. A sketch of the experiment is shown in Fig. 4a.

Fig. 4b shows the optical microscopy image of a GaSe flake on a step defect of HOPG, showing color changes from blue to light yellow. We anticipated that these translocated defects go beyond modifying the optical properties of the GaSe layer, but its catalytic properties should also be affected. To test this hypothesis, we dropped 10  $\mu\text{L}$  of  $\text{AgNO}_3$   $10^{-4}$  M on the sample shown in Fig. 4b and let it react for 3 mins. Afterward,  $\text{AgNO}_3$  was removed and the sample was washed several times with distilled water to remove  $\text{AgNO}_3$  leftovers.

Fig. 4c and 4d show AFM and scanning electron microscopy images of the region of interest after reaction with  $\text{AgNO}_3$ . We see the formation of nanoparticles that selectively accumulate on the strained region and at the GaSe edge. Elemental analysis was carried out by energy dispersive X-ray analysis (EDX) (Fig. 4e, f, g, and h). These results show that GaSe catalytic activity was largely enhanced in the substrate-induced strained regions since EDX detected no Ag on the non-strained GaSe layers. It is worth noting that the distribution of Ag is not homogeneous. On the strained areas near the edge, the concentration of Ag is 4.4 %, while it is only 0.4 % far from the edge. This 10-fold increase in Ag deposition for the flake edges and the absence of Ag on non-strained regions show an emerging application in 2D materials engineering due to mechanical deformation, that is, straintronics [62]. Beyond providing a versatile substrate for electronic, morphological, and spectroscopic nanoscale characterization of 2D materials, the strong interaction makes it possible to investigate the strain in 3D structures by patterning HOPG.

The selective reaction of  $\text{AgNO}_3$  with laser-irradiated GaSe enhances the photocatalytic properties, which are limited in unmodified GaSe [43]. After calculating dissociation and solvation energies during the cation exchange reaction, reported by Rivest *et al.* [63], we postulate that the reaction between  $\text{AgNO}_3$  and GaSe is driven by cation exchange in the following way:



GaSe  $\rightarrow$  Ga + Se dissociation energy: 207.44 kJ/mol; [64].

$\text{Ag}^+ \rightarrow$  Ag desolvation energy: 350 kJ/mol; [65].

$2\text{Ag} + \text{Se} \rightarrow \text{Ag}_2\text{Se}$  association energy:  $-210$  kJ/mol; [65].

$\text{Ga} \rightarrow \text{Ga}^{2+}$  solvation energy:  $-1678.97$  kJ/mol, calculated as in the report by Marcus [66].

The total Gibbs energy for equation (2) is:  $207.44 + 350 - 210 - 1678.97 = -1331.53$  kJ/mol. The negative value implies that the reaction is spontaneous at room temperature and thermodynamically favorable [67]. The Raman spectra of GaSe at different locations are shown in Fig. 4i. Crystalline GaSe has three main vibrational modes at 132, 212, and 307  $\text{cm}^{-1}$ , shown in location 1. The Raman spectrum at location 2 shows three characteristic peaks, with one small peak rising at 230  $\text{cm}^{-1}$ , corresponding to the Se-Se vibration mode in  $\text{Ag}_2\text{Se}$  [68]. In contrast to spot 2, the Raman spectrum at spot 1 shows a significant rise of peaks at 230 and 250  $\text{cm}^{-1}$ , corresponding to the Se-Se vibration mode in  $\text{Ag}_2\text{Se}$  [68] and the  $E'(\text{LO})$  mode activated by defects, respectively [51]. This also confirms the formation of  $\text{Ag}_2\text{Se}$  nanoparticles on GaSe strained regions. The possibility to drive chemical reactions using the most abundant energy source at our disposal is of fundamental importance. Therefore, we further investigated the photocatalytic activity of newly formed Ag-GaSe nanostructures using 4-nitrobenzenethiol (4-NBT) as a model molecular system for photocatalysis [69].

The conversion of 4-NBT to 4-aminobenzenethiol (4-ABT) and p,p'-dimercaptoazobenzene (DMAB) under laser irradiation has been studied intensively [70,71]. Raman spectroscopy is ideal for this investigation since we can simultaneously induce the chemical reaction and monitor the photocatalytic conversion thanks to the distinct vibrational modes between the reactant and products. 4-NBT has several prominent peaks

at 1077, 1110, and 1340  $\text{cm}^{-1}$ , contributing to in-plane C—H bending modes, and  $\text{NO}_2$  mode, while the peak at 1575  $\text{cm}^{-1}$  arises from the C—C stretching mode [72].

Our Raman spectroscopy results in Fig. 4k show that none of the 4-NBT, 4-ABT, or DMAB species were detected on flat non-strained GaSe (like point 3). This further confirms that no Ag was on the flat GaSe surface, but the substrate-induced strain made the GaSe wrinkles catalytically active as evidenced by the Raman spectra at points 1 and 2. The spectra in those regions match that of DMAB. We should also consider the intrinsic activity of steps in HOPG that have coordinatively unsaturated sites with a higher density of states. Even though these edges are underneath GaSe, their characteristics could enhance photocatalytic activity. Therefore, a control experiment was performed on bare HOPG, with no GaSe, to rule out contributions from HOPG steps reactivity. Our analysis shows that there was no detectable photocatalytic activity from HOPG steps confirming that the enhanced activity in this system is due to strained GaSe decorated with Ag NPs. Indeed, we discovered a new venue for a clean and versatile way to engineer defects on 2D materials by either exploiting graphite steps and natural defects or pre-patterning a HOPG substrate. After depositing the 2D material on a patterned HOPG the defects translocate to the 2D. These results show that the strong interaction between the 2D material and pre-existing defects in HOPG can be exploited in straintronics, giving rise to localized changes in reactivity, optical, and electronic properties.

In this work, we chose the mechanical transfer method because of its low cost, simplicity, speed, and versatility in investigating the intrinsic properties of 2D material. Moreover, transferring 2D materials onto substrate allows investigating any 2D materials regardless of their growth method, especially those not synthesized yet, such as naturally-occurring layered minerals. Also, we can transfer arbitrary 2D flakes onto steps of HOPG for strain engineering, which is demonstrated in this work and cannot be realized by directly growing them on a HOPG substrate. Nevertheless, the unique chemical and temperature stability of HOPG could also open the door for the direct growth of 2D materials with compatible methods such as electrochemistry and other chemical and physical growth techniques. This is indeed a perspective that we aim to explore next.

In summary, this work has several novelty points that were possible thanks to using HOPG as the substrate for 2D investigation. For example, it is the first time that: 1) the new 2D material zinc indium sulfide is investigated in its large-area layered single-crystal form; 2) the same substrate is used for all the nanoscale characterization methods we showed without any additional sample preparation steps, and the deposition from the bulk taking literally just a few seconds; 3) substrate-induced strain engineering is reported for the two-dimensional semiconductor GaSe activating its photocatalytic properties; 4) achieved visualization of single-layers without the optical interference of the conventional  $\text{SiO}_2/\text{Si}$  substrate; 5) evidence that 2D materials can become transparent to structural defects of the substrate underneath.

### 3. Conclusion

We comprehensively investigated the optical and electronic properties of several two-dimensional materials, including GaSe,  $\text{MoS}_2$ ,  $\text{Zn}_2\text{In}_2\text{S}_5$ , talc, and h-BN (see Supporting information), using HOPG as a substrate. We demonstrated HOPG advantages for investigating 2D materials with various state-of-the-art nanoscale methods. The optical contrast of layered structures on HOPG with thickness ranging from single to few layers and its visibility on the graphite surface was elucidated. We performed a layer thickness vs. optical contrast evaluation for fast estimation of the thickness of 2D material on the HOPG substrate via optical contrast dependence with the layer number. Using KPFM and DFM, for the first time, we investigated electronic properties such as the work function and majority carrier type of a widely known 2D semiconductor GaSe and the novel two-dimensional material  $\text{Zn}_2\text{In}_2\text{S}_5$ . For the latter, we also demonstrated the influence of handmade and



transferred defects on its work function, offering mechanical patterning and energy levels engineering possibilities. In addition, PL and Raman spectroscopy for MoS<sub>2</sub> was conducted to discuss intensity (PL) and peak position shifting (Raman) dependent on the number of layers showing no significant effects when using HOPG compared to the conventional Si/SiO<sub>2</sub>. This could be done thanks to HOPG's Raman spectrum, which does not overlap with low-frequency Raman bands of 2D materials (usually lower than 600 cm<sup>-1</sup>). The van der Waals nature of HOPG gave rise to a strong 2D material interaction that goes beyond the realm of van der Waals forces into the chemical range, opening new routes for 2D material engineering. Finally, the strong interaction and the multistep nature of the HOPG surface were exploited for strain engineering on GaSe for localization of photocatalytic properties enhancement by selective catalytic growth of Ag nanostructures from AgNO<sub>3</sub> on strained regions. The multifunctionality added by Ag nanostructures was further exploited in the photocatalytic 4-NBT conversion. We anticipate that these eye-opening demonstrations will motivate the active research community working on 2D materials to discover and manipulate new phenomena using an old but still unexplored substrate material as a platform.

#### 4. Materials and methods

Natural solid crystals of MoS<sub>2</sub> were used for the preparation of flakes. GaSe crystal was grown by the Bridgman method. Zn<sub>2</sub>In<sub>2</sub>S<sub>5</sub> single crystal was synthesized by a chemical transport method. Synthetic hBN single crystals were acquired from HQ Graphene. Natural talc (steatite) single crystals were used to obtain thin talc layers. The mechanical exfoliation method was used to transfer all the flakes to the HOPG surface (except talc and h-BN). Talc and h-BN were transferred *via* the PDMS stamping method (Figure. S1 in Supporting Information). Exfoliated nanolayers first have been observed by the optical microscope. Optical contrast between flakes and HOPG and the absence of light interference are the indicators of nanoscale flakes. Then, samples were scanned by the NTEGRA NT-MDT AFM system in contact topography mode to verify their thickness and measured by conductive modes SCM and KPFM. In SCM and KPFM, samples were scanned in intermittent contact mode (tapping-mode), and conductive NSG01/Pt cantilevers with force constant of 1.45–15.1 N/m. All AFM cantilevers were purchased from NT-MDT. Raman measurements on MoS<sub>2</sub> were acquired using the Horiba - LabRam Evolution setup. AFM topography images, including talc and h-BN, were obtained using an AIST-NT scanning probe microscope. **Silver deposition:** 10 μL of 1 mM AgNO<sub>3</sub> was dropped on the GaSe flake on HOPG. After 3 mins, AgNO<sub>3</sub> was sucked out, and the sample was washed to remove residual AgNO<sub>3</sub>. Photocatalysis experiment: 4-NBT 10<sup>-3</sup> M was prepared by mixing 7.75 mg in 25 mL distilled water and 25 mL ethanol. The sample was immersed in solution 4-NBT for 3 h; after that, the sample was washed with distilled water and measured in the Raman mode in the NTEGRA NT-MDT AFM system.

#### CRedit authorship contribution statement

**Tuan-Hoang Tran:** Conceptualization, Data curation, Formal analysis, Investigation, Methodology, Visualization, Writing – original draft. **Raul D. Rodriguez:** Supervision, Validation, Conceptualization, Data curation, Formal analysis, Methodology, Funding acquisition, Visualization. **Dmitry Cheshev:** Conceptualization, Data curation, Formal analysis, Investigation, Methodology, Visualization, Writing – original draft. **Nelson E. Villa:** Data curation, Formal analysis, Investigation, Methodology, Writing – original draft. **Muhammad Awais Aslam:** Data curation, Formal analysis, Investigation. **Jelena Pešić:** Data curation, Formal analysis. **Aleksandar Matković:** Data curation, Formal analysis, Validation, Funding acquisition. **Evgeniya Sheremet:** Supervision, Validation, Funding acquisition.

#### Declaration of Competing Interest

The authors declare that they have no known competing financial interests or personal relationships that could have appeared to influence the work reported in this paper.

#### Data availability

Data will be made available on request.

#### Acknowledgments

This work was funded by RFBR and FWF research project No. 19-52-14006. M.A.A. and A.M. acknowledge the support by the Austrian Science Fund (FWF Der Wissenschaftsfonds) through project I4323- N36. We are grateful to the Prof. Mekhman Yusubov and the Chemistry Research School at TPU for support with the acquisition of the AFM/Raman setup. Infrastructural support (Raman-TERS laboratory) by Montanuniversität Leoben is acknowledged. JP acknowledges the funding provided by the Institute of Physics Belgrade, through a grant from the Ministry of Education, Science and Technological Development of the Republic of Serbia. We are grateful to Prof. Bernardo R. A. Neves from the Federal University of Minas Gerais, Brasil, for kindly providing the natural talc (steatite) crystals. We thank Gennadiy Murastov for his assistance with AFM experiments.

#### Appendix A. Supplementary material

Supplementary data to this article can be found online at <https://doi.org/10.1016/j.apsusc.2022.154585>.

#### References

- [1] M. Velický, P.S. Toth, Appl. Mater. Today 8 (2017) 68.
- [2] H.S.N. Jayawardena, S.H. Liyanage, K. Rathnayake, U. Patel, M. Yan, Anal. Chem. 2021 (1889) 93.
- [3] L. Zhang, H. Nan, X. Zhang, Q. Liang, A. Du, Z. Ni, X. Gu, K.K. Ostrikov, S. Xiao, Nat. Commun. 11 (2020) 5960.
- [4] D.J. Late, B. Liu, H.S. Ramakrishna Matte, C.N.R. Rao, V.P. Dravid, Adv. Funct. Mater. 22 (2012) 1894.
- [5] X.F. Fan, W.T. Zheng, V. Chihai, Z.X. Shen, J.-L. Kuo, J. Phys. Condens. Matter 24 (2012), 305004.
- [6] M. Lafkioti, B. Krauss, T. Lohmann, U. Zschieschang, H. Klauk, K.V. Klitzing, J. H. Smet, Nano Lett. 10 (2010) 1149.
- [7] S.B. Desai, S.R. Madhvapathy, M. Amani, D. Kiriya, M. Hettick, M. Tosun, Y. Zhou, M. Dubej, J.W. Ager 3rd, D. Chrzan, A. Javey, Adv. Mater. 28 (2016) 4053.
- [8] K.S. Novoselov, A. Mishchenko, A. Carvalho, A.H. Castro Neto, Science 353 (2016) aac9439.
- [9] X. Gao, Y. Shen, Y. Ma, S. Wu, Z. Zhou, Comput. Mater. Sci. 170 (2019), 109200.
- [10] K.D. Pham, N.N. Hieu, H.V. Phuc, I.A. Fedorov, C.A. Duque, B. Amin, C.V. Nguyen, Appl. Phys. Lett. 113 (2018), 171605.
- [11] M. Kettner, C. Stumm, M. Schwarz, C. Schuschke, J. Libuda, Surf. Sci. 679 (2019) 64.
- [12] J. Cryst. Growth 480 (2017) 13.
- [13] Q. Li, M.A. Brown, J.C. Hemminger, R.M. Penner, Chem. Mater. 18 (2006) 3432.
- [14] C. Herbig, C. Zhang, F. Mujid, S. Xie, Z. Pedramrazi, J. Park, M.F. Crommie, Nano Lett. 21 (2021) 2363.
- [15] L. Meng, Y. Li, T.S. Liu, C. Zhu, Q.Y. Li, X. Chen, S. Zhang, X. Zhang, L. Bao, Y. Huang, F. Xu, R.S. Ruoff, Carbon 156 (2020) 24.
- [16] R. Frisenda, E. Navarro-Moratalla, P. Gant, D. Pérez De Lara, P. Jarillo-Herrero, R. V. Gorbachev, A. Castellanos-Gomez, Chem. Soc. Rev. 47 (2018) 53.
- [17] J.J. Schwartz, H.-J. Chuang, M.R. Rosenberger, S.V. Sivaram, K.M. McCreary, B. T. Jonker, A. Centrone, ACS Appl. Mater. Interfaces 11 (2019) 25578.
- [18] K. Kato, F. Tanno, N. Umemura, Appl. Opt. 52 (2013) 2325.
- [19] H. Li, J. Wu, X. Huang, G. Lu, J. Yang, X. Lu, Q. Xiong, H. Zhang, ACS Nano 7 (2013) 10344.
- [20] F. Huang, J. Phys. Chem. C 123 (2019) 7440.
- [21] J.M. Katzen, M. Velický, Y. Huang, S. Drakeley, W. Hendren, R.M. Bowman, Q. Cai, Y. Chen, L.H. Li, F. Huang, ACS Appl. Mater. Interfaces 10 (2018) 22520.
- [22] X.-L. Li, W.-P. Han, J.-B. Wu, X.-F. Qiao, J. Zhang, P.-H. Tan, Adv. Funct. Mater. 27 (2017) 1604468.
- [23] P. Gant, F. Ghasemi, D. Maeso, C. Munuera, E. López-Elvira, R. Frisenda, D.P. De Lara, G. Rubio-Bollinger, M. Garcia-Hernandez, A. Castellanos-Gomez, Beilstein J. Nanotechnol. 8 (2017) 2357.
- [24] P. Blake, E.W. Hill, A.H. Castro Neto, K.S. Novoselov, D. Jiang, R. Yang, T.J. Booth, A.K. Geim, Appl. Phys. Lett. 91 (2007), 063124.

- [25] P. Hlubina, J. Luňáček, D. Ciprian, R. Chlebus, *Appl. Phys. B* 92 (2008) 203.
- [26] P. Hu, Z. Wen, L. Wang, P. Tan, K. Xiao, *ACS Nano* 6 (2012) 5988.
- [27] M. Nonnenmacher, M.P. O'Boyle, H.K. Wickramasinghe, *Appl. Phys. Lett.* 58 (1991) 2921.
- [28] E. Sheremet, P. Meszmer, T. Blaudeck, S. Hartmann, C. Wagner, B. Ma, S. Hermann, B. Wunderle, S.E. Schulz, M. Hietschold, R.D. Rodriguez, D.R.T. Zahn, *Phys. Status Solidi* 216 (2019) 1900106.
- [29] A. Matković, A. Petritz, G. Schider, M. Krammer, M. Kratzer, E. Karner-Petritz, A. Fian, H. Gold, M. Gärtner, A. Terfort, C. Teichert, E. Zojer, K. Zojer, B. Stadlober, *Adv. Electron. Mater.* 6 (2020) 2000110.
- [30] W. Melitz, J. Shen, A.C. Kummel, S. Lee, *Surf. Sci. Rep.* 66 (2011) 1.
- [31] L. Karvonen, A. Säynätjoki, S. Mehravar, R.D. Rodriguez, S. Hartmann, D.R. Zahn, S. Honkanen, R.A. Norwood, N. Peyghambarian, K. Kieu, H. Lipsanen, J. Riikonen, *Sci. Rep.* (2015) 5, <https://doi.org/10.1038/srep10334>.
- [32] Z. B. Aziza, Z. Ben Aziza, D. Pierucci, H. Henck, M. G. Silly, C. David, M. Yoon, F. Sirotti, K. Xiao, M. Eddrief, J.-C. Girard, A. Ouerghi, *Phys. Rev. B* 2017, 96, DOI 10.1103/physrevb.96.035407.
- [33] M. Rahaman, R.D. Rodriguez, M. Monecke, S.A. Lopez-Rivera, D.R.T. Zahn, *Semicond. Sci. Technol.* 32 (2017), 105004.
- [34] T.-H. Tran, R.D. Rodriguez, M. Salerno, A. Matković, C. Teichert, E. Sheremet, *Carbon* 176 (2021) 431.
- [35] S.K. Chong, F. Long, G. Wang, Y.-C. Lin, S. Bhandari, R. Shahbazian-Yassar, K. Suenaga, R. Pandey, Y.K. Yap, *ACS Appl. Nano Mater.* 1 (2018) 3293.
- [36] Z.I. Alferov, *Russ. Chem. Rev.* 82 (2013) 587.
- [37] Y.Y. Illarionov, T. Knobloch, M. Jech, M. Lanza, D. Akinwande, M.I. Vexler, T. Mueller, M.C. Lemme, G. Fiori, F. Schwierz, T. Grasser, *Nat. Commun.* 11 (2020) 3385.
- [38] J. Zhang, W. Lu, Y.S. Li, J. Cai, L. Chen, *Acc. Chem. Res.* 48 (2015) 1788.
- [39] W. Lu, J. Zhang, Y.S. Li, Q. Chen, X. Wang, A. Hassanien, L. Chen, *J. Phys. Chem. C* 116 (2012) 7158.
- [40] Y. Kang, D. Jeon, T. Kim, *J. Phys. Chem. C* 124 (2020) 18316.
- [41] Z.B. Aziza, Z. Ben Aziza, H. Henck, D. Pierucci, M.G. Silly, E. Lhuillier, G. Patriarche, F. Sirotti, M. Eddrief, A. Ouerghi, *ACS Nano* 10 (2016) 9679.
- [42] M. Zhong, Q. Xia, L. Pan, Y. Liu, Y. Chen, H.-X. Deng, J. Li, Z. Wei, *Adv. Funct. Mater.* 28 (2018) 1870312.
- [43] D. Cheshev, R.D. Rodriguez, A. Matković, A. Ruban, J.-J. Chen, E. Sheremet, *ACS Omega* 5 (2020) 10183.
- [44] R. Bel Hadj Tahar, T. Ban, Y. Ohya, Y. Takahashi, *J. Appl. Phys.* 1998, 83, 2631.
- [45] E. Mercado, Y. Zhou, Y. Xie, Q. Zhao, H. Cai, B. Chen, W. Jie, S. Tongay, T. Wang, M. Kuball, *ACS Omega* 4 (2019) 18002.
- [46] H. Wang, Y. Sun, Y. Wu, W. Tu, S. Wu, X. Yuan, G. Zeng, Z.J. Xu, S. Li, J.W. Chew, *Appl. Catal. B* 245 (2019) 290.
- [47] H. Zhang, S. Xie, J. Hu, X. Wu, Q. Zhang, J. Cheng, Y. Wang, *Chem. Commun.* 56 (2020) 1776.
- [48] S. Yang, Y. Chen, C. Jiang, *InfoMat* 3 (2021) 397.
- [49] B. Vasić, A. Matković, U. Ralević, M. Belić, R. Gajić, *Carbon* 120 (2017) 137.
- [50] Z. Li, Y. Wang, A. Kozbial, G. Shenoy, F. Zhou, R. McGinley, P. Ireland, B. Morganstein, A. Kunkel, S.P. Surwade, L. Li, H. Liu, *Nat. Mater.* 12 (2013) 925.
- [51] R.D. Rodriguez, S. Müller, E. Sheremet, D.R.T. Zahn, A. Villabona, S.A. Lopez-Rivera, P. Tonndorf, S.M. de Vasconcellos, R. Bratschitsch, *J. Vacuum Sci. Technol. B Nanotechnol. Microelectron. Mater. Process. Measur. Phenomena* 32 (2014) 04E106.
- [52] A. Anshul, M. Kumar, A. Raj, *Optik* 212 (2020), 164749.
- [53] T.P. Darlington, C. Carmesin, M. Florian, E. Yanev, O. Ajayi, J. Ardelean, D. A. Rhodes, A. Ghiotto, A. Krayev, K. Watanabe, T. Taniguchi, J.W. Kysar, A. N. Pasupathy, J.C. Hone, F. Jahnke, N.J. Borys, P.J. Schuck, *Nat. Nanotechnol.* 15 (2020) 854.
- [54] A.V. Tyurnina, D.A. Bandurin, E. Khestanova, V.G. Kravets, M. Koperski, F. Guinea, A.N. Grigorenko, A.K. Geim, I.V. Grigorieva, *ACS Photonics* 6 (2019) 516.
- [55] A. Splendiani, L. Sun, Y. Zhang, T. Li, J. Kim, C.-Y. Chim, G. Galli, F. Wang, *Nano Lett.* 10 (2010) 1271.
- [56] H. Li, Q. Zhang, C.C.R. Yap, B.K. Tay, T.H.T. Edwin, A. Olivier, D. Baillargeat, *Adv. Funct. Mater.* 22 (2012) 1385.
- [57] G. Eda, H. Yamaguchi, D. Voiry, T. Fujita, M. Chen, M. Chhowalla, *Nano Lett.* 11 (2011) 5111.
- [58] A. Matković, L. Ludescher, O. E. Peil, A. Sharma, K.-P. Gradwohl, M. Kratzer, M. Zimmermann, J. Genser, D. Knez, E. Fisslthaler, C. Gammer, A. Lugstein, R. J. Bakker, L. Romaner, D. R. T. Zahn, F. Hofer, G. Salvan, J. G. Raith, C. Teichert, *npj 2D Materials and Applications* 2021, 5, DOI 10.1038/s41699-021-00276-3.
- [59] S. Dou, X. Wang, S. Wang, *Small Methods* 3 (2019) 1800211.
- [60] Z. Dai, L. Liu, Z. Zhang, *Adv. Mater.* 31 (2019) 1970322.
- [61] Y. Wu, L. Wang, H. Li, Q. Dong, S. Liu, Strain of 2D materials via substrate engineering, *Chin. Chem. Lett.* 33 (2022) 153–162.
- [62] F. Miao, S.-J. Liang, B. Cheng, *npj quantum mater.* 2021, 6, DOI 10.1038/s41535-021-00360-3.
- [63] J.B. Rivest, P.K. Jain, *Chem. Soc. Rev.* 42 (2013) 89.
- [64] M. Ider, R. Pankajavalli, W. Zhuang, J.Y. Shen, T.J. Anderson, *ECS J. Solid State Sci. Technol.* 4 (2015) Q51.
- [65] N. Chen, M.R. Scimeca, S.J. Paul, S.B. Hafiz, Z. Yang, X. Liu, F. Yang, D.-K. Ko, A. Sahu, *Nanoscale Adv.* 2 (2020) 368.
- [66] Y. Marcus, *J. Chem. Soc., Faraday Trans.* 87 (1991) 2995.
- [67] H. Jin, C. Guo, X. Liu, J. Liu, A. Vasileff, Y. Jiao, Y. Zheng, S.-Z. Qiao, *Chem. Rev.* 118 (2018) 6337.
- [68] M. Pandiaraman, N. Soundararajan, *J. Theor. Appl. Phys.* 6 (2012) 7.
- [69] J.-L. Yang, H.-J. Wang, H. Zhang, Z.-Q. Tian, J.-F. Li, *Cell Rep. Phys. Sci.* 1 (2020), 100184.
- [70] Y. Fang, Y. Li, H. Xu, M. Sun, P. M. Champion, L. D. Ziegler, 2010, DOI 10.1063/1.3482306.
- [71] A.A. Golubev, B.N. Khlebtsov, R.D. Rodriguez, Y. Chen, D.R.T. Zahn, *J. Phys. Chem. C* 122 (2018) 5657.
- [72] K. Kim, I. Lee, S.J. Lee, *Chem. Phys. Lett.* 377 (2003) 201.



ELSEVIER

Contents lists available at ScienceDirect

## Infrared Physics &amp; Technology

journal homepage: [www.elsevier.com/locate/infrared](http://www.elsevier.com/locate/infrared)Plasmon – Phonon interaction in  $\text{ZnSnSb}_2 + \text{Mn}$  semiconductors

Maja Romcevic<sup>a,\*</sup>, Novica Paunovic<sup>a</sup>, Uros Ralevic<sup>a</sup>, Jelena Pesic<sup>a</sup>, Jelena Mitric<sup>a</sup>, Jelena Trajic<sup>a</sup>,  
Lukasz Kilanski<sup>b</sup>, Witold Dobrowolski<sup>b</sup>, Irina Valentinovna Fedorchenko<sup>c,d</sup>,  
Sergey Fedorovich Marenkin<sup>c,d</sup>, Nebojsa Romcevic<sup>a</sup>

<sup>a</sup> Institute of Physics, University of Belgrade, Belgrade, Serbia

<sup>b</sup> Institute of Physics, Polish Academy of Sciences, Warsaw, Poland

<sup>c</sup> Kurnakov Institute of General and Inorganic Chemistry, Russian Academy of Science, Moscow, Russian Federation

<sup>d</sup> College of New Materials and Nanotechnologies, National University of Science and Technology, Moscow, Russian Federation

## ARTICLE INFO

## Keywords:

Semiconductors  
Lattice defects  
Optical properties  
Phonon properties  
Plasmon - phonon interaction

## ABSTRACT

Semiconductors of II-IV-V<sub>2</sub> type with chalcopyrite structure have been studied for several decades. Due to advances in materials synthesis technologies, and doping with various elements, the possibilities of their application have expanded. In this paper, polycrystalline  $\text{ZnSnSb}_2 + \text{Mn}$  was examined with the aim to explain the connection of its high free carrier concentration with the material structure and influence on optical properties. Two samples of  $\text{Zn}_{1-x}\text{Mn}_x\text{SnSb}_2$  with different compositions ( $x = 0.027$  and  $x = 0.076$ ) and significant difference in carrier concentrations were analyzed. Their structural properties were examined by x-ray diffraction, optical microscopy, and AFM. The existence of several different phases -  $\text{ZnSnSb}_2$ ,  $\text{ZnSb}$ ,  $\text{SnSb}$ , and small amounts of  $\text{Sn}$  and  $\text{MnSb}$ , as well as very complex microstructures, were registered. It was found that the high free carrier concentrations are caused by a large number of defects, especially zinc vacancies. Optical properties were analyzed using IR spectroscopy at room temperature. Based on the analysis of IR reflection spectra, the presence of plasmon - phonons interaction was registered. It was determined that three  $\text{ZnSnSb}_2$  phonons of B<sub>2</sub> symmetry interact with plasma, which then leads to the change of their positions. A detailed analysis of this interaction provides insight into the behavior of some other material parameters. Also, vibration modes of  $\text{ZnSb}$  and  $\text{SnSb}$  phases were registered on the spectra. Knowledge of phonon behavior and their interaction with plasma is important for possible applications, especially as a thermoelectric material.

## 1. Introduction

Semiconductors have been widely used thanks to the ability to adapt to different requirements. The II-IV-V<sub>2</sub> chalcopyrite semiconductors have been intensively studied in recent decades [1]. The fields of their application are considerably expanded by doping with various impurities. A significant breakthrough was achieved by the addition of magnetic impurities, whereby ferromagnetism at room temperature was achieved [2,3]. The synthesis technology of this class of compounds has been developed, but it is still adapting to new requirements [4]. Zn-Sn-Sb based alloys have required thermoelectric properties and find application as low-toxic thermoelectric materials [5,6,7]. The engineering of structural, transport, electrical, optical, magnetic properties as well as other material parameters, goes along with the increasing application of this class of semiconductors.

$\text{ZnSnSb}_2$  is II-IV-V<sub>2</sub> type material with the tetragonal chalcopyrite structure, narrow gap of 0.7 eV at room temperature, high

concentration of free carriers ( $10^{21}$ – $10^{22}$  cm<sup>-3</sup>) and inhomogeneous structure [8,9]. In this paper we analyzed ferromagnetic semiconductor  $\text{ZnSnSb}_2 + \text{Mn}$ , which has interesting magnetic properties, such as paramagnet-ferromagnet transition with the Curie temperature about 522 K and the cluster-glass behavior with the transition temperature about 465 K, caused by the formation of  $\text{MnSb}$  clusters in the material [10]. The  $\text{Zn}_{1-x}\text{Mn}_x\text{SnSb}_2$  samples were obtained using direct fusion method, and characterization of their structural, magnetic, optical and phonon properties were done [9]. We chose two samples with different chemical contents,  $x = 0.027$  and  $x = 0.076$ , which we labeled as samples A and B respectively, with the aim to examine their properties in more detail. Main reason was a ten times difference in their free-carrier concentrations ( $p_A = 13 \times 10^{21}$  cm<sup>-3</sup> and  $p_B = 1.2 \times 10^{21}$  cm<sup>-3</sup>). We wanted to determine what the cause of this difference in concentration is, and whether there is a reaction between the free carriers and the crystal lattice. The question of plasmon-phonon interaction is particularly interesting in the study of thermoelectric

\* Corresponding author.

E-mail address: [romcevic@ipb.ac.rs](mailto:romcevic@ipb.ac.rs) (M. Romcevic).

<https://doi.org/10.1016/j.infrared.2020.103345>

Received 3 February 2020; Received in revised form 23 April 2020; Accepted 25 April 2020

Available online 28 April 2020

1350-4495/ © 2020 Elsevier B.V. All rights reserved.

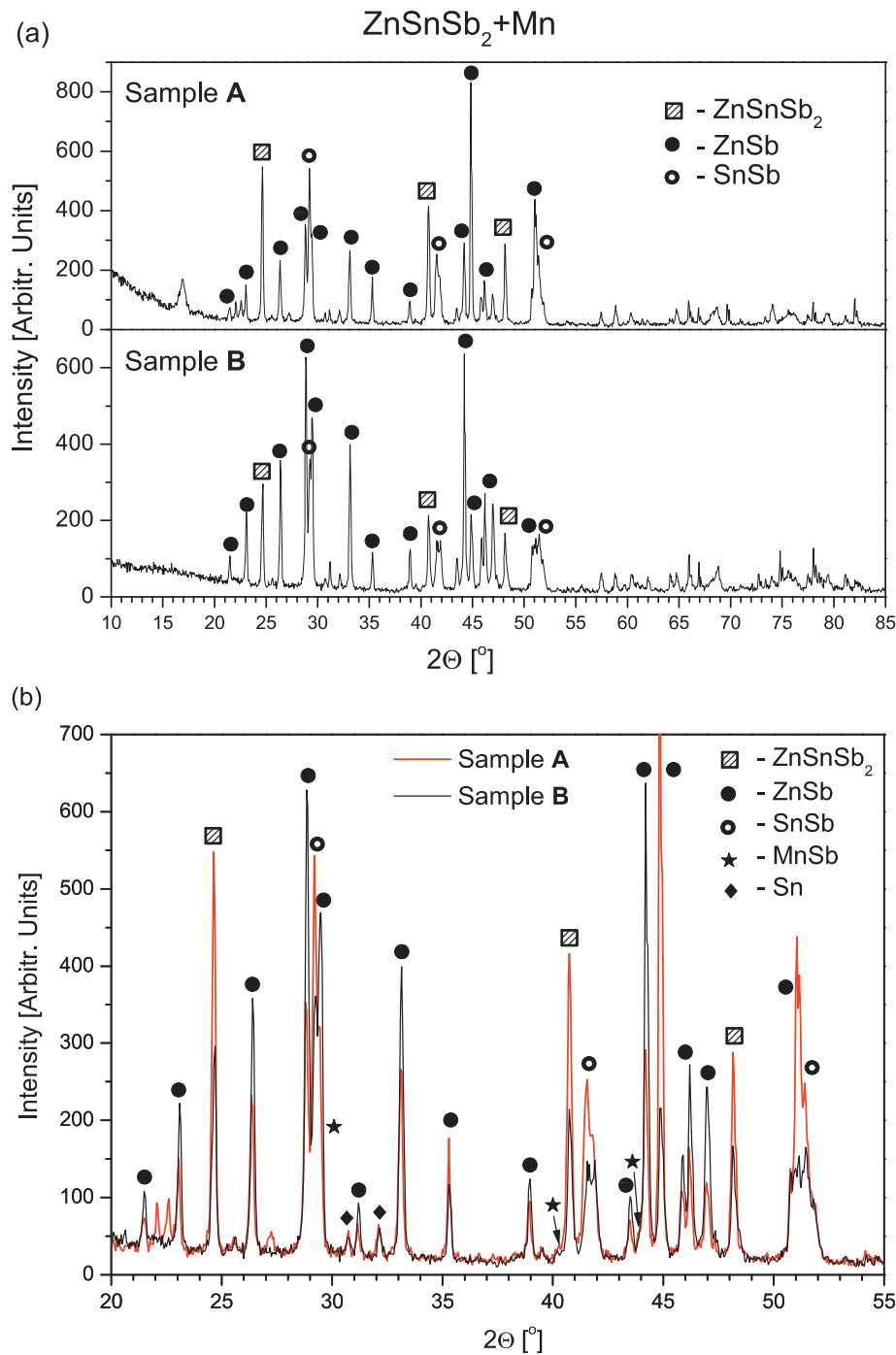


**Fig. 1.** (a) X-ray diffraction pattern for  $\text{ZnSnSb}_2 + \text{Mn}$  samples which contain different amounts of Mn. The registered crystal phases are marked; (b) The two spectra are overlapped to compare their relative intensities.

materials, as well as their electrical and thermal conductivity, and their interdependence.

$\text{ZnSnSb}_2$  is not a homogeneous material, and the consequence is that even two samples from the same crystal can have significantly different properties. This is not surprising given the complicated  $\text{ZnSnSb}_2$  microstructure. Our goal was to analyze the relationship between microstructures, their phonons and free carriers, their conditionality and interactions. For this purpose we used x-ray diffraction, optical microscopy, AFM and IR spectroscopy measurements. Obtained results were analyzed by applying the model for plasmon-phonon interaction.

## 2. Samples and characterization

$\text{ZnSnSb}_2$  semiconductor has a chalcopyrite structure, spatial group I42d, with lattice parameters  $a \approx 6.275 \text{ \AA}$  and  $c \approx 12.55 \text{ \AA}$  and ratio  $c/a$  close to 2.  $\text{ZnSnSb}_2$  melts by a peritectic reaction at  $T = 362 \text{ }^\circ\text{C}$  with a possible phase transformation of the cubic modification into a tetragonal one at  $T = 348 \text{ }^\circ\text{C}$  [11,12]. The  $\text{ZnSnSb}_2 + \text{Mn}$  ferromagnetic semiconductors were synthesized using the method that makes it possible to obtain single crystals at temperatures below the temperature of the peritectic reaction.

The analyzed samples of  $\text{Zn}_{1-x}\text{Mn}_x\text{SnSb}_2$  were synthesized by the direct fusion method. High purity components were used for the

synthesis: zinc single crystals (99.999%), shots of tin (99.999%), anti-mony single crystals (99.999%), and manganese powder (99.999%). They were mixed in stoichiometric ratios.

The reaction mixture was put into a quartz glass tube and heated up to 631 °C. After that, ampoules were quenched to 355 °C and then annealed at 355 °C. This is described in more detail in the papers [12,13]. The synthesized crystals were cut into slices of about 1.5 mm thickness.

The chemical composition of the samples ( $x$ ) was determined using the energy dispersive x-ray fluorescence method (EDXRF) [10]. Obtained results showed that average Mn content ( $x$ ) in the samples is between 0.027 and 0.138. All the studied crystals had the correct stoichiometry of  $Zn_{1-x}Mn_xSnSb_2$  alloy equal to  $1-x : x : 1 : 2$ , within our measurement accuracy of about 10% of the  $x$  value.

Based on the magnetotransport measurements [10] it was found that electrical and magnetotransport parameters, such as resistivity, carrier concentration, and carrier mobility, do not depend linearly on composition, i.e. on the Mn content. Therefore, as mentioned above, two samples with a considerable difference in free-carrier concentrations were selected. The sample with  $x = 0.027$  and  $p = 13 \times 10^{21} \text{ cm}^{-3}$  was labeled as sample A and the one with  $x = 0.076$  and  $p = 1.2 \times 10^{21} \text{ cm}^{-3}$  as sample B. In this way we wanted to determine the connection between the free carriers and the structural and optical properties of the alloy.

The structural properties of these samples were investigated by the XRD powder technique. Measurements were done using a Philips PW 1050 diffractometer equipped with a PW 1730 generator, 40 kV  $\times$  20 mA, using Ni filtered Co K $\alpha$  radiation of 0.1778897 nm at room temperature. The x-ray diffraction patterns were collected during 2 h in the range of 10–100° with a scanning step of 0.05° and 10 s scanning time per step. Phase analysis showed that besides the main phase of chalcopyrite  $ZnSnSb_2$ , the orthorhombic  $ZnSb$ , rhombohedral  $SnSb$ , and hexagonal  $MnSb$  phases are present in the samples. This is consistent with the literature [8,10].

An optical microscope was used to get an insight into the distribution of different phases of the material along the surface. Images were captured using Olympus BH series modular microscope with UIS objective lenses with 50x and 400x enhancement.

The surfaces of  $ZnSnSb_2 + Mn$  samples were examined in detail using Atomic Force Microscope (AFM), NTEGRA prima from NTMDT. The topography and phase images were acquired simultaneously by operating the AFM in semi-contact mode. NSG01 probes with a typical resonant frequency of 150 kHz and 10 nm tip apex curvature radius were used.

The far-infrared (FIR) reflectivity measurements were done with a BOMEM DA-8 Fourier-transform infrared spectrometer in the spectral range from 40 to 450  $\text{cm}^{-1}$  at room temperature. A Hyper beamsplitter and deuterated triglycine sulfate (DTGS) pyroelectric detector were used.

### 3. Results and discussion

It is known that during the preparation of  $ZnSnSb_2$  the polycrystalline material is formed, consisting of the main phase and  $ZnSb$ ,  $SnSb$  and  $\beta$ - $Sn$  inclusions [11].

The structure of the two selected samples was investigated by X-ray diffraction measurements. Obtained results with marked phases are presented in Fig. 1. In Fig. 1(b) the overlap of the results is shown, with the aim to compare their relative intensities. The list of XRD peaks positions and their corresponding Miller indices and phases is given in Table 1 in Supplementary Materials.

Besides the chalcopyrite  $ZnSnSb_2$  phase the orthorhombic  $ZnSb$ , rhombohedral  $SnSb$ ,  $Sn$  have also been registered, as well as weak lines from hexagonal  $MnSb$  inclusions. The idea was to detect differences in the structures of these two samples. It is obvious that diffraction lines corresponding to the  $ZnSnSb_2$  phase (squares) are stronger for sample A

**Table 1**  
Expected values of  $ZnSnSb_2$  phonons of  $B_2$  and E symmetries, from literature [26].

Phonon	$B_2^1$	$B_2^2$	$B_2^3$	$E^1$	$E^2$	$E^3$	$E^4$	$E^5$	$E^6$
Estimated value [ $\text{cm}^{-1}$ ]	189	199	70	189	185	195	111	88	54

as well as lines of  $SnSb$  phase (open circles). Also, it is clear that lines corresponding to  $ZnSb$  (black circles) are mostly stronger for sample B. Existence of the  $Sn$  phase is evident, but lines corresponding  $MnSb$  phase are barely visible.

In order to examine the spatial distribution of the existing different crystal phases, the samples were recorded by an optical microscope with two different magnifications (50  $\times$  and 400  $\times$ ). Obtained micrographs are presented in Fig. 2.

Existing phases are clearly visible and they form multiphase structures. It should be noted that this is a very non-homogeneous material and that images from different parts of the samples differed, so the characteristic ones are selected and shown in Fig. 2.

In our previous work [9] is determined that gray fields are  $ZnSnSb_2$  crystal, white ones correspond  $SnSb$  phase and that dark parts consist of  $ZnSb$ . Micrometric crystals of  $MnSb$  in the shape of dark circles were registered also.

Although microstructures of similar shapes have been formed in both samples, it is apparent that the surfaces significantly differ. Based on previous work [8,9,14], it can be concluded that these spherical and needle like microcrystals are  $ZnSb$ ,  $MnSb$ ,  $Sn$ , and  $Sb$  phases formed during crystallization of the material. As can be seen from Fig. 2, the sample B contains a lot of micron-sizes phases relatively evenly distributed over the surface (volume).

In order to more accurately examine the surface of the samples, we used atomic force microscopy (AFM) measurements. The characteristic results are presented in Fig. 3.

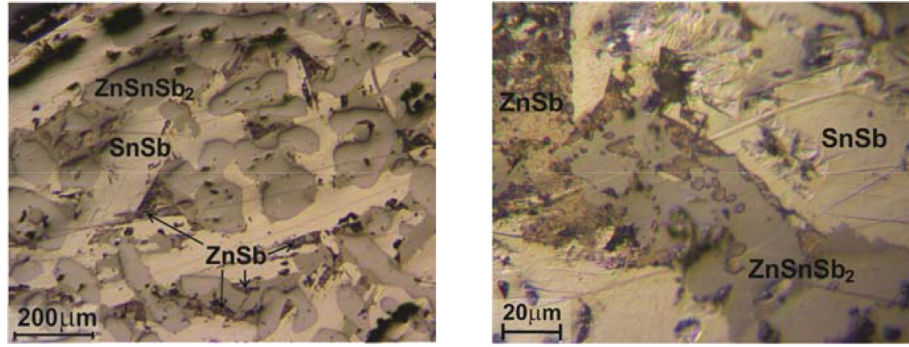
The surfaces of both samples have a granular structure. The sample A has evenly distributed grains over the entire surface with a few larger clusters and an average grain height of around  $\sim 100$  nm (see Fig. 3(a) and the profile in Fig. 3(c)). The phase contrast in Fig. 3(b) originates exclusively from the abrupt changes in the height, indicating that the material properties of the sample A surface are homogeneous. The grains on the surface of the sample B are exclusively arranged into clusters which are not evenly distributed over the surface. The majority of the clusters reach several tens of nm in height, with a few exceptions having a height of  $\sim 100$  nm (see Fig. 3(d) and the profile in Fig. 3(f)). The phase contrast of the sample B surface shows that the larger clusters have a distinct phase shift, seen as dark and white regions in Fig. 3(e), so that clusters have different material properties than the remainder of the surface.

This material is known to be difficult to synthesize and beside  $ZnSnSb_2$  the  $ZnSb$  and  $SnSb$  phases are formed [11,15]. The series of  $Zn_{1-x}Mn_xSnSb_2$  samples were synthesized under the same conditions with the only difference being the starting amounts of manganese and zinc [10]. Obviously, the small variation in the starting mixture causes rather different structures and properties of the materials.

It was found that a large concentration of lattice defects, especially in the cation sublattice, in  $ZnSnSb_2$ , as well as in other II-IV-V<sub>2</sub> semiconductors [16,17], causes a high hole concentration. In particular, Zn vacancies are those defects that lead to a very high concentration of holes [18,19,20]. Typical hole concentration in  $ZnSnSb_2$  is  $10^{20} \text{ cm}^{-3}$  [15–20], in two-component p-type  $ZnSb$  it is  $10^{19} \text{ cm}^{-3}$  [18,19], while  $SnSb$  is a n-type material with metallic character and electron concentration of about  $10^{22} \text{ cm}^{-3}$  at 1.8 K [21]. Evidently, the electronic structure is very complex in this material.

It is difficult to say exactly what is the cause of different hole concentrations in the  $Zn_{1-x}Mn_xSnSb_2$  samples, but it could be assumed that Zn vacancies are the main reason. Sample A has a higher content of

## Sample A



## Sample B

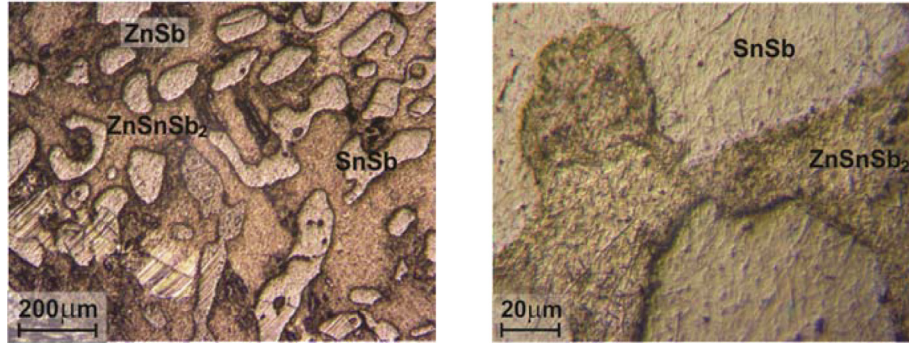


Fig. 2. Micrographs of the ZnSnSb<sub>2</sub> + Mn samples surfaces with magnifications of 50 × and 400 ×.

SnSb, which is related to a higher deficiency of Zn atoms, and therefore higher hole concentration. So, the different concentrations of free carriers in the samples are a consequence of various defects and microstructures which are formed.

In order to examine the interaction of free carriers and a lattice, the far-infrared reflectivity spectra in the range 40–450 cm<sup>-1</sup> at room temperature have been recorded. Obtained spectra are shown in Fig. 4.

It is obvious that the most distinct difference between the spectra relates to wave numbers above 220 cm<sup>-1</sup>, where the high carrier concentration has a main influence. Also, in the range from 120 to 180 cm<sup>-1</sup> the spectrum for sample B (black line) contains some phonon lines which are absent or attenuated in the spectrum for sample A (red line).

A detailed analysis of the obtained results was necessary. For the analysis of the spectra the fitting procedure which includes plasmon-phonon interaction was applied.

#### 4. Plasmon - phonon interaction

In materials with high free carrier concentration a plasmon-phonon interaction should be taken into account, as it significantly affects the properties of the material. Its influence on the dielectric properties of the material is important for the analysis of the reflection spectra.

A theoretical model of the dielectric function in bulk materials [22] has been applied. The dielectric function  $\epsilon(\omega)$  describes dielectric properties of single crystal and includes classical oscillators corresponding to the TO-modes, and Drude part which takes into account the free carrier contribution:

$$\epsilon(\omega) = \epsilon_{\infty} + \sum_{k=1}^l \frac{\epsilon_{\infty}(\omega_{LOk}^2 - \omega_{TOk}^2)}{\omega_{TOk}^2 - \omega^2 - i\gamma_{TOk}\omega} - \frac{\epsilon_{\infty}\omega_p^2}{\omega(\omega + i\Gamma_p)} \quad (1)$$

In this equation  $\epsilon_{\infty}$  is the high-frequency dielectric constant,  $\omega_{TOk}$  and  $\omega_{LOk}$  are the transverse and longitudinal optical-phonon frequencies,  $l$  is the number of phonons,  $\omega_p$  is the plasma frequency,  $\gamma_{TOk}$

and  $\Gamma_p$  are the phonon and plasmon damping. The use of such a dielectric function is valid in multiphase materials, since it is based on a phenomenological approach where the effective values of the material parameters are used, e.g.  $\omega_p^2 = \omega_{p1}^2 + \omega_{p2}^2 + \omega_{p3}^2 + \dots$ .

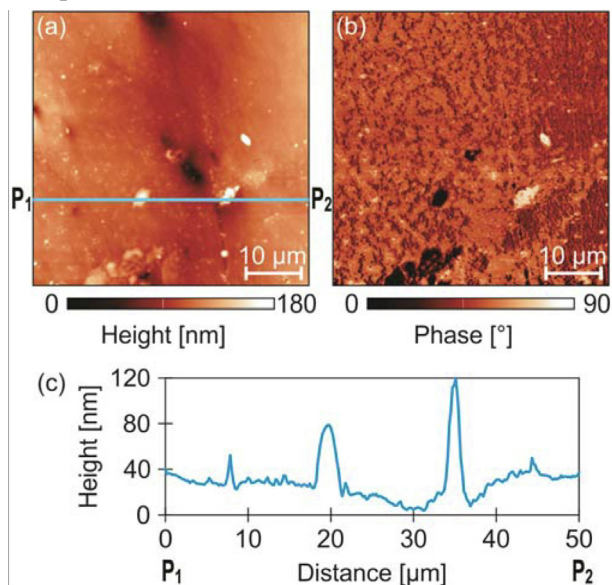
As our ZnSnSb<sub>2</sub> + Mn samples have high concentration of free-carriers ( $p$ ), and therefore high values of  $\omega_p$  ( $\omega_p^2 \sim p$ ), it is expected that plasma interacts with phonons. As a result the phonon frequencies are changed, i.e. their positions are shifted from the expected values. The phonon lines observed at the reflection spectra are these shifted modes i.e. coupled plasmon-phonon modes. So, the situation is much clearer if the dielectric function which takes a plasmon-phonon interaction in advance is used [23,24]. It also allows the possibilities that more than one phonon interact with plasma as well as existence of uncoupled phonons. That dielectric function is:

$$\epsilon(\omega) = \epsilon_{\infty} \frac{\prod_{j=1}^{n+1} (\omega^2 + i\gamma_{ij}\omega - \omega_{ij}^2)}{\omega(\omega + i\Gamma_p) \prod_{i=1}^n (\omega^2 + i\gamma_{ii}\omega - \omega_{ii}^2)} \cdot \prod_{k=1}^s \frac{\omega^2 + i\gamma_{LOk}\omega - \omega_{LOk}^2}{\omega^2 + i\gamma_{TOk}\omega - \omega_{TOk}^2} \quad (2)$$

The first fraction in Eq. (2) describes coupling of a plasmon and  $n$  LO phonons, where parameters  $\omega_{ij}$  and  $\gamma_{ij}$  are eigenfrequencies and damping coefficients of the longitudinal component of the coupled phonons.  $\omega_{ii}$  and  $\gamma_{ii}$  are frequencies and damping of transverse component of these phonons.  $\Gamma_p$  is the plasma damping. The second factor in Eq. (2) represents  $s$  uncoupled phonons of the crystal, wherein  $\omega_{LOk}$  ( $\omega_{TOk}$ ) and  $\gamma_{LOk}$  ( $\gamma_{TOk}$ ) are LO (TO) frequencies and damping coefficients of the  $k$ -th uncoupled phonon of the crystal.

The analysis of the obtained reflection spectra was performed by a fitting procedure, by adjusting the parameters of Eq. (2) in order to obtain a match between the experimental and theoretical curves. The values of  $\omega_{ij}$  and  $\omega_{ii}$  are directly obtained in this way while the  $\omega_p$  and  $\omega_{LO}$  values are calculated [25]. It can be seen that the positions of the  $\omega_{l2}$  and  $\omega_{l4}$  are significantly different for samples A and B. The behavior of phonons and interactions with plasma were analyzed based on the data thus obtained.

Sample A



Sample B

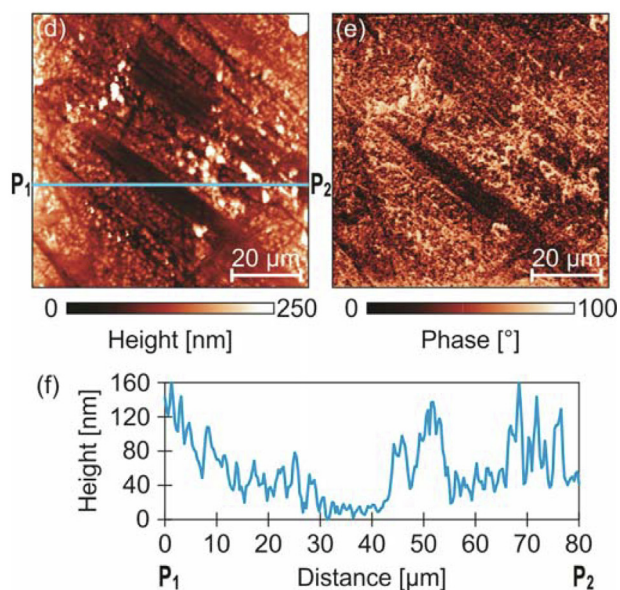


Fig. 3. (a) AFM topography and (b) corresponding phase-contrast image of sample A; (c) Height profile taken along the straight solid line in (a) from point P<sub>1</sub> to point P<sub>2</sub>; Figures (d), (e), and (f) refer to sample B in the same way.

The phonons of ZnSnSb<sub>2</sub> which are IR active are known from literature [26], and they are of B<sub>2</sub> and E symmetries. Their estimated values are given in Table 1.

Plasmon - phonon interaction commonly refers to the coupling of the plasma and one phonon [27]. In that case two coupled modes appear ω<sub>11</sub> and ω<sub>12</sub>, often labeled as ω<sub>+</sub> and ω<sub>-</sub>. In the case of ZnSnSb<sub>2</sub>, based on data obtained by fitting procedure, it was established that the plasma interacts with three phonons of B<sub>2</sub> symmetry [28,29,30]. As a result of that their positions are shifted and instead three B<sub>2</sub> modes there are four coupled modes ω<sub>11</sub>, ω<sub>12</sub>, ω<sub>13</sub> and ω<sub>14</sub>. Obtained values are shown as black points in Fig. 6. Their positions are different for the two samples because of the different influences of the plasma (ω<sub>p</sub><sup>2</sup> ~ p). Because of the high plasma frequency of sample A, the ω<sub>14</sub> has high value of 675 cm<sup>-1</sup> which is outside of the measured range.

For ease of analysis, it is common to draw a dependency diagram of obtained parameters (ω<sub>ij</sub>, ω<sub>b</sub>, ω<sub>TO</sub>, ω<sub>LO</sub>) on plasma frequency ω<sub>p</sub>, as

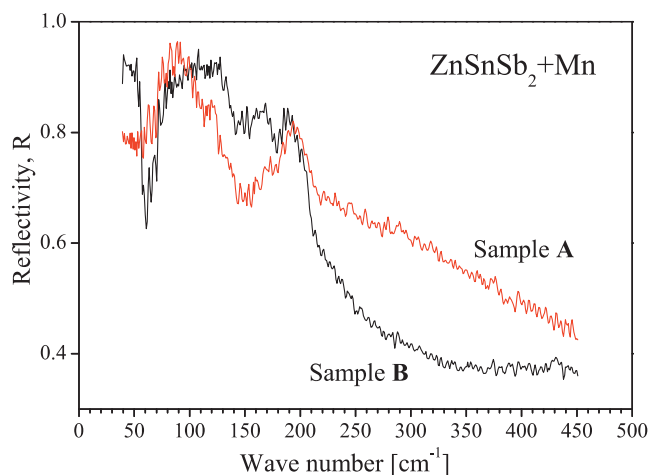


Fig. 4. Far-infrared reflectivity spectra of ZnSnSb<sub>2</sub> + Mn.

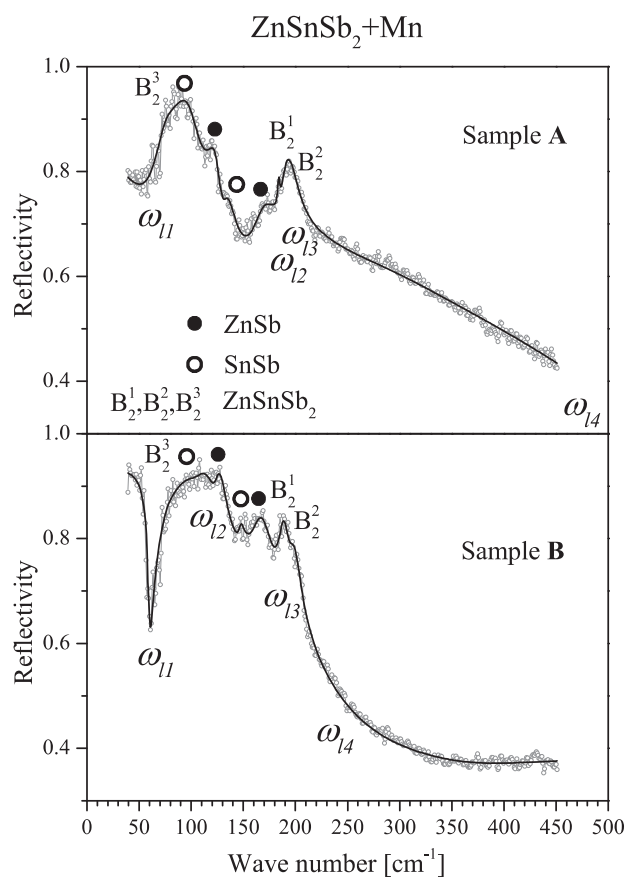
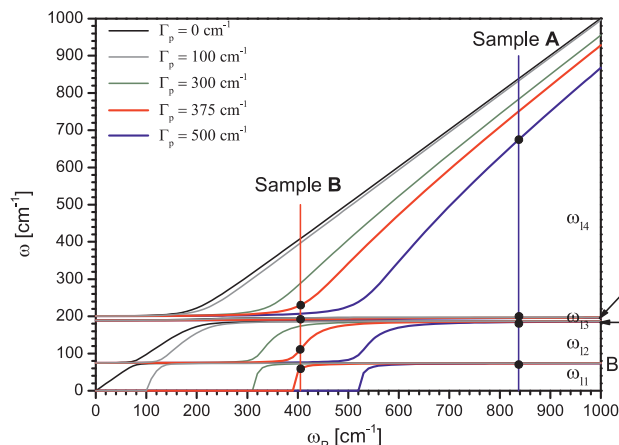


Fig. 5. Analyzed reflection spectra; experimental data are represented by circles while black lines are theoretical curves; registered optical phonons are indicated on the spectra.

shown in Fig. 6. The full lines are solutions of Re{ε(ω)} = 0 from Eq. (1). It should be noted that line ω<sub>13</sub> between B<sub>2</sub><sup>1</sup> and B<sub>2</sub><sup>2</sup> phonons is barely visible because they are very close. The lines are calculated for five different values of plasma damping Γ<sub>p</sub> (Fig. 6) (Γ<sub>p</sub> = 1/τ, where τ is a lifetime of plasmon). This was done to determine Γ<sub>p</sub> interdependence with plasmon - phonon interaction.

The obtained values of plasma damping and plasma frequency of samples A and B are: Γ<sub>pA</sub> = 500 cm<sup>-1</sup>, Γ<sub>pB</sub> = 375 cm<sup>-1</sup>, ω<sub>pA</sub> = 837 cm<sup>-1</sup> and ω<sub>pB</sub> = 405 cm<sup>-1</sup>. It should be noted that these parameters represent the effective values that describe the sample as a



**Fig. 6.** Analysis of plasmon - three-phonons interaction; Full lines are obtained from Eq. (1), as the solutions of  $\text{Re}\{\epsilon(\omega)\} = 0$ , for various values of  $\Gamma_p$ ; Black points represent experimentally obtained data for  $\omega_{ij}$  for both samples (Eq. (2)).

whole. It could be expected (based on  $p_A$  and  $p_B$  values and  $\omega_p^2 \sim p$ ) that  $\omega_{pA}$  and  $\omega_{pB}$  differ about three times, which was not established. Plasma frequency is defined as  $\omega_p^2 = (n_p e^2) / (\epsilon_0 \epsilon_\infty m_{th}^*)$ , i.e. it includes other parameters of the material. Thus, by determining the plasma frequency and plasma damping the other properties of the material can be analyzed.

Besides phonons of  $B_2$  symmetry which interact with plasma, other  $ZnSnSb_2$  phonons are not registered on the IR reflectivity spectra. However, characteristic phonons of the other phases can be identified, as can be seen in Fig. 5. It was necessary that these phonons are not covered by the plasmon - phonon interaction.  $ZnSb$  modes are noticed at about 125 and 165  $\text{cm}^{-1}$ , which is in agreement with results from the literature [31]. Two modes that correspond to  $SnSb$  phase are at about 94 and 145  $\text{cm}^{-1}$ , which matches the previously obtained data [9,32]. The appearance of these modes is expected due to the significant presence of  $ZnSb$  and  $SnSb$  phases in the samples.  $MnSb$  phonons are not registered, i.e. it was not possible to discern them due to the small amount of that phase.

Based on the performed analyses, it can be seen that different microstructures formed in the investigated samples lead to high concentrations of free carriers, but which are ten times different from each other. Those high values cause plasmon -  $B_2$  phonons interaction. That can be used to analyze optical and electrical properties of the materials, as well as other parameters, such as dielectric constants, effective mass of charge carriers and phonon lifetimes. In this way, the multiphase material with different microstructures was analyzed as a whole.

Investigation of thermoelectric properties of  $ZnSnSb_2$  is a current issue [5,15,33]. The analysis of plasmon - phonon interaction performed in this paper can significantly assist in the study and understanding of thermoelectric processes in this as in other semiconducting polycrystalline materials [34].

## 5. Conclusion

Two samples of  $ZnSnSb_2 + Mn$  with different amounts of manganese were analyzed in this paper. The small difference in the initial composition of the material led to a difference of ten times in the free carrier concentrations. Their structural properties were examined by x-ray diffraction, optical microscopy, and AFM. Several different phases were registered -  $ZnSnSb_2$ ,  $ZnSb$ ,  $SnSb$ , and small amounts of  $Sn$  and  $MnSb$ . These phases form different microstructures, which is related to the large irregularities of the lattice. It was found that the high free carrier concentrations are caused by a large number of defects, especially zinc vacancies.

The optical characteristics of these multiphase materials were

examined, whereby the samples were considered as a whole. Based on the analysis of IR reflection spectra the presence of a plasmon - phonons interaction was confirmed. It was determined that three  $ZnSnSb_2$  phonons of  $B_2$  symmetry interact with plasma, which led to the change of their positions. It is clear that strong plasmon - phonon interaction modifies optoelectronic properties of the  $ZnSnSb_2 + Mn$  samples, and that phonon positions depend on a free carrier concentration. A detailed analysis of this interaction also provides insight into the behavior of other material parameters, such as dielectric constants, effective mass of charge carriers and phonon lifetimes. Also, vibration modes of  $ZnSb$  and  $SnSb$  phases were registered on the spectra. Knowledge of phonon behavior in a material, as well as interaction with plasma, is very important for studying its thermoelectric properties.

## Declaration of competing interest

The authors declare that there is no conflict of interest in this paper.

## Acknowledgement

This work was supported under the Agreement of Scientific Collaboration between Polish Academy of Science and Serbian Academy of Sciences and Arts. The work in Serbia was supported by the Serbian Ministry of Education, Science and Technological Development through Project 45003.

## Appendix A. Supplementary material

Supplementary data to this article can be found online at <https://doi.org/10.1016/j.infrared.2020.103345>.

## References

- [1] J.L. Shay, J.H. Wernick, Ternary Chalcopyrite Semiconductors: Growth, Electronic Properties, and Applications, Chapter 3 - Electronic Structure of II-IV-V<sub>2</sub> Compounds, Pergamon Press, New York, 1975, pp. 79–109 <https://doi.org/10.1016/B978-0-08-017883-7.50008-1>.
- [2] W. Dobrowolski, J. Kossut, T. Story. II–VI and IV–VI Diluted Magnetic Semiconductors – New Bulk Materials and Low-Dimensional Quantum Structures. Handbook of Magnetic Materials 15 (2003) pp. 289–377, (Elsevier, Amsterdam, 2003). [https://doi.org/10.1016/S1567-2719\(03\)15003-2](https://doi.org/10.1016/S1567-2719(03)15003-2).
- [3] L. Kilanski, M. Górska, W. Dobrowolski, E. Dynowska, M. Wójcik, B.J. Kowalski, J.R. Anderson, C.R. Rotundu, D.K. Maude, S.A. Varnavskiy, I.V. Fedorchenko, S.F. Marenkin, Magnetism and magnetotransport of strongly disordered  $Zn_{1-x}Mn_xGeAs_2$  semiconductor: The role of nanoscale magnetic clusters, J. Appl. Phys. 108 (2010) 073925, <https://doi.org/10.1063/1.3490231>.
- [4] S.F. Marenkin, A.D. Izotov, I.V. Fedorchenko, V.M. Novotortsev, Manufacture of magnetic granular structures in semiconductor-ferromagnet systems, Russ. J. Inorg. Chem. 60 (2015) 295300, <https://doi.org/10.1134/S0036023615030146>.
- [5] M. Ito, Y. Ohishi, H. Muta, K. Kurosaki, S. Yamanaka, Thermoelectric properties of Zn-Sn-Sb based alloys, Mater. Res. Soc. Symp. Proc. 1314 (2011), <https://doi.org/10.1557/opl.2011.618>.
- [6] P. Balasubramanian, M. Battabyal, D. Sivaprasasam, R. Gopalan, On the formation of phases and their influence on the thermal stability and thermoelectric properties of nanostructured zinc antimonide, J. Phys. D: Appl. Phys. 50 015602 (11 (2017) pp), <https://doi.org/10.1088/1361-6463/50/1/015602>.
- [7] G. Coquil, B. Fraisse, S. Biscaglia, D. Ayme-Perrot, M.T. Sougrati, L. Monconduit,  $ZnSnSb_2$  anode: A solid solution behavior enabling high rate capability in Li-ion batteries, J. Power Sour. 441 (2019) 227165, <https://doi.org/10.1016/j.jpowsour.2019.227165>.
- [8] O. Zobac, J. Sopousek, J. Bursik, A. Zemanova, P. Roupceva, Experimental Study of the Sb-Sn-Zn Alloy System, Metall. Mater. Trans. 45A (2014) 1181–1188, <https://doi.org/10.1007/s11661-013-2104-1>.
- [9] M. Romcevic, M. Gilic, L. Kilanski, W. Dobrowolski, I.V. Fedorchenko, S.F. Marenkin, N. Romcevic, Phonon properties of  $ZnSnSb_2 + Mn$  semiconductors: Raman spectroscopy, J. Raman Spectrosc. 49 (2018) 1678–1685, <https://doi.org/10.1002/jrs.5421>.
- [10] L. Kilanski, M. Górska, A. Slawska-Waniewska, S. Lewinska, R. Szymczak, E. Dynowska, A. Podgorni, W. Dobrowolski, U. Ralevic, R. Gajic, N. Romcevic, I.V. Fedorchenko, S.F. Marenkin, High temperature magnetic order in  $Zn_{1-x}Mn_xSnSb_2 + MnSb$  nanocomposite ferromagnetic semiconductors, J. Phys.:Condens. Matter. 28 (2016) 336004, <https://doi.org/10.1088/0953-8984/28/33/336004>.
- [11] A. Tenga, F.J. Garcia-Garcia, A.S. Mikhaylushkin, B. Espinosa-Arronte, M. Andersson, U. Haussermann, Sphalerite – Chalcopyrite Polymorphism in Semimetallic  $ZnSnSb_2$ , Chem. Mater. 17 (2005) 6080–6085, <https://doi.org/10.1021/cm042031a>.



- 1021/cm0516053.
- [12] A. Tenga, F.J. Garcia-Garcia, Y. Wu, N. Newman, U. Hausermann, Metal-nonmetal transition in the sphalerite-type solid solution  $[\text{ZnSnSb}_2]_{1-x}[\text{2(InSb)}]_x$ , *J. Solid State Chem.* 182 (2009) 1438–1442, <https://doi.org/10.1016/j.jssc.2009.03.015>.
- [13] M. Bostrom, S. Hovmoller, Preparation and Crystal Structure of the Pseudo-Decagonal Approximant  $\text{Mn}_3\text{Ga}_5$ , *J. Solid State Chem.* 153 (2000) 398–403, <https://doi.org/10.1006/jssc.2000.8790>.
- [14] C. Wang, Y. Xu, S. Yang, H. Jiang, J. Li, J. Zhu, S. Yang, X. Liu, Experimental Determination of Phase Equilibria in the Sn-Zn-Sb System, *J. Phase Equil. Diff.* 36 (2015) 350–356, <https://doi.org/10.1007/s11669-015-0387-1>.
- [15] A. Nomura, S. Choi, M. Ishimaru, A. Kosuga, T. Chasapis, S. Ohno, G.J. Snyder, Y. Ohishi, H. Muta, S. Yamanaka, K. Kurosaki, Chalcopyrite  $\text{ZnSnSb}_2$ : A Promising Thermoelectric Material, *ACS Appl. Mater. Interf.* 10 (2018) 43682–43690, <https://doi.org/10.1021/acsami.8b16717>.
- [16] V.N. Brudnyi, Electronic properties and pinning of the Fermi level in irradiated II-IV- $\text{V}_2$  semiconductors, *Semiconductors* 43 (2009) 1146–1154, <https://doi.org/10.1134/S1063782609090085>.
- [17] V.G. Voevodin, S.N. Grinyaev, O.V. Voevodina, Nonstoichiometry and point defects in nonlinear optical crystals  $\text{A}^2\text{B}^4\text{C}_2^5$ , *Mater. Sci. Semicond. Proces.* 6 (2003) 385–388, <https://doi.org/10.1016/j.mssp.2003.07.006>.
- [18] X. Song, M. Schrade, N. Maso, T.G. Finstad, Zn vacancy formation, Zn evaporation and decomposition of  $\text{ZnSb}$  at elevated temperatures: Influence on the microstructure and the electrical properties, *J. Alloys Comp.* 710 (2017) 762–770, <https://doi.org/10.1016/j.jallcom.2017.03.339>.
- [19] L.V. Prokofieva, P.P. Konstantinov, A.A. Shabal'din, On the tin impurity in the thermoelectric compound  $\text{ZnSb}$ : Charge-carrier generation and compensation, *Semicond* 50 (2016) 741–750, <https://doi.org/10.1134/S1063782616060208>.
- [20] L. Bjerg, G.K.H. Madsen, B.B. Iversen, Ab initio Calculations of Intrinsic Point Defects in  $\text{ZnSb}$ , *Chem. Mater.* 24 (2012) 2111–2116, <https://doi.org/10.1021/cm300642t>.
- [21] B. Liu, J. Wu, Y. Cui, H. Wang, Y. Liu, Z. Wang, Z. Ren, G. Cao, Superconductivity in  $\text{SnSb}$  with a natural superlattice structure, *Supercond. Sci. Technol.* 31 (2018) 7, <https://doi.org/10.1088/1361-6668/aae6fe> 125011.
- [22] Abstreiter G., Cardona M., Pinczuk A. Light scattering by free carrier excitations in semiconductors. In: Cardona M., Güntherodt G. (eds) *Light Scattering in Solids IV*. Topics in Applied Physics, vol 54. Springer, Berlin, Heidelberg. (1984) [https://doi.org/10.1007/3-540-11942-6\\_20](https://doi.org/10.1007/3-540-11942-6_20).
- [23] A.A. Kukharskii, Plasmon-phonon coupling in GaAs, *Solid State Commun.* 13 (1973) 1761–1765, [https://doi.org/10.1016/0038-1098\(73\)90724-2](https://doi.org/10.1016/0038-1098(73)90724-2).
- [24] N. Romcevic, M. Romcevic, W.D. Dobrowolski, L. Kilanski, M. Petrovic, J. Trajic, B. Hadzic, Z. Lazarevic, M. Gilic, J.L. Ristic-Djurovic, N. Paunovic, A. Reszka, B.J. Kowalski, I.V. Fedorchenko, S.F. Marenki, Far-infrared spectroscopy of  $\text{Zn}_{1-x}\text{MnxGeAs}_2$  single crystals: Plasma damping influence on plasmon – Phonon interaction, *J. Alloys Comp.* 649 (2015) 375–379, <https://doi.org/10.1016/j.jallcom.2015.07.087>.
- [25] J. Trajic, N. Romcevic, M. Gilic, M. Petrovic Damjanovic, M. Romcevic, V.N. Nikiforov, Optical properties of  $\text{PbTe}_{0.95}\text{S}_{0.05}$  single crystal at different temperatures: Far - infrared study, *Optoelec. Adv. Mater. Rap. Comm.* 6 (2012) 543–546.
- [26] F.W. Ohrendorf, H. Haeuselner, Lattice Dynamics of Chalcopyrite Type Compounds. Part I. Vibrational Frequencies, *Cryst. Res. Technol.* 34 (1999) 339–349, [https://doi.org/10.1002/\(SICI\)1521-4079\(199903\)34:3<339::AID-CRAT339>3.0.CO;2-E](https://doi.org/10.1002/(SICI)1521-4079(199903)34:3<339::AID-CRAT339>3.0.CO;2-E).
- [27] Klein M.V. Electronic Raman Scattering. In: Cardona M. (eds) *Light Scattering in Solids*. Topics in Applied Physics, vol 8. Springer, Berlin, Heidelberg (1975). [https://doi.org/10.1007/978-3-540-37568-5\\_4](https://doi.org/10.1007/978-3-540-37568-5_4).
- [28] M. Petrovic, N. Romcevic, J. Trajic, W.D. Dobrowolski, M. Romcevic, B. Hadzic, M. Gilic, A. Mycielski, Far-infrared spectroscopy of  $\text{CdTe}_{1-x}\text{Se}_x(\text{In})$ : Phonon properties, *Infrared Phys. Tech.* 67 (2014) 323–326, <https://doi.org/10.1016/j.infrared.2014.08.010>.
- [29] M. Romcevic, N. Romcevic, W. Dobrowolski, L. Kilanski, J. Trajic, D.V. Timotijevic, E. Dynowska, I.V. Fedorchenko, S.F. Marenkin, Optical properties and plasmon – Two different phonons coupling in  $\text{ZnGeAs}_2 + \text{Mn}$ , *J. Alloys Comp.* 548 (2013) 33–37, <https://doi.org/10.1016/j.jallcom.2012.09.017>.
- [30] I.J. Luxmoore, C.H. Gan, P.Q. Liu, F. Valmorra, P. Li, J. Faist, G.R. Nash, Strong coupling in the far-infrared between graphene plasmons and the surface optical phonons of silicon dioxide, *ACS Photonics* 1 (2014) 1151, <https://doi.org/10.1021/ph500233s>.
- [31] D.V. Smirnov, D.V. Mashovets, S. Pasquier, J. Leotin, P. Puech, G. Landa, Yu.V. Roznovan, Long-wavelength optical phonons of  $\text{Cd}_x\text{Zn}_{1-x}\text{Sb}$  mixed crystals, *Semicond. Sci. Technol.* 9 (1994) 333–337.
- [32] P. Nithyadharseni, M.V. Reddy, B. Nalini, M. Kalpana, B.V.R. Chowdari, Sn-based Intermetallic Alloy Anode Materials for the Application of Lithium Ion Batteries, *Electrochim. Acta* 161 (2015) 261–268, <https://doi.org/10.1016/j.electacta.2015.02.057>.
- [33] Yu M. BasalaeV, Ab Initio Study of the  $\text{ZnSnSb}_2$  Semiconductor, *Semiconductors* 52 (2018) 1715–1720, <https://doi.org/10.1134/S1063782618130043>.
- [34] Q. Xu, J. Zhou, T.H. Liu, G. Chen, Effect of electron-phonon interaction on lattice thermal conductivity of SiGe alloys, *Appl. Phys. Lett.* 115 (2019) 023903, <https://doi.org/10.1063/1.5108836>.

# Selected transport, vibrational, and mechanical properties of low-dimensional systems under strain **F**

Cite as: J. Appl. Phys. **125**, 154301 (2019); <https://doi.org/10.1063/1.5054120>

Submitted: 29 August 2018 • Accepted: 15 March 2019 • Published Online: 16 April 2019

 V. Celebonovic,  J. Pesic, R. Gajic, et al.

## COLLECTIONS

**F** This paper was selected as Featured



View Online



Export Citation



CrossMark

## ARTICLES YOU MAY BE INTERESTED IN

[Strain engineering in functional 2-dimensional materials](#)

Journal of Applied Physics **125**, 082402 (2019); <https://doi.org/10.1063/1.5053795>

[Strain-tuning of the electronic, optical, and vibrational properties of two-dimensional crystals](#)

Applied Physics Reviews **8**, 021318 (2021); <https://doi.org/10.1063/5.0037852>

[Strain engineering in monolayer WS<sub>2</sub>, MoS<sub>2</sub>, and the WS<sub>2</sub>/MoS<sub>2</sub> heterostructure](#)

Applied Physics Letters **109**, 173105 (2016); <https://doi.org/10.1063/1.4966218>



Time to get excited.  
Lock-in Amplifiers – from DC to 8.5 GHz

[Find out more](#)

 Zurich  
Instruments

# Selected transport, vibrational, and mechanical properties of low-dimensional systems under strain

Cite as: J. Appl. Phys. **125**, 154301 (2019); doi: [10.1063/1.5054120](https://doi.org/10.1063/1.5054120)

Submitted: 29 August 2018 · Accepted: 15 March 2019 ·

Published Online: 16 April 2019



View Online



Export Citation



CrossMark

V. Celebonovic,<sup>1,a)</sup> J. Pesic,<sup>2</sup> R. Gajic,<sup>2</sup> B. Vasic,<sup>2</sup> and A. Matkovic<sup>2,3</sup>

## AFFILIATIONS

<sup>1</sup>LEX Laboratory, Institute of Physics, University of Belgrade, Pregrevica 118, 11080 Belgrade, Serbia

<sup>2</sup>Graphene Laboratory, Center for Solid State Physics and New Materials, Institute of Physics, University of Belgrade, Pregrevica 118, 11080 Belgrade, Serbia

<sup>3</sup>Institute of Physics, Montanuniversität Leoben, Franz Josef Strasse 18, Leoben 8700, Austria

<sup>a)</sup>[vladan@ipb.ac.rs](mailto:vladan@ipb.ac.rs)

## ABSTRACT

The aim of the present paper is to discuss some recent results concerning the behavior of low-dimensional materials under strain. This concerns the electrical conductivity calculations of 1D structures under strain, within the Hubbard model, as well as *ab initio* investigations of phonon, electron-phonon, and superconducting properties of doped graphene and MgB<sub>2</sub> monolayer. Two different experimental approaches to strain engineering in graphene have been considered regarding local strain engineering on monolayer flakes of graphene using atomic force microscopy and dynamic plowing lithography technique as well as the effects of mechanical straining on liquid phase exfoliated graphene and change of sheet resistance of graphene films.

Published under license by AIP Publishing. <https://doi.org/10.1063/1.5054120>

## I. INTRODUCTION

Strain engineering is widely used in materials science to tune various properties of materials and eventually enhance the performance of devices. Engineering of strain in low-dimensional materials promises to revolutionize the field of nanotechnology with the possibility of creating new artificial materials. Two-dimensional materials are a remarkable ground to study the influence of strain, as they can sustain very large deformations without breaking. The unique mechanical properties of graphene present an excellent opportunity for research of strain-induced modifications; for example, graphene is the strongest 2D material ever measured, with Young's modulus of 1 TPa and an intrinsic strength of 130 GPa.<sup>1</sup> What is more important is its ability to sustain reversible elastic tensile strain as large as 25%<sup>1</sup> and this allows the possibility for strain engineering in order to modify or tune graphene properties for specific applications. Since its discovery in 2004 with the size of a micrometer,<sup>2</sup> graphene has attracted increased attention. It is a truly two-dimensional (2D) plane of sp<sub>2</sub>-hybridized carbon atoms arranged in a honeycomb lattice. The unit cell has two identical

carbon atoms giving rise to electronic linear dispersion near the Fermi level and peculiar massless electron dynamics governed by the Dirac–Weyl relativistic equations.<sup>3,4</sup> This unique lattice of graphene leads to many extraordinary properties that include exceptionally high charge carrier mobility,<sup>2,3</sup> high mechanical strength and elasticity,<sup>1,5</sup> optical transparency,<sup>6,7</sup> and a wide variety of possible chemical modifications.<sup>8–10</sup> All of these properties make graphene an ideal material to investigate not only fundamental scientific problems in condensed matter physics, but also practically a wide variety of applications including flexible electronics,<sup>11–14</sup> optoelectronics,<sup>15,16</sup> sensors, and transistors.<sup>17,18</sup> The outstanding stretchability of graphene has made it suitable for application in flexible electronic devices as well as in superconducting electronics based on 2D materials since the electron-phonon (e-ph) coupling is greatly enhanced by the biaxial strain causing the change of superconducting critical temperatures.<sup>19–23</sup>

In this paper, we study and discuss selected transport, vibrational, and mechanical properties of low-dimensional systems under strain with the main focus on strain-induced changes on

conductivity. In Sec. II, we present theoretical approaches for strain engineering in low-dimensional systems. Section II A discusses the effects of the application of strain on conductivity studied in the one-dimensional Hubbard model. Section II B presents the *ab initio* study of the effects of the biaxial strain on doped graphene and isostructural new material  $\text{MgB}_2$  monolayer, namely, both materials are considered superconducting,<sup>24–26</sup> and here it is demonstrated that biaxial strain can cause softening of the phonons, affecting the total electron-phonon interaction and resulting in a significantly higher critical transition temperature. These two-dimensional materials not only share a similar structure, a hexagonal structure with an adatom in the center of a hexagon, but also have a similar electronic structure, and very interestingly, both are electron-phonon mediated superconductors.<sup>1,34–39</sup> Engineering of strain in those materials opens the road to new artificial structures with the improved electron-phonon coupling and higher critical temperatures.

Application of the strain in graphene and 2D materials is an intensively studied topic, both theoretically and experimentally;<sup>1,40,41</sup> for example, application of the strain on graphene can induce changes in the vibrational properties,<sup>42,43</sup> in the electronic bandgaps<sup>44,45</sup> and significant changes in conductivity at both local and macroscopic levels.<sup>46–48</sup> The type of the strain is a very important feature, since the graphene lattice symmetry determines its band structure. The breaking of the hexagonal symmetry will modify the band structure of graphene,<sup>49,50</sup> causing the opening of the bandgap and many other effects.<sup>51,52</sup>

In intercalated graphene, it is known that not all types of intercalant atoms produce superconductivity or significantly increase  $T_c$ . In Li-intercalated graphene (Li-GIC), a strong confinement for electrons along the z-axis exists and it prevents the occupation of the interlayer state. In the monolayer,<sup>24,35</sup> there is a significant reduction of a charge transfer that is beneficial for superconductivity. The charge transfer from the interlayer state formed by the presence of the adatom is a crucial ingredient. Though it is necessary, the completion of the charge transfer is deleterious for the enhancement of the superconductivity.<sup>24,35</sup> For example, in the Li-GIC, a strong confinement along the z-axis exists and it prevents the occupation of the interlayer state. When the quantum confinement is removed as in the monolayer, it results in the reduction of charge transfer which is beneficial for the superconductivity. In Sec. III, we discuss the effects of strain, as shown above, on the most prominent example of low-dimensional materials, graphene.

We present two different experimental approaches to strain engineering in graphene. In Sec. III A, we discuss local strain engineering on monolayer flakes of graphene produced by micromechanical exfoliation using atomic force microscopy (AFM) and dynamic plowing lithography (DPL). In Sec. III B, we present the effects of mechanical straining on the liquid phase exfoliated graphene and the change of sheet resistance graphene films obtained in that way. These two techniques are diametrically different, both in results and in the procedure. Micromechanical exfoliation is a clean technique where high-quality, well-defined monolayer samples are produced using the Scotch tape method.<sup>1</sup> However, samples produced this way though very pure, ideal monolayer without vacancies, are small in scale (maximally, hundreds of

micrometers), making this technique excellent for state-of-the-art nanodevices and fundamental research. Nonetheless, for applications, especially macroscopic ones, this kind of production technique is not applicable. Liquid phase exfoliation (LPE) is an alternative where solution processing of graphite flakes breaks van der Waals forces creating liquid graphene dispersion. Samples produced from this dispersion can be very large in scale, macroscopic; however, they are not monolayers, but few-layer graphene flakes overlap in between forming graphene films.<sup>27,28</sup> We study how strain can be engineered in both samples, where in the first experimental section we focus more on a fine technique for the induction of the local strain in monolayer samples, and in the second one, where strain can be induced and engineered in a much more simple way (since we can work with macroscopic samples), the spotlight is on the effect of the strain quality of the film and eventually on sheet resistance, hence conductivity. Straining the monolayer graphene sample shows that a high enough local pressure induced by an AFM tip will result in protrusion at a neighboring point. The generated local strain introduced in this way is well controlled, and it is expected to affect conductivity along protrusion. The other presented case, the sample of which is produced in LPE, shows the change of resistivity with the application of strain, as it is presented that this is not the intrinsic strain of single graphene flakes but is more of a macroscopic effect. The small flakes that the film consists of are deposited onto the elastic substrate, and when mechanical strain is applied, the substrate surface stretches but individual flakes do not get strained. The total resistance of LPE films comes from the points of the overlap between neighboring flakes, and stretching the LPE graphene film results in effective pulling apart of individual flakes, and thus an increase in the sheet resistivity of the whole film (and vice versa).

## II. THEORY

### A. Effects of strain on the conductivity in 1D system—The Hubbard model study

Toward the middle of the last century, the metal to insulator transition was one of the outstanding problems of condensed matter physics. A general model of the metal to insulator transition was proposed by John Hubbard, in a series of papers starting from Ref. 29. Apart from the metal to insulator transition, the Hubbard model has found applications in studies of transport processes in 1D and 2D correlated electron systems. These calculations have often been performed using the memory function method. A detailed review is available in Ref. 30, while the main results are given in the following.

The initial point for a study of the transport properties of any system is the knowledge of its Hamiltonian. Using the second quantization formalism, the Hamiltonian of the 1D Hubbard model has the following form:

$$H = -t \sum_{i=1, \sigma}^N (c_{i+1, \sigma}^{\dagger} c_{i, \sigma} + c_{i, \sigma}^{\dagger} c_{i+1, \sigma}) + U \sum_l n_{l \uparrow} n_{l \downarrow}. \quad (1)$$

The symbols  $N$ ,  $t$ , and  $U$  denote the number of nodes in a lattice, the mean kinetic energy of the electrons (the so-called hopping

energy), and the interaction energy of pairs of electrons with opposing spins on the same lattice node;  $\sigma$  stands for the electron spin. The symbols in the parenthesis denote the creation and annihilation operators.

Calculations of the electrical conductivity have been performed using the memory function method.<sup>30</sup> These basic expressions are

$$\chi_{AB} = \ll A; B \gg = -i \int_0^\infty e^{izt} \langle [A(t), B(0)] \rangle dt, \quad (2)$$

$$\sigma(\omega) = i \frac{\omega_p^2}{4\pi z} \times \left[ 1 - \frac{\chi(z)}{\chi(0)} \right]. \quad (3)$$

The symbol  $\omega_p^2 = \frac{4\pi n_e e^2}{m_e}$  denotes the square of the plasma frequency

and  $\chi_0 = \frac{n_e}{m_e}$  is the zero frequency limit of the dynamical susceptibility.

Expression (2) is the general definition of the linear response of a physical quantity corresponding to operator  $A$  to the perturbation by another physical quantity described by operator  $B$ .  $A(t)$  denotes the Heisenberg representation of operator  $A$ . Inserting  $A = B = [j, H]$ , with  $j$  denoting the current operator and  $H$  the Hamiltonian, leads to the definition of the current-current correlation function. Details of the calculation of the electrical conductivity are presented in Ref. 30. The final result is

$$\sigma_R(\omega_0) = \left( \frac{1}{2\chi_0} \right) \left( \frac{\omega_p^2}{\pi} \right) \frac{1}{\omega_0^2 - (bt)^2} \left( \frac{Ut}{N^2} \right)^2 \times S, \quad (4)$$

where  $S$  denotes the following function:

$$S = \frac{42.49916}{(1 + \exp[\beta(-\mu - 2t)])^2} + \frac{78.2557}{(1 + \exp[\beta(-\mu + 2t) \cos(1 + \pi)])^2} + \frac{bt}{\omega_0 + bt} \left[ \frac{4.53316}{(1 + \exp[\beta(-\mu - 2t)])^2} + \frac{24.6448}{(1 + \exp[\beta(-\mu + 2t) \cos(1 + \pi)])^2} \right]. \quad (5)$$

The symbol  $\mu$  denotes the chemical potential of the electron gas on a 1D lattice, given by the following (Ref. 30 and references therein):

$$\mu = \frac{(\beta t)^6 (ns - 1) |t|}{1.1029 + 0.1694(\beta t)^2 + 0.0654(\beta t)^4}. \quad (6)$$

*The practical calculation of the conductivity:* Inserting values of material parameters into Eqs. (4)–(6) leads to the electrical conductivity expressed as a function of these parameters. Some examples of such calculations have been discussed in Refs. 32–35 and references therein.

As this paper focuses on nanomaterials under strain, this section considers the problem of treating the material under strain within the Hubbard model. This problem is not only of academic, but also of practical, interest. There already exist examples of stretchable electronics (some examples are given in Refs. 31 and 33). By changing an initial material length from  $l_0$  to  $l$ , the strain is defined as

$$\varepsilon = \frac{l - l_0}{l_0}. \quad (7)$$

If a material is subdued to nonzero strain, the overlap between wave functions of electronic wave functions in adjacent atoms changes, leading to changes in the hopping energy and all material parameters which contain the lattice constant. The dependence of the hopping on the interatomic distance is represented by<sup>31</sup>

$$t = t_0 \times \left[ 1 + r + \frac{1}{3} r^2 \right] \exp[-r], \quad (8)$$

where the distance is expressed in Bohr radii.

All expressions used in the calculations discussed in this section are analytically tractable but too long to be explicitly stated here. Therefore, only a few resulting graphs are presented (Fig. 1).

Figure 1 shows the electrical conductivity of a 1D Hubbard model expressed as a function of the strain to which it is exposed. The data are normalized to 1 at  $n = 1.25$ ,  $t = 0.01$ ,  $T = 116$ ,  $\varepsilon = 0$ .

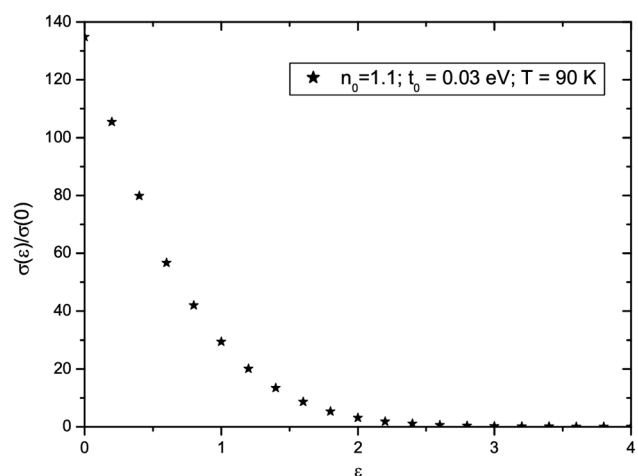


FIG. 1. Normalized conductivity of 1D HM as a function of strain.

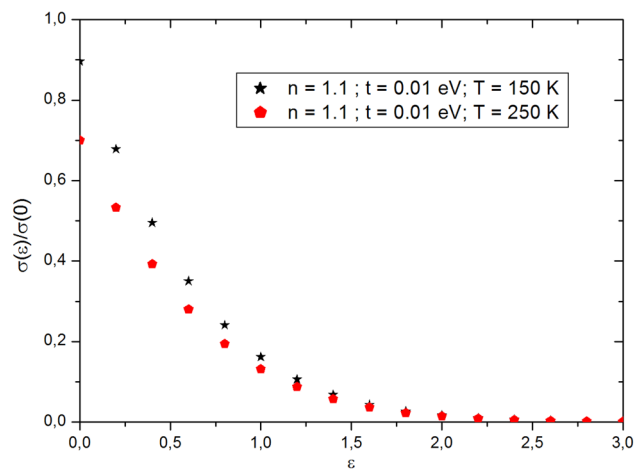


FIG. 2. Normalized conductivity for  $T = 150$  K and  $T = 250$  K.

Figure 2 taken from Ref. 31 shows the behavior of the conductivity for two values of the temperature  $T$ . It could be objected here that extending the value of the strain up to  $\varepsilon = 3$  in Fig. 2 is unphysical, as no real material can withstand such a large value of strain. Indeed, this should be understood just as a mathematical extension. The values of various constants needed for the calculation leading to Fig. 2 are given in Ref. 31.

Figure 3 shows the normalized conductivity for a fixed value of the strain,  $\varepsilon = 0.05$ , and the band filling factor,  $n = 0.9$ . The conductivity is normalized to 1 at  $T = 116$  K,  $n = 1.25$ .

Note that there is a big difference in the behavior of curves presented in Figs. 2 and 3. The curve in Fig. 3 changes sign at a certain point (at  $T \cong 100 - 110$  K).

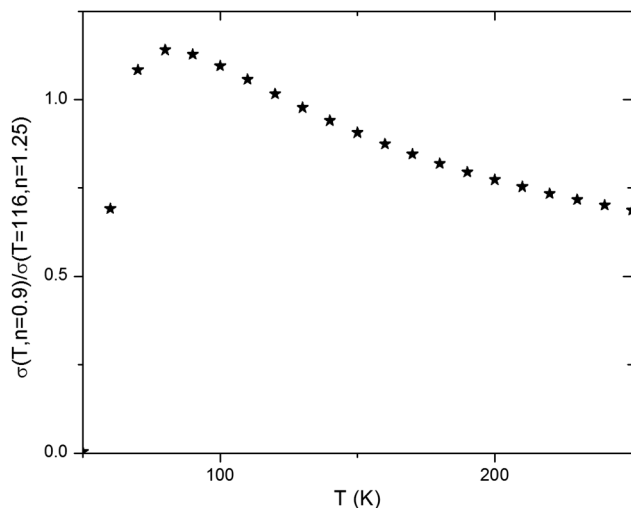


FIG. 3. Normalized conductivity for strain 0.05.

This result has considerable theoretical importance. Namely, practical attempts in applications of stretchable and flexible electronics may require such changes of material characteristics for different sets of material parameters. Therefore, results presented here, and some more which are forthcoming, can contribute to the development of various applications.

## B. Strain effects on vibrational properties in 2D structures—*Ab initio* calculations

In this section, we study the effect of strain on vibrational properties and electron-phonon coupling in two-dimensional materials. The low-dimensional materials are characterized by strong covalent in-plane bonds and weak interlayer van der Waals interactions which give them a layered structure. An application of homogenous strain in bulk materials would be practically impossible outside of the theoretical discussion, and in low-dimensional material, it is rather simple.

Based on this concept, we present computational study within the density functional theory framework of the effects of the (equi) biaxial strain on the two isostructural two-dimensional materials, Li-intercalated graphene and magnesium-diboride monolayer. We used Quantum Espresso software package<sup>53</sup> with both local-density approximation (LDA) and generalized gradient approximation (GGA) Perdew-Burke-Ernzerhof (PBE) functionals and vibrational properties and the electron-phonon interaction is calculated using density functional perturbation theory implemented in this software package.

Here, it is shown that tensile biaxial strain causes softening of the phonons, affecting the total electron-phonon interaction and resulting in significantly a higher critical temperature. In particular, in Li-doped graphene, the in-plane phonons will be dramatically softened, whereas the out-of-plane ones will be less affected.<sup>52</sup> By application of strain, we achieve the increase of the density of states at the Fermi level and softening of the modes.<sup>54,55</sup> Without drastically modifying the structure, this results in great effects on the electron-phonon coupling constant.<sup>55,56</sup> In principle, both these effects can be achieved rather easily in low-dimensional systems.

In order to strain the  $\text{LiC}_6$ -mono and increase the lattice constant, the in-plane distance between C atoms is increased leaving the hexagonal symmetry unaffected. The Li adatom is placed above the H site in graphene (the center of a hexagon). The modification of the lattice constant does not interfere with the Li adatom position which remains fixed in the center of the hexagon, leaving the symmetry unbroken. Due to the expansion of the carbon atom distances and the invariance of the hexagonal symmetry the Li adatom shifts only along the z-axis. The change in the distance between the carbon plane and the Li adatom is presented in Table I. The obtained results are in agreement with other similar studies and experimental results.<sup>24,36,54</sup>

The effects of several values of the strain, which increase the lattice constant by 3%, 5%, 7%, and 10%, are studied. Larger strains are not applied due to the instabilities that occur after the attempt of geometrical optimization and relaxation.<sup>57</sup> The distance between the Li adatom and graphene decreases with the strain, as the Li adatom moves down deeper toward graphene. When the strain is applied, the distance between neighboring C atoms increases and the graphene pi bonds repulse the Li adatom less, which then

**TABLE I.** Changes of bond lengths in Li-doped graphene with application on tensile equibiaxial strain.

Strain %	Distance between Li adatom and carbon layer (Å)	Carbon-carbon bond length (Å)
0	1.80	1.42
3	1.69	1.46
5	1.64	1.49
7	1.61	1.52
10	1.54	1.57

moves down along the z-axis. The small shift of the Fermi level is observed with the strain.

In the phonon dispersion spectrum of doped graphene, the three regions can be distinguished: the adatom-related modes are associated with low-energy regions ( $0\text{--}400\text{ cm}^{-1}$ ), where  $300\text{--}400\text{ cm}^{-1}$  are Li modes mixed with the out-of-plane carbon modes ( $C_z$ ), the midregion ( $400\text{--}900\text{ cm}^{-1}$ ) can be associated with  $C_z$  modes and the high-energy region with carbon-carbon stretching modes.<sup>1</sup>

The main contributions to lambda come from the low-energy lithium modes and the carbon vibrations along the z-axis, with an additional contribution from the C-C stretching modes (in agreement with Refs. 24 and 35). When strain is applied, significant softening of phonons occurs, as shown in Fig. 4. In green color, phonon dispersion is depicted for the 3% strained  $\text{LiC}_6\text{-mono}$  and in red for 10%. The softening of the high-energy C-C stretching modes is strongly present with a larger strain. In addition, the consequent increase of the phonon DOS in the low-energy region occurs as well. Although the low-energy modes slightly move upwards in energy, the main effect on the electron-phonon coupling is the softening of graphene high-energy C-C stretching modes.

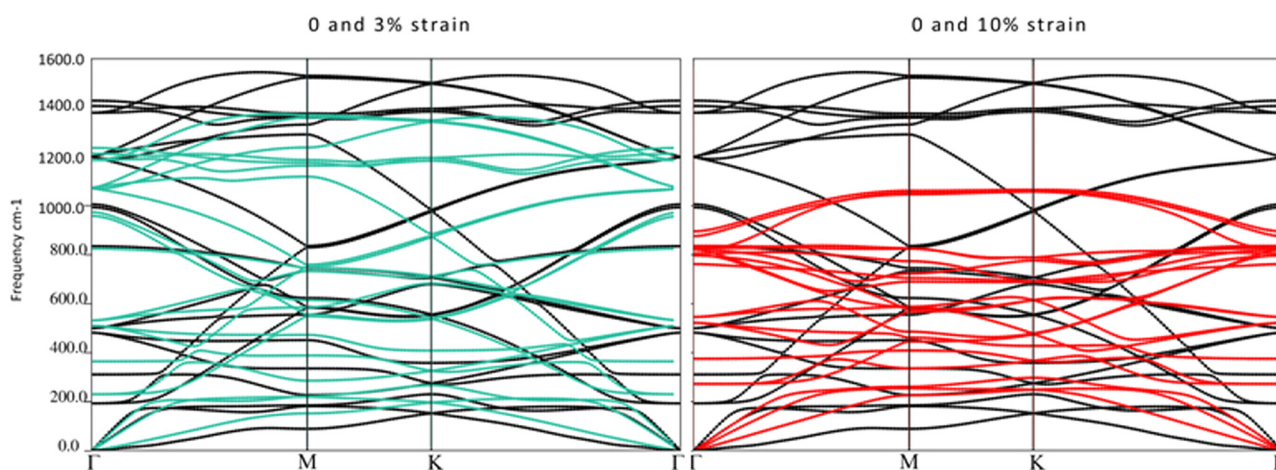
At the same time, with stretching of C-C bonds, another structural change occurs. For the small strain, the Li adatom drops

down toward the center of a hexagon and its orbitals overlap more with the carbon  $\pi$  orbitals. That causes an increase in charge transfer and emptying of the interlayer band, which reduces  $\lambda$ . When more strain is applied, the carbon bonds are elongated and the  $\pi$  orbitals move away, both from each other and the center of the hexagon. The orbital overlap is reduced, and after the certain critical value,  $\lambda$  increases, following the strain. Figure 5 presents the effects of the different strain on electronic localization function (ELF).

The significant changes for the large strain are presented, depicting the above-described effects. For ELF at 10% of the strain, the electron localization region is greatly lowered as graphene and adatom separate one from another and as a C-C bond are elongated. The critical temperature is enhanced with straining of structure, up to  $T_c = 29\text{ K}$  where the electron-phonon coupling constant is  $0.73$ .<sup>34</sup> It is important to stress that this increase in  $T_c$ , achieved by the described mechanism, can be experimentally realized. A pristine graphene is experimentally confirmed to be elastically stretchable up to 25%<sup>1</sup> making here considered strains feasible.

Following structural and electronic similarity we explored the effect of the biaxial strain on the  $\text{MgB}_2$  monolayer.<sup>25</sup> As in graphene the application of the biaxial strain leaves the symmetry of the system unchanged, yet a tensile (compressive) strain moves boron atoms further (closer) from (to) each other in the same proximity, allowing the Mg atom to move along the z-axis. This causes a change in the charge transfer from the magnesium atoms to the boron plane increasing (decreasing) DOS on the Fermi level. The other effects concern the softening (hardening) of modes of the boron atoms due to an elongation (compression) of the B-B bonds.

We compare phonon dispersion for nonstrained  $\text{MgB}_2\text{-mono}$  with compressively and tensely strained ones (Fig. 6). Significant softening (hardening) of high-energy modes is present with elongation (compression) of bonds between boron atoms, following the general trend for phonons, as distances between atoms increase, the interatomic bonds become less stiff, resulting in a decrease

**FIG. 4.** Phonon dispersion for the  $\text{LiC}_6\text{-mono}$ ; black lines are for the nonstrained  $\text{LiC}_6\text{-mono}$ , and green and red for the 3% and 10% tensile biaxial strain, respectively.

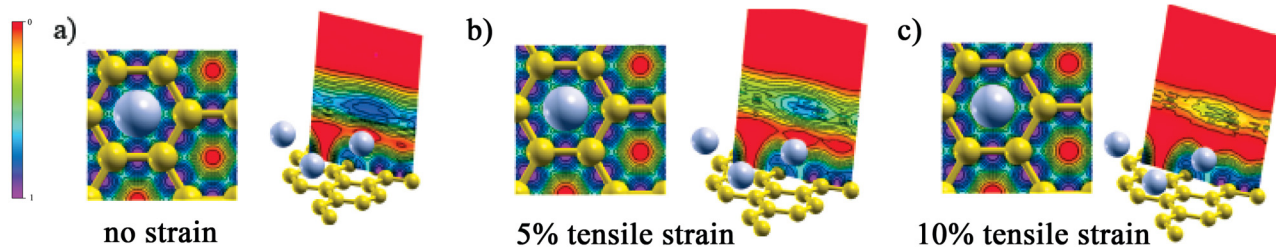


**FIG. 5.** ELF (electron localization function) for the LiC<sub>6</sub>-mono without (a) and with strain [5% (b) and 10% (c)] (first image in pair ELF on the xy direction, second, ELF on the xz direction).

of phonon frequencies (and vice versa). In electron-phonon coupling strongest contribution to coupling comes from E<sub>2</sub> optical mode.<sup>37,38</sup>

In Fig. 6, a significant shift of E<sub>2</sub> mode is visible, it changes frequency for almost 100 cm<sup>-1</sup> with the application of strain. However straining of structure results same as in graphene, not only in a variation of B-B bonds occurs but as well position of Mg adatom above the center of boron hexagon changes. As the distance between B atoms increases (i.e., for tensile strain) Coulomb repulsion is reduced allowing Mg atom to sink deeper towards the center of the hexagon. For compression opposite situation occurs. The repulsion is stronger and the Mg atom gets more remote. This has an effect on charge transfer from Mg to B layer.

To investigate this we study electron localization function (ELF). It is noticeable that straining not only affects ELF in the B layer but as well on the Mg layer. For both compressive and tensile strain in the Mg layer, ELF becomes denser than in the non-strained case. Due to the closing of B atoms in hexagon ELF increases B plane increases for compression (and vice versa) (Fig. 7). As in LiC<sub>6</sub>-mono application of the biaxial strain dramatically increases critical temperature, more than 30 K.<sup>25,26</sup>

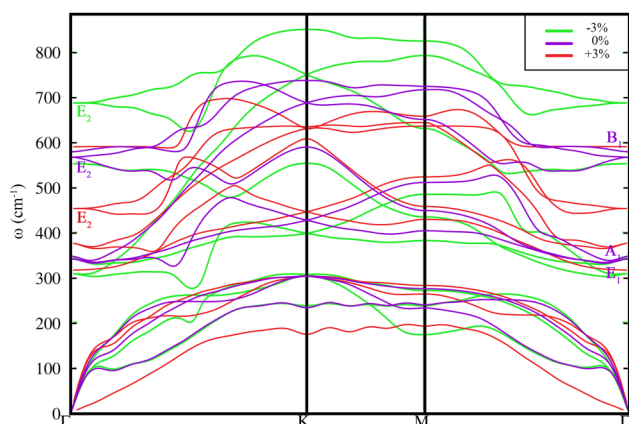


**FIG. 6.** Comparison of phonon dispersion for nonstrained MgB<sub>2</sub> (violet) and compressively (green) and tensely (red) strained (for 3% each).

The question of the reduction of dimensionality of superconducting materials to its limit, a truly atomic-scale 2D system and the consequence of this<sup>57-62</sup> are highly relevant not only to fundamental science but to nanotechnology and it will be crucial for the production of superconducting devices in future. Engineering of strain in such systems could lead to significant improvements in their superconducting properties and pave the way toward new applications.

### III. EXPERIMENT

#### A. Local strain engineering of graphene by atomic force microscopy

A typical way to introduce a local strain into graphene is its transfer on a prepatterned substrate, containing, for example, arrays of nanopillars.<sup>63</sup> Atomic force microscopy (AFM) based lithography offers additional possibilities for graphene reshaping and patterning at the nanoscale. The typical curvature radius of AFM tips is around 5–10 nm making them appropriate for the fabrication of various graphene nanostructures, based on either AFM scratching<sup>64</sup> or AFM based local anodic oxidation.<sup>64-66</sup> In a similar way, a local strain can be introduced into the graphene lattice by applying a local pressure from AFM tips without graphene tearing.<sup>67,68</sup>

Our approach to generating a local strain in graphene is based on the AFM dynamic plowing lithography (DPL),<sup>68</sup> employing the so-called tapping AFM mode. In this mode, the AFM cantilever oscillates above a sample during scanning. The amplitude of the cantilever oscillations, represented by the amplitude set-point, is kept constant during scanning in the tapping mode. In order to hold constant the interaction between the AFM tip and the sample, the AFM scanner together with the sample moves up and down, in the z-direction according to the sample topography. Then, the scanner movement in the z-direction is proportional to the sample topography. On the other hand, during DPL, it is necessary to increase the mechanical interaction between the AFM tip and the considered sample in order to induce local changes in morphology. For this purpose, in order to increase a tip-sample interaction needed for graphene deformation, the free oscillation amplitude of the employed AFM cantilevers is first increased by around 10 times. The tip-sample interaction, controlled by the amplitude set-point in the tapping AFM mode, is then additionally increased by decreasing the set-point by 10–100 times compared to ordinary



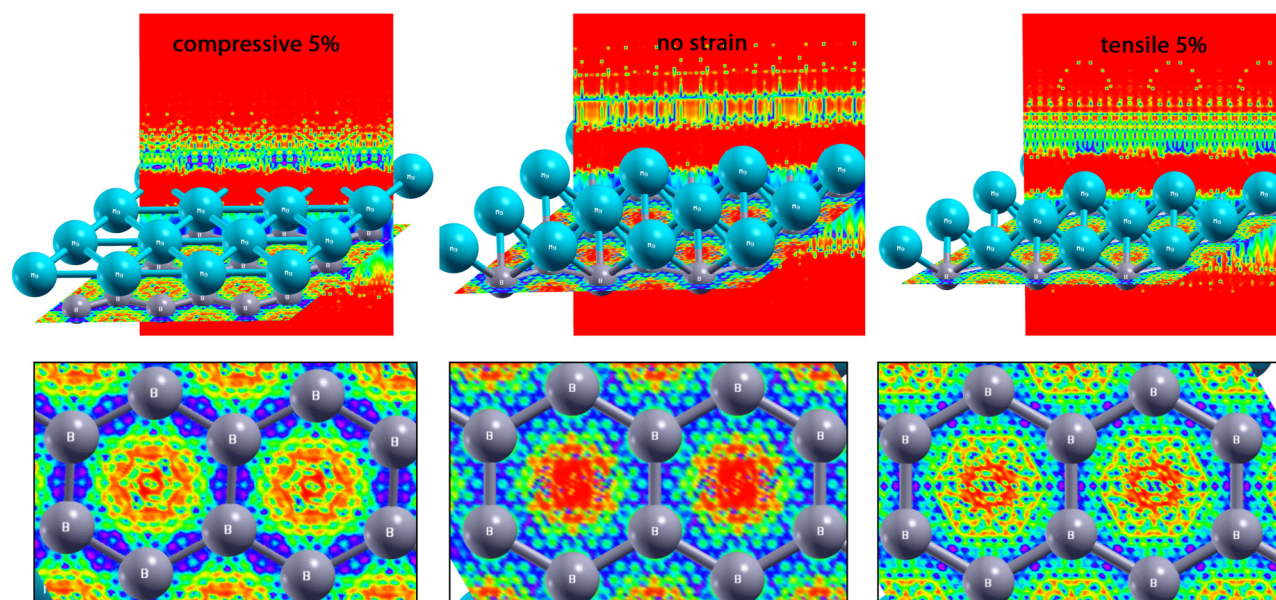


**FIG. 7.** Electron localization function (ELF) for  $\text{MgB}_2$ -mono nonstrained and compressively (left) and tensely (right) strained. Top: 3D projection of ELF with focus on the Mg layer. Bottom: ELF projection on the B layer.

AFM imaging. Benefits of using DPL instead of more traditional AFM scratching lithography stem from the fact that the AFM cantilever is vibrating and not in continuous contact with a sample surface, as in the case of the static plowing (AFM based scratching lithography) employed using the AFM contact mode. As a result, the lateral and friction forces between the AFM tip and the sample surface are minimized, so there is no undesirable dragging, pushing, and pulling of graphene sheet during DPL. At the same time, the AFM cantilever during DPL is free from a torsion caused by lateral forces, which facilitates the fabrication of nanostructures with well-defined edges. AFM imaging and DPL were done using the NTEGRA Prima measuring system, manufactured by NT-MDT ([www.ntmdt-si.com](http://www.ntmdt-si.com)). Since the lithography is based on the mechanical tip-sample interaction, we used robust and wear resistant diamond coated DCP20 probes from NT-MDT.

The selected nanostructures fabricated by DPL of graphene are presented in Fig. 8. All graphene samples were made by the standard mechanical exfoliation onto the Si/SiO<sub>2</sub> substrate. The local strain in graphene can be generated along straight and curved trenches as depicted in Figs. 8(a) and 8(b), respectively, whereas more complex structures can be made by overlapping basic patterns, as presented in Fig. 8(c). DPL can be also used for the fabrication of point-like deformations of graphene, as shown in Fig. 8(d). These deformations were made by local amplitude-distance curves in the tapping mode, with an increased free oscillation amplitude of the employed AFM cantilever and with decreased set-point in order to increase the tip-sample interaction. During the measurement of the amplitude-distance curves, there is no lateral movement and scanning, just a vertical movement of the AFM scanner holding a sample, which finally gives point-like local strain in graphene.

Common for all fabricated nanostructures is a smooth surface without bumps, protrusions, or cuts, implying that the graphene together with the underlying silicon-dioxide substrate is just locally deformed and strained. The only exception is presented in Fig. 8(c) where a small bump appeared parallel and next to the graphene trench. This example shows that for a high enough local pressure,

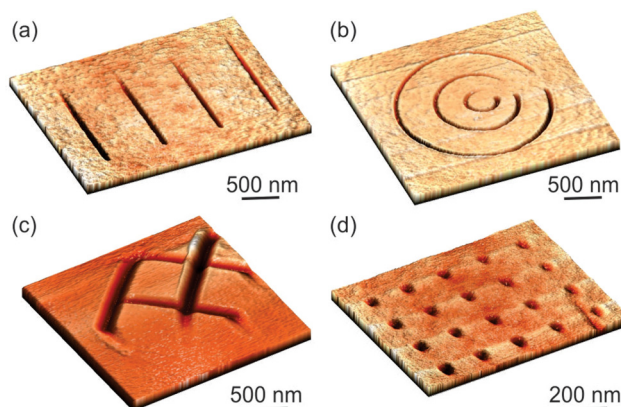


**FIG. 8.** Local strain in graphene nanostructures generated by DPL: (a) straight (z-height 3 nm) and (b) curved trenches (z-height 7 nm), (c) a more complicated pattern obtained by crossing straight trenches (z-height is 11 nm), and (d) point-like local deformation made by DPL during the measurement of amplitude-distance curves in the tapping AFM mode (z-height is 3.5 nm).

the sample compression at one point inevitably results in a protrusion at an adjacent point.

The local strain generated in graphene sheet in percent can be estimated according to the formula  $(L - L_0)/L_0 \times 100\%$ ,<sup>68</sup> where  $L_0$  and  $L$  are the lengths of graphene segments before and after the deformation by DPL, respectively. Therefore,  $L_0$  and  $L$  can be then considered as the graphene trench width and perimeter, respectively, and the values of which can be approximately calculated from measured AFM topographic images (the perimeter can be calculated from the measured trench width and perimeter). For the typical trench widths and depths of around 50–100 nm and several nanometers, respectively, the generated local strain in graphene is in the order of 0.1%. The trench width is dominantly determined by the AFM probe width. In the considered case, since we employed DCP20 probes with a rather large tip radius curvature of 50–70 nm, probably it would not be possible to make narrower trenches. Produced trenches in graphene could be an excellent platform in order to study local changes in graphene conductivity due to strain.<sup>87,88</sup>

## B. Axial strain in liquid phase exfoliated graphene films

Many potential applications of graphene and other 2D materials<sup>27,69,70</sup> rely on continuous films, either polycrystalline or single crystals. Chemical vapor deposition (CVD) techniques are commonly the fabrication methods of choice when large area graphene is considered.<sup>71–73</sup> However, CVD based films require a transfer from a catalyst on which these are grown onto a targeted substrate for their application. Usually, this step introduces many undesired features in the films, such as cracks, wrinkles, and transfer residues, and hinders intrinsic properties of graphene.<sup>74,75</sup>

A low-cost alternative to large area CVD graphene films is based on solution processing of either graphene oxide or graphite flakes.<sup>28,74–80</sup> In particular, LPE using solvers that do not covalently bond with graphene sheets can result with graphene-based films that are very promising for many applications—as strain gauges—where coatings are needed on an industrial scale.<sup>81</sup> Since these

coatings are made out of many overlapping small (100 nm–10  $\mu\text{m}$ ) single-crystal sheets of graphene or multilayer graphene, their response to strain is rather different from the case of continuous films. Understanding the strain mechanisms in these complex nanoscaled systems is crucial for their future applications. In this section, we demonstrate how axial strain of the flexible support affects the electrical properties of LPE graphene films, and similar mechanisms are to be expected for the coatings and films of other 2D materials, fabricated via solution processes.

LPE graphene films were prepared following the route described in Ref. 28. 500  $\mu\text{m}$  mesh high purity and high crystallinity graphite powder was dispersed in N-methylpyrrolidone (15–20 mg/ml), sonicated in a low-power ultrasonic bath for 14 h, and finally centrifuged at 300 rpm. The top part of the resulting solution (with 0.3–0.4 mg/ml graphene concentration) was drop casted on the water surface, and the film formed on a water-air interface was transferred to substrates by the Langmuir–Blodgett technique. Figure 9(a) shows an AFM topography of the film's edge deposited on a  $\text{SiO}_2/\text{Si}$  substrate. The film thickness was estimated from the AFM cross-sections [as presented in Fig. 9(b)], giving  $(4.0 \pm 1.5)$  nm thick films (including also batch-to-batch variations). Typical Raman spectra of the deposited LPE graphene films on a  $\text{SiO}_2/\text{Si}$  substrate are presented in Fig. 9(c), for comparison also showing the spectra obtained from the starting graphite powder (measured within a single graphite flake). Raman spectra were obtained using a TriVista 557S&I GmbH spectrometer ( $\lambda = 532$  nm) under ambient conditions. Intensity ratios of Raman active modes can be used to estimate the quality of the film and to point out the types of defects.<sup>82–85</sup> For the samples used in this study, the  $I(\text{D})/I(\text{G})$  ratio was found to be  $(0.6 \pm 0.1)$ . In particular, the  $I(\text{D})/I(\text{D}')$  ratio of  $(2.8 \pm 0.4)$  was observed, indicating that mainly it is the edges of the flakes that contribute to D mode intensity observed in the spectra.<sup>82</sup>

In order to examine the influence of the uniaxial strain on the electrical conductivity of these LPE graphenes—in the same manner as described above—the films were deposited onto flexible polyethylene terephthalate (PET) foils. Figure 10 gives an example of how LPE graphene films commonly respond to axial strain.

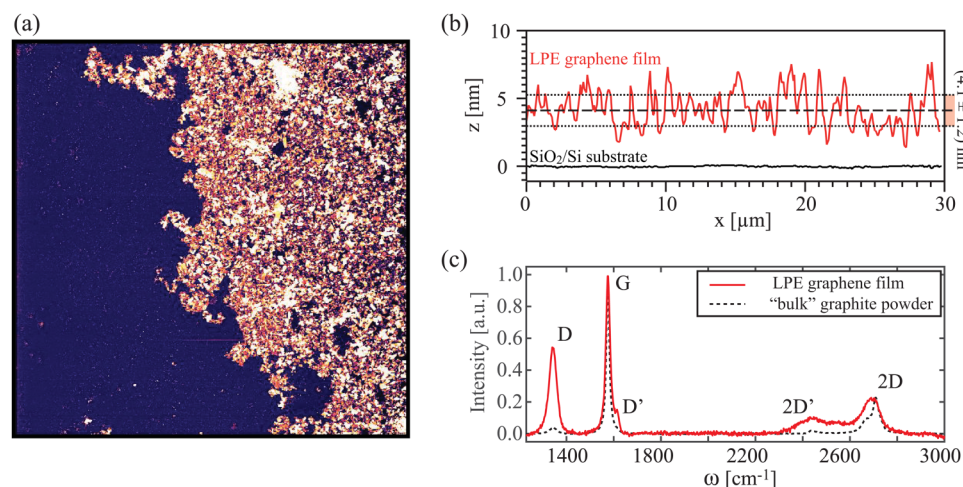


**FIG. 9.**  $50 \times 50 \mu\text{m}^2$  ( $z$  scale 10 nm) of a LPE graphene film edge, deposited on a  $\text{SiO}_2/\text{Si}$  substrate. (b) shows  $30 \mu\text{m}$  long height profiles on the film and on the substrate, averaging  $10 \mu\text{m}$  in width. (c) Raman spectra of the LPE graphene film (solid line) compared with the starting graphite powder (dashed line). Most relevant modes of graphene/graphite are labeled. Spectra are normalized to  $I(\text{G}) = 1$ .

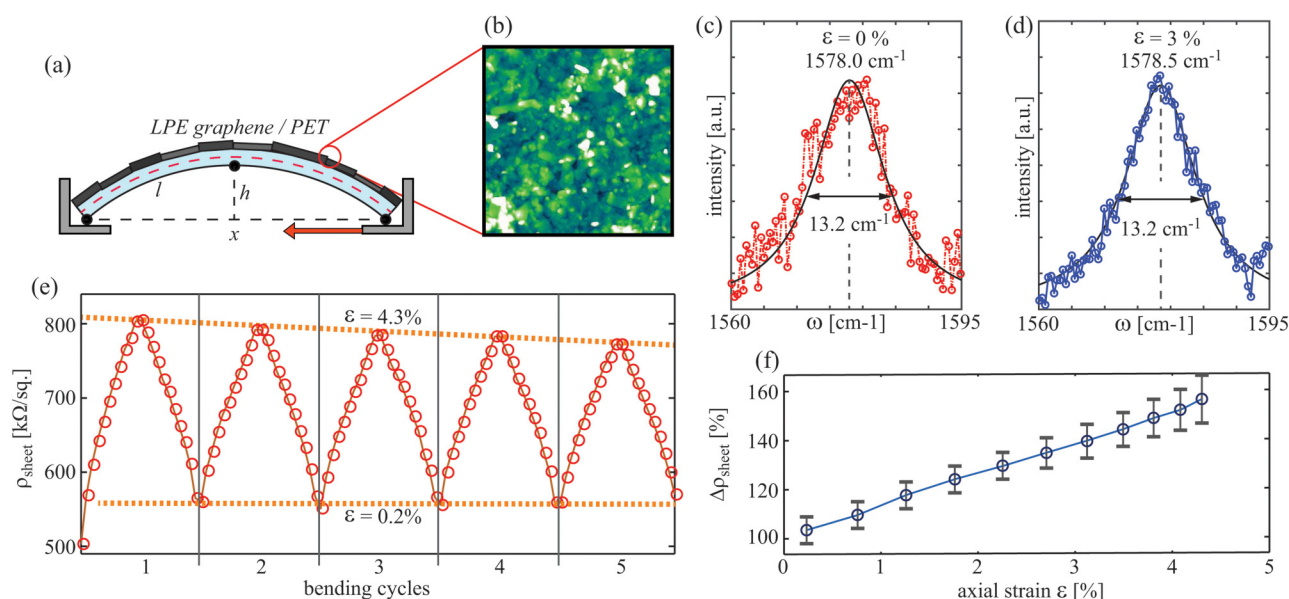


**FIG. 10.** (a) Scheme of the setup used for stretching of LPE graphene films. (b) Typical surface morphology of the films ( $5 \times 5 \mu\text{m}^2$ ,  $z$  scale 40 nm). (c) and (d) Normalized Raman spectra of graphene's G mode without strain, and with 3% of axial strain, respectively. (e) Sheet resistance as a function of alternating axial strain between 0.2% and 4.3%, showing five subsequent bending cycles. (f) Relative sheet resistance (with respect to nominal values) as a function of axial strain, averaged over several LPE films used in this study.

The film was exposed to uniaxial stretching through bending of the PET support, as schematically presented in Fig. 9(a). For this purpose, a micrometer screw was used and controlled by an integrated step motor with the precision down to  $10 \mu\text{m}$ , thus allowing a precise control over the distance between the two fixed points of the PET support. Axial strain that the LPE graphene film exhibits in such a case depends on the bending curvature of the PET support (expressed through geometrical parameters  $x$ ,  $l$ , and  $d$ ) and the thickness of PET ( $200 \pm 20 \mu\text{m}$ ). The structure of the film was investigated using atomic force microscopy [Fig. 9(b)], showing how many small flakes overlap into a continuously conducting film.

A clear fingerprint of stretching the hexagonal lattice of graphene can be obtained from Raman spectroscopy.<sup>82–85</sup> However, in the presented case when many small flakes are deposited onto the PET substrate, the substrate surface stretches but individual flakes are not strained. This can be clearly seen from the lack of both the shift and broadening of graphene's characteristic Raman active mode at  $\sim 1580 \text{ cm}^{-1}$  (G mode).<sup>82–85</sup> By measuring Raman spectra of graphene on PET, while bending the support, effective axial strain was introduced up to  $\sim 3\%$ . Higher values of axial strain during Raman spectroscopy measurements were not possible to reach with a particular setup used in this study. Figures 10(c) and 10(d) show examples of the G mode without and upon 3% of axial strain. The presented spectra have been renormalized, and the spectra of clean PET have been deduced. The G mode was fitted by a single Lorentzian function [solid lines in Figs. 10(c) and 10(d)]. No significant shift (above local variations on the sample) or any

trend of either the mode frequency, intensity, or width was detected within the applied stretching range.

Although individual flakes were not exposed to axial strain in the bending experiments, sheet resistivity of the entire film exhibits a strong dependence on axial strain. Since the main contribution to the total resistance of LPE films comes from the points of overlap between neighboring flakes,<sup>28</sup> stretching the LPE graphene film results in effective pulling apart of individual flakes, and thus an increase in the sheet resistivity of the whole film. Figure 10(e) presents five repeated cycles of stretching and relaxing of the LPE graphene film on PET.

Maximal axial strain applied to the films in the case presented in Fig. 10(e) was estimated to be  $\sim 4.3\%$ . Figure 10(f) shows the dependence of relative sheet resistance increase (with respect to the unstrained value) of the LPE graphene film as a function of axial strain ( $\epsilon$ ). The data were obtained by measuring in a two-point probe configuration by considering several films, with the length of the films varying between 10 mm and 20 mm. The width of the films was fixed to 10 mm. Contact resistance was determined by varying the length of the films and found to be negligible, commonly being over two orders of magnitude smaller than the resistance of LPE graphene films. A strong increase of sheet resistivity was observed upon stretching of the films, increasing linearly by  $\sim 10\%$  for 1% of axial strain. These values are much larger than in the case of CVD graphene,<sup>11</sup> as expected, since the mechanism behind the change in sheet resistance is fundamentally different. Such a large change of resistance upon bending, with the opportunity to further optimize the fabrication, opens up many possibilities

to use LPE graphene films in sensing applications such as strain gauges, pressure sensors, e-skin, and touch screens.<sup>86</sup>

#### IV. CONCLUSION

As we have outlined, strain engineering has an unprecedented ability to manipulate the plethora of properties of low-dimensional materials. Design of new materials with desired features, engineered through the introduction of mechanical deformations, could lead to the production of novel devices and the low-dimensional materials offering a great possibility for manipulation and engineering, especially with techniques that are not available in bulk materials. As demonstrated in this paper, conductivity can be strongly modified with strain. We have shown how electrical conductivity can be tuned with the application of strain in one-dimensional systems. For two-dimensional materials, we demonstrated a significant effect of the biaxial strain on phonons and its drastic modification of superconducting coupling in doped graphene and isostructural MgB<sub>2</sub>-monolayer. We showed that critical temperature of the superconducting state can be enhanced up to several times by the application of strain in order to modify the electron-phonon coupling. All proposed strains are within experimental reach; however, they are beyond the scope of techniques used in this research.

To further understand the effects of strain on realistic 2D materials, we experimentally study an introduction of strain on graphene samples. On two essentially different types of samples, we demonstrate strain effects, both locally and macroscopically. This concerns a possible strain engineering of monolayer graphene by atomic force microscopy and the influence of an axial strain in liquid phase exfoliated graphene films. Manipulation of properties of these different nanomaterials in a controllable fashion through strain engineering has been proven achievable and potentially useful for the design of next generation devices. We showed that AFM produced trenches in graphene could be an excellent platform in order to study local changes in graphene conductivity due to strain. Results of such a study could be related to our theoretical prediction on the effects of strain on conductivity in the 1D-like system. This opens the path for further research on this topic. Application of strain of LPE films has a significant effect on their predicted applications. The sheet resistivity in the entire LPE graphene film exhibits a strong dependence on axial strain. Stretching results in effective pulling apart of individual flakes, and thus an increase in the sheet resistivity of the whole film. This could have a significant impact on their use as flexible electrodes; however, it will open the possibility for a new set of applications such as pressure sensors and strain gauges.

All these results together indicate the effects of the application of strain; tensile and compressive and uniaxial and biaxial strains have significant effects on conductivity and have to be carefully considered depending on the application or concept that we are researching for.

#### ACKNOWLEDGMENTS

DFT calculations were performed using computational resources at Johannes Kepler University, Linz, Austria. This work was supported by the Serbian Ministry of Education, Science and

Technological Development under Project Nos. OI 171005 and III45018. This research was also supported by Qatar National Research Fund, under Grant No. NPRP 7-665-1-125. A.M. acknowledges support from a Lise Meitner fellowship by FWF (Grant No. M2323-N36).

#### REFERENCES

- <sup>1</sup>C. Lee, X. Wei, J. Kysar, and J. Hone, "Measurement of the elastic properties and intrinsic strength of monolayer graphene," *Science* **321**, 385–388 (2008).
- <sup>2</sup>K. S. Novoselov, V. I. Falko, L. Colombo, P. R. Gellert, M. G. Schwab, and K. Kim, *Nature* **490**, 192–200 (2012).
- <sup>3</sup>K. S. Novoselov, A. K. Geim, S. V. Morozov, D. Jiang, Y. Zhang, S. V. Dubonos, I. V. Grigorieva, and A. A. Firsov, "Electric field effect in atomically thin carbon films," *Science* **306**, 666–669 (2004).
- <sup>4</sup>M. I. Katsnelson, "Graphene: Carbon in two dimensions," *Mater. Today* **10**, 1–2 (2007).
- <sup>5</sup>S.-K. Lee, H. Y. Jang, S. Jang, E. Choi, B. H. Hong, J. Lee, S. Park, and J.-H. Ahn, *Nano Lett.* **12**, 3472–3476 (2012).
- <sup>6</sup>R. R. Nair, P. Blake, A. N. Grigorenko, K. S. Novoselov, T. J. Booth, T. Stauber, N. M. R. Peres, and A. K. Geim, *Science* **320**, 1308 (2008).
- <sup>7</sup>S. Bae, H. Kim, Y. Lee, X. Xu, J.-S. Park, Y. Zheng, J. Balakrishnan, T. Lei, H. Ri Kim, Y. I. Song, Y.-J. Kim, K. S. Kim, B. Ozyilmaz, J.-H. Ahn, B. H. Hong, and S. Iijima, *Nat. Nanotechnol.* **5**, 574–578 (2010).
- <sup>8</sup>Z. Sun, D. K. James, and J. M. Tour, *J. Phys. Chem. Lett.* **2**, 2425–2432 (2011).
- <sup>9</sup>K. P. Loh, Q. Bao, P. K. Ang, and J. Yang, *J. Mater. Chem.* **20**, 2277–2289 (2010).
- <sup>10</sup>S. Niyogi, E. Bekyarova, J. Hong, S. Khizroev, C. Berger, W. de Heer, R. C. Haddon, and J. Phys. *Chem. Lett.* **2**, 2487–2498 (2011).
- <sup>11</sup>K. S. Kim, Y. Zhao, H. Jang, S. Y. Lee, J. M. Kim, K. S. Kim, J.-H. Ahn, P. Kim, J.-Y. Choi, and B. H. Hong, *Nature* **457**, 706–810 (2009).
- <sup>12</sup>C.-C. Lu, Y.-C. Lin, C.-H. Yeh, J.-C. Huang, and P.-W. Chiu, *ACS Nano* **6**, 4469–4474 (2012).
- <sup>13</sup>B. J. Kim, H. Jang, S.-K. Lee, B. H. Hong, J.-H. Ahn, and J. H. Cho, *Nano Lett.* **10**, 3464–3466 (2010).
- <sup>14</sup>S.-K. Lee, B. J. Kim, H. Jang, S. C. Yoon, C. Lee, B. H. Hong, J. A. Rogers, J. H. Cho, and J.-H. Ahn, *Nano Lett.* **11**, 4642–4646 (2011).
- <sup>15</sup>P. Avouris, *Nano Lett.* **10**, 4285–4294 (2010).
- <sup>16</sup>F. Bonaccorso, Z. Sun, T. Hasan, and A. C. Ferrari, *Nat. Photonics* **4**, 611–622 (2010).
- <sup>17</sup>Y.-M. Lin, C. Dimitrakopoulos, K. A. Jenkins, D. B. Farmer, H.-Y. Chiu, A. Grill, and P. Avouris, *Science* **327**, 662 (2010).
- <sup>18</sup>F. Schwierz, *Nat. Nanotechnol.* **5**, 487–496 (2010).
- <sup>19</sup>G. G. Naumis, S. Barraza-Lopez, M. Oliva-Leyva, and H. Terrones, "Electronic and optical properties of strained graphene and other strained 2D materials: A review," *Rep. Prog. Phys.* **80**, 096501 (2017).
- <sup>20</sup>C. Si, Z. Suna, and F. Liu, "Strain engineering of graphene: A review," *Nanoscale* **8**, 3207 (2016).
- <sup>21</sup>B. Amorim, A. Cortijo, F. de Juan, A. G. Grushin, F. Guinea, A. Gutiérrez-Rubio, H. Ochoa, V. Parente, R. Roldán, P. San-Jose, J. Schiefele, M. Sturla, and M. A. H. Vozmediano, "Novel effects of strains in graphene and other two dimensional materials," *Phys. Rep.* **617**, 1 (2016).
- <sup>22</sup>M. A. Bissett, M. Tsuji, and H. Ago, "Strain engineering the properties of graphene and other two-dimensional crystals," *Phys. Chem. Chem. Phys.* **16**, 11124 (2014).
- <sup>23</sup>D. Akinwande *et al.*, "A review on mechanics and mechanical properties of 2D materials—Graphene and beyond," *Ext. Mech. Lett.* **13**, 42 (2017).
- <sup>24</sup>G. Profeta, M. Calandra, and F. Mauri, "Phonon-mediated superconductivity in graphene by lithium deposition," *Nat. Phys.* **8**, 131 (2012).
- <sup>25</sup>J. Pesic, "Investigation of superconductivity in graphene and related materials, using ab-initio methods," Ph.D. thesis (University of Belgrade, 2017).

- <sup>26</sup>J. Bekaert, A. Aperis, B. Partoens, P. M. Oppeneer, and M. V. Milosevic, "Evolution of multigap superconductivity in the atomically thin limit: Strain-enhanced three-gap superconductivity in monolayer  $\text{MgB}_2$ ," *Phys. Rev. B* **96**, 094510 (2017).
- <sup>27</sup>Y. Hernandez *et al.*, *Nat. Nanotechnol.* **3**, 563–568 (2008).
- <sup>28</sup>A. Matkovic *et al.*, *2D Mater.* **3**, 015002 (2016).
- <sup>29</sup>J. Hubbard, "Electron correlations in narrow energy bands," *Proc. R. Soc. Lond. A* **276**, 238 (1963).
- <sup>30</sup>V. Celebonovic, "Hubbard model in materials science: Electrical conductivity and reflectivity of models of some 2D materials," in *Advanced 2D Materials*, edited by A. Tiwari and M. Syvajarvi (Scrivener Publishing LLC, 2016), pp. 115–144.
- <sup>31</sup>V. Celebonovic, "The hubbard model: Useful for stretchable nanomaterials?," *J. Phys. Conf. Ser.* **558**, 012006 (2014).
- <sup>32</sup>V. Celebonovic, "Some calculational improvements in applying the hubbard model to nanomaterials," *J. Phys. Conf. Ser.* **794**, 012008 (2017).
- <sup>33</sup>J. van den Brand, M. de Kok, M. Koetse *et al.*, "Flexible and stretchable electronics for wearable health devices," *Solid State Electron.* **113**, 116–120 (2015).
- <sup>34</sup>K. Szalowski, "Critical temperature of  $\text{MgB}_2$  ultrathin superconducting films: BCS model calculations in the tight-binding approximation," *Phys. Rev. B* **74**, 094501 (2006).
- <sup>35</sup>M. Calandra, G. Profeta, and F. Mauri, "Superconductivity in metal-coated graphene," *Phys. Status Solidi B* **12**, 2544 (2012).
- <sup>36</sup>B. M. Ludbrook, G. Levy, P. Nigge, M. Zonno, M. Schneider, D. J. Dvorak, C. N. Veenstra, S. Zhdanovich, D. Wong, P. Dosanjh, C. Strasser, A. Stohr, S. Forti, C. R. Ast, U. Starke, and A. Damascelli, "Evidence for superconductivity in Li-decorated monolayer graphene," *Proc. Natl. Acad. Sci. U.S.A.* **112**(38), 11795–11799 (2015).
- <sup>37</sup>J. Nagamatsu, N. Nakagawa, T. Muranaka, Y. Zentani, and J. Akimitsu, "Superconductivity at 39 K in magnesium diboride," *Nature* **410**, 63–64 (2001).
- <sup>38</sup>J. M. An and W. E. Pickett, "Superconductivity of  $\text{MgB}_2$ : Covalent bonds driven metallic," *Phys. Rev. Lett.* **86**, 4366 (2001).
- <sup>39</sup>Z. H. Ni, T. Yu, Y. H. Lu, Y. Y. Wang, Y. P. Feng, and Z. X. Shen, "Uniaxial strain on graphene: Raman spectroscopy study and band-gap opening," *ACS Nano* **11**, 2301 (2008).
- <sup>40</sup>M. Huang, H. Yan, C. Chen, D. Song, T. F. Heinz, and J. Hone, "Phonon softening and crystallographic orientation of strained graphene studied by Raman spectroscopy," *Proc. Natl. Acad. Sci. U.S.A.* **106**, 7304 (2009).
- <sup>41</sup>V. M. Pereira, A. H. Castro Neto, and N. M. R. Peres, "A tight-binding approach to uniaxial strain in graphene," *Phys. Rev. B* **80**, 045401 (2009).
- <sup>42</sup>F. Ding, H. Ji, Y. Chen, A. Herklotz, K. Dorr, Y. Mei, A. Rastelli, and O. G. Schmidt, "Stretchable graphene: A close look at fundamental parameters through biaxial straining," *Nano Lett.* **10**, 3453 (2010).
- <sup>43</sup>T. M. G. Mohiuddin, A. Lombardo, R. R. Nair, A. Bonetti, G. Savini, R. Jalil, N. Bonini, D. M. Basko, C. Galiotis, N. Marzari, K. S. Novoselov, A. K. Geim, and A. C. Ferrari, "Uniaxial strain in graphene by Raman spectroscopy: G peak splitting, Grüneisen parameters, and sample orientation," *Phys. Rev. B* **79**, 205433 (2009).
- <sup>44</sup>N. Levy, S. A. Burke, K. Meaker, M. L. Panlasigui, A. Zettl, F. Guinea, A. H. C. Neto, and M. F. Crommie, "Strain-induced pseudo-magnetic fields greater than 300 Tesla in graphene nanobubbles," *Science* **329**, 544–547 (2010).
- <sup>45</sup>F. Guinea, M. I. Katsnelson, and A. K. Geim, "Energy gaps and a zero-field quantum Hall effect in graphene by strain engineering," *Nat. Phys.* **6**, 30–33 (2009).
- <sup>46</sup>M. L. Teague, A. P. Lai, J. Velasco, C. R. Hughes, A. D. Beyer, M. W. Bockrath, C. N. Lau, and N.-C. Yeh, "Evidence for strain-induced local conductance modulations in single-layer graphene on  $\text{SiO}_2$ ," *Nano Lett.* **9**, 2542 (2009).
- <sup>47</sup>M. Huang, T. A. Pascal, H. Kim, W. A. Goddard, and J. R. Greer, "Electronic-mechanical coupling in graphene from in situ nanoindentation experiments and multiscale atomistic simulations," *Nano Lett.* **11**, 1241–1246 (2011).
- <sup>48</sup>X.-W. Fu, Z.-M. Liao, J. X. Zhou, Y.-B. Zhou, H.-C. Wu, R. Zhang, G. Jing, J. Xu, X. Wu, W. Guo, and D. Yu, "Strain dependent resistance in chemical vapor deposition grown graphene," *Appl. Phys. Lett.* **99**, 213107 (2011).
- <sup>49</sup>S. Y. Zhou, G. H. Gweon *et al.*, "Substrate-induced band gap opening in epitaxial graphene," *Nat. Mater.* **6**, 770 (2007).
- <sup>50</sup>D. Xiao, W. Yao, and Q. Niu, "Valley-Contrasting physics in graphene: Magnetic moment and topological transport," *Phys. Rev. Lett.* **99**, 236809 (2007).
- <sup>51</sup>G. Gui, J. Li, and J. Zhong, "Band structure engineering of graphene by strain: First-principles calculations," *Phys. Rev. B* **78**, 075435 (2008).
- <sup>52</sup>C. A. Marianetti and H. G. Yevick, "Failure mechanisms of graphene under tension," *Phys. Rev. Lett.* **105**, 245502 (2010).
- <sup>53</sup>P. Giannozzi, A. V. Fedorov, G.-H. Gweon, P. N. First *et al.*, *J. Phys.: Condens. Matter* **21**, 395502 (2009).
- <sup>54</sup>J. Pesic, R. Gajic, K. Hingerl, and M. Belic, "Strain enhanced superconductivity in Li-doped graphene," *Europhys. Lett.* **108**, 67005 (2014).
- <sup>55</sup>J. Pesic, V. Damjanovic, R. Gajic, K. Hingerl, and M. Belic, "Density functional theory study of phonons in graphene doped with Li, Ca and Ba," *Europhys. Lett.* **112**, 67006 (2015).
- <sup>56</sup>C. Si, Z. Liu, W. Duan, and F. Liu, "First-Principles calculations on the effect of doping and biaxial tensile strain on electron-phonon coupling in graphene," *Phys. Rev. Lett.* **111**, 196802 (2013).
- <sup>57</sup>A. Romero-Bermudez and A. M. Garca-Garca, "Size effects in superconducting thin films coupled to a substrate," *Phys. Rev. B* **89**, 064508 (2014).
- <sup>58</sup>A. Bingyun, Z. Zhengjun, T. Tao, and Z. Yiping, "Potential enhancement of superconductivity in  $\text{MgB}_2$  nanosheets: First-principles calculations," *Chem. Phys. Lett.* **591**, 185 (2014).
- <sup>59</sup>C. Zhang, Y. Wang, D. Wang, Y. Zhang, Z.-H. Liu, Q.-R. Feng, and Z.-Z. Gan, "Suppression of superconductivity in epitaxial  $\text{MgB}_2$  ultrathin films," *J. Appl. Phys.* **114**, 023903 (2013).
- <sup>60</sup>N. Acharya, M. A. Wolak, T. Tan, N. Lee, A. C. Lang, M. Taheri, D. Cunnane, B. S. Karasik, and X. X. Xi, " $\text{MgB}_2$  ultrathin films fabricated by hybrid physical chemical vapor deposition and ion milling," *APL Mater.* **4**, 086114 (2016).
- <sup>61</sup>A. Romero-Bermudez and A. M. Garca-Garca, "Shape resonances and shell effects in thin-film multiband superconductors," *Phys. Rev. B* **89**, 024510 (2014).
- <sup>62</sup>D. Valentinis, D. van der Marel, and C. Berthod, "Rise and fall of shape resonances in thin films of BCS superconductors," *Phys. Rev. B* **94**, 054516 (2016).
- <sup>63</sup>A. Reserbat-Plantey, D. Kalita, Z. Han, L. Ferlazzo, S. Autier-Laurent, K. Komatsu, C. Li, R. Weil, A. Ralko, L. Marty, S. Guéron, N. Bendiab, H. Bouchiat, and V. Bouchiat, "Strain superlattices and macroscale suspension of graphene induced by corrugated substrates," *Nano Lett.* **14**, 5044–5051 (2014).
- <sup>64</sup>A. J. M. Giesbers, U. Zeitler, S. Neubeck, F. Freitag, K. S. Novoselov, and J. C. Maan, "Nanolithography and manipulation of graphene using an atomic force microscope," *Solid State Commun.* **147**, 366 (2008).
- <sup>65</sup>L. Weng, L. Zhang, Y. P. Chen, and L. P. Rokhinson, "Atomic force microscope local oxidation nanolithography of graphene," *Appl. Phys. Lett.* **93**, 093107 (2008).
- <sup>66</sup>S. Masubuchi, M. Ono, K. Yoshida, K. Hirakawa, and T. Machida, "Fabrication of graphene nanoribbon by local anodic oxidation lithography using atomic force microscope," *Appl. Phys. Lett.* **94**, 082107 (2009).
- <sup>67</sup>P. Nemes-Incze, G. Kukucska, J. Koltai, J. Kürti, C. Hwang, L. Tapasztó, and L. P. Biró, "Preparing local strain patterns in graphene by atomic force microscope based indentation," *Sci. Rep.* **7**, 3035 (2017).
- <sup>68</sup>B. Vasić, M. Kratzer, A. Matković, A. Nevsad, U. Ralević, D. Jovanović, C. Ganser, C. Teichert, and R. Gajić, "Atomic force microscopy based manipulation of graphene using dynamic plowing lithography," *Nanotechnology* **24**, 015303 (2013).
- <sup>69</sup>A. C. Ferrari *et al.*, *Nanoscale* **7**, 4598–4810 (2014).
- <sup>70</sup>F. Bonaccorso, L. Colombo, G. Yu, M. Stoller, V. Tozzini, A. C. Ferrari, R. S. Ruoff, and V. Pellegrini, *Science* **347**, 1246501 (2015).
- <sup>71</sup>J. Coraux, A. T. N'Diaye, C. Busse, and T. Michely, *Nano Lett.* **8**, 565–570 (2008).
- <sup>72</sup>A. Reina, X. Jia, J. Ho, D. Nezich, H. Son, V. Bulovic, M. S. Dresselhaus, and J. Kong, *Nano Lett.* **9**, 30–35 (2008).
- <sup>73</sup>X. Li *et al.*, *Science* **324**, 1312–1314 (2009).
- <sup>74</sup>A. V. Zaretski and D. J. Lipomi, *Nanoscale* **7**, 9963–9969 (2015).

- <sup>75</sup>M. Kratzer *et al.*, *Appl. Phys. Lett.* **106**, 103101 (2015).
- <sup>76</sup>P. Blake *et al.*, *Nano Lett.* **8**, 1704–1708 (2008).
- <sup>77</sup>S. Stankovich, D. A. Dikin, G. H. Dommett, K. M. Kohlhaas, E. J. Zimney, E. A. Stach, R. D. Piner, S. T. Nguyen, and R. S. Ruoff, *Nature* **442**, 282–286 (2006).
- <sup>78</sup>S. Stankovich, D. A. Dikin, R. D. Piner, K. A. Kohlhaas, A. Kleinhammes, Y. Jia, Y. Wu, S. T. Nguyen, and R. S. Ruoff, *Carbon* **45**, 1558–1565 (2007).
- <sup>79</sup>G. Eda, G. Fanchini, and M. Chhowalla, *Nat. Nanotechnol.* **3**, 270–274 (2008).
- <sup>80</sup>M. Cai, D. Thorpe, D. H. Adamson, and H. C. Schniepp, *J. Mater. Chem.* **22**, 24992–25002 (2012).
- <sup>81</sup>M. Segal, *Nat. Nanotechnol.* **4**, 612–614 (2009).
- <sup>82</sup>A. Eckmann, A. Felten, A. Mishchenko, L. Britnell, R. Krupke, K. S. Novoselov, C. Casiraghi, “Probing the nature of defects in graphene by Raman spectroscopy,” *Nano Lett.* **12**, 3925–3930 (2012).
- <sup>83</sup>A. C. Ferrari and D. M. Basko, *Nature Nanotech.* **8**, 235 (2013).
- <sup>84</sup>T. Mohiuddin, A. Lombardo, R. R. Nair *et al.*, *Phys. Rev. B* **79**, 205433 (2009).
- <sup>85</sup>F. Ding, H. Ji, Y. Chen, A. Herklotz, K. Dorr, Y. Mei, A. Rastelli, and O. G. Schmidt, *Nano Lett.* **10**, 3453–3458 (2010).
- <sup>86</sup>Y. Zang, F. Zhang, C.-a. Di, and D. Zhu, *Mater. Horiz.* **2**, 140–156 (2015).
- <sup>87</sup>M. Huang, T. A. Pascal, H. Kim, W. A. Goddard, and J. R. Greer, *Nano Lett.* **11**, 1241–1246 (2011).
- <sup>88</sup>M. L. Teague, A. P. Lai, J. Velasco, C. R. Hughes, A. D. Beyer, M. W. Bockrath, C. N. Lau, and N. C. Yeh, *Nano Lett.* **9**, 2542–2546 (2009).

## Short-Range Order in $\text{VI}_3$

Sanja Djurdjic Mijin, A. M. Milinda Abeykoon, Andrijana Šolajić, Ana Milosavljević, Jelena Pešić, Yu Liu, Cedomir Petrovic, Zoran V. Popović, and Nenad Lazarević\*

Cite This: *Inorg. Chem.* 2020, 59, 16265–16271

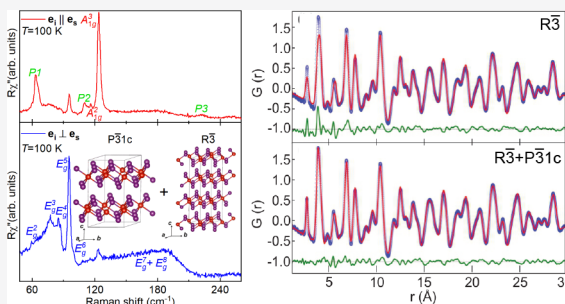
Read Online

ACCESS |

Metrics & More

Article Recommendations

**ABSTRACT:** We present a detailed investigation of the crystal structure of  $\text{VI}_3$ , a two-dimensional van der Waals material of interest for studies of low-dimensional magnetism. As opposed to the average crystal structure that features  $R\bar{3}$  symmetry of the unit cell, our Raman scattering and X-ray atomic pair distribution function analysis supported by density functional theory calculations point to the coexistence of short-range ordered  $P\bar{3}1c$  and long-range ordered  $R\bar{3}$  phases. The highest-intensity peak,  $A_{1g}$ , exhibits a moderate asymmetry that might be traced back to the spin–phonon interactions, as in the case of  $\text{CrI}_3$ .



### INTRODUCTION

A well-known family of transition metal trihalides (TMTs)  $\text{MX}_3$  ( $X = \text{Cr}, \text{B}, \text{or I}$ ) have received a great deal of attention due to potential existence of two-dimensional (2D) ferromagnetism,<sup>1–6</sup> which has been confirmed in  $\text{CrI}_3$ .<sup>7,8</sup> The similar crystal structure and magnetic properties of  $\text{CrI}_3$  and  $\text{VI}_3$  fostered a belief that the same might be found in the latter. In fact, magnetization measurements revealed the 2D ferromagnetic nature of  $\text{VI}_3$  with a Currie temperature ( $T_c$ ) of around 50 K.<sup>9,10</sup> Contrary to a layer-dependent ferromagnetism in  $\text{CrI}_3$ ,<sup>11</sup> the first-principles calculations predict that ferromagnetism in  $\text{VI}_3$  persists down to a single layer,<sup>9</sup> making it a suitable candidate for engineering 2D spintronic devices. Resistivity measurements showed  $\text{VI}_3$  is an insulator with an optical band gap of  $\sim 0.6$  eV.<sup>9,12</sup>

Whereas laboratory X-ray diffraction studies reported three possible high-temperature  $\text{VI}_3$  unit cell symmetries,<sup>9,12–14</sup> high-resolution synchrotron X-ray diffraction confirmed a rhombohedral  $R\bar{3}$  space group.<sup>10</sup> A very recently published Raman spectroscopy study indicated that the  $\text{VI}_3$  crystal structure can be described within the  $C_{2h}$  point group.<sup>15</sup> All results agree on the existence of a phase transition at a temperature of 79 K. However, the subtle<sup>12</sup> structural changes below 79 K are still under debate.

The long-range magnetic order in ultrathin 2D van der Waals (vdW) crystals stems from strong uniaxial anisotropy, in contrast to materials with isotropic exchange interactions where order parameters are forbidden.<sup>16–18</sup> 2D vdW magnetic materials are of interest both as examples of exotic magnetic order<sup>19</sup> and for potential applications in spintronic technology.<sup>2,4,20,21</sup>

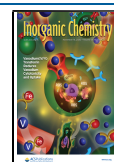
Atomically thin flakes of  $\text{CrCl}_3$  have a magnetic transition temperature that is different from that of bulk crystals possibly

due to the different crystal structure of the monolayer and ultrathin crystals when compared to bulk.<sup>22,23</sup> Similar observations were made on  $\text{CrI}_3$  monolayers.<sup>22,24,25</sup> It has been proposed<sup>23</sup> that the second anomaly in heat capacity in bulk  $\text{CrCl}_3$  arises due to regions close to the surface that host a different crystal structure when compared to bulk;<sup>26,27</sup> however, due to the substantial mass fraction detected in heat capacity measurements, this could also reflect differences between the short-range order and long-range crystallographic order of Bragg planes. The short-range order is determined by the space group that is energetically favorable for a monolayer or a few layers, whereas the long-range crystallographic order is established over large packing lengths.

In this paper, we present an experimental Raman scattering study of the bulk  $\text{VI}_3$  high-temperature structure, supported by density functional theory (DFT) calculations and the X-ray atomic pair distribution function (PDF) analysis. The comparison between the Raman experiment and DFT calculations for each of the previously reported space groups suggested that the high-temperature lattice vibrations of bulk  $\text{VI}_3$  are consistent with a  $P\bar{3}1c$  trigonal structure. Nine ( $2A_{1g} + 7E_g$ ) of 12 observed peaks were assigned on the basis of factor group analysis (FGA) and DFT calculations. The PDF analysis indicated the coexistence of two crystallographic phases at two different interatomic distances, short-range ordered  $P\bar{3}1c$  and

Received: July 12, 2020

Published: October 23, 2020



long-range ordered  $R\bar{3}$ , as two segregated phases and/or as randomly distributed short-range ordered  $P\bar{3}1c$  domains in the long-range ordered  $R\bar{3}$  lattice. Raman data displayed a moderate asymmetry of the  $A_{1g}^3$  phonon line. This behavior was attributed to the spin–phonon interaction, similar to the case for  $\text{CrI}_3$ . The additional peaks in our spectra obey  $A_g$  selection rules and can be described in terms of overtones, as well as the  $A_{2g}$  silent modes “activated” by the symmetry breaking.

## EXPERIMENTAL AND COMPUTATIONAL DETAILS

The preparation of single-crystal  $\text{VI}_3$  samples used in this study is presented elsewhere.<sup>10</sup> For the Raman scattering experiment, a Tri Vista 557 spectrometer was used in the backscattering micro-Raman configuration with a 1800/1800/2400 grooves/mm diffraction grating combination. A Coherent  $\text{Ar}^+/\text{Kr}^+$  ion laser with a 514 nm line was used as an excitation source. Laser beam focusing was achieved through the microscope objective with 50 $\times$  magnification. The direction of the incident (scattered) light coincides with the crystallographic  $c$  axis. The sample, cleaved in open air, was held inside a KONTI CryoVac continuous helium flow cryostat with a 0.5 mm thick window. Raman scattering measurements were performed under high vacuum ( $10^{-6}$  mbar). All of the obtained Raman spectra were corrected by the Bose factor. The spectrometer resolution is comparable to the Gaussian width of  $1\text{ cm}^{-1}$ .

PDF and wide-angle X-ray scattering measurements were carried out in capillary transmission geometry using a PerkinElmer amorphous silicon area detector placed 206 and 983 mm downstream from the sample, respectively, at beamline 28-ID-1 (PDF) of National Synchrotron Light Source II at Brookhaven National Laboratory. The setup utilized a 74.3 keV ( $\lambda = 0.1668\text{ \AA}$ ) X-ray beam.

Two-dimensional diffraction data were integrated using the Fit2D software package.<sup>28</sup> Data reduction was performed to obtain experimental PDFs ( $Q_{\text{max}} = 26\text{ \AA}^{-1}$ ) using the xPDFsuite software package.<sup>29</sup> The Rietveld and PDF analyses were carried out using GSAS-II<sup>30</sup> and PDFgui<sup>31</sup> software packages, respectively.

Density functional theory calculations were performed using the Quantum Espresso software package,<sup>32</sup> employing the PBE exchange–correlation functional<sup>33</sup> and PAW pseudopotentials.<sup>34,35</sup> All calculations are spin-polarized. The cutoff for wave functions and the charge density were set to 48 and 650 Ry, respectively. The  $k$ -points were sampled using the Monkhorst–Pack scheme, on a  $6 \times 6 \times 6$   $\Gamma$ -centered grid for  $R\bar{3}$  and  $C2/m$  structures and a  $12 \times 12 \times 8$  grid for the  $P\bar{3}1c$  structure. Optimization of the lattice parameters and atomic positions in the unit cell was performed until the interatomic forces were  $<10^{-6}$  Ry/ $\text{\AA}$ . To obtain more accurate lattice parameters, treatment of the van der Waals interactions is included using the Grimme-D2 correction. The correlation effects are treated with the Hubbard  $U$  correction (LDA+ $U$ ), using a rotationally invariant formulation implemented in QE,<sup>36</sup> where  $U = 3.68\text{ eV}$ . Band structure plots are calculated at 800  $k$ -points on the chosen path over high-symmetry points. Phonon frequencies were calculated with the linear response method, as implemented in the -homon part of Quantum Espresso.

## RESULTS AND DISCUSSION

The first reported results for  $\text{VI}_3$ , dating from the 1950s,<sup>37–39</sup> indicated that  $\text{VI}_3$  adopts a honeycomb layer-type  $\text{BiI}_3$  structure described with space group  $R\bar{3}$ , which is a structure common in TMTs, also found in the low-temperature phase of  $\text{CrI}_3$ .<sup>6,40</sup>

There have been several proposed unit cell symmetries for  $\text{VI}_3$  in the literature:  $R\bar{3}$ ,<sup>12,13</sup>  $C2/m$ ,<sup>14</sup> and  $P\bar{3}1c$ .<sup>9</sup> Schematic representations of the  $P\bar{3}1c$ ,  $R\bar{3}$ , and  $C2/m$  crystal structures are depicted in Figure 1. The corresponding crystallographic unit cell parameters, previously reported, are listed in Table 1.

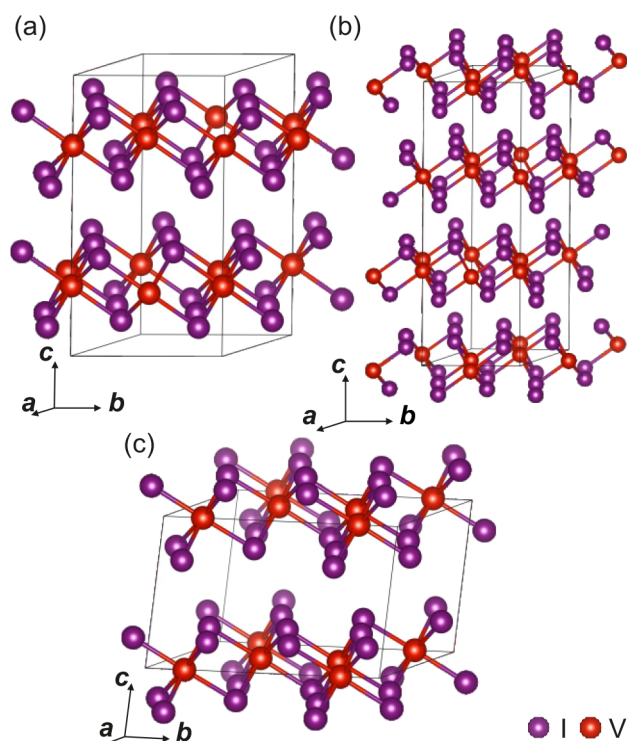


**Figure 1.** Schematic representation of the high-temperature (a)  $P\bar{3}1c$ , (b)  $R\bar{3}$ , and (c)  $C2/m$  structures of  $\text{VI}_3$ . Black solid lines represent unit cells.

Each of the suggested symmetries implies a different distribution of Raman active modes.

According to FGA, eight ( $4A_g + 4E_g$ ), 11 ( $3A_{1g} + 8E_g$ ), and 12 ( $6A_g + 6B_g$ ) Raman active modes are expected to be observed in the light scattering experiment for  $R\bar{3}$ ,  $P\bar{3}1c$ , and  $C2/m$  crystal structures, respectively. Wyckoff positions, irreducible representations, and corresponding tensors of Raman active modes for each space group are listed in Table 2.

The first step in determining the crystal symmetry from the light scattering experiment is to compare the expected and observed Raman active modes, shown in Figure 2. The red solid line represents the spectrum measured in the parallel polarization configuration, whereas the blue line corresponds to the cross polarization configuration. Five of 12 observed peaks emerge only in parallel, whereas five peaks and a broad peak-like structure can be observed for both polarization configurations. The emergence of the  $123.4\text{ cm}^{-1}$  peak in the cross polarization can be understood as a “leakage” of the  $A_{1g}^3$  mode due to a possible finite  $c$  axis projection and/or the presence of defects.

Now the peaks that appear only for the parallel polarization configuration can be assigned as either  $A_{1g}$  or  $A_g$  symmetry modes, assuming the light polarization direction along the main crystal axis of the  $C2/m$  structure for the later. On the basis of the FGA for possible symmetry group candidates, the remaining Raman active modes can be either of  $E_g$  or  $B_g$  symmetry. The selection rules (Table 2) do not allow observation of the  $B_g$  symmetry modes for the parallel polarization configuration. Consequently, the peaks that can be observed in both scattering channels were recognized as  $E_g$  modes. The absence of  $B_g$  modes in the Raman spectra rules out the possibility of the  $\text{AlCl}_3$  type of structure (space group  $C2/m$ ). Two possible remaining crystal symmetries ( $R\bar{3}$  and



Table 1. Previously Reported Experimental and Calculated Unit Cell Parameters for  $P\bar{3}1c$ ,  $R\bar{3}$ , and  $C2/m$  Structures of  $VI_3$ 

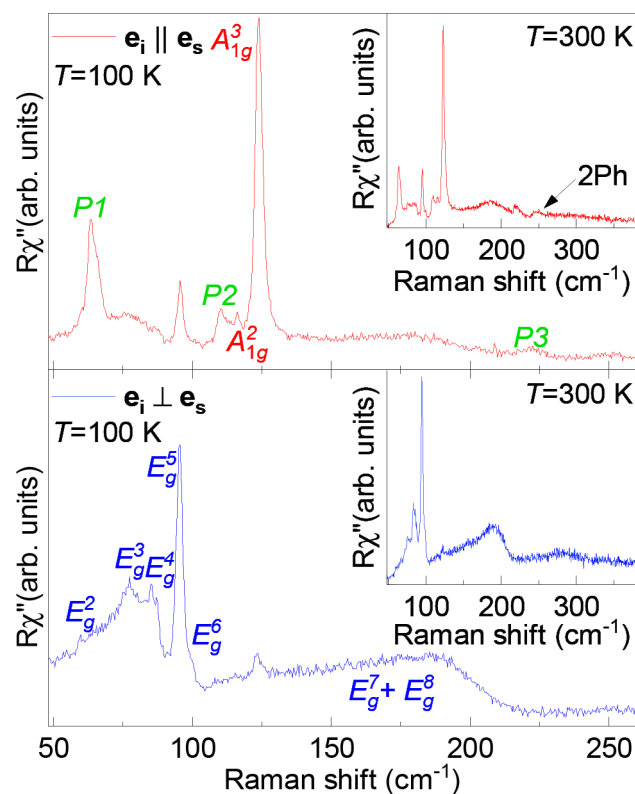
	$P\bar{3}1c$		$R\bar{3}$		$C2/m$	
	calcd	exp. <sup>9</sup>	calcd	exp. <sup>12</sup>	calcd	exp. <sup>14</sup>
<i>a</i> (Å)	6.87	6.89(10)	6.69	6.89(3)	7.01	6.84(3)
<i>b</i> (Å)	6.87	6.89(10)	6.69	6.89(3)	12.14	11.83(6)
<i>c</i> (Å)	13.224	13.289(1)	19.81	19.81(9)	7.01	6.95(4)
$\alpha$ (deg)	90	90	90	90	90	90
$\beta$ (deg)	90	90	90	90	109.05	108.68
$\gamma$ (deg)	120	120	120	120	90	90
cell volume (Å <sup>3</sup> )	559.62	547.74(10)	767.71	814.09(8)	563.33	533.66(36)

Table 2. Wyckoff Positions of Atoms and Their Contributions to the  $\Gamma$ -Point Phonons for the  $R\bar{3}$ ,  $C2/m$ , and  $P\bar{3}1c$  Structures and the Raman Tensors for the Corresponding Space Groups

space group $P\bar{3}1c$		space group $R\bar{3}$		space group $C2/m$	
atom	irreducible representation	atom	irreducible representation	atom	irreducible representation
V (2a)	$A_{2g} + A_{2u} + E_g + E_u$	V (3a)	$A_g + A_u + E_g + E_u$	V (4g)	$A_g + A_u + 2B_g + 2B_u$
V (2c)	$A_{2g} + A_{2u} + E_g + E_u$	V (6c)	$A_g + A_u + E_g + E_u$	I (4i)	$2A_g + A_u + B_g + 2B_u$
I (12i)	$3A_{1g} + 3A_{1u} + 3A_{2g} + 3A_{2u} + 6E_g + 6E_u$	I (18f)	$3A_g + 3A_u + 3E_g + 3E_u$	I (8j)	$3A_g + 3A_u + 3B_g + 3B_u$

$A_{1g} = \begin{pmatrix} a & a & b \end{pmatrix}$ ${}^1E_g = \begin{pmatrix} c & d \\ -c & d \end{pmatrix} {}^2E_g = \begin{pmatrix} -c & -d \\ d & c \end{pmatrix}$	$A_g = \begin{pmatrix} a & a & b \end{pmatrix}$ ${}^1E_g = \begin{pmatrix} c & d & e \\ d & -c & f \\ e & f & -c \end{pmatrix} {}^2E_g = \begin{pmatrix} d & -c & -f \\ -c & -d & e \\ -f & e & d \end{pmatrix}$	$A_g = \begin{pmatrix} a & d \\ c & b \end{pmatrix}$ $B_g = \begin{pmatrix} e & f \\ e & f \end{pmatrix}$
---	--	---



**Figure 2.** Raman spectra of the high-temperature  $VI_3$  single-crystal structure measured in parallel (red solid line) and cross (blue solid line) polarization configurations at 100 K. Peaks crossed in both spectra were identified as  $E_g$  modes, whereas peaks observed only in the red spectrum were assigned as  $A_{1g}$  modes. Additional peaks that obey pure  $A_{1g}$  symmetry are marked as P1–P3.

$P\bar{3}1c$ ) are difficult to single out on the basis of the Raman data symmetry analysis alone. To overcome this obstacle, the DFT method was applied for each of the suggested structures.

It was reported in the literature that  $P\bar{3}1c$   $VI_3$  can have two possible electronic states<sup>9,14,41–43</sup> that both can be obtained using DFT+U calculations by varying the smearing and mixing parameters. This approach resulted in a Mott-insulator state having a lower energy making it the electronic ground state of  $VI_3$ . However, the total energy difference of these two states is small and will not be mentioned further because it is outside of the scope of our analysis. For the sake of completeness, both sets of phonon energies obtained through DFT calculations for these electronic states of the  $P\bar{3}1c$  structure are listed in Table 3 together with the results for the  $R\bar{3}$  and  $C2/m$  space groups as well as the experimental results measured at 100 K.

Now one can see that, even though the Raman mode symmetries for the case of the  $R\bar{3}$  crystal structure can describe our Raman spectra, there is a stronger mismatch in calculated and experimentally determined phonon energies when compared to the results obtained for the  $P\bar{3}1c$  structure. The deviation is largest for the calculated  $A_g^1$  mode. The closest mode in energy, which obeys the same symmetry rules as the calculated  $A_g^1$ , is a peak at  $\sim 64.1$   $cm^{-1}$ , yielding a deviation of  $\sim 30\%$ . Also, the calculated energy of the  $A_g^4$  mode could not be identified within our spectrum, with the closest experimental  $A_g$  peaks being within 20%. Such deviation in theory and experiment,  $>20\%$ , indicates that the room-temperature phonon vibrations in  $VI_3$  do not originate predominantly from the  $BiI_3$  structure type either, leaving  $P\bar{3}1c$  as the only candidate. This indication is further reinforced by the inability to connect the experimentally observed  $E_g$  modes at  $\sim 77$  and  $\sim 86$   $cm^{-1}$  with the  $R\bar{3}$ -calculated modes.

Our experimental data (Table 3) are mostly supported by the phonon energies obtained for possible electronic states of

**Table 3.** Comparison between Calculated Values of Raman Active Phonon Energies for Insulating and Half-Metallic States of the  $P\bar{3}1c$  Structure and Experimentally Obtained Values (left)<sup>a</sup> and Phonon Symmetries and Calculated Phonon Energies for the  $R\bar{3}$  and  $C2/m$  Structures of  $VI_3$ <sup>b</sup>

space group $P\bar{3}1c$				space group $R\bar{3}$		space group $C2/m$	
symmetry	calcd (cm <sup>-1</sup> )	calcd (cm <sup>-1</sup> )	exp. (cm <sup>-1</sup> )	symmetry	calcd (cm <sup>-1</sup> )	symmetry	calcd (cm <sup>-1</sup> )
$E_g^1$	17.2	15.2	–	$E_g^1$	45.2	$A_g^1$	58.1
$A_{2g}^1$ (silent)	35.0	56.8		$E_g^2$	69.9	$B_g^1$	60.0
$E_g^2$	62.2	61.6	59.8	$A_g^1$	99.3	$A_g^2$	82.7
$A_{2g}^2$ (silent)	69.4	72.3		$E_g^3$	99.8	$B_g^2$	82.9
$E_g^3$	74.1	75.9	77.2	$A_g^2$	105.1	$A_g^3$	85.7
$A_{1g}^1$	83.3	84.2	–	$A_g^3$	135.5	$B_g^3$	88.9
$E_g^4$	84.9	86.6	86.7	$A_g^4$	167.9	$A_g^4$	99.3
$E_g^5$	91.5	98.4	95.2	$E_g^4$	176.8	$B_g^4$	99.3
$A_{2g}^3$ (silent)	92.2	96.3				$A_g^5$	122.3
$E_g^6$	97.4	108.3	100.4			$B_g^5$	149.9
$A_{1g}^2$	113.2	119.3	116.8			$B_g^6$	161.0
$A_{1g}^3$	117.1	123.9	123.4			$A_g^6$	164.0
$A_{2g}^4$ (silent)	121.3	147.8					
$E_g^7$	132.2	151.9	c				
$E_g^8$	149.4	166.9	c				
$A_{2g}^5$ (silent)	185.9	212.1					

<sup>a</sup>The experimental values were determined at 100 K. The experimental uncertainty is 0.3 cm<sup>-1</sup>. <sup>b</sup>All calculations were performed at 0 K. <sup>c</sup>See the text for an explanation.

the  $P\bar{3}1c$  trigonal structure with deviations of around 10% and 15%. Nine of 11 Raman modes were singled out and identified, with  $E_g^1$  being not observable in our experimental setup due to its low energy. The  $A_{1g}^1$  mode might be missing due to its low intensity and/or the finite spectrometer resolution. The most striking was the observation of the broad feature at  $\sim 180$  cm<sup>-1</sup>, persisting up to 300 K in both scattering channels. Whereas its line shape resembles those of the two-magnon type of excitation, we believe that scenario is unlikely for a ferromagnetic material. The energy region where the feature was observed may also suggest the possibility of a two-phonon type of excitation. However, their scattering cross sections are usually small and dominated by overtones, thus mostly observed for the parallel scattering configuration.<sup>45</sup> For example, such an excitation was observed at  $\sim 250$  cm<sup>-1</sup> (Figure 2). Finally, the observed feature also falls into the energy region where, as suggested by the numerical calculations, observation of the  $E_g^7$  and  $E_g^8$  modes is expected. We believe that it is actually a complex structure comprising  $E_g^7$  and  $E_g^8$  Raman modes, significantly broadened by the spin-phonon interaction, that is particularly strong on these phonon branches. The proximity of the two very broad, presumably asymmetric peaks hampers their precise assignment.

Closer inspection of other Raman peaks revealed that some of them also exhibit an asymmetric line shape. To further demonstrate this virtue, we have quantitatively analyzed the highest-intensity peak,  $A_{1g}^3$ , using the symmetric Voigt line shape and convolution of a Fano profile and a Gaussian.<sup>44–46</sup> The asymmetric line shape (with a Fano parameter of  $|q| = 12.3$ ) gives a slightly better agreement with the experimental data, as depicted in Figure 3. Considering that the observed asymmetry in similar materials was shown to reflect the spin-phonon interaction,<sup>46,47</sup> we propose it as a possible scenario in  $VI_3$ , as well.

Our findings, based on the inelastic light scattering experiments, at first glance differ from those presented in ref 10. To resolve this discrepancy, we used synchrotron X-ray Rietveld and PDF analysis. Typically, the short-range order

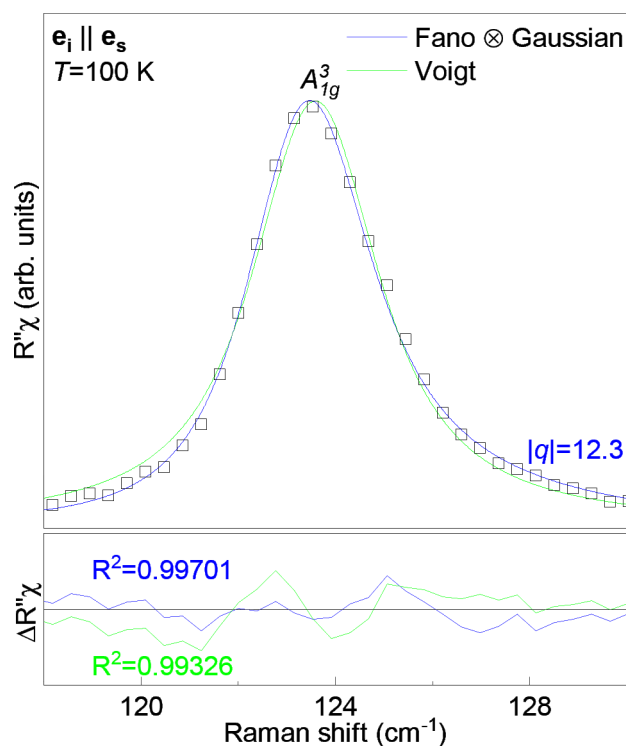


**Figure 3.** Quantitative analysis of the  $A_{1g}^3$  mode. The blue solid line represents the line shape obtained as a convolution of the Fano line shape and the Gaussian, whereas the green one represents a Voigt profile fitted to experimental data ( $\square$ ). For details, see refs 44 and 45.

(SRO) contributes to diffuse scattering under the long-range order (LRO) Bragg peaks when they coexist. Because the diffuse scattering is subtracted as part of the background in the Rietveld refinement, this method is more sensitive to the average structure of materials. In contrast, PDF analysis is performed on the sine Fourier transform of the properly corrected diffraction pattern, including both Bragg and diffuse

components. PDF is a real space function that provides a histogram of interatomic distances, which contain information regarding all length scales.<sup>48–51</sup> The 1–10 and 11–30 Å PDF length scales are more sensitive to SRO and LRO, respectively. For the  $\text{VI}_3$  system, the best Rietveld fit was obtained using the  $R\bar{3}$  space group (Figure 4a), in agreement with that previously

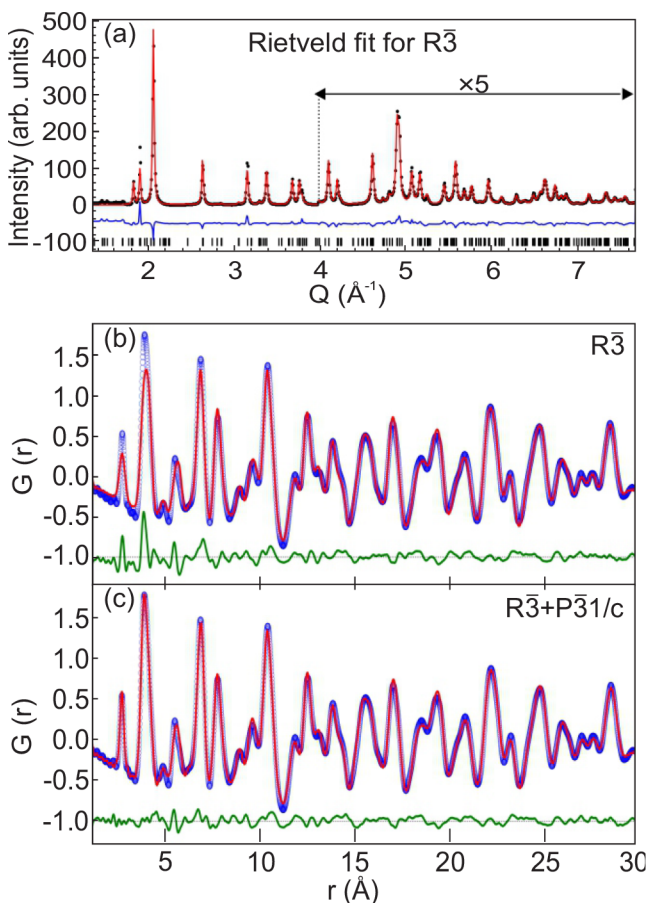


**Figure 4.** Best structural model fits to diffraction data. (a) Rietveld fit using the  $R\bar{3}$  space group with black vertical bars indicating calculated peak positions. (b) PDF fit using the  $R\bar{3}$  space group. (c) Two-phase PDF fit using  $R\bar{3}$  and  $P\bar{3}1c$  space groups to fit LRO and SRO, respectively. Black dots (XRD) and blue dots (PDF) represent experimental data, and red solid lines represent the model-based fits. The fit residues are shown at the bottom of each plot.

observed.<sup>10</sup> Not surprisingly, LRO obtained from the Rietveld refinement showed a good agreement on the PDF length scale of 10–30 Å. However, the  $R\bar{3}$  space group gave a poor fit on the length scale of 1.5–15 Å with refined  $\delta 1$  to account for correlated motion (Figure 4b). In contrast,  $P\bar{3}1c$  gave a better fit to SRO, but a poor fit to LRO. The best PDF fits were obtained by refining a weighted two-phase structural model containing  $\sim 25$  wt % SRO  $P\bar{3}1c$  and  $\sim 75$  wt % LRO  $R\bar{3}$  phases. The refined correlation length of the SRO is  $\sim 15$ –20 Å (Figure 4c). These results suggest two possible scenarios: (1) coexistence of two segregated phases, LRO  $R\bar{3}$  and SRO  $P\bar{3}1c$ , and (2) randomly distributed short-range ordered  $P\bar{3}1c$  domains in the long-range ordered  $R\bar{3}$  lattice. A detailed structural analysis is required to pinpoint scenario 1 and/or 2, which is beyond the scope of this work.

In addition to the peaks already assigned to  $\Gamma$ -point Raman active phonons of the  $P\bar{3}1c$  crystal structure (Table 2), three

additional peaks at  $64.2\text{ cm}^{-1}$  ( $P_1$ ),  $110.1\text{ cm}^{-1}$  ( $P_2$ ), and  $220.6\text{ cm}^{-1}$  ( $P_3$ ) are observed (see Figure 2). According to the results of DFT, energies of these modes correspond well to those calculated for silent  $A_{2g}^2$ ,  $A_{2g}^3$ , and  $A_{2g}^5$  modes. Their observability in Raman data may come from the release of the symmetry selection rules by breaking of the (translation) symmetry as suggested by the PDF in both scenarios.<sup>52–55</sup> However, as previously discussed, these peaks obey  $A_{1g}$  selection rules, indicating the possibility for them to be overtones in nature. In this less likely scenario, the phonon–phonon coupling is enhanced by the spin–phonon interaction and/or by the structural imperfections, thus enhancing the Raman scattering rate for the two-phonon processes.<sup>45</sup> Hence, the observed Raman modes reflect the symmetry of phonon vibrations related to the SRO.<sup>56,57</sup> It is interesting to note that, besides a possible short-range crystallography that is different from the average,  $\text{VI}_3$  might also feature short-range magnetic order above 79 K.<sup>14</sup>

## CONCLUSION

In summary, room-temperature phonon vibrations of  $\text{VI}_3$  stem from the  $P\bar{3}1c$  symmetry of the unit cell. The PDF analysis suggested the coexistence of two phases, short-range ordered  $P\bar{3}1c$  and long-range ordered  $R\bar{3}$ , as two segregated phases and/or as randomly distributed short-range ordered  $P\bar{3}1c$  domains in the long-range ordered  $R\bar{3}$  lattice. Nine of 12 observed peaks in the Raman spectra were assigned in agreement with  $P\bar{3}1c$  symmetry calculations. Three additional peaks, which obey  $A_{1g}$  symmetry rules, could be explained as either overtones or as activated  $A_{2g}$  silent modes caused by a symmetry breaking. The asymmetry of one of the  $A_{1g}$  phonon modes, together with the anomalous behavior of  $E_g^7$  and  $E_g^8$ , indicates strong spin–phonon coupling, which has already been reported in similar 2D materials.<sup>46,58</sup>

## AUTHOR INFORMATION

### Corresponding Author

Nenad Lazarević – Institute of Physics Belgrade, University of Belgrade, 11080 Belgrade, Serbia; [orcid.org/0000-0001-6310-9511](https://orcid.org/0000-0001-6310-9511); Email: [nenadl@ipb.ac.rs](mailto:nenadl@ipb.ac.rs)

### Authors

Sanja Djurdjić Mijin – Institute of Physics Belgrade, University of Belgrade, 11080 Belgrade, Serbia

A. M. Milinda Abeykoon – National Synchrotron Light Source II, Brookhaven National Laboratory, Upton, New York 11973, United States

Andrijana Solajić – Institute of Physics Belgrade, University of Belgrade, 11080 Belgrade, Serbia

Ana Milosavljević – Institute of Physics Belgrade, University of Belgrade, 11080 Belgrade, Serbia

Jelena Pešić – Institute of Physics Belgrade, University of Belgrade, 11080 Belgrade, Serbia

Yu Liu – Condensed Matter Physics and Materials Science Department, Brookhaven National Laboratory, Upton, New York 11973-5000, United States; [orcid.org/0000-0001-8886-2876](https://orcid.org/0000-0001-8886-2876)

Cedomir Petrović – Condensed Matter Physics and Materials Science Department, Brookhaven National Laboratory, Upton, New York 11973-5000, United States; [orcid.org/0000-0001-6063-1881](https://orcid.org/0000-0001-6063-1881)

Zoran V. Popović – Institute of Physics Belgrade, University of Belgrade, 11080 Belgrade, Serbia; Serbian Academy of Sciences and Arts, 11000 Belgrade, Serbia

Complete contact information is available at:  
<https://pubs.acs.org/10.1021/acs.inorgchem.0c02060>

## Notes

The authors declare no competing financial interest.

## ACKNOWLEDGMENTS

The authors acknowledge funding provided by the Institute of Physics Belgrade, through a grant from the Ministry of Education, Science and Technological Development of the Republic of Serbia, Project F-134 of the Serbian Academy of Sciences and Arts, and the Science Fund of the Republic of Serbia, PROMIS, 6062656, StrainedFeSC. DFT calculations were performed using computational resources at Johannes Kepler University (Linz, Austria). Materials synthesis was supported by the U.S. DOE-BES, Division of Materials Science and Engineering, under Contract DE-SC0012704 (BNL). This research used beamline 28-ID-1 of National Synchrotron Light Source II, a U.S. DOE Office of Science User Facility operated for the DOE Office of Science by Brookhaven National Laboratory under Contract DE-S.




## REFERENCES

- (1) Seyler, K. L.; Zhong, D.; Klein, D. R.; et al. Ligand-field helical luminescence in a 2D ferromagnetic insulator. *Nat. Phys.* **2018**, *14*, 277–281.
- (2) Klein, D. R.; MacNeill, D.; Lado, J. L.; Soriano, D.; Navarro-Moratalla, E.; Watanabe, K.; et al. Probing magnetism in 2D van der Waals crystalline insulators via electron tunneling. *Science* **2018**, *360*, 1218–1222.
- (3) Huang, B.; Clark, G.; Klein, D. R.; MacNeill, D.; Navarro-Moratalla, E.; Seyler, K. L.; et al. Electrical control of 2D magnetism in bilayer CrI<sub>3</sub>. *Nat. Nanotechnol.* **2018**, *13*, 544–548.
- (4) Jiang, S.; Li, L.; Wang, Z.; Mak, K. F.; Shan, J. Controlling magnetism in 2D CrI<sub>3</sub> by electrostatic doping. *Nat. Nanotechnol.* **2018**, *13*, 549–553.
- (5) McGuire, M. A.; Clark, G.; KC, S.; Chance, W. M.; Jellison, G. E.; Cooper, V. R.; Xu, X.; Sales, B. C. Magnetic behavior and spin-lattice coupling in cleavable van der Waals layered CrCl<sub>3</sub> crystals. *Phys. Rev. Materials* **2017**, *1*, 014001.
- (6) Djurdjic-Mijin, S. D.; Solajić, A.; Pešić, J.; Šćepanović, M.; Liu, Y.; Baum, A.; et al. Lattice dynamics and phase transition in CrI<sub>3</sub> single crystals. *Phys. Rev. B: Condens. Matter Mater. Phys.* **2018**, *98*, 104307.
- (7) Thiel, L.; Wang, Z.; Tschudin, M.; Rohner, D.; Gutierrez-Lezama, I. G.; Ubrig, N.; et al. Probing magnetism in 2D materials at the nanoscale with single-spin microscopy. *Science* **2019**, *364*, 973–976.
- (8) Lin, G. T.; Luo, X.; Chen, F. C.; Yan, J.; Gao, J. J.; Sun, Y.; et al. Critical behavior of two-dimensional intrinsically ferromagnetic semiconductor CrI<sub>3</sub>. *Appl. Phys. Lett.* **2018**, *112*, 072405.
- (9) Son, S.; Coak, M. J.; Lee, N.; Kim, J.; Kim, T. Y.; Hamidov, H.; et al. Bulk properties of the van der Waals hard ferromagnet VI<sub>3</sub>. *Phys. Rev. B: Condens. Matter Mater. Phys.* **2019**, *99*, 041402.
- (10) Liu, Y.; Abeykoon, M.; Petrovic, C. Critical behavior and magnetocaloric effect in VI<sub>3</sub>. *Phys. Rev. Research* **2020**, *2*, 013013.
- (11) Huang, B.; Clark, G.; Navarro-Moratalla, E.; Klein, D. R.; Cheng, R.; Seyler, K. L.; et al. Layer-dependent ferromagnetism in a van der Waals crystal down to the monolayer limit. *Nature* **2017**, *546*, 270–273.
- (12) Kong, T.; Stolze, K.; Timmons, E. I.; Tao, J.; Ni, D.; Guo, S.; et al. VI<sub>3</sub> – a New Layered Ferromagnetic Semiconductor. *Adv. Mater.* **2019**, *31*, 1808074.
- (13) Doležal, P.; Kratochvílová, M.; Holý, V.; Čermak, P.; Sechovský, V.; Dušek, M.; et al. Crystal structures and phase transitions of the van der Waals ferromagnet VI<sub>3</sub>. *Phys. Rev. Materials* **2019**, *3*, 121401.
- (14) Tian, S.; Zhang, J.-F.; Li, C.; Ying, T.; Li, S.; Zhang, X.; et al. Ferromagnetic van der Waals Crystal VI<sub>3</sub>. *J. Am. Chem. Soc.* **2019**, *141*, 5326–5333.
- (15) Wang, Y.-M.; Tian, S.-J.; Li, C.-H.; Jin, F.; Ji, J.-T.; Lei, H.-C.; Zhang, Q.-M. Raman scattering study of two-dimensional magnetic van der Waals compound VI<sub>3</sub>. *Chin. Phys. B* **2020**, *29*, 056301.
- (16) Lee, I.; Utermohlen, F. G.; Weber, D.; Hwang, K.; Zhang, C.; van Tol, J.; Goldberger, J. E.; Trivedi, N.; Hammel, P. C. Fundamental Spin Interactions Underlying the Magnetic Anisotropy in the Kitaev Ferromagnet CrI<sub>3</sub>. *Phys. Rev. Lett.* **2020**, *124*, 017201.
- (17) Xu, C.; Feng, J.; Xiang, H.; Bellaiche, L. Interplay between Kitaev interaction and single ion anisotropy in ferromagnetic CrI<sub>3</sub> and CrGeTe<sub>3</sub> monolayers. *npj Comput. Mater.* **2018**, *4*, 57.
- (18) Mermin, N. D.; Wagner, H. Absence of Ferromagnetism or Antiferromagnetism in One- or Two-Dimensional Isotropic Heisenberg Models. *Phys. Rev. Lett.* **1966**, *17*, 1133–1136.
- (19) Pershoguba, S. S.; Banerjee, S.; Lashley, J. C.; Park, J.; Ågren, H.; Aeppli, G.; Balatsky, A. V. Dirac Magnons in Honeycomb Ferromagnets. *Phys. Rev. X* **2018**, *8*, 011010.
- (20) Liu, J.; Shi, M.; Mo, P.; Lu, J. Electrical-field-induced magnetic Skyrmion ground state in a two-dimensional chromium tri-iodide ferromagnetic monolayer. *AIP Adv.* **2018**, *8*, 055316.
- (21) Jiang, S.; Li, L.; Wang, Z.; Shan, J.; Mak, K. Spin tunnel field-effect transistors based on two-dimensional van der Waals heterostructures. *Nature Electronics* **2019**, *2*, 159.
- (22) Klein, D. R.; MacNeill, D.; Song, Q.; Larson, D. T.; Fang, S.; Xu, M.; Ribeiro, R. A.; Canfield, P. C.; Kaxiras, E.; Comin, R.; Jarillo-Herrero, P. Enhancement of interlayer exchange in an ultrathin two-dimensional magnet. *Nat. Phys.* **2019**, *15*, 1255–1260.
- (23) Wang, Z.; Gibertini, M.; Dumcenco, D.; Taniguchi, T.; Watanabe, K.; Giannini, E.; Morpurgo, A. Determining the phase diagram of atomically thin layered antiferromagnet CrCl<sub>3</sub>. *Nat. Nanotechnol.* **2019**, *14*, 1116.
- (24) Ubrig, N.; Wang, Z.; Teyssier, J.; Taniguchi, T.; Watanabe, K.; Giannini, E.; Morpurgo, A. F.; Gibertini, M. Low-temperature monoclinic layer stacking in atomically thin CrI<sub>3</sub> crystals. *2D Mater.* **2020**, *7*, 015007.
- (25) Sun, Z.; et al. Giant nonreciprocal second-harmonic generation from antiferromagnetic bilayer CrI<sub>3</sub>. *Nature* **2019**, *572*, 497–501.
- (26) McGuire, M. A.; Clark, G.; KC, S.; Chance, W. M.; Jellison, G. E.; Cooper, V. R.; Xu, X.; Sales, B. C. Magnetic behavior and spin-lattice coupling in cleavable van der Waals layered CrCl<sub>3</sub> crystals. *Phys. Rev. Materials* **2017**, *1*, 014001.
- (27) Kuhlow, B. Magnetic Ordering in CrCl<sub>3</sub> at the Phase Transition. *physica status solidi (a)* **1982**, *72*, 161–168.
- (28) Hammersley, A. P.; Svensson, S. O.; Hanfland, M.; Fitch, A. N.; Hausermann, D. Two-dimensional detector software: From real detector to idealised image or two-theta scan. *High Pressure Res.* **1996**, *14*, 235–248.
- (29) Yang, X.; Juhas, P.; Farrow, C. L.; Billinge, S. J. L. *xPDFsuite: an end-to-end software solution for high throughput pair distribution function transformation, visualization and analysis*; 2014.
- (30) Toby, B. H.; Von Dreele, R. B. GSAS-II: the genesis of a modern open-source all purpose crystallography software package. *J. Appl. Crystallogr.* **2013**, *46*, 544–549.
- (31) Farrow, C. L.; Juhas, P.; Liu, J. W.; Bryndin, D.; Božin, E. S.; Bloch, J.; Proffen, T.; Billinge, S. J. L. PDFfit2 and PDFgui: computer programs for studying nanostructure in crystals. *J. Phys.: Condens. Matter* **2007**, *19*, 335219.
- (32) Giannozzi, P.; et al. QUANTUM ESPRESSO: a modular and open-source software project for quantum simulations of materials. *J. Phys.: Condens. Matter* **2009**, *21*, 395502.
- (33) Perdew, J. P.; Burke, K.; Ernzerhof, M. Generalized Gradient Approximation Made Simple. *Phys. Rev. Lett.* **1996**, *77*, 3865–3868.

- (34) Blöchl, P. E. Projector augmented-wave method. *Phys. Rev. B: Condens. Matter Mater. Phys.* **1994**, *50*, 17953–17979.
- (35) Kresse, G.; Joubert, D. From ultrasoft pseudopotentials to the projector augmented-wave method. *Phys. Rev. B: Condens. Matter Mater. Phys.* **1999**, *59*, 1758–1775.
- (36) Cococcioni, M.; de Gironcoli, S. Linear response approach to the calculation of the effective interaction parameters in the LDA + U method. *Phys. Rev. B: Condens. Matter Mater. Phys.* **2005**, *71*, 035105.
- (37) Juza, D.; Giegling, D.; Schäfer, H. Über die Vanadinjodide VJ<sub>2</sub> und VJ<sub>3</sub>. *Z. Anorg. Allg. Chem.* **1969**, *366*, 121–129.
- (38) Berry, K. O.; Smardzewski, R. R.; McCarley, R. E. Vaporization reactions of vanadium iodides and evidence for gaseous vanadium(IV) iodide. *Inorg. Chem.* **1969**, *8*, 1994–1997.
- (39) Klemm, W.; Krose, E. Die Kristallstrukturen von ScCl<sub>3</sub>, TiCl<sub>3</sub> und VCl<sub>3</sub>. *Z. Anorg. Chem.* **1947**, *253*, 218–225.
- (40) Liu, Y.; Petrovic, C. Three-dimensional magnetic critical behavior in CrI<sub>3</sub>. *Phys. Rev. B: Condens. Matter Mater. Phys.* **2018**, *97*, 014420.
- (41) He, J.; Ma, S.; Lyu, P.; Nachtigall, P. Unusual Dirac half-metallicity with intrinsic ferromagnetism in vanadium trihalide monolayers. *J. Mater. Chem. C* **2016**, *4*, 2518–2526.
- (42) Wang, Y.-P.; Long, M.-Q. Electronic and magnetic properties of van der Waals ferromagnetic semiconductor VI<sub>3</sub>. *Phys. Rev. B: Condens. Matter Mater. Phys.* **2020**, *101*, 024411.
- (43) Li, Y.; Liu, Y.; Wang, C.; Wang, J.; Xu, Y.; Duan, W. Electrically tunable valleytronics in quantum anomalous Hall insulating transition metal trihalides. *Phys. Rev. B: Condens. Matter Mater. Phys.* **2018**, *98*, 201407.
- (44) Lazarević, N.; Popović, Z. V.; Hu, R.; Petrovic, C. Evidence for electron-phonon interaction in Fe<sub>1-x</sub>M<sub>x</sub>Sb<sub>2</sub> (M = Co and Cr 0 ≤ x ≤ 0.5) single crystals. *Phys. Rev. B: Condens. Matter Mater. Phys.* **2010**, *81*, 144302.
- (45) Baum, A.; Milosavljević, A.; Lazarević, N.; Radonjić, M. M.; Nikolić, B.; Mitschek, M.; Maranloo, Z. I.; Šćepanović, M.; Grujić-Brojčin, M.; Stojilović, N.; Opel, M.; Wang, A.; Petrovic, C.; Popović, Z. V.; Hackl, R. Phonon anomalies in FeS. *Phys. Rev. B: Condens. Matter Mater. Phys.* **2018**, *97*, 054306.
- (46) Milosavljević, A.; Solajic, A.; Pešić, J.; Liu, Y.; Petrovic, C.; Lazarević, N.; Popović, Z. V. Evidence of spin-phonon coupling in CrSiTe<sub>3</sub>. *Phys. Rev. B: Condens. Matter Mater. Phys.* **2018**, *98*, 104306.
- (47) McCarty, K. F.; Radousky, H. B.; Hinks, D. G.; Zheng, Y.; Mitchell, A. W.; Folkerts, T. J.; Shelton, R. N. Electron-phonon coupling in superconducting Ba<sub>0.6</sub>K<sub>0.4</sub>BiO<sub>3</sub>: A Raman scattering study. *Phys. Rev. B: Condens. Matter Mater. Phys.* **1989**, *40*, 2662–2665.
- (48) Proffen, T.; Page, K. L.; McLain, S. E.; Clausen, B.; Darling, T. W.; TenCate, J. A.; Lee, S.-Y.; Ustundag, E. Atomic pair distribution function analysis of materials containing crystalline and amorphous phases. *Z. Kristallogr.* **2005**, *220*, 1002–1008.
- (49) Bordet, P. Application of the pair distribution function analysis for the study of cultural heritage materials. *C. R. Phys.* **2018**, *19*, 561–574.
- (50) Bozin, E. S.; Yin, W. G.; Koch, R. J.; Abeykoon, M.; Hor, Y. S.; Zheng, H.; Lei, H. C.; Petrovic, C.; Mitchell, J. F.; Billinge, S. J. L. Local orbital degeneracy lifting as a precursor to an orbital-selective Peierls transition. *Nat. Commun.* **2019**, *10*, 3638.
- (51) Egami, T.; Billinge, S. J. L. *Underneath the Bragg Peaks: Structural Analysis of Complex Materials*; 2003; p 16.
- (52) Jin, F.; Lazarević, N.; Liu, C.; Ji, J.; Wang, Y.; He, S.; Lei, H.; Petrovic, C.; Yu, R.; Popović, Z. V.; Zhang, Q. Phonon anomalies and magnetic excitations in BaFe<sub>2</sub>Se<sub>2</sub>O. *Phys. Rev. B: Condens. Matter Mater. Phys.* **2019**, *99*, 144419.
- (53) Moskovits, M.; Dilella, D. Surface-enhanced Raman spectroscopy of benzene and benzene-d<sub>6</sub> adsorbed on silver. *J. Chem. Phys.* **1980**, *73*, 6068–6075.
- (54) Dubroka, A.; Humlíček, J.; Abrashev, M. V.; Popović, Z. V.; Sapiña, F.; Cantarero, A. Raman and infrared studies of La<sub>1-y</sub>Sr<sub>y</sub>Mn<sub>1-x</sub>M<sub>x</sub>O<sub>3</sub> (M = Cr, Co, Cu, Zn, Sc or Ga): Oxygen disorder and local vibrational modes. *Phys. Rev. B: Condens. Matter Mater. Phys.* **2006**, *73*, 224401.
- (55) Souza Filho, A. G.; Faria, J. L. B.; Guedes, I.; Sasaki, J. M.; Freire, P. T. C.; Freire, V. N.; Mendes Filho, J.; Xavier, M. M.; Cabral, F. A. O.; de Araújo, J. H.; da Costa, J. A. P. Evidence of magnetic polaronic states in La<sub>0.70</sub>Sr<sub>0.30</sub>Mn<sub>1-x</sub>Fe<sub>x</sub>O<sub>3</sub> manganites. *Phys. Rev. B: Condens. Matter Mater. Phys.* **2003**, *67*, 052405.
- (56) Lekgoathi, M.; Kock, L. Effect of short and long range order on crystal structure interpretation: Raman and powder X-ray diffraction of LiPF<sub>6</sub>. *Spectrochim. Acta, Part A* **2016**, *153*, 651–654.
- (57) Wolverton, C.; Zunger, A.; Lu, Z.-W. Long-versus short-range order in Ni<sub>3</sub>V and Pd<sub>3</sub>V alloys. *Phys. Rev. B: Condens. Matter Mater. Phys.* **1994**, *49*, 16058.
- (58) Webster, L.; Liang, L.; Yan, J.-A. Distinct spin-lattice and spin-phonon interactions in monolayer magnetic CrI<sub>3</sub>. *Phys. Chem. Chem. Phys.* **2018**, *20*, 23546–23555.

Article

# Ab Initio Study of the Electronic, Vibrational, and Mechanical Properties of the Magnesium Diboride Monolayer

Jelena Pešić<sup>1,\*</sup> , Igor Popov<sup>1,2</sup> , Andrijana Šolajić<sup>1</sup>, Vladimir Damljanović<sup>1</sup> , Kurt Hingerl<sup>3</sup>, Milivoj Belić<sup>4</sup> and Radoš Gajić<sup>1</sup>

<sup>1</sup> Laboratory for graphene, other 2D materials and ordered nanostructures, Center for Solid State Physics and New Materials, Institute of Physics Belgrade, University of Belgrade, 11080 Belgrade, Serbia; popov@ipb.ac.rs (I.P.); solajic@ipb.ac.rs (A.Š.); damlja@ipb.ac.rs (V.D.); rgajic@ipb.ac.rs (R.G.)

<sup>2</sup> Institute for Multidisciplinary Research, University of Belgrade, Kneza Višeslava 1, 11030 Belgrade, Serbia

<sup>3</sup> Center for Surface and Nanoanalytics, Johannes Kepler University, 4040 Linz, Austria; Kurt.Hingerl@jku.at

<sup>4</sup> Science Program, Texas A&M University at Qatar, Doha P.O. Box 23874, Qatar; milivoj.belic@qatar.tamu.edu

\* Correspondence: yelena@ipb.ac.rs

Received: 15 March 2019; Accepted: 1 April 2019; Published: 2 April 2019



**Abstract:** Magnesium diboride gained significant interest in the materials science community after the discovery of its superconductivity, with an unusually high critical temperature of 39 K. Many aspects of the electronic properties and superconductivity of bulk MgB<sub>2</sub> and thin sheets of MgB<sub>2</sub> have been determined; however, a single layer of MgB<sub>2</sub> has not yet been fully theoretically investigated. Here, we present a detailed study of the structural, electronic, vibrational, and elastic properties of monolayer MgB<sub>2</sub>, based on ab initio methods. First-principles calculations reveal the importance of reduction of dimensionality on the properties of MgB<sub>2</sub> and thoroughly describe the properties of this novel 2D material. The presence of a negative Poisson ratio, higher density of states at the Fermi level, and a good dynamic stability under strain make the MgB<sub>2</sub> monolayer a prominent material, both for fundamental research and application studies.

**Keywords:** magnesium diboride; 2D materials; density functional theory

**PACS:** 71.15.Mb; 74.70.Ad

## 1. Introduction

Magnesium diboride was first synthesized and had its structure confirmed in 1953 [1]. An interest in its properties has grown ever since 2001, when it was discovered that MgB<sub>2</sub> exhibits the highest superconducting transition temperature  $T_c$  of all metallic superconductors. It is an inter-metallic s-wave compound superconductor with a quasi-two dimensional character [2] and a critical temperature of superconductive transition at  $T_c = 39$  K. The experimental confirmation of the isotope effect [3] in MgB<sub>2</sub> indicated that it is a phonon-mediated BCS superconductor. A better definition would describe MgB<sub>2</sub> as self-doped semimetal with a crucial  $\sigma$ -bonding band that is nearly filled [4]. The basic aspects of the electronic structure and pairing is in a rather strong coupling of high frequency boron–boron stretch modes to the bonding electronic boron–boron states at the Fermi surface. The phonon-mediated mechanism with different coupling strengths between a particular phonon mode and selected electronic bands, boron  $\sigma$ - and  $\pi$ -bands [5–13], results in the presence of two superconducting gaps at the Fermi level. MgB<sub>2</sub> has already been fabricated in bulk, as single crystals, and as a thin film, and shows potential for practical applications.

The discovery of graphene in 2004 [14] sparked an interest in 2D materials and their properties. A variety of new properties, which distinguished graphene from graphite [14–22], inspired a search for other low-dimensional limits of layered materials and possibilities they offered. Interest in a low-dimensional limit of  $\text{MgB}_2$  has arisen in past years, showing that it is superconductive even in a monolayer [23,24].

$\text{MgB}_2$  has a distinct layer structure, where boron atoms form a honeycomb layer and magnesium atoms are located above the center of the hexagons, between every boron plane. The boron layers alternate with a triangular lattice of magnesium layers. There is a noticeable structural similarity of  $\text{MgB}_2$  to graphite-intercalated compounds (GICs), some of which also exhibit superconductivity [25–29]. Both monolayer and two-layer graphene, decorated/intercalated with atoms of alkali and alkaline earth metals, exhibit superconductivity and have been thoroughly studied using ab initio methods and isotropic and anisotropic Eliashberg theory [30–32].

Furthermore, a similarity in the electronic structure between GICs and  $\text{MgB}_2$  exists. The peculiar and unique property of  $\text{MgB}_2$  is a consequence of the incomplete filling of two  $\sigma$  bands corresponding to strongly covalent  $sp^2$ -hybrid bonding within the graphite-like boron layers [33].

Here, we present a comprehensive study of the electronic, vibrational, and mechanical properties of  $\text{MgB}_2$  using ab initio methods, in order to provide its detail description.

## 2. Computational Details

$\text{MgB}_2$  has a hexagonal unit cell and consists of graphite-like  $\text{B}_2$  layers stacked with the Mg atoms in between, as shown in Figure 1. The first-principles calculations were performed within the density functional theory (DFT) formalism, using a general gradient approximation (GGA) to calculate the electronic structure. For all electronic and phonon structure, the Quantum Espresso software package [34] was used with ultra-soft pseudopotentials and a plane-wave cutoff energy of 30 Ry. All calculated structures are relaxed to their minimum energy configuration, following the internal force on atoms and stress tensor of the unit cell. We used the Monkhorst-Pack  $48 \times 48 \times 48$  and  $40 \times 40 \times 1$  k-meshes, for the calculations of the electronic structure of the  $\text{MgB}_2$  bulk and  $\text{MgB}_2$  monolayer, respectively. The phonon frequencies are calculated using Density Functional Perturbation Theory (DFPT) on the  $12 \times 12 \times 12$  and  $20 \times 20 \times 1$  phonon wave vector mesh for the bulk and monolayer structures, respectively. In two-dimensional systems, the van der Waals (vdW) interaction was found to play an important role on the electronic structure [35]; however, as this is study on monolayer  $\text{MgB}_2$ , we do not treat vdW interactions, especially since, in this case, the effects are minor and including them would add additional computational costs but would not yield more accurate results.

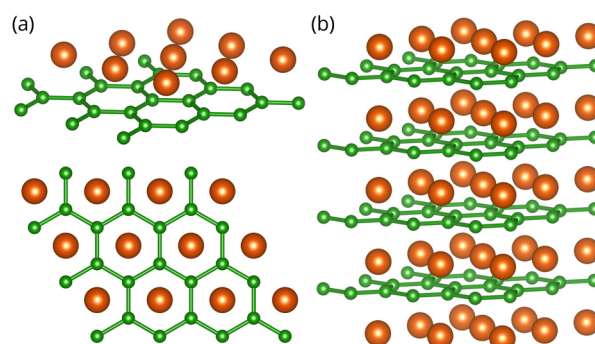


**Figure 1.** Crystal structure of the  $\text{MgB}_2$  monolayer (a) and bulk  $\text{MgB}_2$  (b), with a hexagonal unit cell. Green (orange) spheres represent Boron (Magnesium) atoms. Color online.

The crystal structure of  $\text{MgB}_2$  and the  $\text{MgB}_2$  monolayer are presented in Figure 1. The lattice parameters for the bulk  $\text{MgB}_2$  are in agreement with the experimental results,  $a = 3.083 \text{ \AA}$  and

$c/a = 1.142$  [9]. In order to avoid an interlayer interaction due to the periodicity and to simulate a 2D material, an artificial vacuum layer was set to be 25 Å. When the monolayer is modelled, the structure is geometrically optimized, allowing the atoms to reach a minimum potential energy state. The bond length between neighbouring atoms remained to be 1.78 Å, but the distance from the boron layer to the Mg atoms changed from  $h = 1.76$  Å to  $h = 1.60$  Å.

For the molecular dynamics (MD) study, the Siesta code was utilized [36]. The super-cell is built by repeating the unit cell three times in both in-plane directions, whereas the lattice vector in the perpendicular direction is 15 Å, providing a large enough vacuum space between the 2D material and its periodic replica in order to avoid their mutual interaction. The lattice parameters and the geometry of the unit cell are initially optimized using the conjugate gradient method. The Perdew-Burke-Ernzerhof form of the exchange-correlation functional [37], the double-zeta polarized basis set, and the Troulier-Martins pseudopotentials [38] were used in all MD calculations.

The second-order elastic constants were calculated using the ElaStic software package [39]. First, the direction is projected from the strain tensor and total energies for each deformation are calculated. Elastic constants are then calculated using the second derivatives of the energy curves, dependent on the parameter  $\eta$ . In our calculations, the maximum positive and negative amplitudes of 5% Lagrangian strain were applied, with a step of 0.1%.

For the 2D square, rectangular, or hexagonal lattices, the non-zero second-order elastic constants, in Voigt notation, are  $c_{11}$ ,  $c_{22}$ ,  $c_{12}$ , and  $c_{66}$ . Due to symmetry, in hexagonal structures  $c_{11} = c_{22}$  and  $c_{66} = \frac{1}{2}(c_{11} - c_{12})$ ; so, we have 2 independent elastic constants. The layer modulus, which represents the resistance of a 2D material to stretching, is given as

$$\gamma = \frac{1}{4}(c_{11} + c_{22} + 2c_{12}).$$

The 2D Young modulus  $Y$  for strains in the (10) and (01) directions, Poisson's ratio  $\nu$  and the shear modulus  $G$  are obtained from the following relations,

$$Y = \frac{c_{11}^2 - c_{12}^2}{c_{11}}, \quad \nu = \frac{c_{12}}{c_{22}}, \quad G = c_{66}.$$

Units for elastic constants and those parameters are N/m.

### 3. Results and Discussion

In order to determine the stability of a single layer of MgB<sub>2</sub>, we perform MD simulations based on DFT and the super-cell approach. Besides the system with optimized (pristine) lattice parameters, we also consider a biaxially stretched system (up to 3% of tensile strain) and biaxially compressed system (up to 5% of compressive strain). The MD simulations are conducted in the range of temperatures between 50–300 K, with a step of 50 K, using the Nosé–Hoover thermostat [40].

Figure 2a shows the average distance between Mg and B atomic layers, as evolved over a time of 1 ps. Throughout the simulation time, there is no further evolution of the z-coordinate and the Mg atom shows only oscillatory movement around the equilibrium positions (as is shown in Figure 2) Importantly, the separation indicates that the Mg atoms do not leave the surface of the MgB<sub>2</sub> crystal. The plane in which the Mg atoms reside shifts away from the plane of the B atoms on average by 0.09 Å in a compressed crystal, while the distance between the planes decreases on average by 0.42 Å in the stretched system. This (relatively larger) shift in the latter case can be understood by analysing the details of the MgB<sub>2</sub> atomic structure. When the crystal is biaxially stretched, its Mg–B bond lengths increase, which is partially compensated by the nesting of the Mg atoms in the hollow sites closer to the B sublattice. Despite these atomic shifts, the MD simulations show the structural stability of the system. The stability from the MD simulations can be further quantitatively derived from the global Lindemann index, the dependence of which on temperature is shown in Figure 2b. It is calculated



for the pristine crystal, with a compressive strain of 5% and a tensile strain of 3%, from the local Lindemann indices, given by the formula

$$q_i = \frac{1}{N-1} \sum_{j \neq i} \frac{\sqrt{\langle r_{ij}^2 \rangle - \langle r_{ij} \rangle^2}}{\langle r_{ij} \rangle},$$

by averaging over all atoms. Here  $q_i$  is the local Lindemann index of atom  $i$ ,  $N$  is number of atoms,  $r_{ij}$  is a separation between atoms  $i$  and  $j$ , and the angle brackets denote averaging over time (i.e., MD steps) [41]. The linear behaviour of the Lindemann indices indicate that systems are stable, at least up to room temperature.

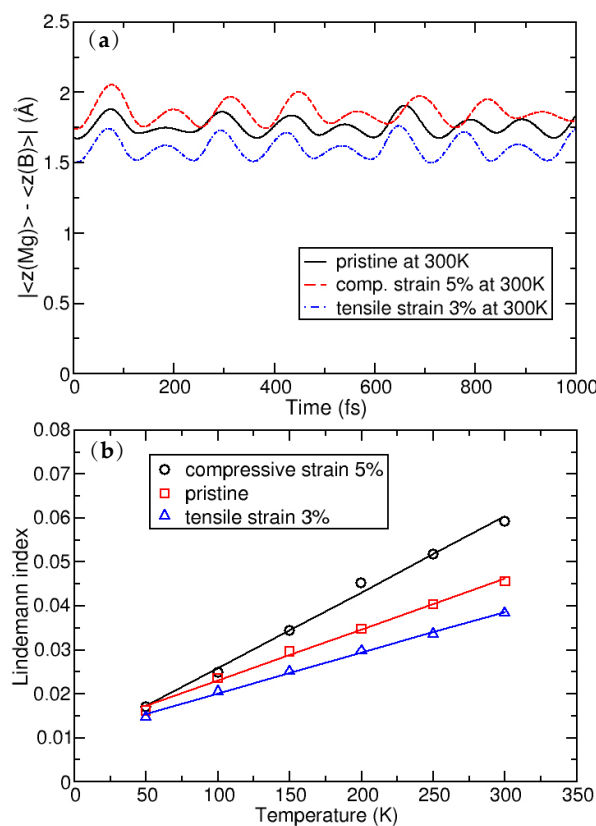


**Figure 2.** (a): Average distance between the Mg and B atomic layers; and (b): the dependence of the global Lindemann index as a function of temperature.

The calculated second-order elastic constants and other structural parameters for monolayer  $\text{MgB}_2$  are given in Table 1. All elastic constants related to the bulk material (those that have 3, 4, or 5 in their subscripts), are calculated close to zero, as is expected for the monolayer. Compared to similar 2D materials, the layer modulus of  $\text{MgB}_2$  of 30.18 N/m is relatively small (in the range of Silicene and Germanene), roughly five times smaller than that of graphene or h-BN, for example [42,43]. Similar results are obtained for the Young modulus. Compared to borophene (two-dimensional boron sheets with rectangular structures) [44], which is a hard and brittle 2D material that exhibits an extremely large Young's modulus of 398 N/m along the  $a$  direction [45], the  $\text{MgB}_2$  monolayer has a significantly smaller value of 63.29 N/m. The most interesting observation in the elastic properties of the  $\text{MgB}_2$  monolayer is that the  $c_{12}$  constant is negative, which gives a negative Poisson ratio in the  $a$  and  $b$  directions, too—although, with a very small negative value of  $-0.05$ . However, compared to 2D borophene, which has an out-of-plane negative Poisson's ratio (that effectively holds the strong boron bonds lying along the  $a$  direction and makes the boron sheet show superior mechanical flexibility along

the  $b$  direction [46]), we obtain similar values [45]. For comparison, graphene has a Young modulus of 352.2 N/m and a Poisson ratio of 0.185 [42]. After confirming its stability and determining the elastic properties of the  $\text{MgB}_2$  monolayer, we study its electronic properties. In Figure 3, the electronic structures of bulk  $\text{MgB}_2$  and the  $\text{MgB}_2$  monolayer are presented. The band structures for the bulk along the high-symmetry points  $\Gamma$ -K-M- $\Gamma$ -A-L, and for the monolayer along  $\Gamma$ -K-M- $\Gamma$  were calculated. The Fermi level is set to zero. The band structure of the bulk is in full agreement with previous studies [10,47–49]. The two bands crossing the Fermi level play a crucial role in the electronic properties of  $\text{MgB}_2$ . The density of the states around  $E_f$  are predominantly related to the B atoms and their  $p$ -orbitals, whereas the Mg atom contribution is negligible in this region. Previous studies described Mg as fully ionized and showed that the electrons donated to the system are not localized on the anion but, rather, are distributed over the whole crystal [6]. A similarity to graphite can be observed, with three  $\sigma$  bands, corresponding to the in-plane  $sp_xp_y$  ( $sp^2$ ) hybridization in the boron layer and two  $\pi$ -bands of boron  $p_z$  orbitals [33]. Boron  $p_{x(y)}$  and  $p_z$  orbitals contribute as  $\sigma$  and  $\pi$  states. Analysing projected DOS, one concludes that the  $\sigma$  states are considerably involved in the total density of states at the Fermi level, while the  $\pi$  states have only a partial contribution. It is worth emphasizing that the bulk bands of this material at the K-point above the Fermi level present a formation similar to the Dirac cones in graphene.

In the monolayer, there is an increase in the total density of states at the Fermi level from  $N(E_f)_{\text{bulk}} = 0.72$  states/eV to  $N(E_f)_{\text{mono}} = 0.97$  states/eV. In the same manner as in the bulk, the monolayer Mg atoms negligibly contribute to the density of states at the Fermi level, and the main contribution comes from the B  $p$ -orbitals. The characteristic Dirac cone-like structure is still present and closer to the Fermi level.  $D_{g77}$ , as the symmetry group of the  $\text{MgB}_2$  monolayer, hosts a Dirac-like dispersion in the vicinity of the K-point in the hexagonal Brillouin zone, if the orbital wave functions belong to the 2D representation E of the  $C_{3v}$  point group of the wave vector [50,51]. In the tight-binding case, the  $p_x$  and  $p_y$  orbitals of two boron ions give rise to one E-representation (and to two one-dimensional representations), while the s-orbitals form a basis for one E-representation and  $p_z$ -orbitals form a basis for one E-representation as well. This explains the presence of the Dirac cones at the K-point in the band structure of the  $\text{MgB}_2$  monolayer (as shown in Figure 3b).

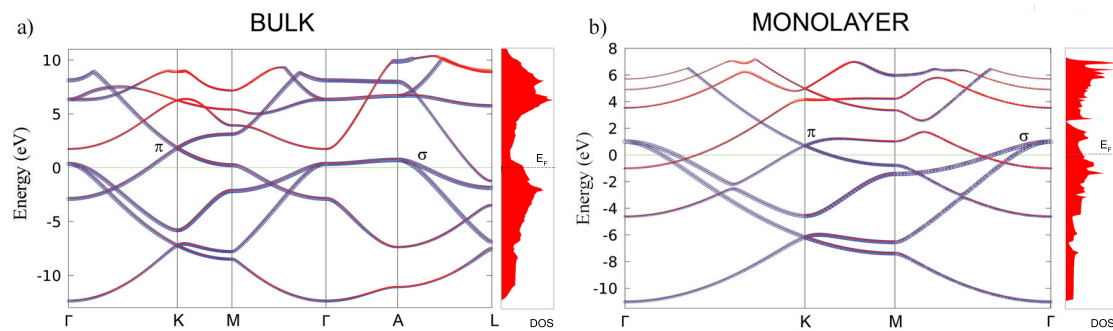


**Figure 3.** The electronic band structure and total density of states in bulk  $\text{MgB}_2$  (a) and the  $\text{MgB}_2$  monolayer (b). The blue and red colors represent the B and Mg atoms contributions to the electronic dispersion, respectively.

**Table 1.** The calculated elastic stiffness constants, layer modulus  $\gamma$ , Young’s modulus  $Y$ , Poisson’s ratio  $\nu$ , and shear modulus  $G$  for the  $\text{MgB}_2$  monolayer. All parameters are in units of N/m.

$c_{11}$	$c_{12}$	$c_{66}$	$\gamma$	$Y$	$\nu$	$G$
63.4	−3.1	33.3	30.18	63.29	−0.05	33.3

Figure 4 shows the phonon dispersions for both the bulk and monolayer. For the bulk (in Figure 4a), there are four optical modes at the  $\Gamma$  point. Due to the light atomic mass of the B

atoms and the strong B–B coupling, the two high-frequency modes almost have a pure boron character. The in-plane stretching mode  $E_{2g}$  and the out-of-plane mode (where the atoms move in opposite directions  $B_{1g}$ ) are the boron atom modes.  $E_{2g}$  is a doubly-degenerate Raman active mode and experimental studies [6,9] showed that this mode is very sensitive to structural changes and it has a strong electron-phonon coupling. The low-frequency modes ( $A_{2u}$ ) and double degenerate ( $E_{1u}$ ) are infrared active and they do not involve changes on in-plane bonds. In Figure 4b, the phonon dispersion of the  $MgB_2$  monolayer is presented. In the phonon spectrum there are no imaginary frequencies, which confirms, once again, the dynamical stability of the system (also demonstrated earlier by the MD calculations).

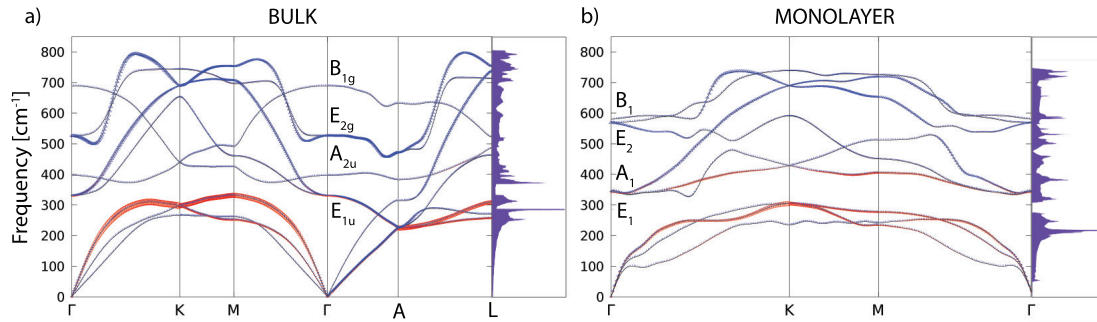


**Figure 4.** The phonon dispersion and the phonon density of states for the  $MgB_2$  bulk (a) and monolayer (b). The blue and red colours represent the B and Mg atom contributions in the phonon dispersion, respectively.

At the  $\Gamma$  point, there are three acoustic and six optical modes (from which two pairs are doubly degenerate). The optical modes  $A_1$ ,  $B_1$ ,  $E_1$ , and  $E_2$  are related to the optical modes of the parent material. Two significant differences between the bulk and monolayer spectrum can be observed: The  $E_1$  and  $A_1$  mode become energy degenerate in the monolayer, resulting in either a slight softening (hardening) of the modes which leads to nearly equal frequencies, which opens a gap in the phonon density of states (DOS) between the acoustic and optical modes. A more significant effect concerns the softening of the  $B_1$  mode and hardening of the  $E_2$  mode. As in the bulk  $E_{2g}$  mode, the monolayer  $E_2$  mode is strongly coupled to electrons, causing the superconductivity in the monolayer in a similar fashion as in the bulk. In Figure 5, the vibrational frequencies and normal coordinates for the  $MgB_2$  monolayer are presented. The symmetry group is  $C_{6v}$ , and the acoustic modes are  $A_1$  and  $E_1$ . The optical modes at the  $\Gamma$  point are  $A_1$ ,  $B_1$ ,  $E_1$ , and  $E_2$ , where the infrared-active ones are  $A_1$  and  $E_1$ . The Raman-active modes are  $A_1$ ,  $E_1$ , and  $E_2$ , and  $B_1$  is silent. In Table 2, the Raman tensor for the  $MgB_2$  monolayer is presented [52]. Similar to graphene, the phonon eigenvectors and the normal coordinates at the  $\Gamma$ -point are determined by symmetry rules and, therefore, are a model independent.

**Table 2.** Raman tensor of the  $MgB_2$  monolayer.

Raman Tensors	
<b><math>MgB_2</math>-mono</b> $Dg77 = TC_{6v}$ $O_z \parallel C_6$ $O_x \parallel \sigma_v$	$\begin{pmatrix} a & 0 & 0 \\ 0 & a & 0 \\ 0 & 0 & b \end{pmatrix} \begin{pmatrix} 0 & 0 & c \\ 0 & 0 & 0 \\ c & 0 & 0 \end{pmatrix} \begin{pmatrix} 0 & 0 & 0 \\ 0 & 0 & c \\ 0 & c & 0 \end{pmatrix} \begin{pmatrix} d & 0 & 0 \\ 0 & -d & 0 \\ 0 & 0 & 0 \end{pmatrix} \begin{pmatrix} 0 & -d & 0 \\ -d & 0 & 0 \\ 0 & 0 & 0 \end{pmatrix}$

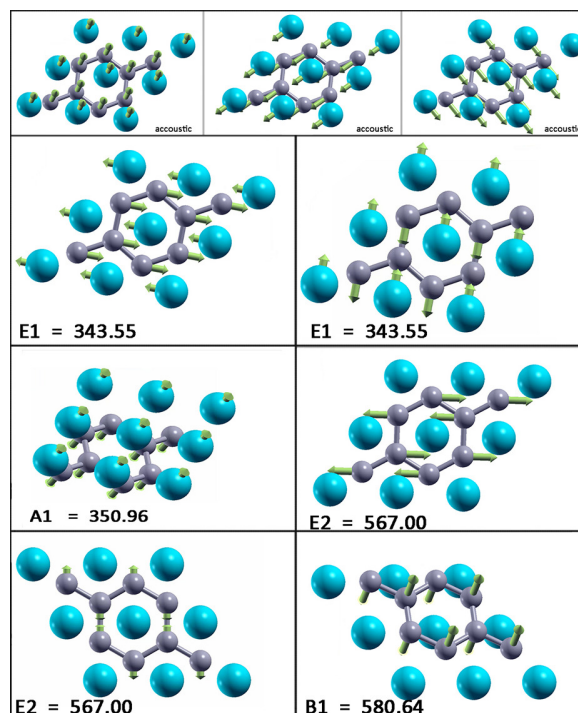


**Figure 5.** Vibrational frequencies (in wavenumbers) and the vibration normal coordinates at  $\Gamma$  for the  $\text{MgB}_2$  monolayer.

#### 4. Conclusions

The electronic band structure, density of states, phonon dispersion, and elastic constants have been calculated for the  $\text{MgB}_2$  monolayer and compared to the bulk material, using first-principles calculations within the DFT framework. We demonstrated an increase of electronic density of states at the Fermi level in the monolayer (compared to the bulk) and determined its stability under various strains. These two features are crucial for the enhancement of electron–phonon coupling and they enable significant mechanical modification that increases the critical superconducting temperature. Establishing stability and offering insight into this novel 2D material, we focus on the effects of ultimate lowering of the dimensionality. The question of reduction of dimensionality to its limit, a truly atomic-scale 2D system, and the consequences of this [53–61] are highly relevant, not only to fundamental science but also to applications in nanotechnology.

**Author Contributions:** Conceptualization, J.P. and R.G.; Validation, K.H., M.B., R.G.; Investigation, J.P., I.P., A.Š. and V.D.; Writing—Original Draft Preparation, J.P., I.P., A.Š. and V.D.; Writing—Review & Editing, J.P.; Supervision, R.G.; Funding Acquisition, K.H., M.B. and R.G.

**Funding:** This research is supported by Serbian Ministry of Education, Science and Technological Development under projects OI 171005, III 45018, and III 45016 and by the Qatar National Research Fund, cycle 11, under grant number NPRP 11S-1126-170033. K.H. acknowledges the support of the European Commission under the H2020 grant TWINFUSYON.GA692034.

**Acknowledgments:** The DFT calculations were performed using the computational resources at Johannes Kepler University, Linz, Austria. This work was supported by the Serbian Ministry of Education, Science and Technological Development under projects OI 171005, III 45018, and III 45016.

**Conflicts of Interest:** The authors declare no conflict of interest.

## References

1. Jones, M.E.; Marsh R.E. The preparation and structure of magnesium boride,  $MgB_2$ . *J. Am. Chem. Soc.* **1953**, *76*, 5. [[CrossRef](#)]
2. Nagamatsu, J.; Nakagawa, N.; Muranaka, T.; Zenitani, Y.; Akimitsu, J. Superconductivity at 39 K in magnesium diboride. *Nature* **2001**, *410*, 63. [[CrossRef](#)] [[PubMed](#)]
3. Bud'ko, S.L.; Lapertot, G.; Petrovic, C.; Cunningham, C.E.; Anderson, N.; Canfield, P.C. Boron Isotope Effect in Superconducting  $MgB_2$ . *Phys. Rev. Lett.* **2001**, *86*, 1877. [[CrossRef](#)] [[PubMed](#)]
4. Pickett, W. Superconductivity: 2D Physics, Unknown Mechanisms, Current Puzzles. *Emerg. Phenom. Correl. Matter Lect. Notes Autumn School Corr. Electron.* **2013**, *2013*, 45.
5. Choi, H.J.; Roundy, D.; Sun, H.; Cohen, M.L.; Steven Louie, G. The origin of the anomalous superconducting properties of  $MgB_2$ . *Nature* **2002**, *418*, 758. [[CrossRef](#)]
6. Kortus, J.; Mazin, I.I.; Belaichenko, K.D.; Antropov, V.P.; Boyer, L.L. Superconductivity of Metallic Boron in  $MgB_2$ . *Phys. Rev. Lett.* **2001**, *86*, 4656. [[CrossRef](#)]
7. An, J.M.; Pickett, W.E. Superconductivity of  $MgB_2$ : Covalent Bonds Driven Metallic. *Phys. Rev. Lett.* **2001**, *86*, 4366. [[CrossRef](#)] [[PubMed](#)]
8. Liu, A.Y.; Mazin, I.I.; Kortus, J. Beyond Eliashberg Superconductivity in  $MgB_2$ : Anharmonicity, Two-Phonon Scattering, and Multiple Gaps. *Phys. Rev. Lett.* **2001**, *87*, 087005. [[CrossRef](#)] [[PubMed](#)]
9. Kong, Y.; Dolgov, O.V.; Jepsen, O.; Andersen, O.K. Electron-phonon interaction in the normal and superconducting states of  $MgB_2$ . *Phys. Rev. B* **2001**, *64*, 020501. [[CrossRef](#)]
10. Bohnen, K.-P.; Heid, R.; Renker, B. Phonon Dispersion and Electron-Phonon Coupling in  $MgB_2$  and  $AlB_2$ . *Phys. Rev. Lett.* **2001**, *86*, 5771. [[CrossRef](#)] [[PubMed](#)]
11. Kunc, K.; Loa, I.; Syassen, K.; Kremer, R.K.; Ahn, K.  $MgB_2$  under pressure: phonon calculations, Raman spectroscopy, and optical reflectance. *J. Phys. Condens. Matter* **2001**, *13*, 9945. [[CrossRef](#)]
12. Choi, H.J.; Roundy, D.; Sun, H.; Cohen, M.L.; Louie, S.G. First-principles calculation of the superconducting transition in  $MgB_2$  within the anisotropic Eliashberg formalism. *Phys. Rev. B* **2002**, *66*, 020513. [[CrossRef](#)]
13. Canfield, P.C.; Crabtree, G.W. Magnesium Diboride: Better Late than Never. *Phys. Today* **2003**, *56*, 34. [[CrossRef](#)]
14. Novoselov, K.S.; Geim, A.K.; Morozov, S.V.; Jiang, D.; Zhang, Y.; Dubonos, S.V.; Grigorieva, I.V.; Firsov, A.A. Electric Field Effect in Atomically Thin Carbon Films. *Science* **2004**, *306*, 666–669. [[CrossRef](#)]
15. Katsnelson, M.I.; Novoselov, K.S.; Geim, A.K. Chiral tunnelling and the Klein paradox in graphene. *Nat. Phys.* **2006**, *2*, 620–625. [[CrossRef](#)]
16. Katsnelson, M.I. Zitterbewegung, chirality, and minimal conductivity in graphene. *Eur. Phys. J. B* **2006**, *51*, 157–160. [[CrossRef](#)]
17. Rusin, T.M.; Zawadzki, W. Zitterbewegung of electrons in graphene in a magnetic field. *Phys. Rev. B* **2008**, *78*, 125419. [[CrossRef](#)]
18. Pisana, S.; Lazzeri, M.; Casiraghi, C.; Novoselov, K.S.; Geim, A.K.; Ferrari, A.C.; Mauri, F. Breakdown of the adiabatic Born-Oppenheimer approximation in graphene. *Nat. Mater.* **2007**, *6*, 198–201. [[CrossRef](#)] [[PubMed](#)]
19. Piscanec, S.; Lazzeri, M.; Mauri, F.; Ferrari, A.C.; Robertson, J. Kohn Anomalies and Electron-Phonon Interactions in Graphite. *Phys. Rev. Lett.* **2004**, *93*, 85503. [[CrossRef](#)]
20. Novoselov, K.S.; Jiang, Z.; Zhang, Y.; Morozov, S.V.; Stormer, H.L.; Zeitler, U.; Maan, J.C.; Boebinger, G.S.; Kim, P.; Geim, A.K. Room-temperature quantum Hall effect in graphene. *Science* **2007**, *315*, 1379. [[CrossRef](#)]
21. Zhou, S.Y.; Gweon, G.-H.; Fedorov, A.V.; First, P.N.; de Heer, W.A.; Lee, D.-H.; Guinea, F.; Castro Neto, A.H.; Lanzara, A.; et al. Substrate-induced bandgap opening in epitaxial graphene. *Nat. Mater.* **2007**, *6*, 770–775. [[CrossRef](#)]
22. Zhang, Y.; Tan, Y.; Stormer, H.L.; Kim, P. Experimental observation of the quantum Hall effect and Berry's phase in graphene. *Nature* **2005**, *438*, 201–204. [[CrossRef](#)]
23. Bekaert, J.; Aperis, A.; Partoens, B. Oppeneer, P.M.; Milošević, M.V. Evolution of multigap superconductivity in the atomically thin limit: Strain-enhanced three-gap superconductivity in monolayer  $MgB_2$ . *Phys. Rev. B* **2017**, *96*, 094510.
24. Morshedloo, T.; Roknabadi, M.R.; Behdani, M. First-principles study of the superconductivity in  $MgB_2$  bulk and in its bilayer thin film based on electron-phonon coupling. *Physica C* **2015**, *509*. [[CrossRef](#)]

25. Calandra, M.; Profeta, G.; Mauri, F. Superconductivity in metal-coated graphene. *Phys. Status Solidi (b)* **2012**, *249*, 2544. [[CrossRef](#)]
26. Ludbrook, B.M.; Levy, G.; Nigge, P.; Zonno, M.; Schneider, M.; Dvorak, D.J.; Veenstra, C.N.; Zhdanovich, S.; Wong, D.; Dosanjh, P.; et al. Evidence for superconductivity in Li-decorated monolayer graphene. *Proc. Natl. Acad. Sci. USA* **2015**, *112*, 11795. [[CrossRef](#)] [[PubMed](#)]
27. Profeta, G.; Calandra, M.; Mauri, F. Phonon-mediated superconductivity in graphene by lithium deposition. *Nat. Phys.* **2012**, *8*, 131–134. [[CrossRef](#)]
28. Pešić, J.; Gajić, R.; Hingerl, K.; Belić, M. Strain-enhanced superconductivity in Li-doped graphene. *Europhys. Lett.* **2014**, *108*, 67005. [[CrossRef](#)]
29. Szczesniak, D.; Durajski, A.P.; Szczesniak, R. Influence of lithium doping on the thermodynamic properties of graphene based superconductors. *J. Phys-Condens. Mat.* **2014**, *26*, 255701. [[CrossRef](#)]
30. Durajski, A.; Skoczylas, K.; Szczesniak, R. Superconductivity in bilayer graphene intercalated with alkali and alkaline earth metals. *Phys. Chem. Chem. Phys.* **2019**, *21*, 5925. [[CrossRef](#)] [[PubMed](#)]
31. Zheng, J.-J.; Margine, E.R. First-principles calculations of the superconducting properties in Li-decorated monolayer graphene within the anisotropic Migdal-Eliashberg formalism. *Phys. Rev. B* **2016**, *94*, 064509. [[CrossRef](#)]
32. Margine, E.R.; Lambert, H.; Giustino, F. Electron-phonon interaction and pairing mechanism in superconducting Ca-intercalated bilayer graphene. *Sci. Rep.* **2016**, *6*, 21414. [[CrossRef](#)]
33. Mazin, I.I.; Antropov, V.P. Electronic structure, electron-phonon coupling, and multiband effects in MgB<sub>2</sub>. *Phys. C Supercond.* **2003**, *385*, 49–65. [[CrossRef](#)]
34. Giannozzi, P.; Andreussi, O.; Brumme, T.; Bunau, O.; Buongiorno, N.M.; Calandra, M.; Car, R.; Cavazzoni, C.; Ceresoli, D.; Cococcioni, M. et al. Quantum espresso: A modular and open-source software project for quantum simulations of materials. *J. Phys. Condensed Matter* **2009**, *21*, 395502. [[CrossRef](#)] [[PubMed](#)]
35. Lu, N.; Guo, H.; Zhuo, Z.; Wang, L.; Wu, X.; Zeng, X.C. Twisted MX<sub>2</sub>/MoS<sub>2</sub> heterobilayers: effect of van der Waals interaction on the electronic structure. *Nanoscale* **2017**, *9*, 19131–19138. [[CrossRef](#)] [[PubMed](#)]
36. Soler, J.M.; Artacho, E.; Gale, J.D.; García, A.; Junquera, J.; Ordejón, P.; Sánchez-Portal, D. The SIESTA method for ab initio order-N materials simulation. *J. Phys. Condens. Matter.* **2002**, *14*, 2745. [[CrossRef](#)]
37. Perdew, J.P.; Burke, K.; Ernzerhof, M. Generalized Gradient Approximation Made Simple. *Phys. Rev. Lett.* **1996**, *77*, 3865–3868. [[CrossRef](#)]
38. Troullier, N.; Martins, J.L. Efficient pseudopotentials for plane-wave calculations. *Phys. Rev. B* **1991**, *43*, 1993–2006. [[CrossRef](#)]
39. Golezorkhtabar, R.; Pavone, P.; Spitaler, J.; Puschnig, P.; Draxl, C. ElaStic: A tool for calculating second-order elastic constants from first principles. *Comput. Phys. Commun.* **2013**, *184*, 1861–1873. [[CrossRef](#)]
40. Nosé, S. A unified formulation of the constant temperature molecular dynamics methods. *J. Chem. Phys.* **1984**, *81*, 511. [[CrossRef](#)]
41. Lindemann, F.A. The calculation of molecular vibration frequencies. *Phys. Z.* **1910**, *11*, 609.
42. Andrew, R.C.; Mapasha, R.E.; Ukpong, A.M.; Chetty, N. Mechanical properties of graphene and boronitrene. *Phys. Rev. B* **2012**, *85*, 125428. [[CrossRef](#)]
43. Zhang, Z.; Yang, Y.; Penev, E.S.; Yakobson, B.I. Elasticity, Flexibility, and Ideal Strength of Borophenes. *Adv. Func. Mater.* **2017**, *27*, 1605059. [[CrossRef](#)]
44. Zhong, H.; Huang, K.; Yu, G.; Yuan, S. Electronic and mechanical properties of few-layer borophene. *Phys. Rev. B* **2018**, *98*, 054104. [[CrossRef](#)]
45. Mannix, A.J.; Zhou, X.F.; Kiraly, B.; Wood, J.D.; Alducin, D.; Myers, B.D.; Liu, X.; Fisher, B.L.; Santiago, U.; Guest, J.R.; et al. Synthesis of borophenes: Anisotropic, two-dimensional boron polymorphs. *Science* **2015**, *350*, 1513–1516. [[CrossRef](#)]
46. Wang, H.; Li, Q.; Gao, Y.; Miao, F.; Zhou, X.-F.; Wan, X.G. Strain effects on borophene: Ideal strength, negative Poisson's ratio and phonon instability. *New J. Phys.* **2016**, *18*, 073016. [[CrossRef](#)]
47. De la Pena-Seaman, O.; de Cross, R.; Heid, R.; Bohnen, K.-P. Effects of Al and C doping on the electronic structure and phonon renormalization in MgB<sub>2</sub>. *Phys. Rev. B* **2009**, *79*, 134523. [[CrossRef](#)]
48. Ponce, S.; Margine E.R., Verdi, C.; Giustino, F. EPW: Electron-phonon coupling, transport and superconducting properties using maximally localized Wannier functions. *Comp. Phys. Commun.* **2016**, *209*, 116–133. [[CrossRef](#)]

49. Margine, E.R.; Giustino, F. Anisotropic Migdal-Eliashberg theory using Wannier functions. *Phys. Rev. B* **2013**, *87*, 024505. [[CrossRef](#)]
50. Damljanovic, V.; Gajic, R. Existence of Dirac cones in the Brillouin zone of diperiodic atomic crystals according to group theory. *J. Phys. Condens. Matter* **2016**, *28*, 085502. [[CrossRef](#)]
51. Damljanovic, V.; Gajic, R. Addendum to 'Existence of Dirac cones in the Brillouin zone of diperiodic atomic crystals according to group theory'. *J. Phys. Condens. Matter* **2016**, *28*, 439401. [[CrossRef](#)]
52. Poulet, H.; Mathieu, J.P. *Vibration Spectra and Symmetry of Crystals*; Gordon and Breach: New York, NY, USA, 1976.
53. Szalowski, K. Critical temperature of MgB<sub>2</sub> ultrathin superconducting films: BCS model calculations in the tight-binding approximation. *Phys. Rev. B* **2006**, *74*, 094501. [[CrossRef](#)]
54. Zhang, C.; Wang, Y.; Wang, D.; Zhang, Y.; Liu, Z.-H.; Feng, Q.-R.; Gan, Z.-Z. Suppression of superconductivity in epitaxial MgB<sub>2</sub> ultrathin films. *J. Appl. Phys.* **2013**, *114*, 023903. [[CrossRef](#)]
55. Ao, B.; Zhang, Z.; Tang, T.; Zhao, Y. Potential enhancement of superconductivity in MgB<sub>2</sub> nanosheets: First-principles calculations. *Chem. Phys. Lett.* **2014**, *591*, 185–188. [[CrossRef](#)]
56. Romero-Bermudez, A.; Garcia-Garcia, A.M. Shape resonances and shell effects in thin-film multiband superconductors. *Phys. Rev. B* **2014**, *89*, 024510. [[CrossRef](#)]
57. Romero-Bermudez, A.; Garcia-Garcia, A.M. Size effects in superconducting thin films coupled to a substrate. *Phys. Rev. B* **2014**, *89*, 064508. [[CrossRef](#)]
58. Acharya, N.; Wolak, M.A.; Cunnane, D.P.; Karasik, B.S.; Xi, X.X. MgB<sub>2</sub> ultrathin films fabricated by hybrid physical chemical vapor deposition and ion milling. *APL Mater.* **2016**, *4*, 086114. [[CrossRef](#)]
59. Valentinis, D.; van der Marel, D.; Berthod, C. Rise and fall of shape resonances in thin films of BCS superconductors. *Phys. Rev. B* **2016**, *94*, 054516. [[CrossRef](#)]
60. Narlikar, A.V. Small Superconductors: Introduction. In *The Oxford Handbook of Small Superconductors*, 1st ed.; Narlikar, A.V., Ed.; Oxford University Press: Oxford, UK, 2017.
61. Gariglio, S.; Scheurer, M.; Schmalian, J.; Monteiro, A.M.R.V.L.; Goswami, S.; Caviglia, A. Surface and Interface Superconductivity. In *The Oxford Handbook of Small Superconductors*, 1st ed.; Narlikar, A.V., Ed.; Oxford University Press: Oxford, UK, 2017.



© 2019 by the authors. Licensee MDPI, Basel, Switzerland. This article is an open access article distributed under the terms and conditions of the Creative Commons Attribution (CC BY) license (<http://creativecommons.org/licenses/by/4.0/>).

PAPER

## Peculiar symmetry-protected electronic dispersions in two-dimensional materials

To cite this article: V Damjanović *et al* 2020 *J. Phys.: Condens. Matter* **32** 485501

View the [article online](#) for updates and enhancements.

### You may also like

- [Investigation of normal and superconducting states in noncentrosymmetric  \$\text{Re}\_2\text{Ti}\_5\$](#)   
C S Lue, H F Liu, C N Kuo *et al.*
- [Topological superconductors: a review](#)  
Masatoshi Sato and Yoichi Ando
- [Superconductivity and spin-orbit coupling in non-centrosymmetric materials: a review](#)  
M Smidman, M B Salamon, H Q Yuan *et al.*



# Peculiar symmetry-protected electronic dispersions in two-dimensional materials

V Damljanović<sup>1,3</sup> , N Lazic<sup>2</sup> , A Šolajić<sup>1</sup> , J Pešić<sup>1</sup> , B Nikolić<sup>2</sup>  and M Damjanović<sup>2</sup> 

<sup>1</sup> Institute of Physics Belgrade, University of Belgrade, Pregrevica 118, 11080 Belgrade, Serbia

<sup>2</sup> NanoLab, Faculty of Physics, University of Belgrade, PO Box 44, Belgrade 11001, Serbia

E-mail: [damlja@ipb.ac.rs](mailto:damlja@ipb.ac.rs)

Received 16 June 2020, revised 23 July 2020

Accepted for publication 30 July 2020

Published 8 September 2020



## Abstract

Symmetry indicates that low energy spectra of materials could be richer than well-known Dirac, semi-Dirac, or quadratic, hosting some unusual quasiparticles. Performing the systematic study of exact forms of low energy effective Hamiltonians and dispersions in high-symmetry points with fourfold degeneracy of bands, we found new, previously unreported dispersion, which we named poppy flower (PF) after its shape. This massless fermion exists in non-magnetic two-dimensional (2D) crystals with spin-orbit coupling (SOC), which are invariant under one of the proposed ten noncentrosymmetric layer groups. We suggest real three-dimensional (3D) layered materials suitable for exfoliation, having layers that belong to these symmetry groups as candidates for realization of PF fermions. In 2D systems without spin-orbit interaction, fortune teller (FT)-like fermions were theoretically predicted, and afterward experimentally verified in the electronic structure of surface layer of silicon. Herein, we show that such fermions can also be hosted in 2D crystals with SOC, invariant under additional two noncentrosymmetric layer groups. This prediction is confirmed by density functional based calculation: layered BiIO<sub>4</sub>, which has been synthesized already as a 3D crystal, exfoliates to stable monolayer with symmetry  $pb2_1a$ , and FT fermion is observed in the band structure. Analytically calculated density of states (DOS) of the PF shows semimetallic characteristic, in contrast to metallic nature of FT having non-zero DOS at the bands contact energy. We indicate possibilities for symmetry breaking patterns which correspond to the robustness of the proposed dispersions as well as to the transition from Dirac centrosymmetric semimetal to PF.

Keywords: electronic dispersions, spin-orbit coupling, symmetry, new fermions

(Some figures may appear in colour only in the online journal)

## 1. Introduction

Electronic dispersion essentially determines crystal properties and it is well known that it is assigned by quantum numbers of the underlying symmetry group. These are space, layer (including wallpaper) or line groups, referring respectively to dimensionality of crystals: 3D, quasi-2D (Q2D), or quasi-1D. Probably the most famous example of a low-dimensional material is graphene (there are also related single layers, such as borophene [1], borophosphene [2], graphynes

[3], etc), which hosts Dirac like (linear in quasi-momentum) dispersion in the vicinity of high symmetry Dirac points. Such shape of energy bands, besides being responsible for some intriguing phenomena, provides material realization of relativistic electron. This triggered numerous investigations of the connection between symmetry of materials and appearance of Dirac and Weyl points in their band structures. These points are attributed to existence of rotational [4], nonsymmorphic [5], mirror [6], space-time inversion [7, 8], time-reversal plus fractional translation [9], and generalized chiral symmetry [10]. There are also results on the search for Weyl and Dirac

<sup>3</sup> Author to whom any correspondence should be addressed.

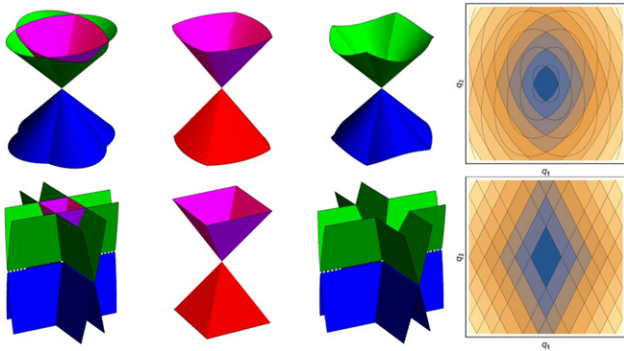


**Figure 1.** PF (up) and FT (bottom) dispersions (given by equations (3.1)): from left to right are all bands, bands  $E_{\pm 1,+1}$ , bands  $E_{\pm 1,-1}$  and horizontal sections of the bands (iso-energetic lines).

points according to group theoretical criteria in Brillouin zones (BZs) of all space [11], layer [12–14] or wallpaper groups [15].

In addition, geometrical symmetries impose conditions that lead to the emergence of unconventional quasiparticles in condensed matter systems. In 3D materials, enforced by space groups, double Dirac points [16], three-component [17, 18] or hourglass fermions [19] are found, inspiring further theoretical and experimental research [20–25]. Concerning Q2D systems, besides Dirac (as in graphene [26]), there are also semi-Dirac (Dirac-like in one direction, and quadratic in the orthogonal one, as in black phosphorus [27]), quadratic (as in molybdenum disulphide [28]), and fortune teller (FT) dispersions [29], which corresponds to the coexistence of a nodal point and lines. Namely, symmetry analysis of the possible completely linear dispersions in non-magnetic, Q2D materials with negligible spin–orbit coupling (SOC) has shown that only completely massless fermions appearing in layers are Dirac and FT [29]. Recently, FT dispersion has been experimentally confirmed in a surface layer of silicon [30].

A question arises whether new types of fermions are possible in Q2D materials by inclusion of SOC? With help of layer double groups (LDGs) and time-reversal symmetry (TRS) (i.e. gray LDG), we made a quite general search for linear dispersions in the vicinity of high symmetry points (HSPs); since no reference to nonsymmorphic symmetries is made, the topological (hour-glass like) band crossing mechanisms are not *a priori* assumed, as it is usual. Indeed, it turns out that there are two peculiar types (figure 1) featuring twelve nonsymmorphic and noncentrosymmetric groups: two groups support previously predicted FT, and the remaining ones poppy flower (PF) dispersion (generalizing both FT and Dirac types).

After a brief overview of necessary group-theoretical methods, the obtained results are discussed on the basis of effective low-energy model, calculated densities of states and symmetry breaking patterns. Also, a list of material candidates supporting the new dispersions is provided. The predicted effect is justified by density functional based relaxation and band structure calculation in BiIO<sub>4</sub> monolayer. Synthesis of this layered 3D material was reported around a decade ago [31]. Numerical band structure con-

firms our group theoretical prediction, which may be the motivation for future laboratory synthesis of this material as monolayer.

## 2. Method

Symmetry determines Bloch Hamiltonian in the vicinity of high-symmetry BZ wave vector through the allowed irreducible representations (IRs) of the little group [32]. Allowed IRs of LDGs are subduced from the corresponding space groups IRs (found on Bilbao Crystallographic Server [33]), and also independently constructed by POLSym code [34]. Concerning LDGs with TRS, the dimensions [33, 35] of the allowed IRs (actually co-representations) are 1, 2 or 4, and for generic ones, giving bands degeneracy, this is 1 or 2. Here we focus on the band structures near quadruple points at high-symmetry momenta. Further, we do not consider generically degenerate bands, giving double degenerate Dirac dispersion (precisely, it consists of two double spinfull degenerate cones meeting at one fourfold degenerate point); this automatically excludes centrosymmetric crystals, as Kramers degeneracy in them forbids non-degenerate bands [36]. Among the remaining groups, only twelve are with special points with four-dimensional allowed (co)representation.

Analysis of all allowed IRs  $R$  of little groups  $G(\mathbf{k}_0)$  of HSPs  $\mathbf{k}_0$  in LDG lacking the inversion symmetry gives the following conditions for quadruple point:  $\mathbf{k}_0$  is time-reversal invariant momentum,  $R$  is two-dimensional, either real or complex IR. Therefore, we consider  $\hat{H}(\mathbf{k})$  being Hamiltonian of the system  $\hat{H}_0$  (including spin–orbit) in the basis  $\{|\Psi_1\rangle, |\Psi_2\rangle, |\theta\Psi_1\rangle, |\theta\Psi_2\rangle\}$ , where the spinors  $|\Psi_i\rangle = |\Psi_i(\mathbf{k})\rangle$  ( $i = 1, 2$  counts two bands touching each other at  $\mathbf{k}_0$  also in the absence of TRS) belong to  $R$  at  $\mathbf{k}_0$  and  $\theta$  is an anti-unitary operator of TRS, for which we used  $\theta^2 = -\hat{\sigma}_0$ , since spinfull case is considered. Throughout the text  $\hat{\sigma}_0$  is two-by-two unit matrix, and  $\hat{\sigma}_1, \hat{\sigma}_2, \hat{\sigma}_3$  are Pauli matrices. Denoting the little group elements by  $\ell = (h|\mathbf{r}_{\hat{h}} + \mathbf{b})$ , where  $h$  is crystallographic double point group element, while  $\mathbf{r}_{\hat{h}}$  and  $\mathbf{b}$  are fractional and lattice translation, respectively, one gets the conditions imposed by time-reversal and geometrical symmetries on  $\hat{H}(\mathbf{k}_0 + \mathbf{q})$  in the vicinity of  $\mathbf{k}_0$  (therefore, the wavevector  $\mathbf{q}$  is small):

$$\hat{H}^*(\mathbf{k}_0 + \mathbf{q}) = \hat{T}^\dagger \hat{H}(\mathbf{k}_0 - \mathbf{q}) \hat{T}, \quad (2.1)$$

$$\hat{H}(\mathbf{k}_0 + \mathbf{q}) = \hat{D}^\dagger(\ell) \hat{H}(\mathbf{k}_0 + \hat{h}'\mathbf{q}) \hat{D}(\ell). \quad (2.2)$$

Here,  $\hat{D} = \text{diag}(\hat{R}, \hat{R}^*)$ , and  $\hat{h}'$  is an operator reduction of vector representation  $\hat{h}$  to 2D BZ, while  $\hat{T} = -i\hat{\sigma}_2 \otimes \hat{\sigma}_0$  represents the action of  $\theta$  on the basis of spinors.

To focus on the terms linear in  $\mathbf{q}$ , Hamiltonian is expanded in the form  $\hat{H}(\mathbf{k}_0 + \mathbf{q}) \approx \sum_{i=1,2} q_i \frac{\partial \hat{H}(\mathbf{k}_0 + \mathbf{q})}{\partial q_i} \Big|_{\mathbf{q}=0}$  (energy scale is conveniently shifted such that  $\hat{H}(\mathbf{k}_0) = 0$ ). To incorporate symmetry, the matrix elements of the Hamiltonian gradient are arranged into the four-by-eight matrix  $\hat{W}$ , which entries  $w_{pq} = (w_{pq}^1 \ w_{pq}^2)$  are pairs  $w_{pq}^i = \frac{\partial H_{pq}(\mathbf{k}_0 + \mathbf{q})}{\partial q_i} \Big|_{\mathbf{q}=0}$ . The form

**Table 1.** Groups providing dispersions (3.1). Notations for layer (columns 1 and 2) and space groups (columns 4, 5 and 6) are according to [37, 38] respectively. IR notation in the eighth column is as in Bilbao Crystallographic Server [33]. Effective Hamiltonian is indicated in the last column by the nonzero parameters (and their interrelations) of (2.5). For the last four groups  $a = c$  while  $\bar{M}_6$  and  $\bar{M}_7$  are conjugated pair of IRs.

Layer double group			Corresponding space double group				Dispersion	Nonzero $v_{pq}^i$	
Group	IR	Group	Plane	IR	IR				
21	$p2_12_12$	$\bar{S}_5$	18	$P2_12_12$	$D_2^3$	$z = 0$	$\bar{S}_5$	(3.1a)	$v_{13}^1, v_{23}^1, v_{33}^1, v_{11}^2, v_{21}^2, v_{31}^2$
25	$pba2$	$\bar{S}_5$	32	$Pba2$	$C_{2v}^8$	$z = 0$	$\bar{S}_5$	(3.1a)	$v_{13}^1, v_{23}^1, v_{33}^1, v_{11}^2, v_{21}^2, v_{31}^2$
28	$pm2_1b$	$\bar{Y}_5, \bar{S}_5$	26	$Pmc2_1$	$C_{2v}^2$	$y = 0$	$\bar{Z}_5, \bar{U}_5$	(3.1a)	$v_{11}^1, v_{21}^1, v_{31}^1, v_{10}^2, v_{20}^2, v_{30}^2$
29	$pb2_1m$	$\bar{Y}_5, \bar{S}_5$	26	$Pmc2_1$	$C_{2v}^2$	$x = 0$	$\bar{Z}_5, \bar{T}_5$	(3.1b)	$v_{11}^1, v_{21}^1, v_{31}^1, v_{10}^2, v_{20}^2, v_{30}^2$
30	$pb2b$	$\bar{Y}_5, \bar{S}_5$	27	$Pcc2$	$C_{2v}^3$	$x = 0$	$\bar{Z}_5, \bar{T}_5$	(3.1a)	$v_{11}^1, v_{21}^1, v_{31}^1, v_{10}^2, v_{20}^2, v_{30}^2$
32	$pm2_1n$	$\bar{Y}_5$	31	$Pmn2_1$	$C_{2v}^7$	$y = 0$	$\bar{Z}_5$	(3.1a)	$v_{13}^1, v_{23}^1, v_{33}^1, v_{10}^2, v_{20}^2, v_{30}^2$
33	$pb2_1a$	$\bar{Y}_5$	29	$Pca2_1$	$C_{2v}^5$	$y = 0$	$\bar{Z}_5$	(3.1b)	$v_{13}^1, v_{23}^1, v_{33}^1, v_{10}^2, v_{20}^2, v_{30}^2$
34	$pb2n$	$\bar{Y}_5$	30	$Pnc2$	$C_{2v}^6$	$x = 0$	$\bar{Z}_5$	(3.1a)	$v_{13}^1, v_{23}^1, v_{33}^1, v_{10}^2, v_{20}^2, v_{30}^2$
54	$p42_12$	$(\bar{M}_6, \bar{M}_7)$	90	$P42_12$	$D_4^2$	$z = 0$	$(\bar{M}_6, \bar{M}_7)$	(3.1a)	$\left\{ \begin{array}{l} v_{02}^1 = v_{02}^2 = v_{31}^1 = -v_{31}^2 \\ v_{10}^1 = v_{10}^2 = v_{23}^1 = -v_{23}^2 \\ v_{13}^1 = -v_{13}^2 = -v_{20}^1 = -v_{20}^2 \end{array} \right\}$
56	$p4bm$	$(\bar{M}_6, \bar{M}_7)$	100	$P4bm$	$C_{4v}^2$	$z = 0$	$(\bar{M}_6, \bar{M}_7)$	(3.1a)	
58	$p\bar{4}2_1m$	$(\bar{M}_6, \bar{M}_7)$	113	$P\bar{4}2_1m$	$D_{2d}^3$	$z = 0$	$(\bar{M}_6, \bar{M}_7)$	(3.1a)	
60	$p\bar{4}b2$	$(\bar{M}_6, \bar{M}_7)$	117	$P\bar{4}b2$	$D_{2d}^7$	$z = 0$	$(\bar{M}_6, \bar{M}_7)$	(3.1a)	

$$\hat{W} = \begin{pmatrix} w_{11} & w_{12} & w_{13} & w_{14} \\ w_{12}^* & w_{22} & w_{14} & w_{24} \\ w_{13}^* & w_{14}^* & -w_{11} & -w_{12}^* \\ w_{14}^* & w_{24}^* & -w_{12} & -w_{22} \end{pmatrix} \quad (2.3)$$

follows from the relation (2.1), together with  $w_{pq}^i = w_{qp}^{i*}$  corresponding to the requirement that Hamiltonian  $\hat{H}$  is a Hermitian operator. Note that the form (2.3) of  $\hat{W}$  leads to the traceless Hamiltonian: it excludes the scalar term (which imposes the tilt of the bands). The geometrical symmetries are incorporated by (2.2), which is rewritten [11, 29] as an efficient fixed point condition

$$\left| \hat{W} \right\rangle = \hat{D} \otimes \hat{D}^* \otimes \hat{h}' \left| \hat{W} \right\rangle, \quad (2.4)$$

on the column vector  $(32 \times 1)$  form  $\left| \hat{W} \right\rangle$  of  $\hat{W}$ . The equation (2.4) is solved with help of the group projection operators for all of the twelve noncentrosymmetric groups hosting quadruple points at high symmetry momenta; in this way, the symmetry determines form of  $\hat{W}$ . To explicate this, it is more convenient to use another general expansion of the effective low energy Hamiltonian,

$$\hat{H}(\mathbf{q}) = \sum_{p,q=0}^3 \sum_{i=1}^2 q_i v_{pq}^i \hat{\sigma}_p \otimes \hat{\sigma}_q, \quad (2.5)$$

and find the constraints imposed by symmetry on the real coefficients  $v_{pq}^i$  (simply interrelated with  $w_{pq}^i$ ).

### 3. Results and discussion

#### 3.1. Symmetry adapted Hamiltonians and dispersions

Groups hosting new dispersions are listed in table 1. Besides intrinsic layer group notation (the first part), the space group

of the system obtained by periodic repetition of the layer along axis perpendicular to it (column plane) according to Bilbao Crystallographic Server is also given (second part), where the directions  $x$ ,  $y$  and  $z$  are along axes of orthorhombic/tetragonal 3D primitive unit cell. On the other hand, in POLSym approach we used convention that layers are in  $xy$ -plane. Orthogonal lattice vectors  $\mathbf{a}_1$  and  $\mathbf{a}_2$  span primitive rectangular/square 2D unit cell, while reciprocal lattice vectors  $\mathbf{k}_1$  and  $\mathbf{k}_2$  satisfy  $\mathbf{a}_j \cdot \mathbf{k}_l = 2\pi\delta_{jl}$  and  $q_1, q_2$  are projections of  $\mathbf{q}$  along  $\mathbf{k}_1$  and  $\mathbf{k}_2$ . Relevant BZs are in figure 2.

Effective Hamiltonians allowed by symmetry group in the special points of Brillouin's zone are presented in the last column of the table 1: the nonzero real coefficients  $v_{pq}^i$  in the expansion (2.5) are specified, together with the constraints among them. The listed forms correspond to the group settings (lattice vectors and coordinate origin) and double valued irreducible co-representations obtained by POLSym code. In fact, this enabled flexibility in the choice of generators (coordinate system and translational periods), which finally results in the form of irreducible co-representations. These are chosen such to get the same form of the effective Hamiltonian whenever it is possible (for different groups). Equivalent (but different) settings (and co-representations) produce different (still equivalent with respect to dispersions) Hamiltonian forms. Clearly, the exact values of the nonzero coefficients  $v_{pq}^i$  (listed in the last column of the table 1) are material dependent. The groups' generators and their representative matrices in the allowed co-representations associated to the specified high-symmetry points are in the table 2. It should be remarked that in all the considered cases this point is fixed by the whole gray group, i.e. the little group is the gray (double) group, and the allowed co-representations of the little group are simultaneously the irreducible co-representations of the gray group. The matrices of the relevant co-representations are four-dimensional. In all the cases time-reversal corresponds to the matrix  $\hat{T}$ ; all other generators are represented by the block-diagonal

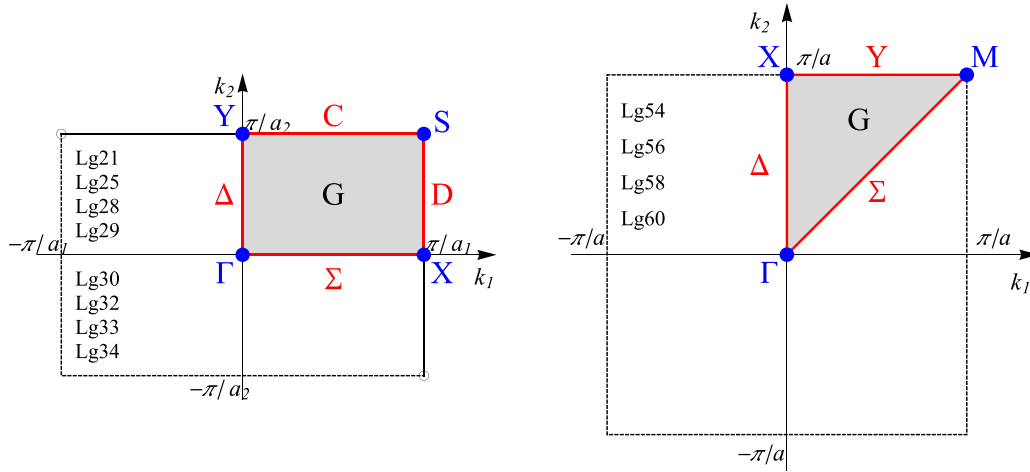


**Figure 2.** BZs of the groups (listed in table 1) supporting dispersions (3.1). For layer groups 28, 29, 30, 32, 33 and 34 vector  $k_2$  is along (screw) axis of order two.

matrices  $\hat{D} = \text{diag}(\hat{R}, \hat{R}^*)$ , with mutually conjugated  $2 \times 2$  blocks. Therefore, only this block,  $\hat{R}$ , is given in the table 2.

The described technique leads to two new types of dispersions (figure 1; crossings are taken at  $E = 0$ ). The first one is PF, with four bands (obtained for  $u, v = \pm 1$ ):

$$E_{v,u}(\mathbf{q}) = v\sqrt{aq_1^2 + cq_2^2 + ub|q_1q_2|}. \quad (3.1a)$$

The expression under the square root is non-negative since  $a, b$  and  $c$  are positive quantities (functions of  $v_{pq}^i$ ) such that  $b^2 - 4ac < 0$ . For quadratic layer groups (54, 56, 58, 60)  $c = a$ , and above dispersion degenerates to the isotropic one  $E_{v,u} = v\sqrt{aq^2 + ub|q_1q_2|}$ . Two groups, 29 and 33, enforce  $b^2 - 4ac = 0$ , hosting thus FT dispersions (with bands counted by  $u, v = \pm 1$ ):

$$E_{v,u}(\mathbf{q}) = v|f|q_1| + ug|q_2||, \quad (3.1b)$$

with  $f, g$  positive quantities, also functions of  $v_{pq}^i$ . Note that on the other side, the limit  $b \rightarrow 0^+$  gives Dirac dispersion.

### 3.2. Density of states

Dispersion (3.1), differing from the well-known Dirac, semi-Dirac or quadratic, impose specific physical properties. In this context, one must take into account the range of validity of these forms, describing the realistic band structures only in the vicinity of high-symmetry point. In particular, corresponding density of states (DOS) near  $E = 0$  are:

$$\rho_{\text{PF}}^{\text{SOC}} = \frac{2|E|}{\pi\sqrt{4ac - b^2}}, \quad (3.2a)$$

$$\rho_{\text{FT}}^{\text{SOC}} \approx \frac{L}{4\pi^2\sqrt{f^2 + g^2}}. \quad (3.2b)$$

Unlike to PF, but similarly to 3D nodal semimetals [39], exact calculation of DOS of FT is prevented due to the non-circular iso-energetic lines (figure 1). Thus, the last expression corresponds to realistic situations where the horizontal parts of band crossing lines are of the length  $L$  (this is an effective

range of approximation). In non-SOC case calculation of DOS gives doubled results (3.2), since each energy is spin degenerate, which is then decoupled from the orbital one. Non zero DOS of FT near  $E = 0$  is in contrast to DOS of Dirac or PF dispersions being proportional to  $|E|$ , as well as to semi-Dirac which is proportional to  $\sqrt{|E|}$ . This affects many properties, to mention only charge and spin transport. Further, it can be shown that the electron effective mass, obtained from band curvatures, for all dispersions (3.1) vanishes. Let us emphasize that the higher order terms, neglected in derivation cannot change the obtained band topology (figure 1), though may distort bands slightly.

### 3.3. Symmetry breaking

Despite the obtained dispersions are essential, i.e. resistant to symmetry preserving perturbation, an interesting additional insight is gained by considering symmetry breaking. Herein, taking into account group-subgroup relations, we discuss the possibilities of robustness or switching between various dispersions at the same BZ-point by lowering the symmetry, e.g. due to strain. It is expected that decreasing the number of symmetry elements leads to relaxing the constraints imposed on Hamiltonians, and consequently increasing (or preserving) the number of independent parameters. In this context, taking into account the number of non-zero parameters  $v_{pq}^i$  of (2.5) given in table 1, it is meaningful to consider the transitions from FT to anisotropic PF, as well as from isotropic PF to FT, when the symmetry is lowered. Precisely, the allowed four-band model Hamiltonian diagonalizing in PF dispersion have six real independent parameters, which are reduced to three for quadratic groups; similarly, there are 4 real independent Hamiltonian parameters for FT. Before proceeding, let us take a brief look into the robustness of FT and PF.

Regarding groups 29 and 33 supporting FT dispersion, symmetry reduction in which either nonsymmorphic glide plane or screw axis (but not both) is retained causes that FT at the  $Y$  point splits into two non-degenerate conical dispersions. Opposite out-of-plane shifts of the adjacent nuclei positioned

**Table 2.** Allowed irreducible co-representations: for each group and corresponding HSP, the generators are listed, and the block-diagonal part  $\hat{R}$  of double valued co-representation  $\hat{D}$  representing these generators (in the same order). Here,  $C_{n\hat{n}}$  is rotation for  $2\pi/n$  around axis  $\hat{n}$  (which is  $\hat{x}, \hat{y}, \hat{z}$ , or  $\hat{c} = \frac{1}{\sqrt{2}}(\hat{x} + \hat{y})$ ),  $m_{\hat{n}}$  is vertical mirror plane which contains  $\hat{n}$  axis,  $m_h$  is horizontal mirror plane, and  $S_n = C_{n\hat{z}}m_h$ .

Group	HSP	Generators		$\hat{R}$			
21	$S$	$(C_{2\hat{x}} \frac{1}{2}0)$	$(C_{2\hat{y}} 0\frac{1}{2})$	$\hat{\sigma}_3$	$\hat{\sigma}_1$		
25	$S$	$(m_{\hat{x}} \frac{1}{2}0)$	$(m_{\hat{y}} 0\frac{1}{2})$	$\hat{\sigma}_3$	$\hat{\sigma}_1$		
28	$Y$	$(I 10)$	$(C_{2\hat{y}} 0\frac{1}{2})$	$m_{\hat{y}}$	$\hat{\sigma}_0$	$-\hat{\sigma}_3$	$-i\hat{\sigma}_2$
28	$S$	$(I 10)$	$(C_{2\hat{y}} 0\frac{1}{2})$	$m_{\hat{y}}$	$-\hat{\sigma}_0$	$-\hat{\sigma}_3$	$-i\hat{\sigma}_2$
29	$Y$	$(I 10)$	$(C_{2\hat{y}} 0\frac{1}{2})$	$m_h$	$\hat{\sigma}_0$	$-\hat{\sigma}_3$	$-i\hat{\sigma}_2$
29	$S$	$(I 10)$	$(C_{2\hat{y}} 0\frac{1}{2})$	$m_h$	$-\hat{\sigma}_0$	$-\hat{\sigma}_3$	$-i\hat{\sigma}_2$
30	$Y$	$(I 10)$	$(m_{\hat{y}} 0\frac{1}{2})$	$C_{2\hat{y}}$	$\hat{\sigma}_0$	$-\hat{\sigma}_3$	$-i\hat{\sigma}_2$
30	$S$	$(I 10)$	$(m_{\hat{y}} 0\frac{1}{2})$	$C_{2\hat{y}}$	$-\hat{\sigma}_0$	$-\hat{\sigma}_3$	$-i\hat{\sigma}_2$
32	$Y$	$(I 10)$	$(m_h \frac{1}{2}\frac{1}{2})$	$m_{\hat{y}}$	$\hat{\sigma}_0$	$-\hat{\sigma}_3$	$-i\hat{\sigma}_2$
33	$Y$	$(m_h \frac{1}{2}0)$	$(C_{2\hat{y}} 0\frac{1}{2})$		$i\hat{\sigma}_3$	$\hat{\sigma}_1$	
34	$Y$	$(I 10)$	$(m_h \frac{1}{2}\frac{1}{2})$	$C_{2\hat{y}}$	$\hat{\sigma}_0$	$-\hat{\sigma}_3$	$-i\hat{\sigma}_2$
54	$M$	$(I 10)$	$(C_{2\hat{c}} \frac{1}{2}\frac{1}{2})$	$C_{4\hat{z}}$	$-\hat{\sigma}_0$	$-i\hat{\sigma}_2$	$e^{-i\frac{3\pi}{4}}$ diag(1, i)
56	$M$	$(I 10)$	$(m_{\hat{c}} \frac{1}{2}\frac{1}{2})$	$C_{4\hat{z}}$	$-\hat{\sigma}_0$	$-i\hat{\sigma}_2$	$e^{-i\frac{3\pi}{4}}$ diag(1, i)
58	$M$	$(I 10)$	$(m_{\hat{c}} \frac{1}{2}\frac{1}{2})$	$S_4$	$-\hat{\sigma}_0$	$-i\hat{\sigma}_2$	$e^{-i\frac{3\pi}{4}}$ diag(1, i)
60	$M$	$(I 10)$	$(C_{2\hat{c}} \frac{1}{2}\frac{1}{2})$	$S_4$	$-\hat{\sigma}_0$	$-i\hat{\sigma}_2$	$e^{-i\frac{3\pi}{4}}$ diag(1, i)

in the mirror plane, transforms mirror into a glide plane, while doubling the lattice constant; this in turn halves primitive vector  $\mathbf{k}_1$  of the reciprocal lattice. Group 29 reduces to 33 and the  $S$  point in 29 becomes  $Y$  point in 33. Consequently, FT in  $Y$  and  $S$  points in 29 are robust against lowering the symmetry to group 33. Similarly, concerning the PF, any homogeneous stretching along  $\mathbf{a}_1$  or  $\mathbf{a}_2$  axis deforms square primitive cell to rectangular, reducing the symmetries of layer groups 54 and 58 (56 and 60) to the group 21 (25) and causes PF to change from isotropic to anisotropic form, which implies direction-dependent electronic and related properties.

Since PF is a generalized form of FT, one could expect that the parameters of these dispersions can be interrelated by tuning. However, continuous transformation from FT to PF at the same point of the BZ is not possible, since neither of groups supporting FT is a subgroup of any of groups allowing PF, nor vice-versa. The expression (3.2a) for DOS of PF shows that the changing parameters such that PF approaches to FT results in a singularity at zero energy. In the other words, if opposite would hold, arbitrarily small displacements of nuclei, being sufficient to lower the symmetry, would cause a jump of (graphene-like) negligible DOS of PF to a finite and constant DOS of FT, which we found unlikely. At the same time, such obstruction from DOS does not forbid the transition between Dirac (double degenerate cones with four-fold degenerate point) and PF, nor it forbids splitting of FT and PF into two non-degenerate conical dispersions (with double degenerate point).

Following the above arguments, it is expected that transition from Dirac cone to PF may be realized by lowering the symmetry, since Dirac dispersions has less independent parameters than PF. According to [5] Dirac semimetals in time-reversal invariant two-dimensional systems with strong SOC are possible in nonsymmorphic groups with inversion symmetry. E.g. let us consider the layer group 46 ( $pmmn$ ), hosting Dirac cones

at  $X$ ,  $Y$  and  $S$  HSPs (the BZ is the same as this one given on the left panel in figure 2). It is expected that the violation of the inversion symmetry leads to Weyl points or node [5]. However, listing all subgroups, it turns out that the two of the subgroups, 32 and 21, actually host PF in the points  $Y$  and  $S$ , respectively. Indeed, in [46], using spinfull tight-binding model with four sites (with s-orbitals) per unit cell, authors show that at fillings 2, 6, system invariant under double layer group 21 is semimetal, which hosts one fourfold degenerate and four Weyl points. A plethora of such cases, where groups allowing PF from the table 1 are subgroups of symmetry groups of Dirac semimetals, indicates candidates for transitions between centrosymmetric and noncentrosymmetric crystals with protected four-fold band crossing point. Moreover, the existence of such essential fourfold degenerate point simultaneously with double degenerate Weyl points in the same system, makes that the layers from our list represent possible two-dimensional materials suitable for the study of their interplay.

### 3.4. Material realization

Despite the fabrication of freestanding layers is not always feasible, the above theoretical predictions required material realizations, or at least numerical simulations. To find realistic material with layer groups from table 1 we searched the list [41] of 3D layered materials, synthesis of which has been reported in the literature. In the table 3 we listed potential material candidates with symmetry groups allowing the predicted peculiar dispersions. These are laboratory fabricated 3D crystals with layered structures, which could be easily or potentially exfoliated into layers.

It is interesting to single out our group-theoretical findings indicated that dispersions (3.1) are not preserved when SOC is neglected, except for the LDG 33, which supports FT dispersion also in that case [29]. Inclusion of SOC moves FT from

**Table 3.** Material candidates: layered systems with symmetry groups hosting the dispersions (3.1). Layer and corresponding space groups are listed for materials given by a formula and materials project ID. Abbreviations EE and PE stand for easily and potentially exfoliable, respectively, according to [41].

Layer group	Space group	Formula	ID	EE/PE		
21	$p2_12_12$	18	$P2_12_12$	As <sub>2</sub> SO <sub>6</sub>	mp-27230	EE
				MgMoTeO <sub>6</sub>	mp-1210722	EE
25	$pba2$	32	$Pba2$	Au <sub>2</sub> Se <sub>2</sub> O <sub>7</sub>	mp-28095	EE
				Re <sub>2</sub> S <sub>2</sub> O <sub>13</sub> -I	mp-974650	EE
28	$pm2_1b$	26	$Pmc2_1$	TIP <sub>5</sub>	mp-27411	EE
				KO <sub>2</sub> H <sub>4</sub> F	mp-983327	PE
				NaGe <sub>3</sub> P <sub>3</sub>	mp-1104707	PE
29	$pb2_1m$	26	$Pmc2_1$	WO <sub>2</sub> Cl <sub>2</sub>	mp-32539	EE
32	$pm2_1n$	31	$Pmn2_1$	CuCOCl	mp-562090	EE
33	$pb2_1a$	29	$Pca2_1$	BiIO <sub>4</sub>	mp-1191266	PE
				KPSe <sub>6</sub>	mp-18625	EE
58	$p\bar{4}2_1m$	113	$P\bar{4}2_1m$	LiReO <sub>2</sub> F <sub>4</sub>	mp-554108	EE

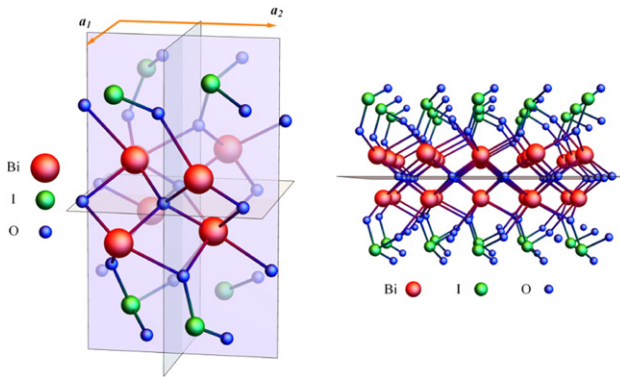


**Figure 3.** Crystal structure of BiIO<sub>4</sub> mono-layer: elementary cell (left) and a part of layer (right).

BZ corners to the  $Y$ -point. The material BiIO<sub>4</sub> belongs to corresponding space group 29 and has layers parallel to the  $y = 0$  plane. Consequently, it should exfoliate to layer group 33 so we choose it for further DFT investigations, as an example of achievements of our theory. Since IRs from table 1 are the only extra IRs in these BZ points, the dispersions (3.1) are unavoidable for crystals with symmetry of these groups. On the other hand, the position of Fermi level cannot be determined solely by symmetry arguments, nor it can be guaranteed that no other bands cross or touch the Fermi level.

We determined crystal (figure 3) and band structure (figure 4) of BiIO<sub>4</sub> mono-layer configuration using DFT calculations: full relaxation and bands calculations were performed by QUANTUM ESPRESSO software package [42], full relativistic PAW pseudopotentials [43, 44], with the Perdew–Burke–Ernzerhof exchange–correlation functional [45]. The energy cutoff for electron wavefunction and charge density of 47 Ry and 476 Ry were chosen, respectively. The band structures were found in 500  $k$ -points on selected path, and 2500  $k$ -points for 2D band structure plots in the vicinity of HSPs.

Crystal structure of mono-layer is shown in figure 3. It belongs to rectangular lattice of the group 33, with nearly equal  $a_1 = 0.566$  nm and  $a_2 = 0.575$  nm. Band structure of BiIO<sub>4</sub>

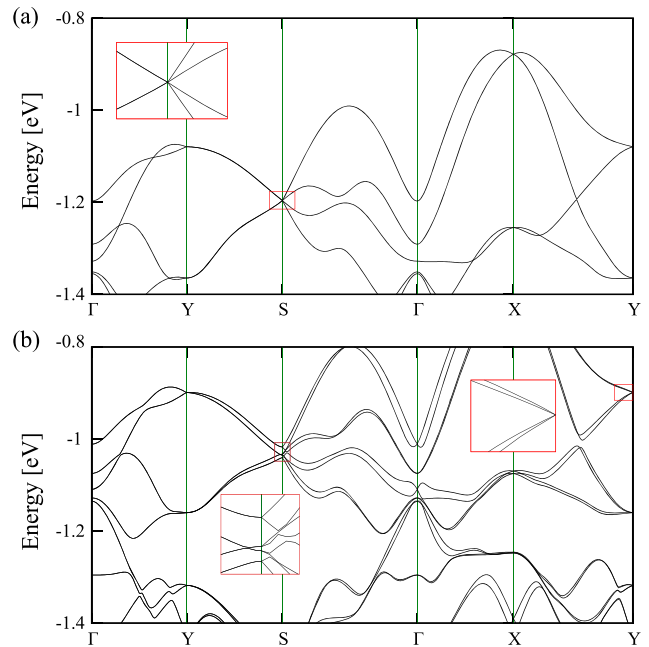


**Figure 4.** Band structure of BiIO<sub>4</sub> mono-layer without SOC (top) and with SOC (bottom), with insets showing magnified FT and split FT dispersions. The Fermi level is set to zero eV.

mono-layer with and without SOC is shown in figure 4. It turns out that the system is insulating in undoped and ungated regime. The closest to Fermi level FT state is at  $-0.9$  eV. When SOC is neglected energy at the point  $S$  is eightfold degenerate (including spin), which gives electron filling of  $8n$  that is necessary for insulating systems [40]. With inclusion of SOC the eightfold spinfull degeneracy at  $S$  is lifted, but sets of eight non-degenerate bands each, form *cat's cradle* structure along  $\Gamma X$  line, as predicted in reference [46]. This gives again electron filling of  $8n$  [46, 47]. Our electron filling of 184, derived from DFT calculations, is indeed divisible by 8. Electron filling for DLG 33 prevents FT to be the only dispersion at the Fermi level, while for remaining groups in table 1 the filling condition necessary for Fermi surface consisting of isolated points is  $\nu = 4n + 2$ .

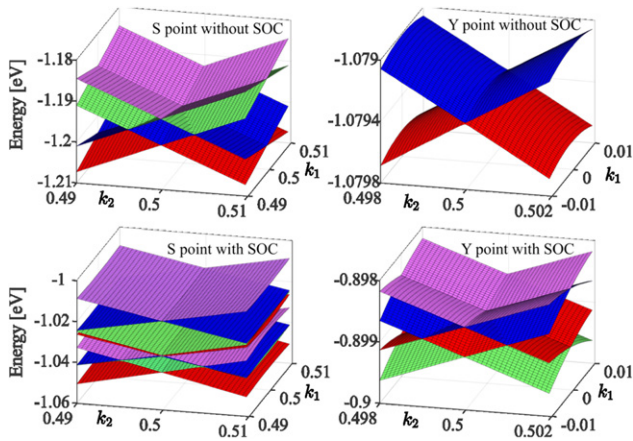


**Figure 5.** Band structures of BiIO<sub>4</sub> mono-layer without and with SOC near points *S* and *Y*. Inclusion of SOC turns FT dispersion into nodal lines in *S*, and degenerate Dirac line into FT in *Y*.

Behavior of FT states with inclusion of SOC is shown in figure 5. In non-SOC case, two pairs of Dirac lines meet at the point *S* and form the FT states. SOC splits eightfold degenerate band at *S* into four double degenerate ones. Near point *Y*, SOC splits fourfold spinfull degenerate Dirac line into one FT state. Since SOC strength is proportional to the fourth power of the atomic number [48], heavy elements in the material induced observable splitting.

#### 4. Conclusions

Characterized by band crossings (touching) points (lines) at Fermi level from which energies disperse linearly, nodal metals/semimetals take an important role in investigations of various topological properties of crystals. Among them, symmetry-enforced ones represent a class of materials hosting such dispersions in HSPs due to increased degeneracy. In the language of group theory, while the spinless case is described by the ordinary group of geometrical transformations, the spinfull situation, when system is robust on spin-orbit perturbation, needs double groups. Additional inclusion of TRS leads to gray magnetic ordinary or double group. The increased degeneracy of energy is enabled by higher dimensional allowed irreducible (co)representations of the corresponding underlying crystal symmetry.

New fermions in 2D materials revealed by application of full gray double layer group symmetry contribute to the interesting physical phenomena of layered systems: two new types of dispersions beyond Dirac, PF and FT, accompany the fourfold degeneracy of bands in high-symmetry points. Our findings single out list of twelve nonsymmorphic and non-centrosymmetric layer groups that support such unusual linear electronic dispersions. As the method is not based on the topological mechanism (invoking nonsymmorphic symmetry), the result is general, verifying *a posteriori* the necessity of nonsymmorphic elements for the considered dispersions. Providing this list, numerical simulations aimed to find material realizations of the peculiar dispersions are facilitated, which is of a great importance to achieve corresponding physical properties. PF dispersion occurs in ten groups; in particular, there

are single isolated HSP hosting it in the groups  $p_{21}2_12$ ,  $pba2$  (point *S*),  $pm2_1n$ ,  $pb2n$  (*Y*), and  $p4_212$ ,  $p4bm$ ,  $p4_21m$ ,  $p4b2$  (*M*), while the groups  $pm2_1b$  and  $pb2b$  have two such points (*Y*, *S*). On the other hand, the FT type of dispersion in the group  $pb2_1a$  is hosted in single (*Y*), and in the group  $pb2_1m$  in two HSPs (*Y*, *S*).

Particularly interesting are groups  $pb2_1a$ , supporting FT dispersion both with and without SOC, as well as  $pba2$  and  $p4bm$ , which are also wallpaper groups, preserved even when perpendicular, homogenous electric field is applied (e.g. due to gating). Moreover, coexistence of degenerate point and lines at the same energy in FT dispersion may lead to some new phenomena. FT dispersion has constant contribution to DOS, manifested as a plateau nearby zero energy in FT. This may be important in technological applications, especially when electron and/or spin transport are looked for, like materials for solar cells [49], spintronic etc. On the contrary, PF dispersion, similarly to Dirac ones, contributes by linear DOS with no states on zero energy. It has both isotropic and anisotropic forms which may be continuously transformed into each other by crystal deformations.

Our numerical calculations show that layered BiIO<sub>4</sub> 3D crystal, exfoliates to stable mono-layer having a symmetry group from our list. Band structure of BiIO<sub>4</sub> mono-layer confirms theoretical prediction, but further efforts are necessary in order to place the Fermi level at right energy.

#### Acknowledgments

Authors VD, AŠ and JP acknowledge funding provided by the Institute of Physics Belgrade, through the Grant by the Ministry of Education, Science and Technological Development of the Republic of Serbia. NL, BN and MD were supported by the Serbian Ministry of Education, Science and Technological Development under Project Number OI171035. DFT calculations were performed using computational resources at Johannes Kepler University, Linz, Austria.

#### ORCID iDs

V Damjanović <https://orcid.org/0000-0001-7517-6439>  
 N Lazić <https://orcid.org/0000-0002-3634-0301>  
 A Šolajić <https://orcid.org/0000-0002-0553-0858>  
 J Pešić <https://orcid.org/0000-0002-8600-7187>  
 B Nikolić <https://orcid.org/0000-0002-7241-3248>  
 M Damjanović <https://orcid.org/0000-0003-2806-253X>

#### References


- [1] Gupta S, Kutana A and Yakobson B I 2018 Dirac cones and nodal line in borophene *J. Phys. Chem. Lett.* **9** 2757–62
- [2] Zhang Y, Kang J, Zheng F, Gao P-F, Zhang S-L and Wang L-W 2019 Borophosphene: a new anisotropic Dirac cone mono-layer with a high Fermi velocity and a unique self-doping feature *J. Phys. Chem. Lett.* **10** 6656–63
- [3] Zhang L Z, Wang Z F, Wang Z M, Du S X, Gao H-J and Liu F 2015 Highly anisotropic Dirac fermions in square graphynes *J. Phys. Chem. Lett.* **6** 2959–62

- [4] Fang C, Gilbert M J, Dai X and Andrei Bernevig B 2012 Multi-Weyl topological semimetals stabilized by point group symmetry *Phys. Rev. Lett.* **108** 266802
- [5] Young S M and Kane C L 2015 Dirac semimetals in two dimensions *Phys. Rev. Lett.* **115** 126803
- [6] van Miert G and Smith C M 2016 Dirac cones beyond the honeycomb lattice: a symmetry-based approach *Phys. Rev. B* **93** 035401
- [7] Wang J 2017 Antiferromagnetic Dirac semimetals in two dimensions *Phys. Rev. B* **95** 115138
- [8] Kim J, Baik S S, Jung S W, Sohn Y, Ryu S H, Choi H J, Yang B-J and Kim K S 2017 Two-dimensional Dirac fermions protected by space-time inversion symmetry in black phosphorus *Phys. Rev. Lett.* **119** 226801
- [9] Young S M and Wieder B J 2017 Filling-enforced magnetic Dirac semimetals in two dimensions *Phys. Rev. Lett.* **118** 186401
- [10] Kawarabayashi T, Aoki H and Hatsugai Y 2019 Topologically protected doubling of tilted Dirac fermions in two dimensions *Phys. Status Solidi B* **256** 1970025
- [11] Mañes J L 2012 Existence of bulk chiral fermions and crystal symmetry *Phys. Rev. B* **85** 155118
- [12] Damljanović V and Gajić R 2016 Existence of Dirac cones in the Brillouin zone of diperiodic atomic crystals according to group theory *J. Phys.: Condens. Matter* **28** 085502
- [13] Damljanović V and Gajić R 2016 Addendum to existence of Dirac cones in the Brillouin zone of diperiodic atomic crystals according to group theory *J. Phys.: Condens. Matter* **28** 439401
- [14] Park S and Yang B-J 2017 Classification of accidental band crossings and emergent semimetals in two-dimensional noncentrosymmetric systems *Phys. Rev. B* **96** 125127
- [15] Wieder B J, Bradlyn B, Wang Z, Cano J, Kim Y, Kim H-S D, Rappe A M, Kane C L and Andrei Bernevig B 2018 Wallpaper fermions and the nonsymmorphic Dirac insulator *Science* **361** 246–51
- [16] Wieder B J, Kim Y, Rappe A M and Kane C L 2016 Double Dirac semimetals in three dimensions *Phys. Rev. Lett.* **116** 186402
- [17] Bradlyn B, Cano J, Wang Z, Vergniory M G, Felser C, Cava R J and Andrei Bernevig B 2016 Beyond Dirac and Weyl fermions: unconventional quasiparticles in conventional crystals *Science* **353** aaf5037
- [18] Zhu Z, Winkler G W, Wu Qian S, Ju L and Alexey A 2016 Soluyanov. Triple point topological metals *Phys. Rev. X* **6** 031003
- [19] Wang Z, Alexandradinata A, Cava R J and Andrei Bernevig B 2016 Hourglass fermions *Nature* **532** 189–94
- [20] Lv B Q *et al* 2017 Observation of three-component fermions in the topological semimetal molybdenum phosphide *Nature* **546** 627–31
- [21] Barik R K, Shinde R and Singh A K 2018 Multiple triple-point fermions in Heusler compounds *J. Phys.: Condens. Matter* **30** 375702
- [22] Yang Y *et al* 2019 Topological triply degenerate point with double Fermi arcs *Nat. Phys.* **15** 645–9
- [23] Ma J *et al* 2017 Experimental evidence of hourglass fermion in the candidate nonsymmorphic topological insulator KHgSb *Sci. Adv.* **3** e1602415
- [24] Wang S-S, Liu Y, Yu Z-M, Sheng X-L and Yang S A 2017 Hourglass Dirac chain metal in rhenium dioxide *Nat. Commun.* **8** 1844
- [25] Singh B, Ghosh B, Su C, Lin H, Agarwal A and Bansil A 2018 Topological hourglass Dirac semimetal in the nonpolar phase of  $\text{Ag}_2\text{BiO}_3$  *Phys. Rev. Lett.* **121** 226401
- [26] Novoselov K S, Geim A K, Morozov S V, Jiang D, Zhang Y, Dubonos S V, Grigorieva I V and Firsov A A 2004 Electric field effect in atomically thin carbon films *Science* **306** 666–9
- [27] Kim J *et al* 2015 Observation of tunable band gap and anisotropic Dirac semimetal state in black phosphorus *Science* **349** 723–6
- [28] Wang Z M 2014 *MoS<sub>2</sub> Materials, Physics and Devices* (Berlin: Springer)
- [29] Damljanović V, Popov I and Gajić R 2017 Fortune teller fermions in two-dimensional materials *Nanoscale* **9** 19337–45
- [30] Kopciuszynski M, Krawiec M, Żurawek L and Zdyb R 2020 Experimental evidence of a new class of massless fermions *Nanoscale Horiz.* **5** 679–82
- [31] Nguyen S D, Yeon J, Kim S-H and Shiv Halasyamani P 2011  $\text{BiO}(\text{IO}_3)$ : a new polar iodate that exhibits an Aurivillius-type  $(\text{Bi}_2\text{O}_2)^{2+}$  layer and a large SHG response *J. Am. Chem. Soc.* **133** 12422–5
- [32] Cornwell J F 1984 *Group Theory in Physics* (New York: Academic)
- [33] Elcoro L *et al* 2017 Double crystallographic groups and their representations on the Bilbao Crystallographic Server *J. Appl. Crystallogr.* **50** 1457–77
- [34] Damljanović M and Milošević I 2015 Full symmetry implementation in condensed matter and molecular physics—modified group projector technique *Phys. Rep.* **581** 1–43
- [35] Litvin D B and Wike T R 1991 *Character Tables and Compatibility Relations of the Eighty Layer Groups and Seventeen Plane Groups* (New York: Plenum)
- [36] Dresselhaus M S, Dresselhaus G and Jorio A 2008 *Group Theory* (Berlin: Springer)
- [37] Kopsky V and Litvin D B 2002 *International Tables of Crystallography Volume E: Subperiodic Groups* (Dordrecht: Kluwer)
- [38] Hahn T 2005 *International Tables of Crystallography Volume A: Space-Group Symmetry* (Berlin: Springer)
- [39] Burkov A A, Hook M D and Leon B 2011 Topological nodal semimetals *Phys. Rev. B* **84** 235126
- [40] Watanabe H, Po H C, Zaletel M P and Vishwanath A 2016 Filling-enforced gaplessness in band structures of the 230 space groups *Phys. Rev. Lett.* **117** 096404
- [41] Mounet N *et al* 2018 Two-dimensional materials from high-throughput computational exfoliation of experimentally known compounds *Nat. Nanotechnol.* **13** 246–52
- [42] Giannozzi P *et al* 2009 QUANTUM ESPRESSO: a modular and open-source software project for quantum simulations of materials *J. Phys.: Condens. Matter* **21** 395502
- [43] Blöchl P E 1994 Projector augmented-wave method *Phys. Rev. B* **50** 17953–79
- [44] Kresse G and Joubert D 1999 From ultrasoft pseudopotentials to the projector augmented-wave method *Phys. Rev. B* **59** 1758–75
- [45] Perdew J P, Burke K and Ernzerhof M 1996 Generalized gradient approximation made simple *Phys. Rev. Lett.* **77** 3865–8
- [46] Wieder B J and Kane C L 2016 Spin-orbit semimetals in the layer groups *Phys. Rev. B* **94** 155108
- [47] Watanabe H, Po H C, Vishwanath A and Zaletel M 2015 Filling constraints for spin-orbit coupled insulators in symmorphic and nonsymmorphic crystals *Proc. Natl Acad. Sci.* **112** 14551–6
- [48] Yang S A 2016 Dirac and Weyl materials: fundamental aspects and some spintronic applications *SPIN* **06** 1640003
- [49] Boriskina S, Zhou J, Ding Z and Chen G 2018 Efficiency limits of solar energy harvesting via internal photoemission in carbon materials *Photonics* **5** 4



## RESEARCH ARTICLE

Vacancies and spin–phonon coupling in  $\text{CrSi}_{0.8}\text{Ge}_{0.1}\text{Te}_3$ 

Ana Milosavljević<sup>1</sup>  | Andrijana Šolajić<sup>1</sup> | Bojana Višić<sup>1</sup> | Marko Opačić<sup>1</sup> | Jelena Pešić<sup>1</sup> | Yu Liu<sup>2</sup> | Cedomir Petrović<sup>2</sup> | Zoran V. Popović<sup>1,3</sup> | Nenad Lazarević<sup>1</sup>

<sup>1</sup>Institute of Physics Belgrade, University of Belgrade, Pregrevica 118, Belgrade, 11080, Serbia

<sup>2</sup>Condensed Matter Physics and Materials Science Department, Brookhaven National Laboratory, Upton, New York, 11973-5000, USA

<sup>3</sup>Serbian Academy of Sciences and Arts, Knez Mihailova 35, Belgrade, 11000, Serbia

**Correspondence**

Ana Milosavljević, Institute of Physics Belgrade, University of Belgrade, Pregrevica 118, 11080 Belgrade, Serbia.  
Email: ana.milosavljevic@ipb.ac.rs

**Funding information**

Serbian Academy of Sciences and Arts, Grant/Award Number: F-134; Slovenian Research Agency, Grant/Award Number: P1-0099; Ministry of Education, Science and Technological Development of the Republic of Serbia U.S. DOE-BES, Division of Materials Science and Engineering, Grant/Award Number: DE-SC0012704

**Abstract**

We report temperature-dependent Raman scattering and magnetization studies of van der Waals ferromagnetic compound  $\text{CrSi}_{0.8}\text{Ge}_{0.1}\text{Te}_3$ . Magnetic susceptibility measurements revealed dominant ferromagnetic interactions below  $T_C$  which shift to the lower values due to the presence of vacancies. A Raman active mode, additional to the ones predicted by symmetry in the parent compounds, has been observed. This  $A_g$  symmetry mode most likely emerges as a consequence of the atomic vacancies on Si/Ge site. Presence of the strong spin–phonon coupling at temperature around 210 K is indicated by deviations from conventional phonon self-energy temperature dependence of all analysed modes.

**KEYWORDS**

magnetism, phonons, raman spectroscopy, van der Waals materials

**1 | INTRODUCTION**

Considerable progress has been made in the field of material science through developing new materials and revealing their properties in the last decade. Namely, in the recent years, large family of van der Waals materials with inherent magnetism became the focus of experimental and theoretical research, because they seem suitable for numerous technical applications.<sup>[1–7]</sup> The family includes  $\text{Fe}_{3-x}\text{GeTe}_2$  metallic materials with high magnetic transition temperature,<sup>[8–10]</sup> semiconductors  $\text{CrXTe}_3$  ( $X = \text{Si, Ge, Sn}$ ) and  $\text{CrX}_3$  ( $X = \text{Cl, Br, I}$ ) monolayers<sup>[2,11–13]</sup> and heterostructures.<sup>[14]</sup>

$\text{CrSiTe}_3$  and  $\text{CrGeTe}_3$  are ferromagnetic (FM) semiconductors with band gap of 0.4 and 0.7 eV and Curie temperatures ( $T_C$ ) of 32 and 61 K, respectively.<sup>[15–18]</sup> Twinning of  $\text{CrSiTe}_3$  single crystals along  $c$ -axes was revealed by X-ray diffraction experiment as well as  $\text{Cr}^{3+}$  ions magnetic order.<sup>[15]</sup> Recently, through high-resolution angle-resolved photoemission spectroscopy (ARPES), it was possible to identify full electronic structure near the Fermi level. Due to spin–orbit coupling,  $\text{CrSiTe}_3$  is a Mott-type FM insulator.<sup>[19]</sup> Electronic structure of  $\text{CrGeTe}_3$  single crystals was also investigated by ARPES.<sup>[20]</sup> It was shown that the low-lying valence bands are centred around the  $\Gamma$  point and are mainly formed from Te 5p orbitals.

Raman scattering studies of  $\text{CrSiTe}_3$  reveal strong spin–lattice coupling in the paramagnetic phase<sup>[15,21]</sup> as a consequence of a short-range magnetic order in this compound. In addition to renormalization of energies and linewidths of observed Raman active modes, coupling of doubly degenerate  $E_g$  mode with magnetic continuum was found.<sup>[21]</sup> The coupling results in an asymmetric phonon line shape up to 180 K. Besides the splitting of two low-energy  $E_g$  modes in the magnetic phase of  $\text{CrGeTe}_3$  and unconventional behaviour of phonon properties around transition temperature, experimental results indicate spin–phonon coupling effect with magnetic quasi-elastic scattering.<sup>[22]</sup> Pressure-dependent Raman scattering study of  $\text{CrGeTe}_3$  showed a decrease in bond length, the deviation of Cr–Te–Cr angle, and reduction of phase transition temperature.<sup>[23]</sup>

Change of the carrier concentration plays an important role in the physics of semiconducting materials as it can lead to surprising physical properties. Very small variations in dopant concentrations can lead to structural modifications and considerable changes in magnetic transition temperature. Here, we report a Raman scattering and magnetization studies of  $\text{CrSi}_{0.8}\text{Ge}_{0.1}\text{Te}_3$ . Our scanning electron microscopy (SEM) measurements reveal 10% of Ge atoms concentration and 10% of vacancies. Vacancies induced a decrease in  $T_C$  was detected within magnetic susceptibility measurements. In the Raman scattering results, we identified three  $A_g$  and four  $E_g$  symmetry modes. Additional peak of the  $A_g$  symmetry is also observed in our spectra. This mode may be traced to vacancies and possible inhomogeneous distribution of Ge atoms substitution on Si atomic site at nano-scale. Energies of modes predicted by symmetry analysis are found between the experimental values of parent compounds  $\text{CrSiTe}_3$  and  $\text{CrGeTe}_3$ , reported previously in Milosavljević et al.<sup>[21]</sup> The presence of the strong spin–phonon interaction at temperature around 210 K is indicated in small deviations from conventional temperature-dependent behaviour of the observed modes energies and linewidths, including additional one.

## 2 | EXPERIMENT AND NUMERICAL METHOD

$\text{CrSi}_{0.8}\text{Ge}_{0.1}\text{Te}_3$  single crystals were grown as described previously.<sup>[24]</sup> Magnetic properties were measured in a Quantum Design MPMS-XL5 system.

SEM measurements were performed using FEI HeliosNanolab 650. This microscope is equipped with an Oxford Instruments energy dispersive spectroscopy (EDS) system with an X-max SSD detector operating at 20 kV. Measurements were performed on as-cleaved samples

deposited on a graphite tape. The elemental composition EDS mapping was obtained on crystals that appeared to be uniform for several tens of microns. The maps show the presence of Cr, Ge, Te and Si.

For Raman scattering experiment, Tri Vista 557 spectrometer was used in the subtractive backscattering micro-Raman configuration. The combination of gratings was 1800/1800/2400 grooves/mm and the entrance slit of 80  $\mu\text{m}$ . Solid state laser with 532-nm line was used as an excitation source. In our scattering configuration, plane of incidence is  $ab$ -plane, where  $|a|=|b|$  ( $\angle(a,b)=120^\circ$ ), with incident (scattered) light propagation direction along  $c$ -axes. Samples were cleaved in the air before being placed in vacuum. All measurements were performed in high vacuum ( $10^{-6}$  mbar) using a KONTI CryoVac continuous Helium flow cryostat with 0.5-mm thick window. Laser beam focusing was achieved using microscope objective with  $\times 50$  magnification. All spectra were corrected for Bose factor.

Spin-polarized density functional theory calculations were performed in Quantum Espresso software package,<sup>[25]</sup> based on plane waves and pseudopotentials, using Perdew–Burke–Ernzerhof (PBE) exchange–correlation functional<sup>[26]</sup> and projector augmented wave (PAW) pseudopotentials.<sup>[27,28]</sup> The cutoff for wavefunctions and the charge density of 85 and 425 Ry were chosen, respectively. The  $k$ -point were sampled using the Monkhorst–Pack scheme, on  $8 \times 8 \times 8$   $\Gamma$  centred grid used for both structures. Optimization of the lattice parameters and atomic positions in unit cell was performed until the interatomic forces were minimized down to  $10^{-6}$  Ry/Å. Treatment of the van der Waals interactions is included using the Grimme-D2 correction, in order to obtain the lattice parameters more accurately. Phonon wave numbers were calculated within the linear response method, as implemented in PHonon part of Quantum Espresso.

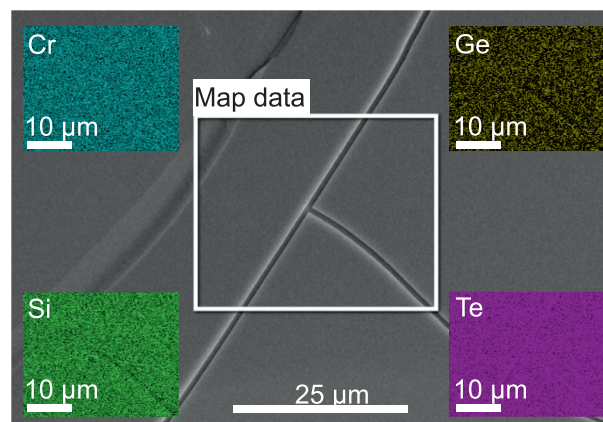


**FIGURE 1** Energy dispersive spectroscopy (EDS) mapping on a  $\text{CrSi}_{0.8}\text{Ge}_{0.1}\text{Te}_3$  single crystal [Colour figure can be viewed at [wileyonlinelibrary.com](http://wileyonlinelibrary.com)]

### 3 | RESULTS AND DISCUSSION

In order to investigate uniformity and elemental composition of  $\text{CrSi}_{0.8}\text{Ge}_{0.1}\text{Te}_3$  sample, SEM measurements were performed on as-cleaved crystals. EDS mapping presented in Figure 1 shows that the ratio of Cr:Si:Ge:Te (averaged over 10 measurements) is 1:0.8:0.1:3. This result reveals the presence of 10% Ge atomic vacancies in the sample.

Figure 2a,b presents the temperature dependence of zero-field cooling (ZFC) magnetic susceptibility  $\chi(T) = M(T)/H$  measured in 1-kOe magnetic field applied parallel to *a* (a) and *c* (b) crystallographic axes. Curie–Weiss law  $\chi = \frac{C}{T-\theta}$  fit at high temperatures yields Weiss temperatures  $\theta_a = 61(2)$  K,  $\theta_c = 70(2)$  K and high temperature paramagnetic moments  $\mu_{\text{eff},a} = 4.14(2)\mu_B$  and  $\mu_{\text{eff},c} = 3.91(2)\mu_B$  for  $\text{CrSi}_{0.8}\text{Ge}_{0.1}\text{Te}_3$ , consistent with dominant FM interactions below  $T_c$  and in line with the observed FM  $T_c$  and magnetic hysteresis loops.<sup>[13,24]</sup> The approximate  $T_c$  value can be determined from the minima of the  $d\chi/dT$  curves insets in Figure 2(a,b). It should be noted

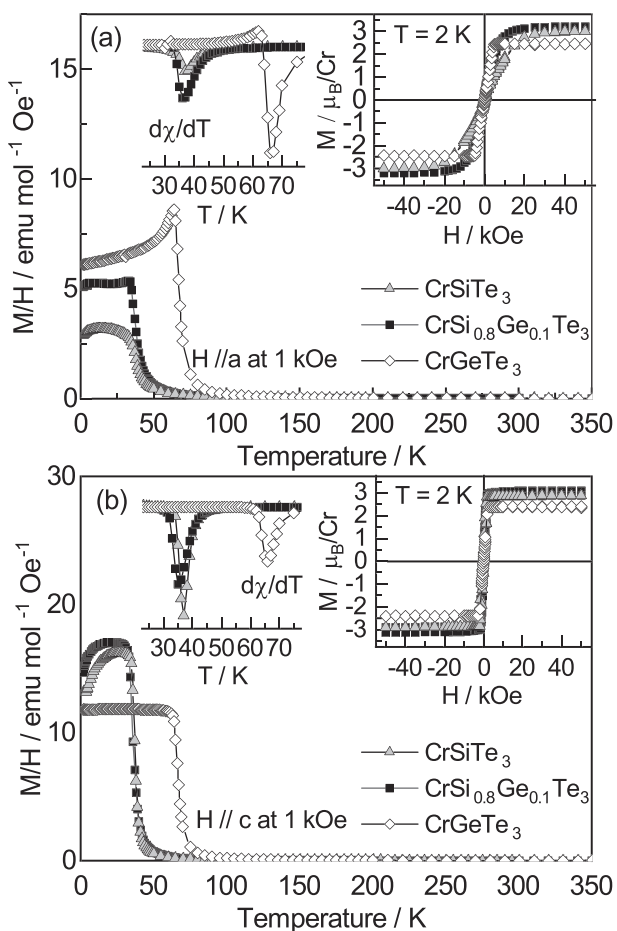


**FIGURE 2** Temperature dependence of zero-field cooling (ZFC)  $\chi=M/H$  for  $\text{CrSiTe}_3$ ,  $\text{CrSi}_{0.8}\text{Ge}_{0.1}\text{Te}_3$  and  $\text{CrGeTe}_3$  in 1-kOe magnetic field applied in-plane (a) and along the *c*-axis (b). Insets show transition temperatures of ferromagnetic orders ( $d\chi/dT$ ) and magnetic hysteresis loops taken at 2 K

that, instead of monotonous rise, there is a weak but discernible shift to lower temperature in  $d\chi/dT$  in  $\text{CrSi}_{0.8}\text{Ge}_{0.1}\text{Te}_3$  when compared with  $\text{CrSiTe}_3$ . This small reduction in FM transition temperature is likely induced by the presence of vacancies, as suggested by the EDS data. The presence of vacancies in this class of materials usually disarrange magnetic exchange due to disorder increment, which leads to the reduction of  $T_c$ .<sup>[29]</sup>

Isostructural parent compounds  $\text{CrSiTe}_3$  and  $\text{CrGeTe}_3$  crystallize in the rhombohedral crystal structure, described with space group  $R\bar{3}(C_{3i}^2)$ .<sup>[30]</sup> According to factor group analysis, five  $A_g$  and five double degenerate  $E_g$  symmetry modes are expected to be observed in the light scattering experiment. Detailed symmetry analysis, phonon mode distribution and selection rules for parent compounds ( $\text{CrSiTe}_3$  and  $\text{CrGeTe}_3$ ) can be found in Milosavljević et al.<sup>[21]</sup> In our scattering configuration, the plane of incidence is *ab* plane, where  $|a|=|b|$  ( $\angle(a,b) = 120^\circ$ ) (inset in Figure 3), and the direction of incident (scattered) light propagation is along *c*-axes. According to the selection rules for this scattering configuration,<sup>[21]</sup> all Raman active modes may be observed, having in mind that  $A_g$  symmetry modes can be detected only in parallel polarization configuration. The  $E_g$  symmetry modes are expected to appear in both the parallel and cross polarization configurations. Raman spectra of  $\text{CrSi}_{0.8}\text{Ge}_{0.1}\text{Te}_3$ , obtained by continuous change of the angle between polarization vectors of incident and

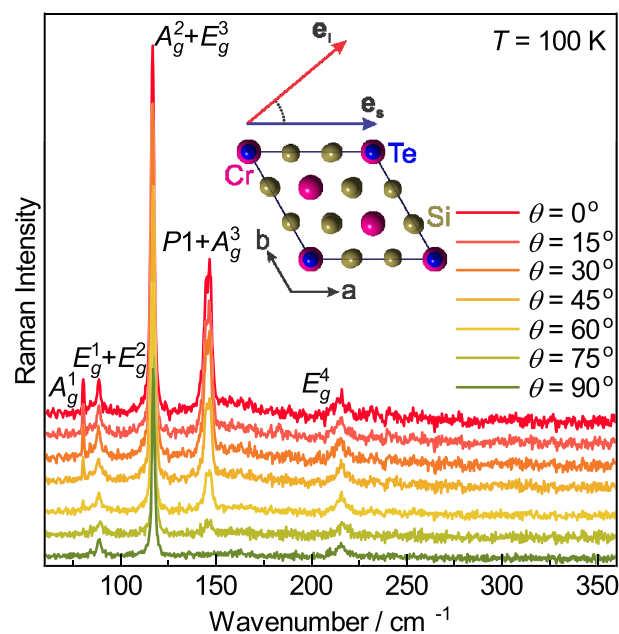


**FIGURE 3** Raman spectra of  $\text{CrSi}_{0.8}\text{Ge}_{0.1}\text{Te}_3$  single crystal, measured at 100 K, as a function of angle  $\theta$ , between incident and scattered light polarization. Inset: schematic representation of the incident and scattered light polarization with respect to the crystal orientation [Colour figure can be viewed at wileyonlinelibrary.com]

scattered light,  $\theta = \angle(\mathbf{e}_i, \mathbf{e}_s)$ , ( $0^\circ \leq \theta \leq 90^\circ$ ) at 100 K, are shown in Figure 3. It can be seen that by changing this angle, starting from  $\theta = 0^\circ$ , the intensities of the peaks at energies 80.2, 116.4 and  $145.5 \text{ cm}^{-1}$  continuously decrease and completely vanish for polarization angle of  $90^\circ$ . Therefore, these excitations obey pure  $A_g$  symmetry. On the other hand, the peaks at energies of 84.5, 88.3, 117.2 and  $215.0 \text{ cm}^{-1}$  are not influenced by change of polarization angle, so they can be identified as  $E_g$  symmetry modes.

Here, one should note that the feature observed at around  $117 \text{ cm}^{-1}$  in both scattering configurations is actually a two-peak structure comprising of  $116.4 \text{ cm}^{-1}$   $A_g$  and  $117.2 \text{ cm}^{-1}$   $E_g$  symmetry modes. Detailed analysis of the structure for two scattering configurations is presented in Figure A1 of Appendix. Furthermore, closer inspection of the data revealed that peak at energy of  $145.5 \text{ cm}^{-1}$ , which obeys pure  $A_g$  symmetry, is also composed of two modes,  $P1$  ( $144.6 \text{ cm}^{-1}$ ) and  $A_g^3$  ( $146.7 \text{ cm}^{-1}$ ), as shown in Figure A2 of Appendix.

Calculated optical phonon wavenumbers of the parent compounds,  $\text{CrSiTe}_3$  and  $\text{CrGeTe}_3$ , together with their experimental Raman active values as well as Raman mode energies of  $\text{CrSi}_{0.8}\text{Ge}_{0.1}\text{Te}_3$ , are compiled in Table 1. As expected, experimental values of  $\text{CrSi}_{0.8}\text{Ge}_{0.1}\text{Te}_3$  Raman active modes are found between the values of the observed modes in parent compounds.<sup>[21]</sup> Figure 4a shows compositional evolution of the peaks with highest

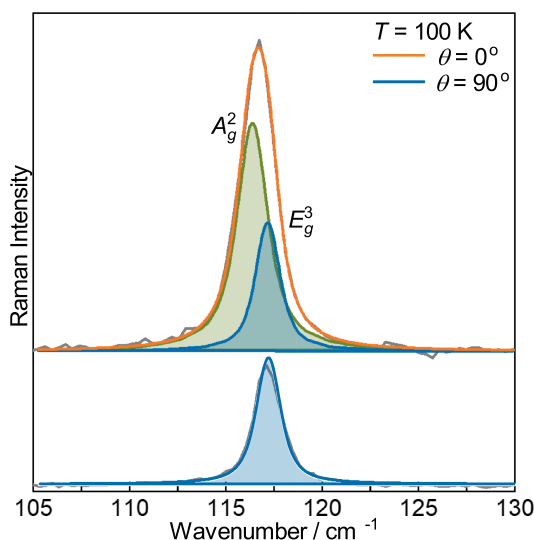


**FIGURE A1** Decomposition of unresolved  $A_g^2$  and  $E_g^3$  symmetry modes obtained by simultaneous modelling in parallel and cross polarization configuration. Grey line represents the measured data, Voigt line of  $A_g^2$  mode is shown by green, and blue lines represent the  $E_g^3$  symmetry mode in parallel (upper panel) and cross (lower panel) polarization. The orange line is the superposition of these two lines [Colour figure can be viewed at [wileyonlinelibrary.com](http://wileyonlinelibrary.com)]

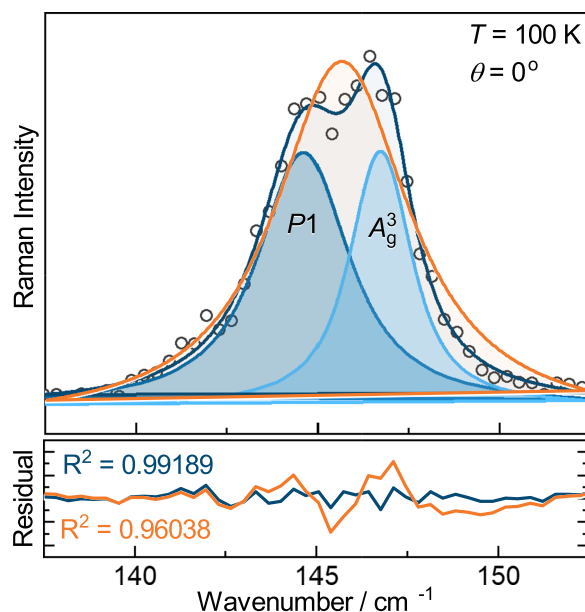


**FIGURE A2** Decomposition of phonon mode in parallel scattering configuration on two  $A_g$  symmetry modes. Open circles represent the measured data and the blue one sum of two Voigt profile line shapes. Data modelled with one Voigt profile line shape (orange line) deviates significantly from measured data [Colour figure can be viewed at [wileyonlinelibrary.com](http://wileyonlinelibrary.com)]

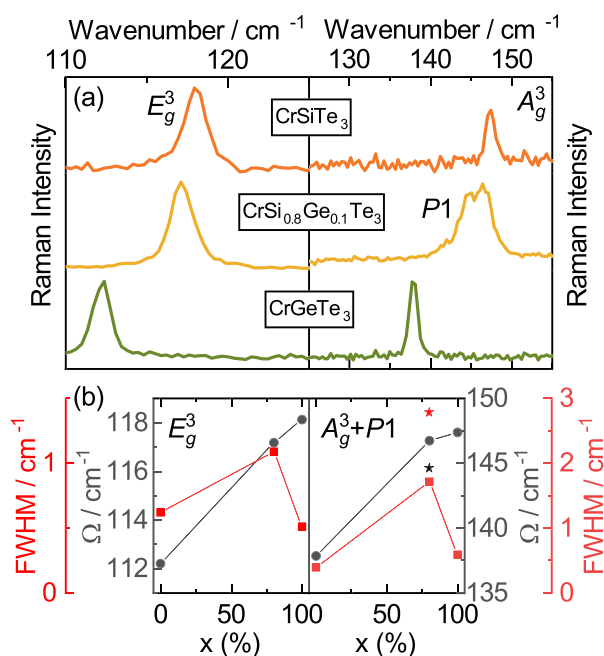
intensity, assigned as  $E_g^3$  and  $A_g^3$  symmetry modes in parent compounds. The  $E_g^3$  mode energy changes almost linearly (Figure 4b), as a consequence of change in lattice parameters and “change of mass” effect. The observed energy shift is followed by doubling of the linewidth, dominantly induced by the significant crystalline disorder. The similar type of behaviour, with somewhat larger increase in the linewidth, was also observed for the  $A_g^3$  symmetry mode. The most striking feature was the additional  $A_g$  symmetry mode (denoted as  $P1$ , see Figure A2 of the Appendix), observed in the doped sample. Generally, both the substitutional defects and vacancies may have similar impact on the Raman modes energy and linewidth. Here, the appearance of  $P1$  peak can be understood as a consequence of the presence of vacancies on Si/Ge atomic site and their inharmonic distribution at nano-scale. The mode “splitting” is detected only for the  $A_g^3$  but not for other observed modes, due to the fact that different nature of these vibrations results in different values of energy shifts. In the case of other modes, the difference between the shifts for corresponding domains is smaller than the spectral resolution of the instrument ( $\sim 1.8 \text{ cm}^{-1}$ ), and therefore, the separate modes can not be resolved.

Figure 5 shows  $\text{CrSi}_{0.8}\text{Ge}_{0.1}\text{Te}_3$  Raman scattering spectra measured at various temperatures. For clarity, spectra obtained for cross polarization configuration are

**TABLE 1** Phonon symmetry, calculated ( $T=0$  K) and experimental ( $T=100$  K) Raman active phonon wavenumbers of parent compounds  $\text{CrSiTe}_3$  and  $\text{CrGeTe}_3$ .<sup>[21]</sup> Experimental values for Raman active phonons of  $\text{CrSi}_{0.8}\text{Ge}_{0.1}\text{Te}_3$  at 100 K are shown in the last column

Raman active modes					
Symmetry	Calculations		Experiment		
	$\text{CrSiTe}_3$	$\text{CrGeTe}_3$	$\text{CrSiTe}_3$	$\text{CrGeTe}_3$	$\text{CrSi}_{0.8}\text{Ge}_{0.1}\text{Te}_3$
$A_g^1$	88.2	84.2	—	—	80.2
$E_g^1$	93.5	82.0	88.9	83.5	84.5
$E_g^2$	96.9	90.8	—	—	88.3
$E_g^3$	118.3	114.2	118.2	112.2	117.2
$A_g^2$	122.0	105.9	—	—	116.4
$A_g^3$	148.0	134.8	147.4	137.9	146.7
$A_g^4$	208.7	200.3	—	—	—
$E_g^4$	219.5	209.6	217.2	217.5	215.0
$E_g^5$	357.4	229.8	—	—	—
$A_g^5$	508.9	290.7	—	296.6	—

Note: All values are given in  $\text{cm}^{-1}$ .



**FIGURE 4** (a) Raman scattering spectra of  $E_g^3$  and  $A_g^3$  phonon modes of  $\text{CrSiTe}_3$  (orange line),  $\text{CrSi}_{0.8}\text{Ge}_{0.1}\text{Te}_3$  (yellow line) and  $\text{CrGeTe}_3$  (green line) at  $T=100$  K measured in cross (left panel) and parallel (right panel) scattering configuration, respectively. (b) Energy (grey line) and linewidth (red line) of these two modes with respect to the percentage of Si atoms concentration. Energy and linewidth of  $P1$  mode are marked with black and red star, respectively [Colour figure can be viewed at [wileyonlinelibrary.com](http://wileyonlinelibrary.com)]

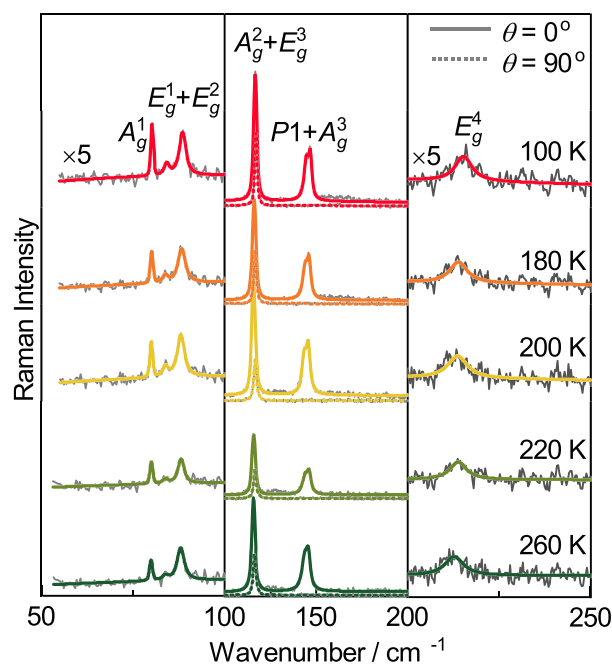


**FIGURE 5** Raman spectra of  $\text{CrSi}_{0.8}\text{Ge}_{0.1}\text{Te}_3$  single crystal measured at various temperatures. The spectra were analysed by using multiple Voigt peak functions and a single  $\chi''_{cont} = a\Gamma\omega/(\Gamma^2 + \omega^2) + b\omega$  function, for parallel ( $\theta=0^\circ$ , solid coloured lines) and cross ( $\theta=90^\circ$ , dashed coloured lines) scattering configuration. For clarity, higher and lower energy ranges (left and right panel) are multiplied by the factor of five [Colour figure can be viewed at [wileyonlinelibrary.com](http://wileyonlinelibrary.com)]

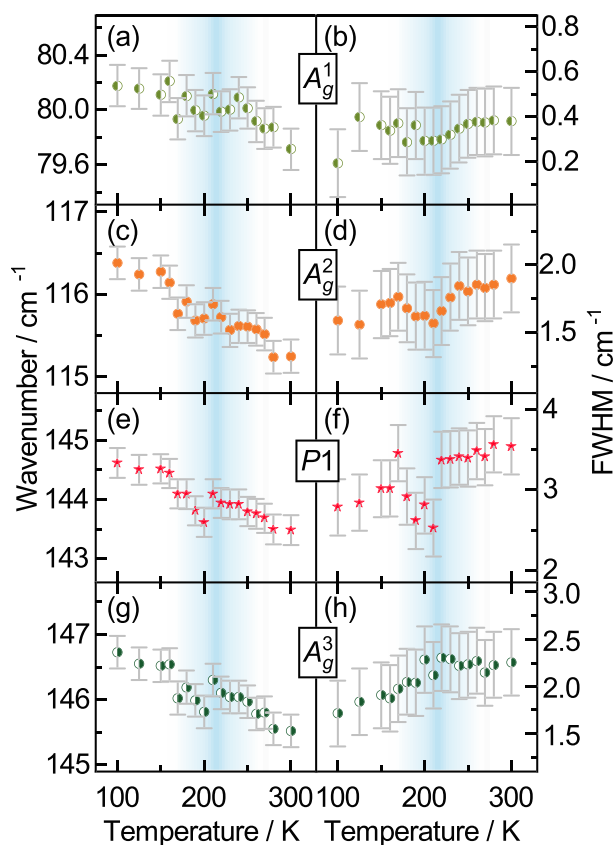


**FIGURE 6** Energy and linewidth temperature dependence of  $A_g^1$  (a,b),  $A_g^2$  (c,d),  $P1$  (e,f) and  $A_g^3$  (g,h) Raman modes [Colour figure can be viewed at [wileyonlinelibrary.com](http://wileyonlinelibrary.com)]

only shown for the mid-energy range. Temperature dependence of energies and linewidths of all the observed  $A_g$  symmetry modes, including  $P1$ , are presented in Figure 6. By heating the sample from 100 K to approximately 210 K, monotonous decrease in energy of all the  $A_g$  symmetry modes is present, dominantly driven by thermal expansion.<sup>[31]</sup> In the temperature region around 210 K, these modes' energy exhibit small deviation, followed by a continuous decrease up to room temperature. In the same temperature region, deviation from expected anharmonic type of behaviour is observed for all the  $A_g$  symmetry modes linewidth. This effect is more pronounced for higher energy modes where the anharmonicity is expected to be higher. Similar response of analysed  $E_g$  symmetry modes is present and shown in Figure 7.

Concerning previously reported strong spin-phonon coupling in  $\text{CrSiTe}_3$ ,<sup>[15,21]</sup> which persists up to 180 K, we believe that this unconventional behaviour of energies and linewidths can be attributed to the coupling of the phonon modes to the spin system.<sup>[32]</sup> Due to the doping and presence of vacancies, strong magnetic correlations in  $\text{CrSi}_{0.8}\text{Ge}_{0.1}\text{Te}_3$  are sustained up to 210 K.

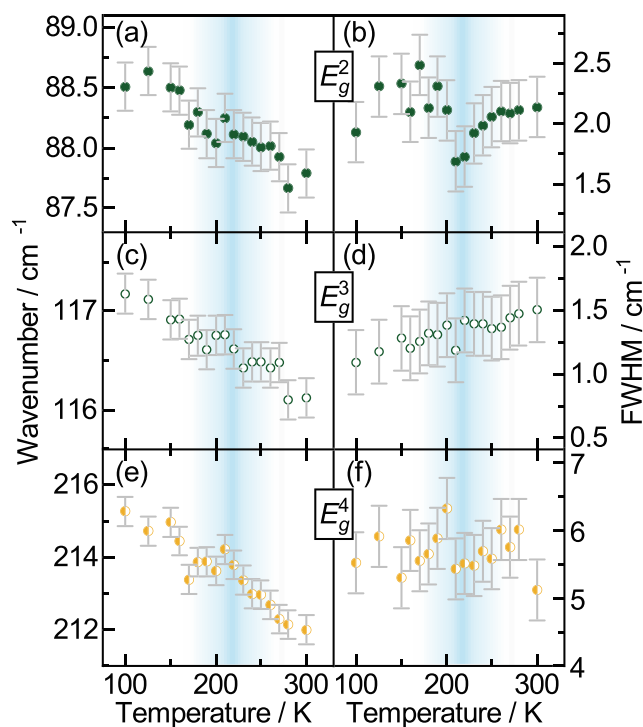


**FIGURE 7** Energy and linewidth temperature dependence of  $E_g^2$  (a,b),  $E_g^3$  (c,d) and  $E_g^4$  (e,f) symmetry modes [Colour figure can be viewed at [wileyonlinelibrary.com](http://wileyonlinelibrary.com)]

## 4 | CONCLUSIONS

In summary, we presented temperature-dependent Raman scattering and magnetization studies of doped van der Waals ferromagnet  $\text{CrSi}_{0.8}\text{Ge}_{0.1}\text{Te}_3$ . SEM measurements revealed the presence of 10% vacancies on Si/Ge atomic site. As a consequence, magnetization measurements detected small but clear decrease in  $T_C$ . Seven out of 10 Raman active modes have been assigned in our Raman spectra. Temperature dependence of all the observed modes shows the persistence of magnetic correlations up to 210 K. In addition, the results revealed the appearance of the peak that obey pure  $A_g$  symmetry, which is attributed to the possible inhomogeneous distribution of Ge atoms and vacancies at nano-scale. This study provides an insight into the impact of doping and presence of vacancies on magnetic and lattice properties in this class of materials.

## ACKNOWLEDGEMENTS

This work was supported by the Ministry of Education, Science and Technological Development of the Republic of Serbia and project no F-134 of the Serbian Academy of Sciences and Arts. DFT calculations were performed using computational resources at Johannes Kepler University, Linz, Austria. Electron microscopy was performed at Jozef Stefan Institute, Ljubljana, Slovenia,

under Slovenian Research Agency contract P1-0099 (B. V.). Work at BNL (crystal synthesis and magnetic characterization) was supported by the U.S. DOE-BES, Division of Materials Science and Engineering, under Contract No. DE-SC0012704.

## ORCID

Ana Milosavljević  <https://orcid.org/0000-0002-8654-0475>

## REFERENCES

- [1] F. Hellman, A. Hoffmann, Y. Tserkovnyak, G. S. Beach, E. E. Fullerton, C. Leighton, A. H. MacDonald, D. C. Ralph, D. A. Arena, H. A. Dürr, P. Fischer, *Rev. Mod. Phys.* **2017**, *89*, 025006.
- [2] N. Sivadas, M. W. Daniels, R. H. Swendsen, S. Okamoto, D. Xiao, *Phys. Rev. B* **2015**, *91*, 235425.
- [3] K. S. Novoselov, A. K. Geim, S. V. Morozov, D. Jiang, Y. Zhang, S. V. Dubonos, I. V. Grigorieva, A. A. Firsov, *Science* **2004**, *306*(5696), 666.
- [4] Q. H. Wang, K. Kalantar-Zadeh, A. Kis, J. N. Coleman, M. S. Strano, *Nat. Nanotechnol.* **2012**, *7*, 699.
- [5] G. Cheng, L. Lin, L. Zhenglu, J. Huiwen, S. Alex, X. Yang, C. Ting, B. Wei, W. Chenzhe, W. Yuan, Z. Q. Qiu, R. J. Cava, G. L. Steven, X. Jing, Z. Xiang, *Nature* **2017**, *546*, 265.
- [6] B. Huang Bevin, G. Clark, E. Navarro-Moratalla, D. R. Klein, R. Cheng, K. L. Seyler, D. Zhong, E. Schmidgall, M. A. McGuire, D. H. Cobden, W. Yao, *Nature* **2017**, *546*, 270.
- [7] K. S. Burch, D. Mandrus, J.-G. Park, *Nature* **2018**, *563*(7729), 47.
- [8] J.-X. Zhu, M. Janoschek, D. Chaves, S. J. C. Cezar, T. Durakiewicz, F. Ronning, Y. Sassa, M. Mansson, B. L. Scott, N. Wakeham, E. D. Bauer, J. D. Thompson, *Phys. Rev. B* **2016**, *93*, 144404.
- [9] B. Chen, J. H. Yang, H. D. Wang, M. Imai, H. Ohta, C. Michioka, K. Yoshimura, M. H. Fang, *J. Phys. Soc. Japan* **2013**, *82*(12), 124711.
- [10] A. Milosavljević, A. Šolajić, S. Djurdjic-Mijin, J. Pešić, B. Višić, Y. Liu, C. Petrovic, N. Lazarević, Z. V. Popović, *Phys. Rev. B* **2019**, *99*, 214304.
- [11] M. A. McGuire, H. Dixit, V. R. Cooper, B. C. Sales, *Chem. Mat.* **2015**, *27*(2), 612.
- [12] H. L. Zhuang, Y. Xie, P. R. C. Kent, P. Ganesh, *Phys. Rev. B* **2015**, *92*, 035407.
- [13] G. T. Lin, H. L. Zhuang, X. Luo, B. J. Liu, F. C. Chen, J. Yan, Y. Sun, J. Zhou, W. J. Lu, P. Tong, Z. G. Sheng, *Phys. Rev. B* **2017**, *95*, 245212.
- [14] M. Gibertini, M. Koperski, A. F. Morpurgo, K. S. Novoselov, *Nat. Nanotech.* **2019**, *14*(5), 408.
- [15] L. D. Casto, A. J. Clune, M. O. Yokosuk, J. L. Musfeldt, T. J. Williams, H. L. Zhuang, M.-W. Lin, K. Xiao, R. G. Hennig, B. C. Sales, J.-Q. Yan, D. Mandrus, *APL Mat.* **2015**, *3*(4), 041515.
- [16] X. Zhang, Y. Zhao, Q. Song, S. Jia, J. Shi, W. Han, *JJpn. J. Appl. Phys.* **2016**, *55*(3), 033001.
- [17] B. Siberchicot, S. Jobic, V. Carreaux, P. Gressier, G. Ouvrard, *Phys. J. Chem.* **1996**, *100*(14), 5863.
- [18] V. Carreaux, F. Moussa, M. Spiessner, *EPL* **1995**, *29*(3), 251.

- [19] J. Zhang, X. Cai, W. Xia, A. Liang, J. Huang, C. Wang, L. Yang, H. Yuan, Y. Chen, S. Zhang, Y. Guo, *Phys. Rev. Lett.* **2019**, *123*, 047203.
- [20] Y. F. Li, W. Wang, W. Guo, C. Y. Gu, H. Y. Sun, L. He, J. Zhou, Z. B. Gu, Y. F. Nie, X. Q. Pan, *Phys. Rev. B* **2018**, *98*, 125127.
- [21] A. Milosavljević, A. Šolajić, J. Pešić, Y. Liu, C. Petrovic, N. Lazarević, Z. V. Popović, *Phys. Rev. B* **2018**, *98*, 104306.
- [22] Y. Tian, M. J. Gray, H. Ji, R. J. Cava, K. S. Burch, *2D Mater.* **2016**, *3*(2), 025035.
- [23] Y. Sun, R. C. Xiao, G. T. Lin, R. R. Zhang, L. S. Ling, Z. W. Ma, X. Luo, W. J. Lu, Y. P. Sun, Z. G. Sheng, *Appl. Phys. Lett.* **2018**, *112*(7), 072409.
- [24] Y. Liu, C. Petrovic, *Phys. Rev. Mater.* **2019**, *3*, 014001.
- [25] P. Giannozzi, S. Baroni, N. Bonini, M. Calandra, R. Car, C. Cavazzoni, D. Ceresoli, G. L. Chiarotti, M. Cococcioni, I. Dabo, A. Dal Corso, *J. Phys. Condens. Matter.* **2009**, *21*(39), 395502.
- [26] J. P. Perdew, K. Burke, M. Ernzerhof, *Phys. Rev. Lett.* **1996**, *77*, 3865.
- [27] P. E. Blöchl, *Phys. Rev. B* **1994**, *50*, 17953.
- [28] G. Kresse, D. Joubert, *Phys. Rev. B* **1999**, *59*, 1758.
- [29] F. A. May, S. Calder, C. Cantoni, H. Cao, M. A. McGuire, *Phys. Rev. B* **2016**, *93*, 014411.
- [30] R. E. Marsh, *J. Solid State Chem.* **1988**, *77*(1), 190.
- [31] M. Opačić, N. Lazarević, M. Šćepanović, H. Ryu, H. Lei, C. Petrovic, Z. V. Popović, *J. Phys. Condens. Matter.*, *48*(27), 485701.
- [32] F. Feng, N. Lazarević, C. Liu, J. Ji, Y. Wang, S. He, H. Lei, C. Petrovic, R. Yu, Z. V. Popović, Q. Zhang, *Phys. Rev. B* **2019**, *99*, 144419.

**How to cite this article:** Milosavljević A, Šolajić A, Višić B, et al. Vacancies and spin-phonon coupling in CrSi<sub>0.8</sub>Ge<sub>0.1</sub>Te<sub>3</sub>. *J Raman Spectrosc.* 2020;51:2153–2160. <https://doi.org/10.1002/jrs.5962>

## APPENDIX: A DECOMPOSITION OF UNRESOLVED MODES

Analysing the spectra of CrSi<sub>0.8</sub>Ge<sub>0.1</sub>Te<sub>3</sub> single crystal, in different polarization configurations (Figure 3), in the energy range around 117 cm<sup>-1</sup>, becomes clear that lower energy part completely disappears in cross polarization configuration, whereas higher energy part persists. Enlarged part of this energy region is shown in Figure A1, in parallel and cross polarization configuration at temperature of 100 K. After simultaneous modelling of these spectra becomes clear that they consist of the A<sub>g</sub><sup>2</sup> and E<sub>g</sub><sup>3</sup> modes, at energies 116.4 and 117.2 cm<sup>-1</sup>, respectively. This is completely supported with theoretical calculations presented in Table 1.

On the other hand, existence of  $P_1$  is not predicted by theoretical calculations, as Raman active peak. Only closer inspection and detailed analysis, presented in

Figure A2, shows that much better agreement with experimental results gives modelling as a superposition of two Voigt lines.



**Evidence of spin-phonon coupling in CrSiTe<sub>3</sub>**A. Milosavljević,<sup>1</sup> A. Šolajić,<sup>1</sup> J. Pešić,<sup>1</sup> Yu Liu (刘育),<sup>2</sup> C. Petrovic,<sup>2</sup> N. Lazarević,<sup>1,\*</sup> and Z. V. Popović<sup>1,3</sup><sup>1</sup>*Center for Solid State Physics and New Materials, Institute of Physics Belgrade, University of Belgrade, Pregrevica 118, 11080 Belgrade, Serbia*<sup>2</sup>*Condensed Matter Physics and Materials Science Department, Brookhaven National Laboratory, Upton, New York 11973-5000, USA*<sup>3</sup>*Serbian Academy of Sciences and Arts, Knez Mihailova 35, 11000 Belgrade, Serbia*

(Received 12 July 2018; published 18 September 2018; corrected 28 March 2019)

We present Raman scattering results on the layered semiconducting ferromagnetic compound CrSiTe<sub>3</sub>. Four Raman-active modes, predicted by symmetry, are observed and assigned. The experimental results are supported by density functional theory calculations. The self-energies of the  $A_g^3$  and the  $E_g^3$  symmetry modes exhibit unconventional temperature evolution around 180 K. In addition, the doubly degenerate  $E_g^3$  mode shows a clear change of asymmetry in the same temperature region. The observed behavior is consistent with the presence of the previously reported short-range magnetic order and strong spin-phonon coupling.

DOI: [10.1103/PhysRevB.98.104306](https://doi.org/10.1103/PhysRevB.98.104306)**I. INTRODUCTION**

Trichalcogenides CrXTe<sub>3</sub> ( $X = \text{Si, Ge}$ ) belong to a rare class of quasi-two-dimensional semiconducting materials with a ferromagnetic order, band gaps of 0.4 eV for Si and 0.7 eV for Ge compounds, and Curie temperatures ( $T_C$ ) of 32 and 61 K, respectively [1–6]. Because of their layered structure, due to van der Waals bonding, they can be exfoliated to mono- and few-layer nanosheets, which, together with their semiconducting and magnetic properties, make an ideal combination for applications in optoelectronics and nanospintronics [7–11]. This was further supported by the observation of giant resistivity modulation of CrGeTe<sub>3</sub>-based devices [12].

From an x-ray diffraction study [1], it was revealed that CrSiTe<sub>3</sub> crystals are twinned along  $c$  axes, the thermal expansion is negative at low temperatures, and the thermal conductivity shows strong magnon-phonon scattering effects. A very small single-ion anisotropy favoring magnetic order along  $c$  axes and spin waves was found in CrSiTe<sub>3</sub> by elastic and inelastic neutron scattering [13]. Spin-wave measurements suggest the absence of three-dimensional correlations above  $T_C$ , whereas in-plane dynamic correlations are present up to 300 K. First-principles calculations suggested the possibility of graphenelike mechanical exfoliation for CrXTe<sub>3</sub> ( $X = \text{Si, Ge}$ ) single crystals with conserved semiconducting and ferromagnetic properties [14]. The exfoliation of CrSiTe<sub>3</sub> bulk to mono- and few-layer two-dimensional crystals onto a Si/SiO<sub>2</sub> substrate has been achieved [15] with a resistivity between 80 and 120 K, depending on the number of layers. Critical exponents for CrSiTe<sub>3</sub> were also determined from theoretical analysis [16].

Spin-phonon coupling in CrGeTe<sub>3</sub> was investigated in Raman scattering experiments [17]. Splitting of the two lowest-energy  $E_g$  modes in the ferromagnetic phase has been observed and ascribed to time-reversal symmetry breaking by

the spin ordering. Furthermore, the significant renormalization of the three higher-energy modes' self-energies below  $T_C$  provided additional evidence of spin-phonon coupling [17]. The external pressure-induced effect on lattice dynamics and magnetization in CrGeTe<sub>3</sub> has also been studied [18].

The Raman spectrum of CrSiTe<sub>3</sub> single crystals was reported in Ref. [1], where three Raman-active modes have been observed. Similar results have also been presented in Ref. [15] for ultrathin nanosheets of CrSiTe<sub>3</sub>. Here, we report a Raman scattering study of CrSiTe<sub>3</sub> single crystals, with the main focus on phonon properties in the temperature range between 100 and 300 K. Our experimental results are qualitatively different from those previously reported [1,15] but consistent with the results obtained for CrGeTe<sub>3</sub> [17,18]. Furthermore, our data reveal the asymmetry of the  $E_g^3$  mode, which is suppressed at higher temperatures. The  $A_g^3$  and  $E_g^3$  symmetry modes exhibit nonanharmonic self-energy temperature dependence in the region around 180 K, related to the strong spin-lattice interaction due to short-range magnetic order [1]. Energies and symmetries of the observed Raman-active modes are in good agreement with theoretical calculations.

**II. EXPERIMENT AND NUMERICAL METHOD**

Single crystals of CrSiTe<sub>3</sub> and CrGeTe<sub>3</sub> were grown as described previously [19]. For a Raman scattering experiment, a Tri Vista 557 spectrometer was used in the backscattering micro-Raman configuration with a 1800/1800/2400 grooves/mm diffraction grating combination. A coherent Verdi G solid-state laser with a 532-nm line was used as the excitation source. The direction of the incident (scattered) light coincides with a crystallographic  $c$  axis. Right before being placed in the vacuum, the samples were cleaved in the air. All measurements were performed in a high vacuum ( $10^{-6}$  mbar) using a KONTI CryoVac continuous-helium-flow cryostat with a 0.5-mm-thick window. Laser-beam focusing was achieved through a microscope objective with  $\times 50$  magnification, a spot size of approximately 8  $\mu\text{m}$ , and a power

\*nenadl@ipb.ac.rs

TABLE I. Calculated and experimental crystallographic lattice parameters for CrSiTe<sub>3</sub> ( $|a| = |b|$ ), bond lengths, interlayer distance ( $d$ ), and van der Waals (vdW) gap.

CrSiTe <sub>3</sub>	Calculation (Å)	Experiment (Å) [20]
$a$	6.87	6.76
$c$	19.81	20.67
Si-Si	2.27	2.27
Si-Te	2.52	2.51
Cr-Te	2.77	2.78
$d$	6.86	6.91
vdW gap	3.42	3.42

<2 mW on the surface of a sample. All spectra were corrected for the Bose factor.

Density functional theory calculations were performed in the Quantum Espresso software package [21], using the PBE exchange-correlation functional [22], PAW pseudopotentials [23,24], and energy cutoffs for wave functions and the charge density of 85 and 425 Ry, respectively. For  $k$ -point sampling, the Monkhorst-Pack scheme was used, with a  $\Gamma$ -centered  $8 \times 8 \times 8$  grid. Optimization of the atomic positions in the unit cell was performed until the interatomic forces were minimized down to  $10^{-6}$  Ry/Å. In order to obtain the parameters accurately, treatment of the van der Waals interactions was included using the Grimme-D2 correction [25]. Phonon frequencies were calculated at the  $\Gamma$  point

TABLE II. (a) Type of atoms, Wyckoff positions, each site's contribution to the phonons at the  $\Gamma$  point, and corresponding Raman tensors for the  $R\bar{3}$  space group of CrSiTe<sub>3</sub>. (b) Phonon symmetry, calculated optical phonon frequencies at 0 K, and experimental values for Raman-active (at 100 K) and infrared (IR)-active (at 110 K) [1] CrSiTe<sub>3</sub> phonons.

(a) Space group $R\bar{3}$ (No. 148)					
Atom(s) (Wyckoff positions)			Irreducible representations		
Cr, Si (6c)			$A_g + E_g + A_u + E_u$		
Te (18f)			$3A_g + 3E_g + 3A_u + 3E_u$		
(b) Raman tensors					
$A_g = \begin{pmatrix} a & 0 & 0 \\ 0 & b & 0 \\ 0 & 0 & c \end{pmatrix}$		$E_g^1 = \begin{pmatrix} c & d & e \\ d & -c & f \\ e & f & 0 \end{pmatrix}$		$E_g^2 = \begin{pmatrix} d & -c & -f \\ -c & -d & e \\ -f & e & 0 \end{pmatrix}$	
Raman active			IR active [1]		
Symmetry	Calc. (cm <sup>-1</sup> )	Expt. (cm <sup>-1</sup> )	Symmetry	Calc. (cm <sup>-1</sup> )	Expt. (cm <sup>-1</sup> )
$A_g^1$	88.2	–	$A_u^1$	91.8	91.0
$E_g^1$	93.5	88.9	$E_u^1$	93.7	–
$E_g^2$	96.9	–	$A_u^2$	116.8	–
$E_g^3$	118.3	118.2	$E_u^2$	117.1	–
$A_g^2$	122.0	–	$A_u^3$	202.4	–
$A_g^3$	148.0	147.4	$E_u^3$	206.2	207.9
$A_g^4$	208.7	–	$A_u^4$	243.7	–
$E_g^4$	219.5	217.2	$E_u^4$	365.8	370.4
$E_g^5$	357.4	–			
$A_g^5$	508.8	–			

within the linear response method implemented in Quantum Espresso. Calculated crystallographic properties obtained by relaxing the structures are in good agreement with x-ray diffraction measurements [20]. A comparison between our, calculated, and experimental results is presented in Table I.

### III. RESULTS AND DISCUSSION

#### A. Polarization dependence

CrSiTe<sub>3</sub> crystallizes in the rhombohedral crystal structure, described by  $R\bar{3}$  ( $C_{3i}^2$ ) [26]. Wyckoff positions of atoms, together with each site's contribution to phonons at the  $\Gamma$  point and corresponding Raman tensors, are listed in Table II. The phonon mode distribution obtained by factor-group analysis for the  $R\bar{3}$  space group is as follows:

$$\Gamma_{\text{Raman}} = 5A_g + 5E_g,$$

$$\Gamma_{\text{IR}} = 4A_u + 4E_u,$$

$$\Gamma_{\text{Acoustic}} = A_u + E_u.$$

Since the plane of incidence is  $ab$ , where  $|a| = |b|$  [ $\angle(a, b) = 120^\circ$ ], and the direction of light propagation is along  $c$  axes, from the selection rules, it is possible to observe all Raman-active modes, i.e., five  $A_g$  modes and five doubly degenerate  $E_g$  modes. According to the Raman tensors presented in Table II,  $A_g$  symmetry modes are observable only in the parallel polarization configuration, whereas  $E_g$  symmetry

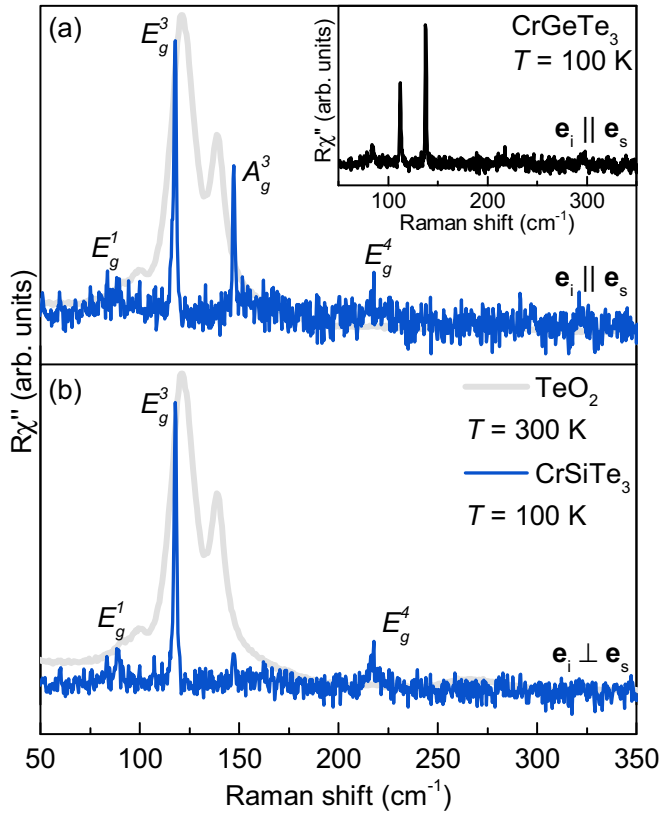


FIG. 1. Raman spectra of CrSiTe<sub>3</sub> single crystals measured at 100 K in (a) parallel and (b) cross polarization configurations. The gray line represents the TeO<sub>2</sub> spectrum measured at 300 K. Inset: Raman spectrum of CrGeTe<sub>3</sub> in the parallel polarization configuration measured at 100 K.

modes can be expected to appear for both in-parallel and cross polarization configurations.

The Raman spectra of CrSiTe<sub>3</sub> for two main linear polarization configurations, at 100 K, are shown in Fig. 1. Four peaks can be observed in the spectra, at energies of 88.9, 118.2, 147.4, and 217.2 cm<sup>-1</sup>. Since only the peak at 147.4 cm<sup>-1</sup> vanishes in the cross polarization configuration, it corresponds to the A<sub>g</sub> symmetry mode. The other three modes appear in both parallel and cross polarization configurations and, thereby, can be assigned as E<sub>g</sub> symmetry modes (Fig. 1).

In order to exclude the possibility that any of the observed features originate from the TeO<sub>2</sub> [17,27], its Raman spectrum is also presented in Fig. 1. It can be noted that no TeO<sub>2</sub> contribution is present in our CrSiTe<sub>3</sub> data. Furthermore, the observed CrSiTe<sub>3</sub> Raman spectra are also consistent with the CrGeTe<sub>3</sub> Raman spectra (see inset in Fig. 1), isostructural to CrSiTe<sub>3</sub>. Five Raman-active modes have been observed for CrGeTe<sub>3</sub>, two A<sub>g</sub> modes, at 137.9 and 296.6 cm<sup>-1</sup>, and three E<sub>g</sub> modes, at 83.5, 112.2, and 217.5 cm<sup>-1</sup>, in agreement with the previously published data [17,18]. The main difference in the spectra of CrSiTe<sub>3</sub> and CrGeTe<sub>3</sub> arises from the change in mass and lattice parameter effects that cause the peaks to shift.

Calculated and observed Raman-active phonon energies are compiled in Table II, together with the experimental energies of the infrared (IR)-active phonons [1], and are found to be in good agreement. Displacement patterns of the A<sub>g</sub>

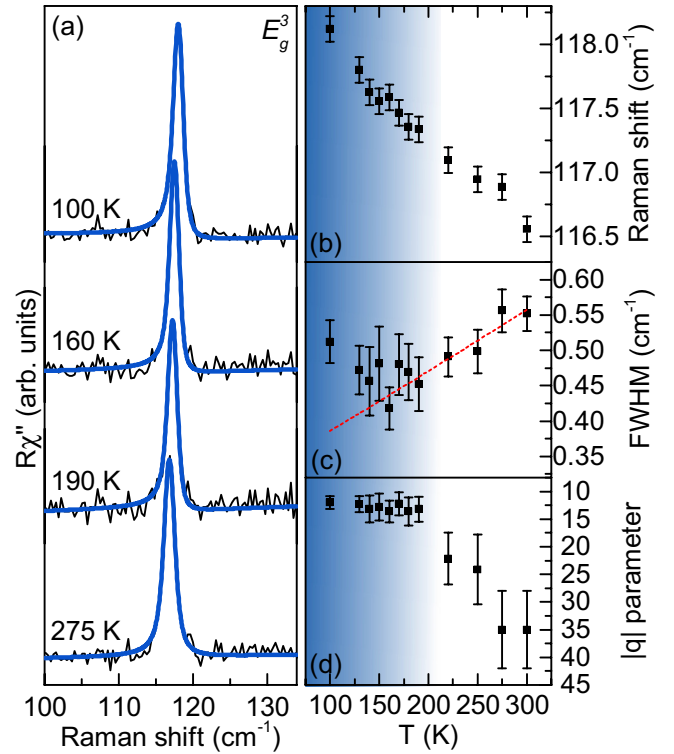


FIG. 2. (a) The E<sub>g</sub><sup>3</sup> mode Raman spectra of CrSiTe<sub>3</sub> at four temperatures measured in the cross polarization configuration. Blue lines represent line shapes obtained as a convolution of the Fano line shape and Gaussian, calculated to fit the experimental data. Temperature dependence of (b) the energy, (c) the line width, and (d) the Fano parameter *q* of the E<sub>g</sub><sup>3</sup> mode. The dashed red line represents standard anharmonic behavior [28,29]. All the parameters show a change in tendency around 180 K.

and E<sub>g</sub> symmetry modes are presented in Fig. 4, in the Appendix.

## B. Temperature dependence

After proper assignment of all the observed CrSiTe<sub>3</sub> Raman-active modes we proceeded with temperature evolution of their properties, focusing on the most prominent ones, E<sub>g</sub><sup>3</sup> and A<sub>g</sub><sup>3</sup>. Figure 2(a) shows the spectral region of the doubly degenerate E<sub>g</sub><sup>3</sup> mode at an energy of 118.2 cm<sup>-1</sup>, at four temperatures. Closer inspection of the 100 K spectra revealed clear asymmetry of the peak on the low-energy side. The presence of defects may result in the appearance of the mode asymmetry [30], however, they would also contribute to the mode line width and, possibly, the appearance of phonons from the edge of the Brillouin zone in the Raman spectra [29]. The very narrow lines and absence of additional features in the Raman spectra of CrSiTe<sub>3</sub> do not support this scenario. The asymmetry may also arise when the phonon is coupled to a continuum [31]. Such a coupling of the E<sub>g</sub><sup>3</sup> phonon mode would result in a line shape given by the convolution of a Fano function and a Gaussian, the latter representing the resolution of the spectrometer [29]. Comparison between the Fano line shape convoluted with a Gaussian, the Voigt line shape, and the experimental data at 100 K is presented in Fig. 5, in the

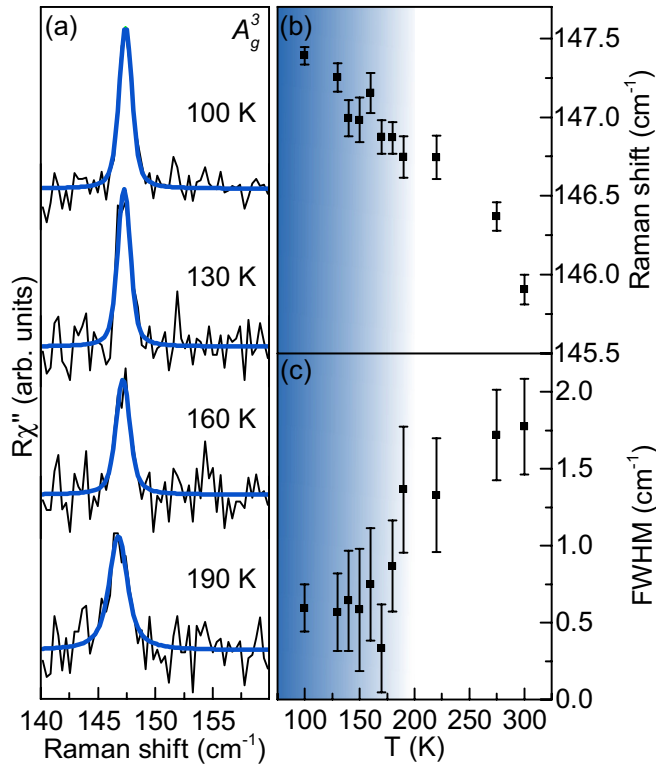


FIG. 3. (a)  $A_g^3$  mode Raman spectra of  $\text{CrSiTe}_3$  at four temperatures measured in the parallel polarization configuration. Blue lines represent Voigt line shapes. (b) Energy and (c) line-width temperature dependence of the  $A_g^3$  mode.

Appendix, with the former yielding better agreement with the experimental data. Furthermore, it fully captures the  $E_g^3$  mode line shape at all temperatures under investigation [Figs. 2(a) and 6].

Upon cooling of the sample, the  $E_g^3$  mode energy hardens [Fig. 2(b)] with a very small discontinuity in the temperature range around 180 K. Down to the same temperature, the line width monotonically narrows in line with the standard anharmonic behavior [dashed red line in Fig. 2(c)]. Upon further cooling, the line width increased, deviating from the expected anharmonic tendency. This indicates activation of an additional scattering mechanism, e.g., spin-phonon interaction. Figure 2(d) shows the evolution of the Fano parameter,  $|q|$ . Whereas in the region below 180 K, it increases slightly but continuously, at higher temperatures it promptly goes to lower values and the mode recovers a symmetric line shape. We believe that the observed behavior of the  $E_g^3$  mode can be traced back to the short-range magnetic correlations, which, according to Ref. [1], persist up to 150 K, and the strong spin-phonon coupling in  $\text{CrSiTe}_3$ . Similar behavior of the energy and line width, which differs from the conventional anharmonic, as well as the  $E_g$  mode Fano-type line shape, was recently reported in  $\alpha\text{-RuCl}_3$  and was interpreted as a consequence of the spin-phonon interaction [32].

Unlike the  $E_g^3$  mode, no pronounced asymmetry was observed for the  $A_g^3$  mode. As can be seen from Figs. 3(b) and 3(c) both the energy and the line width of the  $A_g^3$  mode showed

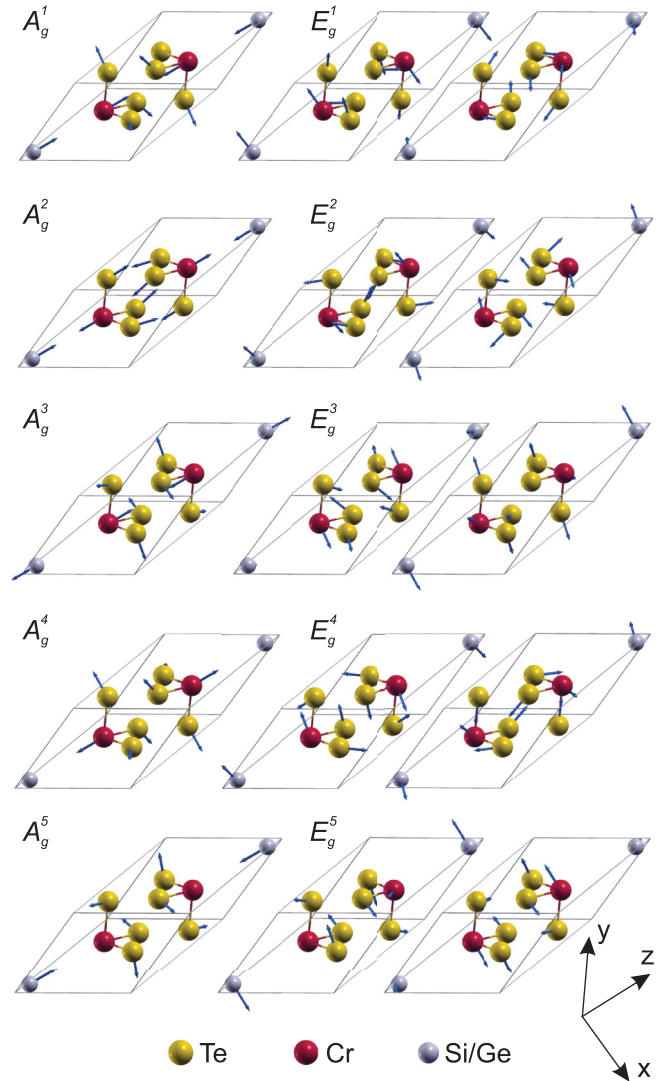


FIG. 4. Unit cell of a  $\text{CrSiTe}_3$  single crystal (solid lines) with the displacement patterns of the  $A_g$  and  $E_g$  symmetry modes. Arrow lengths are proportional to the square root of the interatomic forces.

a similar change in tendency in the same temperature region as the  $E_g^3$  mode, most likely due to the spin-phonon coupling.

#### IV. CONCLUSION

The lattice dynamics of  $\text{CrSiTe}_3$ , a compound isostructural to  $\text{CrGeTe}_3$ , is presented. An  $A_g$  and three  $E_g$  modes were observed and assigned. The experimental results are well supported by theoretical calculations. The temperature dependences of the energies and line widths of the  $A_g^3$  and  $E_g^3$  modes deviate from the conventional anharmonic model in the temperature range around 180 K. In addition, the  $E_g^3$  mode shows clear Fano resonance at lower temperatures. This can be related to the previously reported short-range magnetic correlations at temperatures up to 150 K [1] and the strong spin-phonon coupling.

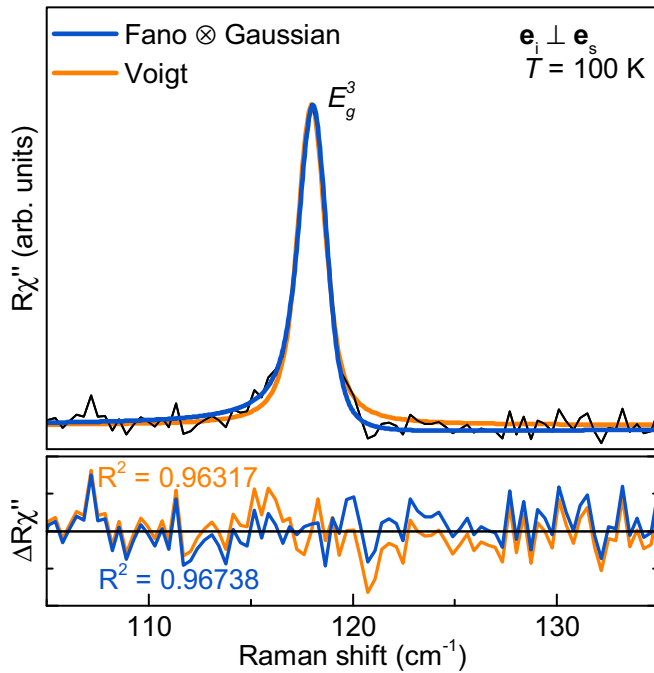


FIG. 5. Analysis of the  $E_g^3$  asymmetry. Measured data are shown as the black line. The solid blue line represents the line shape obtained as a convolution of the Fano line shape and a Gaussian, whereas the orange line represents a Voigt line shape, both calculated to fit the experimental data. The Voigt profile deviates from the experimental data at the peak flanks.

### ACKNOWLEDGMENTS

The work was supported by the Serbian Ministry of Education, Science and Technological Development under Projects III45018 and OI171005. DFT calculations were performed using computational resources at Johannes Kepler University, Linz, Austria. Work at Brookhaven was supported by the US Department of Energy, Office of Basic Energy Sciences as part of the Computation Material Science Program (material synthesis and characterization).

A.M. and N.L. conceived and performed the experiment, analyzed and discussed data, and wrote the paper; A.S. and J.P. calculated phonon energies, analyzed and discussed data, and wrote the paper; Y.L. and C.P. synthesized and characterized the samples; Z.V.P. analyzed and discussed data and wrote the paper. All authors commented on the manuscript.

### APPENDIX

#### 1. Eigenvectors of Raman-active modes

Figure 4 summarizes the  $A_g$  and  $E_g$  symmetry mode displacement patterns of a CrSiTe<sub>3</sub> single crystal ( $R\bar{3}$  space group). Arrow lengths are proportional to the square root of the interatomic forces.

#### 2. Asymmetry of the $E_g^3$ line

The peak at  $118.2 \text{ cm}^{-1}$ , which we assigned as the  $E_g^3$  symmetry mode, at low temperatures shows a significant asymmetry towards lower energies. The possibility of additional

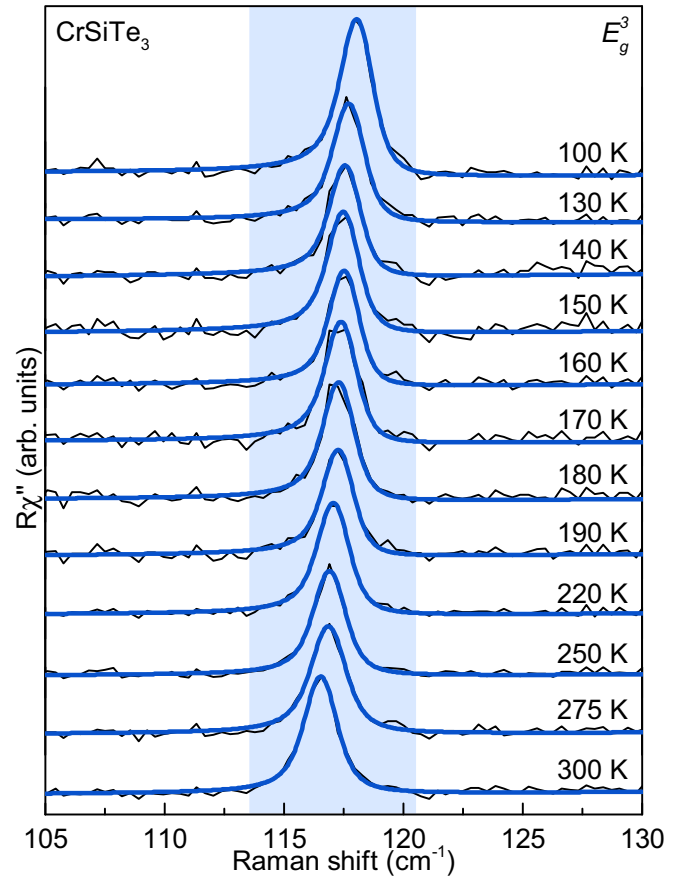


FIG. 6. The  $E_g^3$  mode Raman spectra of CrSiTe<sub>3</sub> at all temperatures measured in the cross polarization configuration. Blue lines represent calculated spectra obtained as the convolution of the Fano line shape and Gaussian.

defect-induced features in Raman spectra can be excluded, since the modes are very narrow, suggesting high crystallinity of the sample. Also, the theoretical calculations do not predict additional Raman-active modes in this energy region. On the other hand, coupling of the phonon mode to a continuum may result in an asymmetric line shape described with the Fano function. Due to the finite resolution of the spectrometer it has to be convoluted with a Gaussian ( $\Gamma_G = 1 \text{ cm}^{-1}$ ). In Fig. 5 we present a comparison of the line obtained as a convolution of the Fano line shape and a Gaussian (blue line) and a Voigt line shape (orange line) fitted to the experimental data. Whereas the Voigt line shape deviates at the peak flanks, excellent agreement has been achieved for convolution of the Fano line shape and a Gaussian.

#### 3. $E_g^3$ mode temperature dependence

Figure 6 shows Raman spectra of CrSiTe<sub>3</sub> in the region of the  $E_g^3$  mode in the cross polarization configuration at various temperatures. Solid blue lines represent the convolution of the Fano line shape and Gaussian fitted to the experimental data. The asymmetry is the most pronounced below 190 K. Above this temperature, the asymmetry is decreasing, and at high temperatures the peak recovers the fully symmetric line shape.

- [1] L. D. Casto, A. J. Clune, M. O. Yokosuk, J. L. Musfeldt, T. J. Williams, H. L. Zhuang, M.-W. Lin, K. Xiao, R. G. Hennig, B. C. Sales, J.-Q. Yan, and D. Mandrus, Strong spin-lattice coupling in CrSiTe<sub>3</sub>, *APL Mater.* **3**, 041515 (2015).
- [2] X. Zhang, Y. Zhao, Q. Song, S. Jia, J. Shi, and W. Han, Magnetic anisotropy of the single-crystalline ferromagnetic insulator Cr<sub>2</sub>Ge<sub>2</sub>Te<sub>6</sub>, *Jpn. J. Appl. Phys.* **55**, 033001 (2016).
- [3] T. Leineweber and H. Kronmüller, Micromagnetic examination of exchange coupled ferromagnetic nanolayers, *J. Magn. Magn. Mater.* **176**, 145 (1997).
- [4] G. Ouvrard, E. Sandre, and R. Brec, Synthesis and crystal structure of a new layered phase: The chromium hexatellurosilicate Cr<sub>2</sub>Si<sub>2</sub>Te<sub>6</sub>, *J. Solid State Chem.* **73**, 27 (1988).
- [5] B. Siberchicot, S. Jobic, V. Carreaux, P. Gressier, and G. Ouvrard, Band structure calculations of ferromagnetic chromium tellurides CrSiTe<sub>3</sub> and CrGeTe<sub>3</sub>, *J. Phys. Chem.* **100**, 5863 (1996).
- [6] V. Carreaux, F. Moussa, and M. Spiesser, 2D Ising-like ferromagnetic behaviour for the lamellar Cr<sub>2</sub>Si<sub>2</sub>Te<sub>6</sub> compound: A neutron scattering investigation, *Europhys. Lett.* **29**, 251 (1995).
- [7] N. Sivasdas, M. W. Daniels, R. H. Swendsen, S. Okamoto, and D. Xiao, Magnetic ground state of semiconducting transition-metal trichalcogenide monolayers, *Phys. Rev. B* **91**, 235425 (2015).
- [8] K. S. Novoselov, A. K. Geim, S. V. Morozov, D. Jiang, Y. Zhang, S. V. Dubonos, I. V. Grigorieva, and A. A. Firsov, Electric field effect in atomically thin carbon films, *Science* **306**, 666 (2004).
- [9] Q. H. Wang, K. Kalantar-Zadeh, A. Kis, J. N. Coleman, and M. S. Strano, Electronics and optoelectronics of two-dimensional transition metal dichalcogenides, *Nat. Nanotechnol.* **7**, 699 (2012), review Article.
- [10] C. Gong, L. Li, Z. Li, H. Ji, A. Stern, Y. Xia, T. Cao, W. Bao, C. Wang, Y. Wang, Z. Q. Qiu, R. J. Cava, S. G. Louie, J. Xia, and X. Zhang, Discovery of intrinsic ferromagnetism in two-dimensional van der Waals crystals, *Nature* **546**, 265 (2017).
- [11] B. Huang, G. Clark, E. Navarro-Moratalla, D. R. Klein, R. Cheng, K. L. Seyler, D. Zhong, E. Schmidgall, M. A. McGuire, D. H. Cobden, W. Yao, D. Xiao, P. Jarillo-Herrero, and X. Xu, Layer-dependent ferromagnetism in a van der Waals crystal down to the monolayer limit, *Nature* **546**, 270 (2017).
- [12] W. Xing, Y. Chen, P. M. Odenthal, X. Zhang, W. Yuan, T. Su, Q. Song, T. Wang, J. Zhong, S. Jia, X. C. Xie, Y. Li, and W. Han, Electric field effect in multilayer Cr<sub>2</sub>Ge<sub>2</sub>Te<sub>6</sub>: A ferromagnetic 2D material, *2D Mater.* **4**, 024009 (2017).
- [13] T. J. Williams, A. A. Aczel, M. D. Lumsden, S. E. Nagler, M. B. Stone, J.-Q. Yan, and D. Mandrus, Magnetic correlations in the quasi-two-dimensional semiconducting ferromagnet CrSiTe<sub>3</sub>, *Phys. Rev. B* **92**, 144404 (2015).
- [14] X. Li and J. Yang, CrXTe<sub>3</sub> (X = Si, Ge) nanosheets: Two dimensional intrinsic ferromagnetic semiconductors, *J. Mater. Chem. C* **2**, 7071 (2014).
- [15] M.-W. Lin, H. L. Zhuang, J. Yan, T. Z. Ward, A. A. Puretzy, C. M. Rouleau, Z. Gai, L. Liang, V. Meunier, B. G. Sumpter, P. Ganesh, P. R. C. Kent, D. B. Geohegan, D. G. Mandrus, and K. Xiao, Ultrathin nanosheets of CrSiTe<sub>3</sub>: A semiconducting two-dimensional ferromagnetic material, *J. Mater. Chem. C* **4**, 315 (2016).
- [16] B. Liu, Y. Zou, S. Zhou, L. Zhang, Z. Wang, H. Li, Z. Qu, and Y. Zhang, Critical behavior of the van der Waals bonded high T<sub>C</sub> ferromagnet Fe<sub>3</sub>GeTe<sub>2</sub>, *Sci. Rep.* **7**, 6184 (2017).
- [17] Y. Tian, M. J. Gray, H. Ji, R. J. Cava, and K. S. Burch, Magnetoelastic coupling in a potential ferromagnetic 2D atomic crystal, *2D Mater.* **3**, 025035 (2016).
- [18] Y. Sun, R. C. Xiao, G. T. Lin, R. R. Zhang, L. S. Ling, Z. W. Ma, X. Luo, W. J. Lu, Y. P. Sun, and Z. G. Sheng, Effects of hydrostatic pressure on spin-lattice coupling in two-dimensional ferromagnetic Cr<sub>2</sub>Ge<sub>2</sub>Te<sub>6</sub>, *Appl. Phys. Lett.* **112**, 072409 (2018).
- [19] Y. Liu and C. Petrovic, Critical behavior of quasi-two-dimensional semiconducting ferromagnet Cr<sub>2</sub>Ge<sub>2</sub>Te<sub>6</sub>, *Phys. Rev. B* **96**, 054406 (2017).
- [20] G. T. Lin, H. L. Zhuang, X. Luo, B. J. Liu, F. C. Chen, J. Yan, Y. Sun, J. Zhou, W. J. Lu, P. Tong, Z. G. Sheng, Z. Qu, W. H. Song, X. B. Zhu, and Y. P. Sun, Tricritical behavior of the two-dimensional intrinsically ferromagnetic semiconductor CrGeTe<sub>3</sub>, *Phys. Rev. B* **95**, 245212 (2017).
- [21] P. Giannozzi, S. Baroni, N. Bonini, M. Calandra, R. Car, C. Cavazzoni, D. Ceresoli, G. L. Chiarotti, M. Cococcioni, I. Dabo, A. D. Corso, S. de Gironcoli, S. Fabris, G. Fratesi, R. Gebauer, U. Gerstmann, C. Gougoussis, A. Kokalj, M. Lazzeri, L. Martin-Samos, N. Marzari, F. Mauri, R. Mazzarello, S. Paolini, A. Pasquarello, L. Paulatto, C. Sbraccia, S. Scandolo, G. Sclauzero, A. P. Seitsonen, A. Smogunov, P. Umari, and R. M. Wentzcovitch, Quantum espresso: A modular and open-source software project for quantum simulations of materials, *J. Phys.: Condens. Matter* **21**, 395502 (2009).
- [22] J. P. Perdew, K. Burke, and M. Ernzerhof, Generalized Gradient Approximation Made Simple, *Phys. Rev. Lett.* **77**, 3865 (1996).
- [23] P. E. Blöchl, Projector augmented-wave method, *Phys. Rev. B* **50**, 17953 (1994).
- [24] G. Kresse and D. Joubert, From ultrasoft pseudopotentials to the projector augmented-wave method, *Phys. Rev. B* **59**, 1758 (1999).
- [25] G. Stefan, Semiempirical GGA-type density functional constructed with a long-range dispersion correction, *J. Comput. Chem.* **27**, 1787 (2006).
- [26] R. E. Marsh, The crystal structure of Cr<sub>2</sub>Si<sub>2</sub>Te<sub>6</sub>: Corrigendum, *J. Solid State Chem.* **77**, 190 (1988).
- [27] N. Lazarević, E. S. Bozin, M. Šćepanović, M. Opačić, Hechang Lei, C. Petrovic, and Z. V. Popović, Probing IrTe<sub>2</sub> crystal symmetry by polarized Raman scattering, *Phys. Rev. B* **89**, 224301 (2014).
- [28] M. Opačić, N. Lazarević, M. Šćepanović, H. Ryu, H. Lei, C. Petrovic, and Z. V. Popović, Evidence of superconductivity-induced phonon spectra renormalization in alkali-doped iron selenides, *J. Phys.: Condens. Matter* **27**, 485701 (2015).
- [29] A. Baum, A. Milosavljević, N. Lazarević, M. M. Radonjić, B. Nikolić, M. Mitschek, Z. Inanloo Maranloo, M. Šćepanović, M. Grujić-Brojčin, N. Stojilović, M. Opel, Aifeng Wang, C. Petrovic, Z. V. Popović, and R. Hackl, Phonon anomalies in FeS, *Phys. Rev. B* **97**, 054306 (2018).

- [30] N. Lazarević, M. Radonjić, M. Šćepanović, Hechang Lei, D. Tanasković, C. Petrovic, and Z. V. Popović, Lattice dynamics of KNi<sub>2</sub>Se<sub>2</sub>, *Phys. Rev. B* **87**, 144305 (2013).
- [31] N. Lazarević, Z. V. Popović, Rongwei Hu, and C. Petrovic, Evidence for electron-phonon interaction in Fe<sub>1-x</sub>M<sub>x</sub>Sb<sub>2</sub> ( $M = \text{Co}$  and  $\text{Cr}$ ;  $0 \leq x \leq 0.5$ ) single crystals, *Phys. Rev. B* **81**, 144302 (2010).
- [32] L. J. Sandilands, Y. Tian, K. W. Plumb, Y.-J. Kim, and K. S. Burch, Scattering Continuum and Possible Fractionalized Excitations in  $\alpha$ -RuCl<sub>3</sub>, *Phys. Rev. Lett.* **114**, 147201 (2015).

*Correction:* Missing support information in the Acknowledgment section has been inserted.

## Lattice dynamics and phase transition in CrI<sub>3</sub> single crystals

S. Djurdjic-Mijin,<sup>1</sup> A. Šolajić,<sup>1</sup> J. Pešić,<sup>1</sup> M. Šćepanović,<sup>1</sup> Y. Liu (刘育),<sup>2</sup> A. Baum,<sup>3,4</sup> C. Petrovic,<sup>2</sup>  
N. Lazarević,<sup>1</sup> and Z. V. Popović<sup>1,5</sup>

<sup>1</sup>Center for Solid State Physics and New Materials, Institute of Physics Belgrade, University of Belgrade,  
Pregrevica 118, 11080 Belgrade, Serbia

<sup>2</sup>Condensed Matter Physics and Materials Science Department, Brookhaven National Laboratory, Upton, New York 11973-5000, USA

<sup>3</sup>Walther Meissner Institut, Bayerische Akademie der Wissenschaften, 85748 Garching, Germany

<sup>4</sup>Fakultät für Physik E23, Technische Universität München, 85748 Garching, Germany

<sup>5</sup>Serbian Academy of Sciences and Arts, Knez Mihailova 35, 11000 Belgrade, Serbia



(Received 9 July 2018; published 18 September 2018; corrected 28 March 2019)

The vibrational properties of CrI<sub>3</sub> single crystals were investigated using Raman spectroscopy and were analyzed with respect to the changes of the crystal structure. All but one mode are observed for both the low-temperature  $R\bar{3}$  and the high-temperature  $C2/m$  phase. For all observed modes the energies and symmetries are in good agreement with DFT calculations. The symmetry of a single layer was identified as  $p\bar{3}1/m$ . In contrast to previous studies we observe the transition from the  $R\bar{3}$  to the  $C2/m$  phase at 180 K and find no evidence for coexistence of both phases over a wide temperature range.

DOI: [10.1103/PhysRevB.98.104307](https://doi.org/10.1103/PhysRevB.98.104307)

### I. INTRODUCTION

Two-dimensional layered materials have gained attention due to their unique properties, the potential for a wide spectrum of applications, and the opportunity for the development of functional van der Waals heterostructures. CrI<sub>3</sub> is a member of the chromium-trihalide family which are ferromagnetic semiconductors [1]. Recently they have received significant attention as candidates for the study of magnetic monolayers. The experimental realization of CrI<sub>3</sub> ferromagnetic monolayers [1] motivated further efforts towards their understanding. CrI<sub>3</sub> features electric field controlled magnetism [2] as well as a strong magnetic anisotropy [3,4]. With the main absorption peaks lying in the visible part of the spectrum, it is a great candidate for low-dimensional semiconductor spintronics [5]. In its ground state, CrI<sub>3</sub> is a ferromagnetic semiconductor with a Curie temperature of 61 K [1,6] and a band gap of 1.2 eV [6]. It was demonstrated that the magnetic properties of CrI<sub>3</sub> mono- and bilayers can be controlled by electrostatic doping [2]. Upon cooling, CrI<sub>3</sub> undergoes a phase transition around 220 K from the high-temperature monoclinic ( $C2/m$ ) to the low-temperature rhombohedral ( $R\bar{3}$ ) phase [3,7]. Although the structural phase transition is reported to be first order, it was suggested that the phases may coexist over a wide temperature range [3]. Raman spectroscopy can be of use here due to its capability to simultaneously probe both phases in a phase-separated system [8–10].

A recent theoretical study predicted the energies of all Raman active modes in the low-temperature and high-temperature structure of CrI<sub>3</sub> suggesting a near degeneracy between the  $A_g$  and  $B_g$  modes in the monoclinic ( $C2/m$ ) structure. Their energies match the energies of  $E_g$  modes in the rhombohedral ( $R\bar{3}$ ) structure [7].

In this article we present an experimental and theoretical Raman scattering study of CrI<sub>3</sub> lattice dynamics. In both phases all but one of the respective modes predicted by

symmetry were observed. The energies for all modes are in good agreement with the theoretical predictions for the assumed crystal symmetry. Our data suggest that the first-order transition occurs at  $T_s \approx 180$  K without evidence for phase coexistence over a wide temperature range.

### II. EXPERIMENT AND NUMERICAL METHOD

The preparation of the single crystal CrI<sub>3</sub> sample used in this study is described elsewhere [11]. The Raman scattering experiment was performed using a Tri Vista 557 spectrometer in backscattering micro-Raman configuration with a 1800/1800/2400 grooves/mm diffraction grating combination. The 532 nm line of a Coherent Verdi G solid state laser was used for excitation. The direction of the incident light coincides with the crystallographic  $c$  axis. The sample was oriented so that its principal axis of the  $R\bar{3}$  phase coincides with the  $x$  axis of the laboratory system. A KONTI CryoVac continuous helium flow cryostat with a 0.5-mm-thick window was used for measurements at all temperatures under high vacuum ( $10^{-6}$  mbar). The sample was cleaved in air before being placed into the cryostat. The obtained Raman spectra were corrected by the Bose factor and analyzed quantitatively by fitting Voigt profiles to the data whereby the Gaussian width  $\Gamma_{\text{Gauss}} = 1 \text{ cm}^{-1}$  reflects the resolution of the spectrometer.

The spin polarized density functional theory (DFT) calculations have been performed in the Quantum Espresso (QE) software package [12] using the Perdew-Burke-Ernzerhof (PBE) exchange-correlation functional [13] and PAW pseudopotentials [14,15]. The energy cutoffs for the wave functions and the charge density were set to be 85 and 425 Ry, respectively, after convergence tests. For  $k$ -point sampling, the Monkhorst-Pack scheme was used with a  $8 \times 8 \times 8$  grid centered around the  $\Gamma$  point. Optimization of the atomic positions in the unit cell was performed until the interatomic forces



were smaller than  $10^{-6}$  Ry/Å. To treat the van der Waals (vdW) interactions a Grimme-D2 correction [16] is used in order to include long-ranged forces between the layers, which are not properly captured within LDA or GGA functionals. This way, the parameters are obtained more accurately, especially the interlayer distances. Phonon frequencies were calculated at the  $\Gamma$  point using the linear response method implemented in QE. The phonon energies are compiled in Table III together with the experimental values. The eigenvectors of the Raman active modes for both the low- and high-temperature phase are depicted in Fig. 5 of the Appendix.

### III. RESULTS AND DISCUSSION

CrI<sub>3</sub> adopts a rhombohedral  $R\bar{3}$  ( $C_{3i}^2$ ) crystal structure at low temperatures and a monoclinic  $C2/m$  ( $C_{2h}^3$ ) crystal structure at room temperature [3], as shown in Fig. 1. The main difference between the high- and low-temperature crystallographic space groups arises from different stacking sequences with the CrI<sub>3</sub> layers being almost identical. In the rhombohedral structure the Cr atoms in one layer are placed above the center of a hole in the Cr honeycomb net of the two adjacent layers. When crossing the structural phase transition at  $T_s$  to the monoclinic structure the layers are displaced along the  $a$  direction so that every fourth layer is at the same place as the first one. The interatomic distances, mainly the interlayer distance, and the vdW gap, are slightly changed by the structural transition. The crystallographic parameters for both phases are presented in Table I. The numerically obtained values are in good agreement with reported x-ray diffraction data [11].

The vibrational properties of layered materials are typically dominated by the properties of the single layers composing the crystal. The symmetry of a single layer can be described by one of the 80 diproperiodic space groups (DG) obtained by

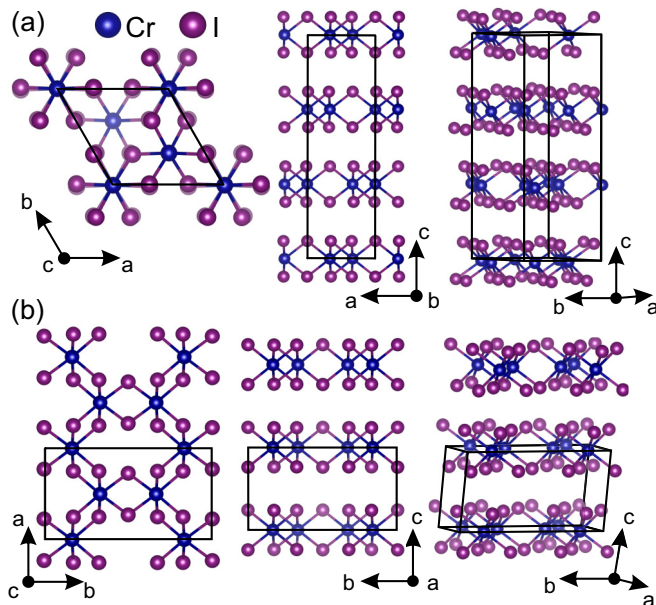


FIG. 1. Schematic representation of (a) the low-temperature  $R\bar{3}$  and (b) the high-temperature  $C2/m$  crystal structure of CrI<sub>3</sub>. Black lines represent unit cells.

TABLE I. Calculated and experimental [11] parameters of the crystallographic unit cell for the low-temperature  $R\bar{3}$  and high-temperature  $C2/m$  phase of CrI<sub>3</sub>.

$T$ (K)	Space group $R\bar{3}$		Space group $C2/m$	
	Calc.	Expt. [11]	Calc.	Expt. [11]
$a$ (Å)	6.87	6.85	6.866	6.6866
$b$ (Å)	6.87	6.85	11.886	11.856
$c$ (Å)	19.81	19.85	6.984	6.966
$\alpha$ (deg)	90	90	90	90
$\beta$ (deg)	90	90	108.51	108.68
$\gamma$ (deg)	120	120	90	90

lifting translational invariance in the direction perpendicular to the layer [17]. In the case of CrI<sub>3</sub>, the symmetry analysis revealed that the single layer structure is fully captured by the  $p\bar{3}1/m$  ( $D_{3d}^1$ ) diproperiodic space group DG71, rather than by  $R\bar{3}2/m$  as proposed in Ref. [7].

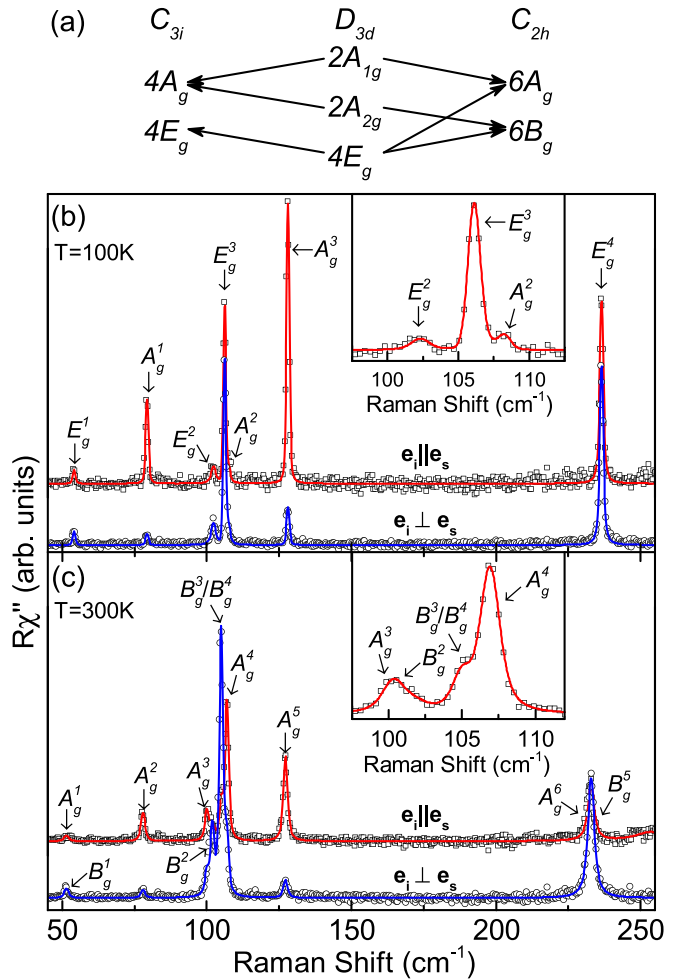


FIG. 2. (a) Compatibility relations for the CrI<sub>3</sub> layer and the crystal symmetries. Raman spectra of (b) the low-temperature  $R\bar{3}$  and (c) the high-temperature  $C2/m$  crystal structure measured in parallel (open squares) and crossed (open circles) polarization configurations at 100 and 300 K, respectively. Red and blue solid lines represent fits of Voigt profiles to the experimental data.

TABLE II. Wyckoff positions of the two types of atoms and their contributions to the  $\Gamma$ -point phonons for the  $R\bar{3}$  and  $C2/m$  as well as the  $p\bar{3}1/m$  diperiodic space group. The second row shows the Raman tensors for the corresponding space groups.

Space group $R\bar{3}$		Diperiodic space group $p\bar{3}1/m$		Space group: $C2/m$	
Atoms	Irreducible representations	Atoms	Irreducible representations	Atoms	Irreducible representations
Cr (6c)	$A_g + A_u + E_g + E_u$	Cr (2c)	$A_{2g} + A_{2u} + E_g + E_u$	Cr (4g)	$A_g + A_u + 2B_g + 2B_u$
I (18f)	$3A_g + 3A_u + 3E_g + 3E_u$	I (6k)	$2A_{1g} + A_{1u} + A_{2g} + 2A_{2u} + 3E_g + 3E_u$	I (4i)	$2A_g + 2A_u + B_g + B_u$
	$A_g = \begin{pmatrix} a & & \\ & a & \\ & & b \end{pmatrix}$		$A_{1g} = \begin{pmatrix} a & & \\ & a & \\ & & b \end{pmatrix}$		$A_g = \begin{pmatrix} a & d \\ & c \\ d & b \end{pmatrix}$
	${}^1E_g = \begin{pmatrix} c & d & e \\ d & -c & f \\ e & f & \end{pmatrix}$		${}^1E_g = \begin{pmatrix} c & & \\ -c & d & \\ d & & \end{pmatrix}$		$B_g = \begin{pmatrix} e & \\ & f \\ e & f \end{pmatrix}$
	${}^2E_g = \begin{pmatrix} d & -c & -f \\ -c & -d & e \\ -f & e & \end{pmatrix}$		${}^2E_g = \begin{pmatrix} & -c & -d \\ -c & & \\ -d & e & \end{pmatrix}$		

According to the factor group analysis (FGA) for a single  $\text{CrI}_3$  layer, six modes ( $2A_{1g} + 4E_g$ ) are expected to be observed in the Raman scattering experiment (see Table II). By stacking the layers the symmetry is reduced and, depending on the stacking sequence, FGA yields a total of eight Raman active modes ( $4A_g + 4E_g$ ) for the  $R\bar{3}$  and 12 Raman active modes ( $6A_g + 6B_g$ ) for the  $C2/m$  crystal symmetry. The correlation between layer and crystal symmetries for both cases is shown in Fig. 2(a) [18,19].

Figure 2(b) shows the  $\text{CrI}_3$  single crystal Raman spectra measured at 100 K in two scattering channels. According to the selection rules for the rhombohedral crystal structure (Table II) the  $A_g$  modes can be observed only in the parallel polarization configuration, whereas the  $E_g$  modes appear in both parallel and crossed polarization configurations. Based on the selection rules the peaks at about 78, 108, and 128  $\text{cm}^{-1}$  were identified as  $A_g$  symmetry modes, whereas the peaks at about 54, 102, 106, and 235  $\text{cm}^{-1}$  are assigned as  $E_g$  symmetry. The weak observation of the most pronounced  $A_g$  modes in crossed polarizations [Fig. 2(b)] is attributed to

the leakage due to a slight sample misalignment and/or the presence of defects in the crystal. The energies of all observed modes are compiled in Table III together with the energies predicted by our calculations and by Ref. [7], and are found to be in good agreement for the  $E_g$  modes. The discrepancy is slightly larger for the low energy  $A_g$  modes. Our calculations in general agree with those from Ref. [7]. The  $A_g^4$  mode of the rhombohedral phase, predicted by calculation to appear at about 195  $\text{cm}^{-1}$ , was not observed in the experiment, most likely due to its low intensity.

When the symmetry is lowered in the high-temperature monoclinic  $C2/m$  phase [Fig. 2(c)] the  $E_g$  modes split into an  $A_g$  and a  $B_g$  mode each, whereas the rhombohedral  $A_g^2$  and  $A_g^4$  modes are predicted to switch to the monoclinic  $B_g$  symmetry. The correspondence of the phonon modes across the phase transition is indicated by the arrows in Table III. The selection rules for  $C2/m$  (see Table II) predict that  $A_g$  and  $B_g$  modes can be observed in both parallel and crossed polarization configurations. Additionally, the sample forms three types of domains which are rotated with respect to each other. We

TABLE III. Phonon symmetries and phonon energies for the low-temperature  $R\bar{3}$  and high-temperature  $C2/m$  phase of  $\text{CrI}_3$ . The experimental values were determined at 100 and 300 K, respectively. All calculations were performed at zero temperature. Arrows indicate the correspondence of the phonon modes across the phase transition.

Space group $R\bar{3}$				Space group $C2/m$			
Symm.	Expt. ( $\text{cm}^{-1}$ )	Calc. ( $\text{cm}^{-1}$ )	Calc. ( $\text{cm}^{-1}$ ) [7]	Symm.	Expt. ( $\text{cm}^{-1}$ )	Calc. ( $\text{cm}^{-1}$ )	Calc. [7] ( $\text{cm}^{-1}$ )
$E_g^1$	54.1	59.7	53	$B_g^1$	52.0	57.0	52
				$A_g^1$	53.6	59.8	51
$A_g^1$	73.33	89.6	79	$A_g^2$	78.6	88.4	79
$E_g^2$	102.3	99.8	98	$A_g^3$	101.8	101.9	99
				$B_g^2$	102.4	101.8	99
$E_g^3$	106.2	112.2	102	$B_g^3$	106.4 <sup>a</sup>	108.9	101
				$A_g^4$	108.3	109.3	102
$A_g^2$	108.3	98.8	88	$B_g^4$	106.4 <sup>a</sup>	97.8	86
$A_g^3$	128.1	131.1	125	$A_g^5$	128.2	131.7	125
$A_g^4$	–	195.2	195	$B_g^5$	–	198.8	195
$E_g^4$	236.6	234.4	225	$A_g^6$	234.6	220.1	224
				$B_g^6$	235.5	221.1	225

<sup>a</sup>Observed as two peak structure.

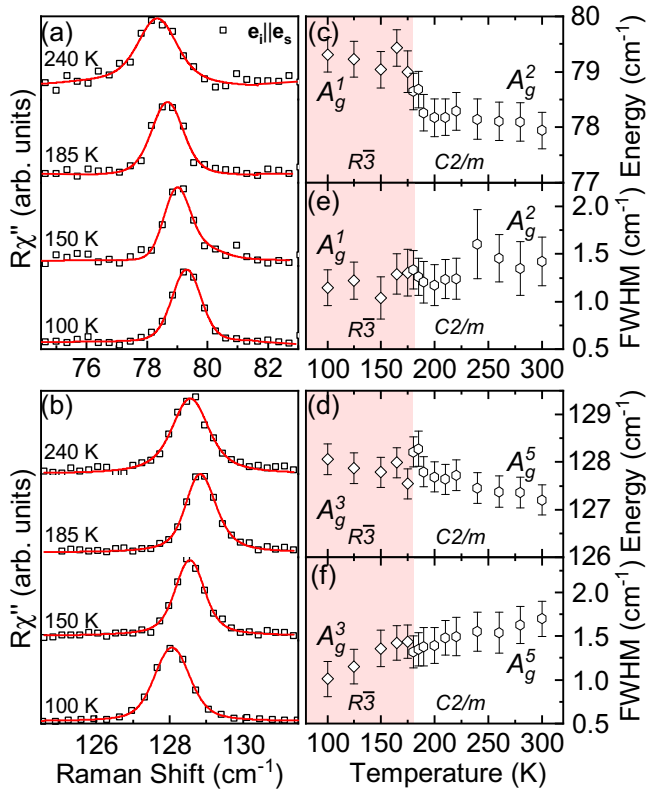


FIG. 3. Temperature dependence of the  $A_g^1$  and  $A_g^3$  phonon modes of the rhombohedral structure and the corresponding  $A_g^2$  and  $A_g^5$  modes of the monoclinic structure, respectively. (a) and (b) Raman spectra at temperatures as indicated. The spectra are shifted for clarity. Solid red lines represent Voigt profiles fitted to the data. (c) and (d) Temperature dependence of the phonon energies and linewidths, respectively. Both modes show an abrupt change in energy at the phase transition at 180 K.

therefore identify the phonons in the  $C2/m$  phase in relation to the calculations and find again good agreement of the energies. The  $B_g^3$  and  $B_g^4$  modes overlap and therefore cannot be resolved separately. As can be seen from the temperature dependence shown below [Fig. 4(b)] the peak at  $106\text{ cm}^{-1}$  broadens and gains spectral weight in the monoclinic phase in line with the expectation that two modes overlap. The missing rhombohedral  $A_g^4$  mode corresponds to the monoclinic  $B_g^5$  mode, which is likewise absent in the spectra.

The temperature dependence of the observed phonons is shown in Figs. 3 and 4. In the low-temperature rhombohedral phase all four  $E_g$  modes as well as  $A_g^1$  and  $A_g^2$  soften upon warming, whereas  $A_g^3$  hardens up to  $T \approx 180\text{ K}$  before softening again. Crossing the first-order phase transition from  $R\bar{3}$  to  $C2/m$  crystal symmetry is reflected in the spectra as a symmetry change and/or renormalization for the non-degenerate modes and lifting of the degeneracy of the  $E_g$  modes as shown in Table II. In our samples, this transition is observed at  $T_s \approx 180\text{ K}$ . The splitting of the  $E_g$  phonons into  $A_g$  and  $B_g$  modes at the phase transition is sharp (Fig. 4). The rhombohedral  $A_g^1$  and  $A_g^3$  phonons show a jump in energy and a small discontinuity in the linewidth at  $T_s$  (Fig. 3). Our spectra were taken during warming in multiple runs after

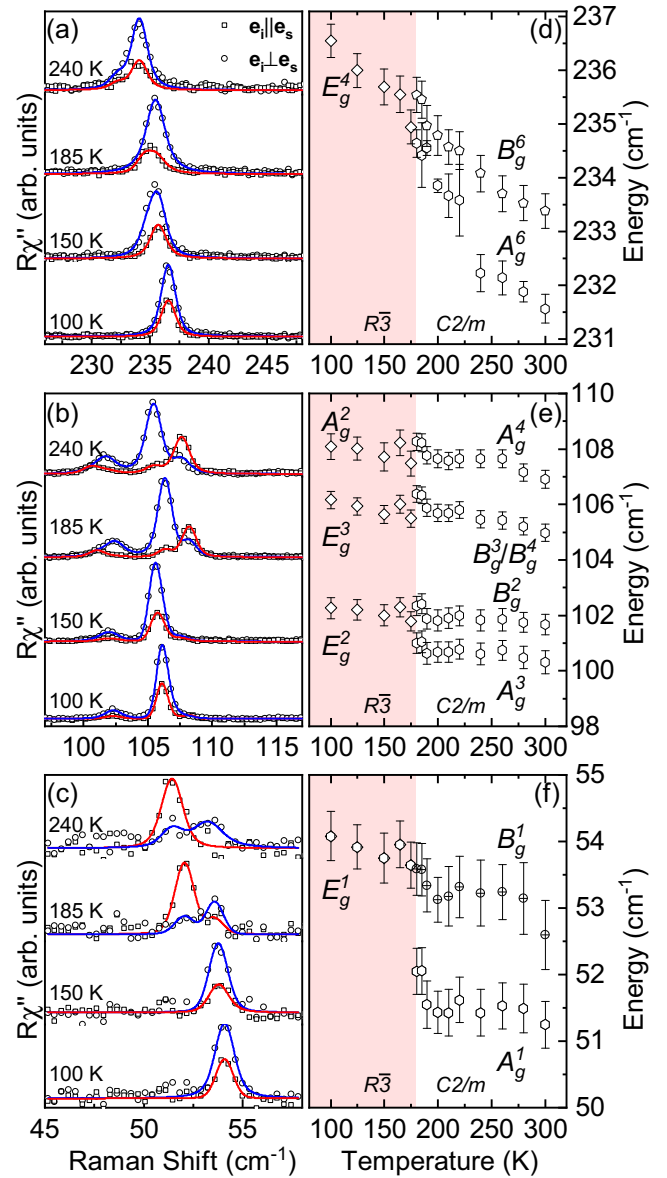


FIG. 4. Temperature dependence of the rhombohedral  $A_g^4$  and  $E_g$  modes. (a)–(c) Raman spectra in parallel (open squares) and crossed (open circles) light polarizations at temperatures as indicated. The spectra are shifted for clarity. Blue and red solid lines are fits of Voigt profiles to the data. Two spectra were analyzed simultaneously in two scattering channels with the integrated intensity as the only independent parameter. (d)–(f) Phonon energies obtained from the Voigt profiles. Each  $E_g$  mode splits into an  $A_g$  and a  $B_g$  mode above 180 K.

cooling to 100 K each time. We found that the temperature dependence for the phonon modes obtained this way was smooth in each phase. McGuire *et al.* [3,20] reported  $T_s$  in the range of 220 K, a coexistence of both phases and a large thermal hysteresis. However, they also noted that the first and second warming cycle showed identical behavior and only found a shift of the transition temperature to higher values for cooling cycles. We therefore consider the difference between the reported transition around 220 K and our  $T_s \approx 180\text{ K}$  significant. To some extent this difference may be attributed

to local heating by the laser. More importantly, we find no signs of phase coexistence in the observed temperature range. The spectra for the low-temperature and high-temperature phases are distinctly different (Fig. 2) and the  $E_g$  modes exhibit a clearly resolved splitting which occurs abruptly at  $T_S$ . We performed measurements in small temperature steps (see Figs. 3 and 4). This limits the maximum temperature interval where the phase coexistence could occur in our samples to approximately 5 K, much less than the roughly 30 to 80 K reported earlier [3,20]. We cannot exclude the possibility that a small fraction of the low-temperature phase could still

coexist with the high-temperature phase over a wider temperature range, whereby weak peaks corresponding to the remains of the low-temperature  $R\bar{3}$  phase might be hidden under the strong peaks of the  $C2/m$  phase.

#### IV. CONCLUSION

We studied the lattice dynamics in single crystalline  $\text{CrI}_3$  using Raman spectroscopy supported by numerical calculations. For both the low-temperature  $R\bar{3}$  and the high-temperature  $C2/m$  phase, all except one of the predicted

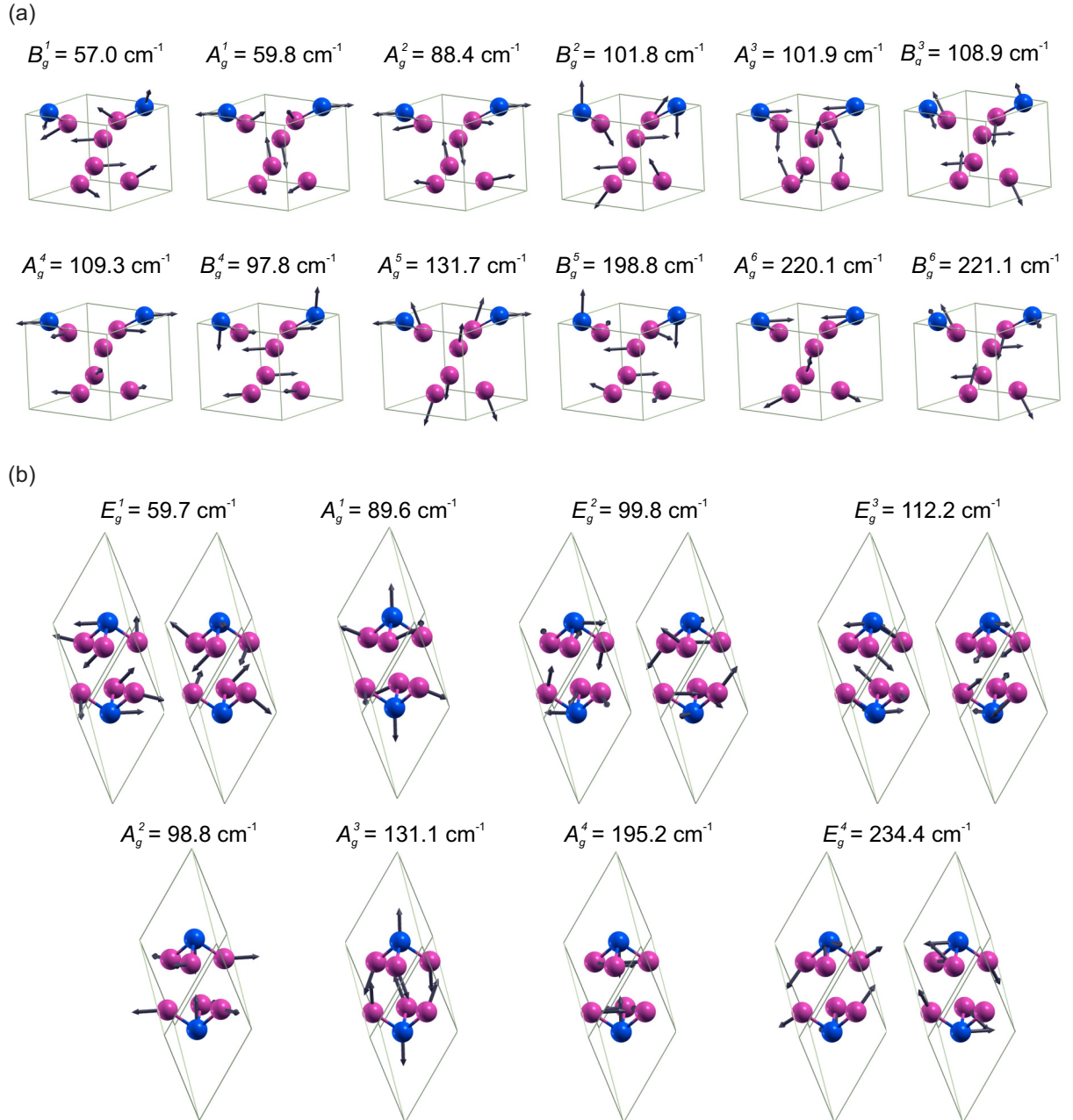


FIG. 5. Raman-active phonons in  $\text{CrI}_3$  for (a) the monoclinic phase hosting  $A_g$  and  $B_g$  modes and for (b) the rhombohedral phase hosting  $A_g$  and  $E_g$  modes. Blue and violet spheres denote Cr and I atoms, respectively. Solid lines represent primitive unit cells. Arrow lengths are proportional to the square root of the interatomic forces. The given energies are calculated for zero temperature.

phonon modes were identified and the calculated and experimental phonon energies were found to be in good agreement. We determined that the symmetry of the single CrI<sub>3</sub> layers is  $p\bar{3}1/m$ . Abrupt changes to the spectra were found at the first-order phase transition which was located at  $T_s \approx 180$  K, lower than in previous studies. In contrast to the prior reports we found no sign of phase coexistence over temperature ranges exceeding 5 K.

### ACKNOWLEDGMENTS

The work was supported by the Serbian Ministry of Education, Science and Technological Development under Projects No. III45018 and No. OI171005. DFT calculations were performed using computational resources at Johannes Kepler University, Linz, Austria. Work at Brookhaven was supported by the US Department of Energy, Office of Basic Energy Sciences as part of the Computation Material Science Program (material synthesis and characterization).

S.Dj.M. and N.L. conceived the experiment, performed the experiment, analyzed and discussed the data, and wrote the paper. A.Š. and J.P. calculated the phonon energies, analyzed and discussed the data, and wrote the paper. Y.L. and C.P. synthesized and characterized the samples. M.Š. performed the experiment and analyzed and discussed the data. A.B. and Z.V.P. analyzed and discussed the data and wrote the paper. All authors commented on the manuscript.

### APPENDIX: EIGENVECTORS

In addition to the phonon energies we also calculated the phonon eigenvectors which are shown in Fig. 5(a) for the high-temperature monoclinic phase and in Fig. 5(b) for the low-temperature rhombohedral phase. The energies, as given, are calculated for zero temperature. The relative displacement of the atoms is denoted by the length of the arrows.

- 
- [1] E. Navarro-Moratalla, B. Huang, G. Clark *et al.*, Layer-dependent ferromagnetism in a van der Waals crystal down to the monolayer limit, *Nature (London)* **546**, 270 (2017).
- [2] S. Jiang, L. Li, Z. Wang, K. F. Mak, and J. Shan, Controlling magnetism in 2D CrI<sub>3</sub> by electrostatic doping, *Nat. Nanotechnol.* **13**, 549 (2018).
- [3] M. A. McGuire, H. Dixit, V. R. Cooper, and B. C. Sales, Coupling of crystal structure and magnetism in the layered, ferromagnetic insulator CrI<sub>3</sub>, *Chem. Mater.* **27**, 612 (2015).
- [4] J. L. Ladno and J. Fernández-Rossier, On the origin of magnetic anisotropy in two dimensional CrI<sub>3</sub>, *2D Mater.* **4**, 035002 (2017).
- [5] W.-B. Zhang, Q. Qu, P. Zhu, and C.-H. Lam, Robust intrinsic ferromagnetism and half semiconductivity in stable two-dimensional single-layer chromium trihalides, *J. Mater. Chem. C* **3**, 12457 (2015).
- [6] J. F. Dillon, Jr. and C. E. Olson, Magnetization, resonance, and optical properties of the ferromagnet CrI<sub>3</sub>, *J. Appl. Phys.* **36**, 1259 (1965).
- [7] D. T. Larson and E. Kaxiras, Raman Spectrum of CrI<sub>3</sub>: An *ab initio* study, *Phys. Rev. B* **98**, 085406 (2018).
- [8] N. Lazarević, M. Abeykoon, P. W. Stephens, H. Lei, E. S. Bozin, C. Petrovic, and Z. V. Popović, Vacancy-induced nanoscale phase separation in K<sub>x</sub>Fe<sub>2-y</sub>Se<sub>2</sub> single crystals evidenced by Raman scattering and powder x-ray diffraction, *Phys. Rev. B* **86**, 054503 (2012).
- [9] H. Ryu, M. Abeykoon, K. Wang, H. Lei, N. Lazarevic, J. B. Warren, E. S. Bozin, Z. V. Popovic, and C. Petrovic, Insulating and metallic spin glass in Ni-doped K<sub>x</sub>Fe<sub>2-y</sub>Se<sub>2</sub> single crystals, *Phys. Rev. B* **91**, 184503 (2015).
- [10] H. Ryu, K. Wang, M. Opacic, N. Lazarevic, J. B. Warren, Z. V. Popovic, E. S. Bozin, and C. Petrovic, Sustained phase separation and spin glass in Co-doped K<sub>x</sub>Fe<sub>2-y</sub>Se<sub>2</sub> single crystals, *Phys. Rev. B* **92**, 174522 (2015).
- [11] Y. Liu and C. Petrovic, Three-dimensional magnetic critical behavior in CrI<sub>3</sub>, *Phys. Rev. B* **97**, 014420 (2018).
- [12] P. Giannozzi, S. Baroni, N. Bonini, M. Calandra, R. Car, C. Cavazzoni, D. Ceresoli, G. L. Chiarotti, M. Cococcioni, I. Dabo, A. D. Corso, S. de Gironcoli, S. Fabris, G. Fratesi, R. Gebauer, U. Gerstmann, C. Gougoussis, A. Kokalj, M. Lazzeri, L. Martin-Samos, N. Marzari, F. Mauri, R. Mazzarello, S. Paolini, A. Pasquarello, L. Paulatto, C. Sbraccia, S. Scandolo, G. Sclauzero, A. P. Seitsonen, A. Smogunov, P. Umari, and R. M. Wentzcovitch, Quantum espresso: A modular and open-source software project for quantum simulations of materials, *J. Phys. Condens. Matter* **21**, 395502 (2009).
- [13] J. P. Perdew, K. Burke, and M. Ernzerhof, Generalized Gradient Approximation Made Simple, *Phys. Rev. Lett.* **77**, 3865 (1996).
- [14] P. E. Blöchl, Projector augmented-wave method, *Phys. Rev. B* **50**, 17953 (1994).
- [15] G. Kresse and D. Joubert, From ultrasoft pseudopotentials to the projector augmented-wave method, *Phys. Rev. B* **59**, 1758 (1999).
- [16] S. Grimme, Semiempirical GGA-type density functional constructed with a long-range dispersion correction, *J. Comput. Chem.* **27**, 1787 (2006).
- [17] E. A. Wood, The 80 diperiodic groups in three dimensions, *Bell Syst. Tech. J.* **43**, 541 (1964).
- [18] W. G. Fateley, N. T. McDevitt, and F. F. Bentley, Infrared and raman selection rules for lattice vibrations: The correlation method, *Appl. Spectrosc.* **25**, 155 (1971).
- [19] N. Lazarević, Z. V. Popović, R. Hu, and C. Petrovic, Evidence of coupling between phonons and charge-density waves in ErTe<sub>3</sub>, *Phys. Rev. B* **83**, 024302 (2011).
- [20] M. A. McGuire, G. Clark, S. KC, W. M. Chance, G. E. Jellison, V. R. Cooper, X. Xu, and B. C. Sales, Magnetic behavior and spin-lattice coupling in cleavable van der Waals layered CrCl<sub>3</sub> crystals, *Phys. Rev. Mater.* **1**, 014001 (2017).

*Correction:* Missing support information in the Acknowledgment section has been inserted.

## Lattice dynamics and phase transitions in $\text{Fe}_{3-x}\text{GeTe}_2$

A. Milosavljević,<sup>1</sup> A. Šolajić,<sup>1</sup> S. Djurdjić-Mijin,<sup>1</sup> J. Pešić,<sup>1</sup> B. Višić,<sup>1</sup> Yu Liu (刘育),<sup>2</sup> C. Petrovic,<sup>2</sup>  
N. Lazarević,<sup>1</sup> and Z. V. Popović<sup>1,3</sup>

<sup>1</sup>*Center for Solid State Physics and New Materials, Institute of Physics Belgrade,*

*University of Belgrade, Pregrevica 118, 11080 Belgrade, Serbia*

<sup>2</sup>*Condensed Matter Physics and Materials Science Department, Brookhaven National Laboratory, Upton, New York 11973-5000, USA*

<sup>3</sup>*Serbian Academy of Sciences and Arts, Knez Mihailova 35, 11000 Belgrade, Serbia*



(Received 23 April 2019; published 17 June 2019)

We present Raman spectroscopy measurements of the van der Waals bonded ferromagnet  $\text{Fe}_{3-x}\text{GeTe}_2$ , together with lattice dynamics. Four out of eight Raman active modes are observed and assigned, in agreement with numerical calculations. The energies and linewidths of the observed modes display an unconventional temperature dependence at about 150 and 220 K, followed by the nonmonotonic evolution of the Raman continuum. Whereas the former can be related to the magnetic phase transition, the origin of the latter anomaly remains an open question.

DOI: [10.1103/PhysRevB.99.214304](https://doi.org/10.1103/PhysRevB.99.214304)

### I. INTRODUCTION

A novel class of magnetism hosting van der Waals bonded materials has recently become of great interest, since the materials are suitable candidates for numbers of technical applications [1–5]. Whereas  $\text{CrXTe}_3$  ( $X = \text{Si, Ge, Sn}$ ) and  $\text{CrX}_3$  ( $X = \text{Cl, Br, I}$ ) classes maintain low phase transition temperatures [1,6–9] even in a monolayer regime [10],  $\text{Fe}_{3-x}\text{GeTe}_2$  has a high bulk transition temperature, between 220 and 230 K [11,12], making it a promising applicant.

The  $\text{Fe}_{3-x}\text{GeTe}_2$  crystal structure consists of  $\text{Fe}_{3-x}\text{Ge}$  sublayers stacked between two sheets of Te atoms, and a van der Waals gap between neighboring Te layers [13,14]. Although the structure contains two different types of Fe atoms, it is revealed that vacancies take place only in the Fe2 sites [13,15].

Neutron diffraction, thermodynamic and transport measurements, and Mössbauer spectroscopy were used to analyze the magnetic and functional properties of  $\text{Fe}_{3-x}\text{GeTe}_2$ , with an Fe atom deficiency of  $x \approx 0.1$  and  $T_C = 225$  K. It is revealed that at a temperature of 1.5 K, magnetic moments of  $1.95(5)\mu_B$  and  $1.56(4)\mu_B$  are directed along the easy magnetic  $c$  axes [16]. In chemical vapor transport (CVT) grown  $\text{Fe}_3\text{GeTe}_2$  single crystals, besides the ferromagnetic (FM)-paramagnetic (PM) transition at a temperature of 214 K, FM layers order antiferromagnetically at 152 K [17]. Close to a ferromagnetic transition temperature of 230 K, a possible Kondo lattice behavior, i.e., coupling of traveling electrons and periodically localized spins, is indicated at  $T_K = 190 \pm 20$  K, which is in good agreement with theoretical predictions of 222 K [18].

Lattice parameters, as well as the magnetic transition temperature, vary with Fe ion concentration. Lattice parameters  $a$  and  $c$  follow the opposite trend, whereas the Curie temperature  $T_C$  decreases with an increase of Fe ion concentration [15]. For flux-grown crystals, the critical behavior was investigated by bulk dc magnetization around the ferromagnetic phase transition temperature of 152 K [13]. The anomalous Hall effect was also studied, where a significant amount of defects produces bad metallic behavior [19].

Theoretical calculations predict a dynamical stability of  $\text{Fe}_3\text{GeTe}_2$  single-layer, uniaxial magnetocrystalline anisotropy that originates from spin-orbit coupling [20]. Recently, anomalous Hall effect measurements on single-crystalline metallic  $\text{Fe}_3\text{GeTe}_2$  nanoflakes with different thicknesses are reported, with a  $T_C$  near 200 K and strong perpendicular magnetic anisotropy [21].

We report  $\text{Fe}_{3-x}\text{GeTe}_2$  single-crystal lattice dynamic calculations, together with Raman spectroscopy measurements. Four out of eight Raman active modes were observed and assigned. Phonon energies are in a good agreement with theoretical predictions. Analyzed phonon energies and linewidths reveal fingerprint of a ferromagnetic phase transition at a temperature around 150 K. Moreover, discontinuities in the phonon properties are found at temperatures around 220 K. Consistently, in the same temperature range, the Raman continuum displays nonmonotonic behavior.

### II. EXPERIMENT AND NUMERICAL METHOD

$\text{Fe}_{3-x}\text{GeTe}_2$  single crystals were grown by the self-flux method as previously described [13]. Samples for scanning electron microscopy (SEM) were cleaved and deposited on graphite tape. Energy dispersive spectroscopy (EDS) maps were collected using a FEI Helios NanoLab 650 instrument equipped with an Oxford Instruments EDS system, equipped with an X-max SSD detector operating at 20 kV. The surface of the as-cleaved  $\text{Fe}_{3-x}\text{GeTe}_2$  crystal appears to be uniform for several tens of microns in both directions, as shown in Fig. 4 of Appendix A. Additionally, the elemental composition maps of Fe, Ge, and Te show a distinctive homogeneity of all the three elements (Fig. 5 of Appendix A).

For Raman scattering experiments, a Tri Vista 557 spectrometer was used in the backscattering micro-Raman configuration. As an excitation source, a solid state laser with a 532 nm line was used. In our scattering configuration, the plane of incidence is the  $ab$  plane, where  $|a| = |b|$  ( $\angle(a, b) = 120^\circ$ ), with the incident (scattered) light propagation direction

TABLE I. Top panel: The type of atoms, Wyckoff positions, each site's contribution to the phonons in the  $\Gamma$  point, and corresponding Raman tensors for the  $P6_3/mmc$  space group of  $\text{Fe}_{3-x}\text{GeTe}_2$ . Bottom panel: Phonon symmetry, calculated optical Raman active phonon frequencies (in  $\text{cm}^{-1}$ ) for the magnetic (M) phase, and experimental values for Raman active phonons at 80 K.

Space group $P6_3/mmc$ (No. 194)		
Fe1 (4e)		$A_{1g} + E_{1g} + E_{2g} + A_{2u} + E_{1u}$
Fe2 (2c)		$E_{2g} + A_{2u} + E_{1u}$
Ge (2d)		$E_{2g} + A_{2u} + E_{1u}$
Te (2c)		$A_{1g} + E_{1g} + E_{2g} + A_{2u} + E_{1u}$
Raman tensors		
$A_{1g} = \begin{pmatrix} a & 0 & 0 \\ 0 & a & 0 \\ 0 & 0 & b \end{pmatrix}$	$E_{1g} = \begin{pmatrix} 0 & 0 & -c \\ 0 & 0 & c \\ -c & c & 0 \end{pmatrix}$	$E_{2g} = \begin{pmatrix} d & -d & 0 \\ -d & -d & 0 \\ 0 & 0 & 0 \end{pmatrix}$
Raman active modes		
Symmetry	Calculations (M)	Experiment (M)
$E_{2g}^1$	50.2	
$E_{1g}^1$	70.3	
$E_{2g}^2$	122.2	89.2
$A_{1g}^1$	137.2	121.1
$E_{1g}^2$	209.5	
$E_{2g}^3$	228.6	214.8
$A_{1g}^2$	233.4	239.6
$E_{2g}^4$	334.3	

along the  $c$  axes. Samples were cleaved in the air, right before being placed in the vacuum. All the measurements were performed in the high vacuum ( $10^{-6}$  mbar) using a KONTI CryoVac continuous helium flow cryostat with a 0.5 mm thick window. To achieve laser beam focusing, a microscope objective with  $\times 50$  magnification was used. A Bose factor correction of all spectra was performed. More details can be found in Appendix C.

Density functional theory (DFT) calculations were performed with the QUANTUM ESPRESSO (QE) software package [22]. We used the projector augmented-wave (PAW) pseudopotentials [23,24] with the Perdew-Burke-Ernzerhof (PBE) exchange-correlation functional [25]. The electron wave function and charge density cutoffs of 64 and 782 Ry were chosen, respectively. The  $k$  points were sampled using the Monkhorst-Pack scheme, with an  $8 \times 8 \times 4$   $\Gamma$ -centered grid. Both magnetic and nonmagnetic calculations were performed, using the experimentally obtained lattice parameters and the calculated values obtained by relaxing the theoretically proposed structure. In order to obtain the lattice parameters accurately, a treatment of the van der Waals interactions is introduced. The van der Waals interaction was included in all calculations using the Grimme-D2 correction [26]. Phonon frequencies in the  $\Gamma$  point are calculated within the linear response method implemented in QE.

### III. RESULTS AND DISCUSSION

$\text{Fe}_{3-x}\text{GeTe}_2$  crystallizes in a hexagonal crystal structure, described with the  $P6_3/mmc$  ( $D_{6h}^4$ ) space group. The atom type, site symmetry, each site's contribution to the phonons

in the  $\Gamma$  point, and corresponding Raman tensors for the  $P6_3/mmc$  space group are presented in Table I.

Calculated displacement patterns of Raman active modes, which can be observed in our scattering configuration, are presented in Fig. 1(a). Since the Raman tensor of the  $E_{1g}$  mode contains only the  $z$  component (Table I), by selection rules, it cannot be detected when measuring from the  $ab$  plane in the backscattering configuration. Whereas  $A_{1g}$  modes include vibrations of Fe and Te ions along the  $c$  axis,  $E_{2g}$  modes include in-plane vibrations of all four atoms. The Raman spectra of  $\text{Fe}_{3-x}\text{GeTe}_2$  in the magnetic phase (M), at 80 K, and nonmagnetic phase (NM), at 280 K, in a parallel scattering configuration ( $\mathbf{e}_i \parallel \mathbf{e}_s$ ), are presented in Fig. 1 (b). As it can be seen, four peaks at 89.2, 121.1, 214.8, and 239.6  $\text{cm}^{-1}$  can be clearly observed at 80 K. According to numerical calculations (see Table I), peaks at 89.2 and 239.6  $\text{cm}^{-1}$  correspond to two out of four  $E_{2g}$  modes, whereas peaks at 121.1 and 239.6  $\text{cm}^{-1}$  can be assigned as two  $A_{1g}$  symmetry modes. One should note that numerical calculations performed by using experimentally obtained lattice parameters in the magnetic phase yield a better agreement with experimental values. This is not surprising since the calculations are performed for the stoichiometric compound as opposed to the nonstoichiometry of the sample. Furthermore, it is known that lattice parameters strongly depend on the Fe atom deficiency [15]. All calculated Raman and infrared phonon frequencies, for the magnetic and nonmagnetic phase of  $\text{Fe}_{3-x}\text{GeTe}_2$ , using relaxed and experimental lattice parameters, together with experimentally observed Raman active modes, are summarized in Table II of Appendix D.

After assigning all observed modes we focused on their temperature evolution. Having in mind finite instrumental

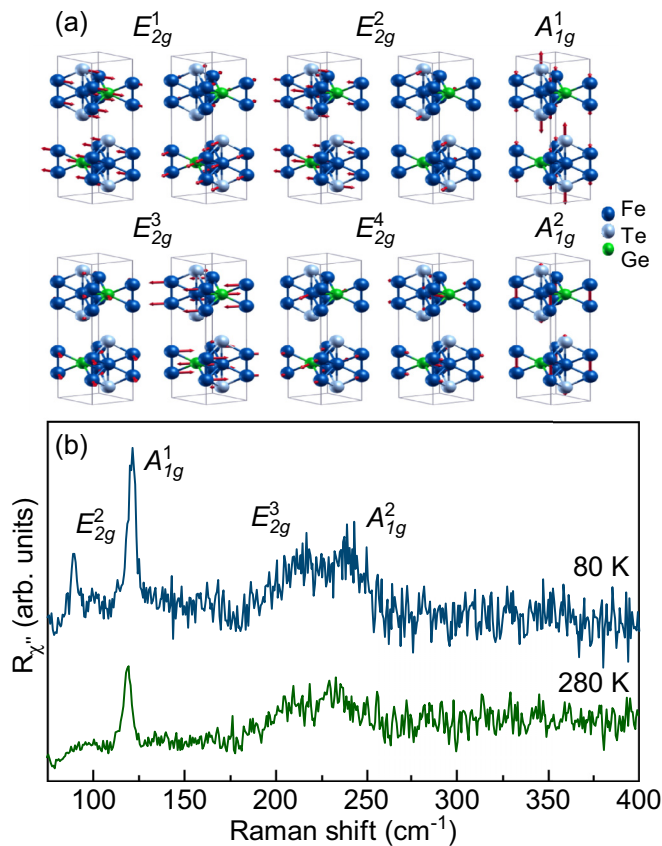


FIG. 1. (a) Displacement patterns of  $A_{1g}$  and  $E_{2g}$  symmetry modes. (b) Raman spectra of  $\text{Fe}_{3-x}\text{GeTe}_2$  single crystal measured at different temperatures in a parallel polarization configuration.

broadening, the Voigt line shape was used for the data analysis [27,28]. The modeling procedure is described in detail in Appendix B and presented in Fig. 6. Figure 2 shows the temperature evolution of the energy and linewidth of the  $A_{1g}^1$ ,  $E_{2g}^3$ , and  $A_{1g}^2$  modes between 80 and 300 K. Upon heating the sample, both the energy and linewidth of  $A_{1g}^1$  and  $A_{1g}^2$  symmetry modes exhibit a small but sudden discontinuity at about 150 K [Figs. 2(a) and 2(e)]. An apparent discontinuity in energy of all analyzed Raman modes is again present at temperatures around 220 K. In the same temperature range the linewidths of these Raman modes show a clear deviation from the standard anharmonic behavior [27–31].

Apart from the anomalies in the phonon spectra, a closer inspection of the temperature-dependent Raman spectra measured in the parallel polarization configuration reveals a pronounced evolution of the Raman continuum [Fig. 3(a)]. For the analysis we have used a simple model including a damped Lorentzian and linear term,  $\chi''_{\text{cont}} \propto a\Gamma\omega/(\omega^2 + \Gamma^2) + b\omega$  [32], where  $a$ ,  $b$ , and  $\Gamma$  are temperature-dependent parameters. Figure 3(b) summarizes the results of the analysis with the linear term omitted (most likely originating from a luminescence). At approximately the same temperatures, where phonon properties exhibit discontinuities, the continuum temperature dependence manifests nonmonotonic behavior. The maximum positions of the curve were obtained by integrating

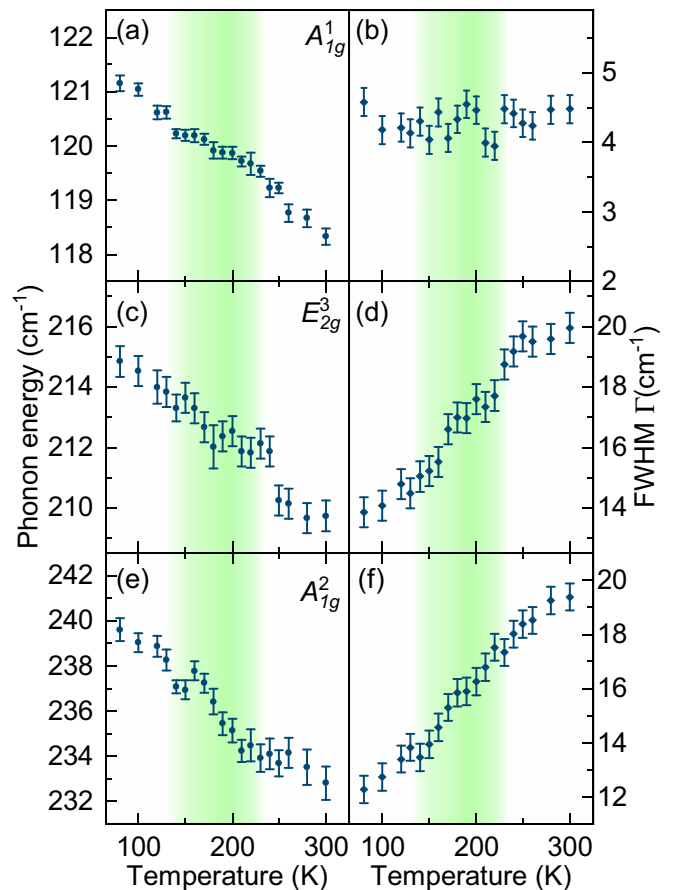


FIG. 2. Energy and linewidth temperature dependence of  $A_{1g}^1$  [(a) and (b)],  $E_{2g}^3$  [(c) and (d)], and  $A_{1g}^2$  [(e) and (f)] phonon modes in  $\text{Fe}_{3-x}\text{GeTe}_2$ .

those shown in Fig. 3(b). The inset of Fig. 3(b) shows the temperature evolution of their displacements. This analysis confirms the presence of discontinuities in the electronic continuum at temperatures around 150 and 220 K, which leaves a trace in the phonon behavior around these temperatures (Fig. 2). While we do not have evidence for the Kondo effect in the  $\text{Fe}_{3-x}\text{GeTe}_2$  crystals we measured, a modification of the electronic background at FM ordering due to localization or the Kondo effect cannot be excluded.

The temperature evolutions of the phonon self-energies and the continuum observed in the Raman spectra of  $\text{Fe}_{3-x}\text{GeTe}_2$  suggest the presence of phase transition(s). Magnetization measurements of the samples were performed as described in Ref. [13], revealing a FM-PM transition at 150 K. Thus, the discontinuity in the observed phonon properties around this temperature can be traced back to the weak to moderate spin-phonon coupling. The question remains open regarding the anomaly observed at about 220 K. As previously reported, the Curie temperature of the  $\text{Fe}_{3-x}\text{GeTe}_2$  single crystals grown by the CVT method is between 220 and 230 K [11,12,14], varying with the vacancy concentration, i.e., a decrease in the vacancy content will result an increment of  $T_C$  [15]. On the other hand, the  $\text{Fe}_{3-x}\text{GeTe}_2$  crystals grown by the self-flux method usually have a lower Curie temperature, since the



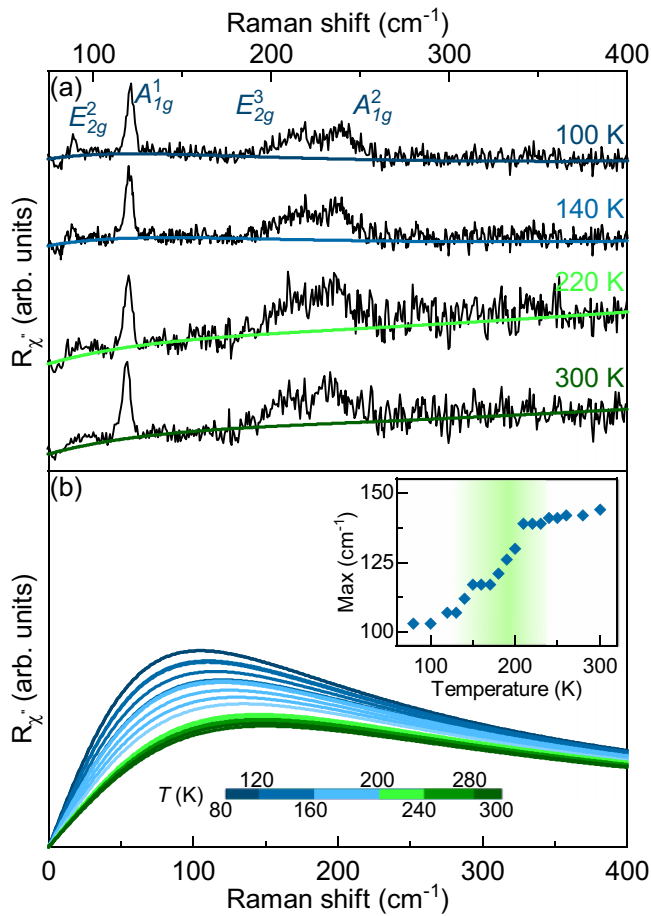


FIG. 3. (a) Raman spectra of  $\text{Fe}_{3-x}\text{GeTe}_2$  at four temperatures measured in a parallel polarization configuration. Solid lines represent the theoretical fit to the experimental data. (b) Temperature evolution of the electronic continuum after omitting the linear term. Inset: Displacement of the maximum of fitted curves.

vacancy content is higher [13,15]. Crystals used in the Raman scattering experiment presented here were grown by the self-flux method with a Fe vacancy content of  $x \approx 0.36$  [13]. This is in good agreement with our EDS results of  $x = 0.4 \pm 0.1$ , giving rise to the FM-PM transition at 150 K. Nevertheless,

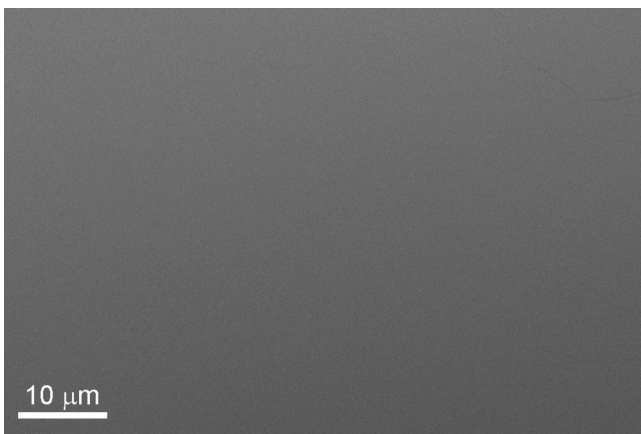


FIG. 4. SEM image of a  $\text{Fe}_{3-x}\text{GeTe}_2$  single crystal.

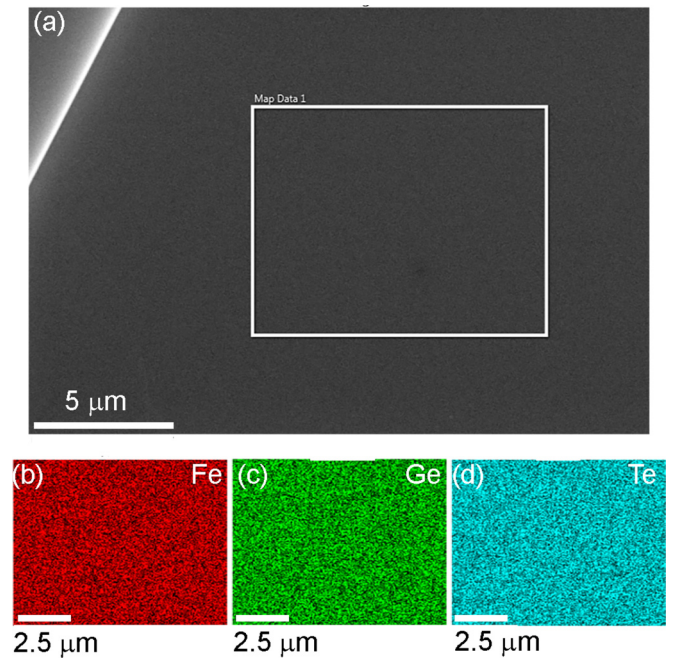


FIG. 5. EDS mapping on a  $\text{Fe}_{3-x}\text{GeTe}_2$  single crystal. (a) Secondary electron image of the crystal with the mapping performed within the rectangle. (b)–(d) Associated EDS maps for Fe, Ge, and Te, respectively.

an inhomogeneous distribution of vacancies may result the formation of vacancy depleted “islands” which in turn would result in an anomaly at 220 K similar to the one observed in our Raman data. However, the EDS data (see Fig. 5) do not support this possibility. At this point we can only speculate that while the long-range order temperature is shifted to a lower temperature by the introduction of vacancies, short-range correlations may develop at 220 K.

#### IV. CONCLUSION

We have studied the lattice dynamics of flux-grown  $\text{Fe}_{3-x}\text{GeTe}_2$  single crystals by means of Raman spectroscopy and DFT. Four out of eight Raman active modes, two  $A_{1g}$  and two  $E_{2g}$ , have been observed and assigned. DFT calculations are in good agreement with experimental results. The temperature dependence of the  $A_{1g}^1$ ,  $E_{2g}^3$ , and  $A_{1g}^2$  mode properties reveals a clear fingerprint of spin-phonon coupling, at a temperature of around 150 K. Furthermore, the anomalous behavior in the energies and linewidths of the observed phonon modes is present in the Raman spectra at temperatures around 220 K with the discontinuity also present in the electronic continuum. Its origin still remains an open question, and requires further analysis.

#### ACKNOWLEDGMENTS

The work was supported by the Serbian Ministry of Education, Science and Technological Development under Projects No. III45018 and No. OI171005. DFT calculations were performed using computational resources at Johannes Kepler University, Linz, Austria. Materials synthesis was supported

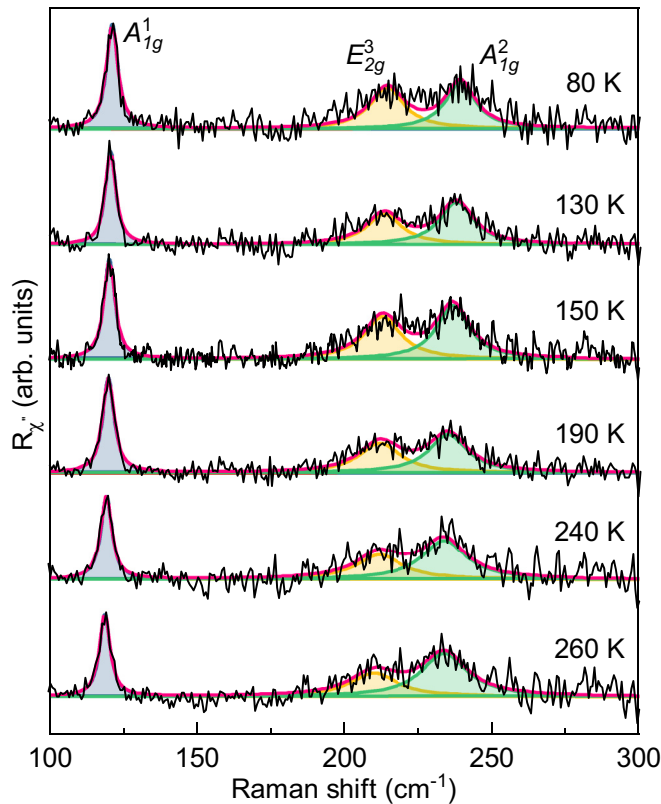


FIG. 6. Modeled Raman spectra of  $\text{Fe}_{3-x}\text{GeTe}_2$  single crystal, after subtracting continuum contributions, obtained at various temperatures. For experimental data modeling, the Voigt line shape was used.

by the US Department of Energy, Office of Basic Energy Sciences as part of the Computation Material Science Program (Y.L. and C.P.). Electron microscopy was performed at Jozef Stefan Institute, Ljubljana, Slovenia under Slovenian Research Agency Contract No. P1-0099 (B.V.). This work has received funding from the European Union's Horizon 2020 research and innovation program under the Marie Skłodowska-Curie Grant Agreement No. 645658 (DAFNEOX Project).

#### APPENDIX A: ELECTRON MICROSCOPY

In order to examine the uniformity of  $\text{Fe}_{3-x}\text{GeTe}_2$ , Scanning electron microscopy (SEM) was performed on as-cleaved crystals. It can be seen from Fig. 4 that the crystals maintain uniformity for several tens of microns. Furthermore, the elemental composition was obtained using EDS mapping, as shown in Fig. 5. The atomic percentage, averaged over ten measurements, is 47%, 17%, and 36% ( $\pm 2\%$ ) for Fe, Ge, and Te, respectively, with the vacancy content  $x = 0.4 \pm 0.1$ . The maps associated with the selected elements appear homogeneous, as they are all present uniformly with no apparent islands or vacancies.

#### APPENDIX B: DATA MODELING

In order to obtain the temperature dependence of the energies and linewidths of the observed  $\text{Fe}_{3-x}\text{GeTe}_2$  phonon modes, the Raman continuum, shown in colored lines in

TABLE II. Top panel: Comparison of calculated energies of Raman active phonons using relaxed (R) and experimental [non-relaxed (NR)] lattice parameters for the magnetic (M) and nonmagnetic phase (NM), given in  $\text{cm}^{-1}$ . Obtained experimental values in the magnetic phase at a temperature of 80 K are given in the last column. Bottom panel: Comparison of calculated energies of infrared optical phonons of  $\text{Fe}_{3-x}\text{GeTe}_2$ .

Raman active modes					
Sym.	Calculations				Experiment (M)
	NM-R	M-R	NM-NR	M-NR	
$E_{2g}^1$	28.4	49.6	33.9	50.2	
$E_{1g}^1$	79.2	70.2	71.7	70.3	
$E_{2g}^2$	115.5	121.0	100.0	122.2	89.2
$A_{1g}^1$	151.7	139.2	131.7	137.2	121.1
$E_{1g}^2$	225.5	206.0	194.3	209.5	
$E_{2g}^3$	238.0	232.6	204.9	228.6	214.8
$A_{1g}^2$	272.0	262.6	235.7	233.4	239.6
$E_{2g}^4$	362.0	337.6	315.4	334.7	
Infrared active modes					
$A_{2u}^1$	70.7	96.6	73.5	92.7	
$E_{1u}^1$	112.5	121.2	89.4	121.6	
$A_{2u}^2$	206.0	162.5	183.1	153.7	
$E_{1u}^2$	226.4	233.6	192.1	231.3	
$A_{2u}^3$	271.8	248.6	240.8	241.0	
$E_{1u}^3$	361.1	336.6	314.7	334.7	

Fig. 3(a), was subtracted for simplicity from the raw Raman susceptibility data (black line). The spectra obtained after the subtraction procedure are presented in Fig. 6 (black line) for various temperatures. Because of the finite resolution of the spectrometer and the fact that line shapes of all the observed phonons are symmetric, the Voigt line shape ( $\Gamma_G = 0.8 \text{ cm}^{-1}$ ) was used for data modeling. Blue, yellow, and green lines in Fig. 6 represent fitting curves for  $A_{1g}^1$ ,  $E_{2g}^3$ , and  $A_{1g}^2$  phonon modes, respectively, whereas the overall spectral shape is shown in the red line.

#### APPENDIX C: EXPERIMENTAL DETAILS

Before being placed in a vacuum and being cleaved, the sample was glued to a copper plate with GE varnish in order to achieve good thermal conductivity and prevent strain effects. Silver paste, as a material with high thermal conductivity, was used to attach the copper plate with the sample to the cryostat. The laser beam spot, focused through an Olympus long-range objective of  $\times 50$  magnification, was approximately  $6 \mu\text{m}$  in size, with a power less than 1 mW at the sample surface. A TriVista 557 triple spectrometer was used in the subtractive mode, with a diffraction grating combination of 1800/1800/2400 grooves/mm and the entrance and second intermediate slit set to  $80 \mu\text{m}$ , in order to enhance stray light rejection and attain good resolution.

## APPENDIX D: CALCULATIONS

In Table II the results of DFT calculations are presented for magnetic (M) and nonmagnetic (NM) relaxed and experimental lattice parameters. For comparison, the

experimental results are shown in the last column. Since the lattice parameters strongly depend on the Fe atom deficiency, the best agreement with experimental results gives the magnetic nonrelaxed solution.

- [1] N. Sivadas, M. W. Daniels, R. H. Swendsen, S. Okamoto, and D. Xiao, Magnetic ground state of semiconducting transition-metal trichalcogenide monolayers, *Phys. Rev. B* **91**, 235425 (2015).
- [2] K. S. Novoselov, A. K. Geim, S. V. Morozov, D. Jiang, Y. Zhang, S. V. Dubonos, I. V. Grigorieva, and A. A. Firsov, Electric field effect in atomically thin carbon films, *Science* **306**, 666 (2004).
- [3] Q. H. Wang, K. Kalantar-Zadeh, A. Kis, J. N. Coleman, and M. S. Strano, Electronics and optoelectronics of two-dimensional transition metal dichalcogenides, *Nat. Nanotechnol.* **7**, 699 (2012).
- [4] C. Gong, L. Li, Z. Li, H. Ji, A. Stern, Y. Xia, T. Cao, W. Bao, C. Wang, Y. Wang, Z. Q. Qiu, R. J. Cava, S. G. Louie, J. Xia, and X. Zhang, Discovery of intrinsic ferromagnetism in two-dimensional van der Waals crystals, *Nature (London)* **546**, 265 (2017).
- [5] B. Huang, G. Clark, E. Navarro-Moratalla, D. R. Klein, R. Cheng, K. L. Seyler, D. Zhong, E. Schmidgall, M. A. McGuire, D. H. Cobden, W. Yao, D. Xiao, P. Jarillo-Herrero, and X. Xu, Layer-dependent ferromagnetism in a van der Waals crystal down to the monolayer limit, *Nature (London)* **546**, 270 (2017).
- [6] M. A. McGuire, H. Dixit, V. R. Cooper, and B. C. Sales, Coupling of crystal structure and magnetism in the layered, ferromagnetic insulator CrI<sub>3</sub>, *Chem. Mater.* **27**, 612 (2015).
- [7] H. L. Zhuang, Y. Xie, P. R. C. Kent, and P. Ganesh, Computational discovery of ferromagnetic semiconducting single-layer CrSnTe<sub>3</sub>, *Phys. Rev. B* **92**, 035407 (2015).
- [8] G. T. Lin, H. L. Zhuang, X. Luo, B. J. Liu, F. C. Chen, J. Yan, Y. Sun, J. Zhou, W. J. Lu, P. Tong, Z. G. Sheng, Z. Qu, W. H. Song, X. B. Zhu, and Y. P. Sun, Tricritical behavior of the two-dimensional intrinsically ferromagnetic semiconductor CrGeTe<sub>3</sub>, *Phys. Rev. B* **95**, 245212 (2017).
- [9] L. D. Casto, A. J. Clune, M. O. Yokosuk, J. L. Musfeldt, T. J. Williams, H. L. Zhuang, M.-W. Lin, K. Xiao, R. G. Hennig, B. C. Sales, J.-Q. Yan, and D. Mandrus, Strong spin-lattice coupling in CrSiTe<sub>3</sub>, *APL Mater.* **3**, 041515 (2015).
- [10] M.-W. Lin, H. L. Zhuang, J. Yan, T. Z. Ward, A. A. Puretzyk, C. M. Rouleau, Z. Gai, L. Liang, V. Meunier, B. G. Sumpter, P. Ganesh, P. R. C. Kent, D. B. Geohegan, D. G. Mandrus, and K. Xiao, Ultrathin nanosheets of CrSiTe<sub>3</sub>: A semiconducting two-dimensional ferromagnetic material, *J. Mater. Chem. C* **4**, 315 (2016).
- [11] J.-X. Zhu, M. Janoschek, D. S. Chaves, J. C. Cezar, T. Durakiewicz, F. Ronning, Y. Sassa, M. Mansson, B. L. Scott, N. Wakeham, E. D. Bauer, and J. D. Thompson, Electronic correlation and magnetism in the ferromagnetic metal Fe<sub>3</sub>GeTe<sub>2</sub>, *Phys. Rev. B* **93**, 144404 (2016).
- [12] B. Chen, J. H. Yang, H. D. Wang, M. Imai, H. Ohta, C. Michioka, K. Yoshimura, and M. H. Fang, Magnetic properties of layered itinerant electron ferromagnet Fe<sub>3</sub>GeTe<sub>2</sub>, *J. Phys. Soc. Jpn.* **82**, 124711 (2013).
- [13] Y. Liu, V. N. Ivanovski, and C. Petrovic, Critical behavior of the van der Waals bonded ferromagnet Fe<sub>3-x</sub>GeTe<sub>2</sub>, *Phys. Rev. B* **96**, 144429 (2017).
- [14] H.-J. Deiseroth, K. Aleksandrov, C. Reiner, L. Kienle, and R. K. Kremer, Fe<sub>3</sub>GeTe<sub>2</sub> and Ni<sub>3</sub>GeTe<sub>2</sub> - Two new layered transition-metal compounds: Crystal structures, HRTEM investigations, and magnetic and electrical properties, *Eur. J. Inorg. Chem.* **2006**, 1561 (2006).
- [15] A. F. May, S. Calder, C. Cantoni, H. Cao, and M. A. McGuire, Magnetic structure and phase stability of the van der Waals bonded ferromagnet Fe<sub>3-x</sub>GeTe<sub>2</sub>, *Phys. Rev. B* **93**, 014411 (2016).
- [16] V. Yu. Verchenko, A. A. Tsirlin, A. V. Sobolev, I. A. Presniakov, and A. V. Shevelkov, Ferromagnetic order, strong magnetocrystalline anisotropy, and magnetocaloric effect in the layered telluride Fe<sub>3-δ</sub>GeTe<sub>2</sub>, *Inorg. Chem.* **54**, 8598 (2015).
- [17] J. Yi, H. Zhuang, Q. Zou, Z. Wu, G. Cao, S. Tang, S. A. Calder, P. R. C. Kent, D. Mandrus, and Z. Gai, Competing antiferromagnetism in a quasi-2D itinerant ferromagnet: Fe<sub>3</sub>GeTe<sub>2</sub>, *2D Mater.* **4**, 011005 (2016).
- [18] Y. Zhang, H. Lu, X. Zhu, S. Tan, W. Feng, Q. Liu, W. Zhang, Q. Chen, Y. Liu, X. Luo, D. Xie, L. Luo, Z. Zhang, and X. Lai, Emergence of Kondo lattice behavior in a van der Waals itinerant ferromagnet, Fe<sub>3</sub>GeTe<sub>2</sub>, *Sci. Adv.* **4**, eaao6791 (2018).
- [19] Y. Liu, E. Stavitski, K. Attenkofer, and C. Petrovic, Anomalous Hall effect in the van der Waals bonded ferromagnet Fe<sub>3-x</sub>GeTe<sub>2</sub>, *Phys. Rev. B* **97**, 165415 (2018).
- [20] H. L. Zhuang, P. R. C. Kent, and R. G. Hennig, Strong anisotropy and magnetostriction in the two-dimensional Stoner ferromagnet Fe<sub>3</sub>GeTe<sub>2</sub>, *Phys. Rev. B* **93**, 134407 (2016).
- [21] C. Tan, J. Lee, S.-G. Jung, T. Park, S. Albarakati, J. Partridge, M. R. Field, D. G. McCulloch, L. Wang, and C. Lee, Hard magnetic properties in nanoflake van der Waals Fe<sub>3</sub>GeTe<sub>2</sub>, *Nat. Commun.* **9**, 1554 (2018).
- [22] P. Giannozzi *et al.*, QUANTUM ESPRESSO: A modular and open-source software project for quantum simulations of materials, *J. Phys.: Condens. Matter* **21**, 395502 (2009).
- [23] P. E. Blöchl, Projector augmented-wave method, *Phys. Rev. B* **50**, 17953 (1994).
- [24] G. Kresse and D. Joubert, From ultrasoft pseudopotentials to the projector augmented-wave method, *Phys. Rev. B* **59**, 1758 (1999).
- [25] J. P. Perdew, K. Burke, and M. Ernzerhof, Generalized Gradient Approximation Made Simple, *Phys. Rev. Lett.* **77**, 3865 (1996).
- [26] S. Grimme, Semiempirical GGA-type density functional constructed with a long-range dispersion correction, *J. Comput. Chem.* **27**, 1787 (2006).
- [27] A. Milosavljević, A. Šolajić, J. Pešić, Y. Liu, C. Petrovic, N. Lazarević, and Z. V. Popović, Evidence of spin-phonon coupling in CrSiTe<sub>3</sub>, *Phys. Rev. B* **98**, 104306 (2018).
- [28] A. Baum, A. Milosavljević, N. Lazarević, M. M. Radonjić, B. Nikolić, M. Mitschek, Z. I. Maranloo, M. Šćepanović, M. Grujić-Brojčin, N. Stojilović, M. Opel, A. Wang,

- C. Petrovic, Z. V. Popović, and R. Hackl, Phonon anomalies in FeS, *Phys. Rev. B* **97**, 054306 (2018).
- [29] M. Opačić, N. Lazarević, M. M. Radonjić, M. Šćepanović, H. Ryu, A. Wang, D. Tanasković, C. Petrovic, and Z. V. Popović, Raman spectroscopy of  $K_xK_{2-y}Se_2$  single crystals near the ferromagnet–paramagnet transition, *J. Phys.: Condens. Matter* **28**, 485401 (2016).
- [30] Z. V. Popović, N. Lazarević, S. Bogdanović, M. M. Radonjić, D. Tanasković, R. Hu, H. Lei, and C. Petrovic, Signatures of the spin-phonon coupling in  $Fe_{1+y}Te_{1-x}Se_x$  alloys, *Solid State Commun.* **193**, 51 (2014).
- [31] Z. V. Popović, M. Šćepanović, N. Lazarević, M. Opačić, M. M. Radonjić, D. Tanasković, H. Lei, and C. Petrovic, Lattice dynamics of  $BaFe_2X_3$  ( $X = S, Se$ ) compounds, *Phys. Rev. B* **91**, 064303 (2015).
- [32] T. P. Devereaux and R. Hackl, Inelastic light scattering from correlated electrons, *Rev. Mod. Phys.* **79**, 175 (2007).

**Probing charge density wave phases and the Mott transition in 1T-TaS<sub>2</sub> by inelastic light scattering**S. Djurdjic Mijin,<sup>1</sup> A. Baum,<sup>2</sup> J. Bekaert,<sup>3</sup> A. Šolajić,<sup>1</sup> J. Pešić,<sup>1</sup> Y. Liu,<sup>4,\*</sup> Ge He,<sup>2</sup> M. V. Milošević,<sup>3</sup> C. Petrovic,<sup>4</sup> Z. V. Popović,<sup>1,5</sup> R. Hackl,<sup>2</sup> and N. Lazarević<sup>1</sup><sup>1</sup>Center for Solid State Physics and New Materials, Institute of Physics Belgrade, University of Belgrade, Pregrevica 118, RS-11080 Belgrade, Serbia<sup>2</sup>Walther Meissner Institut, Bayerische Akademie der Wissenschaften, D-85748 Garching, Germany<sup>3</sup>Department of Physics, University of Antwerp, Groenenborgerlaan 171, B-2020 Antwerp, Belgium<sup>4</sup>Condensed Matter Physics and Materials Science Department, Brookhaven National Laboratory, Upton, New York 11973-5000, USA<sup>5</sup>Serbian Academy of Sciences and Arts, Knez Mihailova 35, RS-11000 Belgrade, Serbia

(Received 10 March 2021; revised 14 June 2021; accepted 16 June 2021; published 22 June 2021)

We present a polarization-resolved, high-resolution Raman scattering study of the three consecutive charge density wave (CDW) regimes in 1T-TaS<sub>2</sub> single crystals, supported by *ab initio* calculations. Our analysis of the spectra within the low-temperature commensurate (C-CDW) regime shows  $P\bar{3}$  symmetry of the system, thus excluding the previously proposed triclinic stacking of the “star-of-David” structure, and promoting trigonal or hexagonal stacking instead. The spectra of the high-temperature incommensurate (IC-CDW) phase directly project the phonon density of states due to the breaking of the translational invariance, supplemented by sizable electron-phonon coupling. Between 200 and 352 K, our Raman spectra show contributions from both the IC-CDW and the C-CDW phases, indicating their coexistence in the so-called nearly commensurate (NC-CDW) phase. The temperature dependence of the symmetry-resolved Raman conductivity indicates the stepwise reduction of the density of states in the CDW phases, followed by a Mott transition within the C-CDW phase. We determine the size of the Mott gap to be  $\Omega_{\text{gap}} \approx 170\text{--}190$  meV, and track its temperature dependence.

DOI: [10.1103/PhysRevB.103.245133](https://doi.org/10.1103/PhysRevB.103.245133)**I. INTRODUCTION**

Quasi-two-dimensional transition metal dichalcogenides (TMDs), such as the various structures of TaSe<sub>2</sub> and TaS<sub>2</sub>, have been in the focus of various scientific investigations over the last 30 years, mostly due to the plethora of charge density wave (CDW) phases [1,2]. Among all TMD compounds 1T-TaS<sub>2</sub> stands out because of its unique and rich electronic phase diagram [3–6]. It experiences phase transitions at relatively high temperatures, making it easily accessible for investigation and, mainly for the hysteresis effects, attractive for potential applications such as data storage [7], information processing [8], or voltage-controlled oscillators [9].

The cascade of phase transitions as a function of temperature includes the transition from the normal metallic to the incommensurate CDW (IC-CDW) phase, the nearly commensurate CDW (NC-CDW) phase, and the commensurate CDW (C-CDW) phase occurring at around  $T_{\text{IC}} = 554$  K,  $T_{\text{NC}} = 355$  K, and in the temperature range from  $T_{\text{C}\downarrow} = 180$  K to  $T_{\text{C}\uparrow} = 230$  K, respectively. Recent studies indicate the possibility of yet another phase transition in 1T-TaS<sub>2</sub> at  $T_H = 80$  K, named the hidden CDW state [10–12]. This discovery led to a new boost in attention for 1T-TaS<sub>2</sub>.

Upon lowering the temperature to  $T_{\text{IC}} = 554$  K, the normal metallic state structure, described by the space group  $P\bar{3}m1$  ( $D_{3d}^d$ ) [13], transforms into the IC-CDW state. As will be

demonstrated here, the IC-CDW domains shrink upon further temperature reduction until they gradually disappear, giving place to the C-CDW ordered state. This region in the phase diagram between 554 and roughly 200 K is characterized by the coexistence of the IC-CDW and C-CDW phases and is often referred to as NC-CDW. At the transition temperature  $T_C$ , IC-CDW domains completely vanish [14] and a new lattice symmetry is established. There is a general consensus about the formation of “star-of-David” clusters with in-plane  $\sqrt{13}a \times \sqrt{13}a$  lattice reconstruction, whereby 12 Ta atoms are grouped around the 13th Ta atom [15,16]. In the absence of any external strain fields, this can be achieved in two equivalent ways (by either clockwise or counterclockwise rotations) thus yielding domains [17]. Despite extensive investigations, both experimental and theoretical, it remains an open question whether the stacking of star-of-David clusters is triclinic, trigonal, hexagonal, or a combination thereof [15,16,18–20]. The C-CDW phase is believed to be an insulator [3,21–23] with a gap of around 100 meV [13]. Very recent theoretical studies based on density-functional theory (DFT) find an additional ordering pattern along the crystallographic  $c$  axis. The related gap has a width of approximately 0.5 eV along  $k_z$  and becomes gapped at the Fermi energy  $E_F$  in the C-CDW phase [24,25].

Nearly all of the previously reported results for optical phonons in 1T-TaS<sub>2</sub> are based on Raman spectroscopy on the C-CDW phase and on temperature-dependent measurements in a narrow range around the NC-CDW to C-CDW phase transition [13,15,18–20]. In this paper we present temperature-dependent polarization-resolved Raman

\*Present address: Los Alamos National Laboratory, Los Alamos, New Mexico 87545, USA.

measurements in the temperature range from 4 to 370 K covering all three CDW regimes of 1T-TaS<sub>2</sub>. Our analysis of the C-CDW phase confirms the symmetry to be  $P\bar{3}$ , while the NC-CDW phase is confirmed as a mixed regime of commensurate and incommensurate domains. The Raman spectra of the IC-CDW phase mainly project the phonon density of states due to the breaking of translation invariance and sizable electron-phonon coupling. The growth of the CDW gap upon cooling, followed by the opening of the Mott gap, is traced via the initial slope of the symmetry-resolved spectra. The size of 170–190 meV and the temperature dependence of the Mott gap are directly determined from high-energy Raman data.

## II. EXPERIMENTAL AND NUMERICAL METHODS

The preparation of the studied 1T-TaS<sub>2</sub> single crystals is described elsewhere [26–29]. Calibrated customized Raman scattering equipment was used to obtain the spectra. Temperature-dependent measurements were performed with the sample attached to the cold finger of a He-flow cryostat. The sample was cooled down to the lowest temperature and then heated. In either case the rates were less than  $\pm 1$  K/min. All measurements were performed in a high vacuum of approximately  $5 \times 10^{-5}$  Pa.

The 575-nm laser line of a diode-pumped Coherent GENESIS MX-SLM solid state laser was used as an excitation source. Additional measurements with the 458- and 514-nm laser lines were performed with a Coherent Innova 304C argon ion laser. The absorbed power was set at 4 mW. All spectra shown are corrected for the sensitivity of the instrument and the Bose factor, yielding the imaginary part of the Raman susceptibility  $R\chi''$ , where  $R$  is an experimental constant. An angle of incidence of  $\Theta_i = 66.0 \pm 0.4^\circ$  and atomically flat cleaved surfaces enable us to measure at energies as low as  $5 \text{ cm}^{-1}$  without a detectable contribution from the laser line since the directly reflected light does not reach the spectrometer. The corresponding laser spot has an area of roughly  $50 \times 100 \mu\text{m}^2$  which prevents us from observing the possible emergence of the domains [17,30]. The inelastically scattered light is collected along the surface normal (crystallographic  $c$  axis) with an objective lens having a numerical aperture of 0.25. In the experiments presented here, the linear polarizations of the incident and scattered light are denoted as  $\mathbf{e}_i$  and  $\mathbf{e}_s$ , respectively. For  $\mathbf{e}_i$  horizontal to the plane of incidence there is no projection on the crystallographic  $c$  axis. For the low numerical aperture of the collection optics  $\mathbf{e}_s$  is always perpendicular to the  $c$  axis. Low-energy data up to  $550 \text{ cm}^{-1}$  were acquired in steps of  $\Delta\Omega = 1 \text{ cm}^{-1}$  with a resolution of  $\sigma \approx 3 \text{ cm}^{-1}$ . The symmetric phonon lines were modeled using Voigt profiles where the width of the Gaussian part is given by  $\sigma$ . For spectra up to higher energies the step width and resolution were set at  $\Delta\Omega = 50 \text{ cm}^{-1}$  and  $\sigma \approx 20 \text{ cm}^{-1}$ , respectively. The Raman tensors for the  $D_{3d}$  point group are given in Table I. Accordingly, parallel linear polarizations project both  $A_{1g}$  and  $E_g$  symmetries, while crossed linear polarizations only project  $E_g$ . The pure  $A_{1g}$  response then can be extracted by subtraction.

We have performed DFT calculations as implemented in the ABINIT package [31]. We have used the Perdew-Burke-Ernzerhof (PBE) functional, an energy cutoff of 50 Ha for the

TABLE I. Raman tensors for trigonal systems (point group  $D_{3d}$ ).

$$A_{1g} = \begin{pmatrix} a & 0 & 0 \\ 0 & a & 0 \\ 0 & 0 & b \end{pmatrix} \quad {}^1E_g = \begin{pmatrix} c & 0 & 0 \\ 0 & -c & d \\ 0 & d & 0 \end{pmatrix} \quad {}^2E_g = \begin{pmatrix} 0 & -c & -d \\ -c & 0 & 0 \\ -d & 0 & 0 \end{pmatrix}$$

plane-wave basis, and we have included spin-orbit coupling by means of fully relativistic Goedecker pseudopotentials [32,33], where Ta- $5d^36s^2$  and S- $3s^23p^4$  states are treated as valence electrons. The crystal structure was relaxed so that forces on each atom were below  $10 \mu\text{eV}/\text{\AA}$  and the total stress on the unit cell below 1 bar, yielding lattice parameters  $a = 3.44 \text{ \AA}$  and  $c = 6.83 \text{ \AA}$ . Subsequently, the phonons and the electron-phonon coupling (EPC) were obtained from density-functional perturbation theory (DFPT) calculations, also within ABINIT [34]. Here, we have used an  $18 \times 18 \times 12$   $\mathbf{k}$ -point grid for the electron wave vectors and a  $6 \times 6 \times 4$   $\mathbf{q}$ -point grid for the phonon wave vectors. For the electronic occupation we employed Fermi-Dirac smearing with broadening factor  $\sigma_{\text{FD}} = 0.01$  Ha, which is sufficiently high to avoid unstable phonon modes related to the CDW phases.

## III. RESULTS AND DISCUSSION

### A. Lattice dynamics of the charge-density wave regimes

Temperature-dependent symmetry-resolved Raman spectra of 1T-TaS<sub>2</sub> are presented in Fig. 1. It is obvious that their evolution with temperature is divided into three distinct ranges (IC-CDW, NC-CDW, and C-CDW) as indicated. The lattice dynamics for each of these ranges will be treated separately in the first part of the section. In the second part we address the electron dynamics.

#### 1. C-CDW phase

At the lowest temperatures 1T-TaS<sub>2</sub> exists in the commensurate C-CDW phase. Here, the atoms form so-called star-of-David clusters. Different studies report either triclinic stacking of these clusters leading to  $P\bar{1}$  unit cell symmetry [16], or trigonal or hexagonal stacking and  $P\bar{3}$  unit cell symmetry [15,18–20]. A factor group analysis predicts 57  $A_g$  Raman-active modes with an identical polarization dependence for  $P\bar{1}$  unit cell symmetry, and alternatively 19  $A_g + 19 E_g$  Raman-active modes for  $P\bar{3}$  unit cell symmetry [13]. Our polarized Raman scattering measurements at  $T = 4$  K, measured in two scattering channels, together with the corresponding cumulative fits are shown in Fig. 2. As it can be seen, we have observed modes of two different symmetries in the related scattering channels. This result indicates trigonal or hexagonal stacking of the star-of-David clusters. The symmetric phonon lines can be described by Voigt profiles, the best fit of which is shown as blue (for parallel light polarizations) and red (crossed polarizations) lines. After fitting Voigt profiles to the Raman spectra, 38 phonon modes were singled out. Following the selection rules for  $A_g$  and  $E_g$  symmetry modes, 19 were assigned as  $A_g$  and 19 as  $E_g$  symmetry, meaning all expected modes could be identified. The contribution from each mode to the cumulative fit is presented in Fig. 2 as green

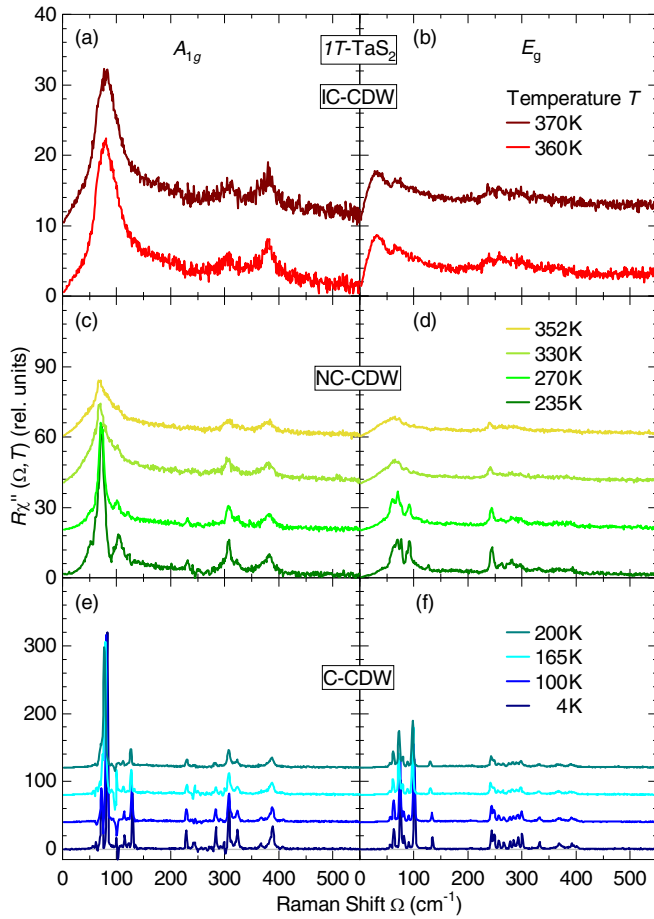


FIG. 1. Symmetry-resolved Raman spectra of  $1T$ -TaS<sub>2</sub> at temperatures as indicated. Both C-CDW (blue lines) and IC-CDW (red lines) domains yield significant contributions to the Raman spectra of the NC-CDW phase (green lines).

TABLE II.  $A_{1g}$  and  $E_g$  Raman mode energies experimentally obtained at  $T = 4$  K.

$n_o$	$\omega_{A_g}$ (cm <sup>-1</sup> )	$\omega_{E_g}$ (cm <sup>-1</sup> )
1	62.6	56.5
2	73.3	63.3
3	83.4	75.3
4	114.9	82.0
5	121.9	90.5
6	129.5	101.1
7	228.7	134.8
8	244.1	244.0
9	271.9	248.9
10	284.2	257.5
11	298.6	266.6
12	307.2	278.3
13	308.2	285.0
14	313.0	292.9
15	321.2	300.5
16	324.2	332.7
17	332.0	369.2
18	367.2	392.6
19	388.4	397.7

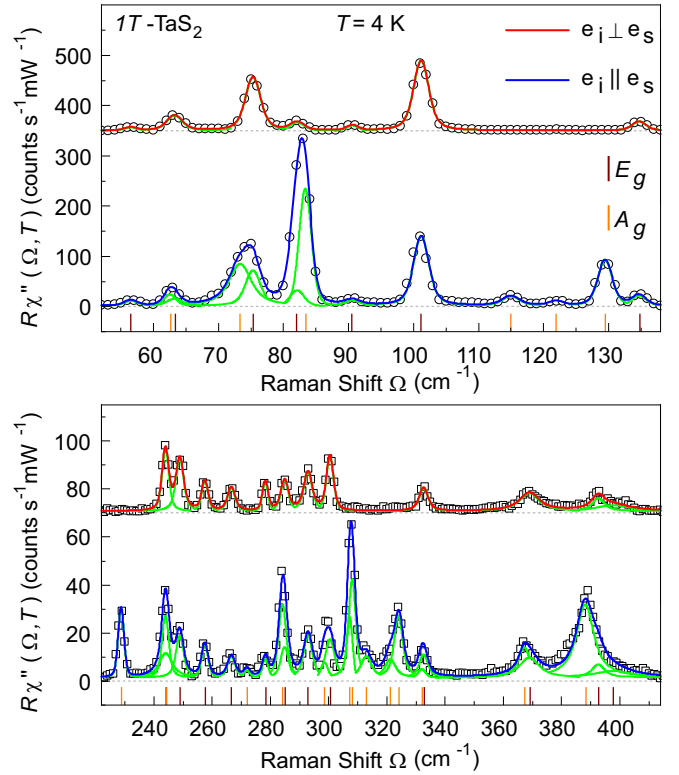


FIG. 2. Raman spectra at  $T = 4$  K, i.e., in the C-CDW phase, for parallel and crossed light polarizations. Red and blue solid lines represent fits of the experimental data using Voigt profiles. Spectra are offset for clarity. The short vertical lines depict central frequencies obtained from the data analysis. The exact energy values are presented in Table II.

lines, whereas the complete list of the corresponding phonon energies can be found in Table II.

## 2. IC-CDW phase

At the highest experimentally accessible temperatures  $1T$ -TaS<sub>2</sub> adopts the IC-CDW phase. Data collected by Raman scattering at  $T = 370$  K, containing all symmetries, are shown as a blue solid line in Fig. 3. As  $1T$ -TaS<sub>2</sub> is metallic in this phase [25] we expect the phonon lines to be superimposed on a continuum of electron-hole excitations which we approximate using a Drude spectrum shown as a dashed line [35,36].

Since the IC-CDW phase arises from the normal metallic phase, described by space group  $P\bar{3}m1$  [13,37], it is interesting to compare our Raman results on the IC-CDW phase to an *ab initio* calculation of the phonon dispersion in the normal phase, shown as an inset in Fig. 3. Four different optical modes were obtained at  $\Gamma$ :  $E_u$  at 189 cm<sup>-1</sup> (double degenerate),  $E_g$  at 247 cm<sup>-1</sup> (double degenerate),  $A_{2u}$  at 342 cm<sup>-1</sup>, and  $A_{1g}$  at 346 cm<sup>-1</sup>. A factor group analysis shows that two of these are Raman active, namely  $E_g$  and  $A_{1g}$  [13].

We observe that the calculated phonon eigenvalues of the simple metallic phase at  $\Gamma$  do not closely match the observed peaks in the experimental spectra of the IC-CDW phase. Rather, these correspond better to the calculated phonon density of states (PDOS), depicted in Fig. 3. There are essentially three different ways to project the PDOS in a Raman

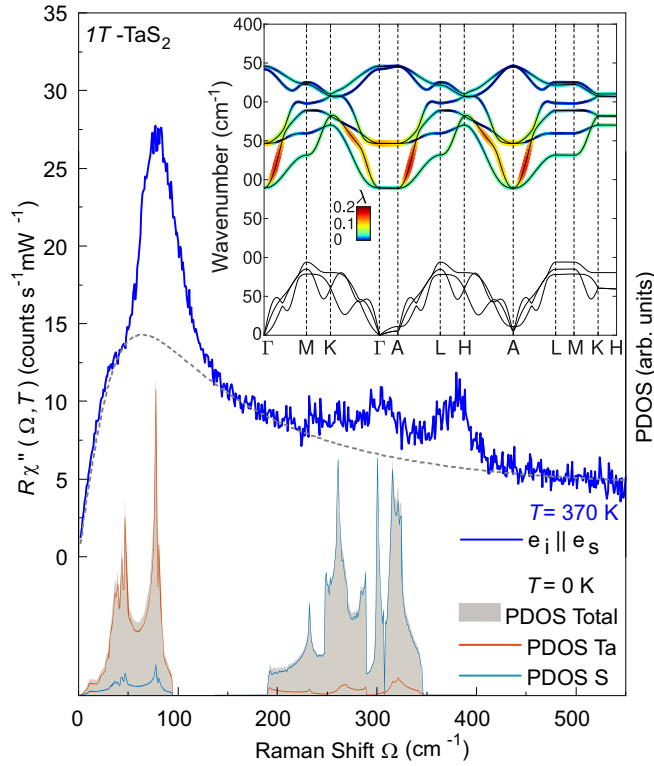


FIG. 3. Raman response for parallel light polarizations in the IC-CDW phase at 370 K (blue line). The dashed line depicts the possible electronic continuum. The contributions of the Ta (dark brown) and S atoms (light brown) to the calculated PDOS (gray area) are shown below. The inset shows the calculated phonon dispersion of 1T-TaS<sub>2</sub> in the simple metallic phase, with the electron-phonon coupling ( $\lambda$ ) of the optical branches indicated through the color scale.

experiment and to overcome the  $q \approx 0$  selection given by the small momentum of visible light: (i) scattering on impurities [38], (ii) enhanced electron-phonon coupling [39], and (iii) breaking of the translational symmetry in the IC-CDW phase. (i) We rule out chemical impurity scattering, expected to exist at all temperatures, as the low-temperature spectra (Fig. 2) show no signs thereof. (ii) The additional scattering channel may come from the electron-phonon coupling (EPC). The calculated EPC,  $\lambda$ , in the optical modes (inset of Fig. 3) is limited, yet not negligible, reaching maxima of  $\sim 0.2$  in the lower optical branches around the Brillouin zone (BZ) points  $\Gamma$  and A. The calculated atom-resolved PDOS shows the acoustic modes to be predominantly due to Ta and the optical modes due to S, as a result of their difference in atomic mass. The acoustic modes display several dips that are signatures of the latent CDW phases, for which the EPC cannot be reliably determined. Significant EPC in the optical modes of 1T-TaS<sub>2</sub> is furthermore supported by experimental results linking a sharp increase in the resistivity above the IC-CDW transition temperature to the EPC [37]. It also corroborates calculated [14] and experimentally obtained [13] values of the CDW gap, which correspond to intermediate to strong EPC [37]. (iii) Although EPC certainly contributes we believe that the majority of the additional scattering channels can be traced back to the incommensurate breaking of the translational in-

variance upon entering IC-CDW. Thus the “weighted” PDOS is projected into the Raman spectrum [see Figs. 1(a) and 1(b)]. These “weighting” factors depend on the specific symmetries along the phonon branches as well as the “new periodicity” and go well beyond the scope of this paper.

### 3. NC-CDW phase

The nearly commensurate phase is seen as a mixed phase consisting of regions of commensurate and incommensurate CDWs [40,41]. This coexistence of high- and low-temperature phases is observable in our temperature-dependent data as shown in Fig. 1. The spectra for the IC-CDW (red curves) and C-CDW phase (blue curves) are distinctly different, as also visible in the data shown above (Figs. 2 and 3). The spectra of the NC-CDW phase ( $235 \text{ K} < T < 352 \text{ K}$ ) comprise contributions from both phases. As 352 K is the highest temperature at which the contributions from the C-CDW phase can be observed in the spectra, we suggest that the phase transition temperature from IC-CDW to NC-CDW phase is somewhere in between 352 and 360 K. This conclusion is in good agreement with experimental results regarding this transition [4–6].

## B. Gap evolution

The opening of a typically momentum-dependent gap in the electronic excitation spectrum is a fundamental property of CDW systems which has also been observed in 1T-TaS<sub>2</sub> [13,37,42]. Here, in addition to the CDW, a Mott transition at the onset of the C-CDW phase leads to an additional gap opening in the bands close to the  $\Gamma$  point [21,43]. Symmetry-resolved Raman spectroscopy can provide additional information here using the momentum resolution provided by the selection rules. To this end, we look at the initial slopes of the electronic part of the spectra.

As shown in Figs. 4(a)–4(c), different symmetries project individual parts of the BZ [36,44]. The vertices given by the hexagonal symmetry of 1T-TaS<sub>2</sub> are derived in Appendix C. The  $A_{1g}$  vertex mainly highlights the area around the  $\Gamma$  point while the  $E_g$  vertices predominantly project the BZ boundaries. The opening of a gap at the Fermi level reduces  $N_F$ , leading to an increase of the resistivity in the case of 1T-TaS<sub>2</sub>. This reduction of  $N_F$  manifests itself also in the Raman spectra which, to zeroth order, are proportional to  $N_F$  [35,44]. As a result, the initial slope changes as shown Figs. 4(d) and 4(e), which zoom in on the low-energy region of the spectra from Fig. 1. The initial slope of the Raman response is  $R \lim_{\Omega \rightarrow 0} \frac{\partial \chi''}{\partial \Omega} \propto N_F \tau_0$ , where  $R$  incorporates only experimental factors [44]. The electronic relaxation  $\Gamma_0^* \propto (N_F \tau_0)^{-1}$  is proportional to the dc resistivity  $\rho(T)$  [45]. If a gap opens up there is vanishing intensity at  $T = 0$  below the gap edge for an isotropic gap. At finite temperature there are thermally excited quasiparticles which scatter. Thus, there is a linear increase at low energies [35]. The black lines in Figs. 4(d)–4(g) represent the initial slopes and their temperature dependences. The lines comprise carrier relaxation and gap effects, and we focus only on the relative changes.

Starting in the IC-CDW phase at  $T = 370 \text{ K}$  [Fig. 4(d)] the initial slope is higher for the  $E_g$  spectrum than for  $A_{1g}$  symmetry. While the CDW gap started to open already at



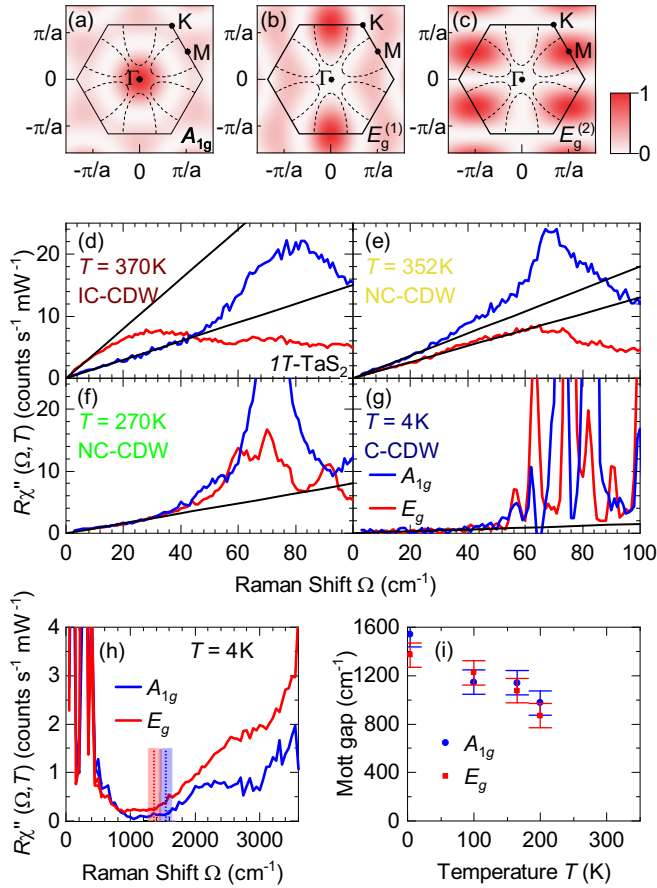


FIG. 4. Evolution of the gaps. (a)–(c) Squared Raman vertices and Fermi surface of  $1T\text{-TaS}_2$  for the indicated symmetries in the normal phase above  $T_C$ . The derivation of Raman vertices is presented in Appendix C. (d)–(g) Low-energy Raman spectra for  $A_{1g}$  symmetry (blue) and  $E_g$  symmetries (red) at temperatures as indicated. The spectra shown are zooms on the data shown in Fig. 1. The black lines highlight the initial slope of the spectra. (h) High-energy spectra at 4 K. Vertical dashed lines and colored bars indicate the approximate size and error bars of the Mott gap for the correspondingly colored spectrum. (i) Temperature dependence of the Mott gap  $\Delta_\mu$  ( $\mu = A_{1g}, E_g$ ).

554 K around the  $M$  points [43], which are highlighted by the  $E_g$  vertex, the Fermi surface projected by the  $E_g$  vertex continues to exist. Thus, we may interpret the different slopes as a manifestation of a momentum-dependent gap in the IC-CDW phase and assume overall intensity effects to be symmetry independent for all temperatures. At  $T = 352$  K [Fig. 4(e)] the slope for  $E_g$  symmetry is substantially reduced to below the  $A_{1g}$  slope due to a strong increase of the CDW gap in the commensurate regions [43] which emerge upon entering the NC-CDW phase. Further cooling also decreases the slope for the  $A_{1g}$  spectrum, as the Mott gap around the  $\Gamma$  point starts to open within the continuously growing C-CDW domains [40,41]. Below  $T = 270$  K the initial slopes are identical for both symmetries and decrease with temperature. Apparently, the Mott gap opens up on the entire Fermi surface in direct correspondence with the increase of the resistivity by approximately an order of magnitude [3]. Finally, at the lowest temperature close to 4 K the initial slopes drop to almost zero

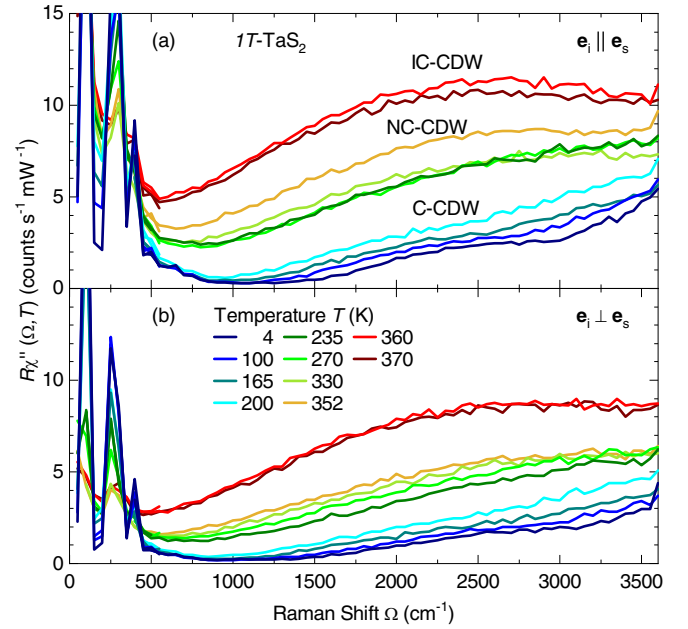


FIG. 5. Raman spectra up to high energies for (a) parallel and (b) crossed polarizations of the incident and scattered light at temperatures as given in the legend.

[Fig. 4(g)], indicating vanishing conductivity or fully gapped bands in the entire BZ.

Concomitantly, and actually more intuitive for the opening of a gap, we observe the loss of intensity in the Raman spectra below a threshold at an energy  $\Omega_{\text{gap}}$ . Below  $30 \text{ cm}^{-1}$  the intensity is smaller than  $0.2 \text{ counts}(\text{mW s})^{-1}$  [Fig. 4(g)] and still smaller than  $0.3 \text{ counts}(\text{mW s})^{-1}$  up to  $1500 \text{ cm}^{-1}$  [Fig. 4(h)]. For a superconductor or a CDW system the threshold is given by  $2\Delta$ , where  $\Delta$  is the single-particle gap, and a pileup of intensity for higher energies,  $\Omega > 2\Delta$  [44]. A pileup of intensity cannot be observed here. Rather, the overall intensity is further reduced with decreasing temperature as shown in Figs. 5 and 6 in Appendixes A and B. In particular, the reduction occurs in distinct steps between the phases and continuous inside the phases with the strongest effect in the C-CDW phase below approximately 210 K (Fig. 5). In a system as clean as  $1T\text{-TaS}_2$  the missing pileup in the C-CDW phase is surprising and argues for an alternative interpretation.

In a Mott system, the gap persists to be observable but the pileup is not a coherence phenomenon and has not been observed yet. In fact, the physics is quite different, and the conduction band is split symmetrically about the Fermi energy  $E_F$  into a lower and an upper Hubbard band. Thus in the case of Mott-Hubbard physics the experimental signatures are more such as those expected for an insulator or semiconductor having a small gap, where at  $T = 0$  there is a range without intensity and an interband onset with a band-dependent shape. At finite temperature there are thermal excitations inside the gap. For  $1T\text{-TaS}_2$  at the lowest accessible temperature, both symmetries exhibit a flat, nearly vanishing electronic continuum below a slightly symmetry-dependent threshold (superposed by the phonon lines at low energies). Above the threshold a weakly structured increase is observed. We interpret this onset as the distance of the lower

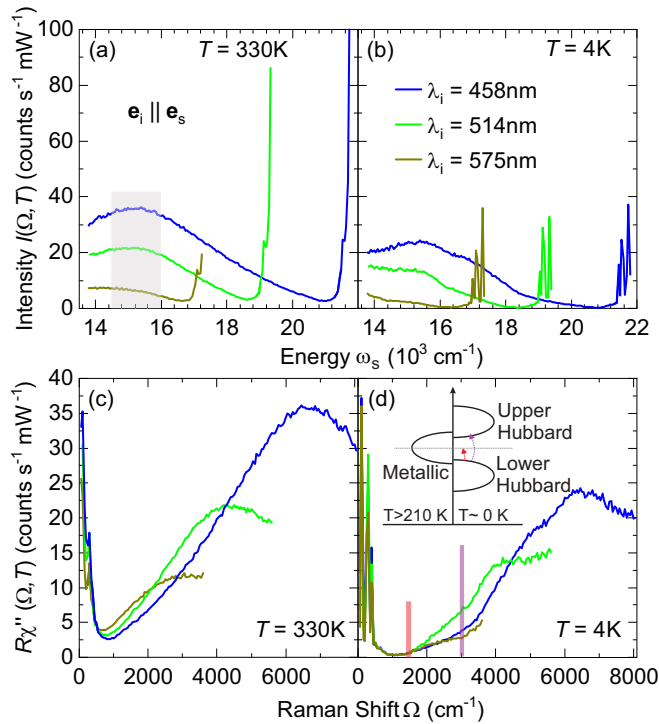


FIG. 6. Luminescence contribution to the Raman data. (a), (b) Intensity as a function of the absolute frequency for (a)  $T = 330$  K and (b)  $T = 4$  K. The approximate peak maximum of the contribution attributed to luminescence is highlighted by the gray shaded area. (c), (d) Raman susceptibility calculated from (a) and (b), respectively, shown as a function of frequency (Raman) shift. The luminescence peak appears at different Raman shifts depending on the wavelength of the laser light. At  $T = 4$  K the spectra are identical up to  $1600$   $\text{cm}^{-1}$  for all laser light wavelengths.

Hubbard band from the Fermi energy  $E_F$  or half of the distance between the lower and the upper Hubbard band, shown as vertical dashed lines at  $1350\text{--}1550$   $\text{cm}^{-1} \equiv 170\text{--}190$  meV [Fig. 4(h)]. The energy is in good agreement with gap obtained from the in-plane angle-resolved photoemission spectroscopy (ARPES) [43], scanning tunneling spectroscopy [46], and infrared spectroscopy [13] which may be compared directly with our Raman results measured with in-plane polarizations. Upon increasing the temperature the size of the gap shrinks uniformly in both symmetries [Fig. 4(i)] and may point to an onset above the C-CDW phase transition, consistent with the result indicated by the initial slope. However, we cannot track the development of the gap into the NC-CDW phase as an increasing contribution of luminescence (see Appendix B) overlaps with the Raman data.

Recently, it was proposed on the basis of DFT calculations that  $1T\text{-TaS}_2$  orders also along the  $c$  axis perpendicular to the planes in the C-CDW state [24,25]. This quasi-one-dimensional (1D) coupling is unexpectedly strong and the resulting metallic band is predicted to have a width of approximately  $0.5$  eV. For specific relative ordering of the star of David patterns along the  $c$  axis this band develops a gap of  $0.15$  eV at  $E_F$  [25], which is intriguingly close to the various experimental observations. However, since our light polarizations are strictly in plane, we have to conclude that the gap

observed here (and presumably in the other experiments) is an in-plane gap. Our experiment cannot detect an out-of-plane gap. Thus, neither a quasimetallic dispersion along the  $c$  axis nor a gap in this band along  $k_z$  may be excluded in the C-CDW phase. However, there is compelling evidence for a Mott-like gap in the layers rather than a CDW gap.

#### IV. CONCLUSIONS

We have presented a study of the various charge density wave regimes in  $1T\text{-TaS}_2$  by inelastic light scattering, supported by *ab initio* calculations. The spectra of lattice excitations in the commensurate CDW (C-CDW) phase determine the unit cell symmetry to be  $P\bar{3}$ , indicating trigonal or hexagonal stacking of the “star-of-David” structure. The high-temperature spectra of the incommensurate CDW (IC-CDW) state are dominated by a projection of the phonon density of states caused by either a significant electron-phonon coupling or, more likely, the superstructure. The intermediate nearly commensurate (NC-CDW) phase is confirmed to be a mixed regime of commensurate and incommensurate regions contributing to the phonon spectra below an onset temperature  $T_{\text{NC}} \approx 352\text{--}360$  K, in good agreement with previously reported values. At the lowest measured temperatures, the observation of a virtually clean gap without a redistribution of spectral weight from low to high energies below  $T_C$  argues for the existence of a Mott metal-insulator transition at a temperature of order  $100$  K. The magnitude of the gap is found to be  $\Omega_{\text{gap}} \approx 170\text{--}190$  meV and has little symmetry, thus momentum, dependence, in agreement with earlier ARPES results [37]. At  $200$  K, on the high-temperature end of the C-CDW phase, the gap shrinks to  $\sim 60\%$  of its low-temperature value. Additionally, the progressive filling of the CDW gaps by thermal excitations is tracked via the initial slope of the spectra, and indicates that the Mott gap opens primarily on the parts of the Fermi surface closest to the  $\Gamma$  point.

Our results demonstrate the potential of using inelastic light scattering to probe the momentum dependence and energy scale of changes in the electronic structure driven by low-temperature collective quantum phenomena. This opens perspectives to investigate the effect of hybridization on collective quantum phenomena in heterostructures composed of different 2D materials, e.g., alternating  $T$  and  $H$  monolayers as in the  $4Hb\text{-TaS}_2$  phase [47].

#### ACKNOWLEDGMENTS

The authors acknowledge funding provided by the Institute of Physics Belgrade through the grant by the Ministry of Education, Science and Technological Development of the Republic of Serbia. The work was supported by the Science Fund of the Republic of Serbia, PROMIS, No. 6062656, StrainedFeSC, and by Research Foundation-Flanders (FWO). J.B. acknowledges support of a postdoctoral fellowship of the FWO, and of the Erasmus + program for staff mobility and training (KA107, 2018) for a research stay at the Institute of Physics Belgrade, during which part of the work was carried out. The computational resources and services used for the first-principles calculations in this work were provided by the VSC (Flemish Supercomputer Center), funded by the

FWO and the Flemish Government – department EWI. Work at Brookhaven is supported by the U.S. DOE under Contract No. DESC0012704. A.B. and R.H. acknowledge support by the German research foundation (DFG) via Projects No. Ha2071/12-1 and No. 107745057 – TRR 80 and by the DAAD via the project-related personal exchange program PPP with Serbia Grant No. 57449106.

### APPENDIX A: RAW DATA

Figure 5 shows Raman spectra at temperatures ranging from  $T = 4$  to 370 K for parallel [Fig. 5(a)] and crossed [Fig. 5(b)] in-plane light polarizations. The spectra were measured in steps of  $\Delta\Omega = 50 \text{ cm}^{-1}$  and a resolution of  $\sigma \approx 20 \text{ cm}^{-1}$ . Therefore neither the shapes nor the positions of the phonon lines below  $500 \text{ cm}^{-1}$  may be resolved. All spectra reach a minimum in the range from 500 to  $1600 \text{ cm}^{-1}$ . At energies above  $500 \text{ cm}^{-1}$  the overall intensities are strongly temperature dependent and decreasing with decreasing temperature. Three clusters of spectra are well separated according to the phases they belong to.

In the C-CDW phase ( $T \leq 200 \text{ K}$ , blue lines) the spectra start to develop substructures at 1500 and  $3000 \text{ cm}^{-1}$ . The spectra at 200 K increase almost linearly with energy. The spectra of the NC- and IC-CDW phases exhibit a broad maximum centered in the region of  $2200\text{--}3200 \text{ cm}^{-1}$  which may be attributed to luminescence (see Appendix B). For clarification we measured a few spectra with various laser lines for excitation.

### APPENDIX B: LUMINESCENCE

Figure 6 shows Raman spectra measured with parallel light polarizations for three different wavelengths  $\lambda_i$  of the incident laser light. Figures 6(a) and 6(b) depict the measured intensity  $I$  (without the Bose factor) as a function of the absolute frequency  $\tilde{\nu}$  of the scattered light.

At high temperature [ $T = 330 \text{ K}$ , Fig. 6(a)] a broad peak can be seen for all  $\lambda_i$  which is centered at a fixed frequency of  $15\,200 \text{ cm}^{-1}$  of the scattered photons (gray shaded area). The peak intensity decreases for increasing  $\lambda_i$  (decreasing energy). Correspondingly, this peak's center depends on the laser wavelength in the spectra shown as a function of the Raman shift [Fig. 6(c)]. This behavior indicates that the origin of this excitation is likely to be luminescence where transitions at fixed absolute final frequencies are expected.

At low temperature [Fig. 6(b)] we can no longer find a structure at a fixed absolute energy. Rather, as already indicated in the main part, the spectra develop additional, yet weak, structures which are observable in all spectra but are particularly pronounced for blue excitation. For green and yellow excitation the spectral range of the spectrometer, limited to 732 nm, is not wide enough for a deeper insight into the luminescence contributions (at energies different from those at high temperature) and no maximum common to all three spectra is observed. If these spectra are plotted as a function of the Raman shift, the changes in slope at 1500 and  $3000 \text{ cm}^{-1}$  are found to be in the same position for all  $\lambda_i$ , values thus arguing for inelastic scattering rather than luminescence. Since we do currently not have the appropriate experimental

tools for an in-depth study, our interpretation is preliminary although supported by the observations in Fig. 6(d).

As shown in the inset of Fig. 6(d) we propose a scenario on the basis of Mott physics. In the C-CDW phase the reduced bandwidth is no longer the largest energy and the Coulomb repulsion  $U$  becomes relevant [22] and splits the conduction band into a lower and upper Hubbard band. We assume that the onset of scattering at  $1500 \text{ cm}^{-1}$  corresponds to the distance of the highest energy of the lower Hubbard band to the Fermi energy  $E_F$ . The second onset corresponds then to the distance between the highest energy of the lower Hubbard band and the lowest energy of the upper Hubbard band. An important question needs to be answered: Into which unoccupied states right above  $E_F$  does the first process scatter electrons? We may speculate that some DOS is provided by the metallic band dispersing along  $k_z$  or by the metallic domain walls between the different types of ordering patterns along the  $c$  axis observed recently by tunneling spectroscopy [46]. These quasi-1D domain walls would provide the states required for the onset of scattering at high energy but are topologically too small for providing enough density of states for a measurable intensity at low energy [Fig. 4(g)] in a location-integrated experiment such as Raman scattering.

### APPENDIX C: DERIVATION OF THE RAMAN VERTICES

Phenomenologically, the Raman vertices can be derived based on lattice symmetry, which are proportional to the Brillouin zone harmonics. They are a set of functions that exhibit the symmetry and periodicity of the lattice structure proposed by Allen [48]. These functions make the  $k$ -space sums and energy integrals more convenient than that of the Cartesian basis or the spherical harmonics basis, especially for those materials who have anisotropic and/or multiple Fermi pockets. The three Cartesian components of the Fermi velocity  $v_k$  are recommended to generate this set of functions since they inherit the symmetry and periodicity of the crystal lattice naturally. However, in most cases, we do not know the details of band dispersion. A phenomenological method is needed to construct such a set of basis functions. Here, we demonstrate a method based on the group theory. The Brillouin zone harmonics can be obtained by the projection operation on specific trial functions.

For a certain group  $G$  with symmetry elements  $R$  and symmetry operators  $\hat{P}_R$ , it can be described by several irreducible representations  $\Gamma_n$ , where  $n$  labels the representation. For each irreducible representation, there are corresponding basis functions  $\Phi_{\Gamma_n}^j$  that can be used to generate representation matrices for a particular symmetry. Here,  $j$  labels the component or partner of the representations. For an arbitrary function  $F$ , we have

$$F = \sum_{\Gamma_n} \sum_j f_j^{\Gamma_n} \Phi_{\Gamma_n}^j. \quad (\text{C1})$$

According to the group theory, we can always define a projection operator by the relation [49]

$$\hat{P}^{\Gamma_n} = \frac{d}{N} \sum_R \chi^{\Gamma_n}(R) * \hat{P}_R, \quad (\text{C2})$$

TABLE III. Symmetry operations  $\hat{P}_R$  and corresponding character table of the  $D_{3d}$  point group.

$\hat{P}_R$	$x'$	$y'$	$z'$	$\chi^{\Gamma_n}(R)$	
				$A_{1g}$	$E_g$
$E$	$x$	$y$	$z$	1	2
$C_3^1$	$-\frac{1}{2}x + \frac{\sqrt{3}}{2}y$	$-\frac{\sqrt{3}}{2}x - \frac{1}{2}y$	$z$	1	-1
$C_3^{-1}$	$-\frac{1}{2}x - \frac{\sqrt{3}}{2}y$	$\frac{\sqrt{3}}{2}x - \frac{1}{2}y$	$z$	1	-1
$C_2'$	$x$	$-y$	$-z$	1	0
$C_2''$	$-\frac{1}{2}x + \frac{\sqrt{3}}{2}y$	$\frac{\sqrt{3}}{2}x + \frac{1}{2}y$	$-z$	1	0
$C_2'''$	$-\frac{1}{2}x - \frac{\sqrt{3}}{2}y$	$-\frac{\sqrt{3}}{2}x + \frac{1}{2}y$	$-z$	1	0
$I$	$-x$	$-y$	$-z$	1	2
$S_6^1$	$\frac{1}{2}x - \frac{\sqrt{3}}{2}y$	$\frac{\sqrt{3}}{2}x + \frac{1}{2}y$	$-z$	1	-1
$S_6^{-1}$	$\frac{1}{2}x + \frac{\sqrt{3}}{2}y$	$-\frac{\sqrt{3}}{2}x + \frac{1}{2}y$	$-z$	1	-1
$\sigma_v'$	$-x$	$y$	$z$	1	0
$\sigma_v''$	$\frac{1}{2}x - \frac{\sqrt{3}}{2}y$	$-\frac{\sqrt{3}}{2}x - \frac{1}{2}y$	$z$	1	0
$\sigma_v'''$	$\frac{1}{2}x + \frac{\sqrt{3}}{2}y$	$\frac{\sqrt{3}}{2}x - \frac{1}{2}y$	$z$	1	0

that satisfies the relation

$$\hat{P}^{\Gamma_n} F = \sum_j f_j^{\Gamma_n} \Phi_{\Gamma_n}^j, \quad (C3)$$

where  $d$  is the dimensionality of the irreducible representation  $\Gamma_n$ ,  $N$  is the number of symmetry operators in the group, and  $\chi^{\Gamma_n}(R)$  is the character of the matrix of symmetry operator  $R$  in irreducible representation  $\Gamma_n$ . By projection operation on a certain irreducible representation  $\Gamma_n$ , we can directly get its basis functions  $\Phi_{\Gamma_n}^j$ .

The basis functions are not unique. In specific physical problems, it is useful to use physical insight to guess an appropriate arbitrary function to find the basis functions for specific

problems.  $1T$ -TaS<sub>2</sub> belongs to the  $D_{3d}$  point group. There are 12 symmetry operators in this group, i.e.,  $E$ ,  $C_3^1$ ,  $C_3^{-1}$ ,  $C_2'$ ,  $C_2''$ ,  $C_2'''$ ,  $I$ ,  $S_6^1$ ,  $S_6^{-1}$ ,  $\sigma_v'$ ,  $\sigma_v''$ ,  $\sigma_v'''$ . The coordinate transformations after symmetry operations and the corresponding character table are listed in Table III.

In order to simulate the periodicity of the Brillouin zone, trigonometric functions are used as trial functions. According to the parity of the irreducible representations, we can choose an appropriate trigonometric function, e.g., a sine function for odd parity representation and cosine function for even parity representation. The combinations of them are also available.

Here, we use  $F = \cos(k_x a)$  as a trial function, where  $a$  is the in-plane crystal constant. The basis function of  $A_{1g}$  can be derived as

$$\Phi_{A_{1g}}(\mathbf{k}) = \frac{1}{3} \left[ \cos(k_x a) + 2 \cos\left(\frac{1}{2}k_x a\right) \cos\left(\frac{\sqrt{3}}{2}k_y a\right) \right]. \quad (C4)$$

With the same method, we obtain a basis function of  $E_g$  as

$$\Phi_{E_g^1}(\mathbf{k}) = \frac{2}{3} \left[ \cos(k_x a) - \cos\left(\frac{1}{2}k_x a\right) \cos\left(\frac{\sqrt{3}}{2}k_y a\right) \right]. \quad (C5)$$

Since the  $E_g$  is a two-dimensional representation, the projection operation provides only one of the two basis functions of the corresponding subspace. The second function is found based on the subspace invariance under the symmetry operations (e.g., if we operate  $\Phi_{E_g^1}$  with  $C_3^1$  symmetry, the result can be presented as a linear combination of  $\Phi_{E_g^1}$  and  $\Phi_{E_g^2}$ ). Thus we obtain

$$\Phi_{E_g^2}(\mathbf{k}) = 2 \sin\left(\frac{1}{2}k_x a\right) \sin\left(\frac{\sqrt{3}}{2}k_y a\right). \quad (C6)$$

- [1] J. C. Tsang, J. E. Smith, M. W. Shafer, and S. F. Meyer, Raman spectroscopy of the charge-density-wave state in  $1T$ - and  $2H$ -TaSe<sub>2</sub>, *Phys. Rev. B* **16**, 4239 (1977).
- [2] C. J. Sayers, H. Hedayat, A. Ceraso, F. Musser, M. Cattelan, L. S. Hart, L. S. Farrar, S. Dal Conte, G. Cerullo, C. Dallera, E. Da Como, and E. Carpene, Coherent phonons and the interplay between charge density wave and Mott phases in  $1T$ -TaSe<sub>2</sub>, *Phys. Rev. B* **102**, 161105(R) (2020).
- [3] A. J. Wilson, J. F. D. Salvo, and S. Mahajan, Charge-density waves and superlattices in the metallic layered transition metal dichalcogenides, *Adv. Phys.* **24**, 117 (1975).
- [4] C. B. Scruby, P. M. Williams, and G. S. Parry, The role of charge density waves in structural transformations of  $1T$ -TaS<sub>2</sub>, *Philos. Mag.* **31**, 255 (1975).
- [5] R. E. Thomson, B. Burk, A. Zettl, and J. Clarke, Scanning tunneling microscopy of the charge-density-wave structure in  $1T$ -TaS<sub>2</sub>, *Phys. Rev. B* **49**, 16899 (1994).
- [6] W. Wen, C. Dang, and L. Xie, Photoinduced phase transitions in two-dimensional charge-density-wave  $1T$ -TaS<sub>2</sub>, *Chin. Phys. B* **28**, 058504 (2019).
- [7] D. Svetin, I. Vaskivskiy, S. Brazovskii, Mertelj, and D. Mihailovic, Three-dimensional resistivity and switching between correlated electronic states in  $1T$ -TaS<sub>2</sub>, *Sci. Rep.* **7**, 46048 (2017).
- [8] D. Svetin, I. Vaskivskiy, P. Sutar, E. Goresnik, J. Gospodaric, T. Mertelj, and D. Mihailovic, Transitions between photoinduced macroscopic quantum states in  $1T$ -TaS<sub>2</sub> controlled by substrate strain, *Appl. Phys. Express* **7**, 103201 (2014).
- [9] G. Liu, B. Debnath, T. R. Pope, T. T. Salguero, R. K. Lake, and A. A. Balandin, A charge-density wave oscillator based on an integrated tantalum disulfide-boron nitride-graphene device operating at room temperature, *Nat. Nanotechnol.* **11**, 845 (2016).
- [10] R. Salgado, A. Mohammadzadeh, F. Kargar, A. Geremew, C.-Y. Huang, M. A. Bloodgood, S. Romyantsev, T. T. Salguero, and A. A. Balandin, Low-frequency noise spectroscopy of charge-density-wave phase transitions in vertical quasi-2D  $1T$ -TaS<sub>2</sub> devices, *Appl. Phys. Express* **12**, 037001 (2019).
- [11] Z. X. Wang, Q. M. Liu, L. Y. Shi, S. J. Zhang, T. Lin, T. Dong, D. Wu, and N. L. Wang, Photoinduced hidden CDW state and relaxation dynamics of  $1T$ -TaS<sub>2</sub> probed by time-resolved terahertz spectroscopy, *arXiv:1906.01500*.
- [12] L. Stojchevska, I. Vaskivskiy, T. Mertelj, P. Kusar, D. Svetin, S. Brazovskii, and D. Mihailovic, Ultrafast switching to a stable

- hidden quantum state in an electronic crystal, *Science* **344**, 177 (2014).
- [13] L. V. Gasparov, K. G. Brown, A. C. Wint, D. B. Tanner, H. Berger, G. Margaritondo, R. Gaál, and L. Forró, Phonon anomaly at the charge ordering transition in  $1T$ -TaS<sub>2</sub>, *Phys. Rev. B* **66**, 094301 (2002).
- [14] O. R. Albertini, R. Zhao, R. L. McCann, S. Feng, M. Terrones, J. K. Freericks, J. A. Robinson, and A. Y. Liu, Zone-center phonons of bulk, few-layer, and monolayer  $1T$ -TaS<sub>2</sub>: Detection of commensurate charge density wave phase through Raman scattering, *Phys. Rev. B* **93**, 214109 (2016).
- [15] S. Uchida and S. Sugai, Infrared and raman studies on a commensurate CDW states in transition metal dichalcogenides, *Physica B+C* **105**, 393 (1981).
- [16] R. Brouwer and F. Jellinek, The low-temperature superstructures of  $1T$ -TaSe<sub>2</sub> and  $2H$ -TaSe<sub>2</sub>, *Physica B+C* **99**, 51 (1980).
- [17] A. Zong, X. Shen, A. Kogar, L. Ye, C. Marks, D. Chowdhury, T. Rohwer, B. Freelon, S. Weathersby, R. Li, J. Yang, J. Checkelsky, X. Wang, and N. Gedik, Ultrafast manipulation of mirror domain walls in a charge density wave, *Sci. Adv.* **4**, eaau5501 (2018).
- [18] J. R. Duffay and R. D. Kirby, Raman scattering from  $1T$ -TaS<sub>2</sub>, *Solid State Commun.* **20**, 617 (1976).
- [19] T. Hirata and F. S. Ohuchi, Temperature dependence of the Raman spectra of  $1T$ -TaS<sub>2</sub>, *Solid State Commun.* **117**, 361 (2001).
- [20] S. L. L. M. Ramos, R. Plumadore, J. Boddison-Chouinard, S. W. Hla, J. R. Guest, D. J. Gosztola, M. A. Pimenta, and A. Luican-Mayer, Suppression of the commensurate charge density wave phase in ultrathin  $1T$ -TaS<sub>2</sub> evidenced by Raman hyperspectral analysis, *Phys. Rev. B* **100**, 165414 (2019).
- [21] B. Sipos, A. F. Kusmartseva, A. Akrap, H. Berger, L. Forró, and E. Tutis, From Mott state to superconductivity in  $1T$ -TaS<sub>2</sub>, *Nat. Mater.* **7**, 960 (2008).
- [22] P. Fazekas and E. Tosatti, Electrical, structural and magnetic properties of pure and doped  $1T$ -TaS<sub>2</sub>, *Philos. Mag. B* **39**, 229 (1979).
- [23] E. Martino, A. Pisoni, L. Čirić, A. Arakcheeva, H. Berger, A. Akrap, C. Putzke, P. J. W. Moll, I. Batistić, E. Tutiš, L. Forró, and K., Preferential out-of-plane conduction and quasi-one-dimensional electronic states in layered  $1T$ -TaS<sub>2</sub>, *npj 2D Mater. Appl.* **4**, 7 (2020).
- [24] P. Darancet, A. J. Millis, and C. A. Marianetti, Three-dimensional metallic and two-dimensional insulating behavior in octahedral tantalum dichalcogenides, *Phys. Rev. B* **90**, 045134 (2014).
- [25] S.-H. Lee, J. S. Goh, and D. Cho, Origin of the Insulating Phase and First-Order Metal-Insulator Transition in  $1T$ -TaS<sub>2</sub>, *Phys. Rev. Lett.* **122**, 106404 (2019).
- [26] Y. Ma, Y. Hou, C. Lu, L. Li, and C. Petrovic, Possible origin of nonlinear conductivity and large dielectric constant in the commensurate charge-density-wave phase of  $1T$ -TaS<sub>2</sub>, *Phys. Rev. B* **97**, 195117 (2018).
- [27] L. J. Li, W. J. Lu, X. D. Zhu, L. S. Ling, Z. Qu, and Y. P. Sun, Fe-doping induced superconductivity in the charge-density-wave system  $1T$ -TaS<sub>2</sub>, *Europhys. Lett.* **98**, 29902 (2012).
- [28] Y. Liu, R. Ang, W. J. Lu, W. H. Song, L. J. Li, and Y. P. Sun, Superconductivity induced by Se-doping in layered charge-density-wave system  $1T$ -TaS<sub>2-x</sub>Se<sub>x</sub>, *Appl. Phys. Lett.* **102**, 192602 (2013).
- [29] R. Ang, Y. Miyata, E. Ieki, K. Nakayama, T. Sato, Y. Liu, W. J. Lu, Y. P. Sun, and T. Takahashi, Superconductivity and bandwidth-controlled Mott metal-insulator transition in  $1T$ -TaS<sub>2-x</sub>Se<sub>x</sub>, *Phys. Rev. B* **88**, 115145 (2013).
- [30] M. Bovet, D. Popović, F. Clerc, C. Koitzsch, U. Probst, E. Bucher, H. Berger, D. Naumović, and P. Aebi, Pseudogapped Fermi surfaces of  $1T$ -TaS<sub>2</sub> and  $1T$ -TaSe<sub>2</sub>: A charge density wave effect, *Phys. Rev. B* **69**, 125117 (2004).
- [31] X. Gonze, B. Amadon, P.-M. Anglade, J.-M. Beuken, F. Bottin, P. Boulanger, F. Bruneval, D. Caliste, R. Caracas, M. Côté, T. Deutsch, L. Genovese, P. Ghosez, M. Giantomassi, S. Goedecker, D. Hamann, P. Hermet, F. Jollet, G. Jomard, S. Leroux *et al.*, ABINIT: First-principles approach to material and nanosystem properties, *Comput. Phys. Commun.* **180**, 2582 (2009).
- [32] S. Goedecker, M. Teter, and J. Hutter, Separable dual-space Gaussian pseudopotentials, *Phys. Rev. B* **54**, 1703 (1996).
- [33] M. Krack, Pseudopotentials for H to Kr optimized for gradient-corrected exchange-correlation functionals, *Theor. Chem. Acc.* **114**, 145 (2005).
- [34] X. Gonze, D. C. Allan, and M. P. Teter, Dielectric Tensor, Effective Charges, and Phonons in  $\alpha$ -Quartz by Variational Density-Functional Perturbation Theory, *Phys. Rev. Lett.* **68**, 3603 (1992).
- [35] A. Zawadowski and M. Cardona, Theory of Raman scattering on normal metals with impurities, *Phys. Rev. B* **42**, 10732 (1990).
- [36] N. Lazarević and R. Hackl, Fluctuations and pairing in Fe-based superconductors: Light scattering experiments, *J. Phys.: Condens. Matter* **32**, 413001 (2020).
- [37] K. Rossnagel, On the origin of charge-density waves in select layered transition-metal dichalcogenides, *J. Phys.: Condens. Matter* **23**, 213001 (2011).
- [38] R. Shuker and R. W. Gammon, Raman-Scattering Selection-Rule Breaking and the Density of States in Amorphous Materials, *Phys. Rev. Lett.* **25**, 222 (1970).
- [39] A. Baum, A. Milosavljević, N. Lazarević, M. M. Radonjić, B. Nikolić, M. Mitschek, Z. I. Maranloo, M. Šćepanović, M. Grujić-Brojčin, N. Stojilović, M. Opel, A. Wang, C. Petrovic, Z. V. Popović, and R. Hackl, Phonon anomalies in FeS, *Phys. Rev. B* **97**, 054306 (2018).
- [40] A. Spijkerman, J. L. de Boer, A. Meetsma, G. A. Wiegers, and S. van Smaalen, X-ray crystal-structure refinement of the nearly commensurate phase of  $1T$ -TaS<sub>2</sub> in  $(3+2)$ -dimensional superspace, *Phys. Rev. B* **56**, 13757 (1997).
- [41] R. He, J. Okamoto, Z. Ye, G. Ye, H. Anderson, X. Dai, X. Wu, J. Hu, Y. Liu, W. Lu, Y. Sun, A. N. Pasupathy, and A. W. Tsen, Distinct surface and bulk charge density waves in ultrathin  $1T$ -TaS<sub>2</sub>, *Phys. Rev. B* **94**, 201108(R) (2016).
- [42] G. Grüner, The dynamics of charge-density waves, *Rev. Mod. Phys.* **60**, 1129 (1988).
- [43] C. Sohrt, A. Stange, M. Bauer, and K. Rossnagel, How fast can a Peierls–Mott insulator be melted?, *Faraday Discuss.* **171**, 243 (2014).
- [44] T. P. Devereaux and R. Hackl, Inelastic light scattering from correlated electrons, *Rev. Mod. Phys.* **79**, 175 (2007).
- [45] M. Opel, R. Nemetschek, C. Hoffmann, R. Philipp, P. F. Müller, R. Hackl, I. Tüttő, A. Erb, B. Revaz, E. Walker, H. Berger, and L. Forró, Carrier relaxation, pseudogap, and superconducting

- gap in high- $T_c$  cuprates: A Raman scattering study, *Phys. Rev. B* **61**, 9752 (2000).
- [46] J. Skolimowski, Y. Gerasimenko, and R. Žitko, Mottness Collapse without Metallization in the Domain Wall of the Triangular-Lattice Mott Insulator  $1T$ -TaS<sub>2</sub>, *Phys. Rev. Lett.* **122**, 036802 (2019).
- [47] A. Ribak, R. M. Skiff, M. Mograbi, P. K. Rout, M. H. Fischer, J. Ruhman, K. Chashka, Y. Dagan, and A. Kanigel, Chiral superconductivity in the alternate stacking compound  $4Hb$ -TaS<sub>2</sub>, *Sci. Adv.* **6**, eaax9480 (2020).
- [48] P. B. Allen, Fermi-surface harmonics: A general method for nonspherical problems. Application to Boltzmann and Eliashberg equations, *Phys. Rev. B* **13**, 1416 (1976).
- [49] M. S. Dresselhaus, G. Dresselhaus, and A. Jorio, *Group Theory* (Springer, Berlin, 2008).

## Evolution of lattice, spin, and charge properties across the phase diagram of $\text{FeSe}_{1-x}\text{S}_x$

N. Lazarević<sup>1,\*</sup>, A. Baum<sup>2,3,\*</sup>, A. Milosavljević<sup>1</sup>, L. Peis<sup>2,3,†</sup>, R. Stumberger<sup>2,3,‡</sup>, J. Bekaert<sup>4</sup>, A. Šolajić<sup>1</sup>, J. Pešić<sup>1</sup>, Aifeng Wang<sup>5</sup>, M. Šćepanović<sup>1</sup>, A. M. Milinda Abeykoon<sup>6</sup>, M. V. Milošević<sup>4</sup>, C. Petrovic<sup>7</sup>, Z. V. Popović<sup>1,8</sup> and R. Hackl<sup>2,3,9</sup>

<sup>1</sup>Center for Solid State Physics and New Materials, Institute of Physics Belgrade, University of Belgrade, Pregrevica 118, 11080 Belgrade, Serbia

<sup>2</sup>Walther Meissner Institut, Bayerische Akademie der Wissenschaften, 85748 Garching, Germany

<sup>3</sup>Fakultät für Physik, Technische Universität München, 85478 Garching, Germany

<sup>4</sup>Department of Physics, University of Antwerp, Groenenborgerlaan 171, B-2020 Antwerp, Belgium

<sup>5</sup>School of Physics, Chongqing University, Chongqing 400044, China

<sup>6</sup>National Synchrotron Light Source II, Brookhaven National Laboratory, Upton, New York 11973, USA

<sup>7</sup>Condensed Matter Physics and Materials Science Department, Brookhaven National Laboratory, Upton, New York 11973-5000, USA

<sup>8</sup>Serbian Academy of Sciences and Arts, Kneza Mihaila 35, 11000 Belgrade, Serbia

<sup>9</sup>IFW Dresden, Helmholtzstr. 20, 01069 Dresden, Germany



(Received 9 March 2022; revised 27 July 2022; accepted 26 August 2022; published 19 September 2022)

A Raman scattering study covering the entire substitution range of the  $\text{FeSe}_{1-x}\text{S}_x$  solid solution is presented. Data were taken as a function of sulfur concentration  $x$  for  $0 \leq x \leq 1$ , of temperature and of scattering symmetry. All types of excitations including phonons, spins, and charges are analyzed in detail. It is observed that the energy and width of the iron-related  $B_{1g}$  phonon mode vary continuously across the entire range of sulfur substitution. The  $A_{1g}$  chalcogenide mode disappears above  $x = 0.23$  and reappears at a much higher energy for  $x = 0.69$ . In a similar way the spectral features appearing at finite doping in  $A_{1g}$  symmetry vary discontinuously. The magnetic excitation centered at approximately  $500 \text{ cm}^{-1}$  disappears above  $x = 0.23$  where the  $A_{1g}$  lattice excitations exhibit a discontinuous change in energy. The low-energy mode associated with fluctuations displays maximal intensity at the nematostructural transition and thus tracks the phase boundary.

DOI: [10.1103/PhysRevB.106.094510](https://doi.org/10.1103/PhysRevB.106.094510)

### I. INTRODUCTION

Iron-based compounds are widely believed to host unconventional superconductivity, thus being similar to cuprates or heavy fermion systems. All are characterized by competing phases including magnetism, crystal symmetry breaking or nematicity, and fluctuations of charge and spin prior to superconductivity [1–3]. While long-range magnetic ordering was found in the majority of the compounds, it is absent in the binary compound FeSe. Yet a nematic and structural phase transition occurs simultaneously at 90 K [4–6]. Below  $T_c = 9 \text{ K}$  superconductivity is observed [7]. Upon applied pressure  $T_c$  increases to approximately 37 K [8]. By substituting sulfur for selenium, the transition temperature to the nematic phase is suppressed to zero for  $x \sim 0.2$  [9], suggesting the existence of a quantum critical point (QCP), and a depression of  $T_c$  to approximately 2 K. For  $x > 0.2$ ,  $T_c$  increases again and

reaches 5 K at  $x = 1$  [10]. Surprisingly enough, FeS displays a metallic variation of the resistivity and a high residual resistivity ratio RRR of approximately 30, and neither structural nor nematic phase transitions occur [11]. Thus,  $\text{FeSe}_{1-x}\text{S}_x$  uniquely offers access to instabilities and critical points and the disappearance thereof while superconductivity survives.

FeSe and FeS are isostructural, thus providing us with the opportunity to probe the evolution of competing order by isoelectronic substitution. We wish to address the question as to which extent the properties and, specifically, superconductivity are interrelated with the other instabilities and how the electronic properties affect the phonons. We employ inelastic light scattering to probe evolution with composition of lattice spin and charge excitations in  $\text{FeSe}_{1-x}\text{S}_x$  [12]. We identify the  $A_{1g}$  and  $B_{1g}$  modes, a two-phonon scattering process as well as additional modes that can be traced to either defect-induced or second-order scattering. The obtained experimental results are in good agreement with numerical calculations. Phonons self-energy temperature dependence supports the results reported in Refs. [13,14] where emerging short-range magnetic order at approximately 20 K was reported.

### II. EXPERIMENT

Single crystals of  $\text{FeSe}_{1-x}\text{S}_x$  were synthesized as described elsewhere [15]. Before the experiment the samples were cleaved in air.

Inelastic light scattering on phonons was performed using a Tri Vista 557 Raman spectrometer with the first

\*These authors contributed equally to this work.

†Present Address: IFW Dresden, Helmholtzstr. 20, 01069 Dresden, Germany.

‡Present Address: Robert Bosch GmbH, Robert-Bosch-Platz 1, 70839 Gerlingen, Germany.

Published by the American Physical Society under the terms of the [Creative Commons Attribution 4.0 International](https://creativecommons.org/licenses/by/4.0/) license. Further distribution of this work must maintain attribution to the author(s) and the published article's title, journal citation, and DOI.

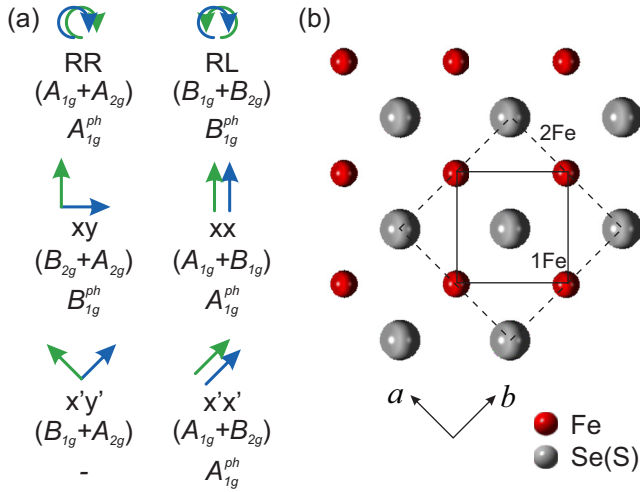


FIG. 1. Crystal structure and selection rules for FeSe(S). Solid and dashed lines represent the 1-Fe and the crystallographic 2-Fe unit cell, respectively. The crystallographic axes are  $a$  and  $b$ . In FeSe and FeS only one  $A_{1g}$  and one  $B_{1g}$  phonon is expected as indicated by  $A_{1g}^{ph}$  and  $B_{1g}^{ph}$ , respectively. The symmetries projected with the polarizations indicated symbolically with respect to the 1-Fe cell are relevant for electronic and spin excitations. The symmetries of the phonons are in brackets.

two monochromators coupled subtractively and the grating combination 1800/1800/2400 grooves/mm. For excitation a Coherent Verdi G solid state laser was used emitting at 532 nm. The samples were mounted in a KONTI CryoVac continuous helium flow cryostat having a 0.5-mm-thick window. The vacuum was pumped to the range of  $10^{-6}$  mbar using a turbo molecular pump. The laser was focused to a spot size of approximately  $8 \mu\text{m}$  using a microscope objective lens with  $\times 50$  magnification. The power absorbed by the sample was  $P_a = 0.75$  mW. In backscattering configuration as used here, the incident and scattered photons propagate parallel to the crystallographic  $c$  axis. All Raman spectra were divided by the Bose factor.

Fluctuations and two magnon excitations were probed with a calibrated scanning spectrometer. The samples were attached to the cold finger of a He-flow cryostat having a vacuum of better than  $10^{-6}$  mbar. A diode-pumped solid state laser emitting at 575 nm (Coherent GENESIS) was used as an excitation source. The laser beam was focused on the sample at an angle of incidence of  $66^\circ$  to a spot of  $2r_f \approx 50 \mu\text{m}$ . Polarization and power of the incoming light were adjusted in a way that the light inside the sample had the proper polarization state and a power of  $P_a = 4$  mW independent of polarization. The ratio  $P_a/r_f$  is similar for the  $\mu$  setup and thus the local heating for both experiments can be estimated to be in the range 3–5 K. All four symmetries of the  $D_{4h}$  group,  $A_{1g}$ ,  $A_{2g}$ ,  $B_{1g}$ , and  $B_{2g}$ , can be accessed using appropriate in-plane polarizations of the incident and scattered light.

The selection rules are dictated by the crystal structure. Here, only polarizations in the  $ab$  plane are relevant, as shown in Fig. 1, with solid and dashed lines representing 1-Fe and 2-Fe unit cells, respectively. For the tetragonal system there are six principal scattering geometries and each probes two symmetry channels. We align our laboratory system with the

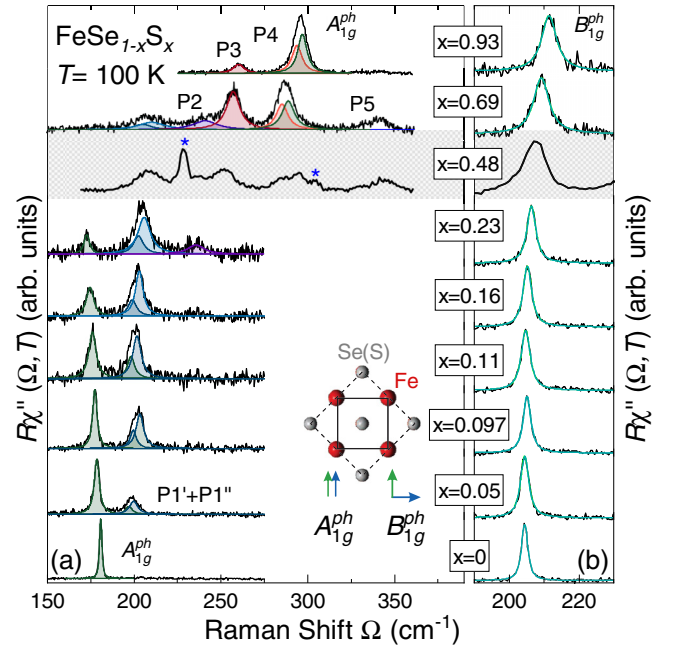


FIG. 2. Phonon spectra of  $\text{FeSe}_{1-x}\text{S}_x$  measured at 100 K. We show  $xx$  and  $xy$  spectra where  $x$  and  $y$  are rotated by  $45^\circ$  with respect to the 2-Fe unit cell, as indicated in the inset, and project  $A_{1g}^{ph}$  and  $B_{1g}^{ph}$ , respectively. (a)  $A_{1g}^{ph}$  spectra. Only for pure FeSe ( $x = 0$ ), a single line is observed at the  $A_{1g}$  energy of  $165 \text{ cm}^{-1}$  expected from lattice dynamics. Above  $x = 0.23$  the Se(S) vibration becomes unobservable and reappears only for  $x \geq 0.69$  at a much higher energy of approximately  $290 \text{ cm}^{-1}$  similar to that in pure FeS. The spectrum at  $x = 0.48$  was measured on the scanning spectrometer and is therefore shaded. There may be an indication of the  $A_{1g}^{ph}$  phonon at about  $290 \text{ cm}^{-1}$ . The peaks other than Raman-active phonons are labeled P1–P5 with increasing energy. Those with asterisks correspond to maxima in the phonon density of states (Fig. 6). Solid lines represent the best fits to the data using Voigt profiles. (b)  $B_{1g}^{ph}$  spectra. Energy and linewidth vary continuously with sulfur content.

1-Fe unit cell. As a consequence, the  $B_{1g}$  phonon ( $B_{1g}^{ph}$ ) is observable in the  $xy$  configuration which corresponds to the  $B_{2g}$  symmetry channel in the 2-Fe cell (Fig. 1). We decided to use this orientation since our main focus here is electronic and spin excitations for which the 1-Fe unit cell is more appropriate.  $A_{1g}^{ph}$  is the fully symmetric in-phase Se(S) mode with elongations along the  $c$  axis;  $B_{1g}^{ph}$  corresponds to the out-of-phase vibration of the Fe atoms parallel to the  $c$  axis.

### III. RESULTS AND DISCUSSION

#### A. Lattice excitations

First, the focus is placed on lattice excitations observable in the  $xx$  and  $xy$  scattering configuration projecting  $A_{1g}^{ph}$  and  $B_{1g}^{ph}$  in the spectral range characteristic for phonons. Figure 2 shows the evolution of the spectra with doping  $x$ , where  $x$  indicates the sulfur concentration. Additional spectra for  $x = 0.48$  and, for convenience,  $x = 1$  are shown in Fig. 7. In order to minimize the thermal broadening of the modes while staying above the nematic phase transition, the spectra



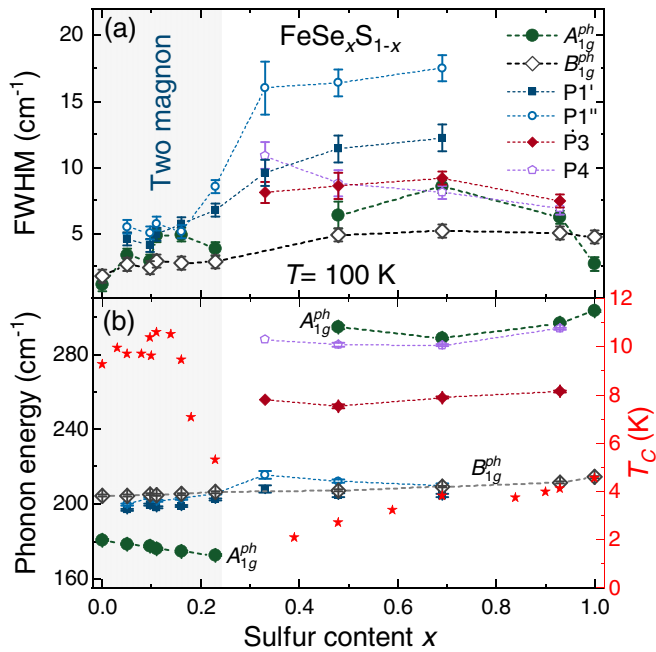


FIG. 3. Energies and linewidths of the Raman-active modes and  $T_c$  in  $\text{FeSe}_{1-x}\text{S}_x$  as a function of sulfur content  $x$  at 100 K. (a) Peak widths (FWHM) and (b) energies as obtained from the fits (left axis). The  $T_c$  values of the corresponding solid solution are taken from Ref. [16].

were recorded at 100 K. In pure stoichiometric compounds only one  $A_{1g}^{ph}$  and one  $B_{1g}^{ph}$  phonon mode is expected (see Fig. 1). This is indeed the case for FeSe [Fig. 2(a), bottom] as described by Gnezdilov *et al.* [17] and corroborated here. In contrast, in pure FeS ( $x = 1$ ) additional modes exist in the  $xx$  spectrum which were assigned to two-phonon scattering ( $265 \text{ cm}^{-1}$ ) and a projection of the phonon density of states (PDOS) ( $\sim 300 \text{ cm}^{-1}$ ) [18] as reproduced in Fig. 7(b). The  $xy$  spectra show only the  $B_{1g}^{ph}$  mode for all doping levels displayed here [see also Fig. 7(a)]. It hardens monotonously and exhibits a weak maximum of the linewidth at  $x = 0.69$  and  $x = 0.93$  highlighting the effect of disorder as summarized in Figs. 3(a) and 3(b).

The  $xx$  spectra display a much more complex doping dependence. Upon substituting only a small amount of sulfur ( $x = 0.05$ ) for selenium an additional structure appears at about  $200 \text{ cm}^{-1}$  [Fig. 2(a)]. Closer inspection of the  $\text{FeSe}_{0.95}\text{S}_{0.05}$  spectra reveals that this feature consists of two peaks denoted as  $P1'$  and  $P1''$ . With increasing  $x$ , these structures gain intensity and harden slightly, whereas the  $A_{1g}$  phonon softens, gradually loses intensity, and becomes undetectable at concentrations above  $x = 0.23$ . It reappears as a clear peak only for  $x \geq 0.69$  at a much higher energy characteristic for FeS [18] and possibly as a remnant structure in the spectrum for  $x = 0.48$  [Fig. 7(a)]. As in FeS the  $A_{1g}^{ph}$  peak overlaps with a weaker structure which is compatible with the PDOS (P4). At  $x = 0.69$  P4 is approximately as strong as the  $A_{1g}$  phonon. Here [and at  $x = 0.48$ , Fig. 7(a)] there is also a broad feature at  $340 \text{ cm}^{-1}$  (P5). For  $x = 0.93$  similar to  $x = 1$  there is another structure at  $250 \text{ cm}^{-1}$  (P3) which gains intensity toward  $x = 0.69$  where it has a weak companion at

$235 \text{ cm}^{-1}$  (P2) being present down to  $x = 0.23$ . As expected, the increase of crystalline disorder due to substitution leads to a broadening of all observed modes to some maximum value before the trend reverses for compositions close to pure FeS. The widths and energies of the stronger modes are summarized in Fig. 3. As opposed to the  $B_{1g}^{ph}$  phonon in  $xy$  configuration, all modes in  $xx$  polarization including the Raman-active phonon depend quasidiscontinuously on substitution.

This dichotomy of the substitution dependence of the phonon part in  $xx$  and  $xy$  configuration is the most remarkable effect of this study. Whereas the continuous evolution of the Fe  $B_{1g}$  line by and large tracks the degree of disorder and lattice contraction, the Se/S  $A_{1g}$  mode varies counterintuitively. Naively one would expect a continuous (not necessarily trivial) increase in the phonon frequency and maximal broadening for doping levels around  $x = 0.5$  similar to what is observed in isotopically substituted semiconductors [19]. However, the line disappears after a continuous loss of intensity at approximately  $x = 0.23$  and  $172 \text{ cm}^{-1}$  and reappears (presumably) at  $x = 0.48$  slightly below  $300 \text{ cm}^{-1}$ . At low doping the  $A_{1g}$  energy decreases by 4% although S is lighter than Se by a factor of 2.13 and the lattice contracts. Above  $x = 0.48$  the energy of the  $A_{1g}$  phonon varies as expected [see Fig. 3(b)].

The structures appearing in addition to the allowed phonons are rather difficult to interpret in detail. There are essentially two possibilities for intensity to appear in addition to the phonons: defect-induced scattering projecting the PDOS on the site of the defect or overtone (combination) scattering [20]. In FeS one of the peaks (P3) is in the gap between the acoustic and the optical branches and was therefore assigned to an overtone, whereas P4 may originate from the PDOS [18]. The two features depend in the same fashion on doping as the  $A_{1g}$  phonon, and the assignment may be maintained. This is plausible on the basis of the PDOS (Fig. 6) although the PDOS of a solid solution cannot be calculated straightforwardly. If we argue that the extra lines vary as discontinuously as the phonon,  $P1'$  and  $P1''$  would have both an overtone and a PDOS component. Interestingly,  $P1'$  and  $P1''$  have the expected doping dependence [see Fig. 3(b)].

The anomalous doping dependence of the  $A_{1g}$  phonon may indicate an enhanced electron-phonon coupling which manifests itself also in the linewidth (on top of the inhomogeneous broadening) [Fig. 3(a)]. The slightly enhanced electron-phonon coupling may boost  $T_c$  a little bit until the structure becomes unstable and  $T_c$  decreases rapidly for  $x > 0.16$ . There is, in fact, a kink in the  $c/a$  ratio at  $x = 0.23$  which may be related to the structural instability [15]. In a recent preprint the collapse of  $T_c$  is almost precipitous and coincides with the end of the nematic phase [21], and one may speculate about the position of the quantum critical point and its impact. Yet, further work is necessary to finally clarify the issue.

## B. Spin excitations and fluctuations

Second, we focus on the electronic  $B_{1g}$  symmetry channel projected in the  $x'y'$  (1-Fe) configuration. Figure 4 shows the doping dependence of the high-energy Raman spectra at approximately 4 K. The  $A_{2g}$  contribution can be neglected in these materials [22]. A broad excitation centered at about

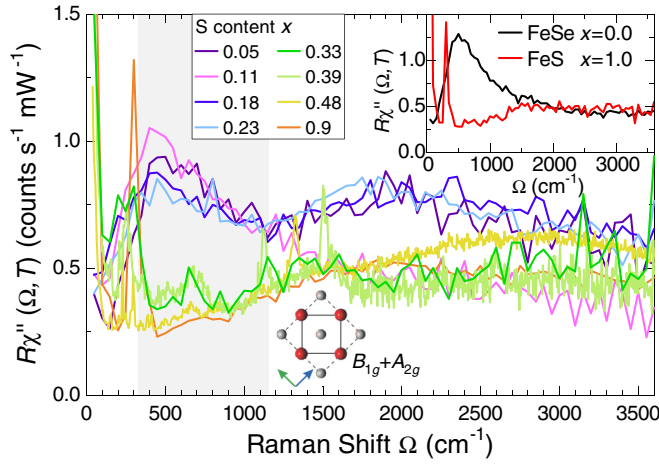


FIG. 4. Doping dependence of the high-energy spectra of  $\text{FeSe}_{1-x}\text{S}_x$  in  $xy$  ( $2\text{-Fe}$ ) configuration at 4 K, except for  $x = 0.33$ ,  $x = 0.39$ , and  $x = 0.48$  which were obtained at 100 K. For the electronic unit cell (full line in Fig. 1) relevant here the  $B_{1g}$  and  $A_{2g}$  symmetries are projected where  $A_{2g}$  is negligibly weak. The doping levels are indicated. The inset compares the high-energy spectra of pure FeSe [22] and FeS. The maximum in the range  $500\text{ cm}^{-1}$  is compatible with two-magnon scattering [23], whereas the broad shoulder around  $2000\text{ cm}^{-1}$  appearing in three out of ten (including all doping levels) spectra was identified as luminescence by using various laser lines for excitation. The peaks in the range  $700\text{--}1550\text{ cm}^{-1}$  observed only for the doping levels  $x = 0.33$ ,  $x = 0.39$ , and  $x = 0.48$  may originate from either overtones of the phonon density of states [20,24] or from magnetic excitations in the paramagnetic state above the magnetic phase which was observed recently below  $20\text{--}40\text{ K}$  [25,26]. Since the measuring temperature is well above the magnetic transition the former is more likely.

$500\text{ cm}^{-1}$  dominates the spectrum at  $x = 0$  which was interpreted in terms of two-magnon scattering [22]. Since the ratio of the nearest to the next-nearest-neighbor exchange coupling  $J_1$  and  $J_2$  is close to 0.5 [27] the system is a nearly frustrated antiferromagnet. Consequently the two-magnon Raman peak is pushed to energies well below  $3J_1$  [23]. No comparable feature is observed in FeS (see inset in Fig. 4).

Upon doping, the two-magnon peak remains relatively robust up to  $x = 0.23$  and is absent for higher doping levels. This goes in line with the fact that for  $x = 0$ , the Fermi velocity in the  $d_{xy}$  band,  $v_F^{(xy)}$ , is significantly smaller than  $v_F^{(xz)}$  or  $v_F^{(yz)}$  and increases by only 10% for  $x \leq 0.20$ . For  $x > 0.20$   $v_F^{(xy)}$  increases significantly towards FeS [28]. Generally,  $v_F^{(xy)}$  in FeSe is smaller than  $v_F^{(xy)}$  in  $\text{Ba}(\text{Fe}_{1-x}\text{Co}_x)_2\text{As}_2$  for instance [29], in agreement with theoretical predictions [30–32]. Thus FeSe is close to the localization limit, and the two-magnonlike response may result from the rather slow carriers on the  $d_{xy}$  band. In contrast, the more itinerant carriers in the pnictides condense into a stripelike spin density wave (SDW) which becomes manifest in a gap and a coherence peak [22,33].

In the energy region  $\Omega < 200\text{ cm}^{-1}$  extra intensity is observed for low temperatures. In FeSe it becomes clearly visible below 200 K and fills the spectral gap below the magnon at  $500\text{ cm}^{-1}$ . Below approximately 100 K an isolated

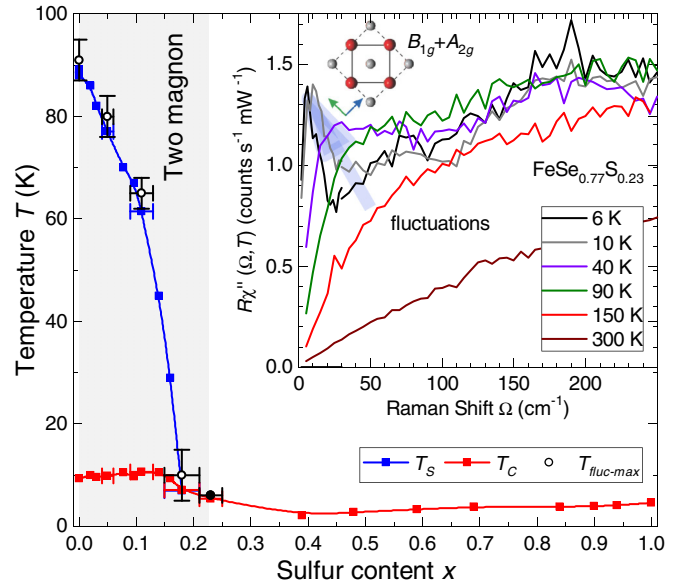


FIG. 5. Phase diagram of  $\text{FeSe}_{1-x}\text{S}_x$  with  $T_{\text{fluct,max}}$  tracing  $T_S$  in the region where the two-magnon feature was observed in the Raman scattering experiment.  $T_c$  taken from Ref. [15]. The full circle represents the lowest accessible temperature. Inset: Low-energy Raman spectrum showing the temperature dependence of the fluctuation contribution at  $x = 0.23$ . Spectra for all doping levels  $0 \leq x \leq 0.23$  are shown in Fig. 8.

peak may be observed for  $x = 0$  which continuously softens above the structural transformation at  $T_s = 90\text{ K}$ , fades away below  $T_s$ , and almost vanishes at 21 K [22,34]. The line shape and the temperature dependence above  $T_s$  can be described quantitatively in terms of critical fluctuations in a similar fashion as in  $\text{Ba}(\text{Fe}_{1-x}\text{Co}_x)_2\text{As}_2$  [22,33,35]. For increasing doping, this extra intensity starts to develop at lower temperatures. However, remarkably enough the temperature where this peak's intensity is maximal,  $T_{\text{fluct,max}}$ , always coincides with the respective transition temperature  $T_s(x)$ . At  $x = 0.23$  the fluctuation response gains intensity down to the lowest accessible temperatures as presented in the inset of Fig. 5. Thus, the phase transition line of the nematic phase can also be tracked by the Raman response. For  $x = 0.33$  (the next available doping level) the fluctuation response cannot be observed any further. Concomitantly, the two-magnon excitation at  $500\text{ cm}^{-1}$  becomes unobservable. The most likely explanation of this coincidence is that the two phenomena have the same origin and result from spin excitations. However, there is no consensus on that view in the literature, and Zhang *et al.* [36] and Chibani *et al.* [34] interpret the same experimental observation in terms of quadrupolar charge fluctuations. Yet, one certainly has to answer the question as to why the fluctuations are not found in the simulations [23].

Most probably, the length scale the simulations can deal with limits the applicability of the exact diagonalization method. Since it was intended to study the temperature dependence the cluster had to be sufficiently small ( $4 \times 4$ ) to keep the time for the simulations finite [23]. For the two-magnon excitations, the  $4 \times 4$  cluster is sufficient because only nearest-neighbor spins are important. However, close to

the transition the correlation length of fluctuations diverges making them inaccessible for the small clusters tractable numerically. Actually, well above the transition there is a shoulder on the low-energy side of the two-magnon peak which may be associated with the fluctuations but the shoulder is lost close to  $T_s$ . Thus, although there are experimental arguments in favor of spin fluctuations at low energy there is no theoretical support for this conjecture.

The last question we wish to address concerns the origin of possible local or quasilocal spin order in  $\text{FeSe}_{1-x}\text{S}_x$  for  $x < 0.3$ . It was observed a while ago that the width of the various bands derived from the orbitals close to the Fermi surface varies by approximately a factor of 3 or more. There are itinerant  $yz$  and  $xz$  bands crossing the Fermi surface at  $E_F$  and a weakly dispersing  $xy$  band just below  $E_F$  [29] on which the nearly localized spins may reside [30,32]. It is an important question to which extent the fluctuations at low energy are related to these spins. As a matter of fact, Ba122 displays itinerant SDW magnetism as manifested by a gap and a coherence peak along with fluctuations [22,33], whereas FeSe exhibits signatures of local spins and also fluctuations at low energies as shown here. In  $\text{FeSe}_{1-x}\text{S}_x$  both phenomena disappear together above  $x > 0.23$ .

#### IV. CONCLUSION

Raman results covering the entire substitution range  $0 \leq x \leq 1$  in  $\text{FeSe}_{1-x}\text{S}_x$  were presented. The main goal was the study of the physics around the QCP where the nematic instability approached zero transition temperature in the range  $0.16 \leq x \leq 0.23$ . We find a striking signature of this transition in both the phonon and the electronic spectra. Whereas the  $B_{1g}$  phonon varies continuously with S substitution, the  $A_{1g}$  phonon and all structures in the  $xx$  spectra show a discontinuity above  $x = 0.23$ . Similarly, the electronic spectra dominated by spin excitations change abruptly here. Both the two-magnon excitations and the low-energy fluctuations disappear. We argue that they are interrelated. Since we could not observe gap excitation for  $x > 0$ , statements about the evolution of the superconducting pairing are currently not possible. Another issue is the exact position of the quantum critical transition and its sharpness.

#### ACKNOWLEDGMENTS

We acknowledge valuable discussions with T. Böhm and D. Jost. The authors acknowledge funding provided by the Institute of Physics Belgrade through a grant by the Ministry of Education, Science and Technological Development of the Republic of Serbia and and SASA Project No. F-134. The work was supported by the Science Fund of the Republic of Serbia, PROMIS, No. 6062656, StrainedFeSC, by Research Foundation-Flanders (FWO), and COST actions CA16218 and CA21144. Further support came from the German research foundation (DFG) via projects Ha2071/8-1, Ha2071/12-1, and 107745057-TRR 80 and from the DAAD via the project-related personal exchange program PPP with Serbia Grant No. 57449106. J.B. is Senior Postdoctoral Fellow of the FWO, and further acknowledges the Erasmus+ program for staff mobility and training (KA107, 2018) for a

research stay at the Institute of Physics Belgrade. The computational resources and services used for the first-principles calculations in this work were provided by the VSC (Flemish Supercomputer Center), funded by the FWO and the Flemish Government, department EWI. Work at Brookhaven National Laboratory is supported by the U.S. DOE under Contract No. DESC0012704 (materials synthesis).

#### APPENDIX A: PHONON DISPERSION AND DENSITY OF STATES

We have performed density functional theory (DFT) calculations as implemented in the ABINIT package [38]. We have used the Perdew-Burke-Ernzerhof functional tailored for solids [39] and optimized norm-conserving pseudopotentials [40,41], where Fe  $3s^2 3p^6 3d^6 4s^2$ , S  $3s^2 3p^4$ , and Se  $3d^{10} 4s^2 4p^4$  are treated as valence electrons. The energy cutoff for the plane-wave basis was set to 50 Ha. The lattice parameters and atomic positions used in the calculations were directly obtained from our x-ray diffraction measurements (performed at 300 K). Following previous first-principles studies on phonons in, for example, FeS [18], the crystal structures were not further relaxed, to achieve optimal characterization of the phonon frequencies. Here, both FeS and FeSe adopt the simple tetragonal space group  $P4/nmm$  (No. 129), where Fe occupies Wyckoff position  $2a$  and S/Se position  $2c$ . The latter comprises an additional degree of freedom, namely, the height of the chalcogen atoms S and Se with respect to the Fe plane, denoted as  $z$ . An overview of the lattice parameters that were used in the calculations is provided in Table I.

Subsequently, the phonon dispersions were obtained from density functional perturbation theory (DFPT) calculations, also within ABINIT. Here, we have used a  $15 \times 15 \times 9$   $k$ -point grid for the electron wave vectors and a  $5 \times 5 \times 3$   $q$ -point grid for the phonon wave vectors. For the electronic occupation we employed Fermi-Dirac smearing with broadening factor  $\sigma = 0.01$  Ha.

The results of these calculations are shown in Fig. 6. FeS is found to have phonon frequencies stretching up to  $344 \text{ cm}^{-1}$  [Fig. 6(a)], which is significantly higher than the maximum phonon value of  $273 \text{ cm}^{-1}$  obtained for FeSe [Fig. 6(b)], owing to the higher atomic mass of Se compared to S. The atom-resolved phonon densities of states (DOS) of both compounds reveal a mixture of iron and chalcogen contribution throughout the entire phonon spectrum [Figs. 6(c) and 6(d)]. Interestingly, there is a change of dominant phonon character, with the lower modes dominated by Fe in FeS, while the lower modes have predominant Se character in FeSe. This reversal can be understood from the fact that the atomic number of Fe ( $Z = 26$ ) lies in between those of S ( $Z = 16$ ) and Se ( $Z = 34$ ). These differences in atomic masses lead moreover

TABLE I. Lattice parameters, obtained from x-ray diffraction measurements, used in the DFT and DFPT calculations.

Compound	$a$ (Å)	$c$ (Å)	$z$ (units of $c$ )
FeS	3.6795	5.0321	0.2578
FeSe	3.7707	5.5202	0.2671

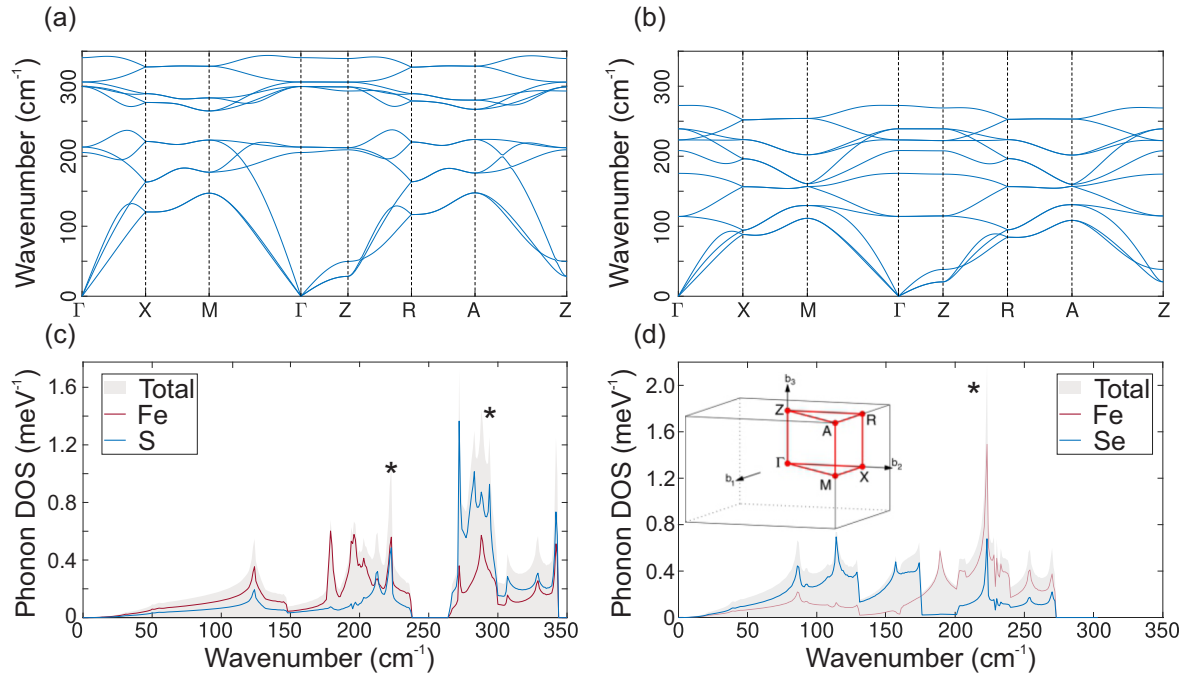


FIG. 6. Calculated phonon band structures of (a) FeS and (b) FeSe. Phonon DOS of (c) FeS and (d) FeSe, including partial contributions from Fe and S/Se. The Brillouin zone of both structures depicted in black is shown in the inset of (d), with the irreducible Brillouin zone, along which the band structures are plotted, in red [37]. The energies of the extra peaks in Fig. 7 are also indicated here by asterisks.

to a small energy gap between Fe- and S-dominated modes in FeS (between 238 and 265  $\text{cm}^{-1}$ ), which is entirely absent in FeSe.

#### APPENDIX B: $\text{FeSe}_{0.52}\text{S}_{0.48}$ AND FeS

For convenience we show here additional doping levels in Fig. 7. The spectrum for  $x = 1$  in panel (b) was already published elsewhere [18]. Note that for  $x \neq 1$  both  $A_{1g}^{ph}$  and  $B_{1g}^{ph}$  are projected and that the labels for the symmetry-forbidden peaks P3 and P4 are different from those in the earlier paper [18].  $x = 0.48$  [Fig. 7(a)] is in the middle between FeSe and FeS, and one can therefore expect the strongest contribution from defect-induced scattering. This interpretation is supported by the presence of structures in both configurations. All peaks resolved at  $x = 0.69$  in  $xx$  configuration are also observed here. In addition there are two lines marked by asterisks which appear only at  $x = 0.48$ . Since they appear also for  $xy$  we interpret them in terms of contributions from the PDOS as shown in Fig. 6 where the respective energies correspond to a high DOS of either FeSe or FeS. Structure P5 may be related to the high-energy part of FeS.

#### APPENDIX C: FLUCTUATION RESPONSE

The Raman response from fluctuations was studied by various authors [22,36,42]. While the experiments agree by and large, the interpretation is still controversial. Here we show that the fluctuations appear along with the two-magnon excitations at approximately 500  $\text{cm}^{-1}$  from a frustrated spin system [22,23]. Above  $x = 0.23$  we could neither observe fluctuations nor two-magnon excitations (see Fig. 4). We cannot entirely exclude that the fluctuations are masked by in-

sufficient stray-light rejection in the more disordered samples but consider it unlikely.

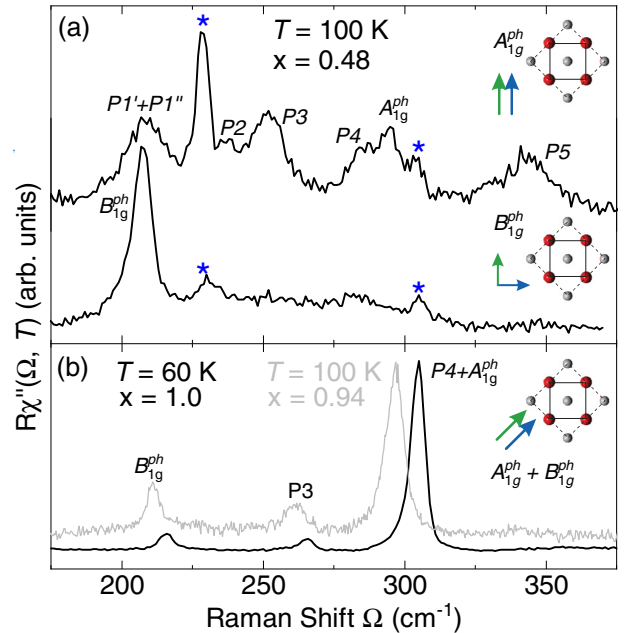


FIG. 7.  $\text{FeSe}_{1-x}\text{S}_x$  for  $x = 0.48$ ,  $x = 0.94$ , and  $x = 1$ . (a)  $A_{1g}^{ph}$  ( $xx$ ) and  $B_{1g}^{ph}$  ( $xy$ ) spectra for  $\text{FeSe}_{0.52}\text{S}_{0.48}$ . In addition to the phonons and the structures observed at the other doping levels there are two relatively sharp lines (marked by asterisks) which we associate with the PDOS. They may also arise from a nearly ordered superstructure close to 50% doping.

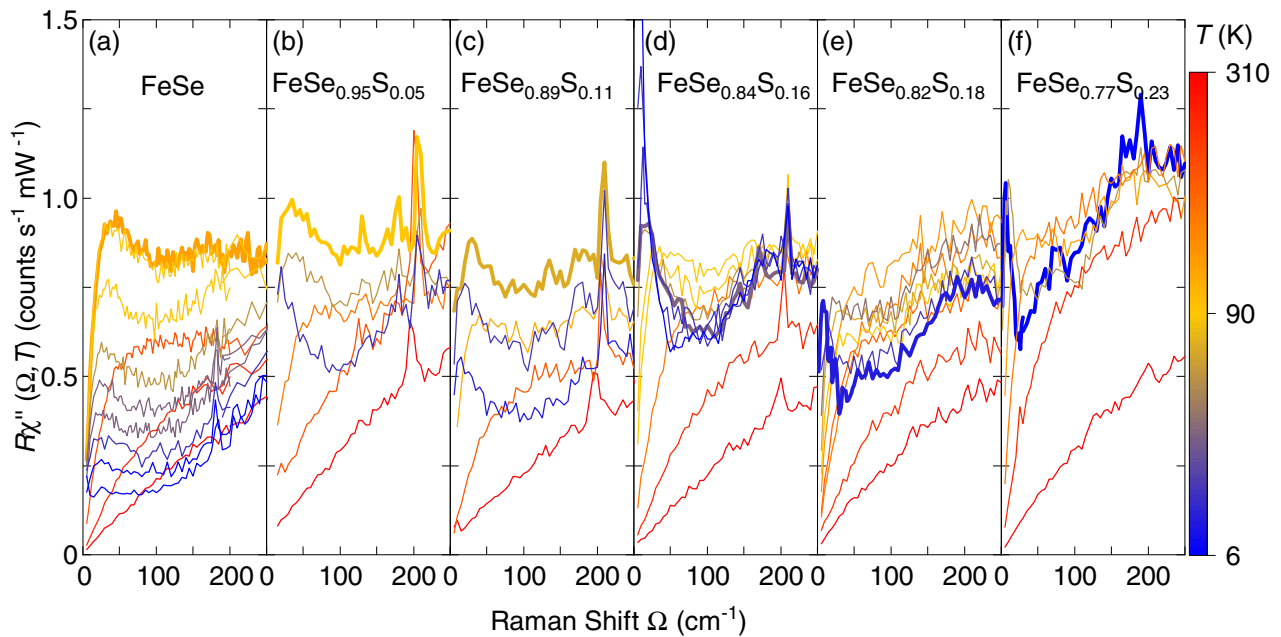


FIG. 8. Fluctuation response of  $\text{FeSe}_{1-x}\text{S}_x$  for  $0 \leq x \leq 0.23$ . The spectra with the maximal intensity in the fluctuations are highlighted. The respective temperatures are (a) 91 K, (b) 80 K, (c) 65 K, (d) 25 K, (e) 10 K, and (f) 6 K, where 6 K was the lowest accessible temperature. The temperatures are compiled in Fig. 5 and track the transition to the nematic phase.

If excitations are very close to zero energy one encounters two difficulties: (1) The experimentally accessible quantity is the differential cross section,  $d^2\sigma/(d\Omega d\omega) \propto S(q=0, \omega)$ . The dynamical structure factor or Van Hove function  $S(q=0, \omega)$  is related to the imaginary part of the Raman response function  $\text{Im}\chi(q=0, \omega)$  through the fluctuation-dissipation theorem as  $S(q=0, \omega) = \pi^{-1}\{1 + n(\omega, T)\}\text{Im}\chi(q=0, \omega)$  [43]. The Bose factor  $1 + n(\omega, T)$  increases rapidly towards  $\omega = 0$  for  $\hbar\omega < k_B T$  and conceals all spectral features below  $k_B T$ . Since the fluctuation-dissipation theorem is derived on purely statistical arguments the response function contains exactly the same information as the structure factor but makes features at low energy visible. Thus it is sensible to show  $\text{Im}\chi(q=0, \omega)$  rather than  $S(q=0, \omega)$ . (2) If the surface is not atomically flat there is stray light from insufficient rejection of the laser. The problem is aggravated

when atoms of the residual gas accumulate on the surface at low temperature. In panels (a), (b), and (d) of Fig. 8 this effect can be observed. Fortunately, it can be distinguished from the desired response which always goes through zero linearly for causality reasons. (a) In FeSe only the spectra at 10 K show a slight increase which, however, is separated from the fluctuation peak at finite energy. (b) The increase at 10 K is partially resulting from stray light but the maximal intensity is already observed at 80 K. (c) There is little contribution from stray light. (d) Here the stray light becomes strong below 20 K. In (e) and (f) the stray light is negligible.

Remarkably, the overall intensity of all spectra is approximately the same, whereas the maximal intensity in the fluctuation peak is observed at different temperatures as indicated in Fig. 8. These temperatures compare well with the boundary of the nematic phase as shown in Fig. 5.

- 
- [1] D. J. Scalapino, A common thread: The pairing interaction for unconventional superconductors, *Rev. Mod. Phys.* **84**, 1383 (2012).
- [2] E. Fradkin, S. A. Kivelson, and J. M. Tranquada, *Colloquium: Theory of intertwined orders in high temperature superconductors*, *Rev. Mod. Phys.* **87**, 457 (2015).
- [3] S. Lederer, Y. Schattner, E. Berg, and S. A. Kivelson, Enhancement of Superconductivity near a Nematic Quantum Critical Point, *Phys. Rev. Lett.* **114**, 097001 (2015).
- [4] A. E. Böhrner, T. Arai, F. Hardy, T. Hattori, T. Iye, T. Wolf, H. v. Löhneysen, K. Ishida, and C. Meingast, Origin of the Tetragonal-to-Orthorhombic Phase Transition in FeSe: A Combined Thermodynamic and NMR Study of Nematicity, *Phys. Rev. Lett.* **114**, 027001 (2015).
- [5] T. M. McQueen, A. J. Williams, P. W. Stephens, J. Tao, Y. Zhu, V. Ksenofontov, F. Casper, C. Felser, and R. J. Cava, Tetragonal-to-Orthorhombic Structural Phase Transition at 90 K in the Superconductor  $\text{Fe}_{1.01}\text{Se}$ , *Phys. Rev. Lett.* **103**, 057002 (2009).
- [6] M. D. Watson, T. K. Kim, A. A. Haghighirad, N. R. Davies, A. McCollam, A. Narayanan, S. F. Blake, Y. L. Chen, S. Ghannadzadeh, A. J. Schofield *et al.*, Emergence of the nematic electronic state in FeSe, *Phys. Rev. B* **91**, 155106 (2015).
- [7] F.-C. Hsu, J.-Y. Luo, K.-W. Yeh, T.-K. Chen, T.-W. Huang, P. M. Wu, Y.-C. Lee, Y.-L. Huang, Y.-Y. Chu, D.-C. Yan, and M.-K. Wu, Superconductivity in the PbO-type structure  $\alpha$ -FeSe, *Proc. Natl. Acad. Sci. USA* **105**, 14262 (2008).

- [8] S. Medvedev, T. M. McQueen, I. A. Troyan, T. Palasyuk, M. I. Erements, R. J. Cava, S. Naghavi, F. Casper, V. Ksenofontov, G. Wortmann, and C. Felser, Electronic and magnetic phase diagram of  $\beta$ -Fe<sub>1,01</sub>Se with superconductivity at 36.7 K under pressure, *Nat. Mater.* **8**, 630 (2009).
- [9] Y. Sato, S. Kasahara, T. Taniguchi, X. Xing, Y. Kasahara, Y. Tokiwa, Y. Yamakawa, H. Kontani, T. Shibauchi, and Y. Matsuda, Abrupt change of the superconducting gap structure at the nematic critical point in FeSe<sub>1-x</sub>S<sub>x</sub>, *Proc. Natl. Acad. Sci. USA* **115**, 1227 (2018).
- [10] X. Lai, H. Zhang, Y. Wang, X. Wang, X. Zhang, J. Lin, and F. Huang, Observation of superconductivity in tetragonal FeS, *J. Am. Chem. Soc.* **137**, 10148 (2015).
- [11] U. Pachmayr, N. Fehn, and D. Johrendt, Structural transition and superconductivity in hydrothermally synthesized FeX (X = S, Se), *Chem. Commun.* **52**, 194 (2016).
- [12] N. Lazarević and R. Hackl, Fluctuations and pairing in Fe-based superconductors: Light scattering experiments, *J. Phys.: Condens. Matter* **32**, 413001 (2020).
- [13] S. Hohenstein, U. Pachmayr, Z. Guguchia, S. Kamusella, R. Khasanov, A. Amato, C. Baines, H.-H. Klauss, E. Morenzoni, D. Johrendt, and H. Luetkens, Coexistence of low-moment magnetism and superconductivity in tetragonal FeS and suppression of  $T_c$  under pressure, *Phys. Rev. B* **93**, 140506(R) (2016).
- [14] F. K. K. Kirschner, F. Lang, C. V. Topping, P. J. Baker, F. L. Pratt, S. E. Wright, D. N. Woodruff, S. J. Clarke, and S. J. Blundell, Robustness of superconductivity to competing magnetic phases in tetragonal FeS, *Phys. Rev. B* **94**, 134509 (2016).
- [15] A. Wang, A. Milosavljevic, A. M. M. Abeykoon, V. Ivanovski, Q. Du, A. Baum, E. Stavitski, Y. Liu, N. Lazarevic, K. Attenkofer *et al.*, Suppression of superconductivity and nematic order in Fe<sub>1-y</sub>Se<sub>1-x</sub>S<sub>x</sub> ( $0 \leq x \leq 1$ ;  $y \leq 0.1$ ) crystals by anion height disorder, *Inorg. Chem.* **61**, 11036 (2022).
- [16] A. Wang, L. Wu, V. N. Ivanovski, J. B. Warren, J. Tian, Y. Zhu, and C. Petrovic, Critical current density and vortex pinning in tetragonal FeS<sub>1-x</sub>Se<sub>x</sub> ( $x = 0, 0.06$ ), *Phys. Rev. B* **94**, 094506 (2016).
- [17] V. Gnezdilov, Y. G. Pashkevich, P. Lemmens, D. Wulferding, T. Shevtsova, A. Gusev, D. Chareev, and A. Vasiliev, Interplay between lattice and spin states degree of freedom in the FeSe superconductor: Dynamic spin state instabilities, *Phys. Rev. B* **87**, 144508 (2013).
- [18] A. Baum, A. Milosavljević, N. Lazarević, M. M. Radonjić, B. Nikolić, M. Mitschek, Z. I. Maranloo, M. Šćepanović, M. Grujić-Brojčin, N. Stojilović *et al.*, Phonon anomalies in FeS, *Phys. Rev. B* **97**, 054306 (2018).
- [19] M. Cardona and M. L. W. Thewalt, Isotope effects on the optical spectra of semiconductors, *Rev. Mod. Phys.* **77**, 1173 (2005).
- [20] G. Turrell, *Infrared and Raman Spectra of Crystals* (Academic, London/New York, 1972).
- [21] Y. Mizukami, M. Haze, O. Tanaka, K. Matsuura, D. Sano, J. Böker, I. Eremin, S. Kasahara, Y. Matsuda, and T. Shibauchi, Thermodynamics of transition to BCS-BEC crossover superconductivity in FeSe<sub>1-x</sub>S<sub>x</sub>, [arXiv:2105.00739](https://arxiv.org/abs/2105.00739).
- [22] A. Baum, H. N. Ruiz, N. Lazarević, Y. Wang, T. Böhm, R. Hosseinian Ahangharnejhad, P. Adelman, T. Wolf, Z. V. Popović *et al.*, Frustrated spin order and stripe fluctuations in FeSe, *Commun. Phys.* **2**, 14 (2019).
- [23] H. Ruiz, Y. Wang, B. Moritz, A. Baum, R. Hackl, and T. P. Devereaux, Frustrated magnetism from local moments in FeSe, *Phys. Rev. B* **99**, 125130 (2019).
- [24] W. Spengler and R. Kaiser, First and second order Raman scattering in transition metal compounds, *Solid State Commun.* **18**, 881 (1976).
- [25] F. Nabeshima, Y. Kawai, N. Shikama, Y. Sakishita, A. Suter, T. Prokscha, S. E. Park, S. Komiya, A. Ichinose, T. Adachi, and A. Maeda, Sulfur-induced magnetism in FeSe<sub>1-x</sub>S<sub>x</sub> thin films on LaAlO<sub>3</sub> revealed by muon spin rotation/relaxation, *Phys. Rev. B* **103**, 184504 (2021).
- [26] X. Yi, X. Xing, L. Qin, J. Feng, M. Li, Y. Zhang, Y. Meng, N. Zhou, Y. Sun, and Z. Shi, Hydrothermal synthesis and complete phase diagram of FeSe<sub>1-x</sub>S<sub>x</sub> ( $0 \leq x \leq 1$ ) single crystals, *Phys. Rev. B* **103**, 144501 (2021).
- [27] J. K. Glasbrenner, I. I. Mazin, H. O. Jeschke, P. J. Hirschfeld, R. M. Fernandes, and R. Valentí, Effect of magnetic frustration on nematicity and superconductivity in iron chalcogenides, *Nat. Phys.* **11**, 953 (2015).
- [28] A. I. Coldea, Electronic nematic states tuned by isoelectronic substitution in bulk FeSe<sub>1-x</sub>S<sub>x</sub>, *Frontiers Phys.* **8**, 594500 (2021).
- [29] M. Yi, Z.-K. Liu, Y. Zhang, R. Yu, J.-X. Zhu, J. Lee, R. Moore, F. Schmitt, W. Li, S. Riggs *et al.*, Observation of universal strong orbital-dependent correlation effects in iron chalcogenides, *Nat. Commun.* **6**, 7777 (2015).
- [30] Z. P. Yin, K. Haule, and G. Kotliar, Kinetic frustration and the nature of the magnetic and paramagnetic states in iron pnictides and iron chalcogenides, *Nat. Mater.* **10**, 932 (2011).
- [31] K. M. Stadler, Z. P. Yin, J. von Delft, G. Kotliar, and A. Weichselbaum, Dynamical Mean-Field Theory Plus Numerical Renormalization-Group Study of Spin-Orbital Separation in a Three-Band Hund Metal, *Phys. Rev. Lett.* **115**, 136401 (2015).
- [32] S. L. Skornyakov, V. I. Anisimov, D. Vollhardt, and I. Leonov, Effect of electron correlations on the electronic structure and phase stability of FeSe upon lattice expansion, *Phys. Rev. B* **96**, 035137 (2017).
- [33] F. Kretzschmar, T. Böhm, U. Karahasanović, B. Muschler, A. Baum, D. Jost, J. Schmalian, S. Caprara, M. Grilli, C. Di Castro *et al.*, Critical spin fluctuations and the origin of nematic order in Ba(Fe<sub>1-x</sub>Co<sub>x</sub>)<sub>2</sub>As<sub>2</sub>, *Nat. Phys.* **12**, 560 (2016).
- [34] S. Chibani, D. Farina, P. Massat, M. Cazayous, A. Sacuto, T. Urata, Y. Tanabe, K. Tanigaki, A. E. Böhmer, P. C. Canfield *et al.*, Lattice-shifted nematic quantum critical point in FeSe<sub>1-x</sub>S<sub>x</sub>, *npj Quantum Mater.* **6**, 37 (2021).
- [35] U. Karahasanovic, F. Kretzschmar, T. Böhm, R. Hackl, I. Paul, Y. Gallais, and J. Schmalian, Manifestation of nematic degrees of freedom in the Raman response function of iron pnictides, *Phys. Rev. B* **92**, 075134 (2015).
- [36] W. Zhang, S. Wu, S. Kasahara, T. Shibauchi, Y. Matsuda, and G. Blumberg, Quadrupolar charge dynamics in the nonmagnetic FeSe<sub>1-x</sub>S<sub>x</sub> superconductors, *Proc. Natl. Acad. Sci. USA* **118**, e2020585118 (2021).
- [37] W. Setyawan and S. Curtarolo, High-throughput electronic band structure calculations: Challenges and tools, *Comput. Mater. Sci.* **49**, 299 (2010).
- [38] X. Gonze, B. Amadon, G. Antonius, F. Arnardi, L. Baguet, J.-M. Beuken, J. Bieder, F. Bottin, J. Bouchet, E. Bousquet *et al.*, The ABINIT project: Impact, environment and recent developments, *Comput. Phys. Commun.* **248**, 107042 (2020).

- [39] J. P. Perdew, A. Ruzsinszky, G. I. Csonka, O. A. Vydrov, G. E. Scuseria, L. A. Constantin, X. Zhou, and K. Burke, Restoring the Density-Gradient Expansion for Exchange in Solids and Surfaces, *Phys. Rev. Lett.* **100**, 136406 (2008).
- [40] D. R. Hamann, Optimized norm-conserving Vanderbilt pseudopotentials, *Phys. Rev. B* **88**, 085117 (2013).
- [41] M. van Setten, M. Giantomassi, E. Bousquet, M. Verstraete, D. Hamann, X. Gonze, and G.-M. Rignanese, The PseudoDojo: Training and grading a 85 element optimized norm-conserving pseudopotential table, *Comput. Phys. Commun.* **226**, 39 (2018).
- [42] P. Massat, D. Farina, I. Paul, S. Karlsson, P. Strobel, P. Toulemonde, M.-A. Méasson, M. Cazayous, A. Sacuto, S. Kasahara *et al.*, Charge-induced nematicity in FeSe, *Proc. Natl. Acad. Sci. USA* **113**, 9177 (2016).
- [43] L. D. Landau and E. M. Lifshitz, *Electrodynamics of Continuous Media* (Pergamon, Oxford, 1960), p. 377.

## Spin-phonon interaction and short-range order in $\text{Mn}_3\text{Si}_2\text{Te}_6$

S. Djurdjic Mijin,<sup>1</sup> A. Šolajić,<sup>1</sup> J. Pešić,<sup>1,\*</sup> Y. Liu,<sup>2,†</sup> C. Petrovic,<sup>2</sup> M. Bockstedte,<sup>3</sup> A. Bonanni,<sup>4</sup>  
Z. V. Popović,<sup>1,5</sup> and N. Lazarević<sup>1</sup>

<sup>1</sup>*Institute of Physics Belgrade, University of Belgrade, Pregrevica 118, 11080 Belgrade, Serbia*

<sup>2</sup>*Condensed Matter Physics and Materials Science Department, Brookhaven National Laboratory, Upton, New York 11973-5000, USA*

<sup>3</sup>*Institute for Theoretical Physics, Johannes Kepler University Linz, Altenbergerstrasse 69, 4040 Linz, Austria*

<sup>4</sup>*Institute of Semiconductor and Solid-State Physics, Johannes Kepler University Linz, Altenbergerstrasse 69, 4040 Linz, Austria*

<sup>5</sup>*Serbian Academy of Sciences and Arts, Knez Mihailova 35, 11000 Belgrade, Serbia*



(Received 7 September 2022; revised 31 January 2023; accepted 3 February 2023; published 21 February 2023)

The vibrational properties of ferrimagnetic  $\text{Mn}_3\text{Si}_2\text{Te}_6$  single crystals are investigated using Raman spectroscopy and density functional theory calculations. Eighteen Raman-active modes are identified, 14 of which are assigned according to the trigonal symmetry. Four additional peaks, obeying the  $A_{1g}$  selection rules, are attributed to the overtones. The unconventional temperature evolution of the  $A_{1g}^5$  mode self-energy suggests a competition between different short-range magnetic correlations that significantly impact the spin-phonon interaction in  $\text{Mn}_3\text{Si}_2\text{Te}_6$ . The research provides comprehensive insight into the lattice properties, studies their temperature dependence, and shows arguments for the existence of competing short-range magnetic phases in  $\text{Mn}_3\text{Si}_2\text{Te}_6$ .

DOI: [10.1103/PhysRevB.107.054309](https://doi.org/10.1103/PhysRevB.107.054309)

### I. INTRODUCTION

Layered magnetic van der Waals materials have lately received widespread attention due to their potential application in spintronics, magnetoelectronics, data storage, and biomedicine [1–7]. Recent experimental confirmation of a long-range magnetism persisting down to a monolayer in  $\text{CrI}_3$  [8] further affirmed these materials as a platform for magneto-optoelectronic devices [9], and as candidates for studying low-dimensional magnetism [10].

$\text{Mn}_3\text{Si}_2\text{Te}_6$  single crystals were first synthesized in 1985 [11]. However, few studies were carried out on this compound since. It was only recently that the attention has shifted to them, mainly through comparisons with quasi-two-dimensional materials, specifically  $\text{CrSiTe}_3$ . The vast majority of recent studies were focused on explaining the magnetism in  $\text{Mn}_3\text{Si}_2\text{Te}_6$  and determining its crystal structure. It was revealed that  $\text{Mn}_3\text{Si}_2\text{Te}_6$  crystallizes in a trigonal structure described by the  $P\bar{3}1c$  (No. 163) space group [11,12]. According to various magnetization studies,  $\text{Mn}_3\text{Si}_2\text{Te}_6$  is an insulating ferrimagnetic with Curie temperature  $T_c$  between 74 and 78 K [12–15]. First-principles calculations suggested a competition between the ferrimagnetic ground state and three additional magnetic configurations, originating from the antiferromagnetic exchange for the three nearest Mn-Mn pairs [15]. Additionally, both magnetization and diffuse neutron scattering experiments point at the existence of strong spin correlations well above  $T_c$ , which may be associated with

short-range order or to the preserved correlated excitations in the paramagnetic region [12,15].

Here, we present an experimental and theoretical Raman scattering study of  $\text{Mn}_3\text{Si}_2\text{Te}_6$  single crystals, with the focus on phonon properties in the temperature range from 80 to 320 K. Out of 18 observed modes, 14 ( $5A_{1g} + 9E_g$ ) are identified and assigned in agreement with the  $P\bar{3}1c$  space group. Phonon energies are in a good agreement with the theoretical predictions. Two most prominent Raman modes,  $A_{1g}^4$  and  $A_{1g}^5$ , are used to study the temperature evolution of phonon properties, and reveal three subsequent phase transitions at  $T_1 = 142.5$  K,  $T_2 = 190$  K, and  $T_3 = 285$  K. Furthermore, the  $A_{1g}^5$  mode exhibits strong asymmetry, most likely originating from enhanced spin-phonon coupling. Interestingly, the  $A_{1g}^5$  phonon line is symmetric in the temperature range  $T_1$ – $T_2$ , while becoming more asymmetric above  $T_3$ , potentially indicating that the strength of spin-phonon interaction changes with temperature. We speculate that the observed phenomenon, shown in the  $A_{1g}^5$  phonon, originates from the shift in dominance between competing magnetic states, that are found to be very close in energy [15].

### II. EXPERIMENTAL AND COMPUTATIONAL DETAILS

The  $\text{Mn}_3\text{Si}_2\text{Te}_6$  single-crystal samples used in this study are prepared according to the procedure described in Ref. [12]. The Raman spectra have been obtained with a Tri Vista 557 spectrometer (Teledyne Princeton Instruments, Trenton, NJ, USA) with a 1800/1800/2400 grooves/mm diffraction grating combination in a backscattering configuration. The 514-nm line of a Coherent  $\text{Ar}^+/\text{Kr}^+$  ion laser (Coherent, Santa Clara, CA, USA) is utilized as the excitation source. The direction of the incident (scattered) light coincides with

\*Corresponding author: [jelena.pesic@ipb.ac.rs](mailto:jelena.pesic@ipb.ac.rs)

†Present address: Los Alamos National Laboratory, Los Alamos, New Mexico 87545, USA.



TABLE I. Wyckoff positions of atoms and their contributions to the  $\Gamma$ -point phonons together with the corresponding Raman tensors for the  $P\bar{3}1c$  space group of  $Mn_3Si_2Te_6$ .

Space group: $P\bar{3}1c$	
Atoms	Irreducible representations
Mn (2c)	$A_{2g} + A_{2u} + E_g + E_u$
Mn (4f)	$A_{1g} + A_{1u} + A_{2g} + A_{2u} + 2E_g + 2E_u$
Si (4e)	$A_{1g} + A_{1u} + A_{2g} + A_{2u} + 2E_g + 2E_u$
Te (12i)	$3A_{1g} + 3A_{1u} + 3A_{2g} + 3A_{2u}$ $+ 6E_g + 6E_u$
Raman tensors	
	$A_{1g} = \begin{pmatrix} a & & \\ & a & \\ & & b \end{pmatrix}$
${}^1E_g = \begin{pmatrix} c & & \\ & -c & d \\ & d & \end{pmatrix}$	${}^2E_g = \begin{pmatrix} & -c & -d \\ & & \\ -c & & d \end{pmatrix}$

the crystallographic  $c$  axis. Laser-beam focusing is achieved through a microscope objective with  $50\times$  magnification. The temperature-dependent Raman scattering measurements have been performed under high vacuum ( $10^{-6}$  mbar), with the sample being placed inside of a KONTI CryoVac continuous helium flow cryostat (CryoVac GmbH & Co. KG, Troisdorf, Germany) with a 0.5-mm-thick window. The samples are cleaved in air before being placed into the cryostat. The obtained Raman spectra are corrected by a Bose factor. The spectrometer resolution is comparable to a Gaussian width of  $1\text{ cm}^{-1}$ .

The calculations are based on the density functional theory (DFT) formalism as implemented in the Vienna *ab initio* simulation package (VASP) [16–19], with the plane-wave basis truncated at a kinetic energy of 520 eV, using the Perdew-Burke-Ernzerhof (PBE) exchange-correlation functional [20] and projector augmented-wave (PAW) method [19,21]. The Monkhorst and Pack scheme of  $k$ -point sampling is employed to integrate over the first Brillouin zone with  $12 \times 12 \times 10$  at the  $\Gamma$ -centered grid. The convergence criteria for energy and force have been set to  $10^{-6}$  eV and  $0.001\text{ eV \AA}^{-1}$ , respectively. The DFT-D2 method of Grimme is employed for van der Waals (vdW) corrections [22]. The vibrational modes are calculated using density functional perturbation theory implemented in VASP and PHONOPY [23]. Previous DFT results found the energy of the ferrimagnetic state to be well above an eV per Mn below that of the nonmagnetic state [15], thus this configuration is considered in this study.

### III. RESULTS AND DISCUSSION

#### A. Polarization measurements

$Mn_3Si_2Te_6$  crystallizes in a trigonal  $P\bar{3}1c$  crystal structure [11,12]. The Wyckoff positions of the atoms and their contributions to the  $\Gamma$ -point phonons, together with the corresponding Raman tensors, are listed in Table I. In total, there are 16 Raman-active modes ( $5A_{1g} + 11E_g$ ) and 17 infrared-active modes ( $6A_{2u} + 11E_u$ ). According to the Raman tensors presented in Table I, in our scattering configuration and with

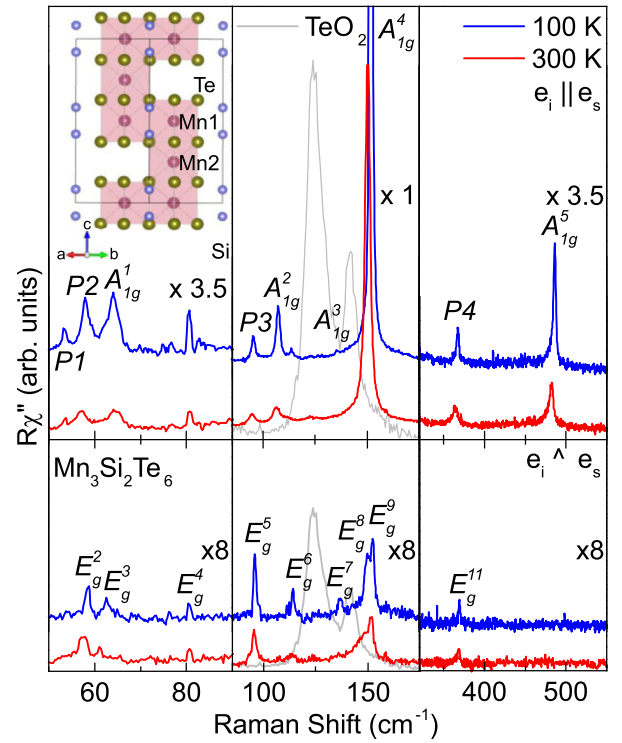


FIG. 1. Raman spectra of  $Mn_3Si_2Te_6$  single crystal measured in two scattering geometries at  $T = 100\text{ K}$  (blue solid line) and  $T = 300\text{ K}$  (red solid lines) with incident light being directed along  $[100]$ . Peaks observed in both geometries are identified as  $E_g$  modes, whereas peaks observed only for the parallel polarization configuration are assigned as  $A_{1g}$  modes. Gray line:  $TeO_2$  spectrum at  $300\text{ K}$ , scaled for clarity. The crystal structure of  $Mn_3Si_2Te_6$  viewed laterally along the  $c$  axis is presented in the inset.

Raman scattering events within the crystallographic  $ab$  plane,  $E_g$  symmetry modes can be observed in the Raman spectra measured in both parallel and crossed polarization configurations, whereas  $A_{1g}$  modes arise only for those in parallel polarization configuration.

As depicted in Fig. 1, nine phonon lines are observed in a parallel polarization configuration only, and identified as  $A_{1g}$  symmetry modes. According to the symmetry analysis only five  $A_{1g}$  symmetry modes are expected, resulting in four excess modes at  $53.3$ ,  $57.9$ ,  $95.3$ , and  $366.7\text{ cm}^{-1}$ . These modes may arise from infrared/silent phonons activated by disorder and from the relaxation of the symmetry selection rules [24–27]. However, it is more likely they are overtones. Overtones, which are always observable in  $A$  symmetries, but can also be observed in other symmetries, can become observable in Raman spectra due to disorder and/or enhanced coupling of the phonons to other excitations such as in the case of spin-phonon coupling [28].

Aside from the discussed  $A_{1g}$  symmetry modes, our spectra host nine modes which obey the  $E_g$  selection rules. Therefore, nine out of the expected 11  $E_g$  modes have been singled out and identified. The absence of two  $E_g$  modes might be attributed to their low intensity and/or the finite resolution of the spectrometer.

Calculated and experimental phonon energies are collected in Table II, and are found to be in good agreement with each

TABLE II. Phonon symmetries and phonon frequencies of  $\text{Mn}_3\text{Si}_2\text{Te}_6$  phonons. The experimental values are determined at 100 K. All calculations have been performed at zero 0 K. The experimental uncertainty is  $0.3 \text{ cm}^{-1}$ .

Space group $P\bar{3}1c$			
$n_0$	Symm.	Expt. ( $\text{cm}^{-1}$ )	Calc. ( $\text{cm}^{-1}$ )
1	$E_g^1$		53.1
2	$P1$	53.3	
3	$P2$	57.9	
4	$E_g^2$	58.7	58.5
5	$E_g^3$	62.6	61.8
6	$A_{1g}^1$	64.2	62.3
7	$E_g^4$	80.4	82.7
8	$P3$	95.3	
9	$E_g^5$	95.9	90.3
10	$A_{1g}^2$	107.3	104.3
11	$E_g^6$	114.0	106.5
12	$A_{1g}^3$	135.4	134.2
13	$E_g^7$	136.6	136.1
14	$E_g^8$	149.8	143.4
15	$A_{1g}^4$	151.8	147.3
16	$E_g^9$	152.6	146.6
17	$E_g^{10}$		352.7
18	$P4$	366.7	
19	$E_g^{11}$	368.7	354.5
20	$A_{1g}^5$	486.7	475.8

other, with the discrepancy being below 8% for all observed modes.

Our data significantly differ from those presented in Ref. [14] where two Raman-active modes were reported, one at  $118.4 \text{ cm}^{-1}$  and the other at  $136.9 \text{ cm}^{-1}$ , assigned as  $E_g$  and  $A_{1g}$ , respectively. The  $E_g$  and  $A_{1g}$  modes in our spectra closest (in terms of energy) to those reported in Ref. [14] are the peaks at  $\sim 114.3$  and  $135.4 \text{ cm}^{-1}$  (Table II). Although the discrepancy in phonon energy is not significant, the observed phonon linewidths strongly deviate from those presented in Ref. [14]. A possible explanation for the discrepancy is the presence of  $\text{TeO}_2$  in samples presented in Ref. [14], as the peaks reported there match rather well with the Raman response of  $\text{TeO}_2$  (Fig. 1). In order to avoid potential contamination in our study, measurements have been repeated on multiple crystals, and no oxide traces have been identified in the spectra.

### B. Temperature dependence

Some of the modes represented in Fig. 1 exhibit an asymmetric line shape. Although the appearance of a mode asymmetry can be attributed to the presence of defects [29], this would have a significant impact also on the linewidths of other modes in the spectrum, which is not the case here. The asymmetry may arise from coupling between the phonon and other elementary excitations [30–32]. The line shape originating from such a coupling is given by the Fano

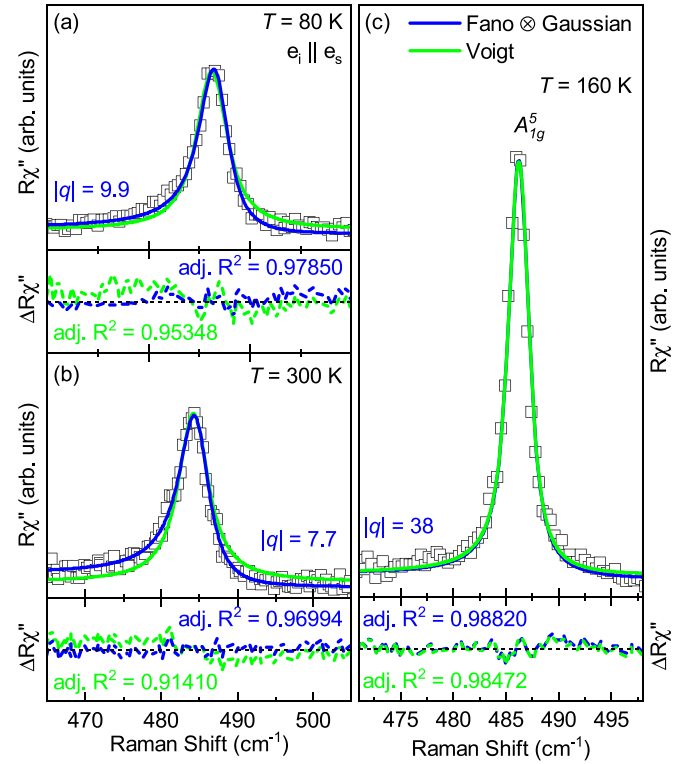


FIG. 2. Raman response as a function of the Raman shift. Quantitative analysis of the  $A_{1g}^5$  mode at temperatures as indicated. (a) and (b) The blue solid lines represent the line shape obtained as a convolution of Fano profiles and Gaussian, whereas the green solid lines represent Voigt profiles. (c) Comparison between asymmetric (deep blue) and symmetric (light blue) line shapes obtained as a Fano-Gaussian convolution and a Voigt profile. Experimental data are represented by open squares.

profile [33–36]

$$I(\omega) = I_0 \frac{(q + \epsilon)^2}{1 + \epsilon^2},$$

where  $\epsilon(\omega) = 2(\omega - \omega_0)/\Gamma$ . Here,  $\omega_0$  is the phonon frequency in the absence of interaction,  $\Gamma$  is the full width at half maximum (FWHM),  $I_0$  is the amplitude, and  $q$  is the Fano parameter. The Fano parameter and FWHM depend on the interaction strength between the phonon and the elementary excitation, and therefore can be used as its indicator. To include the finite spectral resolution of the experimental setup, the Fano profile is convoluted with a Gaussian function as demonstrated in Ref. [28].

The high-intensity peak at  $486.7 \text{ cm}^{-1}$ , identified as the  $A_{1g}^5$  symmetry mode, does not overlap with any other mode. The quantitative analysis of this peak is performed using both the symmetric Voigt profile and the Fano-Gaussian convolution mentioned above. The comparison between the two models and the experimental data at 80 and 300 K are presented in Figs. 2(a) and 2(b), respectively. The asymmetric line shapes provide a satisfactory description of the measured phonon line shape, suggesting the presence of an additional scattering mechanism in  $\text{Mn}_3\text{Si}_2\text{Te}_6$ .

The spectral region of the  $A_{1g}^5$  Raman-active mode in the temperature range of interest is presented in Fig. 3(a). The

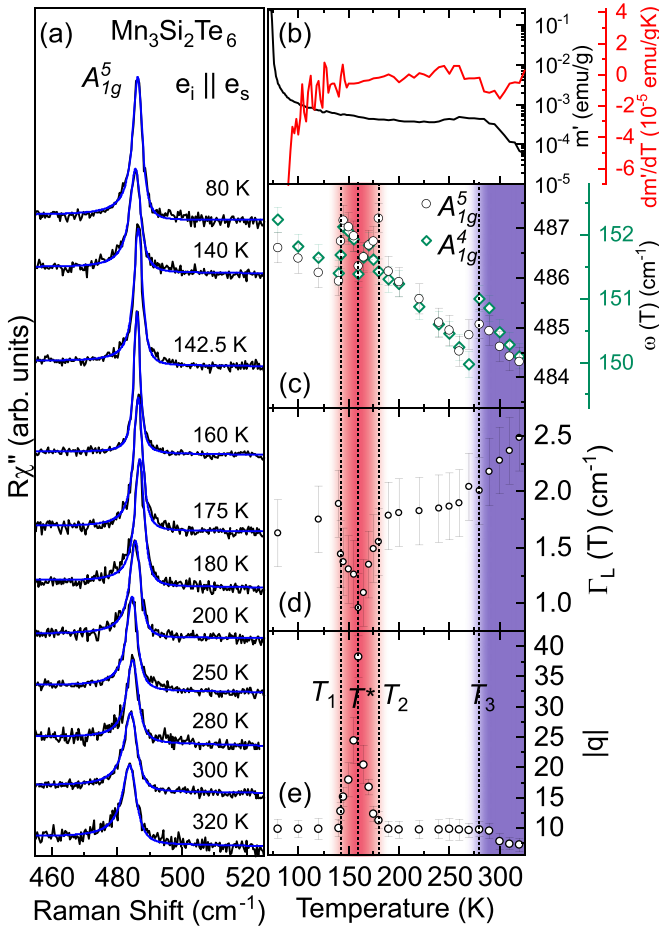


FIG. 3. (a) The spectral region of the  $A_{1g}^5$  Raman-active mode of  $\text{Mn}_3\text{Si}_2\text{Te}_6$  at indicated temperatures measured in the parallel polarization configuration. Green solid lines represent line shapes obtained as a convolution of the Fano line shape and Gaussian, calculated to fit the experimental data. (b) Temperature dependence of ac susceptibility real part  $m'(T)$  and its temperature derivative plotted as a function of temperature with  $\mathbf{H} \parallel \mathbf{ab}$ . Temperature dependence of (c) the energy of the  $A_{1g}^4$  and  $A_{1g}^5$  as well as (d) the linewidth, and (e) the Fano parameter  $|q|$  of the  $A_{1g}^5$  mode.

blue solid lines represent fits to the experimental data obtained using the Fano-Gaussian line shape. The temperature dependence of the phonon energy, linewidth, and the Fano parameter  $|q|$  of the  $A_{1g}^5$  mode are depicted in Figs. 3(c)–3(e), respectively. By increasing the temperature above 80 K, the  $A_{1g}^5$  mode broadens and softens up to  $T_1 = 142.5$  K, where it abruptly narrows and shifts to higher energies followed by further softening and narrowing up to  $T^* = 160$  K. Additional heating leads to a broadening and hardening before the drop in phonon energy at  $\sim T_2 = 190$  K. In the region  $T_2$  the mode softens and broadens with an additional jump in phonon energy at  $T_3 = 285$  K. A similar trend is also observed for the  $A_{1g}^4$  mode, as evidenced in Fig. 3(b).

This intriguing temperature dependence is also manifested in the asymmetry, i.e., the Fano parameter  $|q|$  [Fig. 3(d)] of the  $A_{1g}^5$  peak. At the lowest experimental temperature, 80 K, the  $A_{1g}^5$  mode exhibits strong asymmetry with a Fano parameter  $|q| = 9.9$ . Upon heating the sample to  $\sim T_1$  a Fano parameter

remains nearly constant before the significant increase in the temperature range between  $T_1$  and  $T^*$  resulting in a symmetric line shape [ $|q| = 38$ , Fig. 3(c)]. A further temperature increase leads to a strong decrease of  $|q|$  up to  $T_2$ , where the asymmetry is restored ( $|q| = 9.9$ ), remaining almost constant up to  $T_3$ . At higher temperatures, the line shape becomes more asymmetric, reaching  $|q| \sim 8$  at the highest experimentally accessible temperature  $T = 320$  K.

While the ferrimagnetic order in  $\text{Mn}_3\text{Si}_2\text{Te}_6$  is established only at  $T_c = 78$  K [12,14], the asymmetry of the mode can be observed at all experimental temperatures. Based on the research done on  $\text{Mn}_3\text{Si}_2\text{Te}_6$  and related materials, the most probable scenario is the one in which the observed asymmetry can be traced to an enhanced spin-phonon interaction related to short-range correlations, that can survive up to temperatures well above  $T_c$  [24,37–39]. We may speculate, according to the results presented in Ref. [15], that these short-range correlations are likely in terms of the antiferromagnetic exchange interaction between the three nearest Mn-Mn pairs (as depicted in Fig. 1) in the paramagnetic background. However, this alone cannot explain sudden changes in the properties of the  $A_{1g}^5$  phonon mode. Rather, the existence of competing short-range magnetic phases may be responsible for the observed behavior of the phonon modes. The first phonon mode anomaly at  $T_3 = 285$  K corresponds to the anomaly in  $m'(T)_{ab}$  [Fig. 3(b)] and can be seen as the outlet of additional short-range order in the paramagnetic domains [40] and possibly change of their nature of previously established ones. The onset in temperature with the magnetization anomaly near 330 K [14,41] is likely the consequence of local disorder. At  $T_2$ ,  $\text{Mn}_3\text{Si}_2\text{Te}_6$  becomes locally magnetically frustrated, resulting in the change in magnetostriction and a rapid decrease of the spin-phonon interaction that is manifested in the strong evolution of the phonon self-energy (Fig. 3). At this temperature both the magnetoresistance and nonlinearity of Hall resistance become observable [41]. In this scenario, by further lowering the temperature, at  $T_1$  a new short-range magnetic order and the strong spin-phonon interaction are established. The new magnetic order is most likely antiferromagnetic [15]. In order to fully understand the complex evolution of the short-range magnetic correlation in  $\text{Mn}_3\text{Si}_2\text{Te}_6$  that is manifested through the anomalous temperature development of the  $A_{1g}^5$  mode, further investigations are required.

#### IV. CONCLUSION

The lattice dynamic in single-crystalline  $\text{Mn}_3\text{Si}_2\text{Te}_6$  using Raman spectroscopy in analyzed. Five  $A_{1g}$  modes and nine  $E_g$  modes are observed and assigned according to the  $P\bar{3}1c$  symmetry group. Four additional peaks to the ones assigned to the  $P\bar{3}1c$  symmetry group, obeying  $A_{1g}$  selection rules, are attributed to overtones. There is a pronounced asymmetry of the  $A_{1g}^5$  phonon mode at 100 and 300 K. The unconventional temperature evolution of the  $A_{1g}^5$  Raman mode reveals three successive, possibly magnetic, phase transitions that may significantly impact the strength of the spin-phonon interaction in  $\text{Mn}_3\text{Si}_2\text{Te}_6$ . These are likely caused by the competition between the various magnetic states, close in energy. This paper provides comprehensive insight into the lattice properties, their temperature dependence, and shows arguments

for the existence of competing short-range magnetic phases in  $\text{Mn}_3\text{Si}_2\text{Te}_6$ .

### ACKNOWLEDGMENTS

The authors acknowledge funding provided by the Institute of Physics Belgrade, through a grant from the Ministry of Science, Technological Development and Innovations of the Republic of Serbia, the Serbian Academy of Sciences and Arts - Project No. F-134, the Science Fund of the Republic of

Serbia, PROMIS, 6062656, StrainedFeSC, Austrian Science Fund (FWF) through Project No. P31423, and the support of Austrian Academy of Sciences' Joint Excellence in Science and Humanities (JESH) Program (J.P.). DFT calculations were performed using computational resources at Johannes Kepler University (Linz, Austria). Materials synthesis was supported by the U.S. DOE-BES, Division of Materials Science and Engineering, under Contract No. DE-SC0012704 (BNL). The authors would like to thank Dr. Rudi Hackl for useful discussions that contributed to the finalized version of the manuscript.

- [1] Z. Guguchia, Unconventional magnetism in layered transition metal dichalcogenides, *Condensed Matter* **5**, 42 (2020).
- [2] Q. H. Wang, K. Kalantar-Zadeh, A. Kis, J. N. Coleman, and M. S. Strano, Electronics and optoelectronics of two-dimensional transition metal dichalcogenides, *Nat. Nanotechnol.* **7**, 699 (2012).
- [3] W. Han, R. K. Kawakami, M. Gmitra, and J. Fabian, Graphene spintronics, *Nat. Nanotechnol.* **9**, 794 (2014).
- [4] W. Zhang, R. Mazzarello, M. Wuttig, and E. Ma, Designing crystallization in phase-change materials for universal memory and neuro-inspired computing, *Nat. Rev. Mater.* **4**, 150 (2019).
- [5] C. Zhu, G. Yang, H. Li, D. Du, and Y. Lin, Electrochemical sensors and biosensors based on nanomaterials and nanostructures, *Anal. Chem.* **87**, 230 (2015).
- [6] X. J. Zhou, Magnetism in medicine: A handbook, second completely revised and enlarged edition, *Med. Phys.* **34**, 4978 (2007).
- [7] Q. H. Wang, A. Bedoya-Pinto, M. Blei, A. H. Dismukes, A. Hamo, S. Jenkins, M. Koperski, Y. Liu, Q.-C. Sun, E. J. Telford, H. H. Kim, M. Augustin, U. Vool, J.-X. Yin, L. H. Li, A. Falin, C. R. Dean, F. Casanova, R. F. L. Evans, M. Chshiev *et al.*, The magnetic genome of two-dimensional van der Waals materials, *ACS Nano* **16**, 6960 (2022).
- [8] B. Huang, G. Clark, E. Navarro-Moratalla, D. R. Klein, R. Cheng, K. L. Seyler, D. Zhong, E. Schmidgall, M. A. McGuire, D. Cobden, W. Yao, D. Xiao, P. Jarillo-Herrero, and X. Xu, Layer-dependent ferromagnetism in a van der Waals crystal down to the monolayer limit, *Nature (London)* **546**, 270 (2017).
- [9] S. Jiang, L. Li, Z. Wang, K. F. Mak, and J. Shan, Controlling magnetism in 2D  $\text{CrI}_3$  by electrostatic doping, *Nat. Nanotechnol.* **13**, 549 (2018).
- [10] N. Sethulakshmi, A. Mishra, P. Ajayan, Y. Kawazoe, A. K. Roy, A. K. Singh, and C. S. Tiwary, Magnetism in two-dimensional materials beyond graphene, *Mater. Today* **27**, 107 (2019).
- [11] H. Vincent, D. Leroux, and D. Bijaoui, Crystal structure of  $\text{Mn}_3\text{Si}_2\text{Te}_6$ , *J. Solid State Chem.* **63**, 349 (1986).
- [12] Y. Liu and C. Petrovic, Critical behavior and magnetocaloric effect in  $\text{Mn}_3\text{Si}_2\text{Te}_6$ , *Phys. Rev. B* **98**, 064423 (2018).
- [13] R. Rimet, C. Schlenker, and H. Vincent, A new semiconducting ferrimagnet: A silicon manganese telluride, *J. Magn. Magn. Mater.* **25**, 7 (1981).
- [14] L. M. Martinez, H. Iturriaga, R. Olmos, L. Shao, Y. Liu, T. T. Mai, C. Petrovic, A. R. Hight Walker, and S. R. Singamaneni, Enhanced magnetization in proton irradiated  $\text{Mn}_3\text{Si}_2\text{Te}_6$  van der Waals crystals, *Appl. Phys. Lett.* **116**, 172404 (2020).
- [15] A. F. May, Y. Liu, S. Calder, D. S. Parker, T. Pandey, E. Cakmak, H. Cao, J. Yan, and M. A. McGuire, Magnetic order and interactions in ferrimagnetic  $\text{Mn}_3\text{Si}_2\text{Te}_6$ , *Phys. Rev. B* **95**, 174440 (2017).
- [16] G. Kresse and J. Hafner, *Ab initio* molecular dynamics for liquid metals, *Phys. Rev. B* **47**, 558 (1993).
- [17] G. Kresse and J. Furthmüller, Efficiency of ab-initio total energy calculations for metals and semiconductors using a plane-wave basis set, *Comput. Mater. Sci.* **6**, 15 (1996).
- [18] G. Kresse and J. Furthmüller, Efficient iterative schemes for *ab initio* total-energy calculations using a plane-wave basis set, *Phys. Rev. B* **54**, 11169 (1996).
- [19] G. Kresse and D. Joubert, From ultrasoft pseudopotentials to the projector augmented-wave method, *Phys. Rev. B* **59**, 1758 (1999).
- [20] J. P. Perdew, K. Burke, and M. Ernzerhof, Generalized Gradient Approximation Made Simple, *Phys. Rev. Lett.* **77**, 3865 (1996).
- [21] P. E. Blöchl, Projector augmented-wave method, *Phys. Rev. B* **50**, 17953 (1994).
- [22] S. Grimme, Semiempirical GGA-type density functional constructed with a long-range dispersion correction, *J. Comput. Chem.* **27**, 1787 (2006).
- [23] A. Togo and I. Tanaka, First principles phonon calculations in materials science, *Scr. Mater.* **108**, 1 (2015).
- [24] F. Jin, N. Lazarević, C. Liu, J. Ji, Y. Wang, S. He, H. Lei, C. Petrovic, R. Yu, Z. V. Popović, and Q. Zhang, Phonon anomalies and magnetic excitations in  $\text{BaFe}_2\text{Se}_2\text{O}$ , *Phys. Rev. B* **99**, 144419 (2019).
- [25] M. Moskovits and D. Dilella, Surface-enhanced Raman spectroscopy of benzene and benzene- $d_6$  adsorbed on silver, *J. Chem. Phys.* **73**, 6068 (1980).
- [26] A. Dubroka, J. Humlíček, M. V. Abrashev, Z. V. Popović, F. Sapiña, and A. Cantarero, Raman and infrared studies of  $\text{La}_{1-y}\text{Sr}_y\text{Mn}_{1-x}\text{M}_x\text{O}_3$  ( $M = \text{Cr, Co, Cu, Zn, Sc, or Ga}$ ): Oxygen disorder and local vibrational modes, *Phys. Rev. B* **73**, 224401 (2006).
- [27] A. G. Souza Filho, J. L. B. Faria, I. Guedes, J. M. Sasaki, P. T. C. Freire, V. N. Freire, J. Mendes Filho, M. M. Xavier, F. A. O. Cabral, J. H. de Araújo, and J. A. P. da Costa, Evidence of magnetic polaronic states in  $\text{La}_{0.70}\text{Sr}_{0.30}\text{Mn}_{1-x}\text{Fe}_x\text{O}_3$  manganites, *Phys. Rev. B* **67**, 052405 (2003).
- [28] A. Baum, A. Milosavljević, N. Lazarević, M. M. Radonjić, B. Nikolić, M. Mitschek, Z. I. Maranloo, M. Šćepanović, M. Grujić-Brojčin, N. Stojilović, M. Opel, A. Wang, C. Petrovic,

- Z. V. Popović, and R. Hackl, Phonon anomalies in FeS, *Phys. Rev. B* **97**, 054306 (2018).
- [29] N. Lazarević, M. Radonjić, M. Šćepanović, H. Lei, D. Tanasković, C. Petrovic, and Z. V. Popović, Lattice dynamics of  $\text{KNi}_2\text{Se}_2$ , *Phys. Rev. B* **87**, 144305 (2013).
- [30] M. Balkanski, K. P. Jain, R. Beserman, and M. Jouanne, Theory of interference distortion of Raman scattering line shapes in semiconductors, *Phys. Rev. B* **12**, 4328 (1975).
- [31] D. Olego and M. Cardona, Self-energy effects of the optical phonons of heavily doped  $p$ -GaAs and  $p$ -Ge, *Phys. Rev. B* **23**, 6592 (1981).
- [32] E. H. Hasdeo, A. R. T. Nugraha, M. S. Dresselhaus, and R. Saito, Breit-Wigner-Fano line shapes in Raman spectra of graphene, *Phys. Rev. B* **90**, 245140 (2014).
- [33] U. Fano, Effects of configuration interaction on intensities and phase shifts, *Phys. Rev.* **124**, 1866 (1961).
- [34] P. H. M. van Loosdrecht, J. P. Boucher, G. Martinez, G. Dhalenne, and A. Revcolevschi, Inelastic Light Scattering from Magnetic Fluctuations in  $\text{CuGeO}_3$ , *Phys. Rev. Lett.* **76**, 311 (1996).
- [35] M. Braden, B. Hennion, W. Reichardt, G. Dhalenne, and A. Revcolevschi, Spin-Phonon Coupling in  $\text{CuGeO}_3$ , *Phys. Rev. Lett.* **80**, 3634 (1998).
- [36] J. W. Ager, W. Walukiewicz, M. McCluskey, M. A. Plano, and M. I. Landstrass, Fano interference of the Raman phonon in heavily boron-doped diamond films grown by chemical vapor deposition, *Appl. Phys. Lett.* **66**, 616 (1995).
- [37] S. Djurdjić Mijin, A. M. M. Abeykoon, A. Šolajić, A. Milosavljević, J. Pešić, Y. Liu, C. Petrovic, Z. V. Popović, and N. Lazarević, Short-range order in  $\text{VI}_3$ , *Inorg. Chem.* **59**, 16265 (2020).
- [38] L. J. Sandilands, Y. Tian, K. W. Plumb, Y.-J. Kim, and K. S. Burch, Scattering Continuum and Possible Fractionalized Excitations in  $\alpha$ - $\text{RuCl}_3$ , *Phys. Rev. Lett.* **114**, 147201 (2015).
- [39] A. Milosavljević, A. Šolajić, J. Pešić, Y. Liu, C. Petrovic, N. Lazarević, and Z. V. Popović, Evidence of spin-phonon coupling in  $\text{CrSiTe}_3$ , *Phys. Rev. B* **98**, 104306 (2018).
- [40] Y. Liu, Z. Hu, M. Abeykoon, E. Stavitski, K. Attenkofer, E. D. Bauer, and C. Petrovic, Polaronic transport and thermoelectricity in  $\text{Mn}_3\text{Si}_2\text{Te}_6$  single crystals, *Phys. Rev. B* **103**, 245122 (2021).
- [41] Y. Ni, H. Zhao, Y. Zhang, B. Hu, I. Kimchi, and G. Cao, Colossal magnetoresistance via avoiding fully polarized magnetization in the ferrimagnetic insulator  $\text{Mn}_3\text{Si}_2\text{Te}_6$ , *Phys. Rev. B* **103**, L161105 (2021).



# Ab-initio calculations of electronic and vibrational properties of Sr and Yb intercalated graphene

Andrijana Šolajić<sup>1</sup> · Jelena Pešić<sup>1</sup> · Radoš Gajić<sup>1</sup>

Received: 14 October 2017 / Accepted: 14 June 2018 / Published online: 20 June 2018  
© Springer Science+Business Media, LLC, part of Springer Nature 2018

## Abstract

Since the 1960s, Graphite intercalation compounds (GIC) have been extensively studied, showing many new properties and exotic physics. This inspired many to investigate a single or few-layer intercalated graphene. Intercalated graphene has many extraordinary properties and it is different compared to pristine graphene or bulk GICs, with great spectra of characteristics induced by various intercalants. This method opens new possibilities for research and applications in electronics and photonics. Here we present the results of a DFT study on electronic and vibrational properties of the graphene doped with Sr and Yb adatoms, taking into account that only their corresponding bulk compounds have been investigated so far. The calculations were performed in Quantum Espresso software package.

**Keywords** Graphene · DFT · Electronic properties · 2D materials

## 1 Introduction

Since the experimental discovery in Novoselov et al. (2004), graphene has been attracting enormous attention. The relativistic behaviour of the low-energy excitations (the so-called *Dirac fermions*) leads to many interesting effects and the linear electronic dispersion of graphene in the vicinity of the K-point mimics the physics of the massless fermions in quantum electrodynamics, at speed 300 times smaller than the speed of light. Therefore, many unusual properties can be observed in graphene, such are the Klein paradox (Katsnelson et al. 2006) or the anomalous integer quantum Hall effect (Gusynin and Sharapov 2005; Neto et al. 2006) which can be observed at room temperatures (Novoselov et al. 2007).

---

This article is part of the Topical Collection on Focus on Optics and Bio-photonics, Photonica 2017.

---

Guest Edited by Jelena Radovanovic, Aleksandar Krmpot, Marina Lekic, Trevor Benson, Mauro Pereira, Marian Marciniak.

---

✉ Andrijana Šolajić  
solajic@ipb.ac.rs

<sup>1</sup> Laboratory for Graphene, Other 2D Materials and Ordered Nanostructures, Center for Solid State Physics and New Materials, Institute of Physics Belgrade, University of Belgrade, Pregrevica 118, Belgrade 11080, Serbia

Graphene has excellent thermal conductivity, high electron mobility (Bolotin et al. 2008) and transparency, and at the same time it is one of the strongest materials known (Lee et al. 2008), about 200 times stronger than structural steel, yet very flexible and stretchable. With all its unique properties, graphene has various potential applications in almost all research fields, especially in electronics and optoelectronics (Ferrari 2015; Blake et al. 2008; Todorović et al. 2015). With high electrical and optical conductivity, it is promising candidate for applications in energy storage (Bonaccorso et al. 2015), detectors (Sassi et al. 2017; Liu et al. 2014), or even for the flexible touch screen technology (Ahn and Hong 2014; Bae et al. 2010). Ultra-thin graphitic films are also well researched for applications in photonics with high transparency and electrical conductivity (Matković et al. 2016).

Already extraordinary characteristics of graphene can be tailored and enhanced in many ways—by various types of disorders, controlling the type of edges (Peres et al. 2006; Wakabayashi et al. 1996, 2009), number of layers, by doping, applying the strain (Levy et al. 2010; Choi et al. 2010; Settnes et al. 2016; Masir et al. 2013), etc. Among them, doping graphene is an excellent way to make graphene suitable for various applications (Sharma and Ahn 2013; Wang et al. 2010; Qu et al. 2010; Jeong et al. 2011; Cui et al. 2011). Especially interesting is intercalation of various species in a few layer graphene (or doping a single layer graphene with adatoms), in a similar manner to the graphite intercalation compounds (GIC). This provides very high level of doping and leads to many interesting effects that are not present in pristine graphene, offering a new way to design various materials with magnetic, highly conductive or superconducting properties. Doping via adsorption is also very convenient, as the graphene can host various adatoms or small molecules while preserving its own structure, and at the same time drastically change its electronic properties. By covering the graphene sheet with the layer of adatoms, significant structural changes are avoided, as the dopant atoms are not fitted in the graphene lattice instead of the carbon atoms. However, adsorbed atoms can strongly affect the electronic properties of graphene, dominantly through the  $p_z$  orbitals. Therefore, it is an excellent tool for tuning the properties of graphene in a wide range and obtain new effects. GIC have been extensively researched since the 1960s (Rüdrorf 1959; Enoki et al. 2003; Dresselhaus and Dresselhaus 2002), but the interest for them has significantly raised with discovery of the superconductivity in some of the alkali or alkaline earth metal intercalated graphite structures, among which are  $\text{CaC}_6$  and  $\text{YbC}_6$  (Weller et al. 2005) with relatively high critical temperatures of  $T_c = 11.5$  K and  $T_c = 6.5$  K. As research of 2D materials has raised in the last decade, the superconductivity in GIC imposed a question of investigating the monolayer graphene doped with alkali and alkaline earth metal adatoms, searching for the atomically thin superconductors. The electrical characteristics of the doped graphene depend strongly on the species of the used adatom. Reports on related structures suggest the occurrence of superconductivity in some of them, usually with alkali or alkaline earth metals doping, similar to the GICs. The explanation for the emergence of the superconductivity in the alkali doped graphene lies in the electron-phonon coupling that arises from the new intercalant-derived band and the graphene  $\pi$ -bands at the Fermi level. Among first researched doped graphene structures was Li decorated graphene (Profeta et al. 2012; Pešić et al. 2015), which is superconducting with the critical temperature of  $T = 5.9$  K. It can also be enhanced by applying the strain (Pešić et al. 2014). The experimental evidence of superconductivity in the Li doped graphene (Ludbrook 2015) inspired many to search for other 2D superconducting structures (Calandra et al. 2012; Penev et al. 2016; Shimada et al. 2017; Saito et al. 2016). Graphene doped with the Ca atoms is also reported to be superconducting as the doped monolayer (Profeta et al. 2012) and bilayer intercalated graphene (Mazin and Balatsky 2010; Margine et al. 2016), there are also reports for a

few-layer potassium doped graphene (Xue et al. 2012). Among other similar structures, the heavily n-doped graphene was also predicted to be superconducting (Margine and Giustino 2014), the combination of biaxial strain with charge doping, which leads to the superconductor with  $T_c$  estimated to be up to 30 K (Si et al. 2013), or the hole-doped graphene which was predicted to be a high  $T_c$  superconductor, with a critical temperature in range 60–80 K (Durajski 2015). However, many possible structures based on doped graphene with potential superconducting properties are not considered yet.

In this paper we studied the electronic and vibrational properties of Sr and Yb doped graphene using the density functional theory approach. We were motivated by the fact that both structures are known as superconductors in their corresponding bulk compounds,  $\text{YbC}_6$  with critical temperature of  $T_c = 6.5$  K (Weller et al. 2005) and  $\text{SrC}_6$  with up to  $T_c = 3.03$  K (Calandra and Mauri 2006). We are first to report the results for a monolayer graphene doped with those adatoms.

## 2 Computational details

All calculations were performed using the Quantum Espresso software package (Giannozzi et al. 2009), based on the plane waves and pseudopotentials. We used norm-conserving pseudopotentials (Perdew and Zunger 1981) and LDA exchange-correlation functional. The plane wave energy cutoff is 120 Ry for  $\text{SrC}_6$ -mono and 160 Ry for  $\text{YbC}_6$ -mono. The unit cell for both structures is modelled as  $\sqrt{3} \times \sqrt{3}R30^\circ$  supercell of the graphene unit cell, with adatoms positioned in the H-site. This is the favorable adsorption site for both adatoms, according to the DFT study (Nakada and Ishii 2011). The value of the hexagonal cell parameter  $a$  is  $4.26\text{\AA}$  taken theoretically, as there are no experimental realization of those structures. The top and side view of the structures are shown in Fig. 1. In order to avoid interactions between layers, the hexagonal cell parameter  $c$  of the unit cell was chosen to be sufficiently large,  $c = 11.4\text{\AA}$  for  $\text{SrC}_6$ -mono and  $11.3\text{\AA}$  for  $\text{YbC}_6$ -mono. Prior to any calculations, the ionic positions in systems are fully relaxed to their minimum energy configuration, using the Broyden-Fletcher-Goldfarb-Shanno (BFGS) algorithm. Obtained vertical distance between graphene layer and the adsorbed atom is  $h = 2.22\text{\AA}$  for  $\text{SrC}_6$ -mono and  $h = 2.25\text{\AA}$  for  $\text{YbC}_6$ -mono. Phonon properties are obtained with the Density

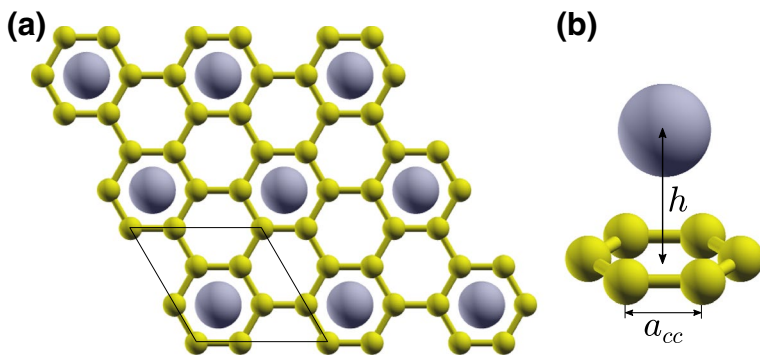


**Fig. 1** **a** Top view of the graphene structure with the adatoms adsorbed in the H-site. Unit cell is marked with the black line, **b** side view of the one hexagon with the adatom above



Functional Perturbation Theory (DFPT) implemented in the PHonon part of the Quantum Espresso software.

### 3 Results and discussion

As we said in Sect. 2, the unit cell for our H-site doped structures is enlarged compared to the pristine graphene. Due to the increase in the size of the primitive cell in direct space, basis vector lengths in reciprocal space are reduced. As a consequence, the K-point of the Brillouin zone of graphene is folded to the  $\Gamma$  point of the Brillouin zone of H-site doped graphene. Brillouin zones of the graphene unit cell and the H-site doped graphene are shown in Fig. 2.

#### 3.1 Electronic properties

Electronic dispersions along  $\Gamma$ -M-K- $\Gamma$  high symmetry points for  $\text{SrC}_6$ -mono and  $\text{YbC}_6$ -mono are shown in Fig. 3. Fermi level is set to zero in all figures. Folding the  $\pi$  and  $\pi^*$  bands of graphene from K-point to  $\Gamma$ -point, the inner and outer carbon  $\pi$  and  $\pi^*$  bands are obtained, crossing at the  $\Gamma$  point. For both structures, lower bands from the  $\sigma$  bonds in the valence band are almost unaffected, as expected, and they are not shown in figures. The Fermi level is shifted up in both structures. By deposition of adatoms on top of graphene, new interlayer band derived from the Yb or Sr adatoms is formed around the Fermi level, showing a nearly free-electron-like dispersion. They are placed at 2.2 and 1.5 eV below the Fermi level in the  $\text{YbC}_6$ -mono and  $\text{SrC}_6$ -mono, respectively, being partially occupied. The density of states on Fermi level is also raised. The carbon  $\pi$  bands are not affected by the presence of the adatoms. Previously unoccupied  $\pi^*$  bands now intersect the new up-shifted Fermi level and are strongly hybridized with the new band derived from the adsorbed atoms. In  $\text{YbC}_6$ -mono,  $4f$  orbitals coming from the Yb atoms form a set of flat non-dispersive bands, similar to the bulk  $\text{YbC}_6$  (Csányi et al. 2005). Those flat bands are characteristic for most lanthanides. They are localized at 0.7 eV below the Fermi level with the corresponding peak clearly observed in the density of states. As reported for the bulk  $\text{YbC}_6$ , calculations with the Hubbard+U corrections do not give significant changes and result only in slightly shifting down those bands, so the same is expected for the monolayer. The Dirac points from graphene are folded to the  $\Gamma$  point in the H-site doped graphene, and

**Fig. 2** Brillouin zones of graphene (black) and the H-site doped graphene (red). (Color figure online)

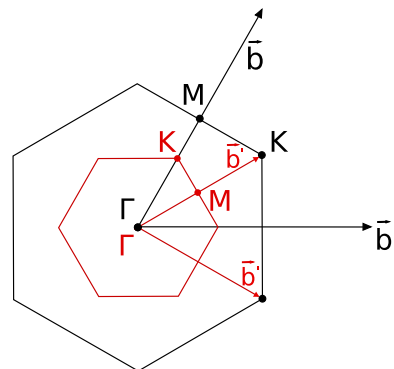
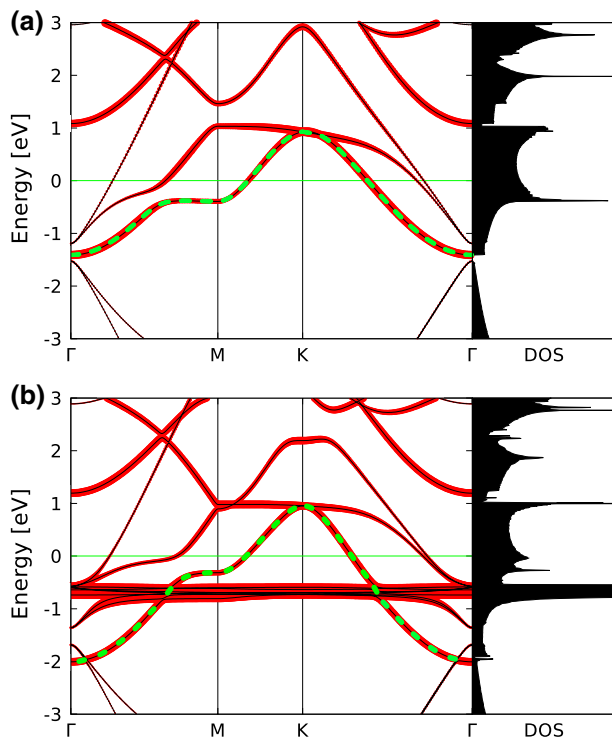


**Fig. 3** Electronic dispersions of **a** SrC<sub>6</sub>-mono and **b** YbC<sub>6</sub>-mono. Thickness of the red lines is proportional to the Sr/Yb character and the interlayer band is marked in green dotted line. (Color figure online)



they are now below the Fermi level. Due to the adatom presence, the symmetry is broken and a gap is opened. In the SrC<sub>6</sub>, interlayer band is placed between the  $\pi$  and  $\pi^*$  and a very small gap can be observed in the density of states, while in the YbC<sub>6</sub>-mono, the new interlayer band intersect the  $\pi$  band and the gap is closed.

### 3.2 Phonon properties

The symmetry group of graphene with adatoms adsorbed in the H-site is  $Dg77 = T' C_{6v}$ , which is a subgroup of the diperiodic group of graphene,  $Dg80 = TD_{6h}$  (Damljanović et al. 2014). In order to connect the phonon modes of the H-site doped graphene with the corresponding phonon modes of graphene, the corresponding irreducible representation of group  $Dg77$  of graphene to its subgroup  $Dg80$  (Damljanović et al. 2014). The modes from the  $\Gamma$  point,  $\Gamma E_{2g}$  and  $\Gamma B_{1g}$  correspond to  $\Gamma E_2$  and  $\Gamma B_1$ . For the modes of graphene in the K point,  $KA'_1$  corresponds to the modes  $A_1$  and  $B_2$ ,  $KA'_2$  to  $A_2$  and  $B_1$ ,  $KE'$  and  $KE''$  to  $E_1$  and  $E_2$  (Altmann and Herzig 1994; Damljanović and Gajić 2012). The modes  $A_1$  and  $E_1$  are both infrared and Raman active, while  $E_2$  modes are only Raman active. The symmetry classification of optical modes and Raman tensors for H-site doped graphene are given in Table 1. The displacement patterns of the SrC<sub>6</sub>-mono and YbC<sub>6</sub>-mono, in the  $\Gamma$  point are shown in Fig. 4. Those modes have displacement patterns similar to those of graphene phonons at  $\Gamma$  and K points, which happens due to the Brillouin zone folding. As the K point of graphene is folded to the  $\Gamma$  point of the new Brillouin zone in the H-site doped graphene, the phonon modes in graphene at the  $\Gamma$  and K points correspond to the  $\Gamma$  modes in the H-site doped

**Table 1** Raman tensors and symmetry classification of optical modes

Raman tensors			
Graphene	$A_{1g}$	$E_{1g}$	$E_{2g}$
$Dg80 = TD_{6h}$	$\begin{pmatrix} a & 0 & 0 \\ 0 & a & 0 \\ 0 & 0 & b \end{pmatrix}$	$\begin{pmatrix} 0 & 0 & 0 \\ 0 & 0 & c \\ 0 & c & 0 \end{pmatrix}$	$\begin{pmatrix} 0 & 0 & -c \\ 0 & 0 & 0 \\ c & 0 & 0 \end{pmatrix}$
$O_z \parallel C_6$			
$O_x \parallel C_2$			
$A\alpha$	$A_1$	$E_1$	$E_2$
$Dg77 = TC_{6v}$	$\begin{pmatrix} a & 0 & 0 \\ 0 & a & 0 \\ 0 & 0 & b \end{pmatrix}$	$\begin{pmatrix} 0 & 0 & c \\ 0 & 0 & 0 \\ c & 0 & 0 \end{pmatrix}$	$\begin{pmatrix} 0 & 0 & 0 \\ 0 & -d & 0 \\ 0 & 0 & 0 \end{pmatrix}$
$O_z \parallel C_6$			
$O_x \parallel \sigma_v$			
Optical modes	$\Gamma_{opt} = 2A_1 + A_2 + 2B_1 + B_2 + 3E_1 + 3E_2$		

structures. This is valid for all H-site doped graphene structures as the unit cell is the type. As the Kohn anomaly is present in graphene at  $\Gamma$  and K points in  $E_{2g}$  and  $KA'_1$  modes, we expect it to be present in the H-site doped graphene structures for the modes related to these two. Modes with Kohn anomaly can not be calculated precisely using the density functional theory as the DFT is based on the adiabatic Born-Oppenheimer approximation which is in this case broken. Comparing the calculated phonon modes for graphene at K and  $\Gamma$  point, with the corresponding phonon modes at the  $\Gamma$  point of the  $SrC_6$  and  $YbC_6$  monolayers, we can observe small differences in the corresponding frequencies. Some of these are lower than in pristine graphene and some frequencies are split. For example, frequencies of  $E_2$  mode in Sr and Yb doped graphene are  $1470\text{ cm}^{-1}$  and  $1488\text{ cm}^{-1}$ , respectively, while the frequency of  $E_{2g}$  in pristine graphene is  $1550\text{ cm}^{-1}$ ; Frequency of  $E'$  mode in graphene is  $1200\text{ cm}^{-1}$ , and corresponding modes in doped graphene are  $E_2$  at  $1180\text{ cm}^{-1}$  and  $E_1$  at  $1200\text{ cm}^{-1}$ ;  $E''$  mode in graphene is at  $580\text{ cm}^{-1}$ , and corresponding modes in doped graphene are  $E_2$  at  $495\text{ cm}^{-1}$  and  $E_1$  at  $510\text{ cm}^{-1}$  for  $SrC_6$ -mono and  $E_2$  at  $477\text{ cm}^{-1}$  and  $E_1$  at  $500\text{ cm}^{-1}$  for  $YbC_6$ -mono. This can be ascribed to the adatoms impact, and in general, it depends on the type of the adatom.

### 4 Conclusion

Using the density functional theory approach, we calculated the electronic and phonon properties of the Sr and Yb doped graphene, in a similar manner to the GICs. Their corresponding bulk compounds have been studied so far and we are first to investigate the monolayer graphene doped with those adatoms. The electronic and phonon properties are of essential interest for electron-phonon coupling as well as the guidelines for experimental research. From the electronic band structure calculations, we can observe a new adatom-derived interlayer band crossing the Fermi level in both structures, which hybridize strongly with the carbon  $p_z$  orbitals. Density of states on the Fermi level is also raised. Those results can be indicating a possible superconductivity and can be inspiring for further research of those structures. Displacement patterns calculated in the  $\Gamma$  point are similar to those in the K and  $\Gamma$  point of the pristine graphene, as a consequence of the zone folding effect, but due to the adatoms impact we can observe some differences in frequencies and the splitting of

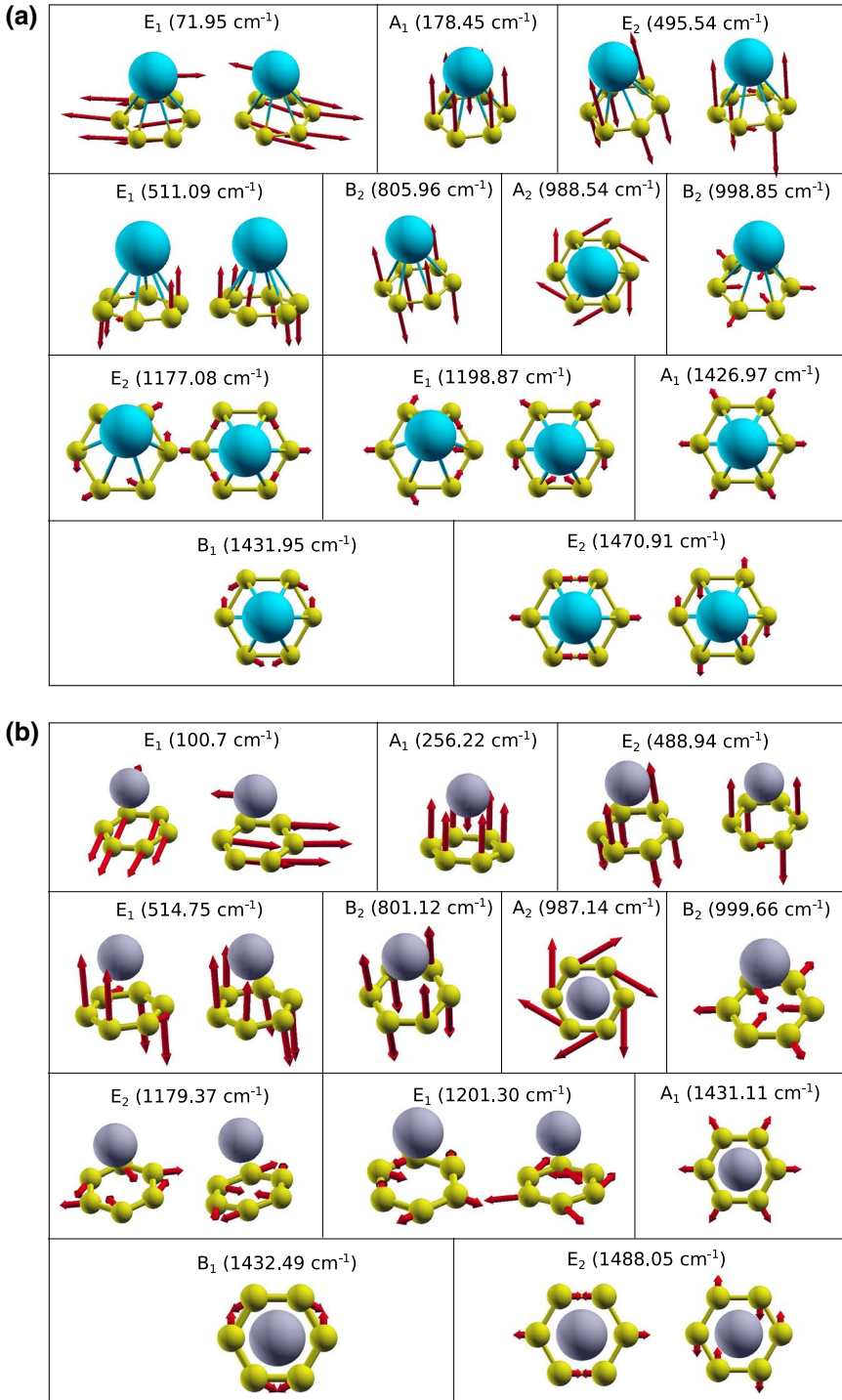


**Fig. 4** Displacement patterns of **a** SrC<sub>6</sub>-mono and **b** YbC<sub>6</sub>-mono. Acoustic modes ( $\omega = 0$ ) are not shown in pictures

some modes. The results obtained in this paper are important base for further theoretical and experimental research of those two structures, as well for future research of similar structures of graphene doped with other metal adatoms.

**Acknowledgements** This work is supported by the Serbian MPNTR through Project OI 171005 and by Qatar National Research Foundation through Project NPRP 7-665-1-12.

## References

- Ahn, J.H., Hong, B.H.: Graphene for displays that bend. *Nat. Nanotechnol.* **9**(10), 737–738 (2014)
- Altmann, S., Herzog, P.: *Point-Group Theory Tables*. Oxford Science Publications, Clarendon Press, Oxford (1994)
- Bae, S., Kim, H., Lee, Y., Xu, X., Park, J.S., Zheng, Y., Balakrishnan, J., Lei, T., Kim, H.R., Song, Y.I., et al.: Roll-to-roll production of 30-inch graphene films for transparent electrodes. *Nat. Nanotechnol.* **5**(8), 574–578 (2010)
- Blake, P., Brimicombe, P.D., Nair, R.R., Booth, T.J., Jiang, D., Schedin, F., Ponomarenko, L.A., Morozov, S.V., Gleeson, H.F., Hill, E.W., Geim, A.K., Novoselov, K.S.: Graphene-based liquid crystal device. *Nano Lett.* **8**(6), 1704–1708 (2008)
- Bolotin, K., Sikes, K., Jiang, Z., Klima, M., Fudenberg, G., Hone, J., Kim, P., Stormer, H.: Ultrahigh electron mobility in suspended graphene. *Solid State Commun.* **146**(9), 351–355 (2008)
- Bonaccorso, F., Colombo, L., Yu, G., Stoller, M., Tozzini, V., Ferrari, A.C., Ruoff, R.S., Pellegrini, V.: Graphene, related two-dimensional crystals, and hybrid systems for energy conversion and storage. *Science* **347**(6217), 1246501 (2015)
- Calandra, M., Mauri, F.: Possibility of superconductivity in graphite intercalated with alkaline earths investigated with density functional theory. *Phys. Rev. B* **74**, 094507 (2006)
- Calandra, M., Profeta, G., Mauri, F.: Superconductivity in metal-coated graphene. *Physica Status Solidi (B)* **249**(12), 2544–2548 (2012)
- Choi, S.M., Jhi, S.H., Son, Y.W.: Effects of strain on electronic properties of graphene. *Phys. Rev. B* **81**, 081407 (2010)
- Csányi, G., Littlewood, P., Nevidomskyy, A.H., Pickard, C.J., Simons, B.: The role of the interlayer state in the electronic structure of superconducting graphite intercalated compounds. *Nat. Phys.* **1**(1), 42–45 (2005)
- Cui, T., Lv, R., Huang, Z.H., Zhu, H., Zhang, J., Li, Z., Jia, Y., Kang, F., Wang, K., Wu, D.: Synthesis of nitrogen-doped carbon thin films and their applications in solar cells. *Carbon* **49**(15), 5022–5028 (2011)
- Damljanović, V., Kostić R., Gajić R.: Characters of graphenes symmetry group dg80. *Physica Scr.* **2014**(T162), 014022 (2014)
- Damljanović, V., Gajić, R.: Phonon eigenvectors of graphene at high-symmetry points of the brillouin zone. *Physica Scr.* **2012**(T149), 014067 (2012)
- Dresselhaus, M.S., Dresselhaus, G.: Intercalation compounds of graphite. *Adv. Phys.* **51**(1), 1–186 (2002)
- Durajski, A.P.: Influence of hole doping on the superconducting state in graphane. *Supercond. Sci. Technol.* **28**(3), 035002 (2015)
- Enoki, T., Suzuki, M., Endo, M.: *Graphite Intercalation Compounds and Applications*, pp. 1–456. Oxford University Press, Oxford (2003)
- Ferrari, A.C., et al.: Science and technology roadmap for graphene, related two-dimensional crystals, and hybrid systems. *Nanoscale* **7**, 4598–4810 (2015)
- Giannozzi, P., et al.: Quantum espresso: a modular and open-source software project for quantum simulations of materials. *J. Phys. Condens. Matter* **21**(39), 395–502 (2009)
- Gusynin, V.P., Sharapov, S.G.: Unconventional integer quantum hall effect in graphane. *Phys. Rev. Lett.* **95**, 146801 (2005)
- Jeong, H.M., Lee, J.W., Shin, W.H., Choi, Y.J., Shin, H.J., Kang, J.K., Choi, J.W.: Nitrogen-doped graphene for high-performance ultracapacitors and the importance of nitrogen-doped sites at basal planes. *Nano Lett.* **11**(6), 2472–2477 (2011)
- Katsnelson, M., Novoselov, K., Geim, A.: Chiral tunnelling and the klein paradox in graphene. *Nat. Phys.* **2**(9), 620–625 (2006)

- Lee, C., Wei, X., Kysar, J.W., Hone, J.: Measurement of the elastic properties and intrinsic strength of monolayer graphene. *Science* **321**(5887), 385–388 (2008)
- Levy, N., Burke, S.A., Meaker, K.L., Panlasigui, M., Zettl, A., Guinea, F., Neto, A.H.C., Crommie, M.F.: Strain-induced pseudo-magnetic fields greater than 300 tesla in graphene nanobubbles. *Science* **329**(5991), 544–547 (2010)
- Liu, C.H., Chang, Y.C., Norris, T.B., Zhong, Z.: Graphene photodetectors with ultra-broadband and high responsivity at room temperature. *Nat. Nanotechnol.* **9**(4), 273–278 (2014)
- Ludbrook, B.M., et al.: Evidence for superconductivity in li-decorated monolayer graphene. *Proc. Nat. Acad. Sci.* **112**(38), 11795–11799 (2015)
- Margine, E.R., Giustino, F.: Two-gap superconductivity in heavily *n*-doped graphene: Ab initio migdal-elishberg theory. *Phys. Rev. B* **90**, 014518 (2014)
- Margine, E., Lambert, H., Giustino, F.: Electron-phonon interaction and pairing mechanism in superconducting ca-intercalated bilayer graphene. *Sci. Rep.* **6**, 21414 (2016)
- Masir, M.R., Moldovan, D., Peeters, F.: Pseudo magnetic field in strained graphene: revisited. *Solid State Commun.* **175**, 76–82 (2013)
- Matković, A., Milošević, I., Milićević, M., Tomašević-Ilić, T., Pešić, J., Musić, M., Spasenović, M., Jovanović, D., Vasić, B., Deeks, C., Panajotović, R., Belić, M.R., Gajić, R.: Enhanced sheet conductivity of Langmuir-Blodgett assembled graphene thin films by chemical doping. *2D Mater.* **3**(1), 015002 (2016)
- Mazin, I., Balatsky, A.: Superconductivity in Ca-intercalated bilayer graphene. *Philos. Mag. Lett.* **90**(10), 731–738 (2010)
- Nakada, K., Ishii, A.: DFT calculation for adatom adsorption on graphene. In: Gong, J.R. (ed.) *Graphene Simulation*. InTech, Rijeka, Croatia (2011)
- Neto, A.H.C., Guinea, F., Peres, N.M.R.: Edge and surface states in the quantum hall effect in graphene. *Phys. Rev. B* **73**, 205408 (2006)
- Novoselov, K.S., Geim, A.K., Morozov, S.V., Jiang, D., Zhang, Y., Dubonos, S.V., Grigorieva, I.V., Firsov, A.A.: Electric field effect in atomically thin carbon films. *Science* **306**(5696), 666–669 (2004)
- Novoselov, K.S., Jiang, Z., Zhang, Y., Morozov, S.V., Stormer, H.L., Zeitler, U., Maan, J.C., Boebinger, G.S., Kim, P., Geim, A.K.: Room-temperature quantum hall effect in graphene. *Science* **315**(5817), 1379–1379 (2007)
- Penev, E.S., Kutana, A., Yakobson, B.I.: Can two-dimensional boron superconduct? *Nano Lett.* **16**(4), 2522–2526 (2016)
- Perdew, J.P., Zunger, A.: Self-interaction correction to density-functional approximations for many-electron systems. *Phys. Rev. B* **23**, 5048–5079 (1981)
- Peres, N.M.R., Neto, A.H.C., Guinea, F.: Conductance quantization in mesoscopic graphene. *Phys. Rev. B* **73**, 195411 (2006)
- Pešić, J., Gajić, R., Hingerl, K., Belić, M.: Strain-enhanced superconductivity in li-doped graphene. *EPL (Europhys. Lett.)* **108**(6), 67005 (2014)
- Pešić, J., Damljanović, V., Gajić, R., Hingerl, K., Belić, M.: Density functional theory study of phonons in graphene doped with Li, Ca and Ba. *EPL (Europhys. Lett.)* **112**(6), 67006 (2015)
- Profeta, G., Calandra, M., Mauri, F.: Phonon-mediated superconductivity in graphene by lithium deposition. *Nat. Phys.* **8**(2), 131–134 (2012)
- Qu, L., Liu, Y., Baek, J.B., Dai, L.: Nitrogen-doped graphene as efficient metal-free electrocatalyst for oxygen reduction in fuel cells. *ACS Nano* **4**(3), 1321–1326 (2010)
- Rüddorf, W.: *Graphite Intercalation Compounds*. *Advances in Inorganic Chemistry and Radiochemistry*, pp. 223–266. Academic Press, Cambridge (1959)
- Saito, Y., Nojima, T., Iwasa, Y.: Highly crystalline 2d superconductors. *Nat. Rev. Mater.* **2**, 16094 (2016)
- Sassi, U., Parret, R., Nanot, S., Bruna, M., Borini, S., De Fazio, D., Zhao, Z., Lidorikis, E., Koppens, F., Ferrari, A., et al.: Graphene-based mid-infrared room-temperature pyroelectric bolometers with ultra-high temperature coefficient of resistance. *Nature Commun.* **8**, 14311 (2017)
- Settnes, M., Power, S.R., Jauho, A.P.: Pseudomagnetic fields and triaxial strain in graphene. *Phys. Rev. B* **93**, 035456 (2016)
- Sharma, B.K., Ahn, J.H.: Graphene based field effect transistors: efforts made towards flexible electronics. *Solid-State Electron.* **89**(Supplement C), 177–188 (2013)
- Shimada, N.H., Minamitani, E., Watanabe, S.: Theoretical prediction of phonon-mediated superconductivity with  $T_c = 25\text{K}$  in Li-intercalated hexagonal boron nitride bilayer. *Appl. Phys. Express* **10**(9), 093101 (2017)
- Si, C., Liu, Z., Duan, W., Liu, F.: First-principles calculations on the effect of doping and biaxial tensile strain on electron-phonon coupling in graphene. *Phys. Rev. Lett.* **111**, 196802 (2013)

- Todorović, D., Matković, A., Milićević, M., Jovanović, D., Gajić, R., Salom, I., Spasenović, M.: Multilayer graphene condenser microphone. *2D Mater* **2**(4), 045013 (2015)
- Wakabayashi, K., Fujita, M., Kusakabe, K., Nakada, K.: Magnetic structure of graphite ribbon. *Czech J. Phys.* **46**(4), 1865–1866 (1996)
- Wakabayashi, K., Takane, Y., Yamamoto, M., Sigrist, M.: Edge effect on electronic transport properties of graphene nanoribbons and presence of perfectly conducting channel. *Carbon* **47**(1), 124–137 (2009)
- Wang, Y., Shao, Y., Matson, D.W., Li, J., Lin, Y.: Nitrogen-doped graphene and its application in electrochemical biosensing. *ACS Nano* **4**(4), 1790–1798 (2010)
- Weller, T.E., Ellerby, M., Saxena, S.S., Smith, R.P., Skipper, N.T.: Superconductivity in the intercalated graphite compounds  $C_6Yb$  and  $C_6Ca$ . *Nat. Phys.* **1**(1), 39–41 (2005)
- Xue, M., Chen, G., Yang, H., Zhu, Y., Wang, D., He, J., Cao, T.: Superconductivity in potassium-doped few-layer graphene. *J. Am. Chem. Soc.* **134**(15), 6536–6539 (2012)



# DFT study of optical properties of MoS<sub>2</sub> and WS<sub>2</sub> compared to spectroscopic results on liquid phase exfoliated nanoflakes

Jelena Pešić<sup>1</sup> · Jasna Vujin<sup>1</sup> · Tijana Tomašević-Ilić<sup>1</sup> · Marko Spasenović<sup>1</sup> · Radoš Gajić<sup>1</sup>

Received: 1 November 2017 / Accepted: 23 June 2018 / Published online: 4 July 2018  
© Springer Science+Business Media, LLC, part of Springer Nature 2018

## Abstract

We calculate the dielectric function within the framework of the random-phase approximation (RPA) based on DFT ground-state calculations, starting from eigenvectors and eigenvalues. The final goal of our theoretical work is a comparison to corresponding experimental data. We compare our computational results with optical measurements on MoS<sub>2</sub> and WS<sub>2</sub> nanoflakes. MoS<sub>2</sub> and WS<sub>2</sub> were exfoliated by ultrasonic treatment in high-boiling point organic solvent and characterized using UV–VIS spectrophotometry. We find that DFT-RPA yields a good, computationally inexpensive first approximation of the imaginary part of the dielectric function, although excitonic effects require more complex code and extra computing power.

**Keywords** DFT optical properties · MoS<sub>2</sub> and WS<sub>2</sub> · 2D materials

## 1 Introduction

Even though graphene is being the most promising two-dimensional material, absence of the gap has imposed limitations of its applications in nanoelectronics and nanophotonics. Transition metal dichalcogenide crystals (TMDCs) emerged as important alternative as a layered 2D materials family with the finite gap and received considerable attention owing to their extraordinary potential for applications in electronics and optics (Pospischil et al. 2014; Baugher et al. 2014; Britnell et al. 2013; Koppens et al. 2014; Ross et al. 2014; Shi 2013; Zhang 2016; Huang 2016; He 2016; Szczesniak 2017). MoS<sub>2</sub> and WS<sub>2</sub> are part of the family of transition

---

Topical Collection on Focus on Optics and Bio-photonics, Photonica 2017.

---

Guest Edited by Jelena Radovanovic, Aleksandar Krmpot, Marina Lekic, Trevor Benson, Mauro Pereira, Marian Marciniak.

---

✉ Jelena Pešić  
yelena@ipb.ac.rs

<sup>1</sup> Graphene Laboratory (GLAB) of Center for Solid State Physics and New Materials, Institute of Physics Belgrade, University of Belgrade, Pregrevica 118, 11080 Belgrade, Serbia



metal dichalcogenide crystals. They display distinctive properties at a thickness of one and few layers (Butler et al. 2013; Wang et al. 2012; Xu et al. 2014) and very peculiar physics, ranging from trions (Mak et al. 2013) to superconductivity (Szczesniak et al. 2018). They have also attracted much interest for applications in optoelectronics as detectors, photovoltaic devices and light emitters (Pospischil et al. 2014; Baugher et al. 2014; Britnell et al. 2013; Koppens et al. 2014; Ross et al. 2014). MoS<sub>2</sub> and WS<sub>2</sub> are layered crystals in hexagonal structure, consisting of metal atoms sandwiched between two chalcogenide atoms, with covalent interaction within layer and van der Waals interaction between layers. For many applications knowledge of the optical properties is of fundamental importance. Spectroscopic techniques are among the most important methods for research in the field of nanoscience and nanotechnologies. Parallel with the development of experimental methods, computational science becomes a very valuable tool in pursuit for new low-dimensional materials and their characterization. Employing high-end modeling codes, it is possible to simulate from first principles more than a few spectroscopic techniques. The most basic description of light-matter interactions in TMDC thin layers is given by the materials complex dielectric function. Importance of the dielectric function is not only in understanding theoretical concepts underlying interesting properties of TMDCs but it is crucial for the characterization of these materials i.e. the imaginary part of dielectric function is directly related to the absorption. The observed double-peak structure in the optical absorption spectra of monolayer TMDCs is connected to excitonic excitations. These excitons are due to the vertical transition at the K point of the Brillouin zone from a spin-orbit-split valence band to doubly degenerate conduction band (Zhu et al. 2011). For experimental approach, spectroscopic ellipsometry allows determination of material's optical properties in nondestructive manner (Tompkins and McGahan 1999; Liu et al. 2014). The liquid-phase exfoliation is a simple and effective method to exfoliate bulk layered materials into mono- and/or few-layer 2D nanosheets. In this work, high quality TMDC, MoS<sub>2</sub> and WS<sub>2</sub> were prepared in NMP with the similar procedure as our previous works (Matković et al. 2016; Tomašević-Ilić et al. 2016). UV–VIS spectroscopic measurements effectively characterize dispersions by their absorption spectra. Using approaches based on density functional theory (DFT), implemented in the Quantum Espresso software package (Giannozzi et al. 2009), we study optical properties of low-dimensional materials, MoS<sub>2</sub> and WS<sub>2</sub>. We calculate the dielectric function within the framework of the random-phase approximation (RPA) (Brener 1975) based on DFT ground-state calculations, starting from eigenvectors and eigenvalues. Although the tight-binding approximation prove their efficiency and accuracy in describing low-dimensional bands and energy gaps in TDMC materials (Liu et al. 2013; Shanavas et al. 2015; Szczesniak et al. 2016), even for study of the optical properties (Ghader et al. 2015) we rely on DFT based methods due to their applicability on large spectra of systems joint with simplicity of use. The final goal of this study is a comparison to corresponding experimental data provided by spectroscopic measurements of liquid exfoliated nanoflakes of MoS<sub>2</sub> and WS<sub>2</sub>. We use our results for analysis of optical properties of liquid phase exfoliated MoS<sub>2</sub> and WS<sub>2</sub> nanoflakes, as a proven method for analysis of basic optical properties of 2D materials (Pešić et al. 2016).

## 2 Computational details

For presented analysis, Quantum Espresso (QE) code (Giannozzi et al. 2009), based on DFT, was used. The approach is established on an iterative solution of the Kohn–Sham equations of the DFT in a plane-wave basis set. The ionic positions in the

cell are fully relaxed, in all calculations, to their minimum energy configuration using the Broyden–Fletcher–Goldfarb–Shanno (BFGS) algorithm. We modeled monolayer MoS<sub>2</sub> and WS<sub>2</sub> with hexagonal unit cell with 3 atoms per unit cell (Fig. 1). For presented analysis, GGA exchange–correlation functional, Perdew–Burke–Ernzerhof (PBE) (Krack 2005) was used. This parameter-free GGA functional, PBE, is known for its general applicability and gives rather accurate results for a wide range of systems. Compared to hybrid, PBE potential is significantly faster, hence more convenient for qualitative description we aim in this discussion. Although LDA is computationally even more affordable, GGA (i.e. PBE) has proven to be closer to experimental results for spectra of properties in low-dimensional materials (Rasmussen 2015; Molina-Sanchez et al. 2015). Additional accuracy that would be obtained with addition of spin orbit correction, however it would lead to significant increase in computational costs (Rasmussen 2015) making this approach obsolete, since we use it for its efficiency. Namely, many-body calculations applying the GW approximation and Bethe–Salpeter equation give good agreement for optical properties, but their computational costs is great comparing to DFT + RPA. Our computationally inexpensive approach gives qualitatively satisfying description. The hexagonal cell parameter  $c$  was set to be very large (10–12 Å) in order to simulate vacuum and two-dimensional system and avoid an interaction due to periodicity. The plane wave kinetic energy cutoff of 70 Ry was used and the uniform k-point grid was composed of 4096 points in the first Brillouin zone. In TMDCs van der Waals interaction (Lu et al. 2017) have an important effect on the electronic structure, and in case of multilayer, structures were relaxed to their minimum position, with van der Waals interaction included to obtain proper interlayer distance (using Grimme scheme Grimme 2006). In case of monolayer, there was no need for inclusion of it. Dielectric function  $\epsilon(\omega)$  was calculated, in the range 1–20 eV, within the framework of the RPA (Brener 1975) based on DFT ground-state calculations, starting from eigenvectors and eigenvalues, implemented in Quantum Espresso (QE) code as epsilon.x post-processing utility. Matrix elements were accounted only for interband transitions. RPA does not include the nonlocal part of the pseudo-potential and it is not able to include in the calculation the non-local field and excitonic effects. We are interested in the study of the optical properties of this two materials using DFT as a computational inexpensive method for the qualitative description. In QE implementation of the RPA, frequency dependence is computed from an explicit summation of dipole matrix elements and transition energies. Similar theoretical methods were already used to describe the bulk TMDCs (Molina-Sanchez et al. 2015, 2013).

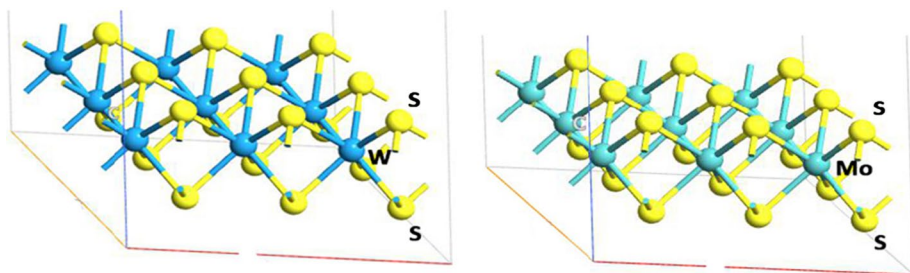


**Fig. 1** Structure of monolayer of WS<sub>2</sub> and MoS<sub>2</sub>

### 3 Synthesis of MoS<sub>2</sub> and WS<sub>2</sub> dispersions

Liquid Phase Exfoliation (LPE) is the physico-chemical process where thin sheets of van der Waals materials, i.e. MoS<sub>2</sub> and WS<sub>2</sub> are exfoliated from their corresponding bulk materials by ultrasonic treatment in liquids such as organic solvents (Fig. 2). In liquid dispersion flakes mainly range from monolayer to few-layer flakes. For the fabrication of both MoS<sub>2</sub> and WS<sub>2</sub> dispersion, we followed the protocol described in earlier papers (Matković et al. 2016; Tomašević-Ilić et al. 2016; Panajotović et al. 2016; Vujin et al. 2016). An initial concentration of powders are: MoS<sub>2</sub> powder (Sigma Aldrich, Product No. 69860) 24 mg/ml and WS<sub>2</sub> powder (Sigma Aldrich Product No.243639) was 12 mg/ml. The mixture was sonicated in a low power sonic bath (Branson CPXH Ultrasonic 8 Cleaning Bath) for 14 h in *N*-Methyl-2-pyrrolidone (NMP) (Sigma Aldrich-328634) for both materials. In order to prevent reaggregation and reduce the amount of unexfoliated material, the solutions were centrifuged for MoS<sub>2</sub> 1000 rpm for 30 min and WS<sub>2</sub> 15 min at 3000 rpm and second centrifuge 6000 rpm for 15 min after we decanted excess of liquid.

### 4 Characterization of MoS<sub>2</sub> and WS<sub>2</sub> dispersions

Large quantities of TMDC flakes were observed as few-layer layered nanosheets, confirming the high quality of the prepared LPE samples. The aggregated nanosheets are absent in these SEM images (Fig. 3), which is in favor of quality of exfoliation procedure.

The UV–visible absorption spectra of the nanosheet dispersions in NMP was measured using the UV–VIS Spectrophotometer (Perkin-Elmer Lambda 4B). The quality of the obtained TMDC nanosheets was characterized by SEM (Tescan MIRA3 field-emission gun SEM). Two typical characteristic absorption peaks of MoS<sub>2</sub> and WS<sub>2</sub> are clearly observed at the region of 600 nm (Fig. 4, which correspond to the A1 and B1 direct excitonic transitions of the TMDC originated from the energy split of valence-band and spin-orbit coupling (Zhu et al. 2011; Coleman et al. 2011). Noteworthy, the splitting between A and B excitonic peaks of WS<sub>2</sub> is larger than that of MoS<sub>2</sub> because of the much heavier mass of the W atom (Shi 2013). These two peaks indicate that the TMDC are dispersed in NMP as the 2H-phase. The Lambert-Beer law was applied to UV–VIS absorption spectra to calculate TMDCs concentration by estimating the absorbance at distinctive peak (MoS<sub>2</sub> at 672 nm and WS<sub>2</sub> at 629 nm) by using a cell length of 1 cm and the extinction coefficient of MoS<sub>2</sub> ( $\alpha = 34.00 \text{ mL mg}^{-1} \text{ m}^{-1}$ ), WS<sub>2</sub> ( $\alpha = 27.56 \text{ mL mg}^{-1} \text{ m}^{-1}$ ), in NMP solutions, which corresponds to previously reported values (Coleman et al. 2011). The concentration of exfoliated MoS<sub>2</sub> is  $343 \mu\text{g ml}^{-1}$  and WS<sub>2</sub> is  $237 \mu\text{g ml}^{-1}$ .

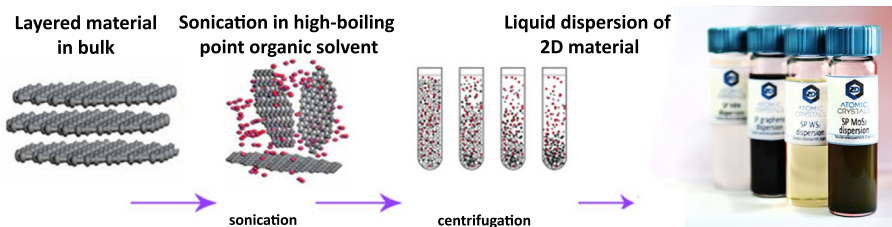
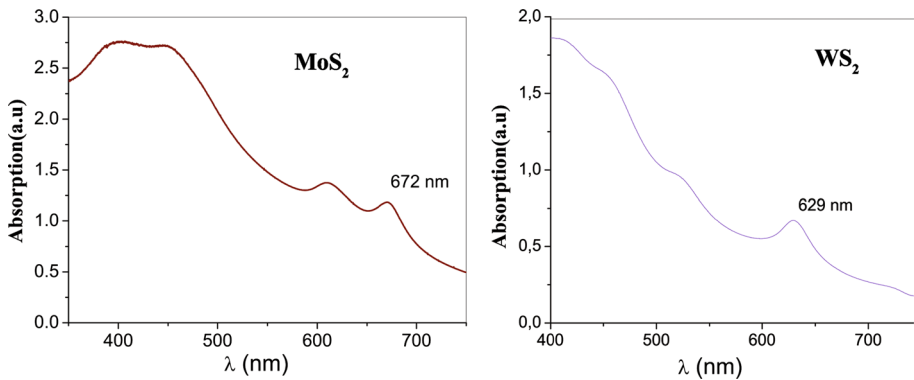


Fig. 2 Procedure of liquid phase exfoliation



**Fig. 3** MoS<sub>2</sub> (up) and WS<sub>2</sub> (down) flakes on Si/SiO<sub>2</sub> substrate—Tescan MIRA3 field-emission gun SEM-left. Photos of MoS<sub>2</sub> and WS<sub>2</sub> dispersions-right



**Fig. 4** UV–VIS spectra were taken using Perkin–Elmer Lambda 4B UV–VIS spectrophotometer with quartz cuvettes

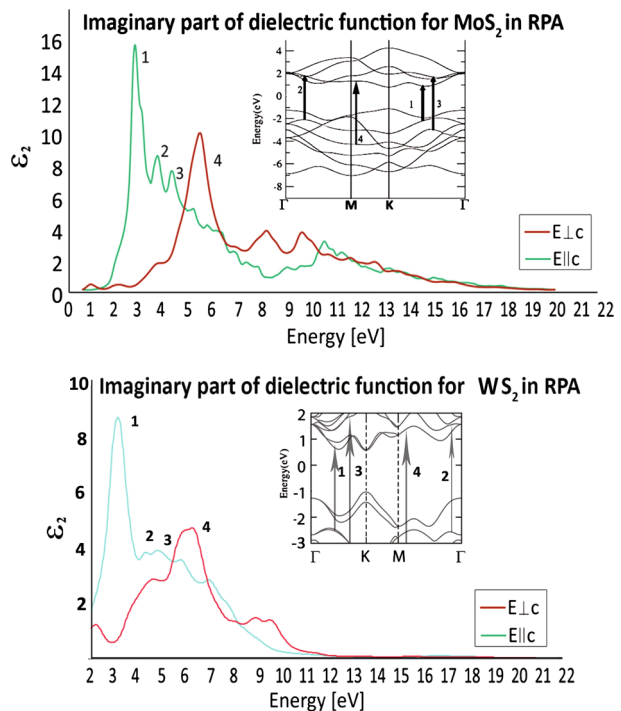
## 5 Results and Discussion

First we calculate the dielectric function for the MoS<sub>2</sub> and WS<sub>2</sub> monolayer (Fig. 5a). On example of MoS<sub>2</sub> monolayer we shall discuss dielectric function. The imaginary part of the

dielectric function for the  $\mathbf{E}$  vector perpendicular to the  $c$  axis is presented in the red color and  $\mathbf{E}$  parallel to the  $c$  axis is presented in the green on Fig. 5. Four distinct structures on Fig. 5, at 1(2.7), 2(3.7), 3(4.2) and 4(5.3 eV) can be connected to the interband transitions, marked on the inset of the electronic band structure, with 1, 2, 3 and 4 as well. All the interband transition depicted here are mainly due to the transition from the  $p$  valence bands of sulfur to the  $d$  conduction bands of the molybdenum (Kumar et al. 2012). The peak 1 is determined by the interband transitions from the valence bands I, II below the Fermi energy to the conduction bands I, II and III above the Fermi energy along  $\Gamma M$  and  $K\Gamma$  direction. The peak 2 is due the interband transitions from the valence bands II below the Fermi energy to the conduction bands II and III above the Fermi energy along  $\Gamma M$  direction and near the  $M$ . The peak 3 exists due to the interband transitions from the valence bands III below the Fermi energy to the conduction bands II and III above the Fermi energy along  $K\Gamma$  direction. Peak 4 is determined by the interband transitions from the valence bands IV below the Fermi energy to the conduction band I above the Fermi energy in the vicinity of the  $M$  high symmetry point. Our calculations are in agreement with the other similar DFT studies (Kumar et al. 2012) and experimental research as well (Li et al. 2014). All TMDCs have similar band structure and corresponding analysis can be applied on  $\text{WS}_2$  monolayer. In Fig. 5 imaginary part of dielectric function of  $\text{WS}_2$  is presented. Same as for  $\text{MoS}_2$ , there are present four distinct peaks originating in same transitions as in  $\text{MoS}_2$ .

Next we compare the imaginary part of the dielectric function in  $\text{MoS}_2$  and  $\text{WS}_2$  with experimental results. Figure 6 qualitatively compares experimental results of  $\text{MoS}_2$  and  $\text{WS}_2$  LPE with DFT+RPA calculations and results obtained using the Kramers–Kronig analysis (Li et al. 2014). The green line represent experimental results, UV–VIS spectra of LPE flakes. Violet lines are DFT + RPA model of  $\text{MoS}_2$  and  $\text{WS}_2$ . The red line is

**Fig. 5** The calculated imaginary part of the dielectric function for  $\text{MoS}_2$  and  $\text{WS}_2$



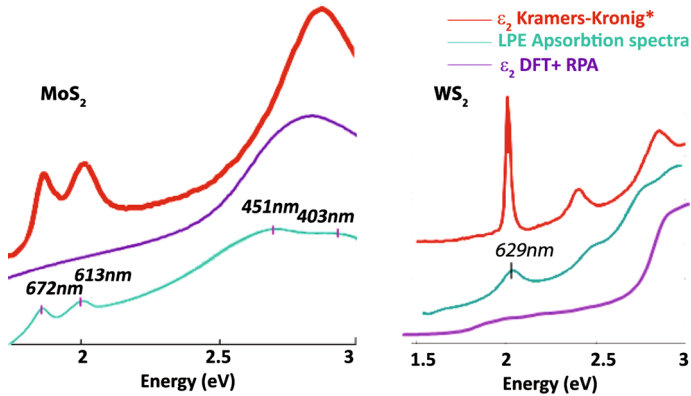
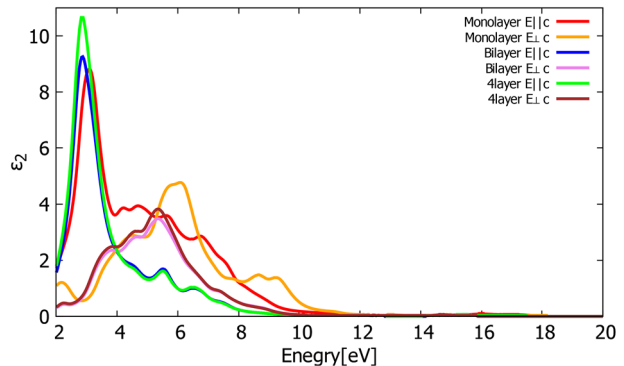


**Fig. 6** The qualitative comparison of imaginary part of experimental results and theoretical calculations for MoS<sub>2</sub> and WS<sub>2</sub>. Asterisks corresponds to result for the reference Li et al. (2014)

**Fig. 7** The calculated imaginary part of the dielectric function for few layers of WS<sub>2</sub>



imaginary part of the dielectric function obtained using Kramers–Kronig analysis from the reference Li et al. (2014). Due to the nature of approximation, excitonic effects are not clearly visible in DFT+RPA calculation and characteristic A and B peaks are not present. However both for MoS<sub>2</sub> and WS<sub>2</sub> peaks at around 400 nm (which originate in electronic transitions) are well described.

After analysis of monolayer we proceeded with calculations of few layer structures to observe changes in the imaginary part of dielectric function with increase of number of layers. We compared monolayer with bilayer and 4-layer WS<sub>2</sub>, Fig. 7 and conclude its thickness-dependent nature. It can be noticed that thicker structures have higher  $\epsilon_2$  in the low energy area. This regular change shows a good agreement with the variation tendency of the density of WS<sub>2</sub> films, as demonstrated in the XRD analysis in ref (Li et al. 2017). Being aware of this effect, a referent model for various thicknesses of TMDCs sheets (ie. number of layers) could be made using DFT-based approach. It is planned to be used as a guide in comparison with UV–VIS spectrophotometry measurement for rapid assessment of thickness of nanoflakes in dispersion.

## 6 Conclusion

In this paper we studied optical properties i.e. the dielectric function of the monolayer MoS<sub>2</sub> and WS<sub>2</sub> as a monolayer TMDCs, using DFT based techniques. Many effects present due to the excitonic effects demand detail and advanced approach based addition of GW approximation and Bethe–Salpeter equation (but computationally significantly more expensive, time-demanding and resource-consuming), in this kind of the calculations they have been completely neglected. Thickness-dependent nature of MoS<sub>2</sub> and WS<sub>2</sub> dielectric function was revealed. However, we can conclude that DFT+RPA techniques can be used for quick analysis of the optical properties of these and similar 2D materials, and they provide the reliable and computationally non-expensive solution for the suitable qualitative description.

**Acknowledgements** This work is supported by the Serbian MPNTR through Project OI 171005 and by Qatar National Research Foundation through Projects NPRP 7-665-1-125. DFT calculations are performed using computational resources at Johannes Kepler University, Linz, Austria.

## References

- Baughner, B.W.H., et al.: Optoelectronic devices based on electrically tunable p-n diodes in a monolayer dichalcogenide. *Nat. Nano* **9**(4), 262–267 (2014)
- Brener, N.E.: Random-phase-approximation dielectric function for diamond, with local field effects included. *Phys. Rev. B* **12**(4), 1487–1492 (1975)
- Britnell, L., et al.: Strong light-matter interactions in heterostructures of atomically thin films. *Science* **340**(6138), 1311–1314 (2013)
- Butler, S.Z., et al.: Challenges, and opportunities in two-dimensional materials beyond graphene. *ACS Nano* **7**(4), 2898–2926 (2013)
- Coleman, J.N., et al.: Two-dimensional nanosheets produced by liquid exfoliation of layered materials. *Science* **331**(6017), 568–571 (2011)
- Ghader, D., et al.: The electronic band structures and optical absorption spectra for incommensurate twisted few-layers graphene. [arXiv:1504.01347v1](https://arxiv.org/abs/1504.01347v1) (2015)
- Giannozzi, P., et al.: QUANTUM ESPRESSO: a modular and open-source software project for quantum simulations of materials. *J. Phys. Condens. Matter* **21**, 395502 (2009). <http://www.quantum-espresso.org>
- Grimme, S.: Semiempirical GGA-type density functional constructed with a longrange dispersion correction. *J. Comp. Chem.* **27**(15), 1787–1799 (2006)
- He, X.: Strain engineering in monolayer WS<sub>2</sub>, MoS<sub>2</sub>, and the WS<sub>2</sub>/MoS<sub>2</sub> heterostructure. *Apl. Phys. Lett.* **109**(17), 173105 (2016)
- Huang, G.Q.: Dynamical stability and superconductivity of Li-intercalated bilayer MoS<sub>2</sub>: A first-principles prediction. *Phys. Rev. B* **93**(10), 104511 (2016)
- Koppens, F.H.L., et al.: Photodetectors based on graphene, other two-dimensional materials and hybrid systems. *Nat. Nano* **9**, 780–793 (2014)
- Krack, M.: Pseudopotentials for H to Kr optimized for gradient-corrected exchange-correlation functionals. *Theor. Chem. Acc.* **114**(1–3), 145–152 (2005)
- Kumar, A., et al.: A first principle comparative study of electronic and optical properties of 1HMoS<sub>2</sub> and 2HMoS<sub>2</sub>. *Mat. Chem. Phys.* **135**, 755–761 (2012)
- Li, Y., et al.: Measurement of the optical dielectric function of monolayer transition-metal dichalcogenides: MoS<sub>2</sub>, MoSe<sub>2</sub>, WS<sub>2</sub>, and WSe<sub>2</sub>. *Phys. Rev. B* **90**(20), 205422 (2014)
- Li, W., et al.: Broadband optical properties of large-area monolayer CVD molybdenum disulfide. *Phys. Rev. B* **90**(19), 195434 (2014)
- Li, Da-Hai, et al.: Dielectric functions and critical points of crystalline WS<sub>2</sub> ultrathin films with tunable thickness. *Phys. Chem. Chem. Phys.* **19**, 12022 (2017)

- Liu, G.-B., et al.: Three-band tight-binding model for monolayers of group-VIB transition metal dichalcogenides. *Phys. Rev. B* **88**(8), 085433 (2013)
- Liu, H.-L., et al.: Optical properties of monolayer transition metal dichalcogenides probed by spectroscopic ellipsometry. *Appl. Phys. Lett.* **105**, 20 (2014)
- Lu, N., et al.: Twisted MX<sub>2</sub>/MoS<sub>2</sub> heterobilayers: effect of van der Waals interaction on the electronic structure. *Nanoscale* **9**, 19131–19138 (2017)
- Mak, K.F., et al.: Tightly bound trions in monolayer MoS<sub>2</sub>. *Nat. Mater.* **12**(3), 207–211 (2013)
- Matković, A., et al.: Enhanced sheet conductivity of LangmuirBlodgett assembled graphene thin films by chemical doping. *2D Mater.* **3**(1), 015002 (2016)
- Molina-Sanchez, A., et al.: Effect of spin-orbit interaction on the optical spectra of single-layer, double-layer, and bulk MoS<sub>2</sub>. *Phys. Rev. B* **88**(4), 045412 (2013)
- Molina-Sanchez, A., et al.: Vibrational and optical properties of MoS<sub>2</sub>: from monolayer to bulk. *Surf. Sci. Rep.* **70**(4), 554–586 (2015)
- Panajotović, R., et al.: Modifications of Lipid/2D-Material Heterostructures by SEM, Book of Abstracts, SPIG 2016, 182–185 (2016)
- Pešić, J., et al.: Ab-initio study of the optical properties of the Li-intercalated graphene and MoS<sub>2</sub>. *Opt Quant Electron* **48**, 368 (2016)
- Pospischil, A., et al.: Solar-energy conversion and light emission in an atomic monolayer p-n diode. *Nat. Nano* **9**(4), 257–261 (2014)
- Rasmussen, F.A.: Computational 2D materials database: electronic structure of transition-metal dichalcogenides and oxides. *J. Phys. Chem. C* **119**, 13169–13183 (2015)
- Ross, J., et al.: Electrically tunable excitonic light-emitting diodes based on monolayer WSe<sub>2</sub> p-n junctions. *Nat. Nano* **9**(4), 268–272 (2014)
- Shanavas, K.V., et al.: Effective tight-binding model for MX<sub>2</sub> under electric and magnetic fields. *Phys. Rev. B* **91**(23), 235145 (2015)
- Shi, H.: Quasiparticle band structures and optical properties of strained monolayer MoS<sub>2</sub> and WS<sub>2</sub>. *Phys. Rev. B* **87**(15), 155304 (2013)
- Szczesniak, D., et al.: Complex band structures of transition metal dichalcogenide monolayers with spin-orbit coupling effects. *J. Phys. Condens. Matter* **28**(35), 355301 (2016)
- Szczesniak, R.: Metallization and superconductivity in Ca-intercalated bilayer MoS<sub>2</sub>. *J. Phys. Chem. Solids* **111**, 254–257 (2017)
- Szczesniak, R., Durajski, A.P., Jarosik, M.W.: Strong-coupling superconductivity induced by calcium intercalation in bilayer transition-metal dichalcogenides. *Front. Phys.* **13**(2), 137401 (2018)
- Tomašević-Ilić, T., et al.: Transparent and conductive films from liquid phase exfoliated graphene. *Opt. Quant. Electron.* **48**, 319 (2016)
- Tompkins, H.G., McGahan, W.A.: *Spectroscopic ellipsometry and reflectometry: a users guide*. Wiley, New York (1999)
- Vujin, J., et al.: Physico-Chemical Characterization Of Lipid-2d-Materials Self-Assembly For Biosensors, Book of Abstracts RAD 2016, 58 (2016)
- Wang, Q.H., et al.: Electronics and optoelectronics of two-dimensional transition metal dichalcogenides. *Nat. Nano* **7**, 699–712 (2012)
- Xu, X., et al.: Spin and pseudospins in layered transition metal dichalcogenides. *Nat. Phys.* **10**, 343–350 (2014)
- Zhang, J.-J.: Strain-enhanced superconductivity of MoX<sub>2</sub>(X=S or Se) bilayers with Na intercalation. *Phys. Rev. B* **93**(15), 155430 (2016)
- Zhu, Z.Y., Cheng, Y.C., Schwingenschlogl, U.: Giant spin-orbit-induced spin splitting in two-dimensional transition-metal dichalcogenide semiconductors. *Phys. Rev. B* **84**(15), 153402 (2011)





# Optical and mechanical properties and electron–phonon interaction in graphene doped with metal atoms

Andrijana Šolajić<sup>1</sup> · Jelena Pešić<sup>1</sup> · Radoš Gajić<sup>1</sup>

Received: 31 October 2019 / Accepted: 5 March 2020 / Published online: 14 March 2020  
© Springer Science+Business Media, LLC, part of Springer Nature 2020

## Abstract

Graphene, the first experimentally realized 2D material with outstanding mechanical and electrical properties as well an excellent optical transparency, is predicted to have many applications in various scientific fields. Furthermore, there are numerous ways for modifications of pure graphene that allow precise tuning of its properties or observation of some new effects, including the applied strain, various types of controlled defects, exposure to electrical or magnetic field, or doping. It is known that graphene with alkali metal atoms adsorbed on its surface becomes superconducting with due to enhanced electron–phonon coupling. The question remains what happens with optical and mechanical properties of such structures, can we preserve or enhance these superb properties while making graphene superconducting at the same time. Here we investigate structures based on graphene doped with several metal atoms—Sr, and some transition metal atoms such are Y and Sc. Using the density functional theory, we analyze the optical and elastic properties of those structures, discussing the influence of adsorbed atoms on these properties and calculate the electron–phonon coupling related properties.

**Keywords** Graphene · DFT · Superconductivity · Electron–phonon interaction · Optical properties · 2D materials

## 1 Introduction

Since the experimental discovery in 2004, graphene has been attracting enormous attention, not only as the first experimentally realised 2D material as the large scale samples, but mostly for its many unique properties. With this wide spectra of effects, graphene was also predicted to be suitable for various applications (Ferrari 2015; Blake et al. 2008; Todorović et al. 2015; Bonaccorso et al. 2015; Sassi et al. 2017; Liu et al. 2014). Monolayer graphene

---

This article is part of the Topical Collection on Advanced Photonics Meets Machine Learning.

Guest edited by Goran Gligoric, Jelena Radovanovic and Aleksandra Maluckov.

---

✉ Andrijana Šolajić  
solajic@ipb.ac.rs

<sup>1</sup> Institute of Physics Belgrade, University of Belgrade, Pregrevica 118, Belgrade 11080, Serbia

formed on various metal surfaces was also extensively researched (Wintterlin and Bocquet 2009; Aizawa et al. 1990a, b; Taleb and Farías 2016) along with intercalation of these supported graphene systems (Gall et al. 1997; Shikin et al. 1998; Farías et al. 1999). Up to today, a couple of thousands papers about graphene are published and it is very well-known today how special graphene is and how its characteristics can be tailored to be suitable for even more suitable use. But in the long list of graphene's remarkable properties (Katsnelson et al. 2006; Gusynin and Sharapov 2005; Castro Neto et al. 2006; Lee et al. 2008), there is one notable effect missing, the superconductivity, which is absent in pristine graphene. Among many attempts to make graphene superconducting, a successful idea came from the so-called Graphite intercalation compounds (GICs). GICs are composed from graphite layers, with metallic atoms nested between. They were extensively studied since the 1960s, but with discovery of the superconductivity in some of the GICs ( $\text{CaC}_6$  with  $T_c = 11.5\text{K}$  and  $\text{YbC}_6$  with  $T_c = 6.5\text{K}$ ), an interest in those structures has raised again. The origin of superconductivity in GICs was debated for a long time, but most suggested was that the pairing mediated by electron–phonon interactions as the mechanism (Mazin 2005; Calandra and Mauri 2005), which was later confirmed by experimental data. As it can be observed, in all superconducting GICs there is an intercalant Fermi surface at the Fermi level, and those electrons are strongly coupled to the phonons. As reported in several studies, similar effects are present when going down to the thinnest limit, case of monolayer graphene doped with alkali adatoms in a similar manner to GICs. The electron–phonon coupling constant,  $\lambda$ ,

$$\lambda = \frac{N(0)D^2}{M\omega_{ph}^2}, \quad (1)$$

is proportional to the density of states at the Fermi level and the deformational potential  $D$ , and inversely proportional to effective atomic mass  $M$  and the frequency of the phonon involved  $\omega_{ph}$ . As the DOS on the Fermi level in graphene is zero and slowly growing in its vicinity, the superconductivity in pristine graphene can not be observed, similar to pristine bulk graphite. However, the situation is changed upon doping with metallic adatoms, similar as in GICs. In the presence of adatoms, new electronic band is formed, the number of carriers is enlarged and, if the interlayer band occurs at the Fermi level, the electron–phonon coupling  $\lambda$  is enhanced and the coupling to carbon out-of-plane vibrations is promoted. Besides DOS, electron–phonon coupling constant also depends on the deformation potential  $D$ , which is inversely related to the distance between the graphene and adatoms. Hence for occurrence of the superconductivity it is favourable for adatoms to be closer to the graphene plane. On the other hand, it was shown that too small distance would result in a complete charge transfer between the graphene and the adatoms, so the interlayer band would be completely empty, as is the case with the bulk  $\text{LiC}_6$  where the strong confinement along the  $z$  axis leads to interlayer band to be completely unoccupied and the superconductivity is suppressed. In contrary, in the  $\text{LiC}_6$  monolayer, the quantum confinement is removed, resulting in partially occupied interlayer band and superconductivity with  $T_c$  up to 8K.

Motivated by these results, we wanted to explore graphene doped with Sr atoms and also with some transition metal atoms such as Sc and Y. Besides the electron–phonon properties crucial for the superconductivity, we were interested to investigate mechanical and optical properties also in order to study effects of added adatoms, questioning can we obtain superconducting material and preserve this superb graphene's properties, which would be of great significance for many applications. Using the density functional theory, we analyse the electron–phonon interaction properties and predict the critical temperature in the framework of the

electron–phonon coupling theory. We analyse the mechanical and optical properties of these structures and discuss the influence of adatoms on these properties.

## 2 Computational details

All calculations were performed in the Quantum Espresso software package (Giannozzi et al. 2009), in the LDA approximation, which is proven to be suitable for graphene systems and often is used. We used norm-conserving pseudopotentials, with the energy cutoff for wavefunctions of 120 Ry, obtained with respect to the convergence test. The unit cell for all doped graphene structures is modelled as  $\sqrt{3} \times \sqrt{3}R30^\circ$  supercell of graphene unit cell, with adatoms positioned above the centres of carbon hexagons, the so-called H-site, as it is the most favourable site for all three atoms, according to the DFT study (Nakada and Ishii 2011). In order to avoid the interactions due to periodicity and to simulate a 2D system, the hexagonal  $c$  parameter was set to be sufficiently large, more than  $c = 10 \text{ \AA}$ . Prior to any further calculations, the structures were relaxed to their minimum energy configuration, using the BFGS algorithm. The dielectric function was calculated within the framework of the random-phase approximation (RPA), as implemented in epsilon.x code of QE, on the uniform k-point grid composed of 4096 k-points. The second-order elastic constants were calculated using the ElaStic code. First, the strain type and strength is chosen, and for each deformation, total energies are calculated. From the second derivatives of energy curves, elastic constants are calculated. Here we used amplitudes of 7% positive and negative Lagrangian strain.

The grid for electron–phonon coupling was used up to  $48 \times 48 \times 1$  electronic  $k$ -mesh and  $12 \times 12 \times 1$  phonon-momentum mesh using the Monkhorst pack. The electron–phonon coupling parameter  $\lambda$  and the critical temperature  $T_c$  are obtained with the isotropic Eliashberg theory. The Eliashberg function is defined as

$$\alpha^2 F(\omega) = \frac{1}{N(0)N_k N_q} \sum_{nk,mq,\nu} |g_{nk,mk+q}^\nu|^2 \times \delta(\epsilon_{nk})\delta(\epsilon_{mk+q})\delta(\omega - \omega_q^\nu) \quad (2)$$

where  $N(0)$  is total density of states per spin,  $N_k$  and  $N_q$  are the total numbers of  $k$  and  $q$  points.  $g_{nk,mk+q}^\nu$  is the electron–phonon matrix element, and electron eigenvalues and the band indexes are labelled with  $n$  and  $m$ , the wavevectors  $\mathbf{k}$  and  $\mathbf{k} + \mathbf{q}$ , the phonon frequencies with the mode number  $\nu$  and the wavevector  $\mathbf{q}$ . From previous equation, the electron–phonon coupling coefficient is given as

$$\lambda(\omega) = 2 \int_0^\omega \frac{\alpha^2 F(\omega')}{\omega'} d\omega' \quad (3)$$

The total electron phonon coupling is obtained for  $\omega \rightarrow \infty$ . The superconducting critical temperature is estimated using the Allen–Dynes formula,

$$T_c = \frac{\omega_{log}}{1.2} \exp \left[ \frac{-1.04(1 + \lambda)}{\lambda(1 - 0.62\mu^*) - \mu^*} \right] \quad (4)$$

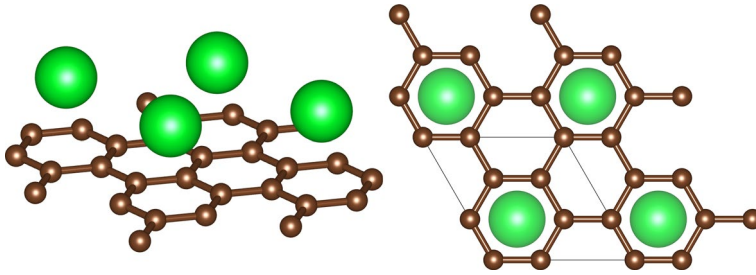


**Fig. 1** The structure of graphene with atoms adsorbed on H-site. On the right, top view of structure is shown, with unit cell marked with black line

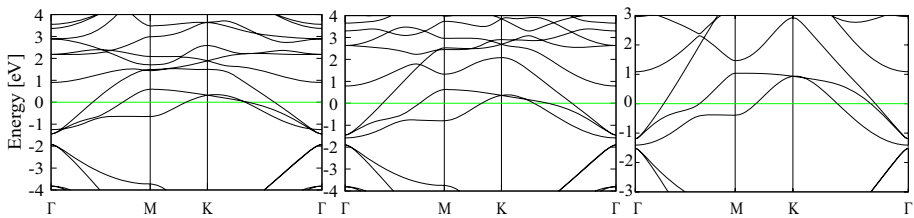


**Fig. 2** Electronic structure of  $\text{ScC}_6$ ,  $\text{YC}_6$  and  $\text{SrC}_6$  along  $\Gamma$ -M-K- $\Gamma$  direction. Fermi level is centered on 0 eV

where  $\mu^*$  is the screened Coulomb pseudopotential and

$$\omega_{\log} = \exp \left[ \frac{2}{\lambda} \int \frac{d\omega}{\omega} \alpha^2 F(\omega) \log \omega \right] \quad (5)$$

is the phonon frequencies logarithmic average.

### 3 Results and Discussion

The atomic structure of  $\text{SrC}_6$  monolayer is consisted of graphene sheet covered with Sr adatoms positioned in the H-site, as shown in Fig. 1. Upon relaxing the systems, obtained distance between the graphene sheet and the adatom are  $h = 2.22 \text{ \AA}$  for  $\text{SrC}_6$ ,  $h = 2.04 \text{ \AA}$  for  $\text{YC}_6$ , and  $h = 1.76 \text{ \AA}$  for  $\text{ScC}_6$ . Comparing to, for example the bulk  $\text{SrC}_6$  compound, where this distance is  $2.475 \text{ \AA}$ , Sr atoms are closer to the graphene plane, more nested in the centres of carbon hexagons.

The electronic structure of  $\text{SrC}_6$  monolayer is discussed in details in our previous work (Šolajić et al. 2018). We have shown the interlayer band that is forming due to the presence of Sr atoms, positioned near the Fermi level, partially occupied. Carbon  $\pi^*$  bands are strongly hybridized with new adatom-derived bands and also the DOS on Fermi level is significantly raised. Very similar are monolayers of  $\text{ScC}_6$  and  $\text{YC}_6$ , without almost any qualitative difference or significant difference in position of the Fermi level. Electronic structure of all three systems are shown in Fig. 2.

Motivated with those results, we proceeded to calculate the phonon dispersion and electron phonon coupling. In Fig. 3 the phonon dispersion of  $\text{SrC}_6$  and phonon density of states for all structures are shown. The adatom contribution to phonon modes is marked

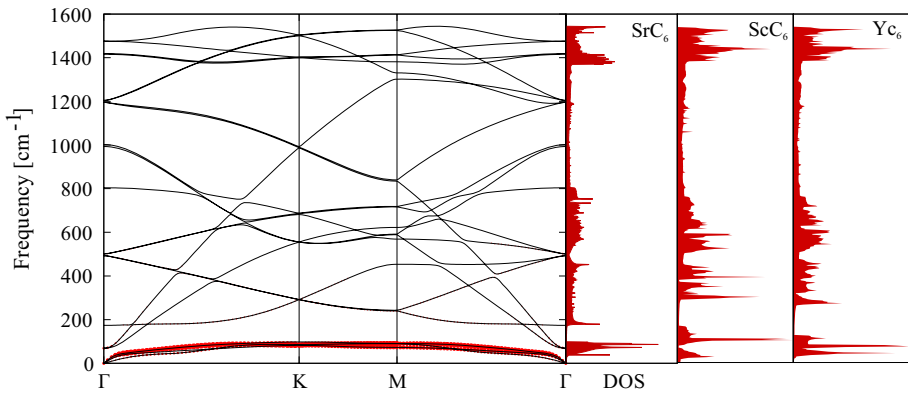


**Fig. 3** Phonon dispersion for SrC<sub>6</sub>-mono and phonon density of states for all three structures

with red circles. The phonon dispersions do not show any negative modes and they suggest that systems are dynamically stable. Similar to other metal doped graphene structures, we can observe three distinguished regions. Lowest region belongs to adatom modes, in the middle region are positioned carbon out-of-plane modes, and highest modes are C–C stretching modes. Since the phonon dispersions show minor differences for all three structures, presented is only SrC<sub>6</sub>. First two modes with lowest energies (degenerated one at  $\approx 70 \text{ cm}^{-1}$  and one at  $\approx 175 \text{ cm}^{-1}$ ) are related to pristine graphene’s acoustic modes. That can be also seen in Fig 4. of our previous study (Šolajić et al. 2018), for the lowest mode at  $70 \text{ cm}^{-1}$ , the in plane displacements of carbon atoms are like TA and LA modes, with the adatom oscillating in opposite direction, and analogue case for the mode at  $175 \text{ cm}^{-1}$ , related to ZA graphene mode. This splitting of ZA-like mode from the lower two is similar to the case where graphene layer is formed on metal substrates, and the gap at the  $\Gamma$  point is introduced due to interaction of graphene with substrate [The shift of ZA mode is seen at  $48 \text{ cm}^{-1}$  in graphene on Cu(111) substrate (Taleb and Fariás 2016) and at  $282 \text{ cm}^{-1}$  for graphene on transition-metal carbides TaC(111), HfC(111) and TiC(111) (Aizawa et al. 1990b)]. We can consider that the splitting of the ZA-like mode can be described in a similar way, representing the interaction between the graphene and adsorbed metal atoms. The formed gap depends on the strength of the graphene-substrate coupling and as given in the following models. For free-standing pristine graphene, the dispersion of the acoustic ZA mode in the vicinity of the  $\Gamma$  point is given by Taleb et al. (2015):

$$\omega_{ZA}^{free}(\mathbf{q}) = \sqrt{\frac{\kappa}{\rho_{2D}} \mathbf{q}^2}, \tag{6}$$

where  $\rho_{2D} = 7.6 \times 10^{-8} \text{ g/cm}^2$  is the two-dimensional mass density of graphene. Coupling to the substrate introduces a gap at a frequency  $\omega_0$  at the  $\Gamma$  point and the dispersion relation is given by Amorim and Guinea (2013)

$$\omega_{ZA}^{free}(\mathbf{q}) = \sqrt{\frac{\kappa}{\rho_{2D}} \mathbf{q}^4 + \omega_0^2}, \tag{7}$$

where  $\omega_0 = \sqrt{g/\rho_{2D}}$  and  $g$  is the coupling strength between graphene and substrate. Following this model, we can approximate the similar interaction of graphene with adsorbed

metal layer and determine the  $g = 0.739 \times 10^{19} \text{ N/m}^3$ . This value is significantly smaller than for graphene on various substrates [from  $g = 5.7 \times 10^{19} \text{ N/m}^3$  for graphene on Cu (Taleb et al. 2015), to the order of  $2 \times 10^{21}$  for the (111) surface of transition metal carbides (Amorim and Guinea 2013)], as somewhat expecting given that the graphene is covered with not so dense placed Sr metal atoms and not suspended on a real surface.

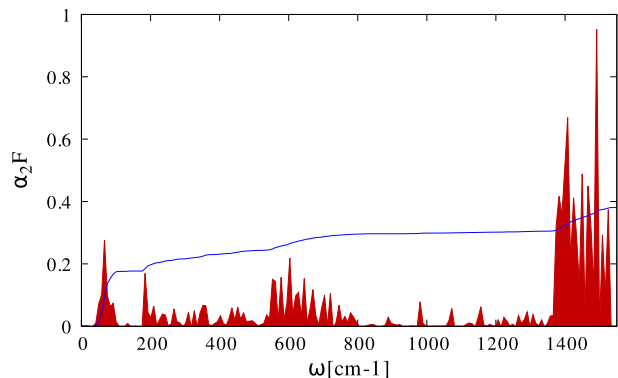
The right side of Fig. 3 shows the phonon DOS for doped graphene structures. For all three structures, the phonon DOS is largest in the adatom region, as well in carbon in-plane modes area. As it can be seen in Eliashberg function, presented in Fig. 4, those modes also have significant contribution in electron–phonon coupling. The choice of adatom does not affect the phonon density of states and, in every of three systems, largest peaks are in low energy region and the highest ones with some minor difference in positions of peaks.

In the Eliashberg function calculated for SrC<sub>6</sub> monolayer, shown in Fig. 4, three distinguished peaks are present as expected, one from the lowest adatom-related modes, one wide and narrow in the middle-energy region, and the highest peak at 1400–1500 cm<sup>-1</sup> related to the carbon in-plane modes. Although the C–C stretching modes are strongly coupled with electronic states at Fermi level, the  $\lambda$  parameter is enhanced most in the low energy region related to adatoms ( $\approx 0.18$ ), given that it depends on the phonon energy inversely, so the low-energy modes have largest contribution to electron–phonon coupling constant. Comparing this to bulk SrC<sub>6</sub> compound (Calandra and Mauri 2006), we can observe slightly softened  $Sr_z$  phonon mode, giving a larger peak in Eliashberg function. However, in the middle region, the contribution of carbon out-of-plane modes is significantly smaller and the contribution to electron–phonon coupling is drastically lowered than in bulk. Very similar case is reported with CaC<sub>6</sub> (Calandra and Mauri 2006; Profeta et al. 2012) where the carbon out-of-plane vibrations are similar in bulk and the monolayer case but overall contribution to  $\lambda$  is decreased in the monolayer. This is also an opposite to the LiC<sub>6</sub> where the removal of confinement gives a rise to the  $\lambda$ .

Overall electron–phonon coupling constant in SrC<sub>6</sub>-monolayer is  $\lambda = 0.38$ , with  $\omega_{log} = 280.9 \text{ cm}^{-1}$ . The superconducting transition temperature, estimated using the Allen–Dynes formula with  $\mu^* = 0.112$  is  $T_c = 0.9 \text{ K}$ , lower than in its bulk counterpart (3K). Both other structures have very similar electronic and phonon structure and enhanced electron–phonon coupling is expected, with critical temperatures in similar range. Further calculations of electron–phonon coupling parameter are needed to be confirmed.

Interested to see what happens with mechanical properties that are superb in graphene, we calculated the elastic constants of our doped structures and compare them

**Fig. 4** Eliashberg function with integrated electron–phonon coupling parameter for SrC<sub>6</sub>-mono



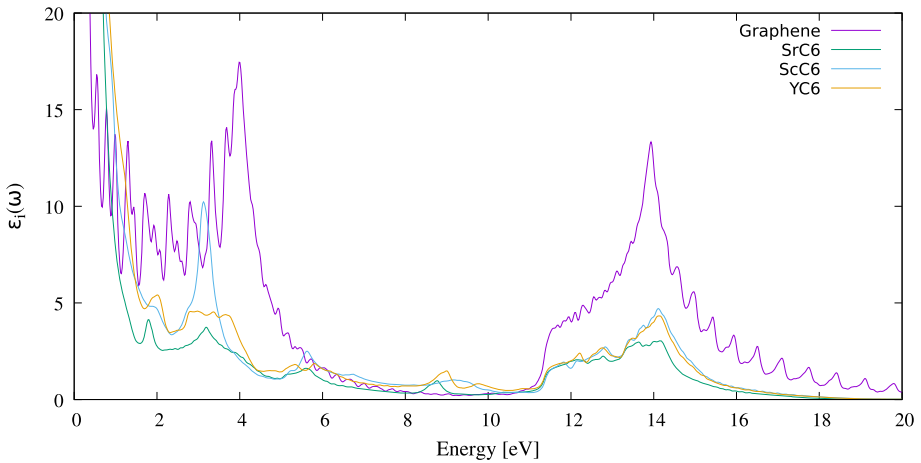


**Fig. 5** Eliashberg function with integrated electron–phonon coupling parameter for SrC6-mono

with pristine graphene, which are shown in Table 1. 2D hexagonal, square and rectangular lattices have 4 non-zero second-order elastic constants,  $c_{11}$ ,  $c_{12}$ ,  $c_{22}$  and  $c_{66}$ , where due to symmetry, in case of hexagonal lattice, only two elastic constants are independent because  $c_{11} = c_{22}$  and  $c_{66} = \frac{1}{2}(c_{11} - c_{22})$ . In this case, the Young modulus and Poisson's ratio are defined according to Wei and Peng (2014) as  $Y = \frac{c_{11}^2 - c_{12}^2}{c_{11}}$  and  $\nu = \frac{c_{21}}{c_{11}}$ . Obtained results for elastic properties of pristine graphene are overall in good agreement with previous experimental and theoretical studies. Calculated elastic constants  $c_{11}$  and  $c_{12}$  are both larger than in literature (estimated to be around 350 and 60 N/m, respectively), so the Young Modulus is also larger (experimentally measured to 342 N/m in Politano et al. 2012 and 340 N/m in Lee et al. 2008). The Poisson's ratio is however accurately obtained to 0.19, presumably due to both  $c_{11}$  and  $c_{12}$  similarly overestimated. Pristine graphene has extraordinary large values of elastic constants and also can be stretched up to roundly 20%. It is clearly observable that upon doping, elastic constants drop to almost half of the pristine graphene ones, as it is somewhat expected due to added adatoms on top of graphene surface. Still, that leaves these parameters very high in comparison to many other similar 2D materials. Moreover, parameters such as Young modulus remains exceptionally good. The elastic constants and Young modulus of doped graphene structures are in range of hBN and slightly larger than SiC (Andrew et al. 2012; Zhang et al. 2017), and still much larger than many other 2D structures, such as MgB<sub>2</sub> (Pešić et al. 2019) or silicene (Zhang et al. 2017). This possibility to

**Table 1** The calculated elastic constants, Young's modulus  $Y$ , Poisson's ratio  $\nu$  and the shear modulus  $G$ , for pristine graphene, ScC<sub>6</sub>, YC<sub>6</sub> and SrC<sub>6</sub> monolayers

	$c_{11}$	$c_{12}$	$c_{66}$	$Y$	$\nu$	$G$
Graphene	462.3	79.6	191.4	448.6	0.19	94.67
ScC <sub>6</sub>	244.8	37.2	103.8	239.2	0.15	103.83
SrC <sub>6</sub>	205.9	33.3	86.3	200.5	0.16	86.26
YC <sub>6</sub>	239.7	38.2	100.8	233.6	0.16	100.77

All parameters are given in units of N/m, except the Poisson's ratio which is dimensionless

strain graphene can be also exploited for tuning superconducting properties, as previously was shown that certain types of strain can enhance the superconducting critical temperature significantly. Pešić et al. (2014).

Calculated imaginary part of dielectric function for our doped structures and pristine graphene, for the electric field vector perpendicular to the  $c$  axis, is shown in Fig. 5. Dielectric function of pristine graphene is discussed before (Marinopoulos et al. 2004) and we will not discuss it in details. Our calculations are in agreement with previous theoretical as well experimental studies, showing clear peaks at 4 eV and 14 eV, originating from  $\pi \rightarrow \pi^*$  and  $\sigma \rightarrow \sigma^*$  interband transitions. The singularity at zero frequency is present and shows metallicity of the system. Upon doping, two small differences can be observed. First, the first peak which is in pristine graphene at 4 eV is shifted to around 3 eV and it is lower intensity in all structures. The second peak at 14 eV does not change position in energy, but drops to much lower intensity in all three structures. These lower intensities and changes in positions of the peaks can be related to Fermi level shift and an adatom influence on  $\pi^*$  bands. Varying the type of dopants however does not make any significant changes in position or intensity of these peaks, except in case of  $\text{ScC}_6$  monolayer where intensity of first peak is slightly smaller than in pristine graphene. Moreover, none of the changes in dielectric function induced by adatoms is crucial for the quality of the optical properties and they remain superb as in pristine graphene.

## 4 Conclusions

In this work we investigated the electron–phonon coupling and possibility of superconductivity in graphene doped with Sr, Y and Sc adatoms, as well their mechanical and optical properties. The bulk  $\text{SrC}_6$  which is superconducting with  $T_c = 3\text{K}$ , was studied theoretically as well experimentally. Moreover, previously studied electronic properties predict the monolayer as good candidate for occurrence of superconductivity. Here we expanded our research by doping with transition metals such as Sc and Y. The phonon dispersion of systems show they are dynamically stable, with no negative frequencies present. Using the isotropic Eliashberg theory, we calculated the total electron–phonon coupling parameter of  $\text{SrC}_6$  monolayer,  $\lambda = 0.38$ . As in bulk  $\text{SrC}_6$  compound, superconductivity is occurring, but with lower  $T_c$ , which is estimated as  $T_c = 0.9\text{K}$  using the Allen–Dynes formula with  $\mu^* = 0.112$ . Other two discussed structures have similar electronic structure and density of states, as well the phonon dispersion too and have potential to have superconducting properties with similar critical temperatures, and need further investigation. Our calculations of elastic constants and mechanical properties show that upon doping graphene, elastic constants and other parameters like Young modulus, drop by half of pristine graphene's, which is still extraordinary good in comparison to many similar structures. Calculated imaginary parts of dielectric constants show no significant changes other than lower intensities of the peaks and slightly shifting in energy. This makes those structures an excellent candidates for potential applications.

**Acknowledgements** The authors acknowledge funding provided by the Institute of Physics Belgrade, through the grant by the Ministry of Education, Science, and Technological Development of the Republic of Serbia. DFT calculations were performed using computational resources at Johannes Kepler University, Linz, Austria.



## References

- Aizawa, T., Souda, R., Otani, S., Ishizawa, Y., Oshima, C.: Anomalous bond of monolayer graphite on transition-metal carbide surfaces. *Phys. Rev. Lett.* **64**, 768–771 (1990a). <https://doi.org/10.1103/PhysRevLett.64.768>
- Aizawa, T., Souda, R., Otani, S., Ishizawa, Y., Oshima, C.: Bond softening in monolayer graphite formed on transition-metal carbide surfaces. *Phys. Rev. B* **42**, 11469–11478 (1990b). <https://doi.org/10.1103/PhysRevB.42.11469>
- Amorim, B., Guinea, F.: Flexural mode of graphene on a substrate. *Phys. Rev. B* **88**(11), 115418–115425 (2013)
- Andrew, R.C., Mapasha, R.E., Ukpong, A.M., Chetty, N.: Mechanical properties of graphene and boron-*nitrene*. *Phys. Rev. B* **85**, 125428–125437 (2012). <https://doi.org/10.1103/PhysRevB.85.125428>
- Blake, P., Brimicombe, P.D., Nair, R.R., Booth, T.J., Jiang, D., Schedin, F., Ponomarenko, L.A., Morozov, S.V., Gleeson, H.F., Hill, E.W., Geim, A.K., Novoselov, K.S.: Graphene-based liquid crystal device. *Nano Lett.* **8**(6), 1704–1708 (2008). <https://doi.org/10.1021/nl080649i>
- Bonaccorso, F., Colombo, L., Yu, G., Stoller, M., Tozzini, V., Ferrari, A.C., Ruoff, R.S., Pellegrini, V.: Graphene, related two-dimensional crystals, and hybrid systems for energy conversion and storage. *Science* (2015). <https://doi.org/10.1126/science.1246501>
- Calandra, M., Mauri, F.: Theoretical explanation of superconductivity in  $c_6$  Ca. *Phys. Rev. Lett.* **95**, 237002–237006 (2005). <https://doi.org/10.1103/PhysRevLett.95.237002>
- Calandra, M., Mauri, F.: Possibility of superconductivity in graphite intercalated with alkaline earths investigated with density functional theory. *Phys. Rev. B* **74**, 094507–094515 (2006). <https://doi.org/10.1103/PhysRevB.74.094507>
- Castro Neto, A.H., Guinea, F., Peres, N.M.R.: Edge and surface states in the quantum hall effect in graphene. *Phys. Rev. B* **73**, 205408–205416 (2006). <https://doi.org/10.1103/PhysRevB.73.205408>
- Fariás, D., Shikin, A.M., Rieder, K.H., Dedkov, Y.S.: Synthesis of a weakly bonded graphite monolayer on ni(111) by intercalation of silver. *J. Phys. Condens. Matter* **11**(43), 8453–8458 (1999). <https://doi.org/10.1088/0953-8984/11/43/308>
- Ferrari, A.C., et al.: Science and technology roadmap for graphene, related two-dimensional crystals, and hybrid systems. *Nanoscale* **7**, 4598–4810 (2015). <https://doi.org/10.1039/C4NR01600A>
- Gall, N.R., Rut'kov, E.V., Tontogode, A.Y.: Two dimensional graphite films on metals and their intercalation. *Int. J. Mod. Phys. B* **11**(16), 1865–1911 (1997). <https://doi.org/10.1142/S0217979297000976>
- Giannozzi, P., et al.: Quantum espresso: a modular and open-source software project for quantum simulations of materials. *J. Phys. Condens. Matter* **21**(39), 395502–395521 (2009)
- Gusynin, V.P., Sharapov, S.G.: Unconventional integer quantum hall effect in graphene. *Phys. Rev. Lett.* **95**, 146801–146805 (2005). <https://doi.org/10.1103/PhysRevLett.95.146801>
- Katsnelson, M., Novoselov, K., Geim, A.: Chiral tunnelling and the klein paradox in graphene. *Nat. Phys.* **2**(9), 620–625 (2006). <https://doi.org/10.1038/nphys384>
- Lee, C., Wei, X., Kysar, J.W., Hone, J.: Measurement of the elastic properties and intrinsic strength of monolayer graphene. *Science* **321**(5887), 385–388 (2008). <https://doi.org/10.1126/science.1157996>
- Liu, C.H., Chang, Y.C., Norris, T.B., Zhong, Z.: Graphene photodetectors with ultra-broadband and high responsivity at room temperature. *Nat. Nanotechnol.* **9**(4), 273–278 (2014)
- Marinopoulos, A.G., Reining, L., Rubio, A., Olevano, V.: Ab initio study of the optical absorption and wave-vector-dependent dielectric response of graphite. *Phys. Rev. B* **69**, 245419–245431 (2004). <https://doi.org/10.1103/PhysRevB.69.245419>
- Mazin, I.I.: Intercalant-driven superconductivity in  $\text{YbC}_6$  and  $\text{CaC}_6$ . *Phys. Rev. Lett.* **95**, 227001–227005 (2005). <https://doi.org/10.1103/PhysRevLett.95.227001>
- Nakada, K., Ishii, A.: DFT calculation for adatom adsorption on graphene. In: Gong, J.R. (ed.) *Graphene Simulation*. InTech, Rijeka, Croatia (2011)
- Pešić, J., Gajić, R., Hingerl, K., Belić, M.: Strain-enhanced superconductivity in li-doped graphene. *Europhys. Lett.: EPL* **108**(6), 67005–67011 (2014)
- Pešić, J., Popov, I., Šolajić, A., Damjanović, V., Hingerl, K., Belić, M., Gajić, R.: Ab initio study of the electronic, vibrational, and mechanical properties of the magnesium diboride monolayer. *Condens. Matter* (2019). <https://doi.org/10.3390/condmat4020037>
- Politano, A., Marino, A.R., Campi, D., Fariás, D., Miranda, R., Chiarello, G.: Elastic properties of a macroscopic graphene sample from phonon dispersion measurements. *Carbon* **50**(13), 4903–4910 (2012). <https://doi.org/10.1016/j.carbon.2012.06.019>
- Profeta, G., Calandra, M., Mauri, F.: Phonon-mediated superconductivity in graphene by lithium deposition. *Nat. Phys.* **8**(2), 131–134 (2012)

- Sassi, U., Parret, R., Nanot, S., Bruna, M., Borini, S., De Fazio, D., Zhao, Z., Lidorikis, E., Koppens, F., Ferrari, A., et al.: Graphene-based mid-infrared room-temperature pyroelectric bolometers with ultra-high temperature coefficient of resistance. *Nat. Commun.* **8**, 14311–14321 (2017)
- Shikin, A.M., Fariás, D., Rieder, K.H.: Phonon stiffening induced by copper intercalation in monolayer graphite on ni(111). *Europhys. Lett.: EPL* **44**(1), 44–49 (1998). <https://doi.org/10.1209/epl/1998-00432-x>
- Šolajić, A., Pešić, J., Gajić, R.: Ab-initio calculations of electronic and vibrational properties of sr and yb intercalated graphene. *Opt. Quantum Electron.* **50**(7), 276–286 (2018). <https://doi.org/10.1007/s11082-018-1541-x>
- Taleb, A.A., Fariás, D.: Phonon dynamics of graphene on metals. *J. Phys. Condens. Matter* **28**(10), 103005–103024 (2016). <https://doi.org/10.1088/0953-8984/28/10/103005>
- Taleb, A.A., Yu, H.K., Anemone, G., Fariás, D., Wodtke, A.M.: Helium diffraction and acoustic phonons of graphene grown on copper foil. *Carbon* **95**, 731–737 (2015). <https://doi.org/10.1016/j.carbon.2015.08.110>
- Todorović, D., Matković, A., Miličević, M., Jovanović, D., Gajić, R., Salom, I., Spasenović, M.: Multilayer graphene condenser microphone. *2D Mater.* **2**(4), 045013–045019 (2015)
- Wei, Q., Peng, X.: Superior mechanical flexibility of phosphorene and few-layer black phosphorus. *Appl. Phys. Lett.* **104**(25), 251915–251920 (2014). <https://doi.org/10.1063/1.4885215>
- Winterlin, J., Bocquet, M.L.: Graphene on metal surfaces. *Surface Science* **603**(10), 1841–1852 (2009). <https://doi.org/10.1016/j.susc.2008.08.037>. (Special Issue of Surface Science dedicated to Prof. Dr. Dr. h.c. mult. Gerhard Ertl, Nobel-Laureate in Chemistry 2007)
- Zhang, Z., Yang, Y., Penev, E.S., Yakobson, B.I.: Elasticity, flexibility, and ideal strength of borophenes. *Adv. Funct. Mater.* **27**(9), 1605059–1605066 (2017). <https://doi.org/10.1002/adfm.201605059>

**Publisher's Note** Springer Nature remains neutral with regard to jurisdictional claims in published maps and institutional affiliations.



# Structural and optical characterization of titanium–carbide and polymethyl methacrylate based nanocomposite

Jelena Pešić<sup>1</sup> · Andrijana Šolajić<sup>1</sup> · Jelena Mitrić<sup>1</sup> · Martina Gilić<sup>1</sup> · Ivan Pešić<sup>2</sup> · Novica Paunović<sup>1</sup> · Nebojša Romčević<sup>1</sup>

Received: 11 October 2021 / Accepted: 10 March 2022 / Published online: 12 May 2022

© The Author(s), under exclusive licence to Springer Science+Business Media, LLC, part of Springer Nature 2022

## Abstract

The rich chemistries and unique morphologies of titanium carbide MXenes, made them strong candidates for many applications like sensors and electronic device materials. During the synthesis procedure, chemical etching, oxidation occurs and residual materials, like titanium-dioxide nanocrystals and nanosheets are often present in resulting material. As titanium-carbide MXenes are suggested to be used as additive in organic polymer matrices for production of nanocomposites, it is essential to consider the presence of the oxides and other residuals together with MXene flakes in synthesis results, and consequently in produced nanocomposite. In this study we present structural and optical characterization of such polymer nanocomposite titanium carbide/PMMA (Polymethyl methacrylate) consisting of  $Ti_3C_2$ ,  $TiC_2$  MXenes and  $TiC$ , and  $TiO_2$  residues of synthesis in PMMA matrix, as a multicomponent nanocomposite. Using XRD, infra-red and Raman spectroscopy, followed by comparative study on the vibrational properties using density functional theory calculations, we characterize this nanocomposite. Further, the SEM measurements are performed, demonstrating the produced titanium-carbide-based flakes in nanocomposite are well defined and separated to nanosized grains, allowing us to use Maxwell–Garnet model to analyse infrared spectrum. This enables us to determine the presence of the optical modification of polymer matrices corresponding to a volume fraction of 0.25.

**Keywords** Titanium-carbide nanoparticles · PMMA composite · Multicomponent nanocomposite

---

This article is part of the Topical Collection on Photonics:Current Challenges and Emerging Applications.

---

Guest edited by Jelena Radovanovic, Dragan Indjin, Maja Nestic, Nikola Vukovic and Milena Milosevic.

---

✉ Jelena Pešić  
yelena@ipb.ac.rs

<sup>1</sup> Institute of Physics Belgrade, University of Belgrade, Pregrevice 118, Belgrade 11080, Serbia

<sup>2</sup> Faculty of Technology and Metallurgy, University of Belgrade, Belgrade 11000, Serbia

## 1 Introduction

Nanocomposites are the combination of two or more different materials where a minimum of one of the components has dimension less than 100 nm Twardowski (2007). The polymer nanocomposites are made of organic polymer matrix (in this research, polymethyl methacrylate—PMMA) and inorganic components (titanium carbide nanoparticles). The properties of the obtained nanocomposites depend on the individual properties of each component, morphology and the interface characteristics. In an attempt to improve the properties of conventional polymer materials and extend the fields of their applications, functionalization has emerged as important method in improvement of their not satisfactory electronic, thermal and mechanical properties Tamborra et al. (2004); Hussain et al. (2006). In addition to typical advantages of polymers (such are light-weight, low cost, and good processability), the improvement of electrical properties (e.g., electrical conductivity) with the addition of a small amount of conductive fillers into polymer matrices have promoted polymer nanocomposites into versatile multifunctional materials. Many applications like household electronics, memory and microwave devices are potentially available with addition of metal oxide nanoparticles to polymer. This enables the modification of the polymer's physical properties as well as the implementation of new features in the polymer matrix creating new type of materials known as the polymer nanocomposites. PMMA as a thermoplastic polymer, has many extraordinary properties, like great transparency and ultraviolet resistance, high abrasion resistance, hardness and stiffness and making it widely used in many applications ranging from everyday items to high tech devices. Further, PMMA is nondegradable and biocompatible which makes it an excellent candidate in medical applications like tissue engineering with typical applications such as fracture fixation, intraocular lenses and dentures Peppas and Langer (1994).

Multicomponent nanocomposites based of layered and 2D materials have drawn significant attention in past decade with promises of various applications. Reduction of dimensionality of the system to the truly atomic-scale 2D is related to the occurrence of all new amazing properties in low-dimensional material, since the reduction of available phase space and decreased screening lead to enhancement of quantum effects and increased correlations. Low-dimensional materials have been studied intensively both for their fundamental properties and insight in basic principles of matter but as well for their colossal potential for applications. A discovery of true two-dimensional material graphene Novoselov et al. (2004) and its remarkable properties like and experimental observation of Klein tunnelling, quantum Hall effect and superconductivity Novoselov et al. (2004); Katsnelson et al. (2006); Zhang et al. (2005); Durajski et al. (2019); Pešić et al. (2014); Margine et al. (2016); Durajski et al. (2020) paved the way for investigation of a new family of materials in low-dimensional physics. The new field of two-dimensional materials research has arose and investigated not only graphene but many more crystal structures where, just like in graphene, cells are connected in at least one direction by the van der Waals' forces Novoselov et al. (2016).

Transition metal carbides are important group of materials for applications since they possess some desired characteristics such as thermal stability, wear and corrosion resistance, electronic, magnetic as well as catalytic properties. Titanium-carbide powders are generally used for manufacturing cutting tools, used in treatment of metals and as abrasive-resistant materials. In 2011 Naguib et al. (2011), the group of early transition metal carbides and/or carbo-nitrides labeled as MXenes. MXenes are produced by the etching out of the A layers from MAX phases Naguib et al. (2011, 2012, 2013). Name MAX phase

comes from its chemical composition:  $M_{n+1}AX_n$ , where M is an early transition metal, A is mainly a group IIIA or IVA (i.e., groups 13 or 14) element, X is carbon and/or nitrogen, and  $n = 1, 2, \text{ or } 3$ .

During the synthesis of titanium-carbide MXenes by chemical etching, oxidation can occur which results in presence of  $TiO_2$  consisted of nanosheets and numerous  $TiO_2$  nanocrystals Naguib et al. (2014). There are several studies Zhu et al. (2016); Gao et al. (2015) whose researched is focused in possible applications of  $TiO_2$ -MXene structures. It is demonstrated the joint effects of  $Ti_3C_2$  and  $TiO_2$  endowed  $TiO_2$ - $Ti_3C_2$  nanocomposites with excellent properties and improved functionalities Zhu et al. (2016). In this work we investigate the structural and optical properties of polymer nanocomposites prepared by the incorporation of titanium-carbide nanoparticles consisting of  $Ti_3C_2$ ,  $TiC_2$   $TiC$  and  $TiO_2$  into the matrices of polymer PMMA. The sample of nanocomposite material was prepared, the PMMA matrix with titanium-carbide particles, PMMA/ $TiC$ . As for similar materials Shan et al. (2021, 2020, 2021); Tan et al. (2021); Jafari et al. (2020); Tan et al. (2021) proper understanding of composition of materials used in composite is crucial and XRD analysis for the titanium-carbide flakes. The structural and morphology studies of the nanocomposites were carried out by SEM and Raman spectroscopy. Infrared spectroscopy is a very powerful technique in analysis of various nanoparticle and nanocomposite materials prepared in various techniques Dastan (2015); Dastan and Chaure (2014); Dastan et al. (2014); Dastan and Chaure (2017). To further understand properties of our inhomogeneous nanocomposite we used infrared spectroscopy with Maxwell–Garnet model. To further support optical characterization, calculations based on density functional theory were performed.

## 2 Samples preparation and structural characterization

### 2.1 Titan-carbide/PMMA composite synthesis

In this work, titanium-carbide/PMMA nanocomposite sample was made from mixture of MXene based titanium-carbide nanoflakes in PMMA matrix. Production of layered titanium-carbide flakes is based on MXene synthesis by selective etching of Al atomic layers from  $Ti_3AlC_2$  MAX phase, we used the so-called 'mild' method with lithium fluoride (LiF) and hydrochloric acid (HCl) Tu et al. (2018). This method was described in Naguib et al. (2011). Procedure of composite preparation is described in Fig. 1.

Commercially available PMMA Acryrex CM205 (Chi Mei Corp. Korea, ( $M_w \approx 90400$  g/mol,  $n = 1.49$ ,  $\lambda = 633$  nm) pellets were used as a matrix for sample preparation.  $Ti_3AlC_2$  MAX phase was processed and kindly donated from Layered Solids Group, Drexel University. Titanium-carbide flakes were obtained by sonification in the water and drying the supernatant in a Petri dish in the oven for 30 minutes on  $90^\circ\text{C}$ .

Composite was prepared with 10 wt% PMMA solution in acetone (Carlo Erbe Reagents, Spain) and added dried titanium-carbide flakes. After stirring the solution was poured in Petri dish Cao et al. (2017) and dried in oven 24h on  $40^\circ\text{C}$ . Content of titanium-carbide flakes in the sample was 1.7 wt%.

The morphology of the produced composite has been investigated by FESEM using high resolution electron microscope MIRA3 TESCAN. Samples display separated nano-sized grains. Fig. 2a presents FESEM image of MXene flakes delaminated in water showing morphology of obtained flakes, b FESEM image of the PMMA/titanium-carbide

**Fig. 1** Schematic describing the synthesis process of MXenes from MAX phases and preparation of composite

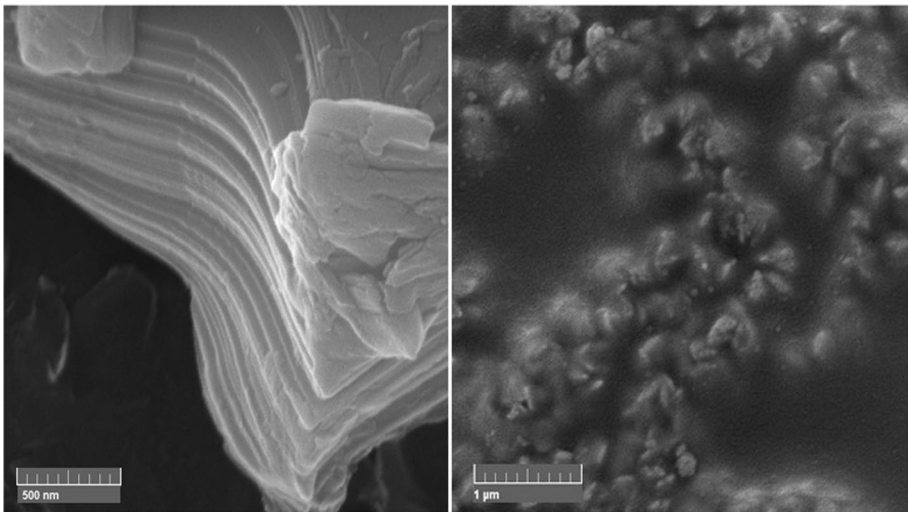
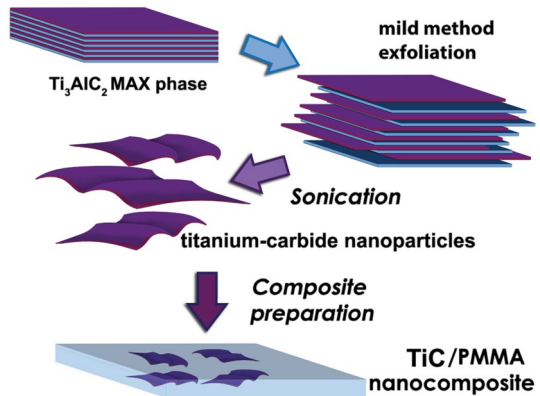


**Fig. 2** FESEM photos of **a** Flakes delaminated in water; **b** PMMA composite prepared with titanium-carbide flakes

nanocomposite. Characteristic layered structure of MXenes is visible on FESEM image and confirming success of delamination and exfoliation procedures. Obtained flakes demonstrate multilayered structure with few  $\mu\text{m}$  in diameter. In Fig. 2b typical accordion like structure can be indicated in nanosize grain-like structures, clustered in PMMA matrix.

## 2.2 XRD

X-ray diffraction powder (XRD) technique was used to determine structural characteristics of titanium-carbide based flakes to be used in composites. Philips PW 1050 diffractometer equipped with a PW 1730 generator was used. The same conditions were used for all samples, 40 kV $\times$ 20 mA, using Ni filtered Co K $\alpha$  radiation of 0.1778897 nm at room temperature. Measurements were carried out in the  $2\theta$  range of 20–80° with a scanning step

**Fig. 3** XRD pattern for titanium-carbide flakes, starting material for PMMA/TiC composite

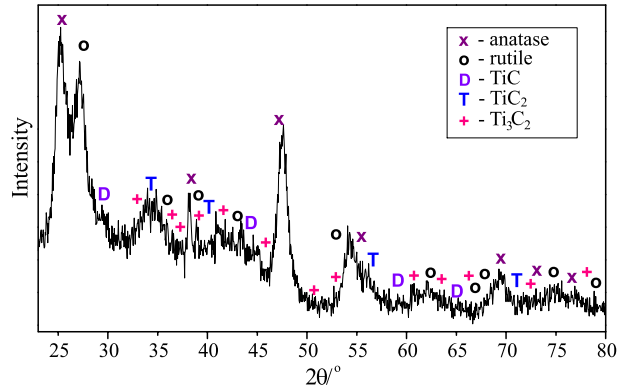
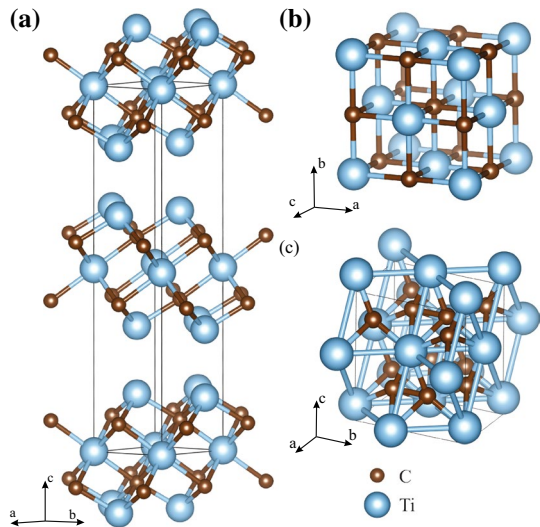


**Fig. 4** Schematic representation of Titanium-carbide structures present at composite **a**  $\text{Ti}_3\text{C}_2$ , **b** TiC and **c**  $\text{TiC}_2$



of  $0.05^\circ$  and 10 s scanning time per step. In Fig. 3 is presented XRD pattern for titanium-carbide flakes, starting material for composite. The different phases of titanium carbide can be noticed from diffractogram— $\text{Ti}_3\text{C}_2$ , TiC and  $\text{TiC}_2$  together with  $\text{TiO}_2$ .  $\text{TiO}_2$  is widely present as anatase and rutile and it is confirmed that they belong to space groups  $P6_3/mmc$  (194),  $Fm\bar{3}m$  (225)  $Fm2m$  (42),  $I4_1/amd$  (141),  $P4_2/mnm$  (136), respectively. The unit cells of MXene structures  $\text{Ti}_3\text{C}_2$ , TiC and  $\text{TiC}_2$  are presented in Fig. 4. These structures were further used in DFT analysis of optical spectroscopy results in Sect. 3.3.

### 3 Results and discussion

#### 3.1 Raman spectroscopy

The micro-Raman spectra were taken in the backscattering configuration and analyzed by the TriVista 557 system equipped with a nitrogen cooled charge-coupled-device

detector. As an excitation source, we used the 532 nm line of Ti:Sapphire laser. Excitation energy is in the off-resonance regime for all the considered materials. The Raman spectra of the PMMA, PMMA/TiC, and titanium-carbide flakes, measured in the spectral range of 100–1100  $\text{cm}^{-1}$  at room temperature, are presented in Fig. 5.

The Raman spectrum of PMMA is presented in Fig. 5a. Intense modes at 235, 300, 362, 400, 484, 560, 603, 660, 733, 815, 839, 864, 911, 967, 985, 1063 and 1091  $\text{cm}^{-1}$  were detected. The obtained results are in a good agreement with the values given in the literature Willis et al. (1969); Thomas et al. (2008); Ćurčić et al. (2020).

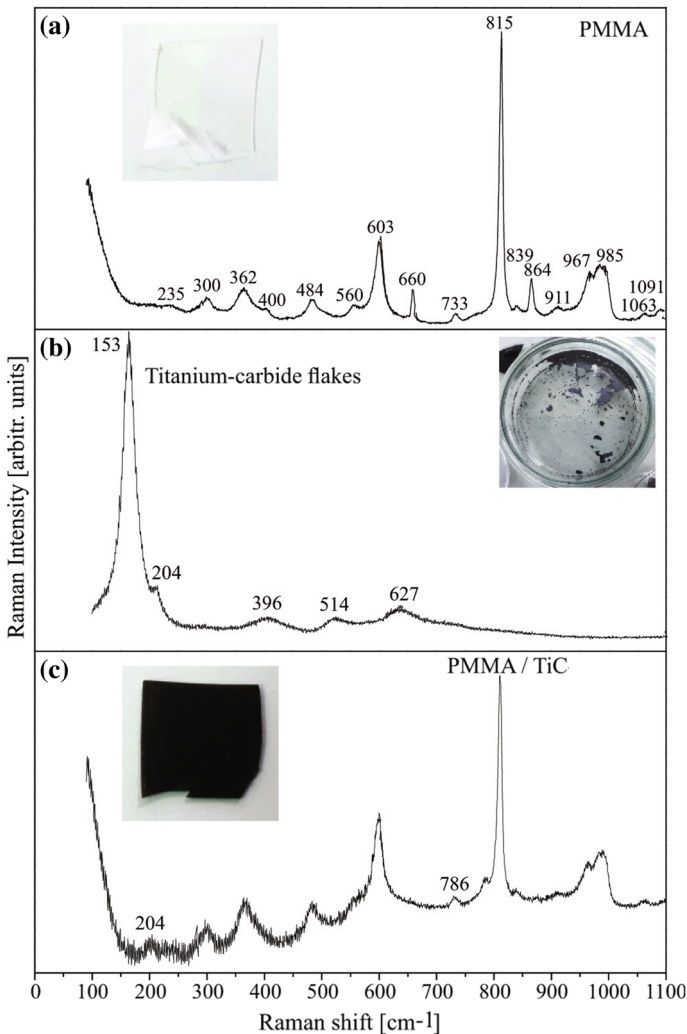


**Fig. 5** Raman spectra with photo of the sample of **a** PMMA, **b** Titanium-carbide flakes, **c** PMMA/TiC composite. Only titanium-carbide related peaks are marked in this spectrum. Unassigned peaks correspond to PMMA from **a** spectrum



In Fig. 5b spectrum of titanium-carbide flakes after etching procedure is presented. Several characteristic peaks can be distinguished on  $153\text{ cm}^{-1}$ ,  $204\text{ cm}^{-1}$ ,  $396\text{ cm}^{-1}$ ,  $514\text{ cm}^{-1}$  and  $627\text{ cm}^{-1}$ . Peaks at  $153\text{ cm}^{-1}$  and  $627\text{ cm}^{-1}$  correspond to doubly degenerated  $E_{2g}$  modes of  $\text{Ti}_3\text{C}_2$ . The frequency associated with  $E_{2g}$  modes is calculated to be at  $161\text{ cm}^{-1}$  for the bare  $\text{Ti}_3\text{C}_2$ . Since their main contribution is from in-plane vibrations of Ti and C atoms, it can be influenced by the vibrations of the terminal atoms (as a residue of synthesis procedure) weaken the in-plane motion of the Ti and C atoms, hence there is shift to lower frequency. The terminal groups play significant roles for the vibrational modes: the terminal atoms weakening the motions in which the surface Ti atoms are involved while strengthening the out-of-plane vibration of the C atoms; the corresponding vibrational frequencies dramatically change with the various terminal atoms Zhao et al. (2016). This is consistent with XRD results suggesting significant amount of  $\text{TiO}_2$  as a residue of synthesis procedure as described in introduction. This can be also visible in Raman spectrum of titanium-carbide flakes on  $204\text{ cm}^{-1}$  and  $514\text{ cm}^{-1}$ . The doubly degenerated modes at  $621\text{ cm}^{-1}$  correspond to the in-plane vibration of the C atoms Hu et al. (2015). In Fig. 5c spectrum of PMMA/TiC is presented, only titanium-carbide related peaks at  $204$  and  $786\text{ cm}^{-1}$  are marked in this spectrum. Unassigned peaks correspond to PMMA peaks marked on a) panel.

As XRD analysis demonstrated, obtained flakes contain both MXene flakes and titanium-dioxide as the residue of synthesis procedure. To further understand and assign this spectra we performed theoretical analysis of all materials identified in XRD pattern using density functional theory calculations. Calculations provided us a guide for identification of peaks and all results are summarized in Table 1.

### 3.2 Far-infrared spectroscopy

Far-infrared reflection spectra were measured at room temperature in the spectral range from  $40$  to  $600\text{ cm}^{-1}$ , carried out with a BOMEM DA 8 spectrometer. The experimental data are represented at Fig. 6a and by circles at Fig. 6b–d. As expected, the reflection spectra of nanocomposites are by intensity placed between the starting composites. In order to analyse far-infrared spectra we have used the classical oscillator model with free carrier contribution, as a base for Maxwell–Garnet effective medium approximation Abstreiter (1984); Carter and Bate (1971). The low-frequency dielectric properties of single crystals are described by classical oscillators corresponding to the TO modes, to which the Drude part is superimposed to take into account the free carrier contribution:

$$\epsilon_s(\omega) = \epsilon_\infty + \sum_{k=1}^l \frac{\epsilon_\infty S_k}{\omega_{TOk}^2 - \omega^2 - i\gamma_{TOk}\omega} - \frac{\epsilon_\infty \omega_p^2}{\omega(\omega + i\Gamma_p)}, \quad (1)$$

where  $\epsilon_\infty$  is the bound charge contribution and it is assumed to be a constant,  $\omega_{TOk}^2$  is the transverse optical-phonon frequency,  $\omega_p^2$  the plasma frequency,  $\gamma_{TOk}$  is damping,  $\Gamma_p$  is the plasmon mode damping coefficient, and  $S_k$  is the oscillator strength.

In general, the optical properties of an inhomogeneous material are described by the complex dielectric function that depends on 3D distribution of constituents. The investigated mixture consists of two materials with two different dielectric components. One is treated as a host, and the other as the inclusions. The characterization of the inhomogeneous material by the two dielectric functions is not useful, since one need to know the exact geometrical arrangement of the constituents of the material. However, if the wavelength of

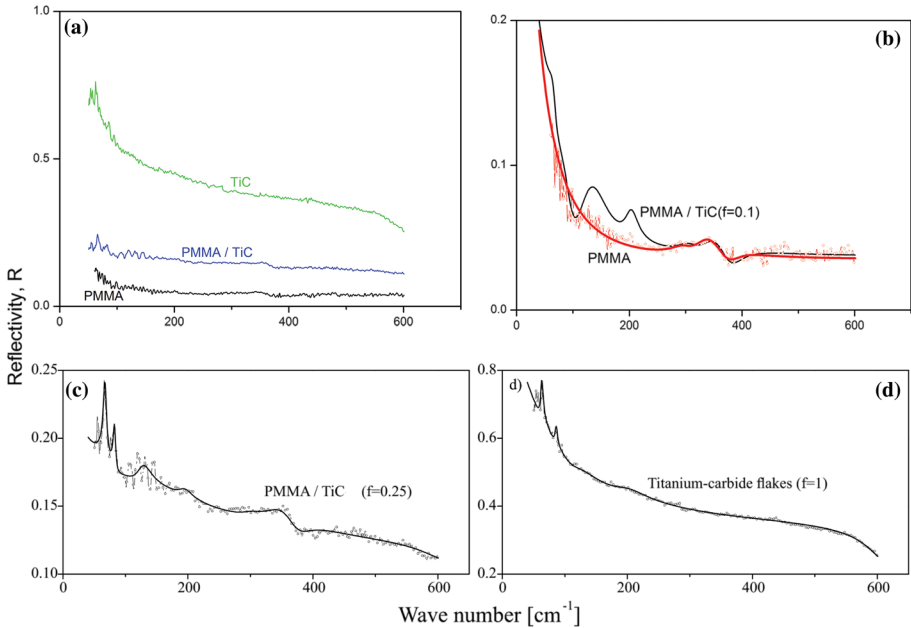


**Fig. 6** Infrared analysis: **a** Infrared spectra of Titanium-carbide flakes (green) and composites PMMA/TiC (blue) and pure PMMA (black), **b**, **c**, and **d** circles represent experimental data and solid lines are fit obtained by Maxwell–Garnet model as described in Sect. 3.2

**Table 1** Raman and infrared spectrum analysis and modes assignation for synthesized titanium-carbide flakes and PMMA/TiC composite

	Titanium-carbide flakes		PMMA/TiC		Description
	Raman	IR	Raman	IR	
$\omega_1$		62.4	66		$E_u, Ti_3C_2$
$\omega_2$		85.8	81		$B_1, TiO_2$ rutile
$\omega_3$		119	127		$A_{2u}, Ti_3C_2$ and $B_1 TiC_2$
$\omega_4$	153				$E_g, Ti_3C_2$
$\omega_5$	204	200	204	195	$E, TiO_2$ anatase
$\omega_6$	396				$A_2, TiC_2; E, TiO_2$ anatase
$\omega_7$	514				$A_1, TiO_2$ anatase
$\omega_8$		620		615	$E_u, Ti_3C_2$
$\omega_9$	627				$E_g, Ti_3C_2$
$\omega_{10}$			786		$A_g, TiO_2$ rutile
$\omega_p$		80		150	
f		1		0.25	

Infrared modes fit is obtained by Maxwell–Garnet model. Modes assignation is performed using values obtained using DFT calculations

the electromagnetic radiation is much larger than the size of inclusions, classical theories of inhomogeneous material presume that the material can be treated as a homogeneous substance with an effective dielectric function. In the literature, many mixing models can

be found for the effective permittivity of such mixture. Some are present in ref Sihvola (1999). Optical properties of such materials depend upon the properties of constituents, as well as their volume fraction. Since our samples are well defined and separated nanosized grains (as demonstrated on FESEM images, Fig. 2), we used Maxwell–Garnet model for present case. For the spherical inclusions case, the prediction of the effective permittivity of mixture,  $\epsilon_{eff}$ , according to the Maxwell–Garnet mixing rule is Garnett (1904):

$$\epsilon_{eff} = \epsilon_1 + 3f\epsilon_1 \frac{\epsilon_2 - \epsilon_1}{\epsilon_2 + 2\epsilon_1 - f(\epsilon_2 - \epsilon_1)} \quad (2)$$

Here, spheres of permittivity  $\epsilon_2$  (Titanium-carbide) are located randomly in homogeneous environment  $\epsilon_1$  (PMMA) and occupy a volume fraction  $f$ .

Solid lines in Fig. 6 are calculated spectra obtained by a fitting procedure based on the previously presented model. The agreement of the theoretical model obtained in this manner with the experimental results is excellent.

To demonstrate the model, together with the infrared spectrum of PMMA, Fig. 6b is given the theoretical spectrum of PMMA/TiC nanocomposites for  $f = 0.1$ . The properties of TiC structures are clearly visible. A larger share of TiC structures leads to the spectrum in Fig 6c, which was obtained for  $f = 0.25$ . In Fig. 6d, for  $f=1$  of course there is no effect from PMMA.

### 3.3 Discussion

In Table 1 are summarized results from spectroscopic measurements of obtained nanocomposites. As stated above, for infrared measurements the agreement of the theoretical model with obtained spectra is excellent and best fit parameters are presented in this table.

To further support our results we performed DFT based calculations and calculated vibrational frequencies in  $\Gamma$  point for all materials present after titanium-carbide flakes exfoliation, which we determined are present using XRD, Fig. 3. Obtained values are compared to experimental Raman and infrared spectrum and modes have been assigned. Results are summarized in Table 1. We presented only modes that can be assigned to peaks from the spectra. In infrared spectra we can notice good agreement with theoretical calculations, specially for low-energy  $E_u$  and  $A_{2u}$  mode of  $Ti_3C_2$  which is present the composite spectrum (Fig. 6b, c) as in starting titanium-carbide material (Fig. 6d). As shown in XRD we notice peaks originating from  $TiO_2$  and  $TiC_2$  in mid-energy region. High-energy mode  $E_u$  on  $620\text{ cm}^{-1}$  is present in spectrum of PMMA/TiC. In Table 2 are summarized calculated optical modes for  $Ti_3C_2$  with symmetry 194 group used in analysis.

DFT calculations were performed using the Quantum Espresso software package Gianozzi (2009), based on the plane waves and pseudopotentials. The PBE (Perdew, Burke and Ernzerhof) Perdew et al. (1996) exchange-correlation functional was employed and PAW (Projector augmented waves) pseudopotentials were used. Energy cutoff for wavefunctions and charge density were set to 52 Ry and 575 Ry to ensure the convergence. The Brillouin zone was sampled using the Monkhorst-Pack scheme, with  $8 \times 8 \times 8$  k-points mesh for  $TiC_2$ ,  $8 \times 8 \times 4$  for  $Ti_3C_2$ ,  $12 \times 12 \times 12$  for TiC, and  $8 \times 8 \times 8$  for  $TiO_2$  (Rutile and Anatase structures). Phonon frequencies are calculated within the DPFT (Density Functional Perturbation Theory) implemented in Quantum Espresso Baroni et al. (2001). In order to obtain the lattice parameters more accurately, van der Waals forces were treated using the Grimme-D2 correction Grimme (2006)

**Table 2** Vibrational modes for  $\text{Ti}_3\text{C}_2$  with symmetry group 194, calculated from the measured data

$\text{Ti}_3\text{C}_2$ (P6 <sub>3</sub> /mmc)		
cm <sup>-1</sup>	Symmetry	Raman or IR active
65.0	E <sub>u</sub>	I
135.2	A <sub>2u</sub>	I
160.6	E <sub>g</sub>	R
161.4	E <sub>g</sub>	R
229.9	A <sub>1g</sub>	R
269.3	A <sub>1g</sub>	R
271.1	E <sub>u</sub>	I
271.7	E <sub>u</sub>	I
371.4	A <sub>2u</sub>	I
382.4	A <sub>2u</sub>	I
549.1	A <sub>2u</sub>	I
554.4	A <sub>2u</sub>	I
611.2	E <sub>g</sub>	R
620.4	E <sub>g</sub>	R
624.1	E <sub>u</sub>	I
626.4	E <sub>u</sub>	I
653.2	A <sub>1g</sub>	R
658.3	A <sub>1g</sub>	R

Optical spectroscopy results supported with the DFT numerical calculation confirm that produced composites PMMA/TiC show optical modification comparing to pure PMMA. Our X-ray diffraction investigation of synthesized nanomaterials identified presence of  $\text{Ti}_3\text{C}_2$  and  $\text{TiC}_2$  MXenes and residual  $\text{TiO}_2$  and TiC from the synthesis procedure, which can be also supported from the optical spectroscopy results.

## 4 Conclusion

In this paper, we present results of optical and structural investigation of composite based on titanium-carbide nanoflakes ( $\text{Ti}_3\text{C}_2$ ,  $\text{TiC}_2$  TiC and  $\text{TiO}_2$ ) in PMMA matrix. X-ray diffraction (XRD) investigation of synthesized nanomaterials identified presence of  $\text{Ti}_3\text{C}_2$  and  $\text{TiC}_2$  MXenes and residual  $\text{TiO}_2$  and TiC from the synthesis procedure. The optical properties were studied by Raman and infrared spectroscopy at room temperature. The analysis of the Raman spectra was made by the fitting procedure. For analysis of infrared spectra we used Maxwell–Garnet model. In order to identify and assign vibrational modes, vibrational frequencies of all identified materials were calculated using density functional theory, and compared with experimental results. We confirmed optical modification in composite structure compared to pure PMMA. Further analysis that goes beyond the scope of this publication studies mechanical properties of composite materials, confirming improvements compared to pure PMMA. The obtained composite showed enhanced hardness, elastic modulus and tensile strength compared with pure PMMA Pestic et al. (2019).

**Acknowledgements** The authors acknowledge funding provided by the Institute of Physics Belgrade and Faculty of Technology and Metallurgy, through the grant by the Ministry of Education, Science and Technological Development of the Republic of Serbia. All calculations were performed using computational resources at Johannes Kepler University, Linz, Austria.

**Author Contributions** Conceptualization, JP and NR; investigation JP, AŠ, JM, MG, IP, NP; validation, JP, NP, NR; formal analysis, JP, AŠ, JM, MG, NP, NR; writing JP and AŠ; writing–review and editing, JP, AŠ, NP, NR; visualization, AŠ; supervision, NR; project administration, NR; funding acquisition, NR. All authors have read and agreed to the published version of the manuscript.

**Funding** The authors acknowledge funding provided by the Institute of Physics Belgrade and Faculty of Technology and Metallurgy, through the grant by the Ministry of Education, Science and Technological Development of the Republic of Serbia.

**Data availability** All additional material is available at authors on request.

**Code availability** Not applicable.

## Declarations

**Conflict of interest** The Authors declare no conflict of interest.

**Ethical approval** Not applicable.

**Informed consent** Not applicable.

**Consent for publication** All authors consent to publication results presented in manuscript.

## References

- Abstreiter, G.: Light Scattering in Solids IV. Springer, New York (1984)
- Baroni, S., de Gironcoli, S., Dal Corso, A., Giannozzi, P.: Phonons and related crystal properties from density-functional perturbation theory. *Rev. Mod. Phys.* **73**, 515–562 (2001)
- Cao, Y., Deng, Q., Liu, Z., Shen, D., Wang, T., Huang, Q., Du, S., Jiang, N., Lin, C.-T., Yu, J.: Enhanced thermal properties of poly (vinylidene fluoride) composites with ultrathin nanosheets of mxene. *RSC Adv.* **7**(33), 20494–20501 (2017)
- Carter, D.L., Bate, R.T.: *The Physics of Semimetals and Narrow-gap Semiconductors: Proceedings*, vol. 32. Pergamon, Texas, USA (1971)
- Ćurčić, M., Hadžić, B., Gilić, M., Radojević, V., Bjelajac, A., Radović, I., Timotjević, D., Romčević, M., Trajić, J., Romcevic, N.: Surface optical phonon (sop) mode in ZnS/poly (methylmethacrylate) nanocomposites. *Physica E* **115**, 113708 (2020)
- Dastan, D.: Nanostructured anatase titania thin films prepared by sol-gel dip coating technique. *J. Atom. Mol. Condens. Matter Nano Phys.* **2**, 109–114 (2015)
- Dastan, D., Chauré, N.B.: Influence of surfactants on TiO<sub>2</sub> nanoparticles grown by sol-gel technique. *Int. J. Mater. Mech. Manuf.* **2**, 21 (2014)
- Dastan, D., Chauré, N.: Kartha: Surfactants assisted solvothermal derived titania nanoparticles: synthesis and simulation. *J. Mater. Sci.* **28**, 7784–7796 (2017)
- Dastan, D., Londhe, P.U., Chauré, N.B.: Characterization of TiO<sub>2</sub> nanoparticles prepared using different surfactants by sol-gel method. *J. Mater. Sci.* **25**, 3473–3479 (2014)
- Durajski, A.P., Skoczylas, K.M., Szczaeniak, R.: Superconductivity in bilayer graphene intercalated with alkali and alkaline earth metals. *Phys. Chem. Chem. Phys.* **21**, 5925–5931 (2019). <https://doi.org/10.1039/C9CP00176J>
- Durajski, A.P., Auguscik, A.E., Szczaeniak, R.: Tunable electronic and magnetic properties of substitutionally doped graphene. *Physica E* **119**, 113985 (2020). <https://doi.org/10.1016/j.physe.2020.113985>
- Gao, Y., Wang, L., Zhou, A., Li, Z., Chen, J., Bala, H., Hu, Q., Cao, X.: Hydrothermal synthesis of TiO<sub>2</sub>/Ti<sub>3</sub>C<sub>2</sub> nanocomposites with enhanced photocatalytic activity. *Mater. Lett.* **150**, 62–64 (2015)

- Garnett, J.M.: XII. Colours in metal glasses and in metallic films. *Philosoph. Trans. R. Soc. Lond. Ser. A* **203**, 385–420 (1904)
- Giannozzi, P., et al.: QUANTUM ESPRESSO: a modular and open-source software project for quantum simulations of materials. *J. Phys. Condens. Matter* **21**(39), 395502 (2009)
- Grimme, S.: Semiempirical GGA-type density functional constructed with a long-range dispersion correction. *J. Comput. Chem.* **27**(15), 1787–1799 (2006)
- Hu, T., Wang, J., Zhang, H., Li, Z., Hu, M., Wang, X.: Vibrational properties of  $\text{t}_3\text{c}_2$  and  $\text{t}_3\text{c}_2\text{t}_2$  ( $t = \text{o}, \text{f}, \text{oh}$ ) monosheets by first-principles calculations: a comparative study. *Phys. Chem. Chem. Phys.* **17**(15), 9997–10003 (2015)
- Hussain, F., Hojjati, M., Okamoto, M., Gorga, R.E.: Review article: polymer-matrix nanocomposites, processing, manufacturing, and application: an overview. *J. Compos. Mater.* **40**(17), 1511–1575 (2006). <https://doi.org/10.1177/0021998306067321>
- Jafari, A., Tahani, K., Dastan, D., Asgary, S., Shi, Z., Yin, X.-T., Zhou, W.-D., Garmestani, H.: Ştefan Ţălu: Ion implantation of copper oxide thin films; statistical and experimental results. *Surf. Interfaces* **18**, 100463 (2020)
- Katsnelson, M.I., Novoselov, K.S., Geim, A.K.: Chiral tunnelling and the Klein paradox in graphene. *Nat. Phys.* **2**, 620–625 (2006)
- Margine, E.R., Lambert, H., Giustino, F.: Electron-phonon interaction and pairing mechanism in superconducting ca-intercalated bilayer graphene. *Sci. Rep.* **6**, 21414 (2016)
- Naguib, M., Kurtoglu, M., Presser, V., Lu, J., Niu, J., Heon, M., Hultman, L., Gogotsi, Y., Barsoum, M.W.: Two-dimensional nanocrystals produced by exfoliation of  $\text{t}_3\text{alc}_2$ . *Adv. Mater.* **23**(37), 4248–4253 (2011). <https://doi.org/10.1002/adma.201102306>
- Naguib, M., Mashtalir, O., Carle, J., Presser, V., Lu, J., Hultman, L., Gogotsi, Y., Barsoum, M.W.: Two-dimensional transition metal carbides. *ACS Nano* **6**(2), 1322–1331 (2012). <https://doi.org/10.1021/nn204153h>
- Naguib, M., Halim, J., Lu, J., Cook, K.M., Hultman, L., Gogotsi, Y., Barsoum, M.W.: New two-dimensional niobium and vanadium carbides as promising materials for li-ion batteries. *J. Am. Chem. Soc.* **135**(43), 15966–15969 (2013). <https://doi.org/10.1021/ja405735d>
- Naguib, M., Mashtalir, O., Lukatskaya, M.R., Dyatkin, B., Zhang, C., Presser, V., Gogotsi, Y., Barsoum, M.W.: One-step synthesis of nanocrystalline transition metal oxides on thin sheets of disordered graphitic carbon by oxidation of mxenes. *Chem. Commun.* **50**, 7420–7423 (2014)
- Novoselov, K.S., Geim, A.K., Morozov, S.V., Jiang, D., Zhang, Y., Dubonos, S.V., Grigorieva, I.V., Firsov, A.A.: Electric field effect in atomically thin carbon films. *Science* **306**(5696), 666–669 (2004). <https://doi.org/10.1126/science.1102896>
- Novoselov, K.S., Mishchenko, A., Carvalho, A., Castro Neto, A.H.: 2d materials and van der Waals heterostructures. *Science* **353**, 6298 (2016). <https://doi.org/10.1126/science.aac9439>
- Peppas, N., Langer, R.: New challenges in biomaterials. *Science* **263**(5154), 1715–1720 (1994). <https://doi.org/10.1126/science.8134835>
- Perdew, J.P., Burke, K., Ernzerhof, M.: Generalized gradient approximation made simple. *Phys. Rev. Lett.* **77**, 3865–3868 (1996)
- Pesic, I., Radojevic, V., Barsoum, N. M. Tomic, Romcevic, N.: Preparation, characterization and mechanical properties of mxene/pmma composite. TechConnect World Innovation Conference and Expo, Boston, MA, USA. <https://www.techconnectworld.com/World2019/wednesday.htmlW6.26> (2019)
- Pešić, J., Gajić, R., Hingerl, K., Belić, M.: Strain-enhanced superconductivity in li-doped graphene. *EPL (Europhys. Lett.)* **108**(6), 67005 (2014). <https://doi.org/10.1209/0295-5075/108/67005>
- Shan, K., Yi, Z.-Z., Yin, X.-T., Dastan, D., Dadkhah, S., Coates, B.T., Garmestani, H.: Mixed conductivities of a-site deficient Y, Cr-doubly doped  $\text{srTiO}_3$  as novel dense diffusion barrier and temperature-independent limiting current oxygen sensors. *Adv. Powder Technol.* **31**(12), 4657–4664 (2020)
- Shan, K., Yi, Z.-Z., Yin, X.-T., Cui, L., Dastan, D., Garmestani, H., Alamgir, F.M.: Diffusion kinetics mechanism of oxygen ion in dense diffusion barrier limiting current oxygen sensors. *J. Alloy. Compd.* **855**, 157465 (2021)
- Shan, K., Zhai, F., Yi, Z.-Z., Yin, X.-T., Dastan, D., Tajabadi, F., Jafari, A., Abbasi, S.: Mixed conductivity and the conduction mechanism of the orthorhombic CAZRO3 based materials. *Surf. Interfaces* **23**, 100905 (2021)
- Sihvola, A.H.: *Electromagnetic Mixing Formulas and Applications*, vol. 47. IET, UK (1999)
- Tamborra, M., Striccoli, M., Comparelli, R., Curri, M., Petrella, A., Agostiano, A.: Optical properties of hybrid composites based on highly luminescent CDS nanocrystals in polymer. *Nanotechnology* **15**(4), 240 (2004)

- Tan, G.-L., Tang, D., Dastan, D., Jafari, A., Shi, Z., Chu, Q.-Q., Silva, J.P.B., Yin, X.-T.: Structures, morphological control, and antibacterial performance of tungsten oxide thin films. *Ceram. Int.* **47**(12), 17153–17160 (2021)
- Tan, G.-L., Tang, D., Dastan, D., Jafari, A., Silva, J.P.B., Yin, X.-T.: Effect of heat treatment on electrical and surface properties of tungsten oxide thin films grown by HFCVD technique. *Mater. Sci. Semicond. Process.* **122**, 105506 (2021)
- Thomas, K., Sheeba, M., Nampoori, V., Vallabhan, C., Radhakrishnan, P.: Raman spectra of polymethyl methacrylate optical fibres excited by a 532 nm diode pumped solid state laser. *J. Opt. A Pure Appl. Opt.* **10**(5), 055303 (2008)
- Tu, S., Jiang, Q., Zhang, X., Alshareef, H.N.: Large dielectric constant enhancement in mxene percolative polymer composites. *ACS Nano* **12**(4), 3369–3377 (2018)
- Twardowski, T.E.: *Introduction to Nanocomposite Materials: Properties, Processing, Characterization*, DEStech Publications Inc, Lancaster, USA (2007)
- Willis, H., Zichy, V., Hendra, P.: The laser-Raman and infra-red spectra of poly (methyl methacrylate). *Polymer* **10**, 737–746 (1969)
- Zhang, Y., Tan, Y.-W., Stormer, H.L., Kim, P.: Experimental observation of the quantum hall effect and Berry's phase in graphene. *Nature* **438**, 201–204 (2005)
- Zhao, T., Zhang, S., Guo, Y., Wang, Q.:  $\text{TiC}_2$ : a new two-dimensional sheet beyond mxenes. *Nanoscale* **8**(1), 233–242 (2016)
- Zhu, J., Tang, Y., Yang, C., Wang, F., Cao, M.: Composites of  $\text{TiO}_2$  nanoparticles deposited on  $\text{Ti}_3\text{C}_2$  mxene nanosheets with enhanced electrochemical performance. *J. Electrochem. Soc.* **163**(5), 785–791 (2016)

**Publisher's Note** Springer Nature remains neutral with regard to jurisdictional claims in published maps and institutional affiliations.

PAPER

## Novel wide spectrum light absorber heterostructures based on hBN/In(Ga)Te

To cite this article: A Šolajić and J Pešić 2022 *J. Phys.: Condens. Matter* **34** 345301

View the [article online](#) for updates and enhancements.

### You may also like

- [Ultrahigh sensitivity and gain white light photodetector based on GaTe/Sn : CdS nanoflake/nanowire heterostructures](#)  
Weichang Zhou, Yong Zhou, Yuehua Peng et al.
- [Temperature-induced phase transition of two-dimensional semiconductor GaTe](#)  
Xiaoyu Wang, , Xue Wang et al.
- [Effects of interlayer interactions on the nanoindentation response of freely suspended multilayer gallium telluride](#)  
Jin Zhang, Yan Zhou, Penghua Ying et al.



# Novel wide spectrum light absorber heterostructures based on hBN/In(Ga)Te

A Šolajić\*  and J Pešić 

Center for Solid State Physics and New Materials, Institute of Physics Belgrade, University of Belgrade, Pregrevica 118, 11080 Belgrade, Serbia

E-mail: [solajic@ipb.ac.rs](mailto:solajic@ipb.ac.rs)

Received 20 April 2022, revised 2 June 2022

Accepted for publication 16 June 2022

Published 28 June 2022



CrossMark

## Abstract

Two-dimensional group III monochalcogenides have recently attracted quite attention for their wide spectrum of optical and electric properties, being promising candidates for optoelectronic and novel electrical applications. However, in their pristine form they are extremely sensitive and vulnerable to oxygen in air and need good mechanical protection and passivation. In this work we modeled and studied two newly designed van der Waals (vdW) heterostructures based on layer of hexagonal boron nitride (hBN) and GaTe or InTe monolayer. Using density functional theory, we investigate electronic and optical properties of those structures. Their moderate band gap and excellent absorption coefficient makes them ideal candidate for broad spectrum absorbers, covering all from part of IR to far UV spectrum, with particularly good absorption of UV light. The hBN layer, which can be beneficial for protection of sensitive GaTe and InTe, does not only preserve their optical properties but also enhances it by changing the band gap width and enhancing absorption in low-energy part of spectrum. Calculated binding energies prove that all three stacking types are possible to obtain experimentally, with H-top as the preferable stacking position. Moreover, it is shown that type of stacking does not affect any relevant properties and bandstructure does not reveal any significant change for each stacking type.

Keywords: heterostructures, hBN, 2D materials, InTe, GaTe, light absorption, DFT

(Some figures may appear in colour only in the online journal)

## 1. Introduction

Enormous attention given to the exploration and researching of two-dimensional materials in the past decade has started a whole new era in materials science and countless possibilities for novel devices emerged. After successful exfoliation and experimental confirmation of graphene's extraordinary properties, many van der Waals (vdW) layered materials were regaining the attention, being extensively exploited in order to find more possible 2D structures [1]—hexagonal boron nitride [2, 3], silicene [4, 5], germanene [6, 7], transition

metal dichalcogenides (TMD's) [8–13], MXenes [14, 15]. As a result, many possibilities emerged for more innovations and research of more complex systems such are 2D vdW heterostructures. Those layered structures often have new rich physics and enhanced properties, particularly attractive for countless applications in nanoelectronic [16–18] and optoelectronic devices such are Light-emitting diodes based on vdW heterostructures [19], solar cells [20, 21] and flexible broad-spectrum photodetectors [22, 23].

In last few years, two-dimensional group IIIa monochalcogenides have been extensively researched [24–27]. In their bulk form, they are layered structures with weak vdW binding forces, suitable for mechanical exfoliation down to a single layer. With a wide spectrum of exceptional electronic and

\* Author to whom any correspondence should be addressed.

optical properties in their two dimensional form, they became very desirable candidates for further research and applications. One of the most outstanding materials in this 2D family, InSe, exhibits very high electron mobility [28] and superb optical properties. Previous work revealed it as very promising material for a highly stable field effect transistors [29]. Excellent absorption properties mark InSe favorable for use in broad spectrum flexible photodetectors, covering wide range from UV to the near IR region [30]. With the idea to further enhance their properties to be more suitable for particular devices, research of vdW heterostructures based on 2D group IIIa monochalcogenides brought notable attention. Various combinations of group III monochalcogenides and graphene emerged as an effective and tunable Schottky barrier [31–35] with many possible ways to precisely control the electronic properties—via electric field, external strain or controlling the interlayer distance. Recent work on heterostructures based on InSe/hBN revealed them as excellent absorbers of the visible and UV part of spectrum.

Two members of group III monochalcogenides were more recently explored and theoretically proposed as new 2D structures—monolayers of InTe and GaTe. Both materials are indirect band gap semiconductors with moderate band gaps of 1.29 and 1.75 eV, respectively. In addition to good electrical and optical properties [36–40], those materials also excel in elastic properties, being able to sustain considerable values of both tensile and compressive strain [36, 40, 41], which is already proven as very effective and convenient way to precisely tune electronic and optical properties of 2D materials [42–44]. Suitable for various applications in novel electronic and optoelectronic devices, research of heterostructures based on those materials is very attractive, with huge expectations for achieving new effects or enhancing desired properties of the 2D structures alone. However, pristine monochalcogenides, especially in form of thin films or as a single layer, are very sensitive and vulnerable to oxygen in air—many studies reveal that single layers are oxidized almost instantly after exposure to the air [45–48]. The issue of their challenging stability can be overcome by passivation with adequate material which would ensure the safe encapsulation of monochalcogenides as well as good mechanical protection. One of materials particularly good and widely used for this purpose is hexagonal boron nitride (hBN). Experimental studies confirmed it as effective for protection and passivation of few layers InSe and GaSe, while their electronic and optical properties are preserved or even enhanced [49] hence the similar effects can be expected for different members of the group III monochalcogenide family.

In the next sections, we present newly designed heterostructures, hBN/GaTe and hBN/InTe, based on a single layer of GaTe or InTe and a layer of hBN. Using the density functional theory (DFT), we explore their electronic and optical properties and analyze the influence of hBN layer on GaTe and InTe. Given the facts stated in previous paragraphs, our motivation was to model stable, mechanically protected structures based on those materials, which would excel in their electronic and optical properties in broad spectrum. Based on their lattice

parameters, we expect to obtain structures with good lattice matching, suitable for experimental realization.

## 2. Theoretical methods

Results are obtained using DFT implemented in Quantum Espresso (QE) software package [50], based on plane waves and pseudopotentials. Perdew–Burke–Ernzerhof (PBE) functional [51] and PAW pseudopotentials [52] were used in all calculations. After convergence tests, the energy cutoff for the wavefunction and the charge density were set to 44 Ry and 364 Ry for hBN/InTe heterostructure, and 60 Ry and 480 Ry for hBN/GaTe heterostructure. The Monkhorst–Pack of  $16 \times 16 \times 1$  mesh for k-point sampling is used in geometric optimization, total energy and phonon calculations. For calculations of p-DOS and optical properties, refined mesh of  $64 \times 64 \times 1$  is used. The bandstructure is calculated on 440 k-points along  $\Gamma$ –M–K– $\Gamma$  direction. In order to simulate 2D structure, a vacuum of 20 Å was added along the z-direction to avoid interactions between the layers. Geometry optimization of both atom positions and lattice parameters is performed using BFGS algorithm, with criteria for maximum allowed forces between atoms of  $10^{-6}$  Ry Å<sup>-1</sup>. As the GGA functionals do not take into consideration long range forces as the van der Waals force, Grimme-D2 correction was included to obtain more accurate lattice constants and forces. Optical properties were calculated using epsilon.x code in QE software, based on the random phase approximation (RPA).

## 3. Results and discussion

Both GaTe (InTe) and hBN have hexagonal lattices with  $D_{3h}^1$  symmetry. Lattice constants obtained after the geometric optimizations of  $a = 4.371$  Å for InTe,  $a = 4.047$  Å for GaTe and 2.515 Å for hBN are in agreement with previous reports [25, 37, 40, 53]. The unit cell of In(Ga)Te/hBN heterostructure is modeled as a supercell which contain one layer of InTe( $1 \times 1$ ) or GaTe( $1 \times 1$ ) on top of layer of hBN( $\sqrt{3} \times \sqrt{3}$ ) supercell, resulting in hexagonal unit cell with  $C_3^1$  symmetry. The lattice constant of  $\sqrt{3} \times \sqrt{3}$  supercell of hBN is  $a = 4.347$  Å. In case of hBN/InTe heterostructure, lattice constants of InTe and hBN supercell are excellent matches with close values of 4.371 and 4.347 Å. After geometric optimization, obtained lattice constant of formed heterostructure is  $a = 4.336$  Å. That results in almost ideal lattice matching with induced strain of 0.8% on InTe layer and 0.3% on hBN layer, making this heterostructure a great candidate for experimental realization. With lattice constant of  $a = 4.047$  Å, monolayer of GaTe is a less perfect match with  $a = 4.347$  Å of hBN supercell. However, the obtained lattice constant of formed hBN/GaTe heterostructure is  $a = 4.309$  Å which induces strains of 6.1% on GaTe layer and 0.8% on hBN, making them still possible for fabrication. Hence, both heterostructures are promising in terms of lattice matching and can be modeled with proposed supercell. Phonon dispersion for both heterostructures is also calculated and presented in figure 1 in order to

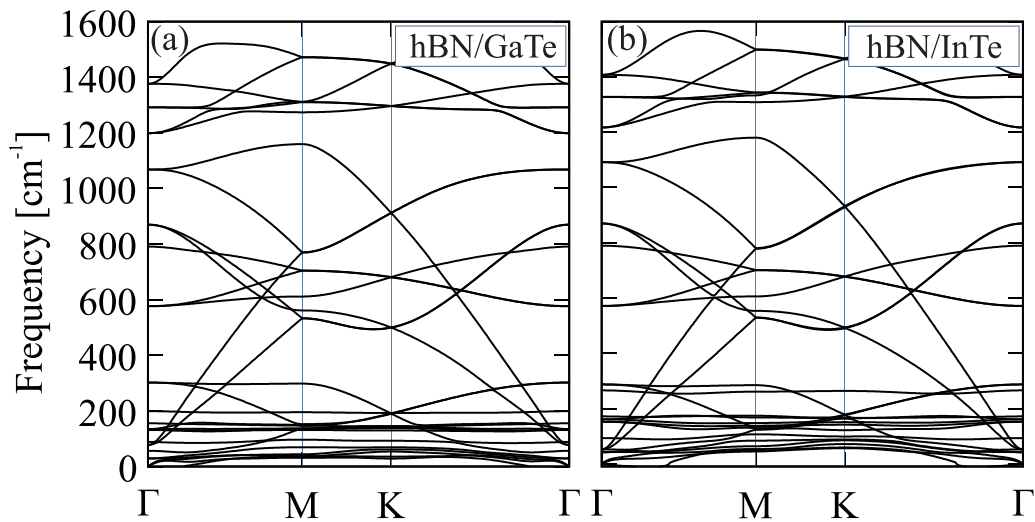


Figure 1. Phonon dispersion of (a) hBN/InTe and (b) hBN/GaTe.

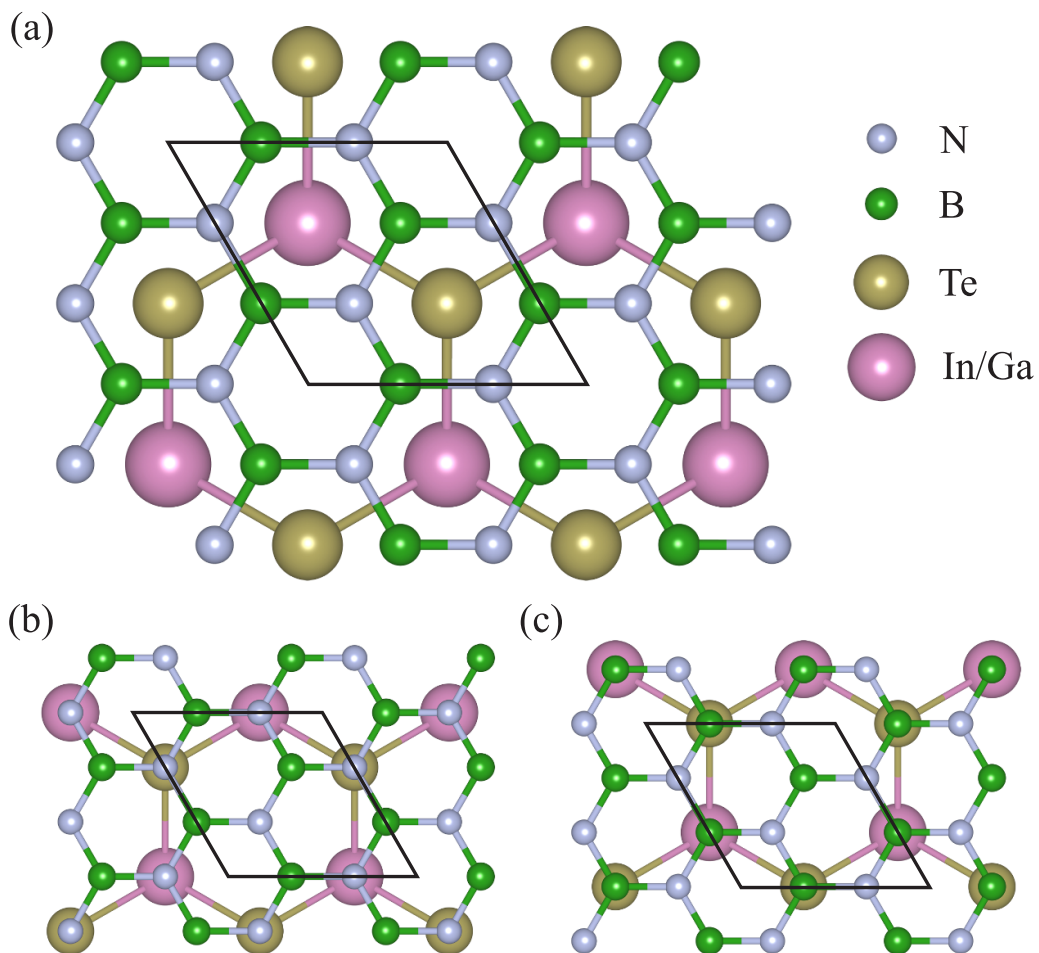
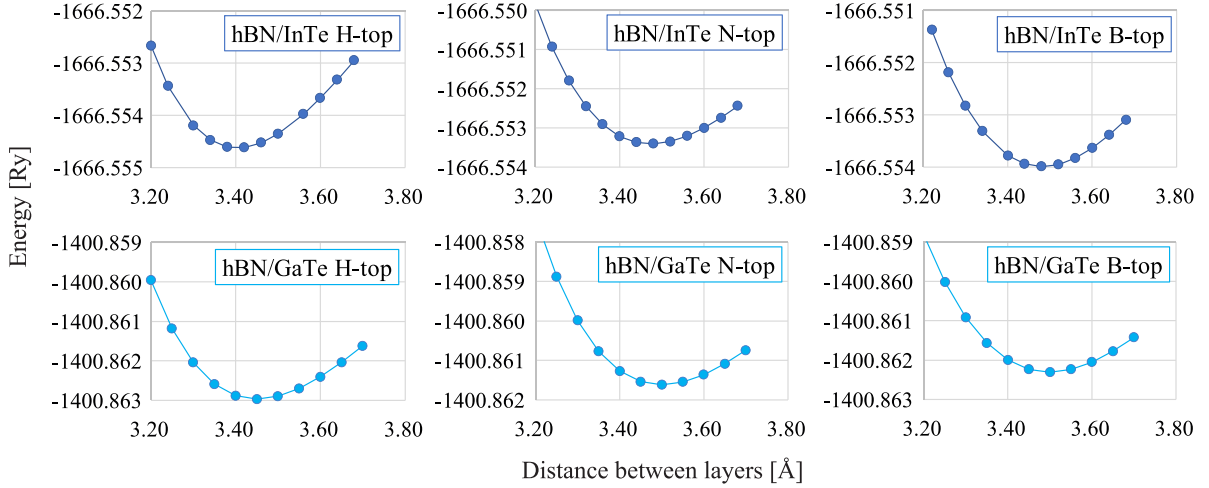


Figure 2. Top view of three possible stacking types, (a) H-top, (b) N-top and (c) B-top.

confirm the structural stability. We do not observe imaginary frequencies, except the small kinks near the Gamma point with low negative values, which are often emerging in calculations of phonons in 2D materials, being a numerical issue and not the real instabilities.

Three possible stacking types are presented in figure 2, the H-top (In/Ga atom being in the center of hBN hexagon), B-top

(In/Ga atom above the B atom of hBN) and N-top (In/Ga atom above the N atom of hBN). We investigated all three types of structure in order to determine the favorable stacking, as well whether the properties are affected by type of stacking, e.g. bandstructure. The optimal distance between the hBN layer and InTe(GaTe) layers (*d*) for both heterostructures and each of their stacking types are obtained previously during the



**Figure 3.** Total energy of the system as a function of the distance between hBN and InTe(GaTe) for different stacking types for hBN/InTe and hBN/GaTe.

geometry optimization, with resulting distances of 3.43–3.52 Å for different stacking positions of hBN/InTe and 3.45–3.52 Å for hBN/GaTe. Total energy of the structure in function of the interlayer distance is shown in figure 3.

In order to confirm the stability of the structures and prove they can be experimentally obtained, we calculated their binding energies ( $E_b$ ) by the following equation:

$$E_b = E_{heterostr.} - E_{In(Ga)Te} - E_{hBN}, \quad (1)$$

where  $E_{heterostr.}$ ,  $E_{In(Ga)Te}$  and  $E_{hBN}$  represent the total energy of hBN/In(Ga)Te heterostructure, InTe or GaTe monolayer and hBN monolayer, respectively. Binding energies, interlayer distance and lattice parameters obtained for each configuration of hBN/InTe and hBN/GaTe heterostructures are summarized in table 1. Negative values of binding energies suggest that both heterostructures are energetically feasible in all stacking configurations. The favorable stacking type for both hBN/InTe and hBN/GaTe heterostructures is H-top with the lowest value of binding energy, but also the total energy of H-top configuration for both heterostructures is  $\approx 8$  and  $\approx 17$  meV lower than in N-top and B-top configurations, respectively. However, the total and binding energies for H-top, N-top and B-top stacking configurations differ just for 10 meV, making all systems convenient for fabrication.

From our calculations, both InTe and GaTe monolayers have an indirect band gap of  $E_g = 1.38$  eV and  $E_g = 1.75$  eV respectively, while hBN has a large direct band gap of 4.63 eV. These results are in agreement with previous theoretical results obtained using the PBE functional [24, 36, 37, 40]. As the PBE functional underestimates the band gap in semiconductors, hybrid functionals such as Heyd–Scuseria–Ernzerhof (HSE) must be used in order to obtain accurate electronic properties. Reports on similar structures show that employing the HSE functional does not change the bandstructure qualitatively, the most significant difference comes from shifted bands above the Fermi level and thus an enlargement of the band gap. Large difference in band gap of InTe(GaTe) and hBN

**Table 1.** Lattice parameters, distance between hBN and In(Ga)Te layers ( $d$ ) and binding energy for all three possible stacking types of hBN/InTe and hBN/GaTe.

	hBN/InTe		
	H-top	N-top	B-top
$a$ (Å)	4.346	4.337	4.337
$d$ (Å)	3.429	3.523	3.479
$E_b$ (meV)	-269.64	-255.49	-259.63
	hBN/GaTe		
	H-top	N-top	B-top
$a$ (Å)	4.309	4.309	4.311
$d$ (Å)	3.451	3.516	3.503
$E_b$ (meV)	-255.62	-241.76	-246.61

as well their alignment of bands make both systems a type-I heterojunctions. This can be also confirmed from the density of states of pristine single layer hBN, InTe and GaTe and projected density of states for both heterostructures, presented in figure 4. As in similar heterostructures [54], the bandstructure does not change with the stacking almost at all—zones near the Fermi level are nearly identical, the band gap does not change and only minor differences can be observed e.g. slightly changed position of some zones below the Fermi level and far above the Fermi level. Bandstructure plots for all three stacking types are shown in figure 5. In further discussion we will focus on the H-top stacking in both hBN/InTe and hBN/GaTe heterostructures.

Atom-decomposed bandstructures of hBN/InTe and hBN/GaTe are presented in figures 6 and 7, alongside their pristine monolayer compounds, InTe and GaTe for easier comparison. Fermi level is set to zero and shown in green line in all figures. Both GaTe and InTe pristine monolayers are indirect band gap semiconductors with valence band maxima close to the  $\Gamma$  point and conduction band minima (CBM) at the M point for GaTe

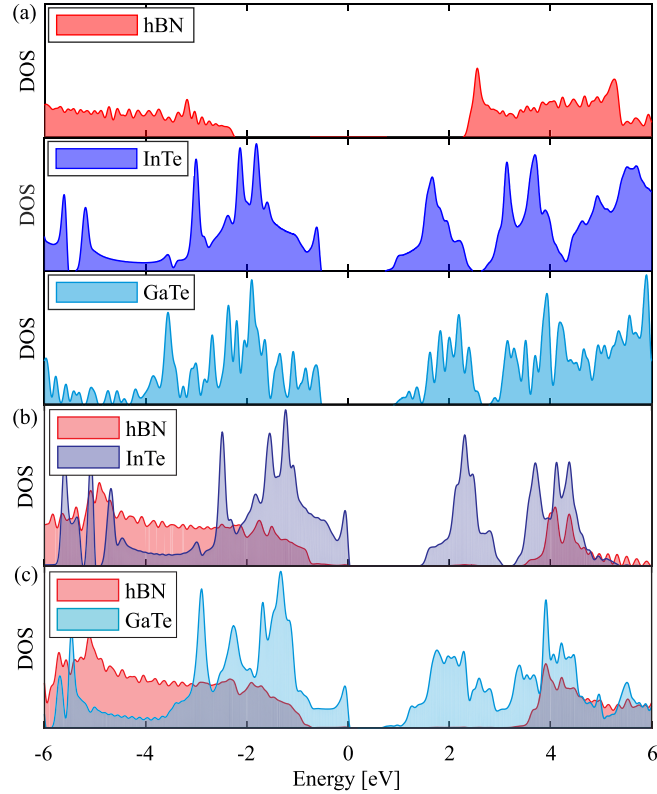


**Figure 4.** Projected density of states for (a) single layer hBN, InTe and GaTe, (b) hBN/InTe heterostructure and (c) hBN/GaTe heterostructure. The contribution from hBN is shown in red lines and red shaded area, while dark blue and turquoise lines and area represent contribution from InTe and GaTe, respectively.

and  $\Gamma$  and M points for InTe. After stacking into heterostructure, the band gap is slightly changed from original GaTe and InTe structures. CBM are shifted to the  $\Gamma$  point in both heterostructures. In the hBN/InTe band gap is slightly enlarged, from 1.38 eV in pure InTe monolayer to 1.54 eV in the heterostructure. This change in band gap is barely visible and bands near the Fermi level have the same shape as in pristine InTe. Hence, upon forming the hBN/InTe heterostructure, there are no important differences in the band structure. States around the Fermi level are almost completely formed by InTe, while the hBN contributions are observed below  $-2$  eV and above 3 eV, similar as in pristine hBN.

More changes can be observed in the second structure—gap of single layer GaTe is 1.59 eV, but after the heterostructure is formed, band gap is reduced to just 0.79 eV. Upon forming the heterostructure, in the vicinity of the  $\Gamma$  point, there are many mixed states around  $-1$  eV, originated from 5p states of Te atoms and 2p states of N atoms, as result of interaction between the hBN and GaTe layers. In addition, valence band is heavily lifted, separating previously grouped states around the  $\Gamma$  point for more than 0.5 eV and significantly reducing the band gap.

The reduction of band gap along with interfacial states can be useful for applications in optoelectronics so we proceeded to analyze the optical properties of these heterostructures. We calculated the absorption coefficients, expecting both structures to have good absorption properties. The

complex dielectric function  $\epsilon(\omega) + \epsilon_R(\omega) + i\epsilon_I(\omega)$  is obtained from calculations in the RPA framework. From these results, we can obtain the absorption coefficient  $\alpha(\omega)$  as the following:

$$\alpha(\omega) = \sqrt{2} \frac{\omega}{c} \sqrt{\sqrt{\epsilon_R^2(\omega) + \epsilon_I^2(\omega)} - \epsilon_I(\omega)}. \quad (2)$$

Results are shown in figure 8 for hBN/InTe and figure 9 for hBN/GaTe heterostructures, both plotted alongside their pristine monolayer compounds. Both structures have very good absorption properties, being able to absorb visible, near and far UV spectrum—the absorption of hBN/GaTe even slightly extends to the IR spectrum. As the PBE functional underestimates band gap, some shift in energy would be noticed compared to HSE calculations. The results though would not be significantly changed, only the reduction in capabilities of absorbing the IR and red part of the visible light is expected.

The highest peaks in absorption function are near 6 eV, primarily originating from the InTe/GaTe, at 11 and at 14 eV as a contribution from hBN layer, with peaks up to  $8 \times 10^5 \text{ cm}^{-1}$ . As a result of smaller band gap in hBN/GaTe heterostructure, slightly enhanced absorption is observed in very low energy region of 1–2 eV. The difference is though, not significant, which is not unexpected as the bandstructures of hBN/InTe and hBN/GaTe do not differ much qualitatively, and band gap

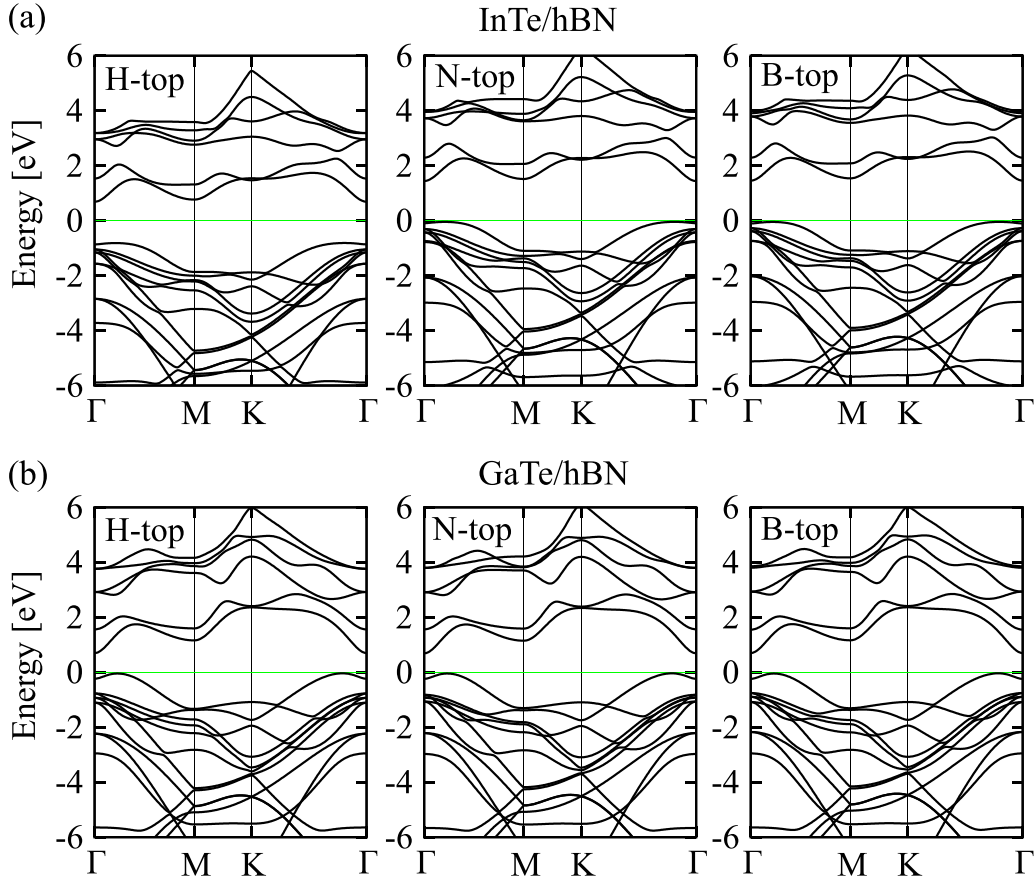


**Figure 5.** Bandstructure for different types of stacking for (a) hBN/InTe and (b) hBN/GaTe heterostructure.

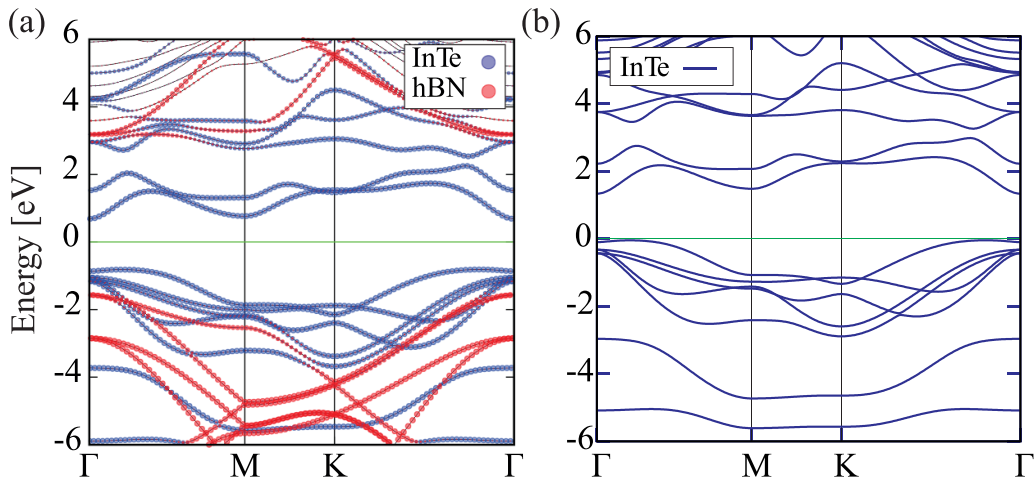


**Figure 6.** (a) Projected bandstructure of hBN/InTe heterostructure and (b) bandstructure of InTe monolayer. The size of circles on the left graph indicate the magnitude of projections of wavefunctions over atomic orbitals—contribution from different atomic orbitals are presented in different colors as shown in the legend.

in GaTe/hBN is primarily reduced due to one single shifted band below the Fermi level. In addition, results obtained using RPA calculations have contribution just from transitions in ground state, any exciton effects cannot be observed. In energy range from 3 to 15 eV, both heterostructures have exceptional values of absorption of  $2\text{--}8 \times 10^5 \text{ cm}^{-1}$ , giving them a huge potential for light absorbers in near and far UV spectrum. This makes both heterostructures excellent candidates for

light absorption-relevant photoelectric applications, such are modern photodetectors. Further, we calculated the reflectance for our heterostructures. The real and imaginary part of dielectric function are related with a complex index of refraction  $n^*(\omega) = n(\omega) + i\kappa(\omega)$  by:

$$\epsilon_R = 2n\kappa, \epsilon_I = n^2 - \kappa^2. \quad (3)$$

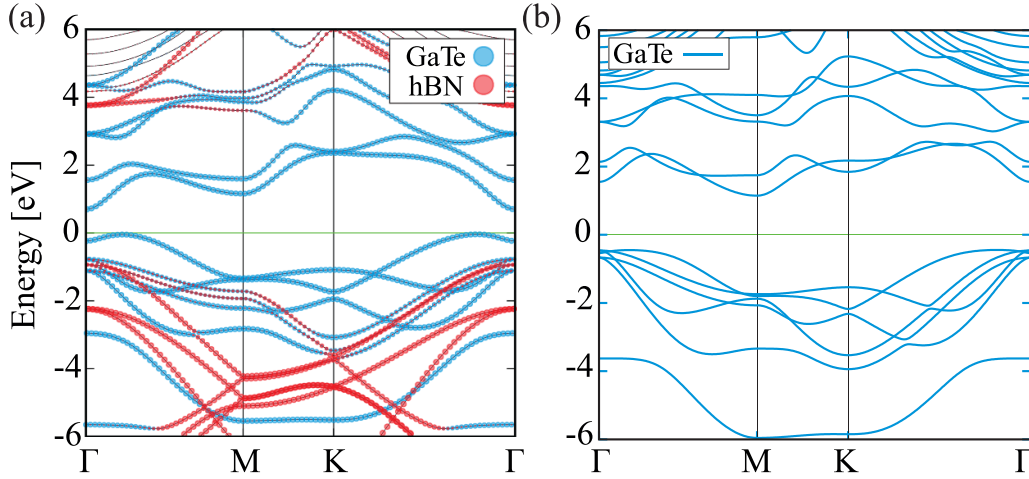


**Figure 7.** (a) Projected bandstructure of hBN/GaTe heterostructure and (b) bandstructure of GaTe monolayer. The size of circles on the left graph indicate the magnitude of projections of wavefunctions over atomic orbitals—contribution from different atomic orbitals are presented in different colors as shown in the legend.

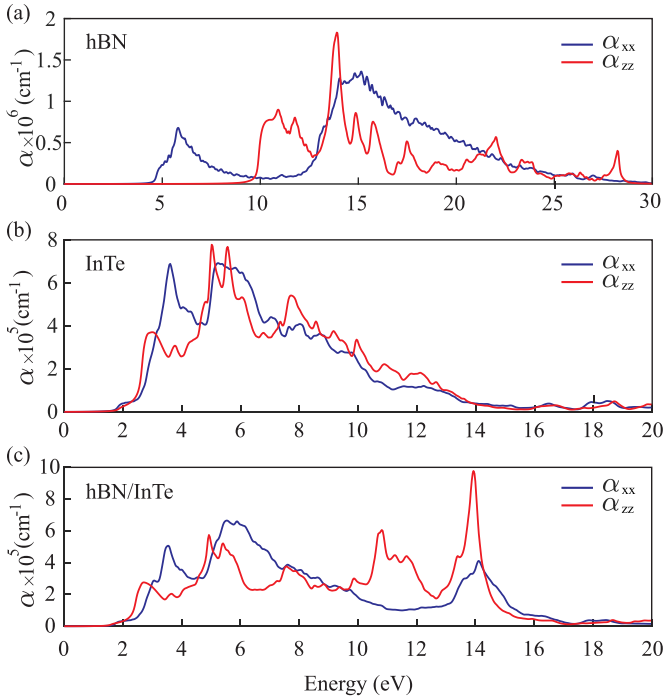


**Figure 8.** Absorption coefficient of (a) hBN, (b) InTe, (c) hBN/InTe heterostructure for in-plane ( $\alpha_{xx}$ ) and out-of-plane ( $\alpha_{zz}$ ) polarizations.

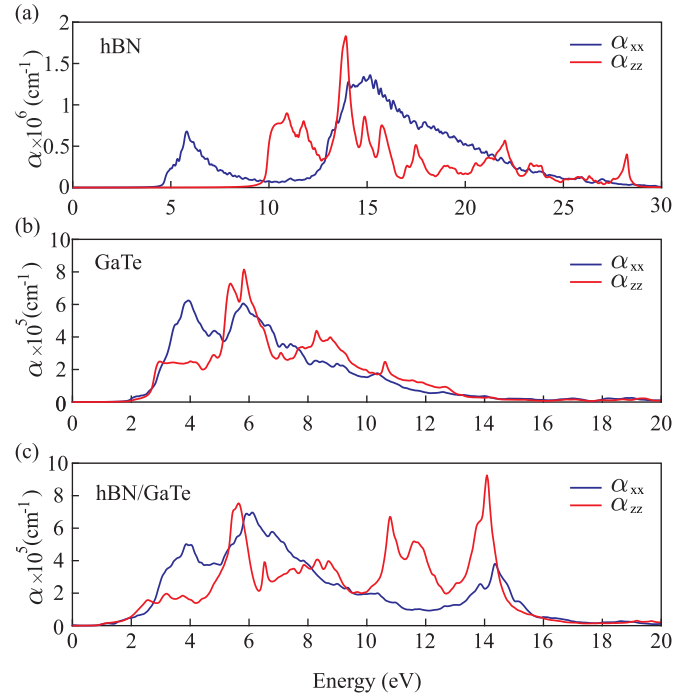


**Figure 9.** Absorption coefficient of (a) hBN, (b) GaTe, (c) hBN/GaTe heterostructure for in-plane ( $\alpha_{xx}$ ) and out-of-plane ( $\alpha_{zz}$ ) polarizations.

The reflectance is now given by:

$$\frac{(n - 1)^2 + \kappa^2}{(n + 1)^2 + \kappa^2}. \quad (4)$$

Figure 10 presents calculated reflectance of hBN/InTe and hBN/GaTe heterostructures. Reflectance of both materials are no larger than 30% for any energy, and are especially low in the low-energy region with 10%, confirming that only a

small amount of light is being reflected at any incidence angle. As both heterostructures have qualitatively similar bandstructures, their reflectances are not much different. However, for z polarization, the small peak at 2.5 eV is flattened in hBN/GaTe dropping to nearly constant values of around 10% in region up to 5 eV, while the peak at 6 eV is narrowed and higher than in hBN/InTe. That can be ascribed as a result of differences in shape and positions of certain bands and different values of band gap.

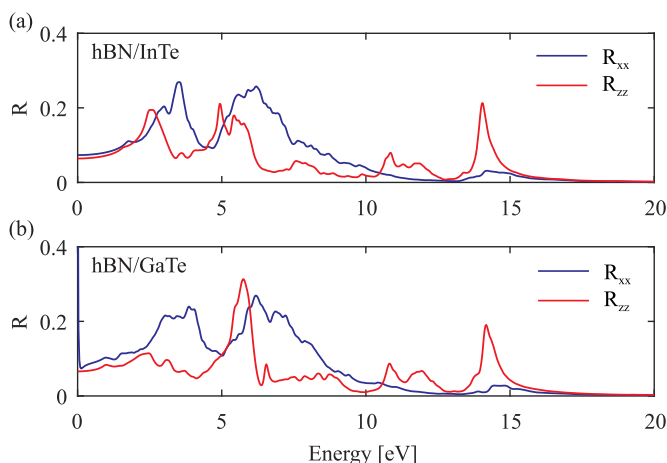


**Figure 10.** Reflectance of (a) hBN/InTe heterostructure and (b) hBN/GaTe, for in-plane ( $\alpha_{xx}$ ) and out-of-plane ( $\alpha_{zz}$ ) polarizations.

#### 4. Conclusions

We report the study of two new heterostructures based on hexagonal boron nitride and InTe/GaTe, by employing first principle calculations. We confirm the structural stability of those systems and show that stacking type does not affect any of the relevant properties and all types of stacking are feasible for fabrication. We investigate their electronic and optical properties, showing the benefit of forming heterostructures of InTe/GaTe with hBN layer. Formation of heterostructure slightly changes the band gap in comparison with pristine monolayer InTe and GaTe, which also enhances absorption in the low-energy region of the spectrum. Both heterostructures have good broad spectrum absorption, with exceptionally good absorbing of the UV light. Hence, their electronic and optical properties reveal them as excellent candidates for field effect transistors based on vdW heterostructures, or modern optoelectronic devices such as flexible broad spectrum photodetectors, solar cells. From the previous studies, the hBN layer is also proven to be beneficial for mechanical protection of sensitive and vulnerable single layers of monochalcogenides like InTe and GaTe, while as we showed, electronic and optical properties are not only preserved but even enhanced. Of special interest is hBN/InTe heterostructure for its remarkably good lattice constant matching between InTe and hBN layers which yields less than 1% of induced strain between the layers. This places hBN/InTe beneficial over similar studied heterostructures with comparable electronic and absorption properties (e.g. hBN/InSe) with significant advantage for future fabrication and experiments as well for their further mechanical manipulation. As both InTe (GaTe) and hBN can withstand a moderate strain, electronic and optical properties can be tuned by applying the strain on the heterostructure or by including electric field, giving these materials a huge value for further research and applications.

#### Data availability statement

All data that support the findings of this study are included within the article (and any supplementary files).

#### Acknowledgments

The authors acknowledge funding provided by the Institute of Physics Belgrade through the grant by the Ministry of Education, Science and Technological Development of the Republic of Serbia. DFT calculations were performed using computational resources at Johannes Kepler University (Linz, Austria).

#### ORCID iDs

A Šolajić  <https://orcid.org/0000-0002-0553-0858>

J Pešić  <https://orcid.org/0000-0002-8600-7187>

#### References

- [1] Liu B and Zhou K 2019 *Prog. Mater. Sci.* **100** 99–169
- [2] Zhang K, Feng Y, Wang F, Yang Z and Wang J 2017 *J. Mater. Chem. C* **5** 11992–2022
- [3] Song L *et al* 2010 *Nano Lett.* **10** 3209–15
- [4] Kara A, Enriquez H, Seitsonen A P, Voon L L Y, Vizzini S, Aufray B and Oughaddou H 2012 *Surf. Sci. Rep.* **67** 1–18
- [5] Zhao J *et al* 2016 *Prog. Mater. Sci.* **83** 24–151
- [6] Acun A *et al* 2015 *J. Phys.: Condens. Matter* **27** 443002
- [7] Derivaz M, Dentel D, Stephan R, Hanf M C, Mehdaoui A, Sonnet P and Pirri C 2015 *Nano Lett.* **15** 2510–6
- [8] Fu Q *et al* 2021 *Adv. Mater.* **33** 1907818
- [9] Li Y, Wang H, Xie L, Liang Y, Hong G and Dai H 2011 *J. Am. Chem. Soc.* **133** 7296–9
- [10] Splendiani A, Sun L, Zhang Y, Li T, Kim J, Chim C Y, Galli G and Wang F 2010 *Nano Lett.* **10** 1271–5
- [11] Li H, Zhang Q, Yap C C R, Tay B K, Edwin T H T, Olivier A and Baillargeat D 2012 *Adv. Funct. Mater.* **22** 1385–90
- [12] Zhao W, Ghorannevis Z, Chu L, Toh M, Kloc C, Tan P H and Eda G 2013 *ACS Nano* **7** 791–7
- [13] Li H, Lu G, Wang Y, Yin Z, Cong C, He Q, Wang L, Ding F, Yu T and Zhang H 2013 *Small* **9** 1974–81
- [14] Anasori B, Lukatskaya M R and Gogotsi Y 2017 *Nat. Rev. Mater.* **2** 1–17
- [15] Pang J, Mendes R G, Bachmatiuk A, Zhao L, Ta H Q, Gemming T, Liu H, Liu Z and Rummeli M H 2019 *Chem. Soc. Rev.* **48** 72–133
- [16] Geim A K and Grigorieva I V 2013 *Nature* **499** 419–25
- [17] Novoselov K, Mishchenko A, Carvalho A and Neto A C 2016 *Science* **353** 14
- [18] Liu Y, Weiss N O, Duan X, Cheng H C, Huang Y and Duan X 2016 *Nat. Rev. Mater.* **1** 1–17
- [19] Withers F *et al* 2015 *Nat. Mater.* **14** 301–6
- [20] Furchi M M, Höller F, Döbusch L, Polyushkin D K, Schuler S and Mueller T 2018 *npj 2D Mater. Appl.* **2** 1–7
- [21] Zheng X, Wei Y, Pang K, Kaner Tolbert N, Kong D, Xu X, Yang J, Li X and Li W 2020 *Sci. Rep.* **10** 1–9
- [22] Qin S, Du Q, Dong R, Yan X, Liu Y, Wang W and Wang F 2020 *Carbon* **167** 668–74
- [23] Dong T, Simoes J and Yang Z 2020 *Adv. Mater. Interfaces* **7** 1901657



- [24] Ren C, Wang S, Tian H, Luo Y, Yu J, Xu Y and Sun M 2019 *Sci. Rep.* **9** 1–6
- [25] Demirci S, Avazl N, Durgun E and Cahangirov S 2017 *Phys. Rev. B* **95** 115409
- [26] Yang Z and Hao J 2019 *Adv. Mater. Technol.* **4** 1900108
- [27] Chen J, Cai S, Xiong R, Sa B, Wen C, Wu B and Sun Z 2020 *Phys. Chem. Chem. Phys.* **22** 7039–47
- [28] Bandurin D A *et al* 2017 *Nat. Nanotechnol.* **12** 223–7
- [29] Jiang J, Li J, Li Y, Duan J, Li L, Tian Y, Zong Z, Zheng H, Feng X, Li Q 2019 *npj 2D Mater. Appl.* **3** 1–8
- [30] Tamalampudi S R, Lu Y-Y, Rajesh Kumar U, Sankar R, Liao C-D, Cheng C-H, Chou F C and Chen Y-T 2014 *Nano Lett.* **14** 2800–6
- [31] Li H, Zhou Z and Wang H 2020 *Nanotechnology* **31** 335201
- [32] Li H, Zhou Z, Zhang K and Wang H 2019 *Nanotechnology* **30** 405207
- [33] Pham K D, Vu-Quang H and Nguyen C V 2019 *Physica B* **555** 69–73
- [34] Pham K D, Hieu N N, Phuc H V, Fedorov I, Duque C, Amin B and Nguyen C V 2018 *Appl. Phys. Lett.* **113** 171605
- [35] Gao X, Shen Y, Ma Y, Wu S and Zhou Z 2019 *Comput. Mater. Sci.* **170** 109200
- [36] Touski S B, Ariapour M and Hosseini M 2020 *Physica E* **118** 113875
- [37] Liao Y, Liu H, Yuan G, Huang Z and Qi X 2020 *Cryst. Res. Technol.* **55** 2000102
- [38] Li K, Xian X, Wang J and Yu N 2019 *Appl. Surf. Sci.* **471** 18–22
- [39] Ariapour M and Touski S B 2019 *Mater. Res. Express* **6** 076402
- [40] Vi V T, Hieu N N, Hoi B D, Binh N T and Vu T V 2020 *Superlattices Microstruct.* **140** 106435
- [41] Jalilian J and Safari M 2017 *Phys. Lett. A* **381** 1313–20
- [42] Zhang J, Lang X, Zhu Y and Jiang Q 2018 *Phys. Chem. Chem. Phys.* **20** 17574–82
- [43] Xiong P *et al* 2020 *Nat. Commun.* **11** 1–12
- [44] Postorino S, Grassano D, D’Alessandro M, Pianetti A, Pulci O and Palummo M 2020 *Nanomater. Nanotechnol.* **10** 1847980420902569
- [45] Rahaman M, Rodriguez R D, Monecke M, Lopez-Rivera S A and Zahn D R T 2017 *Semicond. Sci. Technol.* **32** 105004
- [46] Guo Y, Zhou S and Zhao J 2020 *ChemNanoMat* **6** 838–49
- [47] Guo Y, Zhou S, Bai Y and Zhao J 2017 *J. Chem. Phys.* **147** 104709
- [48] Afaneh T, Fryer A, Xin Y, Hyde R H, Kapuruge N and Gutierrez H R 2020 *ACS Appl. Nano Mater.* **3** 7879–87
- [49] Arora H, Jung Y, Venanzi T, Watanabe K, Taniguchi T, Hubner R, Schneider H, Helm M, Hone J C and Erbe A 2019 *ACS Appl. Mater. Interfaces* **11** 43480–7
- [50] Giannozzi P *et al* 2009 *J. Phys.: Condens. Matter* **21** 395502
- [51] Perdew J P, Burke K and Ernzerhof M 1996 *Phys. Rev. Lett.* **77** 3865–8
- [52] Dal Corso A 2014 *Comput. Mater. Sci.* **95** 337–50
- [53] Wickramaratne D, Weston L and Van de Walle C G 2018 *J. Phys. Chem. C* **122** 25524–9
- [54] Shen N F, Yang X D, Wang X X, Wang G H and Wan J G 2020 *Chem. Phys. Lett.* **749** 137430